Plasma technology

A novel solution for CO_2 conversion?

Proefschrift voorgelegd tot het behalen van de graad van doctor in de
wetenschappen: chemie aan de Universiteit Antwerpen te verdedigen door

Ramses Snoeckx

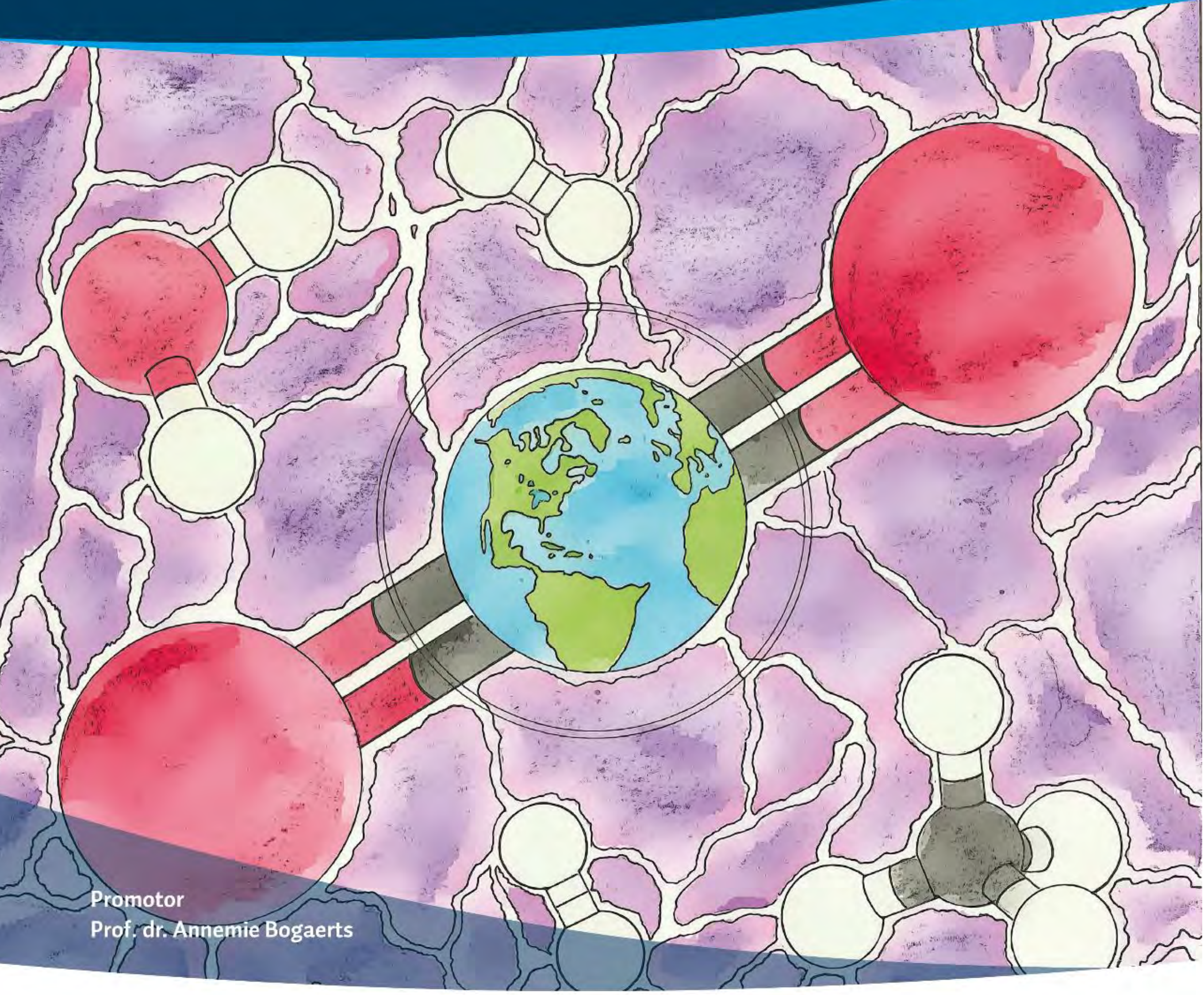

Promotor
Prof. dr. Annemie Bogaerts

Faculteit Wetenschappen
Departement Chemie
Antwerpen 2017

Universiteit
Antwerpen

Universiteit
Antwerpen
Faculteit Wetenschappen
Departement Chemie

Plasma technology

A novel solution for CO_2 conversion?

Plasmatechnologie

Een vernieuwende oplossing voor CO_2 conversie?

Proefschrift voorgelegd tot het behalen van de graad
doctor in de wetenschappen: chemie
aan de Universiteit Antwerpen
te verdedigen door

Ramses Snoeckx

Promotor: prof. dr. Annemie Bogaerts
Antwerpen, 2017

Dit proefschrift werd geëvalueerd door de promotor, de voorzitter en de leden van de doctoraatscommissie en de doctoraatsjury:

promotor: Prof. dr. A. Bogaerts (Universiteit Antwerpen)

commissie: Prof. dr. E. Neyts (Universiteit Antwerpen)

Prof. dr. V. Meynen (Universiteit Antwerpen)

jury: Prof. dr. S. Lenaerts (Universiteit Antwerpen)

Dr. S. Paulussen (VITO)

Prof. dr. Ir. G. Van Rooij (DIFFER)

Prof. dr. F. Reniers (Université libre de Bruxelles)

Contents

Acknowledgments

The requirements for obtaining a PhD state that the individual has to make a significant contribution to the research field, evidently one can never accomplish this fuzzy task without the support of a large group of people. From staff, faculty and colleagues to friends and family, one needs all of these people to survive the minefield through which one has to steer its ship into the safe harbour of successfully finalizing a PhD. Therefore, I would like to take this opportunity to sincerely thank and acknowledge all the people that have supported and helped me along this eventful journey.

First, I would like to thank my advisor Professor Annemie Bogaerts, for giving me the opportunity to pursue a PhD in a research area which combined my passions for chemistry and the environment. Starting from my master thesis, she nourished my interest in the environmental applications of plasma. Professor Bogaerts gave me her full encouragement and support, providing me with enough freedom to examine and explore my research topic, while still offering enough guidance to keep me from losing track. While we may not have always agreed on everything and my (lack of) timing was at times a point of concern, we did make an exceptional team in these past years. I could not have made all these scientific achievements without your mentorship and although it is now time for me to explore further on my own, I am without doubt that our ways will stay connected. Thank you for your support during the emotionally hard times and for all the marvellous opportunities you have given me!

In addition to my supervisor, I would like to thank all the current and past PLASMANT colleagues at the University of Antwerp for being such great people and colleagues. Thank you for the fun times, great talks, interesting discussions, fruitful collaborations and for generating a nice atmosphere.

Some members of the group deserve my special thanks. From the moment I took my first steps in the PLASMANT group, two persons whose professional and personal advise I have always appreciated were Robby and Stefan. I would like to thank them for all the nice memories and helping me develop into a critical researcher from an early stage. Being the inspirational Post-doc he is, Stefan showed me the do’s and don’ts on my first scientific conference in Austin. The both of you were definitely great examples to me. Additionally, I would like to thank Maksudbek, Umedjon and Wesley for the pleasant atmosphere in our office. The many fun walks and discussions about the importance of colours with Wesley were of a big surplus. Thank you, Marleen, Inne, Stijn and Yannick for listening to my advice and even pretending to care when I was just nagging. I wish you all the very best for your future research and I hope to be there when you reach the finish line! Luc Van't Dack always kept an open door, willing to help with any technical problem or concern I might have, as well as being an excellent travel advisor. Similarly, the indispensable administrative support from Nelly Suijerbuijk, Ingrid Swenters and Tania Beyers made all the policies feel less Kafkaesque. The miracle workers of the mechanical workshop who, after laughing with our impossible ideas, always succeeded in turning them into realistic designs. After spending this much time together, many of you have become good friends whom will be missed dearly!

Besides the colleagues of the research group, I would also like to use this opportunity to thank all the amazing people I have met during collaborations, research visits and conferences. These encounters all shaped me into becoming the researcher I am today. It was a pleasure working and discussing together with you, Karen, Xin, Alp, Tom and many others. I immensely enjoyed my research stay in Lisbon, for which a special thanks goes to Nuno Pinhão. For my enriching stay at KAUST I am grateful to Minsuk Cha, and I am exceptionally grateful for having had the opportunity to work together with Alex Fridman, Alex Rabinovich, Greg Fridman and Vandana Miller at the Drexel Plasma Insitute. Special thanks also goes to all the people who showed me around these new places and made me feel at home.

Additionally, I am forever in debt with two professors from the Chemistry department, Wouter Herrebout and Bert Maes, for supporting me through my rocky first two years at university. Without your personal support and kind-heartedness in that stormy period I would not be where I am today.

In my personal life, I would like to thank my family and close friends for their past and ongoing support. First of all, I would not be the person who I am today without my mom. Dearest mom, thank you for giving me all opportunities in life, encouraging me along the way. Both you and grandma are my biggest supporters! I am thankful to Sebastiaan and Matthias, and also Inez who brought me the joy of having adorable nieces in my life. Of course I cannot forget my best friends, Hans, Dean, Yannick, Eva, Victor, Lim, Sophia, Billy, and an additional special thanks to Dimi for designing the beautiful cover art and being the exceptionally inspiring person that you are. Lastly, my deepest thanks belongs to my wife, Andrea. She has been there for the final difficult part of this journey, providing me with the necessary motivation and cheerfulness for the enduring home stretch. I am extremely grateful to have you in my life and I cannot wait to set out on our next of many adventures! Thank you all for bringing so much joy and meaning to my life!

List of figures

List of tables

CHAPTER 1

Background

1. Introduction

Environmental and energy applications of low temperature plasmas are worldwide gaining increasing interest. The central research question is whether plasma-based solutions can yield a valuable alternative to existing thermal processes and whether they can compete with other novel gas conversion technologies. Nowadays, the conversion of CO_2 into chemicals and fuels is a hot topic. The worldwide transition to renewable energy gives plasma processes a clean electricity source, and due to their high operation flexibility, plasmas are very suitable for storing this intermittent renewable energy in a chemical form, i.e. fuels and chemicals.

1.1. CO_2 mitigation and valorisation

Throughout history the use of natural resources has played a major role in the rapid development of the human race. Among those resources, fossil fuels have contributed to a fast and unprecedented development in human society. Still, this comes with a great cost, since burning fossil fuels leads to the emission of large amounts of the greenhouse gas CO_2. Because these anthropogenic CO_2 emissions outpace the natural carbon cycle, the atmospheric CO_2 concentrations have been increasing from 280 ppm since the beginning of the industrial revolution to 400 ppm in 2014.[1] With a high certainty it is this increase that leads to the current adverse global environmental climate changes,[1] which has a growing detrimental effect on our climate and environment, and is a severe threat for our current society and future generations in general.[2–5]

Therefore, the conversion of this main greenhouse gas into value-added chemicals and liquid fuels is considered as one of the main challenges for the 21st century.[1,2] The aim is not only to tackle climate change, but also to provide an answer to our dependence on fossil fuels. As stated by Goeppert *et al.*[6] *"Whether humankind uses up most of the fossil fuel resources (combined with carbon capture) or uses increasingly alternative energies, the need for transportation fuels and materials that we currently obtain from petroleum and natural gas will remain. With increasing population, products based on carbon from plastics to medicines will also be required in increasing quantities. In order to fulfil the demand for carbon based products,* CO_2 *will have to be recycled in an anthropogenic version of nature's own carbon cycle. Carbon capture and recycling (CCR) will capture* CO_2 *from any source, and eventually mainly from the atmosphere, and recycle it to new materials and fuels using any alternative energy source."*

Utilization of this waste and converting it into a new feedstock does not only comply with the framework of sustainable and green chemistry[7,8] but also fits within the "cradle-to-cradle" concept.[9] By generating useful products out of CO_2 we create the possibility to effectively close the carbon loop. This already results in a booming interest for technologies which can convert CO_2 into value-added products,[10–12] since they can effectively convert waste into new feedstocks following the cradle-to-cradle principle.[9]

Besides the traditional thermal CO_2 conversion, several alternative technologies are being investigated, such as electrochemical, solar thermochemical, photochemical and biochemical pathways, either with or without catalysts, and all their possible combinations. Their advantages and disadvantages will be briefly discussed, as they form the context for a novel approach considered to have great potential in recent years, which is based on (non-thermal) plasma.[13,14] Several options are being investigated, including both pure CO_2 splitting into CO and O_2, as well as the reaction with other gases, like CH_4 (dry reforming of methane), H_2 (hydrogenation of CO_2) or H_2O (artificial photosynthesis), aiming for the production of syngas and valuable oxygenates, such as methanol, formaldehyde and formic acid. Most research on plasma-based CO_2 conversion is performed with dielectric barrier discharges (DBD), microwave (MW) plasmas and gliding arc (GA) discharges, as well as others (e.g. corona, glow, spark, radiofrequency and nanosecond pulsed discharges), with a main focus on improving the energy efficiency of the conversion, as well as the selectivity towards value-added chemicals in combination with catalysis.

1.2. Solar fuels

The important difference between the traditional thermal conversion approaches and the emerging technologies is their independence of burning fossil fuels to provide the necessary thermal heat to drive reactions. More precisely, the biochemical pathways rely on the natural photosynthesis process to convert light (either natural or artificial) into biomass, which is harvested and further processed. Other emerging technologies, such as the solar thermochemical and photochemical process, can rely on direct solar energy. The average solar flux striking the earth's surface is 175 W/m^2, which represents more energy striking the earth's surface in two hours, i.e., 640 EJ, than the worldwide energy consumption from all sources combined in 2008, 514 EJ.[15] The solar thermochemical process makes use of concentrated solar heat, while the photochemical process relies on the energy of photons. Finally, the electrochemical and plasmachemical processes rely on electricity. **Figure 1-1** gives an overview of the different novel technologies and their principal use of renewable energy for the conversion of CO_2 in a carbon neutral cycle.

The reliance of electrochemical and plasmachemical conversion on electricity at first seems to limit their use as a greenhouse gas mitigation technology, since currently—in general—producing electricity results in CO_2 emissions. This idea couldn't be further from the truth due to the worldwide transition to renewable energy sources—such as solar and wind energy. In 2014 the estimated renewable energy share of the global final energy consumption was already 19.2 %, and by the end of 2015 the estimated renewable energy share of global electricity production was 23.7 %.[16] It is even so that the large scale adoption of these renewable energy sources poses a challenge for efficient storage and easy transport of the electricity produced, i.e. not only regarding the need for peak shaving, but more importantly the need for technologies to follow the irregular and at times intermittent supply of renewable electricity in a flexible way. While storage in batteries is possible, it is less efficient than chemical storage in fuels.[17] Such fuels, often referred to as carbon neutral fuels or solar fuels, offer a much higher gravimetric and volumetric energy storage capacity, they have much higher energy densities than electrical storage techniques and they match the existing worldwide liquid fuel infrastructure.[12,17]

In first instance, the reactions in which CO_2 is involved can be divided into two categories: the production of chemicals and fuels. The latter is being considered as the most suited target for the conversion of large volumes of CO_2 since its market size is 12–14 times larger than the former. One of the most interesting compounds is methanol, which is positioned exactly in the middle, being at the same time a raw chemical and a fuel—in both combustion engines and fuel cells.[18]

To achieve the transformation of CO_2 into value-added chemicals or fuels, the reactions that are of greatest interest are the conversion of CO_2 with a co-reactant, acting as hydrogen source (like CH_4, H_2 or H_2O). Due to the existing infrastructure, liquid products would be preferable to gases, for most applications. Two approaches can be considered to achieve this, the indirect and direct oxidative pathway. The main product of the former is syngas, a mixture of H_2 and CO, which can be converted to almost any commercial bulk chemical or fuel in a second—albeit again very energy intensive—step through the methanol and/or Fischer-Tropsch synthesis.[10] In this case it is of great importance to have a high sense of control over the H_2/CO ratio to be able to steer the synthesis towards the desired products.[19] The direct oxidative pathway, on the other hand, tries to eliminate this energy intensive middle man by converting the reactants immediately into hydrocarbons, short-chain olefins (e.g. ethylene and propylene) and oxygenated products (e.g. methanol, formaldehyde, dimethyl ether, formic acid, etc.).

Liquid products are more attractive over the gaseous hydrogen, since—while in theory a "Hydrogen Economy" [20] would be very attractive—the latter has a number of serious drawbacks due to its physicochemical properties.[21] Furthermore, the infrastructure needed to safely transport, store and dispense hydrogen would be very expensive to roll out, while liquid chemicals match the existing worldwide fuel infrastructure.[12,17] Hence, especially in the transportation sector, a transition from liquid fossil fuel derived products (e.g. gasoline, diesel fuel, kerosene, etc.) to a renewable and sustainable liquid fuel is highly desirable. Again, methanol is one of the most interesting possible candidates to fulfil these requirements. It is the simplest liquid chemical containing only one carbon. Although to date it is almost exclusively produced from natural gas (and shale gas) for economic reasons, it can easily be obtained from several (future) carbon sources, incl. CO_2, biomass, biogas and landfill gas. Therefore, it has been proposed as a key solar fuel for the above mentioned anthropogenic carbon cycle, in the framework of a "Methanol Economy".[6]

To be economically competitive with the existing structures, the efficient production of these solar fuels will be key during the quest to find an effective CO_2 conversion technology with the potential to be commercialised on a large scale.

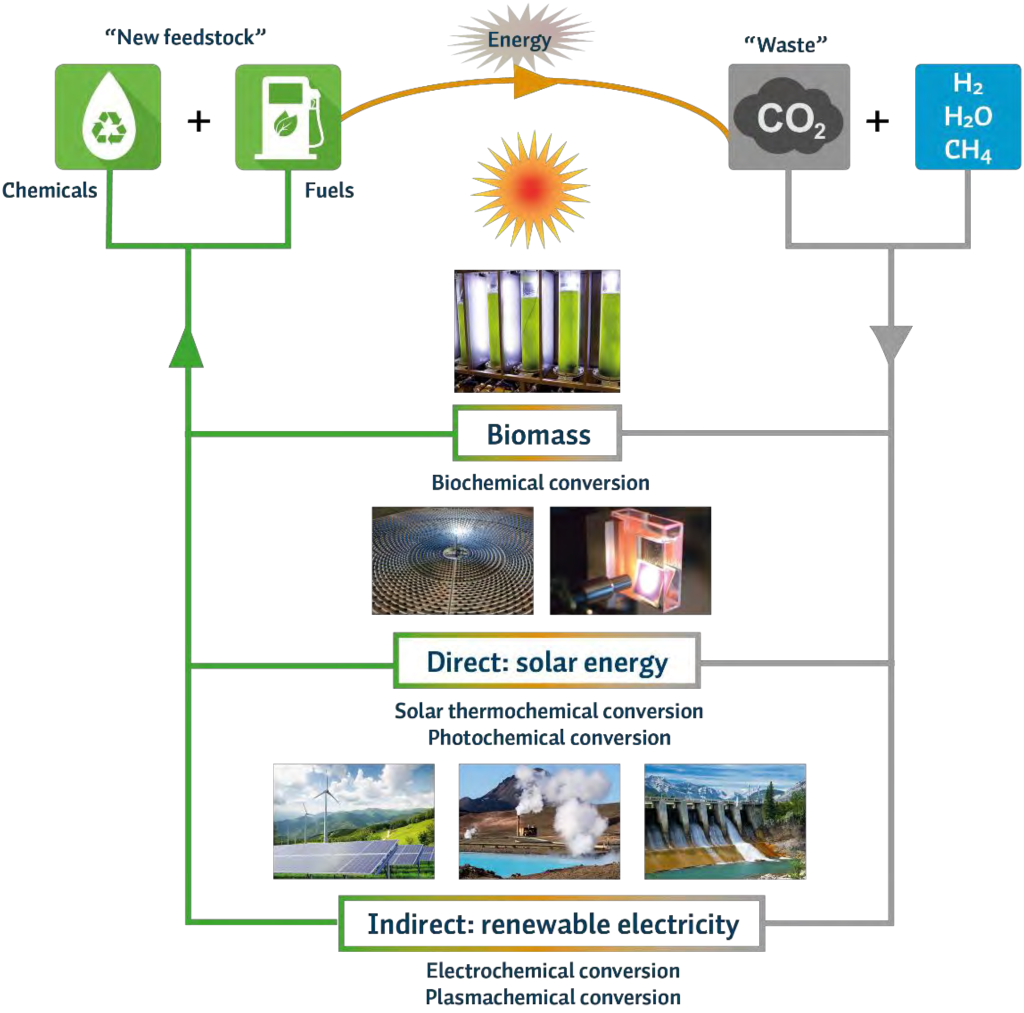

Figure 1-1. Overview of the different novel technologies and their principal use of renewable energy for the conversion of CO_2 in a carbon neutral cycle.

2. Traditional thermal CO_2 conversion approaches

We will first briefly discuss the existing traditional (mainly thermo-catalytic) approaches used on an industrial scale. As such, this section will act as a comparison for the novel technologies under development, such as plasma technology. This section will be subdivided into (1) pure CO_2 splitting and (2) CO_2 conversion in combination with a co-reactant, i.e. CH_4, H_2 and H_2O.

2.1. Pure CO_2 splitting

Thermal CO_2 splitting has not been very effective to date. This is not surprising from a thermodynamic point of view; the carbon-oxygen bonds are relatively strong (783 kJ/mol)[22] and the Gibbs free energy of formation (ΔG^0 = -394 kJ/mol)[17] clearly shows that CO_2 is a highly stable molecule, requiring a substantial energy input, optimized reaction conditions and active catalysts for any chemical conversion to take place. Neither the entropy ($T\Delta S^0$) nor the enthalpy (ΔH^0) term seem favourable for its conversion.[2] The overall reaction is written as:

$$CO_2(g) \rightarrow CO(g) + 1/2\ O_2(g) \qquad \Delta H^0 = +\ 283\ \text{kJ/mol} \qquad (1)$$

Of course the high value of ΔH^0 does not mean that its conversion would not be feasible. Indeed, strongly endothermic chemical reactions can be found in a large number of industrial processes used worldwide, a classic example being the steam reforming of methane (SMR):[17,24]

$$CH_4(g) + H_2O(g) \rightarrow CO(g) + 3\ H_2(g) \qquad \Delta H^0 = +\ 206\ \text{kJ/mol} \qquad (2)$$

This highly endothermic reaction has found worldwide use. In the fertilizer industry the H_2 is used for the production of ammonia, while in the gas industry this reaction is responsible for 95 % of the worldwide H_2 production. This shows there is no reason to dismiss CO_2 splitting, only because it is highly endothermic. Hence, a fair amount of research towards this reaction has already been conducted, of which an overview can be found in the work of Rayne.[22]

It is however clear that, without actively removing one of the products (i.e. CO or O_2), the equilibrium of this reaction lies strongly to the left. Thus, thermal CO_2 splitting is thermodynamically and energetically only favourable at very high temperatures, as can be seen in **Figure 1-2**. At 2000 K for instance, the reaction is not very efficient: we can easily estimate that ca. 92 kJ/mol would be needed to heat 1 mole of CO_2 from 300 to 2000 K. Furthermore, the reaction enthalpy is equal to 245 kJ/mol at 2000 K. Based on a conversion of 1.5 % at this temperature, the energy cost for the total conversion is ~7.9 MJ/mol, yielding an energy efficiency of 4.4 % with respect to the reaction enthalpy of 283 kJ/mol at 300 K. On the other hand, ca. 184 kJ/mol would be needed to heat 1 mole of CO_2 to 3500 K, and at this temperature the reaction enthalpy is equal to 206 kJ/mol. Hence, based on a conversion of 80 % at this temperature, the energy cost of the total conversion is then only ~602 kJ/mol, yielding an energy efficiency of 47 % with respect to the reaction enthalpy of 283 kJ/mol at 300 K. While the conversion continues to increase, above 3500 K the energy efficiency starts to decrease. At 5000 K the conversion is 100 % but the energy efficiency is only 35 %, as can be deduced from **Figure 1-2**.

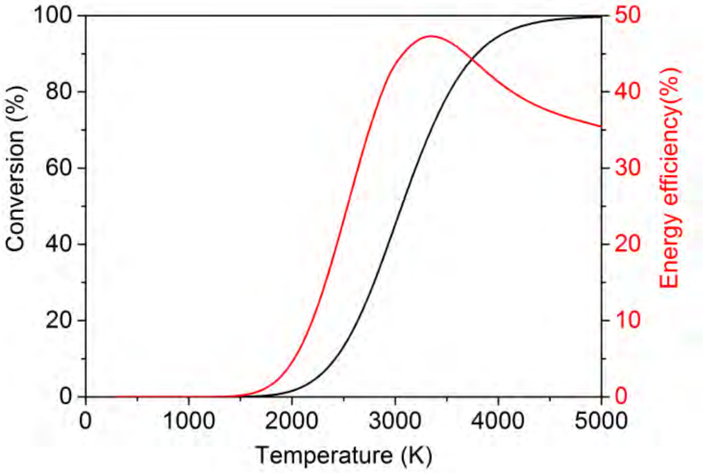

Figure 1-2. Calculated theoretical thermal conversion (left axis) and corresponding energy efficiency (right axis) as a function of temperature for the pure splitting of CO_2 into CO and O_2.

Thus, it is clear that the equilibrium production of CO and O_2 varies from less than 1 % at temperatures below 2000 K up to 45–80 % at 3000–3500 K.[22,23] Therefore, the most pertinent studies regarding thermal CO_2 splitting involve membrane reactor systems. Nigara and Cales[25] used a calcia-stabilized zirconia membrane and CO as sweep gas. At a temperature of 1954 K they were able to reach a conversion of 21.5 %, whereas the equilibrium production is a mere 1.2 % at the same temperature.[25] The overall conversion, however, was much lower due to permeation of O_2 through the membrane, recombining with the CO sweep gas to CO_2. Itoh et al.[26] employed an oxygen permeable yttria-stabilized zirconia membrane and used argon as sweep gas. Unfortunately, despite the removal of oxygen through the membrane, conversions of only up to 0.5 % were obtained for a maximum temperature of 1782 K. Fan et al.[27] used a solid-oxide ($SrCo_{0.5}FeO_3$) membrane reactor and methane as sweep gas. Conversions of up to 10 % were found at a temperature of 1213 K, which is one to two orders of magnitude higher than what would be attained conventionally. Nonetheless, the feed gas was diluted with four parts of helium per part of CO_2, and when this is taken into account, an effective conversion of only 2 % is reached.

To summarize, these studies have demonstrated the possibility of producing CO and O_2 by direct thermal splitting of CO_2—at lower temperatures than the equilibrium predictions—by means of semipermeable membranes to extract oxygen. Nevertheless, the attained overall effective conversions of 0.5–2 % are too low to be considered for successful application on an industrial scale.

Because to date none of the above mentioned alternative approaches to split CO_2 at lower temperatures have realized acceptable conversions and energy efficiencies, thermal-catalytic CO_2 splitting is currently not applied on an industrial scale. The reason is the high energy consumption and in addition also the lack of effective techniques for separating CO and O_2 at high temperatures to avoid ending up with an explosive mixture. Nevertheless, a brief summary of the initial efforts regarding thermal CO_2 splitting was presented here to have a complete understanding of the matter, and because it laid the foundations for one of the novel technologies, i.e. solar thermochemical CO_2 splitting (see further: Section 3.2).

2.2. Conversion of CO_2 with a co-reactant

Due to the inherent high energy consumption and derived low energy efficiency of thermal-catalytic CO_2 splitting, the only practical way to reform CO_2 consists of using a co-reactant. Thermodynamically speaking, it is significantly easier to convert CO_2 when it is paired with a co-reactant that has a higher—less negative—Gibbs free energy.[17] Suitable candidates are for example CH_4 (ΔG^0 = -50.7 kJ/mol) and H_2 (ΔG^0 = 0 kJ/mol). In essence, these hydrogen-bearing energy carriers give up their intrinsic chemical energy to promote the conversion of CO_2.

As such, it is no surprise that the most widely investigated traditional processes to convert CO_2 involve the reaction with either CH_4 or H_2. The former is one of the best known traditional processes for CO_2 reforming into synthesis gas or syngas, which is a mixture of H_2 and CO. The reaction with H_2 is known as the Sabatier reaction, which is a well-known process to generate CH_4 (and H_2O). Additionally, the combination of CO_2 and H_2 can also be used to produce methanol through the methanol synthesis process. A final process of interest is the combined conversion of CO_2 and H_2O, a technique for which there is no real traditional approach. Nevertheless, we briefly mention it here as well, because water is an interesting co-reactant to pursue for the growing array of novel techniques. After all H_2O is not only the most ubiquitous and cheapest hydrogen source, compared to CH_4 and H_2, but converting CO_2 in combination with H_2O to produce value-added products using renewable energy, would successfully mimic natural photosynthesis.[28,29]

2.2.1. $CO_2 + CH_4$: Dry reforming of methane

The combined conversion of CO_2 and CH_4, known as dry reforming of methane (DRM), is named analogous to its sibling steam reforming of methane (SMR; reaction 2 above)—indicating the replacement of water by carbon dioxide:

$$CH_4(g) + CO_2(g) \rightarrow 2\ CO(g) + 2\ H_2(g) \qquad \Delta H^0 = +\ 247\ \text{kJ/mol} \qquad (3)$$

This process is, however, not as straightforward as steam reforming of methane, because CO_2 is a highly oxidized, thermodynamically stable molecule and its reaction partner, CH_4, is chemically inert. Hence, the process needs to be carried out at high temperatures (900 – 1200 K) in the presence of a catalyst, typically containing Ni, Co, precious metals, or Mo_2C as the active phase.[30,31] **Figure 1-3** illustrates the theoretical thermal conversion and energy efficiency as a function of temperature. At 1500 K a complete conversion is achieved with an energy efficiency of 60 %. However, the maximum energy efficiency of 70 % is already obtained at 1000 K, reaching a conversion of 83 %, and it decreases with temperature from then on.

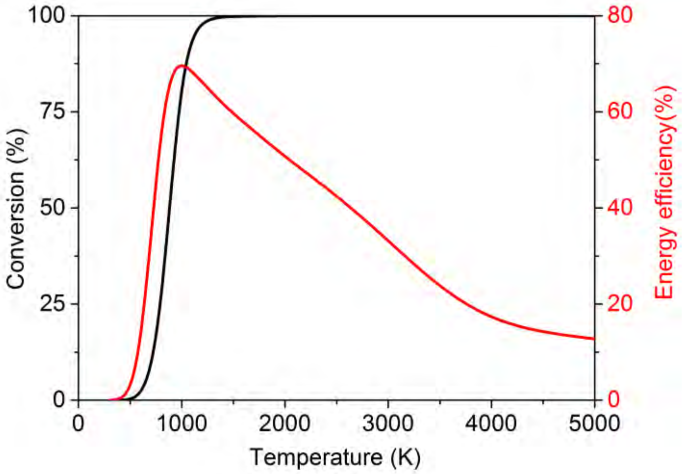

Figure 1-3. Calculated theoretical thermal conversion (left axis) and corresponding energy efficiency (right axis) as a function of temperature for the dry reforming of methane.

Dry reforming of methane (DRM) has quite a history. It was first studied by Fischer and Tropsch in 1928,[31] and it has been a challenge for chemical engineering ever since.[30] Throughout time the rationale for investigating this process has adapted itself several times to the spirit of the age. In its origin it arose from a desire for alternative ways to produce fuels and chemicals (in combination with Fischer-Tropsch synthesis) due to the limited supply of fossil fuels during the second world war.[32] A renewed interest was found in the 70s in the aftermath of the oil crisis,[32] again to circumvent the need for fossil fuels and with the idea of utilizing the cheaper and more abundant natural gas. With the beginning of a new millennium and the increasing concern regarding climate change, DRM was seen as a way to convert the major greenhouse gas CO_2 into useful products with the help of natural gas.[24,33] To date, a true amalgam of environmental and economical motivations exist, such as the conversion of the greenhouse gas CO_2, the capability of using biogas as a feedstock, a convenient way to liquefy CH_4 for easier transport, and the availability of cheap CH_4 through shale gas.[12,24,30,31,33–36]

Alas, despite all the bright outlooks, there is one major pitfall; the process' inherent susceptibility for soot deposition and its detrimental effect: deactivation of the catalyst. Due to this drawback, DRM is to date not yet (widely) used on an industrial scale. Of course, a lot of research is still ongoing towards modified catalysts to circumvent this coking issue, which was originally also a big problem for the currently widely adopted steam reforming of methane. Nevertheless, the inability to transform the alluring promises of DRM into reality through the traditional thermal methods—among other reasons—sparked and fuelled the growing interest for alternative reforming technologies, as will be discussed below.

2.2.2. $CO_2 + H_2$: Hydrogenation of CO_2

Both the complete hydrogenation of CO_2 to CH_4, known as the Sabatier reaction or the methanation of CO_2, and the selective hydrogenation of CO_2 to methanol are well-known commercially interesting processes.[37] The catalytic hydrogenation of CO_2 to methane is a thermodynamically very favourable process:[38]

$$CO_2(g) + 4\ H_2(g) \rightarrow CH_4(g) + 2\ H_2O(g) \qquad \Delta H^0 = -\ 165.3\ \text{kJ/mol} \qquad (4)$$

However, due to the high oxidation of the carbon, its reduction consists of an eight-electron process, significantly limiting the kinetics and requiring a catalyst with high rates and selectivities.[38] The process has been extensively studied using various supported nickel catalysts.[38,39] CO_2 conversions of > 95 %, with methane selectivity going up to 100 % at temperatures of 700 K, have already been achieved.[39] However, for industrial commercialisation this process is only viable when the H_2 is produced from renewable energy and the CO_2 comes from cheap accessible waste streams.[10,39] As mentioned above, 95 % of the worldwide H_2 production, however, comes from steam methane reforming, leading to a problematic flawed loop. Furthermore, the current cost for CO_2 capture, separation and purification from waste streams is too high. Both reasons make this process economically unfeasible.[39]

The selective hydrogenation of CO_2 to methanol, on the other hand, is a process operated on industrial scale. The annual worldwide production of methanol is estimated around 70 M metric tons (2015). The most common commercial catalyst is copper supported on high surface area alumina (often promoted with zinc oxide).[37] Relevant reactions for the selective hydrogenation of CO_2 are:[40]

$$CO_2(g) + H_2(g) \rightarrow CO(g) + H_2O(g) \qquad \Delta H^0 = +\,40.9\ \text{kJ/mol} \qquad (5)$$

$$CO(g) + 2\,H_2(g) \rightarrow CH_3OH(g) \qquad \Delta H^0 = -\,90.8\ \text{kJ/mol} \qquad (6)$$

$$CO_2(g) + 3\,H_2(g) \rightarrow CH_3OH(g) + H_2O(g) \qquad \Delta H^0 = -\,49.9\ \text{kJ/mol} \qquad (7)$$

While the overall reaction (reaction 7) of CO_2 hydrogenation to methanol is exothermic ($\Delta H^0 = -\,49.9$ kJ/mol), the rate determination step is the activation of CO_2 in the reverse water-gas shift (RWGS) reaction 5. Obviously, doping metals which function as catalysts in the RWGS reaction promote CO_2 hydrogenation.[40] As a result, much effort is still focused on investigating the efficacy of Cu-based catalysts promoted with Pd and Ga,[41] with the fundamental materials challenge centring on the fact that, generally, CO_2 and H_2 will only react at high temperatures in multi-component heterogeneous catalysts.[17]

One of the main drawbacks of the selective hydrogenation of CO_2 to methanol in the above case would be the production of water as a by-product (see reaction 7). A third of the H_2 is thus converted to water compared to the complete conversion to methanol when starting from syngas (see reaction 6). Furthermore, the thermodynamics for methanol production from H_2 and CO_2 are not as favourable as those for the production from syngas (cf. reaction 6 and 7).[41] Therefore, on an industrial scale methanol production usually relies on syngas in a 3 to 1 ratio from SMR (reaction 2), while CO_2 is added to deal with the excess H_2 in the feed (compared to reaction 6), and finally the produced water (reaction 7) is recycled via the water-gas shift reaction (reverse reaction of reaction 5).

Nevertheless, to conclude, we can state that currently the selective hydrogenation of CO_2 with H_2 into methanol is the most—not to say only—industrially successful traditional process for the direct reforming of CO_2 into chemicals and fuels.

2.2.3. $CO_2 + H_2O$: Artificial photosynthesis

Although there is no real traditional approach for the combined conversion of CO_2 and H_2O, we present here the main overall reactions of interest for the combined conversion of CO_2 and H_2O, for the sake of completeness and because of their interest for novel technologies (see next section):

$$CO_2(g) + H_2O(g) \rightarrow CO(g) + H_2(g) + 1/2\ O_2(g) \qquad \Delta H^0 = +\,525\ \text{kJ/mol} \qquad (8)$$

$$CO_2(g) + 2\,H_2O(g) \rightarrow CH_3OH(g) + 3/2\ O_2(g) \qquad \Delta H^0 = +\,676\ \text{kJ/mol} \qquad (9)$$

These are clearly the most endothermic overall reactions described in this section, partially explaining the absence of a traditional (thermo-catalytic) reforming approach. **Figure 1-4** clearly illustrates that the same high temperatures are needed for this reaction as for the pure CO_2splitting, while obtaining even somewhat lower energy efficiencies. The highest energy efficiency (40 %) is obtained at 3300 K and a conversion of 60 %. At higher temperatures the energy efficiency decreases to 25 % at 5000 K for total conversion.

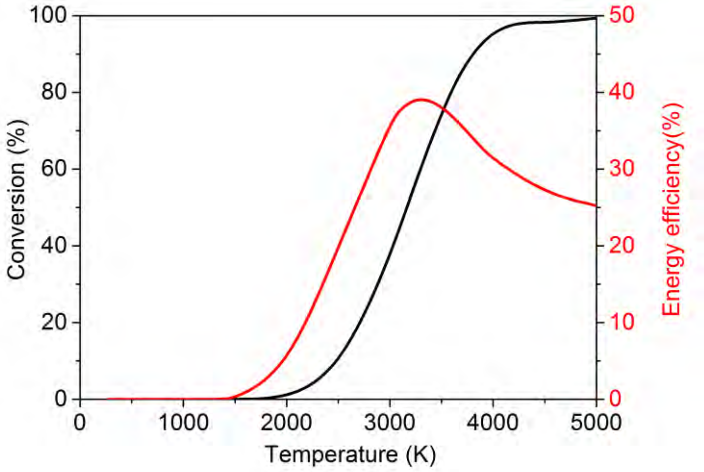

Figure 1-4. Calculated theoretical thermal conversion (left axis) and corresponding energy efficiency (right axis) as a function of temperature for the conversion of CO_2 and H_2O into H_2, CO and O_2.

Nevertheless, a process involving the reaction of CO_2, H_2O, O_2 and CH_4, called tri-reforming, is gaining quite some interest.[17] The novel concept proposed by Song et al.,[24] is a synergetic combination of dry reforming, steam reforming, and partial oxidation of methane in a single reactor, producing syngas in desired ratios (1.5–2.0), while eliminating carbon formation. These two advantages have been demonstrated for a fixed bed flow reactor at 1123 K over supported nickel catalysts.[24]

3. Novel CO_2 conversion approaches

It stands without doubt that the efficient conversion of CO_2 to useful molecules presents an important challenge and a great opportunity for chemistry today. Due to the inability of the traditional thermal approaches to address the worldwide CO_2 and energy challenge, several promising novel technologies are under development. Plasma technology is one among those, but before elaborating on this specific technology in more detail, first, a summary of its main “frenemies” in this domain will be given. For each technology, first a brief explanation of the working principles and current achievements will be given, followed by the major advantages and challenges. From this section it will become clear that there is, indeed, a fierce “competition” in the quest for finding the most effective and efficient CO_2 conversion technology with the potential to be used on an industrial scale. It should be noted that only technologies for CO_2 conversion are described here; for other (in)direct applications and fixation technologies, we refer to other reviews.[12,36]

3.1. Electrochemical conversion

We will kick off with one of the closest competitors for plasma technology, i.e., the electrochemical conversion or reduction of CO_2. This closeness derives from the fact that both technologies rely on the use of (renewable) electrical energy, whereas most of the other novel technologies can take direct advantage of renewable energy, i.e. the sun, either based on its focused radiation heat or its emitted photons. Although significant technical and catalytic advances are still required for its large-scale use, electrochemical conversion is becoming a mature technology for H_2O splitting. For CO_2 reduction, on the other hand, several important challenges remain.[7,34,42–45]

The electrochemical valorisation of CO_2 is an innovative technology, in which electrical energy is supplied to establish a potential between two electrodes, allowing CO_2 to be transformed into value-added chemicals under mild conditions.[7,45] This transformation can occur through a wide variety of pathways, which will be strongly affected by the experimental conditions. The electrochemical reduction of CO_2 can proceed through two-, four-, six-, and eight-electron reduction pathways in gaseous, aqueous, and non-aqueous phases at different cell and electrode configurations.[7,43] **Figure 1-5** shows the three main cell types. **Figure 1-5(a) and (b)** illustrate the principle of a solid proton conducting electrolysis cell (SPCEC) for the combined conversion of CO_2 and H_2O, and of a solid oxide electrolysis cell (SOEC) which can be used for either the pure or combined conversion of CO_2 and H_2O, respectively, while a typical alkaline electrolysis cell for water splitting is shown in **Figure 1-5(c)**. The catalyst and/or electrode materials, the reaction medium, electrolyte solution, buffer strength, pH, CO_2 concentration and pressure, as well as reaction temperature, will all influence and determine the wide variety of products that can be obtained.[43] The major reduction products obtained include carbon monoxide (CO), formic acid (HCOOH) or formate ($HCOO^-$) in basic solution, formaldehyde (CH_2O), methanol (CH_3OH), oxalic acid ($H_2C_2O_4$) or oxalate ($C_2O_4^{2-}$) in basic solution, methane (CH_4), ethylene (C_2H_4) or ethanol (C_2H_5OH).[7,34,43]

There are a number of reasons that makes the electrochemical reduction stand out of the pack. The process is controllable by several reaction parameters, including electrode potential and temperature.[7,34,42–44] Furthermore, a wide variety of valuable products can be made, either in mixtures or more importantly in their pure form. For example, besides direct electrochemical reduction of CO_2 to methanol, it is also possible to produce CO and H_2 at the cathode in a H_2/CO ratio close to 2, while at the anode a valuable pure oxygen stream is generated (see **Figure 1-5(b)**).[34] Another advantage is that electrochemical conversion can make use of a wide variety of (intermittent) renewable electricity sources, i.e., more than only solar energy.[43] Finally, the electrochemical reaction systems are compact, modular, on-demand, and thus easy for small or large scale-up applications.[43]

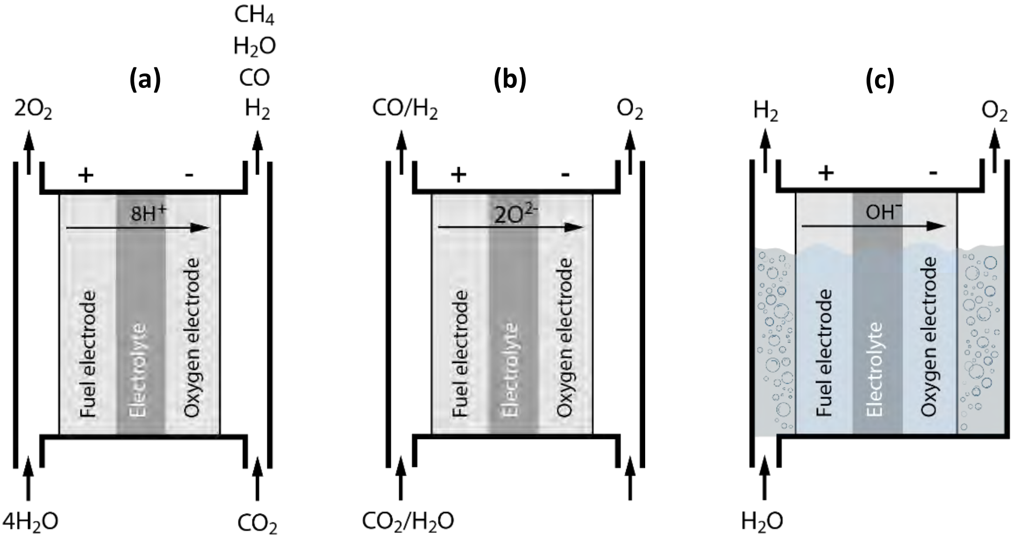

Figure 1-5. Principle of solid proton conducting electrolysis cell (SPCEC) (a), solide oxide electrolysis cell (SOEC) (b) and alkaline electrolysis cell (c), for the conversion of CO_2 and/or H_2O.

Accomplishments to date in the electrochemical reduction of CO_2 have been encouraging and the potential rewards are enormous.[7] Nevertheless, several challenges remain, such as the high overpotential, which is the difference in electrode voltage between the theoretical thermodynamic and actual real-world value to drive a reaction,[42,44] the low solubility of CO_2 in aqueous solutions,[42] the formation of product mixtures, requiring expensive separation steps,[42] the fouling and catalytic deactivation of electrodes by impurities, reaction intermediates and by-products,[7,42,44] the instability of the electrode material,[7] the low Faradeic efficiencies, current densities, and high energy consumption,[42,43] the kinetic barriers leading to low efficiencies,[43,44] and the non-optimized electrode/reactor and system design for practical applications.[43] In general it is recognized that the single biggest challenge is the low performance of the electrocatalysts, due to low activity, low selectivity, and most importantly insufficient stability. The reported stability tests in literature are only in the order of, or below 100 hours, while long-term tests are nonexistent.[43] This makes the development of stable electrocatalyst materials with high activity and selectivity the main priority for this technology.[7,43,46]

It seems that despite the many advances and successful proof-of-concepts, the maturity of electrochemical CO_2 reduction technology is still far from reaching the requirements for commercialization, due to several major technological challenges, as listed above.[7,42,43] Particularly for industrial-scale implementation, the low catalyst stability seems to be the major limitation.[43] As a result, to date no electrocatalysts for the reduction of CO_2 would be useful for a large-scale system.[44] As stated by Qiao et al.[43] "*with continued and extensive efforts focused on developing innovative composite and nanostructured catalyst materials to overcome the challenges of insufficient catalytic activity, product selectivity, and catalytic stability, the technology of CO_2 electroreduction will become practical in the near future.*" Hence, to successfully achieve the transformation of CO_2 to liquid fuels and useful chemicals, new methods and approaches for activating the CO_2 molecule at lower overpotentials are required.[7] In first instance, novel electrodes enabling operation at current densities close to commercially available H_2O electrolysers have to be developed, for which solid oxide electrodes appear to be suitable candidates.[42] Furthermore, a better understanding of the mechanistic role of metal and metal oxides in the reduction process is needed, to open the possibility to design electrodes with certain compositions.[42] To conclude, efforts to optimize system designs and at the same time develop durable catalysts need to be carried out.[43] However, the final grand question remains: can all of this be done with inexpensive earth-abundant metals?[44]

3.2. Solar thermochemical conversion

Another technology which has recently made several huge leaps forward is the solar thermochemical conversion of CO_2. There are several ways to reduce CO_2 with the assistance of renewable solar energy, and those using direct solar light irradiation are probably the most effective methods because there is no addition of extra energy and no negative influence on the environment.[47] Two forms of direct solar energy conversion can be distinguished, i.e., (i) thermal conversion—described here—where work can be extracted after sunlight is absorbed as thermal energy, and (ii) quantum conversion—described in the next section—where the work output can be taken directly from the light absorber (e.g. a semiconductor, a molecule, or an organic compound).[48] For the solar thermochemical conversion, concentrated solar radiation is used as—high temperature heat—energy source to drive the highly endothermic reactions.

The single step thermal dissociation of CO_2 (or H_2O) has been impeded by the need to operate at high temperatures (> 2500 K), as demonstrated in **Figure 1-2** above, and the need for effective separation techniques to avoid ending up with an explosive mixture of CO/O_2 (or H_2/O_2).[48,49] Multi-step thermochemical cycles using metal oxide redox reactions bypass the separation problem and in addition they allow operation at relatively moderate temperatures. More specifically, as shown in **Figure 1-6**, solar process heat at ≥ 1500 K enables a two-step thermochemical cycle using metal oxide redox reactions for CO_2/H_2O-splitting.[48,49] The first—endothermic—step is the solar thermal reduction of the metal oxide MO_{ox} (where M is among others Ce, Zn, or Fe)[50] to the metal or to the lower-valence metal oxide MO_{red}. The second—nonsolar—exothermic step is the oxidation of the reduced metal oxide with CO_2 and/or H_2O to form CO and/or H_2, allowing the (re)oxidized metal oxide to be reused/recycled for the first step.[48,49] In general, two cycle categories can be considered, i.e. volatile and non-volatile. Non-volatile cycles utilize metal oxides which remain in the solid state during reduction, while volatile redox cycles consist of metal oxides that undergo gas–solid phase transitions. The volatile reactions appear more favourable, but the volatile products must be quenched rapidly to avoid recombination, and to date this issue has not been solved in an energetically efficient fashion.[49] For the non-volatile cycles, cerium oxide (ceria, CeO_2) has emerged as a highly attractive redox active material choice for two-step thermochemical cycling.[50,51] Another promising pathway, which operates at lower temperatures than ceria, is the exploration of doped perovskite oxides.[52]

The main advantage of solar thermochemical conversion of CO_2 is obviously the direct use of solar energy. Concentrating solar technologies which are currently applied commercially for large scale (megawatt) power generation can be coupled to high temperature thermochemical reactors with the potential of reaching high solar-to-fuel energy conversion efficiencies and, consequently, producing solar fuels at large scale and at competitive costs.[48] To date solar flux concentration ratios exceeding 2 MW/m^2 are attainable with large-scale solar tower and dish systems. Solar thermochemical applications, although not as far developed as solar thermal electricity generation, employ the same solar concentrating infrastructure, with the solar reactor positioned at the focus of the solar tower (for MW centralized applications) or solar dish (for kW decentralized applications).[48] A recent comprehensive review of the solar concentrating technologies for thermal power and thermochemical fuel production is given by Romero et al.[53] Consequently, these cycles inherently have the potential to realize greater theoretical efficiency than methods using energy vectors or a small part of the solar spectrum and are in addition conceptually simpler.[52,54] This potential to achieve high solar-to-fuel energy conversion efficiencies is primarily related to the fact that solar thermal processes inherently operate at high temperatures and utilize the entire solar spectrum, and as such provide a thermodynamically favourable path to solar fuels production.[48,49] A thermodynamic analysis based solely on the material properties of e.g. CeO_2 indicates that efficiency values in the range of 16–19 % are attainable, even in the absence of sensible heat recovery. These values are close to the 20 % efficiency, which is likely needed for solar fuels to be cost competitive.[55]

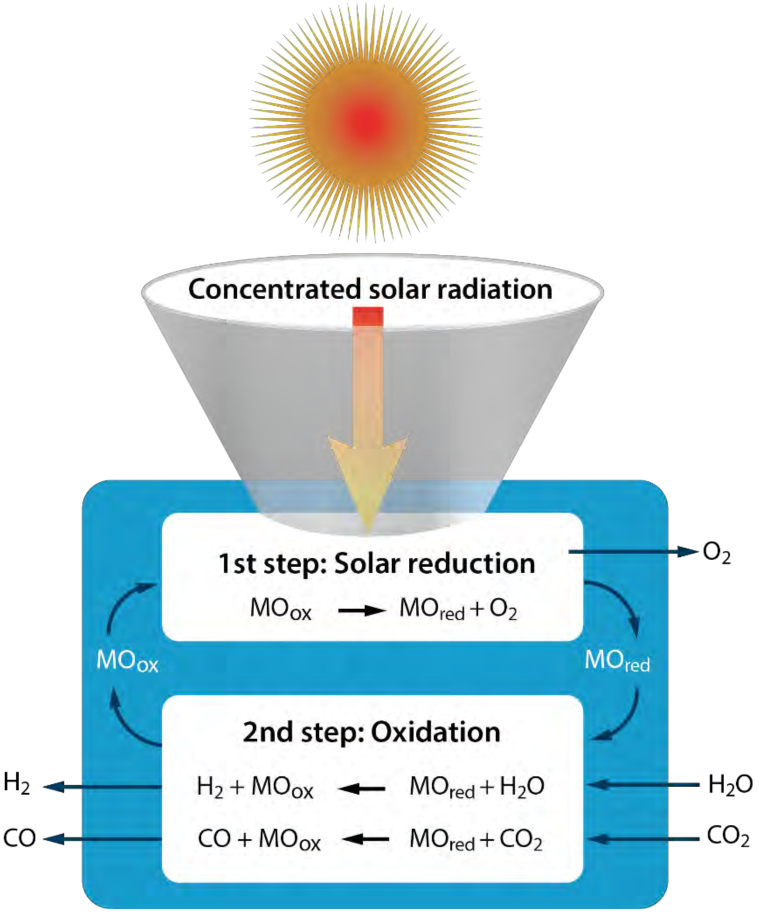

Figure 1-6. Schematic view of the two-step solar thermochemical cycle for CO_2 and H_2O splitting based on metal oxide redox reactions.

Although significant advances have been made in the field of solar thermochemical CO_2 conversion technologies using metal oxides, a lack of fundamental research into the behaviour of the metal oxides under the high temperature conditions present in these cycles has hampered materials development. Basic questions relating to oxygen transport, surface chemistry, structural changes vs. redox reactions, materials synthesis methods, effects of thermochemical cycling on the material, and the role of supports, still have to be addressed.[56] Furthermore, despite its favourable thermodynamics, both the efficiency and the cycling rates in the reactor can be largely limited by thermal losses, resulting from poor conductive and radiative heat transfer across the porous metal oxide structure.[48] Finally, the thermochemical conversion rates are higher than for example the photocatalytic rates, but although conceptually simple, focusing lenses for sunlight and high-temperature reactors incur high initial investment costs.[50]

Solar thermochemistry has clearly emerged as a viable path to utilize concentrated solar technology—currently applied commercially for large-scale power generation—for the conversion of CO_2 (and H_2O) into CO (and H_2). Solar thermochemical cycles for conversion of CO_2 and H_2O via metal oxide redox reaction have favourable thermodynamics, but the ultimate factor dictating commercial viability is a high solar-to-fuel energy conversion efficiency and to date efficiencies above 10 % are still pending experimental demonstration with robust and scalable solar reactors.[48,49,52] Discovery of new materials with large oxygen exchange capabilities at moderate temperatures and their implementation in efficient solar reactors are essential. Additionally, rapid chemical kinetics and material stability over thousands of cycles must be demonstrated for each material considered.[49,57] This is the second key to market viability, because materials must remain active for many thousands of redox cycles in order to avoid high costs associated with frequent replacement. As such, commercial success is again predicated upon materials composed of earth-abundant elements that can operate at lower reduction temperatures than current systems, with sufficient activity to achieve high process efficiency.[52]

3.3. Photochemical conversion

The photochemistry—for the photochemical conversion—differs from (solar) thermochemistry in the way the solar energy is used: the former uses the energy of a photon in the chemical reactions,[50] while the latter uses the absorbed thermal energy to overcome activation barriers and affect chemical equillibria.[48]

Back in 1979, the photoreduction of CO_2 to formaldehyde and methanol in purified water was already reported, using the semiconductors TiO_2, ZnO, CdS, GaP, SiC, and WO_3.[50] Based on the correlation between the conduction band energy potential and the yield of methanol, it was suggested that the photoreduction of CO_2 proceeds by the photoexcited electrons in the conduction band moved to CO_2. This principle mechanism of selective photocatalysts under light irradiation is shown in **Figure 1-7**. The conduction band energy minimum was higher than that for CO_2 photoreductions.[50] Again the efficiency of the photocatalytic materials in their use of sunlight for conversion of CO_2 to fuel is of critical importance.[58] This efficiency is being influenced by several factors, such as catalyst dosage, reactant ratio, reaction temperature, time, system pressure, pH, light intensity and wavelength.[47] A wide variety of reduction products can be obtained, just like with the electrochemical technique, including carbon monoxide (CO), formic acid (HCOOH), formaldehyde (CH_2O), methanol (CH_3OH), methane (CH_4), ethylene (C_2H_4), ethane (C_2H_6), ethanol (C_2H_5OH).[58]

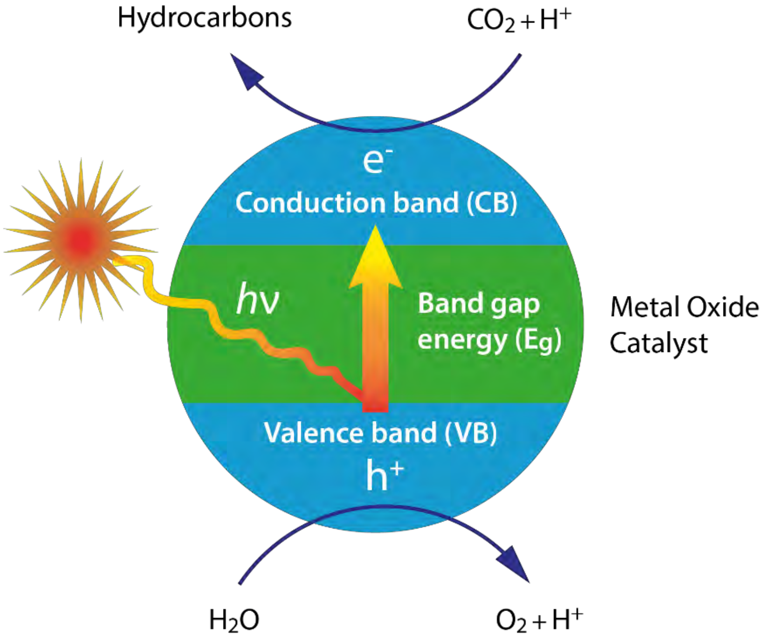

Figure 1-7. Principle of photochemical reduction of CO_2 by water on a photocatalyst.

From a sustainable viewpoint, solar light is the ideal energy source. In combination with photocatalytic H_2O splitting, the solar-driven reduction of CO_2 to fuels is a very attractive approach.[42] The advantages of photochemical systems include the assertion that they are composed of only few parts and are therefore theoretically less likely to fail, if the remaining parts are reliable.[48] The most extensively investigated catalyst for the photoreduction of CO_2 is TiO_2.[50] Several attempts have already been made to enhance the photocatalytic activity of TiO_2, including the use of an added metal, Rh/TiO_2, or $Rh/WO_3–TiO_2$,[50] the use of highly dispersed active Ti ion species,[50] atomically dispersed TiO_2 on zeolites or ordered mesoporous SiO_2 or doped with Pt, Cu, N, I, CdSe, or PbS.[50] The most significant breakthrough has been achieved using nitrogen-doped TiO_2 nanotube arrays cocatalyzed with Cu and/or Pt nanoparticles, in which water vapour saturated CO_2 was reduced to methane and other hydrocarbons without application of an electrical bias.[50,58]

It should be noted, however, that for many oxide semiconductors (incl. TiO_2) this electrical bias is necessary, because unfortunately the conduction band is located below the acceptor level. This is one factor that limits the efficiency of metal oxide materials.[48] Furthermore, most work is performed using artificial (UV) light sources,[47,58] because the large band gap of metal oxides results in a poor photo-responsiveness to visible light.[42,47,48] Theory dictates that a band gap between 2 and 2.4 eV is optimal, which limits the maximum attainable efficiency to about 17 %.[58] However, the solar energy conversion efficiencies obtained to date are much lower (at present < 2 %),[48] e.g. as a result of the energy associated with this electrical bias.[48] Furthermore, a challenge lies in the separation and collection of the hydrogen and oxygen gas produced (often in close proximity).[48] Finally, many of the photocatalysts presently studied are metal complexes employing rare and expensive transition metals, hence efforts must be done using earth-abundant elements that could support large-scale undertakings.[44]

From literature, it becomes clear that encouraging progress has been made toward the photocatalytic conversion of CO_2 using sunlight, but nevertheless, the existing techniques are insufficient and further efforts are required for increasing sunlight-to-fuel photochemical conversion efficiencies.[44,45,47,48,58] This appears to be a general remark for photochemistry: very few examples exist of chemical processes operating on the basis of photocatalysis technology. Not only the photon efficiency of materials and the resulting achievable rates remain insufficient, also sub-optimal photocatalytic reactors often induce inefficiency and limit the practical application.[42] The immediate requirement in this technology is to develop visible light-sensitive photocatalysts, which are prominent in CO_2 recycling.[47] What we seek is a means for achieving high-rate photocatalytic reduction of CO_2, using solar radiation as the only input energy source. Since visible light comprises the majority of the solar spectrum energy, it behoves us to consider photocatalysts sensitive to sunlight.[58] Immediate research opportunities include uniform co-catalyst sensitization of the entire nanotube array surface for enhanced conversion rates, and the design of co-catalysts to improve and control the product selectivity.[58] Although photocatalytic reduction of CO_2 may become an important stepping stone to solar fuel production, much progress remains before it becomes practical as an industrial process.[44] Based on the highest reported activities, one can conclude that game-changing rates have not yet been achieved. Reported turnover frequencies are far from those required for an efficient catalytic process, and an efficiency improvement of at least 3 orders of magnitude is needed.[42] It is clear that photochemical systems have a long way to go to achieve their full potential and thus successfully compete with the alternative approaches to produce fuels from sunlight.[48]

3.4. Biochemical conversion

Another pathway converting solar energy into chemical energy is by ‘natural’ photosynthesis for the production of biofuels.[59] Biological conversion of CO_2 for producing chemicals or fuels is an attractive route. Nevertheless, the use of first generation biofuels has generated a lot of controversy, mainly due to their competition with agriculture for arable land used for food production, impacting global food markets and food security.[59,60] The use of microalgae, on the other hand, could meet the conditions for technically and economically viable biofuel production. More specifically, it should be competitive or cost less than petroleum fuels, it should require low to no additional land use, it should enable air quality improvement and require minimal water use.[59,60] Microalgae can typically be used to capture CO_2 from three different sources: atmospheric CO_2, CO_2 emission from power plants and industrial processes, and CO_2 from soluble carbonate.[60] Pathways for CO_2 fixation have evolved over billions of years and use diverse mechanisms and enzymes for processing CO_2 by making C−H and C−C bonds and cleaving C−O bonds.[37] Furthermore, algae are more photo-synthetically efficient than terrestrial plants, making them without doubt very efficient CO_2 fixers.[61]

Microalgae are currently considered to be one of the most promising alternative sources for biodiesel, hence most of the current research and developmental efforts are focused on microalgae, due to their high growth rate and oil content (up to 77 % of dry cell mass). Algae contain oils, sugars, and functional bioactive compounds that can be used for commercial products. In addition to fuels, the development of the technologies for high efficiency algal biodiesel production is also applicable to biohydrogen, biogas, bioethanol and biomass-to-liquid (BTL) approaches using fast growing algae.[59,60] Furthermore, valuable co-products, such as biopolymers, proteins and animal feed, can be produced during the process.[61,62] Other advantages include very short harvesting cycles (∼1–10 days), allowing multiple or continuous harvests with significantly increased yields. Furthermore, the cultivation can potentially be carried out on marginal or non-arable land and the use of waste water for algal cultivation is also a viable option.[59,60] To obtain the best performing microalgae strains for biofuel production, one can (1) screen a wide range of natural isolates, (2) improve them by metabolic (genetic) engineering or (3) by selection and adaptation. Algae collections worldwide contain thousands of different algal strains that can be accessed.[59]

It should, however, be emphasized that the significant drawback in all the biochemical techniques is the big share of cost for cultivation. Among others, harvesting of algal biomass accounts for the highest proportion of energy input during production, but currently, there are no standard harvesting techniques.[59–61] Therefore, today algal biomass is unsuitable to cultivate it solely for bioenergy applications and must be integrated with the production of other value-added products, e.g. pharmaceutics, cosmetics, food, etc. Unfortunately, processes for the recovery of complex molecules from algal biomass are expensive and a significant technological progress is required before commercial deployment.[63] Algae can be grown in many ways in freshwater, saltwater or wastewater, in closed photobioreactors or open ponds.[59] One key advantage of algae is that its cultivation does not require cropland, but on the other hand, other resources are needed.[62] Other inorganic nutrients required for algae production include nitrogen and phosphorus,[60] resulting in unsustainable inputs of nitrogenous fertilizers, which are produced from fossil fuels and require huge inputs of energy for production.[62] Furthermore, it is reported that between 3.15 and 3650 litres of freshwater are needed to produce the algal biofuel equivalent to 1 litre of gasoline using current technologies. Thus, the integration of upstream production and downstream processing of microalgae, and the framing of these in the context of water savings and net energy gain is required to build up credibility.[62] **Figure 1-8**, shows a schematic overview of the different steps for the application of a photo-bioreactor for CO_2 conversion. Finally, optimization of strain-specific cultivation conditions is of confronting complexity, with many interrelated factors that can each be limiting. These include temperature, mixing, fluid dynamics and hydrodynamic stress, gas bubble size and distribution, gas exchange, mass transfer, light cycle and intensity, water quality, pH, salinity, mineral and carbon regulation/bioavailability, cell fragility, cell density and growth inhibition.[59]

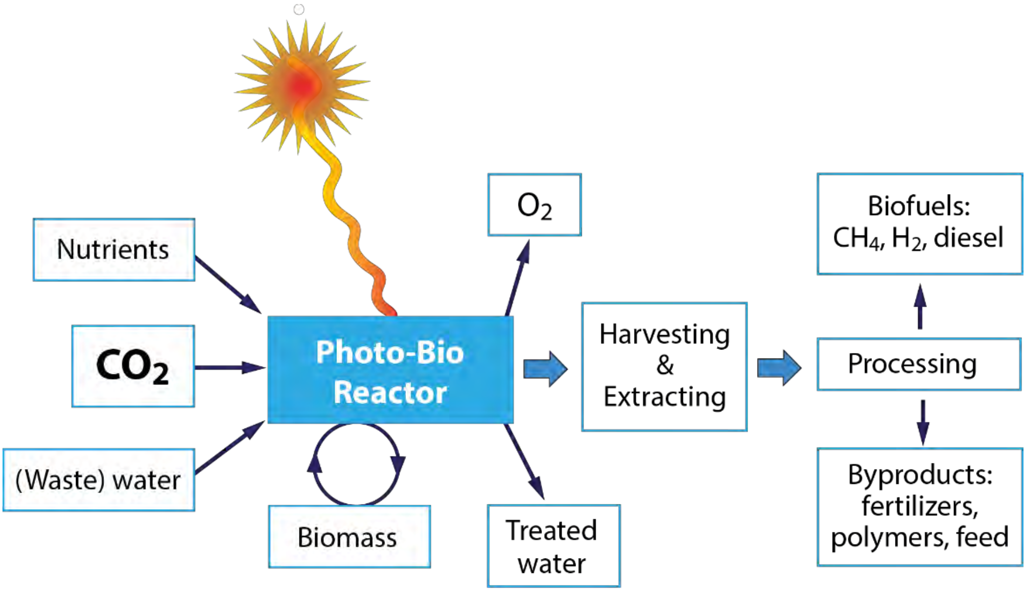

Figure 1-8. Schematic view of photo-bioreactor application for CO_2 conversion.

Despite its inherent potential as a biofuel resource, many challenges have impeded the development of algal biofuel technology to commercial viability that could allow for sustainable production and utilisation.[60] Therefore, large-scale cultivation of algae for biofuel production is still in the research and development phase. The long term potential of this technology can be improved by the following approaches: (1) cost saving growth technologies of oil-rich algae should be identified and developed;[59,62] (2) integrated bio-refineries can be used to produce biodiesel, animal feed, biogas and electrical power, thereby reducing the cost of production;[61,62] (3) selection and successful outdoor large-scale cultivation of a robust microalgal strain by enhancing algal biology by genetic modification and metabolic engineering;[59,61,62] (4) area efficient techniques to capture CO_2 from industrial power plants need to be identified;[62] (5) recycling of nutrients from municipal sewage and industrial wastewaters are required to reduce the demand of fertilizers to grow algae; [59,60,62] (6) economics of microalgae production can be improved by additional revenues from wastewater treatment and greenhouse gas emissions abatement;[62] (7) most importantly, cost-effective and energy-efficient harvesting methods are required to make the whole biofuels production process economical;[61] in this respect, strain selection is an important consideration since certain species are much easier to harvest than others.[59]

3.5. Catalytic conversion

In section 2 we already covered the main traditional thermo-catalytic approaches used. Of course there is still a lot of ongoing research towards finding new improved (thermo-)catalytic pathways for the different processes converting CO_2. There are two main types that can be applied for this process, homogeneous and heterogeneous catalysts. The former (e.g., Ru-, Rh-, and Ir-based catalysts) are efficient for the formation of formic acid and formates, but are more challenging for commercial applications, while the latter (e.g., Fe-, Cu-, and Ni-based catalysts) are more practical for industrial applications, but they frequently suffer from low yields and poor selectivity. As a result, significant improvements in new catalytic systems are necessary to make thermo-catalytic CO_2 reduction economically feasible.[38]

Nonetheless, the catalytic conversion will be briefly discussed here, especially since it is clear from the sections above that catalytic materials can play an important role in the development and further advancement of most novel technologies under study.[18] These scientific advances give rise to intriguing new combinations—and corresponding names—such as electrocatalytic, photocatalytic, biocatalytic, as well as their even more advanced hybrids forms, e.g. photoelectrocatalytic and bioelectrocatalytic processes.[12,43,64] Kumar et al.[44] stated quite frankly that virtually every approach under consideration for the conversion of CO_2 requires catalysts to facilitate the formation and cleavage of chemical bonds, as illustrated by **Figure 1-9**. In general, these required catalysts fall into three classifications: (1) they already exist and show good performance but are too rare/costly to be scaled up; (2) they already exist but in forms that are not optimal or practical for adaptation to an integrated solar fuels system; (3) they do not exist and await discovery.[44]

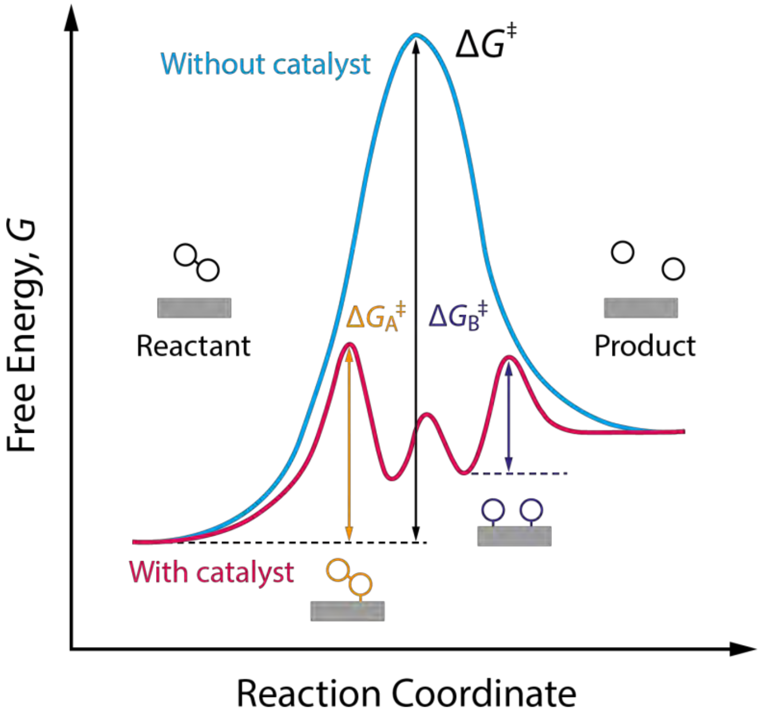

Figure 1-9. Reaction coordinate diagram showing the working principle of a catalyst.

From a scientific point of view, the development of catalysts with inexpensive metals, such as iron and copper compounds, which can also be active in mild conditions, is the grand challenge.[38] Still, it is evident that due to their reliance on thermal heat—derived from burning fossil feedstocks—current pure thermo-catalytic routes can only give a limited net contribution to CO_2 conversion. Hence, techniques based on the use of (in)direct solar energy and other perennial energy sources can contribute to avoiding large volumes of CO_2.[18] One exciting thermo-catalytic advancement—besides the solar thermochemical conversion discussed in section 3.2 above—to circumvent this reliance on fossil fuels is the use of microwaves.[65] The microwave-assisted CO_2 conversion over carbon-based catalysts combines the catalytic and dielectric properties of carbonaceous materials with the advantages of microwave heating, which favours catalytic heterogeneous reactions due to, among other reasons, the generation of hot spots.

Microwave radiation has been shown to have beneficial effects on the reaction rate of heterogeneous (catalytic) reactions.[66,67] The combination of microwave heating and a carbon material acting as both catalyst and microwave receptor gives rise to enhanced conversions, both in the case of CO_2 gasification and dry reforming of methane, compared to conventional heating.[66,67] Fidalgo et al.[67] observed conversions which are a factor 1.6 to 1.9 higher for MW-heating compared to conventional heating. The applied microwave energy is transferred directly to the catalyst, without any heat flux, unlike in conventional heating. As a result, the temperature inside the material is usually higher than the temperature of the surrounding atmosphere near the surface, and the uniformity of heat distribution is improved with respect to conventional heating, as shown in **Figure 1-10**.[67] Furthermore, the formation of hot spots, possibly due to generation of microplasmas within the catalyst bed, with higher temperatures compared to the bulk catalyst, have been reported to be responsible for reaction rate enhancements, higher yields and improved selectivities of heterogeneous (catalytic) reactions.[66,67]

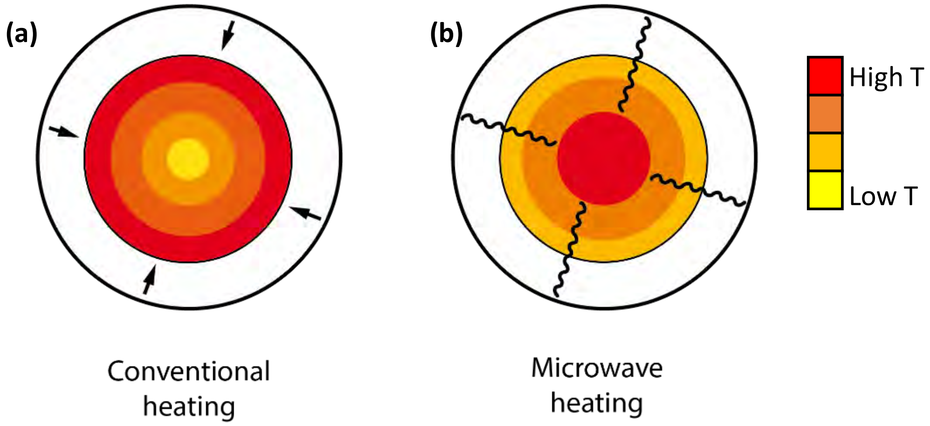

Figure 1-10. Comparison of the temperature gradients produced by conventional (a) and microwave (b) heating.

3.6. Summary

By discussing the main novel technologies for CO_2 conversion, we roughly sketched the current landscape in which we want to orient another emerging technology with potential for CO_2 conversion, i.e. plasmachemical conversion. It is evident that for all technologies discussed above, there are several distinctive up- and downsides. This will not be different for plasma technology—as will become evident from the following Chapters. In the final Chapter of this thesis, we will make a visual comparison between all emerging technologies based on their versatility, the mentioned distinctive advantages and limitations, and—what appears to be most important from an economical point of view—their solar-to-fuel conversion efficiency.

4. Plasma Technology for CO_2 conversion

From the previous section it has become clear that several alternative (non-conventional) CO_2 conversion technologies are—more or less—successfully being investigated. In recent years, another novel technology is being considered, which has not spent much time in the spotlight yet: plasma technology. In this section, first a brief introduction on plasma technology will be given, and its general advantages and unique features for CO_2 conversion will be highlighted. Next, the different kinds of plasma reactors used for CO_2 conversion will be described, focussing on their advantages and disadvantages. Subsequently, the possibly fruitful combination of plasma with catalysts, so-called plasma catalysis, will be discussed. Finally, a critical assessment of plasma-based CO_2 conversion for these different set-ups will be presented in **Chapter 6** for both pure CO_2 splitting and CO_2 conversion with the specified co-reactants.

4.1. Properties of plasma and its unique features for CO_2 conversion

The term *plasma* was first introduced by Irving Langmuir (1928). Plasma is an ionized gas, which means that at least one electron is unbound, creating positively charged ions. In practice, the ionization degree in plasma can vary from fully ionised gases (100 %) to partially ionised gases (e.g. 10^{-4}–10^{-6}). Besides various types of ions (both positive and negative), plasma also consists of a large number of neutral species, e.g. different types of atoms, molecules, radicals and excited species. The latter can lead among other things to the emission of light. More importantly, all these species can interact with each other, making plasma a highly reactive and complex chemical cocktail, which is of interest for many applications.[14,68]

Plasma is also being referred to as the “fourth state of matter”, owing to the observation that with increasing temperature matter transforms in the sequence: solid, liquid, (neutral) gas and finally ionised gas or plasma. Although the concept of plasma is less known than the other states of matter, more than 99 % of the visible matter in the universe is in the plasma state, mainly attributed to interstellar matter and the stars. Hence, our own sun is a perfect example of a plasma. Furthermore, basically, many—not to say all—natural occurring weather phenomena emitting light are plasma, e.g. Saint Elmo’s fire, lightning, red sprites, auroras (Borealis and Australis), with thanks to the excited species for the emission of these colourful lightshows. Other natural plasmas close to home are the earths ionosphere, plasmasphere and the outer magnetosphere.

Beside these natural plasmas, we can distinguish between two main groups of man-made plasmas. The first one are the high-temperature or fusion plasmas, which are in general completely ionised plasmas. Applications include tokomaks, stellarators, plasma pinches, focuses, and so on. The second group comprises the weakly ionized plasmas or so-called gas discharges, which are studied in this PhD thesis.

A second sub-division can be made based on whether the plasma is in thermal equilibrium or not. The temperature in a plasma is determined by the average energies of the different species (electrons, neutrals, ions) and their relevant degrees of freedom (translational, rotational, vibrational, and electronic). Since plasma is a multi-component system, it can exhibit multiple temperatures. When the temperature of all these species is the same in localised areas, the plasma is said to be in 'local thermodynamic equilibrium' (LTE), and these kind of plasmas are usually called thermal plasmas. When the plasma is characterised by multiple different temperatures and thus is far from thermodynamic equilibrium, the plasma is said to be in 'non-local thermodynamic equilibrium' (non-LTE) and these discharges are usually called non-thermal plasmas.

4.1.1. Thermal plasmas

Thermal plasmas can be achieved in two ways, either at high temperature, typically ranging from 4,000 K to 20,000 K, depending on the ease of ionisation, or at high gas pressure. The latter can be explained as follows. Initially, the electrons receive energy from the electric field during their mean free path in between collisions, and they lose a small portion of this energy during collisions with so-called heavy particles (e.g., gas molecules or atoms). Subsequent collisions of this nature, also known as Joule heating, can equilibrate the temperatures to reach equilibrium between the electron and heavy particle temperature. At high pressures the mean free path becomes smaller, so more collisions occur, hence leading to a more efficient energy exchange between the electrons and the heavy particles. More specifically, it is the square of the ratio of the electric field (E) to the pressure (p), i.e., $(E/p)^2$, which is proportional to the temperature difference in gas discharges.[14]

Thermal plasmas have numerous advantages—compared to traditional technologies—due to numerous interesting characteristics, including their high temperature, high intensity non-ionising radiation and high-energy density. The heat source is also directional with sharp interfaces and steep thermal gradients that can be controlled independently of the chemistry. Whereas the upper temperature limit by burning fossil fuels is 2300 K, thermal plasmas can reach temperatures of 20,000 K or more, as mentioned above. As a result, this type of plasma is already being used for a wide range of applications, such as for coating technology, fine powder synthesis, (extractive) metallurgy (e.g., welding, cutting, etc.) and the treatment of hazardous waste materials.[69]

On the other hand, the inherent nature of thermal plasmas makes them unsuitable for the efficient conversion of CO_2. More specifically, the ionisation and chemical processes in thermal plasmas are determined by the temperature. As a result, the maximum energy efficiency is limited to the thermodynamic equilibrium efficiency and corresponding conversion of 47 % and 80 % at 3500 K, respectively (see **Figure 1-2** above). This is in contrast to non-thermal plasmas, where lab-scale efficiencies of up to 90 % have already been reported (see further, section 4.4.1).[14]

4.1.2. Non-thermal plasmas

In non-thermal plasmas the electrons are characterised by a much higher temperature than the heavy particles, leading to the non-LTE condition, as mentioned above. As a result of all the different species, the relationship between all their different temperatures can become quite complex, but conventionally the temperature of the electrons (T_e) is the highest, followed by the vibrationally excited molecules (T_v), while the lowest temperature is being shared by the neutral species (T_0, or simply the gas temperature, T_g), the ions (T_i) and the rotational degrees of freedom of the molecules (T_r); hence: $T_e >> T_v > T_r \approx T_i \approx T_0$.[14] In most cases the electron temperature is in the order of 1 eV (~10,000 K), while the gas temperature remains close to room temperature. This high electron temperature is due to the small mass of the electrons, allowing them to be easily accelerated by the applied electromagnetic fields, whereas the heavy particles—even the ions—are not. Furthermore, due to the large mass difference, the electrons lose less energy during elastic collisions with heavy particles, so they can easily keep their high energy gained from the electric field.

Besides elastic collisions—leading to the aforementioned Joule heating—these highly energetic electrons also give rise to inelastic collisions. Among those, the electron impact ionisation reactions are responsible for sustaining the plasma, with the generation of new electrons and ions, while electron impact dissociation (and excitation) reactions lead to the creation of highly reactive (or energetic) gas species. Hence, the electrons can be considered as the initiators of the highly reactive chemical mixture. This is obviously one of the key advantages of non-thermal plasma technology: it allows gases—even as unreactive as CO_2—to be “activated” at room temperature by the highly energetic electrons.

Accordingly, there is no need to heat the entire reactor or the gas, because the discharge and the associated reactions are easily initiated by applying an electromagnetic field. This results in the second key advantage of non-thermal plasma technology for CO_2 conversion, namely it is a very flexible, or so-called “key-turn” process, since it can easily and—more importantly—instantaneously be switched on and off, with conversion and product yield stabilisation times generally lower than 30 minutes. Furthermore, its power consumption can easily be scaled and adjusted. As such, it has the inherent ability to be(come) one of the most suitable technologies to utilise (excess) intermittent renewable energy (e.g., originating from wind turbines or solar panels) and for storing it in a chemical form. Indeed, this makes it suitable for both peak shaving and—more importantly—grid stabilisation, by adapting to the irregular supply of renewable electricity. Hence, in essence the current transition to renewable energy sources does not only give plasma processes a clean electricity source, but plasma-based CO_2 conversion technology can also provide a solution for the imbalance between energy supply and demand, by storing the electrical energy in a desirable chemical form according to the market needs.

Additional advantages compared to the other emerging technologies for CO_2 conversion, as described in previous section, are the low investment cost for the reactors, they do not rely on rare-earth materials, and last but not least, their simple scalability from watt to megawatt applications, as already demonstrated by the successful development of ozone generators.[70] Due to their extreme scalability, the applications can vary hugely in both scale and application type, starting from small devices such as on board of vehicles, for exhaust treatment or providing on board fuel cell feeds,[71] as well as household scaled devices for indoor air treatment,[72,73] to medium on-demand installations such as the modular containerized plants concept[74] or in-situ CO production,[75] and finally large scale industrial plants. This scalability and flexibility in applications also gives plasma technology a high location flexibility, which is a critical point for carbon capture and utilisation (CCU) techniques.

On the other hand, for the comparison made here with other novel technologies, the reliance of non-thermal plasma technology on indirect solar energy in the form of electricity is a limiting factor for the overall solar-to-fuel efficiency, compared to technologies who can harvest solar energy in a direct form. However, when looking at the broader picture, its ability to rely on multiple energy sources again gives plasma technology a huge advantage regarding location flexibility, not to mention that it can be operated 24/7, even when the sun is not shining.

Although non-thermal plasma is good at creating a non-equilibrium condition by "activating" stable molecules, it is absolutely non-selective in the formation of targeted products. More specifically, the reactive species created by the electrons react according to the laws of chemical kinetics, and as such, they recombine into a (large) number of different products, depending on the reaction conditions—not to mention that the formed products can again be destroyed by new electron collisions. For pure CO_2 splitting, this is not much of an issue, since CO and O_2 (together with small amounts of O_3) are basically the only products that can be formed. However, when combining CO_2 with other reactants, such as CH_4, H_2O or H_2, a wide variety of products can be formed, including syngas (CO and H_2), higher hydrocarbons (C_2H_x, C_3H_y, C_4H_z), as well as several oxygenates, e.g. methanol, ethanol, dimethyl ether, formaldehyde, acetaldehyde and carboxylic acids. For that reason, the combination with catalysis is also highly desirable for plasma technology, when targeting the selective production of specific compounds (see Section 4.3).

4.1.3. Warm plasmas

Conventional thermal and non-thermal discharges cannot simultaneously provide a high level of non-equilibrium and a high electron density, whereas most prospective plasmachemical applications require both, i.e., a high power (translated in a high electron density) for efficient reactor productivity and a high degree of non-equilibrium to selectively populate certain degrees of freedom, like vibrationally excited states (see below).[76] Recent studies have revealed that a transitional type of plasma, so-called “warm discharge” or “warm plasma”, which operates at the boundary—and hence shares properties—of both thermal and non-thermal plasmas, might be very promising for CO_2 conversion. These are non-equilibrium discharges, which are not only able to supply (re)active species, but also some controlled level of translational temperature. Although this translational gas temperature is still much lower than the electron temperature, it is significantly higher than room temperature and can easily reach up to 2000–3000 K. Hence, these warm plasmas are able to create the advantage of a non-equilibrium condition, while at the same time they can influence the chemical kinetics due to this higher gas temperature.

For the application of CO_2 conversion, however, it is not the increased temperature that makes these discharges most interesting, but rather their characteristic electron energy distribution, which leads most of the electron energy going into the vibrational excitation of CO_2, as will be discussed below. The latter is indeed known to provide the most energy efficient and hence most important channel for CO_2 dissociation.[14,77] In fact, in a recent modelling study it was suggested that the higher gas temperature inherent to these warm discharges is actually an unwanted effect.[78–80] As such, the development of “cooler” warm discharges might be beneficial for further increasing the CO_2 conversion and energy efficiency.

4.1.4. CO_2 dissociation channels

For a better understanding about the difference between non-thermal and warm discharges, and specifically between the different discharge types described in the next section, we need to provide an overview of the different channels of energy transferred by electrons to CO_2. As mentioned, the electrons receive their energy from the electric field in non-thermal plasmas, and subsequently—through collisions—this energy is distributed between elastic energy losses and different channels of excitation, ionisation and dissociation. **Figure 1-11** illustrates the fraction of the energy transferred to the different channels of excitation, ionization and dissociation of CO_2, as a function of the reduced electric field (E/n).[81] The reduced electric field is the ratio of the electric field in the plasma over the neutral gas density and has distinctive values for different plasma types. For example, a dielectric barrier discharge (DBD), which is one of the most common types of non-thermal plasmas for CO_2 conversion (see next section) has a reduced electric field in the range above 200 Td (Townsend; 1 Td =10^{-21} V·m^2), whereas microwave (MW) and gliding arc (GA) discharges (which belong to the category of warm plasmas; see next section) typically operate well below this range (about 50 Td).

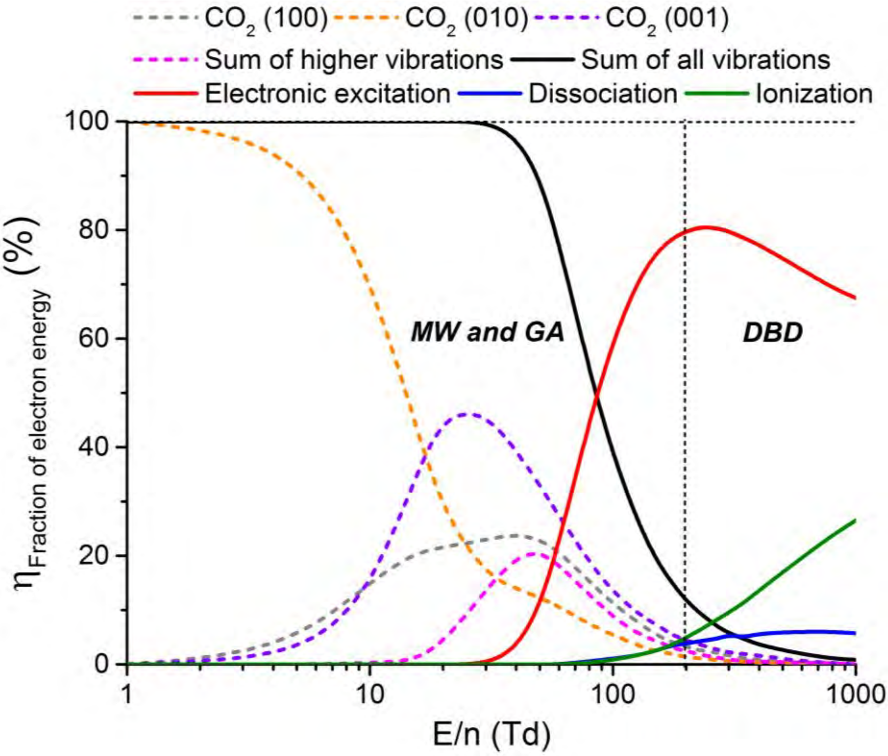

Figure 1-11. Fraction of electron energy transferred to different channels of excitation, as well as ionization and dissociation of CO_2, as a function of the reduced electric field (E/n), as calculated from the corresponding cross sections of the electron impact reactions. The E/n region characteristic for MW and GA plasma and DBD plasma are indicated.

From **Figure 1-11**, it becomes clear that the value of the reduced electric field will have wide implications on the distribution of the electron energy among the different channels. In the region above 200 Td, 70–80 % of the electron energy goes into electronic excitation, about 5 % is transferred to dissociation, 5 % is used for ionisation (increasing with E/n), while only 10 % goes into vibrational excitation (decreasing with E/n). Around 50 Td, however, only 10 % goes into electronic excitation and 90 % of the energy goes into vibrational excitations. It is important to keep in mind that the addition of different gases (e.g. Ar, He, N_2, H_2O, H_2, CH_4, etc.) has an influence on the distribution of these channels.[82] Hence, even during the pure decomposition of CO_2 into CO and O_2, there will be an effect on this distribution.

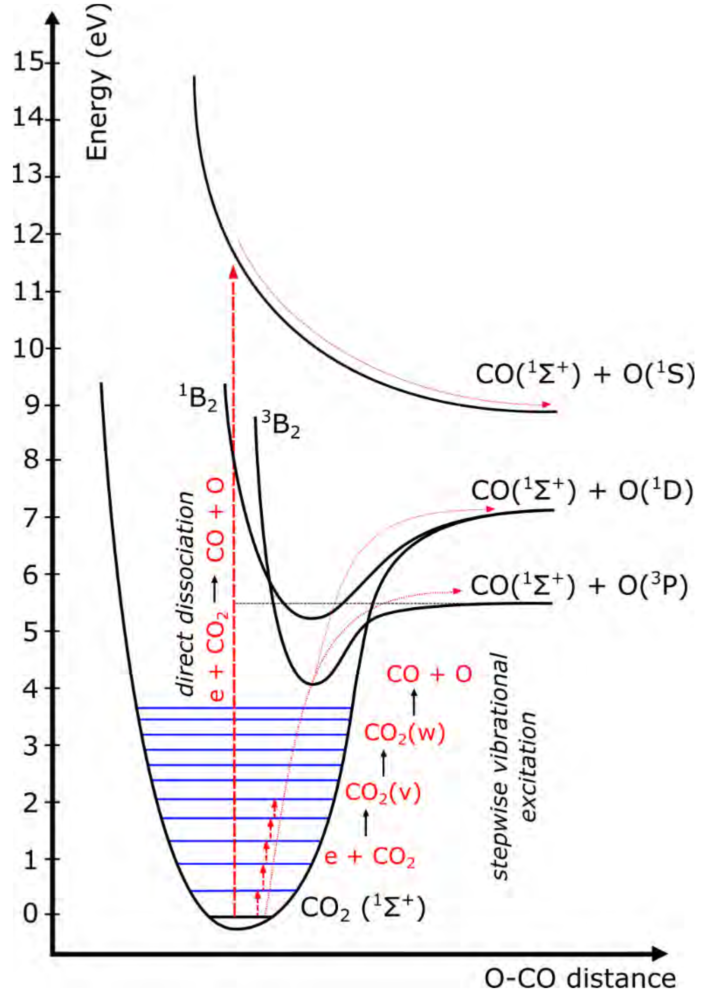

Figure 1-12. Schematic diagram of some CO_2 electronic and vibrational levels, illustrating that much more energy is needed for direct electronic excitation–dissociation than for stepwise vibrational excitation, i.e. the so-called ladder climbing process (Adopted from Bogaerts et al.[81] with permission form the Royal Society of Chemistry).

The distribution of energy into different modes, and especially the fraction going into vibrational excitation is very important, since, as mentioned above, it is known that the vibrational levels of CO_2 can play an important role in the efficient dissociation of CO_2. To achieve direct electron impact dissociation, an electron needs to have enough energy (> 7 eV) to excite CO_2 into a dissociative (i.e., repulsive) electronic state, which will lead to its dissociation into CO and O (see **Figure 1-12**). As such, the amount of energy spent is much higher than the theoretical value necessary for C=O bond breaking (i.e., 5.5 eV). Due to the special nature of the CO_2 molecule, a more efficient dissociation pathway is based on its vibrational excitation. This pathway starts with electron impact vibrational excitation of the lowest vibrational levels, followed by vibrational-vibrational (VV) collisions. This so-called “ladder-climbing” gradually populates the higher vibrational levels, which eventually lead to the dissociation of the CO_2 molecule (see also **Figure 1-12**). In this way it is possible to dissociate CO_2 more efficiently, since only the minimum amount of 5.5 eV for bond breaking is needed, compared to the overshoot in the case of electronic excitation-dissociation.[81]

4.1.5. Plasma chemistry

There are two main types of collisions that can occur in a plasma, i.e. elastic collisions and inelastic collisions. The former constitute collisions during which the internal energies of the colliding particles remain unaltered and thus they conserve the kinetic energy. The latter collisions, on the other hand, result in an energy transfer from the kinetic energy into internal energy (for example ionization processes).

As already mentioned, plasmas consist of a wide variety of species (i.e., molecules, atoms, radicals, ions, electrons, excited species and photons), which can all interact with each other in different ways. First of all, it is important to know that these different species react at varying time scales, based on which we can divide the plasma chemistry into two processes.

The primary process has a time scale around a couple of nanoseconds and generates active species, i.e. radicals, excited species and ions, mainly through collisions with the high energy electrons. This includes ionization, excitation, dissociation and charge transfer processes. During the secondary process, chemical reactions between the primary species, i.e. electrons, radicals, excited molecules and ions, take place, and this is usually completed within approximately 10 ms. A more detailed description of the main plasma chemical processes is listed in **Table 1.1**.

Table 1.1. Overview of the main plasma chemical processes. A and B represent atoms and M stands for a temporary collision partner.[14]

Electron/Molecular Reactions	
Excitation	$e^- + AB \rightarrow AB^* + e^-$
- Vibrational	$e^- + AB(V_1) \leftrightarrow AB^-(V_i) \rightarrow AB(V_2) + e^-$
- Rotational	$e^- + AB(R_1) \leftrightarrow AB^-(R_i) \rightarrow AB(R_2) + e^-$
- Electronic	$e^- + AB(E_1) \leftrightarrow AB^-(E_i) \rightarrow AB(E_2) + e^-$
Dissociation	$e^- + AB \rightarrow A + B + e^-$ $e^- + AB \rightarrow A + B^* + e^-$
Polar dissociation	$e^- + AB \rightarrow A^- + B^+ + e$
Attachment	$e^- + AB \rightarrow AB^-$ $e^- + A + B \rightarrow A^- + B$
Dissociative electron attachment	$e^- + AB \rightarrow (AB^-)^* \rightarrow A^- + B$
Non-dissociative ionization	$e^- + AB \rightarrow AB^+ + e^- + e^-$
Dissociative ionization	$e^- + AB \rightarrow A^+ + B + e^- + e^-$
Step-wise ionization	$e^- + A \rightarrow A^* + e^- \rightarrow A^+ + e^- + e^-$
Electron-ion recombination	$e^- + AB^+ \rightarrow AB$ $e^- + e^- + A^+ \rightarrow A^* + e^-$
Dissociative electron-ion recombination	$e^- + AB^+ \rightarrow (AB)^* \rightarrow A + B^*$
Radiative electron-ion recombination	$e^- + A^+ \rightarrow A^* \rightarrow A + h\upsilon$
Electron impact detachment	$e^- + AB^- \rightarrow AB + e^- + e^-$
Atomic/Molecular Reactions	
Penning dissociation	$M + AB \rightarrow A + B + M$
Penning ionization	$M^* + AB \rightarrow AB^+ + M + e^-$
Charge transfer	$A^+ + B \rightarrow A + B^+$ $A^- + B \rightarrow A + B^-$
Ion-ion recombination	$A^- + B^+ \rightarrow AB$ $A^- + B^+ + M \rightarrow AB + M$
Neutral recombination	$A + B + M \rightarrow AB + M$
Detachment	$A^- + B^* \rightarrow A + B + e^-$
Associative detachment	$A^- + B \rightarrow (AB^-)^* \rightarrow AB + e^-$
Decomposition	
Electronic	$e^- + AB \rightarrow A + B + e^-$
Atomic	$A^* + B_2 \rightarrow AB + B$
Synthesis	
Electronic	$A^* + B \rightarrow AB$
Atomic	$A + B \rightarrow AB$

4.2. Different types of plasma set-ups used for CO_2 conversion

As mentioned above, in recent years, there has been an increasing interest in the use of plasma technology for CO_2 conversion. Experiments are carried out in several types of plasmas. The most common types reported in the literature are dielectric barrier discharges (DBDs), microwave (MW), and gliding arc (GA) discharges, although other types have been used as well (e.g. radiofrequency, corona, glow, spark and nanosecond pulse discharges). A DBD is a typical example of a "non-thermal plasma", where the gas is more or less at room temperature, and the electrons are heated to temperatures of 2−3 eV (~ 20,000–30,000 K) by the strong electric field in the plasma. The MW and GA discharges are examples of "warm plasmas" (see above). The gas can reach temperatures up to 1000 K and more, and the electron temperature is typically up to a few eV. The operating conditions and characteristic features of the three major plasma types for CO_2 conversion will be explained, as well as for some other plasma types that have also been applied for CO_2 conversion.

4.2.1. Dielectric barrier discharge (DBD)

Dielectric barrier discharges (DBDs), also called silent discharges, have been known for more than a century. The first experimental investigations were reported by Siemens in 1857 and concentrated on the most well-known industrial application of DBDs, i.e., ozone generation.[70] For an extensive overview of the history, discharge physics and industrial applications of DBDs, we refer to the review of Kogelschatz et al.[70]

A DBD consists of two plane-parallel or concentric metal electrodes and, as its name suggests, it contains at least one dielectric barrier (e.g. glass, quartz, ceramic material or polymers) in between the electrodes.[68,70,76,83] The purpose of the dielectric barrier is to restrict the electric current and thus prevent the formation of sparks and/or arcs.[83] A gas flow is applied between the (discharge) gap, which can typically vary from 0.1 mm (e.g. in plasma displays), over 1 mm (e.g. for ozone generators) to several cm (e.g. in CO_2 lasers).[68,76] Typical planar (top) and cylindrical (bottom) DBD configurations are shown in **Figure 1-13**. In general, DBDs operate at approximately atmospheric pressure (0.1–10 atm, but usually 1 atm), while an alternating voltage with an amplitude of 1–100 kV and a frequency of a few Hz to MHz is applied between both electrodes.

To ignite the discharge, or more specifically, to transport current in the discharge gap, an electric field high enough to cause breakdown in the gas needs to be applied. This breakdown voltage (V_b) can be determined according to Paschen's Law, and is a function of the pressure (p) and the gap distance (d):

$$V_b = \frac{D \cdot pd}{ln\left(\frac{C \cdot pd}{ln(1/\gamma)}\right)}$$

where C, D and γ are gas (or mixture) specific parameters. Upon breakdown of the gas, most often a non-uniform plasma, consisting of a large number of micro-discharges (or filaments), is observed (indicated as purple in the top left panel of **Figure 1-13**). This mode is called the filamentary mode, and plasma formation is restricted to these micro-discharges. The occurrence of a filamentary mode, as opposed to a homogeneous glow mode, depends on the type of gas. Most gases, including CO_2, give rise to a filamentary mode. It is stated that the volume of the micro-discharges, and hence the plasma volume, comprises about 1–10 % of the total gas volume.[84,85] The rest of the gas is not ionised and serves as background reservoir to absorb the energy dissipated in the micro-discharges and to collect and transport the long-lived species created in the micro-discharges.[70] For a more detailed physical description on the formation of these micro-discharges, we refer to the review of Fridman et al.[76]

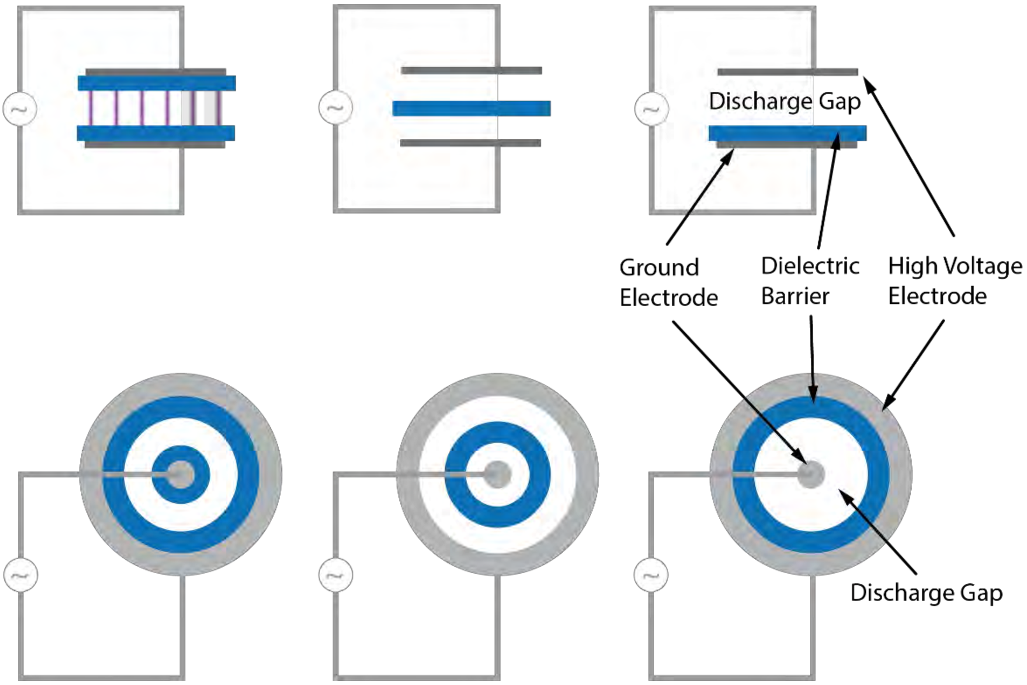

Figure 1-13. Basic planar (top) and cylindrical (bottom) dielectric barrier discharge configurations.

4.2.2. Microwave (MW) discharge

Microwave discharges operate according to a different principle and belong to the group of warm plasmas. They are electrode-less and as their name suggests, the electric power is applied as microwaves, i.e. electromagnetic radiation in the frequency range of 300 MHz to 10 GHz. There exist several different types of MW plasmas, e.g. cavity induced plasmas, free expanding atmospheric plasma torches, electron cyclotron resonance plasmas, surface wave discharges, etc. For more details about the different microwave discharges, we refer to several reviews in the literature.[14,68,83,86]

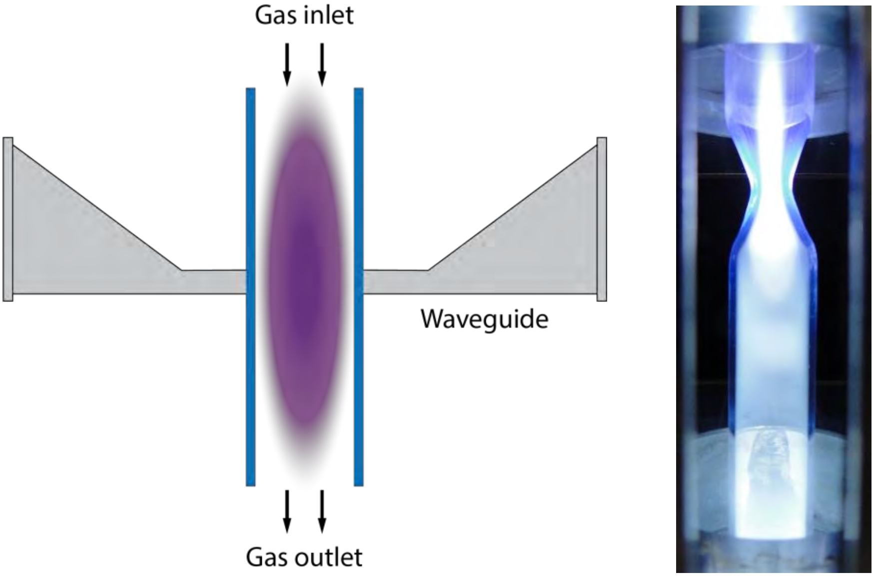

Figure 1-14. Schematic view (left) and picture (right; courtesy of Dutch Institute For Fundamental Energy Research (DIFFER)) of a MW discharge.

In the so-called surface wave discharge, which is most commonly used for CO_2 conversion research, the gas flows through a quartz tube—which is transparent to microwave radiation—intersecting with a rectangular wave guide, where the discharge is initiated, see **Figure 1-14**. This system, also called "guide-surfatron", involves surface waves. The microwaves propagate along the interface between the quartz tube and the plasma column. The wave energy is absorbed by the plasma. Characteristic features are the wavelength (815 MHz or 2.45 GHz), which is comparable to the length of the apparatus, and the short period of the exciting microwave field. Surface wave discharges can be created both at reduced and at atmospheric pressure, but in the pressure regime above 0.1 atm they approach a state of LTE.[68]

4.2.3. Gliding arc (GA) discharge

A gliding arc (GA) discharge is also a warm plasma, combining advantages of thermal and non-thermal plasma systems.[76] It is a transient type of arc discharge. At high currents, the periodic discharge typically evolves during one cycle from arc to a strongly non-equilibrium discharge. The non-equilibrium GA is a very sophisticated physical phenomenon: this transitional quasi-equilibrium/non-equilibrium discharge is essentially non-uniform in time and in space, and includes an internal transition from thermal to non-thermal mechanisms of ionization.[76]

A classical GA plasma is an auto-oscillating periodic discharge, where the gas flows between two diverging flat electrodes. When applying a potential difference between both electrodes, an arc plasma is formed at the narrowest gap, which is dragged by the gas flow towards rising inter-electrode distance, until it extinguishes and a new arc is ignited at the shortest inter-electrode gap. More specifically, the length of the arc column increases together with the voltage until it exceeds its critical value (l_{crit}). At this point, heat losses from the plasma column begin to exceed the supplied energy and it is no longer possible to sustain the plasma in its LTE state, resulting in a fast transition into a non-LTE state. The discharge cools rapidly to gas temperature but the plasma conductivity is maintained by a high value of the electron temperature ($T_e \sim 1$ eV, which is most suitable for efficient vibrational excitation of CO_2). After this fast transition, the GA continues its evolution under non-LTE conditions, until the length reaches a new critical value ($l \sim 3 \cdot l_{crit}$) leading to the decay of the discharge, after which the evolution repeats from the initial breakdown. During this cycle, up to 75–80 % of the energy can be dissipated in the non-LTE zone of the gliding arc. It is this effect that permits the stimulation of chemical reactions in regimes quite different from conventional thermal reaction chemistry. When the GA is operated under milder conditions, i.e. lower currents and high frequencies, this transition to the non-LTE phase can occur in the order of nanoseconds. As a result the GA operates in the non-LTE regime starting almost immediately after its ignition, and a higher fraction of the discharge energy can be consumed by the non-LTE phase.[87–89]

The classical GA plasma, however, also exhibits some disadvantages. The flat 2D electrode geometry makes it less compatible with industrial systems, and the gas conversion is non-uniform and quite limited, because a considerable fraction of the gas does not pass through the active plasma region. Moreover, a high gas flow rate is needed to drag the arc, so the gas residence time is limited, thereby further limiting the conversion. Therefore, a 3D cylindrical GA plasma reactor was developed a few years ago, which makes use of vortex flow stabilization.[90] The gas flows in the reactor through a tangential inlet. An arc is again formed between both electrodes, which is dragged with the tangential gas flow, thereby expanding until it extinguishes, followed by a new cycle. Basically, the arc is again gliding between the anode and cathode, and it is stabilized in the centre of the reactor. Depending on the diameter of the anode tube, a forward or reverse vortex gas flow is created. If the anode diameter is equal to the cathode diameter, the gas can leave the reactor through the anode outlet, leading only to a forward vortex flow. On the other hand, if the anode diameter is smaller than the cathode diameter, the gas cannot immediately leave the reactor, and will first flow upwards close to the walls, in a forward vortex. As this gas is still cold, it creates an isolating and cooling effect, protecting the reactor walls from the warm plasma arc in the centre. When it reaches the upper end of the reactor, it will have lost some speed due to friction and inertia, and when flowing downwards, it moves in a smaller inner vortex, a so-called reverse vortex, where it mixes with the plasma arc, resulting in a more energy-efficient conversion. The reverse vortex flow GA is also called “gliding arc plasmatron” (GAP). **Figure 1.16** shows the difference between these two types of GAs.

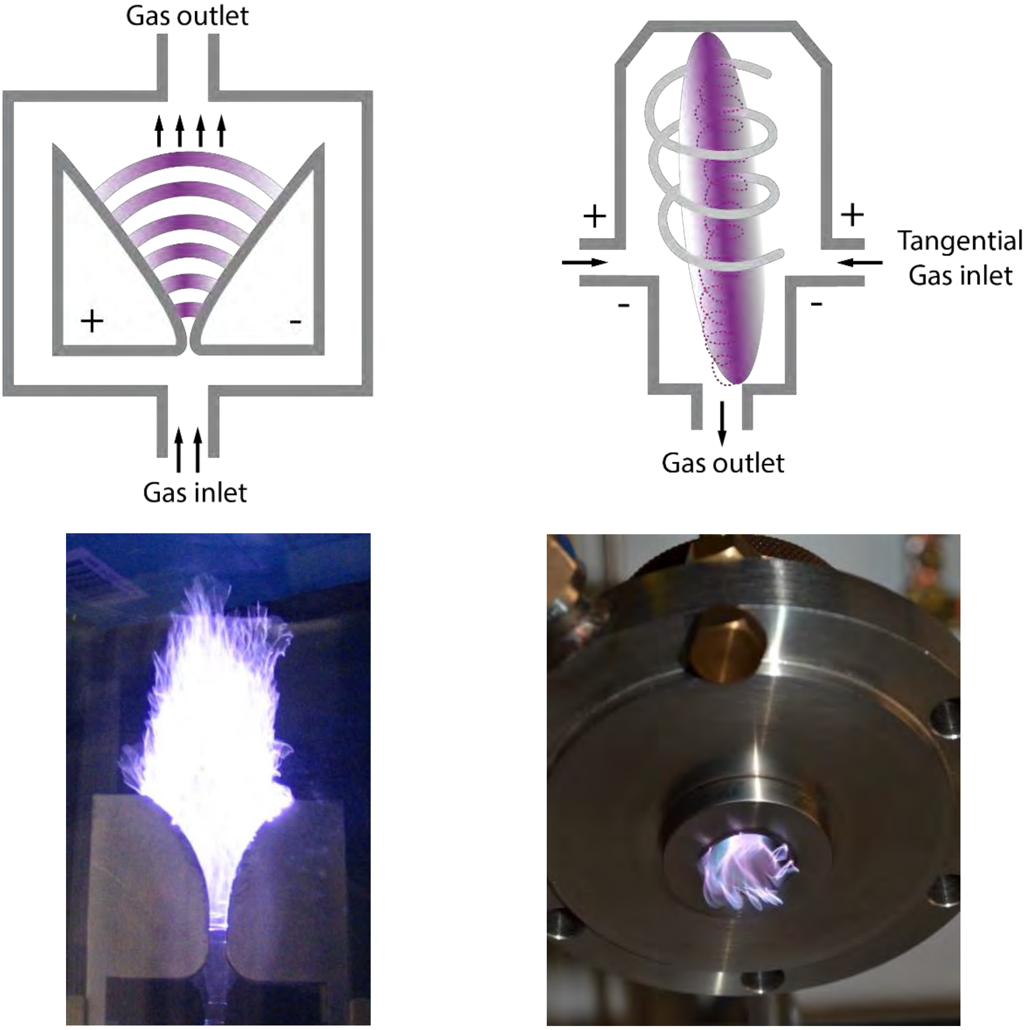

Figure 1-15. Schematic representation of the classical GA (top left), and the GAP (top right) configuration and pictures of the classical GA (bottom left; courtesy of University of Manchester) and GAP (bottom right).

4.2.4. Other plasma types used for CO_2 conversion

Besides the above three main discharge types for CO_2 conversion, some research is also being performed with other plasma types, which will be briefly discussed here. They include the radio frequency (RF) discharge, several different types of atmospheric pressure glow discharges (APGDs), the corona discharge, spark discharge and nanosecond pulsed discharge.

RF discharges usually operate in the 1–100 MHz frequency range, resulting in a corresponding wavelength (300–3 m) which is much larger than the plasma reactor dimensions. The power coupling can be done through capacitive or inductive coupling, resulting in capacitively coupled plasma (CCP) and inductively coupled plasma (ICP). These kind of discharges are mainly applied to thin-film deposition, plasma etching, sputtering of materials and as ion source in mass spectrometry,[86] but some research is also being performed for CO_2 conversion applications, as will be illustrated in **Chapter 6**. An RF source operating at low pressure both with and without the influence of an external magnetic field has been used. The advantages for CO_2 conversion are its capability of obtaining high electron densities at low gas temperature.

When a sufficiently large electric field is applied, corona discharges occur near sharp points, edges or thin wires when used as electrode. When a high negative voltage is applied to the electrode, it is acting as cathode and is considered as a negative corona discharge. When a positive voltage is applied, it is considered as a positive corona discharge. Corona discharges are always non-uniform with a strong electric field, ionization and luminosity close to the electrode, whereas the charged particles are dragged to the other electrode by weak electric fields. They are often operated in a pulsed mode, to increase the power, while inhibiting the transition of streamer formation into sparks.[14] An advantage of corona discharges compared to DBDs is that they are relatively easy to establish, however their performance towards the CO_2 conversion processes is quite similar, as will become clear from **Chapter 6**.

When a streamer is able to connect two electrodes, without the presence of a pulsed power supply (see corona discharge above) or the presence of a dielectric (see DBD), a spark discharge can develop by a further growth of the current.[14] However, when the amount of power provided is restricted, the discharge cannot develop into a stationary (thermal) arc and the discharge extinguishes within several hundred microseconds. Hence, spark discharges consist of an initiation of streamers that develop into highly energetic spark channels, which extinguish and reignite periodically. Lightning is a typical example of a spark discharge.

A wide variety of plasma set-ups fall under APGDs, such as miniaturized direct current (dc) GDs, microhollow cathode dc discharges, RF discharges, as well as DBDs.[68] The main advantage of APGDs is the absence of vacuum conditions compared to regular glow discharges, while operating without elevated temperatures. Depending on the gas mixture and electrode configuration, the discharge can operate in stable homogeneous glow or filamentary glow mode. For example, a DBD can operate in APGD mode, in this case the discharge benefits from the average power densities of a DBD but operating in a uniform homogeneous glow mode, benefiting the uniform gas treatment.[14] This discharge is interesting for DRM due to its special characteristics of electron density ($3x10^{12}$ cm^{-3}), electron temperature (~2 eV, suitable for vibrational excitation of CO_2), and plasma gas temperature (900 K), which is lower than that of thermal plasma but higher than that of DBDs and corona discharges.

Finally, nanosecond pulsed discharges are basically discharges which rely on repetitively pulsed excitation, through nanosecond scale pulse rise time and duration. This leads to a highly non-LTE state with very high plasma densities for a relatively low power consumption due to the short pulse durations. Whereas (sub)microsecond pulsed discharges are initiated by Townsend discharges, nanosecond pulsed discharges ignite instantaneously—without the involvement of secondary electrons. Furthermore, the discharge remains in a glow-like (rather than filamentary) mode despite the high electric field. The interest in shorter pulses, is not because of the duration of the discharge itself, but rather because they offer better control of the electron energy than continuous wave discharges, depending on the pulse length.[91] Thus, more energy can be directed towards the desired dissociation channels.

4.3. Plasma catalysis

As with most of the technologies described in section 3, plasma set-ups can also be combined with a packing material or catalyst, giving rise to plasma catalysis. Plasma catalysis is an emerging branch of plasma processing at the interface of a variety of disciplines, including among others physical chemistry, material science, nanotechnology, catalysis, plasma physics and plasma chemistry. In short, its objective is to enhance plasma reactions by adding a catalyst to the reaction cycle. Theoretically speaking, combining plasma with catalysis offers the best of two worlds. Inert molecules are activated by the plasma under mild conditions, and subsequently the activated species selectively recombine at the catalyst surface to yield the desired products. This will be especially important to further advance and optimize the direct oxidative liquefaction pathway of plasmachemical CO_2 conversion, in order to selectively produce the desired liquid products. In this section we will give a brief overview on the different approaches and possible interactions between plasma and catalyst. For more extensive details we refer to several broad reviews on this specific topic that have recently been published.[73,92–94]

4.3.1. Approaches

Plasmas and catalysts can be combined in two main configurations, as illustrated in **Figure 1-16**. In the first, so-called two-stage configuration (**Figure 1-16(b)**), the catalyst is spatially separated from the plasma region, either upstream or downstream, but the main configuration is downstream. In the second, so-called one-stage configuration (**Figure 1-16(c)**), the catalyst is placed inside the discharge region. In a traditional thermal catalysis experiment, molecules are dissociatively adsorbed onto the catalyst with the energy being supplied in the form of heat. In plasma-assisted catalysis, species are activated by the plasma due to excitation, ionization or dissociation by electrons in the gas phase or on the catalyst surface.

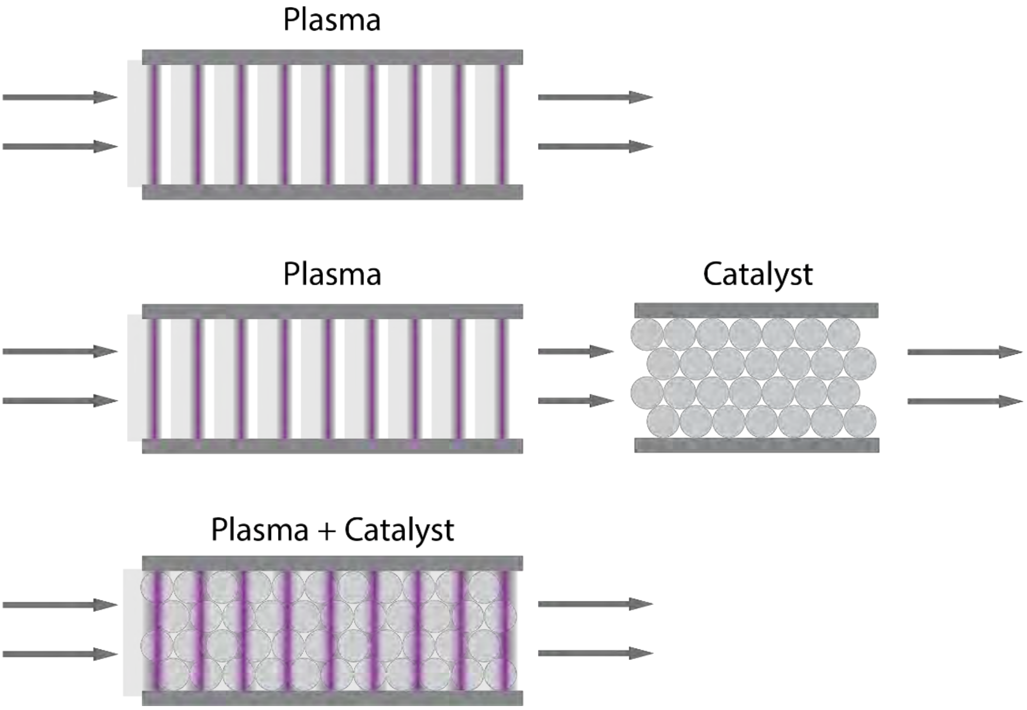

Figure 1-16. Schematic diagram of the different plasma-catalyst configurations, (a) plasma alone without catalyst, (b) catalyst downstream of the discharge, and (c) catalyst directly inside the discharge zone. These examples mainly apply to a DBD. For MW and GA discharges, the catalyst is most commonly placed in the downstream region.

The major difference between the one-stage and two-stage configuration is the kind of species to which the catalyst is exposed. In the two-stage configuration, the end-products and the long-lived intermediates will interact with the catalyst, while in the one-stage configuration, the catalyst can also interact with all the short-lived species, including excited species, radicals, photons, and electrons. Furthermore, in this configuration the catalyst may also be influenced by the plasma and vice-versa (see below). Besides plasma catalysis, the preparation and modification of catalysts by plasma treatments is gaining increased attention, especially for catalysts with a low thermal stability.[93]

The most widely investigated and for this review most interesting configuration is the one-stage, in which the catalyst is placed inside the discharge region, either completely or only partially occupying the discharge zone. The catalyst itself can be introduced in the discharge as pellets, (fine) powders, foams, honeycomb monoliths, different electrode materials and electrode coatings, or coated quartz wool. The ease of implementing a catalyst into the discharge zone greatly varies depending on the type of plasma reactor used. In general, due to their simple geometry and operation close to room temperature, implementation of a catalyst in a DBD reactor is very easy. Although MWs also have a simple geometry, due to the high gas temperature inside the discharge zone (1000–2000 K compared to 300–400 K for DBD) catalysts are often placed downstream, due to their low thermal stability. Finally, GA discharges have rather complex geometries and the same higher gas temperatures, thus catalysts are typically introduced downstream, although the use of a spouted bed is also reported.[95] If these MW and GA discharges can be operated at slightly lower temperatures (≤ 1000 K), this would open the way for using thermal catalysts inside the discharge zone, which would yield new possibilities.

4.3.2. Synergetic effects

The resulting interactions when combining a plasma with a catalyst for plasma-based CO_2 conversion, often yield improved process results in terms of conversion, selectivity, yield and energy efficiency. This surplus effect, as shown in **Figure 1-17**, is a complex phenomenon originating from the interplay between the various plasma-catalyst interactions and is often termed synergy, when the combined effect is larger than the sum of the two separate.[92] Note, that most research to date regarding this effect has been performed for DBDs.

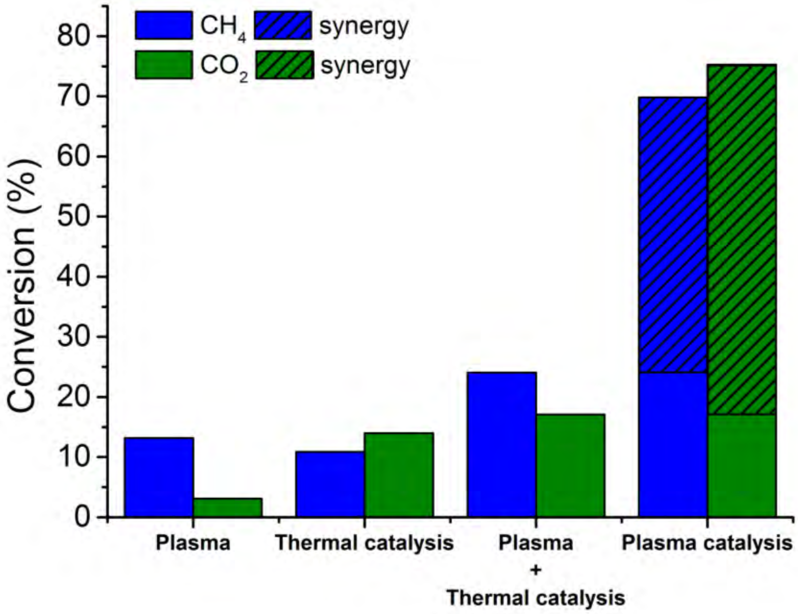

Figure 1-17. Demonstration of the synergy of plasma catalysis for dry reforming of methane, adapted from Zhang et al.[96]

The complex interactions can be subdivided into two categories, i.e., the effects of the plasma on the catalyst, and vice versa, the effects of the catalyst on the plasma.[92,97] Secondly, it is important to distinguish between two types of effects, i.e., physical and chemical effects. While the physical effects are mainly responsible for gaining a better energy efficiency, the chemical effects can lead to an improved selectivity toward targeted products. In the case of CO_2 splitting, mainly CO and O_2 are formed, so the primary added value of the catalyst is to increase the energy efficiency, although the conversion can also be improved by chemical effects, such as enhanced dissociative chemisorption due to catalyst acid/basic sites. When adding a co-reactant (e.g., CH_4, H_2O, H_2), the catalyst allows to modify the selectivity toward targeted products.

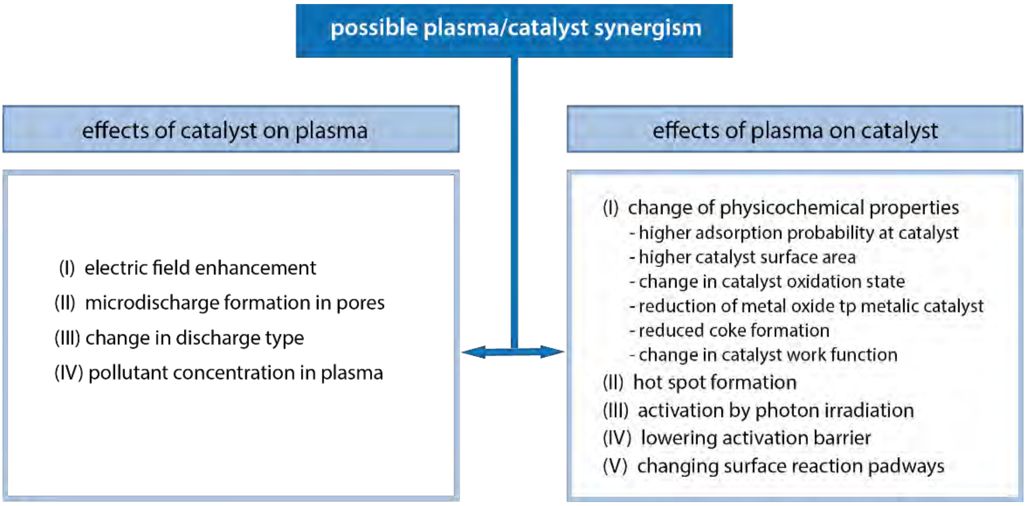

Figure 1-18. An overview of the possible effects of the catalyst on the plasma and vice versa, possibly leading to synergism in plasma catalysis.

An overview of the plasma-catalyst interactions is given in **Figure 1-18**. When adding a catalyst, the following effects on the plasma have been reported: (i) an enhancement of the electric field by geometric distortion and surface roughness; (ii) the formation of microdischarges inside the pores of the catalyst material, due to the very strong electric field inside the pores, leading to different characteristics compared to the bulk; (iii) a change of the discharge type, because the presence of insulating surfaces promotes the development of surface discharges; (iv) the adsorption of species on the catalyst surface, affecting their concentration and conversion due to longer retention times. All the effects of the catalyst on the plasma can thus generally be considered as physical effects. The reported effects of the plasma on the catalyst, on the other hand, are both of a physical and chemical nature. They include (i) changes of its physicochemical properties, such as higher adsorption probability at the catalyst surface, higher catalyst surface area, changed catalyst oxidation state, reduction of metal oxide catalysts to their metallic form, reduced coke formation on the surface and change of the catalyst work function; (ii) the formation of hot spots on the surface due to the formation of strong microdischarges; (iii) catalyst activation by photon irradiation emitted by the excited plasma species (although this effect is probably of minor importance due to the low photon fluxes); (iv) lowered activation barriers due to more reactive vibrationally excited plasma species and consequently the possibility for non-adiabatic barrier crossings; (v) changes in the reaction pathways due to the presence of a wide variety of (re)active species.

While the physical effects have been more extensively studied, such as the plasma behaviour in packed bed DBD reactors[98] or inside catalyst pores,[99] the chemical effects are less understood, mainly because they are often correlated with the physical effects. Indeed, in a DBD, the catalyst is mostly introduced as a packed bed, making it difficult to distinguish between the two effects. Hence, more systematic studies on both the physical and chemical effects of the catalyst material are highly needed.[92] Furthermore, as summarized in **Figure 1-19**, the plasma and catalyst both have their influence on the gas composition, and at the same time the plasma influences the catalyst properties and vice-versa, as mentioned above. Therefore, both the gas composition and the plasma and catalyst properties continuously influence each other, and are influenced by the plasma chemistry and surface chemistry. Hence, it is recommended to develop tailored catalysts for plasma catalysis, rather than simply relying on classical catalysts. This will be discussed further in **Chapter 6.**

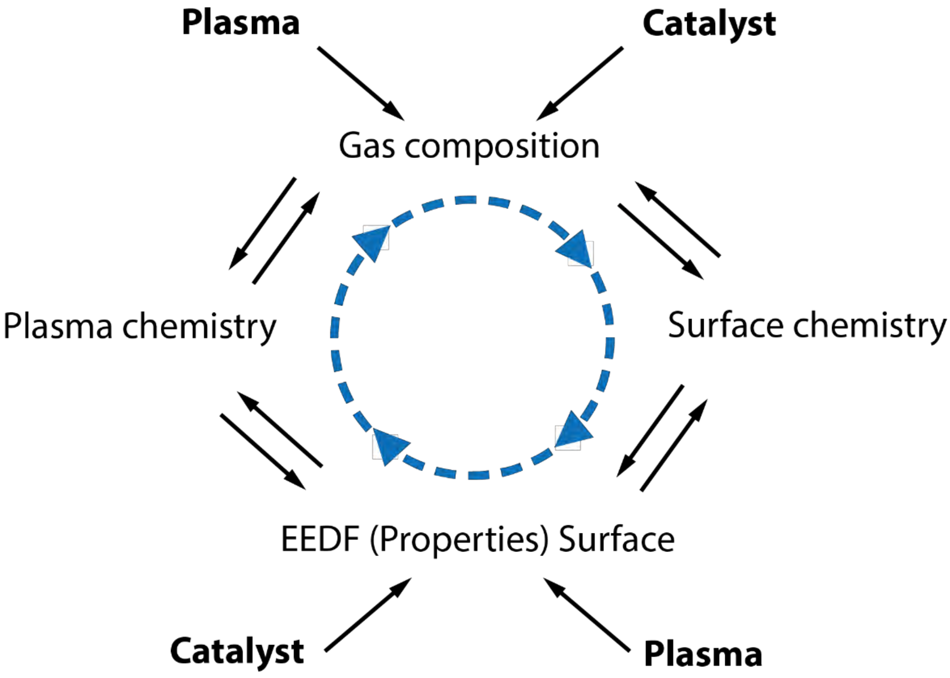

Figure 1-19. Visualization of the continuous influence of plasma and catalyst on the gas conversion process (EEDF = electron energy distribution function).

5. References

1 R. K. Pachauri and L. A. Meyer, *IPCC, 2014: Climate Change 2014: Synthesis Report. Contribution of Working Groups I, II and III to the Fifth Assessment Report of the Intergovernmental Panel on Climate Change*, Geneva, Switzerland, 2014.

2 L. Johnson, J. Grant and P. L. Low, *Two degrees of separation: ambition and reality: Low Carbon Economy Index 2014*, 2014.

3 C. B. Field, V. R. Barros, D. J. Dokken, K. J. Mach, M. D. Mastrandrea, T. E. Bilir, M. Chatterjee, K. L. Ebi, Y. O. Estrada, R. C. Genova, B. Girma, E. S. Kissel, A. N. Levy, S. MacCracken, P. R. Mastrandrea and L. L. White, *IPCC, 2014: Climate Change 2014 Impacts, Adaptation, and Vulnerability. Part A: Global and Sectoral Aspects. Contribution of Working Group II to the Fifth Assessment Report of the Intergovernmental Panel on Climate Change*, Cambridge University Press, 2014.

4 C. Lagarde, *Int. Monet. Fund*, 2013.

5 G. Nichols Roth, *G7 Climate Change The New Economy*, World News -Climate Change The New Economy Ltd., 2015.

6 A. Goeppert, M. Czaun, J.-P. Jones, G. K. Surya Prakash and G. A. Olah, *Chem. Soc. Rev.*, 2014, **43**, 7995–8048.

7 J. Albo, M. Alvarez-Guerra, P. Castaño and A. Irabien, *Green Chem.*, 2015, **17**, 2304–2324.

8 G. Fiorani, W. Guo and A. W. Kleij, *Green Chem.*, 2015, **17**, 1375–1389.

9 W. McDonough, M. Braungart, P. Anastas and J. Zimmerman, *Environ. Sci. Technol.*, 2003, **37**, 434A–441A.

10 G. Centi, E. A. Quadrelli and S. Perathoner, *Energy Environ. Sci.*, 2013, **6**, 1711–1731.

11 G. Centi and S. Perathoner, *Catal. Today*, 2009, **148**, 191–205.

12 M. Mikkelsen, M. Jørgensen and F. C. Krebs, *Energy Environ. Sci.*, 2010, **3**, 43–81.

13 S. Samukawa, M. Hori, S. Rauf, K. Tachibana, P. Bruggeman, G. Kroesen, J. C. Whitehead, A. B. Murphy, A. F. Gutsol, S. Starikovskaia, U. Kortshagen, J.-P. Boeuf, T. J. Sommerer, M. J. Kushner, U. Czarnetzki and N. Mason, *J. Phys. D. Appl. Phys.*, 2012, **45**, 253001.

14 A. Fridman, *Plasma chemistry*, Cambridge University Press, New York, 2008.

15 J. Tsao, N. Lewis and G. Crabtree, 2006, 1–24.

16 J. L. Sawin, K. Seyboth and F. Sverrisson, *Renewables 2016: Global Status Report*, 2016.

17 Z. Jiang, T. Xiao, V. L. Kuznetsov and P. P. Edwards, *Philos. Trans. A. Math. Phys. Eng. Sci.*, 2010, **368**, 3343–64.

18 M. Aresta, A. Dibenedetto and A. Angelini, *Chem. Rev.*, 2014, **114**, 1709–1742.

19 P. L. Spath and D. C. Dayton, *Natl. Renew. Energy Lab.*, 2003, **December**, 1–160.

20 J. Rifkin, *The hydrogen economy: the creation of the worldwide energy web and the redistribution of power on earth*, Putnam, New York, 2002.

21 U. Bossel, *Proc. IEEE*, 2006, **94**, 1826–1836.

22 S. Rayne, *Nat. Preced.*, 2008, 1–17.

23 D. D. Wagman, J. E. Kilpatrick, W. J. Taylor, K. S. Pitzer and F. D. Rossini, *J. Res. Natl. Bur. Stand. (1934).*, 1945, **34**, 143–161.

24 C. Song, *Catal. Today*, 2006, **115**, 2–32.

25 Y. Nigara and B. Cales, *Bull. Chem. Soc. Jpn.*, 1986, **59**, 1997–2002.

26 N. Itoh, M. A. Sanchez, W.-C. Xu, K. Haraya and M. Hongo, *J. Memb. Sci.*, 1993, **77**, 245–253.

27 Y. Fan, J. Ren, W. Onstot, J. Pasale, T. T. Tsotsis and F. N. Egolfopoulos, *Ind. Eng. Chem. Res.*, 2003, **42**, 2618–2626.

28 J. Barber, *Chem. Soc. Rev.*, 2009, **38**, 185–196.

29 S. Berardi, S. Drouet, L. Francàs, C. Gimbert-Suriñach, M. Guttentag, C. Richmond, T. Stoll and A. Llobet, *Chem. Soc. Rev.*, 2014, **43**, 7501–7519.

30 J.-M. Lavoie, *Front. Chem.*, 2014, **2**, 1–17.

31 D. Pakhare and J. Spivey, *Chem. Soc. Rev.*, 2014, **43**, 7813–7837.

32 D. Leckel, *Energy and Fuels*, 2009, **23**, 2342–2358.

33 J. R. H. Ross, *Catal. Today*, 2005, **100**, 151–158.

34 G. A. Olah, A. Goeppert and G. K. S. Prakash, *J. Org. Chem.*, 2009, **74**, 487–498.

35 J. Ma, N. Sun, X. Zhang, N. Zhao, F. Xiao, W. Wei and Y. Sun, *Catal. Today*, 2009, **148**, 221–231.

36 E. A. Quadrelli, G. Centi, J.-L. Duplan and S. Perathoner, *ChemSusChem*, 2011, **4**, 1194–1215.

37 A. M. Appel, J. E. Bercaw, A. B. Bocarsly, H. Dobbek, D. L. Dubois, M. Dupuis, J. G. Ferry, E. Fujita, R. Hille, P. J. a Kenis, C. a. Kerfeld, R. H. Morris, C. H. F. Peden, A. R. Portis, S. W. Ragsdale, T. B. Rauchfuss, J. N. H. Reek, L. C. Seefeldt, R. K. Thauer and G. L. Waldrop, *Chem. Rev.*, 2013, **113**, 6621–6658.

38 W. Wang, S. Wang, X. Ma and J. Gong, *Chem. Soc. Rev.*, 2011, **40**, 3703–3727.

39 M. A. A. Aziz, A. A. Jalil, S. Triwahyono and A. Ahmad, *Green Chem.*, 2015, **17**, 2647–2663.

40 B. Hu, C. Guild and S. L. Suib, *J. CO2 Util.*, 2013, **1**, 18–27.

41 S. G. Jadhav, P. D. Vaidya, B. M. Bhanage and J. B. Joshi, *Chem. Eng. Res. Des.*, 2014, **92**, 2557–2567.

42 E. V. Kondratenko, G. Mul, J. Baltrusaitis, G. O. Larrazabal, J. Perez-Ramirez, G. O. Larrazábal and J. Pérez-Ramírez, *Energy Environ. Sci.*, 2013, **6**, 3112–3135.

43 J. Qiao, Y. Liu, F. Hong and J. Zhang, *Chem. Soc. Rev.*, 2014, **43**, 631–675.

44 B. Kumar, M. Llorente, J. Froehlich, T. Dang, A. Sathrum and C. P. Kubiak, *Annu. Rev. Phys. Chem.*, 2012, **63**, 541–569.

45 I. Ganesh, *Renew. Sustain. Energy Rev.*, 2014, **31**, 221–257.

46 S. Verma, B. Kim, H.-R. 'Molly' Jhong, S. Ma and P. J. A. Kenis, *ChemSusChem*, 2016, **9**, 1972–1979.

47 S. Das and W. M. A. Wan Daud, *RSC Adv.*, 2014, **4**, 20856–20893.

48 G. P. Smestad and A. Steinfeld, *Ind. Eng. Chem. Res.*, 2012, **51**, 11828–11840.

49 J. R. Scheffe and A. Steinfeld, *Mater. Today*, 2014, **17**, 341–348.

50 Y. Izumi, *Coord. Chem. Rev.*, 2013, **257**, 171–186.

51 W. C. Chueh, C. Falter, M. Abbott, D. Scipio, P. Furler, S. M. Haile and A. Steinfeld, *Science (80-.).*, 2010, **330**, 1797–1801.

52 A. H. McDaniel, E. C. Miller, D. Arifin, A. Ambrosini, E. N. Coker, R. O'Hayre, W. C. Chueh and J. Tong, *Energy Environ. Sci.*, 2013, **6**, 2424–2428.

53 M. Romero and A. Steinfeld, *Energy Environ. Sci.*, 2012, **5**, 9234–9245.

54 D. Arifin, V. J. Aston, X. Liang, A. H. McDaniel and A. W. Weimer, *Energy Environ. Sci.*, 2012, **5**, 9438–9443.

55 P. Furler, J. R. Scheffe and A. Steinfeld, *Energy Environ. Sci.*, 2012, **5**, 6098–6103.

56 E. N. Coker, A. Ambrosini, M. a. Rodriguez and J. E. Miller, *J. Mater. Chem.*, 2011, **21**, 10767–10776.

57 B. Meredig and C. Wolverton, *Phys. Rev. B*, 2009, **80**, 245119.

58 S. C. Roy, O. K. Varghese, M. Paulose and C. a Grimes, *ACS Nano*, 2010, **4**, 1259–1278.

59 P. M. Schenk, S. R. Thomas-Hall, E. Stephens, U. C. Marx, J. H. Mussgnug, C. Posten, O. Kruse and B. Hankamer, *BioEnergy Res.*, 2008, **1**, 20–43.

60 L. Brennan and P. Owende, *Renew. Sustain. Energy Rev.*, 2010, **14**, 557–577.

61 R. Halim, M. K. Danquah and P. a. Webley, *Biotechnol. Adv.*, 2012, **30**, 709–732.

62 Y. Shen, *RSC Adv.*, 2014, **4**, 49672–49722.

63 W. M. Budzianowski, *Renew. Sustain. Energy Rev.*, 2012, **16**, 6507–6521.

64 J. A. Martens, A. Bogaerts, N. De Kimpe, P. A. Jacobs, G. B. Marin, K. Rabaey, M. Saeys and S. Verhelst, *ChemSusChem*, 2017, **10**, 1039–1055.

65 A. Navarrete, G. Centi, A. Bogaerts, A. Martin, A. York and G. Stefanidis, *Energy Technol.*, 2017.

66 X. Zhang, C. S. Lee, D. M. P. Mingos and D. O. Hayward, *Catal. Letters*, 2003, **88**, 129–139.

67 B. Fidalgo, A. Domínguez, J. Pis and J. Menéndez, *Int. J. Hydrogen Energy*, 2008, **33**, 4337–4344.

68 A. Bogaerts, E. Neyts, R. Gijbels and J. Van der Mullen, *Spectrochim. Acta - Part B At. Spectrosc.*, 2002, **57**, 609–658.

69 E. Gomez, D. A. Rani, C. R. Cheeseman, D. Deegan, M. Wise and A. R. Boccaccini, *J. Hazard. Mater.*, 2009, **161**, 614–626.

70 U. Kogelschatz, *Plasma Chem. plasma Process.*, 2003, **23**, 1–46.

71 X. Guofeng and D. Xinwei, *Energy*, 2012, **47**, 333–339.

72 O. Koeta, N. Blin-Simiand, W. Faider, S. Pasquiers, A. Bary and F. Jorand, *Plasma Chem. Plasma Process.*, 2012, **32**, 991–1023.

73 H. L. Chen, H. M. Lee, S. H. Chen, M. B. Chang, S. J. Yu and S. N. Li, *Environ. Sci. Technol.*, 2009, **43**, 2216–2227.

74 B. S. Patil, N. Cherkasov, J. Lang, A. O. Ibhadon, V. Hessel and Q. Wang, *Appl. Catal. B Environ.*, 2016, **194**, 123–133.

75 A. Foote, J. Dedrick, D. O’Connell, M. North and T. Gans, in *APS Gaseous Electronics Conference*, 2016.

76 A. Fridman, A. Chirokov and A. Gutsol, *J. Phys. D. Appl. Phys.*, 2005, **38**, R1–

R24.

77 T. Kozák and A. Bogaerts, *Plasma Sources Sci. Technol.*, 2014, **23**, 45004.

78 T. Kozák and A. Bogaerts, *Plasma Sources Sci. Technol.*, 2015, **24**, 15024.

79 A. Berthelot and A. Bogaerts, *J. Phys. Chem. C*, 2017, in press.

80 A. Bogaerts, A. Berthelot, S. Heijkers, S. Kolev, R. Snoeckx, S. R. Sun, G. Trenchev, K. van Laer and W. Wang, *Plasma Sources Sci. Technol.*, 2017, in press.

81 A. Bogaerts, T. Kozák, K. van Laer and R. Snoeckx, *Faraday Discuss.*, 2015, **183**, 217–232.

82 A. Janeco, N. R. Pinhao and V. Guerra, *J. Phys. Chem. C*, 2015, **119**, 109–120.

83 C. Tendero, C. Tixier, P. Tristant, J. Desmaison and P. Leprince, *Spectrochim. Acta Part B At. Spectrosc.*, 2006, **61**, 2–30.

84 A. Bogaerts, W. Wang, A. Berthelot and V. Guerra, *Plasma Sources Sci. Technol.*, 2016, **25**, 55016.

85 R. Aerts, W. Somers and A. Bogaerts, *ChemSusChem*, 2015, **8**, 702–716.

86 H. Conrads and M. Schmidt, *Plasma Sources Sci. Technol.*, 2000, **9**, 441–454.

87 S. R. Sun, H. X. Wang, D. H. Mei, X. Tu and A. Bogaerts, *J. CO2 Util.*, 2017, **17**, 220–234.

88 W. Wang, B. S. Patil, S. Heijkers, V. Hessel and A. Bogaerts, *ChemSusChem*, 2017, in press.

89 X. Tu, H. J. Gallon and J. C. Whitehead, 2011, 28–31.

90 T. Nunnally, K. Gutsol, A. Rabinovich, A. Fridman, A. Gutsol and A. Kemoun, *J. Phys. D. Appl. Phys.*, 2011, **44**, 274009.

91 F. Iza, J. L. Walsh and M. G. Kong, *IEEE Trans. Plasma Sci.*, 2009, **37**, 1289–1296.

92 E. C. Neyts, K. Ostrikov, M. K. Sunkara and A. Bogaerts, *Chem. Rev.*, 2015, **115**, 13408–13446.

93 J. C. Whitehead, *J. Phys. D. Appl. Phys.*, 2016, **49**, 243001.

94 E. C. Neyts and A. Bogaerts, *J. Phys. D. Appl. Phys.*, 2014, **47**, 224010.

95 H. Lee and H. Sekiguchi, *J. Phys. D. Appl. Phys.*, 2011, **44**, 274008.

96 A. Zhang, A. Zhu, J. Guo, Y. Xu and C. Shi, *Chem. Eng. J.*, 2010, **156**, 601–606.

97 E. C. Neyts and K. Ostrikov, *Catal. Today*, 2015, **256**, 23–28.

98 K. Van Laer and A. Bogaerts, *Plasma Sources Sci. Technol.*, 2016, **25**, 15002.

99 Y. R. Zhang, K. Van Laer, E. C. Neyts and A. Bogaerts, *Appl. Catal. B Environ.*, 2016, **185**, 56–67.

CHAPTER 2

Plasma-based CO_2 conversion :

Modelling and experiments

1. Aim of the work and outline of the thesis

The aim of this PhD dissertation is to contribute to the central research question, whether plasma technology can evolve into a valuable technology for the conversion of CO_2—preferably its transformation into value-added chemicals and/or fuels, as outlined in **Chapter 1**. Due to the complexity of the entire process, this question cannot be readily answered and requires a multidisciplinary and integrated approach, conducted in a concerted action by plasma physicists, process engineers, chemists, material scientists, etc. Therefore, it is necessary to first seek answers to some other questions related to specific aspects of this process. A lot of research in this domain is still based on assumptions without a good understanding of the ongoing (chemical and physical) plasma processes, while the latter is obviously an important condition for obtaining progress in this field. As such, there is a clear need for modelling, to better understand and interpret the experimental results and more importantly to improve existing experiments.

By using computer simulations in combination with experiments, this PhD work contributes to the development of several reaction chemistry sets used for a better understanding of the complex plasma chemistry taking place in a dielectric barrier discharge (DBD) and unravelling the underlying chemical reaction pathways. Both the model and the experiments will be outlined in this chapter (**Chapter 2**).

In **Chapter 3** we investigate the process of the combined conversion of CO_2 and CH_4, so called dry reforming of methane (DRM), in a DBD. This is done in two stages. First a study is performed focussing on the chemistry taking place during the discharge pulses and afterglow, ranging from nanoseconds to seconds time scales. Secondly, an extensive optimization study is performed, investigating the effect of several parameters, including the gas mixture ratio, the power, the residence time, the specific energy input (SEI), and the frequency. The obtained results are compared with literature and a critical analysis of the limitations and possibilities of plasma technology for DRM is provided.

Chapter 4 investigates the possibilities of artificial photosynthesis using plasma technology by the combined conversion of CO_2 with H_2O. The effect of water vapour addition on the conversions, selectivity and energy efficiency is analysed for a restricted range, by means of modelling and experiments. Based on these results, the model is used to make predictions for a wide range of gas mixing ratios and SEIs.

The first steps towards the conversion of CO_2 under non-ideal lab-scale situations are taken in **Chapter 5**, where the effect of N_2 both as impurity and admixture concentrations on the conversion of CH_4 and CO_2 is investigated. Attention is mainly focused on the N_2 influence on the energy efficiency and (possibly unwanted NO_x) product formation.

Finally a critical assessment of plasma technology for CO_2 conversion is made in **Chapter 6**. The four main processes, i.e., pure CO_2 splitting, CO_2 + CH_4 (dry reforming of methane), CO_2 + H_2O (artificial photosynthesis, and CO_2 + H_2 (hydrogenation of CO_2) are addressed and compared against the novel technologies examined in **Chapter 1**, to draw conclusions and to provide an outlook on the question: plasma technology – a novel solution for CO_2 conversion?

2. Description of the model

2.1. Physical description of the model

We used Global_kin for the computer simulations, which is a global kinetics plasma simulation code used to address the plasma chemistry in the gas phase, as well as reactions on surfaces.[1,2] We used two basic modules of this model: the Boltzmann equation module and a zero-dimensional plasma chemistry module.

First, a reaction mechanism is defined, based on the most important species occurring in the plasma, and their major production and loss processes. Next, the Boltzmann equation module calculates the values of the reaction rate coefficients for the electron impact reactions, based on the collision cross sections and depending on the electron energy. Subsequently, look-up tables with these rate coefficients as a function of electron energy (or electron temperature) are created. These coefficients will then be used as input in the chemistry module to calculate the source terms for the electron impact gas phase reactions, leading to production and loss of the various plasma species. The rate coefficients for the other gas phase reactions, i.e. between the so-called heavy plasma species, are adopted from literature. Hence, the time-evolution of the number density of the various plasma species is calculated from:

$$\frac{dn_i}{dt} = \sum_j \left\{ \left(a_{ij}^{(R)} - a_{ij}^{(L)} \right) k_j \prod_l n_l^L \right\} \qquad \text{(eq.2-1)}$$

where n_l is the density of species *i*, $a_{ij}^{(R)}$ and $a_{ij}^{(L)}$ are the right-hand side and left-hand side stoichiometric coefficients of species *i* in reaction *j*, k_j is the reaction rate coefficient and n_l^L is the density of the *l*th species in the left-hand side of reaction *j*. Note that no transport is included in this chemistry module. Indeed, the plasma reactor is considered as a batch reactor, with a uniform concentration of species over the entire reactor volume.

The electron induced reactions depend on electron temperature. The latter is determined by heating from the applied power, and by the energy lost in collisions. The electron temperature is thus calculated from:

$$\frac{d}{dt}\left(\frac{3}{2} n_e k_B T_e\right) = \vec{j} \cdot \vec{E} - \sum_i \frac{3}{2} n_e v_{mi} \left(\frac{2m_e}{M_i}\right) k_B (T_e - T_i) + \sum_l n_e k_l N_l \Delta\varepsilon_l \qquad \text{(eq.2-2)}$$

where n_e is the electron density, k_B is Boltzmann's constant, T_e is the electron temperature, $\vec{j}$ and $\vec{E}$ are the current density and the electric field in the discharge, v_{mi} is the electron momentum transfer collision frequency with species i , m_e is the electron mass and M_i and T_i are the mass and temperature of species i . Finally, k_l is the reaction rate coefficient for the l^{th} electron impact process, N_i is the density of the gas phase collision partner and $\Delta\varepsilon_l$ is the corresponding change in the electron energy (hence negative for energy loss). To summarize, the first term expresses the Joule heating, whereas the second and third terms represent the energy loss due to elastic and inelastic collisions, respectively.

Since the model is zero-dimensional, the product of current density with electric field is not used here to calculate the Joule heating, but instead, the ratio of the plasma power (applied in the model) to the plasma volume is used, which is equivalent.

The chemistry module is called every time step, but the Boltzmann module is called less frequently, as defined by the user, preferably when the background gas density has changed significantly.

In this work the Global_kin model was extended with a reaction analysis module, so that an overview can be printed of all absolute contributions of the relevant reactions to the production and loss of every species. For the absolute contributions, equation (1) is used. Next to the absolute contributions, also the relative contributions of the relevant reactions to the production and loss of a species are calculated from:

$$\gamma_{ij} = \left\{\left(a_{ij}^{(R)} - a_{ij}^{(L)}\right) k_j \prod_l n_l^L\right\} / \left(\frac{dn_{ij}}{dt}\right)_{prod/loss} \qquad \text{(eq.2-3)}$$

where γ_{ij} is the relative contribution of reaction j to the production or loss of species i, which is always evaluated versus the total dn_{ij}/dt production or loss rate. All the other parameters have the same meaning as in equation (2-1). It should be mentioned that gas heating was not calculated explicitly in the model, but a fixed gas temperature of 300 K was assumed for the DRM simulations and 323 K for the simulations for the combined conversion of CO_2 and H_2O. We know from experiments that the bulk gas temperature does not rise significantly, i.e. the gas at the outlet is still more or less at room temperature. However, there could be some local heating during one single micro-discharge. For this reason, the influence of temperature on the chemistry was investigated before, and it does not influence the electron impact reactions, which are found to be the most important reactions during the micro-discharge pulse.

The final set of ordinary differential equations (2-1 and 2-2) is then integrated in time using the so-called VODE (Variable-coefficient Ordinary Differential Equation) solver, a stiff equation solver. The time steps chosen for integration are dynamically adjusted to capture the dynamics of the system at any particular time, and it spans > 10^9 orders of magnitude.[3] This entire process is depicted graphically in **Figure 2-1**.

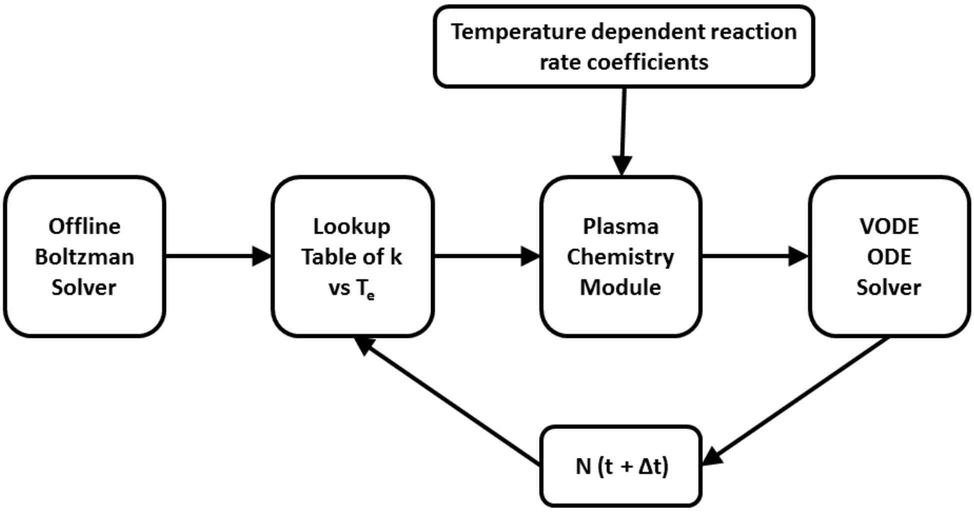

Figure 2-1. Block diagram of the modules of the 0D model Global_kin used in this work.

2.2. Mimicking the power deposition in a filamentary DBD plasma

DBDs typically operate in the filamentary regime, consisting of a large number of micro-discharge filaments, which present themselves in the electrical current waveform as many short peaks with a duration in the nanosecond range, typically around 1–100 ns.[4] From **Figure 2-2** it is clear that several micro-discharge pulses occur per half cycle. Describing these filaments in a plasma model is not straightforward, because of their distribution in time and space. Nonetheless, including a realistic description of these filaments is indispensable to obtain a realistic description of the plasma chemistry, since it is in these micro-discharges that a large fraction of the electron energy is used for excitation, dissociation and ionization of the molecules, and therefore to initiate the chemical reactions. One might argue that a 0D model seems unfit for this task, since it only allows simulating the plasma behaviour as a function of time, and not as a function of space. However, this temporal behaviour can easily be translated into a spatial behaviour, by means of the gas flow, allowing us to mimic the filamentary behaviour by simulating a large number of micro-discharge pulses as a function of time.

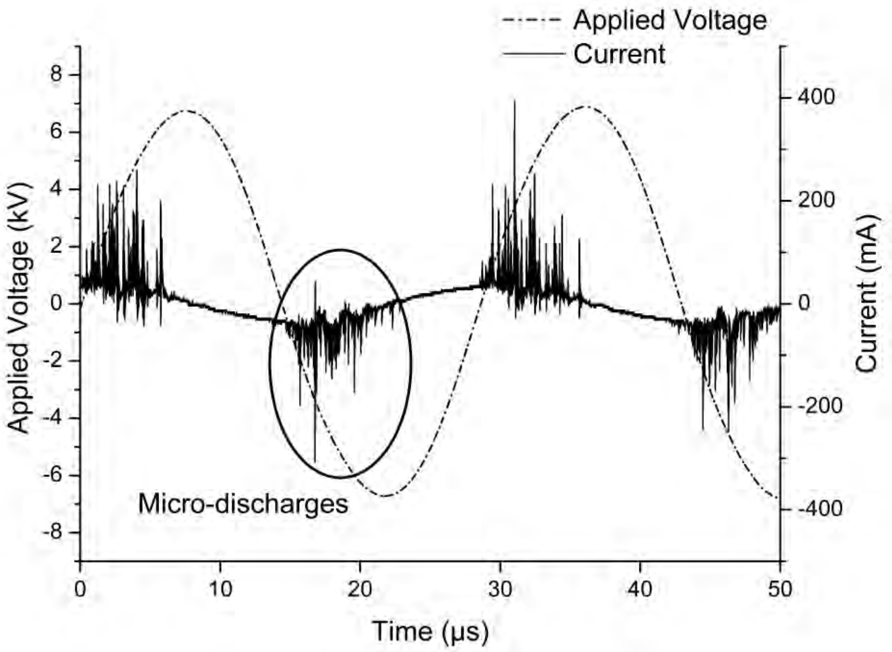

Figure 2-2. Applied voltage (left axis) and resulting current (right axis) as a function of time, for a DBD of 35 kHz and 50 W. The micro-discharge pulses (filaments) are indicated.

Unfortunately, detailed information on the number of micro-discharge pulses that each gas molecule will pass when travelling through the DBD reactor, is not known. For that reason, we started with a basic assumption, which has been adjusted along the way of this PhD research, as more insights on the micro-discharge pulses became available through our own work and through advances found in literature. As starting hypothesis for **Chapter 3**, we assumed that each molecule passes one micro-discharge each half cycle. This would for example correspond to 70,000 micro-discharge pulses per second for an applied frequency of 35 kHz. However, original calculations with this assumption gave values for the electron density (N_e), which were rather on the lower limit of typical experimental values (~10^{12} cm^{-3}), while yielding slightly overestimated conversions in case of DRM. Therefore, additional simulations were performed, yielding the same values of electron temperature (T_e ~ eV), but calculated values for N_e of ~10^{14} cm^{-3}. To achieve this, the pulse frequency was lowered, corresponding to the assumption that each molecule passes one micro-discharge every 100 half cycles instead of every half cycle. This assumption did not only provide better agreement with experiment, but also makes more sense intuitively, since we have spatially divided filaments, which only occupy a low volume in comparison to the total reactor volume. As such, a gas molecule will not pass all these filaments as they are also spread in volume—besides time. At this time, detailed information regarding the exact time evolution of a micro-discharge was not yet known, so we simply assumed a triangular pulse, with a duration of 30 ns, while the maximum power of the pulse was chosen in such a manner that the specific energy input (SEI) could be compared with experimental results for validation. These assumptions were also used for the work in **Chapter 5**. On the other hand, for the modelling work performed in **Chapter 4**, more detailed information regarding the behaviour, the amount and time evolution of the micro-discharge pulses was available through the experimental work performed by A. Ozkan at Université Libre de Bruxelles.[5] Based on this data the total number of micro-discharge filaments for those simulations was set to 475 and the duration of the triangular pulse to 10 ns, while the maximum power per pulse was chosen in the same way as mentioned above. A schematic overview of the modelling methodology is shown in **Figure 2-3**.

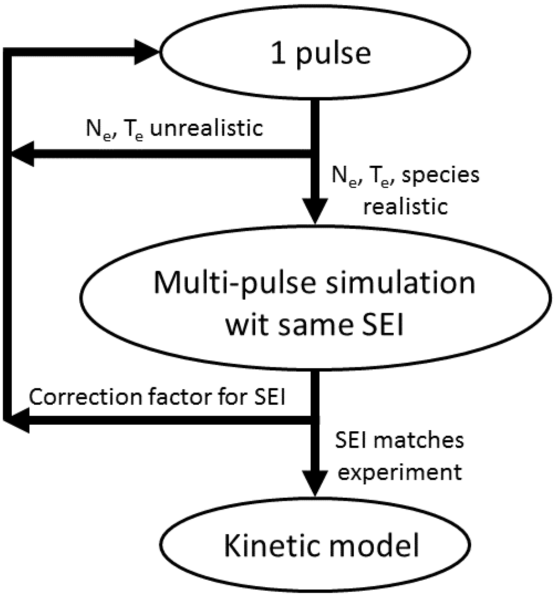

Figure 2-3. Schematic overview of the modelling methodology.

In the first step, an individual pulse is simulated with a certain specific energy input (SEI) for the expected electron temperature and electron density, which can be found in literature. In a second step, the SEI from the experiment is evaluated and fitted by repeating the individual pulse at a certain frequency, until the SEI in the model is the same as in the experiment. In the last step, the accumulation effects are studied; this step is crucial for large power depositions like in greenhouse gas conversion. In this step, the accumulation of the plasma species to unphysically high densities in subsequent pulses is investigated, which would influence the conversion. If unphysically high densities are observed, the frequency of the pulses should probably be lowered.

2.3. Data chemistry sets

In each of the following chapters, there will be a section "Description of the chemical model" specifying the different species (e.g. molecules, ions, radicals, excited species) included in the study under investigation. All the different reactions, the reaction rate coefficients and their corresponding references where the data is collected from can be found in the appendices, i.e., **Appendix I** for the data regarding CO_2/CH_4, **Appendix II** for the data regarding CO_2/H_2O, and **Appendix III** for the data regarding CH_4/N_2. Since the modelling study performed for CO_2/N_2 was performed in collaboration with S. Heijkers[6] we refer to his work regarding this data.

From the different chapters, it will be evident that for each chemistry set, several—possibly non-negligible—species are not included in the models. This is due to the lack of complete data on the specific reaction rate coefficients in literature needed to describe their formation and loss processes. Of course, we could have incorporated these species, but due to the scarcity of coherent input data, their densities would be subject to such large uncertainties that the predictive character of the model would have less to no value. Furthermore, most of the time it concerns species that were not detected in the validation experiments. Nevertheless, we hope that rate coefficients for these missing species will become available in literature in the near future, which would allow us to build even more complete chemistry models, and more importantly, to investigate under which other circumstances these species might be formed.

Closely related to this, one could of course wonder whether it is necessary to keep pursuing hundreds of reactions—with their specific coefficients and so on—to perfect chemical kinetics chemistry models. For example, in **Chapter 4**, section 4.1.4, it was possible to identify 23 different reactions with which a reaction scheme could be compiled and the observed trends explained. This is of course a big difference compared to the 902 different reactions that are included in that specific model. As such one could indeed wonder about the necessity of including all these reactions. However, it is important to realize that this information is evidently only available after the facts, and during the construction of these chemistry sets, missing one—seemingly unimportant—reaction can lead to dramatically wrong outcomes. Therefore, it is absolutely necessary to first build a comprehensive set. Furthermore, building a more complete chemistry set allows this set to be used to model different reactor types and conditions. Notwithstanding, when a relatively complete chemistry model is available in literature—like the ones developed in this thesis—and one wants to optimize a specific set-up, and/or start modelling in two or three dimensions (to include geometry variations for example), it has no use anymore to continue pursuing an as complete model as possible and one should focus on simplifying the chemistry to its bare essence. The latter is necessary, not only to make the interpretation of the results easier to grasp, but also due to computational restraints—it is currently simply impossible to model even a basic reactor in 3D with hundreds of reactions.

3. Experimental set-up

As already mentioned in section 1, the modelling work goes side by side with (validation) experiments. The experimental work in **Chapter 3** was performed by Y. Zeng and Prof. dr. X. Tu at the University of Liverpool, while the experimental work in **Chapter 4** was performed by A. Ozkan at the Université Libre de Bruxelles. The experimental studies in **Chapter 5**, on the other hand, were performed at the University of Antwerp (PLASMANT), with the FTIR NO_X measurements being performed in collaboration with K. Van Wesenbeeck at the University of Antwerp (DuEL). Details of the experimental set-up and the relevant references will be given at the beginning of those chapters, while some general experimental details and background information will be given below.

3.1. Description of the DBD reactor

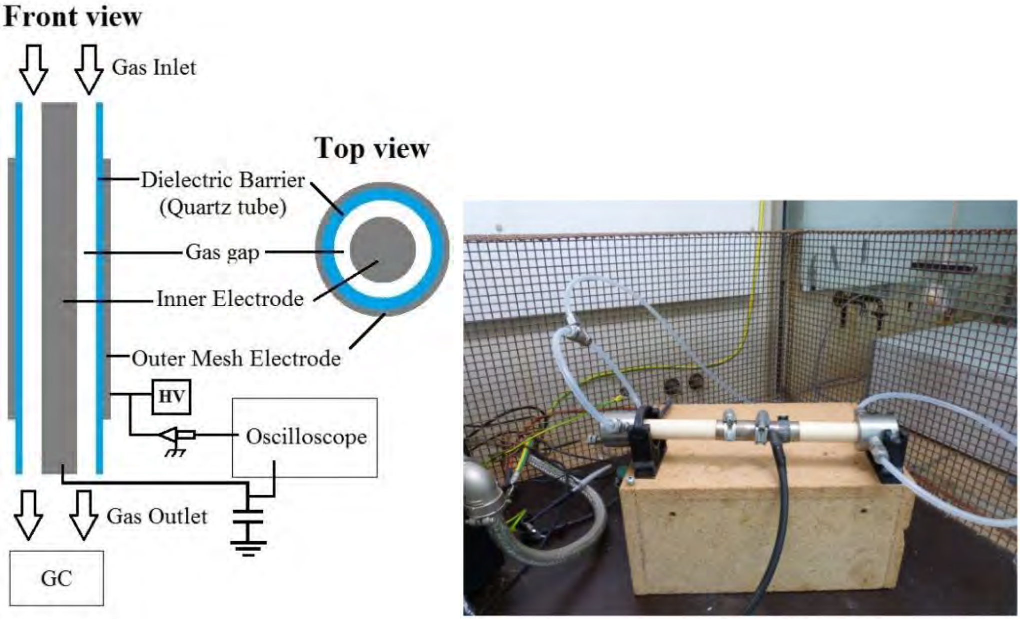

Figure 2-4. Schematic diagram of the experimental set-up for the experiments, in front view and top view (left) as well as a picture of the set-up used for this thesis at PLASMANT (right).

All the experiments were conducted using a coaxial DBD reactor powered by an alternating current (AC) high-voltage power supply. A ground electrode is wrapped over the outside of a quartz or silica tube, while a stainless steel rod is placed in the centre of the tube and used as high voltage electrode. The different feed gases are controlled using separate mass flow controllers. The total current is recorded by a Rogowski-type current monitor (Pearson 4100), while a high voltage probe is used to measure the applied voltage. Furthermore, to obtain the charge generated in the discharge, the voltage on the external capacitor (10 nF) is measured. Finally, all the electrical signals are sampled by a digital oscilloscope and the discharge power is obtained by a control system used to calculate the area of the Q-U Lissajous Figures.[7] As mentioned, the precise experimental conditions can be found in each separate chapter. A schematic picture of the experimental set-up (used for this thesis at PLASMANT) both in front and top view is shown in **Figure 2-4**.

3.2. Gas chromatography analysis

The feed and product gases are analysed by gas chromatography (GC), i.e., based on the separation of gas mixtures into their pure substances. The gas mixture is added to a "mobile phase" and eluted through a "stationary phase". More specifically, helium (He) is used as a mobile phase, which elutes through different columns, representing the stationary phase. By injecting a sample into the column, different gas species pass through the column at different rates, depending on the strength of electrostatic interactions with the walls of the column. As a consequence, the gas mixture becomes separated into individual components that reach the end of the column and are detected at different times.

By measuring the retention time of each species in the column, the component gases can be identified by comparison with chromatograms for known standards. In general, the retention times are affected by the type of column, the gas concentration, pressure as well as temperature; therefore, a selection of the appropriate column materials and operating conditions is critical for the resolution of the gas mixture. A signal is produced by each specific component as it reaches the detector, which results in a peak on the chromatogram at a residence time that is characteristic for that gas. Finally, the relation between the peak area and the gas concentration allows a quantitative measurement.

In this work the detector types used are a thermal conductivity detector (TCD) and a flame ionization detector (FID). A TCD channel containing a Molecular Sieve 5A column is used for the segregation of the molecular gases, O_2, N_2 and CO, while a second TCD channel equipped with a Rt-QBOND column is used for the measurement of CO_2 and C_1-C_2 hydrocarbons. An FID equipped with a Rtx-5 column is used for the measurement of C_1 to C_{10} containing compounds.

4. Definitions

In this section an overview of the different expressions used throughout this thesis for the specific energy input (SEI), conversion (χ), energy efficiency (η), energy cost (EC), selectivity (S) and yield (Y) will be given.

4.1. Specific energy input (SEI)

The specific energy input (expressed in J/cm^3 or kJ/L) is defined as the plasma power divided by the gas flow rate, and this is the dominant determining factor for the conversion and energy efficiency in a plasma process, as will also become clear from the following chapters:

$$SEI\left(\frac{J}{cm^3}\right) = SEI\left(\frac{kJ}{L}\right) = \frac{Power\ (kW)}{Flow\ rate\ (\frac{L}{min})} \cdot 60(\frac{s}{min}) \qquad \text{(eq.2-4)}$$

The SEI is also commonly expressed in electron volt per molecule:

$$SEI\left(\frac{eV}{molecule}\right) = SEI\left(\frac{kJ}{L}\right) \cdot \frac{6{,}24 \cdot 10^{21}\ (eV \cdot kJ^{-1}) \cdot 24{,}5\ (L \cdot mol^{-1})}{6{,}022 \cdot 10^{23} (molecule \cdot mol^{-1})} \qquad \text{(eq.2-5)}$$

Note that the value of 24.5 $L \cdot mol^{-1}$ is only valid for 298 K and 1 atm.

Hence, at reaction conditions of 298 K and 1 atm:

$$SEI\ \left(\frac{J}{cm^3}\right) = SEI\left(\frac{eV}{molecule}\right) \cdot 3.92 \qquad \text{(eq.2-6)}$$

$$\Leftrightarrow SEI\left(\frac{eV}{molecule}\right) = SEI\ \left(\frac{J}{cm^3}\right) \cdot 0.255 \qquad \text{(eq.2-7)}$$

4.2. Absolute and effective conversion

Two types of conversion can be defined. The (absolute) conversion is based on the molar flows of the reactants, i.e. CH_4, CO_2, H_2O and N_2. This is the typical expression used for "conversion" throughout this thesis, and also in general in literature:

$$\chi_{abs,reactant_i} = \frac{\dot{n}_{reactant_i,inlet} - \dot{n}_{reactant_i,outlet}}{\dot{n}_{reactant_i,inlet}} \qquad \text{(eq.2-8)}$$

Where $\dot{n}$ stands for the molar flow rate of reactant specie i.

When more than one gas is present in the feed mixture, the effective conversion takes the dilution into account:

$$\chi_{eff,reactant_i} = \chi_{abs,reactant_i} \cdot \frac{\dot{n}_{reactant_i,inlet}}{\sum_i \dot{n}_{reactant_i,inlet}} \qquad \text{(eq.2-9)}$$

This alternative definition of the conversion is important for comparing the conversion of a specific reactant in different mixtures, since it shows how the conversion rate of the reactant is affected, rather than the absolute value of its conversion.

For an easy comparison of DRM mixtures, it is also interesting to determine the total conversion, which is the sum of the effective conversions:

$$\chi_{Total} = \sum_i \left(\frac{\dot{n}_{reactant_i,inlet}}{\sum_i \dot{n}_{reactant_i,inlet}} \cdot \chi_{abs,reactant_i} \right) = \sum_i \chi_{eff,reactant_i} \qquad \text{(eq.2-10)}$$

4.3. Energy efficiency and energy cost

The energy efficiency and energy cost depend on the process under study. The energy efficiency is a measure for how efficient the process performs compared to the standard reaction enthalpy, based on the specific energy input (SEI):

$$\eta = \frac{\chi_{Total} \cdot \Delta H^0_{298K}\left(kJ \cdot mol^{-1}\right)}{SEI\ \left(kJ \cdot mol^{-1}\right)} = \frac{\chi_{Total} \cdot \Delta H^0_{298K}\left(eV \cdot molecule^{-1}\right)}{SEI\ \left(eV \cdot molecule^{-1}\right)} \qquad \text{(eq.2-11)}$$

As mentioned in Chapter 1, ΔH^0_{298K} is 283 kJ/mol (or 2.93 eV/molecule) for pure CO_2 splitting, 247 kJ/mol (or 2.56 eV/molecule) for DRM, and 525 kJ/mol (or 5.44 eV/molecule) for the combined conversion of CO_2 and H_2O. However, he latter process can easily be divided into its separate components of CO_2 and H_2O splitting, and therefore the following definition is used:

$$\eta = \frac{\chi_{eff,CO_2} \cdot 283\ \left(kJ \cdot mol^{-1}\right) + \chi_{eff,H_2O} \cdot 242\ \left(kJ \cdot mol^{-1}\right)}{SEI\ \left(kJ \cdot mol^{-1}\right)} \qquad \text{(eq.2-12)}$$

The energy cost, on the other hand, is the amount of energy consumed by the process (generally expressed as kJ/converted mol or eV/converted molecule):

$$\mathrm{EC}\ \left(kJ \cdot mol_{conv}{}^{-1}\right) = \frac{\mathrm{SEI}\ \left(kJ \cdot L^{-1}\right) \cdot 24{,}5\ \left(L \cdot mol^{-1}\right)}{\chi_{Total}} \qquad \text{(eq.2-13)}$$

Note that the value of 24.5 $L \cdot mol^{-1}$ is only valid for 298 K and 1 atm.

$$\mathrm{EC}\ \left(eV \cdot molecule_{conv}{}^{-1}\right) = \mathrm{EC}\ \left(kJ \cdot mol_{conv}{}^{-1}\right) \cdot \frac{6{,}24 \cdot 10^{21}\ \left(eV \cdot kJ^{-1}\right) \cdot}{6{,}022 \cdot 10^{23} \left(molecule \cdot mol^{-1}\right)} \qquad \text{(eq.2-14)}$$

4.4. Selectivity and yield

Depending on the process under study and the formed products, it is interesting to look at either the H-, O- or C-based selectivity (denoted as S_H, S_O, S_C, respectively).

For the results in **Chapter 3** on DRM, the following definitions are used:

$$S_{H,H_2} = \frac{\dot{n}_{H_2,out}}{2 \cdot \left(\dot{n}_{CH_4,in} - \dot{n}_{CH_4,out}\right)} \qquad \text{(eq.2-15)}$$

$$S_{C,CO} = \frac{\dot{n}_{CO,out}}{(\dot{n}_{CO_2,in} - \dot{n}_{CO_2,out}) + (\dot{n}_{CH_4,in} - \dot{n}_{CH_4,out})} \qquad \text{(eq.2-16)}$$

$$S_{C,C_xH_y} = \frac{x \cdot \dot{n}_{\mathrm{C_xH_y},out}}{(\dot{n}_{CO_2,in} - \dot{n}_{CO_2,out}) + (\dot{n}_{CH_4,in} - \dot{n}_{CH_4,out})} \qquad \text{(eq.2-17)}$$

$$S_{C,C_xH_yO_z} = \frac{x \cdot \dot{n}_{\,C_xH_yO_z,out}}{(\dot{n}_{CO_2,in} - \dot{n}_{CO_2,out}) + (\dot{n}_{CH_4,in} - \dot{n}_{CH_4,out})} \qquad \text{(eq.2-18)}$$

For the results in **Chapter 4**, on the combined conversion of CO_2 and H_2O, the following definitions are used:

$$S_{O,CO} = \frac{\dot{n}_{CO,out}}{2 \cdot [(\dot{n}_{CO_2,in} - \dot{n}_{CO_2,out}) + 1/2 \cdot (\dot{n}_{H_2O,in} - \dot{n}_{H_2O,out})]} \qquad \text{(eq.2-19)}$$

$$S_{O,O_2} = \frac{\dot{n}_{O_2,out}}{(\dot{n}_{CO_2,in} - \dot{n}_{CO_2,out}) + 1/2 \cdot (\dot{n}_{H_2O,in} - \dot{n}_{H_2O,out})} \qquad \text{(eq.2-20)}$$

$$S_{O,H_2O_2} = \frac{\dot{n}_{H_2O_2,out}}{(\dot{n}_{CO_2,in} - \dot{n}_{CO_2,out}) + 1/2 \cdot (\dot{n}_{H_2O,in} - \dot{n}_{H_2O,out})} \qquad \text{(eq.2-21)}$$

$$S_{H,H_2} = \frac{\dot{n}_{H_2,out}}{(\dot{n}_{H_2O,in} - \dot{n}_{H_2O,out})} \qquad \text{(eq.2-22)}$$

$$S_{H,H_2O_2} = \frac{\dot{n}_{H_2O_2,out}}{(\dot{n}_{H_2O,in} - \dot{n}_{H_2O,out})} \qquad \text{(eq.2-23)}$$

Finally, for the results in **Chapter 5**, on the influence of N_2 on the CH_4 conversion for the hydrogen selectivity, the same equation (2-15) is used, while for the hydrogen yield, the following definition is used:

$$Y_{H_2} = \frac{\dot{n}_{H_2,out}}{2 \cdot n_{CH_4,inlet}} = \chi_{abs,CH_4} \cdot S_{H,H_2} \qquad \text{(eq.2-24)}$$

5. References

1 R. Dorai and M. J. Kushner, *J. Phys. D. Appl. Phys.*, 2003, **36**, 1075–1083.

2 D. S. Stafford and M. J. Kushner, *J. Appl. Phys.*, 2004, **96**, 2451–2465.

3 R. Dorai, PhD Thesis, University of Illinois at Urbana-Champaign, 2002.

4 U. Kogelschatz, *Plasma Chem. plasma Process.*, 2003, **23**, 1–46.

5 A. Ozkan, PhD Thesis, Université Libre de Bruxelles and University of Antwerp, 2016.

6 S. Heijkers, R. Snoeckx, T. Kozák, T. Silva, T. Godfroid, N. Britun, R. Snyders and A. Bogaerts, *J. Phys. Chem. C*, 2015, **119**, 12815–12828.

7 R. Aerts, W. Somers and A. Bogaerts, *ChemSusChem*, 2015, **8**, 702–716.

CHAPTER 3

CO_2 + CH_4 : Dry reforming of methane

This chapter is published as:

- R Snoeckx, R Aerts, X Tu and A Bogaerts, Plasma-Based Dry Reforming: A Computational Study Ranging from the Nanoseconds to Seconds Time Scale, The Journal of Physical Chemistry C 117 (2013) 4957-4970 (14p).
- R Snoeckx, Y X Zeng, X Tu and A Bogaerts, Plasma-Based Dry Reforming: improving the conversion and energy efficiency in a dielectric barrier discharge, RSC Advances 5 (2015) 29799-29808 (10p).

1. Aim of the work

The conversion of the main greenhouse gases, CO_2 and CH_4, into value-added chemicals and liquid fuels is considered as one of the main challenges for the 21st century.[1,2] The combined reforming of both CH_4 and CO_2, i.e., dry reforming of methane (DRM), has therefore gained significant interest over the years because of its (possible) environmental impact.[3,4] Its main advantages over other reforming processes are the use of CO_2 as both a carbon source and oxidizing agent and the production of syngas (H_2/CO) in a ratio which is easily controllable. The main disadvantage for implementing catalytic DRM on an industrial scale is its inherent carbon deposition, which leads to catalyst poisoning.[5] Nevertheless, as stated by Mikkelsen et al.[6] '*The formation of synthesis gas by dry reforming of methane could provide a substantial use for CO_2 from industrial and natural sources. This capture provides a renewable, inexhaustible carbon source and could also provide a means for the continued use of derived carbon fuels in an environmental friendly and carbon neutral way.*' As a result, the interest for alternative (non-conventional) reforming technologies grew quickly and one of the alternatives which is considered to have great potential in this area is plasma technology, as also outlined in **Chapter 1**.

The conversion process of CO_2 and CH_4 is, however, not straightforward. Indeed, CO_2 is a highly oxidated, thermodynamically stable molecule, and its use in redox reactions requires highly energetic reactants or electro-reducing processes.[7] CH_4 is, due to its chemical inertness, currently a highly underutilized source for the production of value-added chemicals. A direct (thermal) synthesis route for hydrocarbons from CH_4 is technically not possible, and the conventional indirect methods are characterized by low yields and they require a high energy input.[8] Nevertheless, the reforming of methane into syngas is worldwide gaining increased attention, due to the versatility of syngas for the production of many fuels and chemicals, such as methanol, but also Fischer-Tropsch fuels, H_2, ethanol, dimethyl ether,…[9]

One of the largest problems of the thermal DRM process is the high amount of carbon deposition at the catalyst material, i.e., much higher than with SMR, giving rise to catalyst poisoning.[5,10] A lot of research is going on in order to find the optimum catalyst materials, as also outlined in **Chapter 1**.[10–12] On the other hand, in recent years there is also growing interest for alternative reforming techniques, based on milder reaction conditions, such as plasma reformers. Both thermal and non-thermal plasma reformers have already been developed.[13–17] The advantage of non-thermal plasmas, compared to the classical catalytic process, is that the gas can remain near room temperature while being "activated" by electron impact excitation, ionization and dissociation reactions, as explained in **Chapter 1**. Furthermore, higher conversions and selectivities can be obtained without problems of carbon deposition.[18] The type of plasma which is currently most often used for DRM (and gas conversion in general) is the dielectric barrier discharge (DBD). Tao et al.[18] calculated that for every mole CO_2 reformed in a DBD, one mole CO_2 would be emitted if the electricity came from methane combustion. Furthermore, we calculated that the energy efficiency of plasma-based DRM would need to achieve a theoretical energy efficiency of at least ~60 % to be competitive with classical DRM, see section 3.3.3.b.

In this chapter, we will study the plasma-based dry reforming process in a DBD reactor, by means of computer simulations validated with experiments. In our investigation we will make use of the zero-dimensional (0D) chemical kinetics model, explained in **Chapter 2**. Simplified calculations for this plasma chemistry have already been performed,[19–22] but they were all based on simplified kinetics, and without a (good) description of the filamentary discharge regime. Therefore, in section 2 we will first carry out an extensive study of the reaction chemistry, while mimicking the filamentary discharge regime. More specifically, we will investigate the plasma chemistry in one micro-discharge pulse and its afterglow, which corresponds to one filament in a DBD, as well as the impact of several consecutive discharge pulses. Subsequently, the model will be applied to long time-scales, corresponding to the typical residence times of gases in a DBD reactor, in order to calculate the conversion of CH_4 and CO_2, the selectivity of the reaction products and the energy cost and energy efficiency of the process. To validate the model, these long time-scale simulations will be compared with experiments.

Finally, in section 3 we perform an extensive computational optimization study for a DBD, based on the developed and validated model. Additionally, some new experiments are performed to support the model in this broader parameter range. The aim of this study is to identify the influence of the operating parameters of a DBD for DRM and to investigate which of these parameters are most promising in terms of energy efficiency and conversion and whether this is eventually sufficient for industrial implementation or whether different plasma set-ups (i.e., packed-bed DBD[23,24] or so-called warm plasmas[18,24–28]) should be pursued.

2. A computational study ranging from the nanoseconds to seconds time scale

2.1. Description of the chemical model

2.1.1. 0D chemical kinetics model

The plasma chemistry set developed in this work is applied to the zero-dimensional (0D) kinetic model, called Global_kin, developed by Kushner and coworkers,[29,30] to describe the underlying reactions taking place. The time-evolution of the species densities is calculated, based on production and loss processes, as defined by the chemical reactions. The rate coefficients of the heavy particle reactions depend on the gas temperature and are calculated by Arrhenius equations. The rate coefficients for the electron impact reactions are a function of the electron temperature, and are calculated in the Boltzmann equation module. Finally, the electron temperature is calculated with an energy balance equation. More details about this model can be found in the work of Kushner et al.[29,30] and in **Chapter 2**, section 2.

2.1.2. Plasma chemistry included in the model

The plasma chemistry described in the model is based on the chemistry set developed by De Bie et al.[31] However, some species and chemical reactions were removed from the model, as they were found to be negligible at the conditions under study. The species included in the present model are listed in **Table 3-1**. They react with each other in 121 electron impact reactions, 87 ion reactions and 290 neutral reactions, which are listed in Appendix I, together with their corresponding rate coefficients and the references where these data were adopted from.

Table 3-1. List of species included in the model for the CH_4/CO_2 gas mixture

Molecules	Charged species	Radicals	Excited species
CH_4	CH_5^+, CH_4^+, CH_3^+, CH_2^+, CH^+	CH_3, CH_2, CH, C	CH_4^*
C_2H_6, C_2H_4, C_2H_2	$C_2H_6^+$, $C_2H_5^+$, $C_2H_4^+$, $C_2H_3^+$, $C_2H_2^+$	C_2H_5, C_2H_3, C_2H	$C_2H_6^*$, $C_2H_4^*$, $C_2H_2^*$
C_3H_8, C_3H_6, C_4H_2		C_3H_7	$C_3H_8^*$
H_2		H	H_2^*
O_2	O_2^+, O^-	O	O^*
CO_2, CO	CO_2^+		CO_2^*, CO^*
H_2O, H_2O_2	H_3O^+, OH^-	OH, HO_2	H_2O^*
CH_2O, CH_3OH,	Electrons	CHO, CH_2OH, CH_3O	
CH_3CHO, CH_2CO		C_2HO, CH_3CO	
		CH_2CHO, $C_2H_5O_2$	

Note: The excited species are only included in the model to describe the energy loss processes, and they are not treated as separate species.

Assuming a typical applied frequency of 35 kHz (as used in the experiments of Tu et al.[32] for validation), this corresponds to a duration of 14 μs for each half cycle. If we assume that each molecule passes one micro-discharge each half cycle, this would correspond to 70,000 micro-discharge pulses per second. That will be our starting assumption in the long time-scale simulations presented in section 2.3.3. Furthermore, as we don't know the exact time evolution of a micro-discharge, we simply assume a triangular pulse, with a duration of 30 ns. The maximum power of the pulse is chosen in such a manner that the specific energy input (SEI) can be compared with experimental results for validation (see below).

First we will investigate in detail the behaviour of one micro-discharge pulse and its afterglow. Subsequently, the accumulation effect of several micro-discharge pulses will be studied, and finally real time-scale simulations will be carried out, with a large number (in the order of hundreds or thousands) of micro-discharge pulses per second, to calculate the conversion of CH_4 and CO_2, the selectivity of the products and the energy cost and energy efficiency of the process. The calculations will be performed for a 1:1 ratio of CH_4/CO_2, to allow a direct comparison and validation with the experimental data obtained by Tu et al.[32]

2.2. Description of the experiments

The experiments used for validation were performed at the University of Liverpool and the description of the experimental procedures were adopted from the work of Tu et al.[32]

The experiment is carried out in a cylindrical DBD reactor. It consists of two coaxial quartz tubes, both of which are covered by a stainless steel mesh electrode. The inner electrode is connected to a high voltage output and the outer electrode is grounded via an external capacitor (22 nF). The length of the discharge region is 55 mm with a discharge gap of 3 mm and discharge volume of 11.4 cm^3. CH_4 and CO_2 are used as feed gases with a total flow rate of 25–100 mL min^{-1} and a mixing ratio of CH_4/CO_2 equal to 1:1. The DBD reactor is supplied by an AC high voltage power supply with a peak-to-peak voltage of 24 kV and a variable frequency of 30–40 kHz. The applied voltage is measured by a high voltage probe, while the total current is recorded by a Rogowski-type current monitor (Bergoz CT-E0.25). The voltage on the external capacitor is measured to obtain the charge generated in the discharge. All the electrical signals are sampled by a four-channel digital oscilloscope (Tektronics TDS2014). A LABVIEW control system is used for the online measurement of the discharge power by the area calculation of the Q-U Lissajous figure.

A trap cooled by solid CO_2 is placed at the exit of the plasma reactor in order to condense any liquid products. The feed and product gases are analysed by two-channel micro-gas chromatography (Agilent 3000A) equipped with two thermal conductivity detectors (TCD). The first channel contains a Molecular Sieve 5A column for the separation of H_2, CO and CH_4, while the second channel is equipped with a Poraplot Q column for the measurement of CO_2 and C_2–C_4 hydrocarbons. The GC is calibrated for a wide range of concentrations for each gaseous component using reference gas mixtures (Agilent Universal Gas Mixture) and other calibrated gas mixes.

2.3. Results and Discussion

2.3.1. Calculated behaviour of one microdischarge pulse and its afterglow

a) Power deposition, electron density, and temperature

Figure 3-1 illustrates the applied power deposition (P), as well as the calculated electron density (N_e) and electron temperature (T_e), as a function of time, for one micro-discharge pulse. At $t = 3 \times 10^{-8}$ s, a triangular pulse of 30 ns is applied, assuming a maximum power deposition of 1.5×10^5 W/cm^3 (**Figure 3-1(a)**). The electron density (**Figure 3-1(b)**) follows the same profile as the power deposition, which is logical as the power is transferred to the electrons, which are heated and give rise to electron impact ionization, creating more electrons. However, the electron density shows a slower decay in the afterglow, indicating that some electrons have a somewhat longer lifetime, or can still be created in the afterglow by heavy-particle reactions. The electron temperature is illustrated in **Figure 3-1(c)**. It shows an initial maximum before the start of the pulse, which is an artefact of the simulations, as the model seems first to overestimate, before converging to the real value of the electron temperature. However, this artefact does not affect the calculation results, because it occurs in the first nanoseconds, where the electron density is still negligible, so it cannot give rise to reactions with the gas molecules. As soon as the discharge pulse starts, the electron temperature reaches a maximum, which is real, because the electrons are heated by the electric field. Upon termination of the pulse, the electron temperature drops to 0.05 eV. The maximum electron temperature is around 2.5–3 eV, which corresponds well with experimental data from literature.[13,27,33] The maximum electron density is about 3×10^{13} cm^{-3}, which is in the same order of magnitude as experimental values (~10^{12}–10^{14} cm^{-3}).[13,27,33] We may therefore conclude that the power deposition assumed for this single discharge pulse correlates well with typical DBD conditions, so that the chemical behaviour of the CH_4/CO_2 mixture can be described in a realistic way.

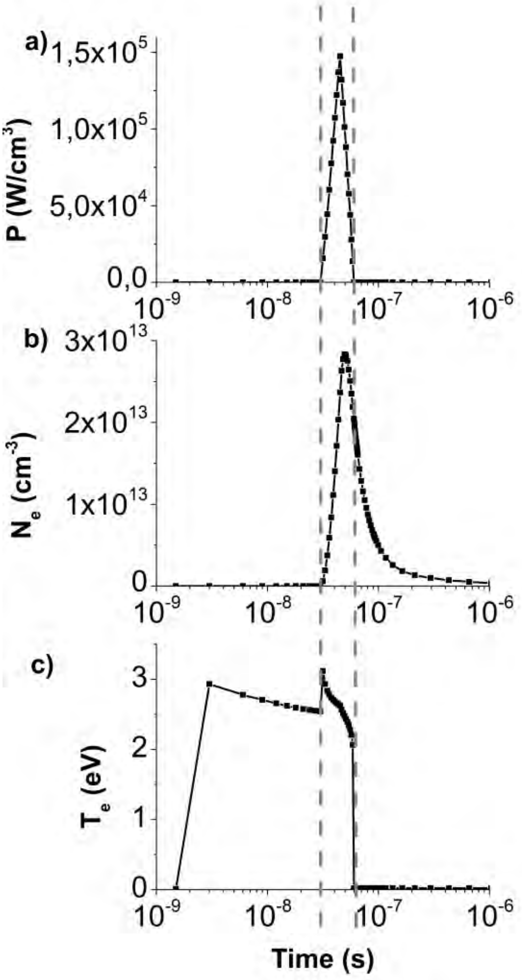

Figure 3-1. Applied power deposition (a), and calculated electron density (b) and electron temperature (c), as a function of time for one pulse and afterglow. The grey dashed lines indicate the start and the end of the micro-discharge pulse.

b) Densities of the plasma species

As illustrated above, electrons are created upon the start of the pulse, and they can give rise to collisions with the gas molecules, thereby forming radicals and ions, as is clear from **Figure 3-2**. During the pulse, the density of the molecules drops slightly (see left axis), whereas the densities of the ions, and especially of the radicals, increase by several orders of magnitude (see right axis). Comparing the ion and radical densities, it is clear that the electron impact reactions mainly create radicals, and that electron impact dissociation will be the dominant loss mechanism for CH_4 and CO_2. In the afterglow, the molecule density rises again, whereas the densities of ions and radicals drop, because they recombine again with the formation of stable molecules. This illustrates that the plasma chemistry is completely different in the afterglow, due to the absence of an electric field. Indeed, the electrons disappear (see figure 2 above) and the chemistry is dominated by heavy particle reactions. The ions have disappeared after 100 μs, whereas the radicals reach a kind of steady state at 5 μs, but drop further after 100 μs. Note that we assume an afterglow of 1 s here, which does probably not correspond to reality (see section 2.1.2. above); hence the accumulation effect of consecutive pulses needs to be examined as well, and these results will be presented in section 2.3.2. below.

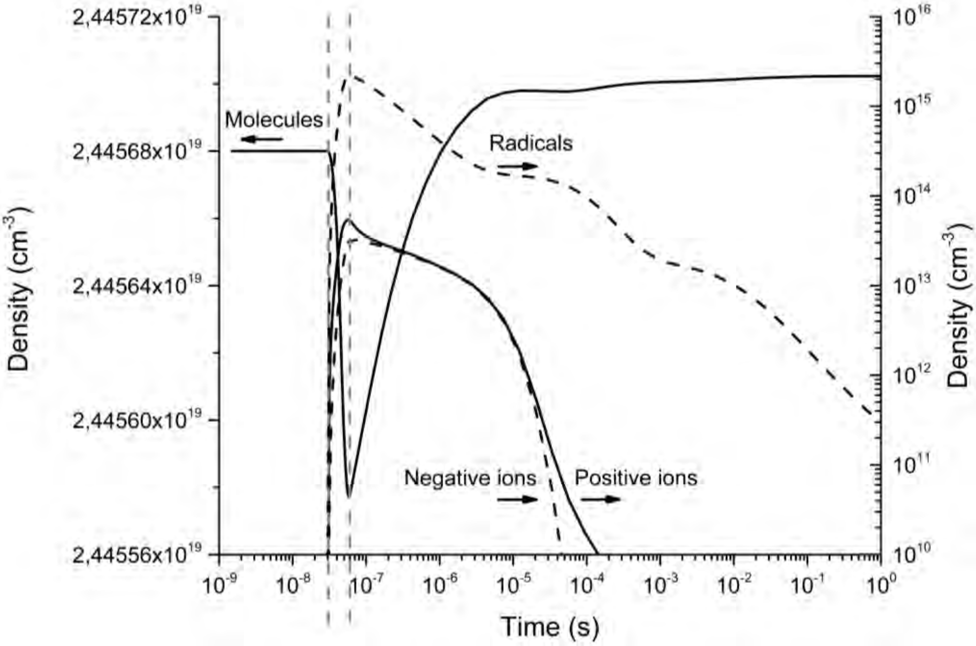

Figure 3-2. Calculated densities of the molecules (left axis) and of the radicals and positive and negative ions (right axis), as a function of time during one pulse and afterglow. The grey dashed lines indicate the start and the end of the micro-discharge pulse.

The densities of CH_4 and CO_2 are plotted as a function of time during one pulse and afterglow in **Figure 3-3**. During the pulse, the dissociation of CH_4 is much more pronounced, which can be attributed to a more efficient dissociation by electron impact for CH_4, or to a competition with production processes for CO_2 during the pulse. The exact reason will be elucidated below, in section 3.3. In the afterglow, however, nearly 74% of the dissociated CH_4 is formed again, due to the recombination of CH_3 and H. The CO_2 dissociation, on the other hand, continues in the afterglow, but after 10 μs an equilibrium is reached between production and loss of CO_2. Our calculations predict that ca. 22 % of the CO_2 dissociation occurs during the pulse, and is attributed to electron impact dissociation, whereas 78 % takes place in the afterglow, and is mainly due to reactions of CO_2 with CH_2 radicals. Nevertheless, overall the conversion of CH_4 is still a factor of 2 higher than for CO_2. After 10 μs, the CH_4 and CO_2 densities reach a steady state value, indicating that the production and/or loss processes compensate each other, or have become all negligible.

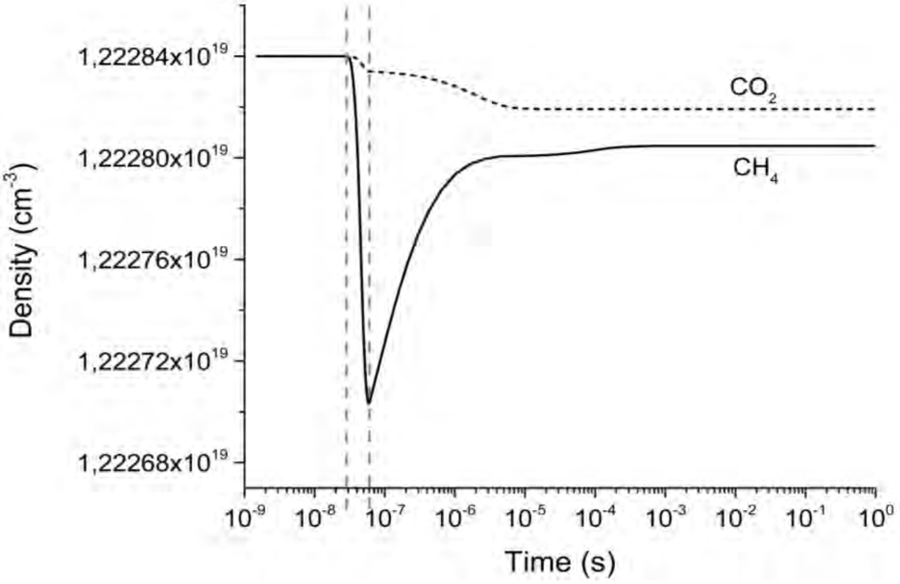

Figure 3-3. Calculated densities of CH_4 and CO_2, as a function of time during one pulse and afterglow. The grey dashed lines indicate the start and the end of the micro-discharge pulse.

Figure 3-4 presents the time evolution of the most important molecule densities, formed out of CH_4 and CO_2. The higher hydrocarbon molecules, C_2H_6, C_2H_4, C_2H_2, C_3H_8 and C_3H_6, are shown in **Figure 3-4(a)**. Note that the considerable density of C_2H_4 before the pulse is again an artefact of the simulations, due to some overestimated starting values, but it has no influence on the results, because it happens before the pulse starts, and the density is 11 orders of magnitude lower than the CH_4 and CO_2 densities. Once the pulse starts, we notify a significant increase in density, over more than 10 orders of magnitude for the hydrocarbon densities. There is, however, some difference between the different hydrocarbons, i.e., the densities of C_2H_6, C_2H_4 and C_2H_2 rise instantaneously upon start of the pulse, whereas the rise in densities of C_3H_8 and C_3H_6 exhibits some delay. This is because the latter molecules are created only after some intermediate products are formed (see reaction path analysis below). In the afterglow, some densities continue to grow, whereas other densities drop slightly, indicating a conversion from lower to higher hydrocarbons. After about 1 ms, all densities reach steady state values.

The densities of the syngas components, CO and H_2, are depicted in **Figure 3-4(b)**. The H_2/CO ratio during the pulse is ~4. However, in the afterglow, the CO density increases more drastically than the H_2 density, due to the continued dissociation of CO_2 (see above), and the final H_2/CO ratio, after about 5 μs, is ~1.4. This ratio is interesting for several industrial applications like for example the dimethyl ether production and Fischer-Tropsch-synthesis.[34]

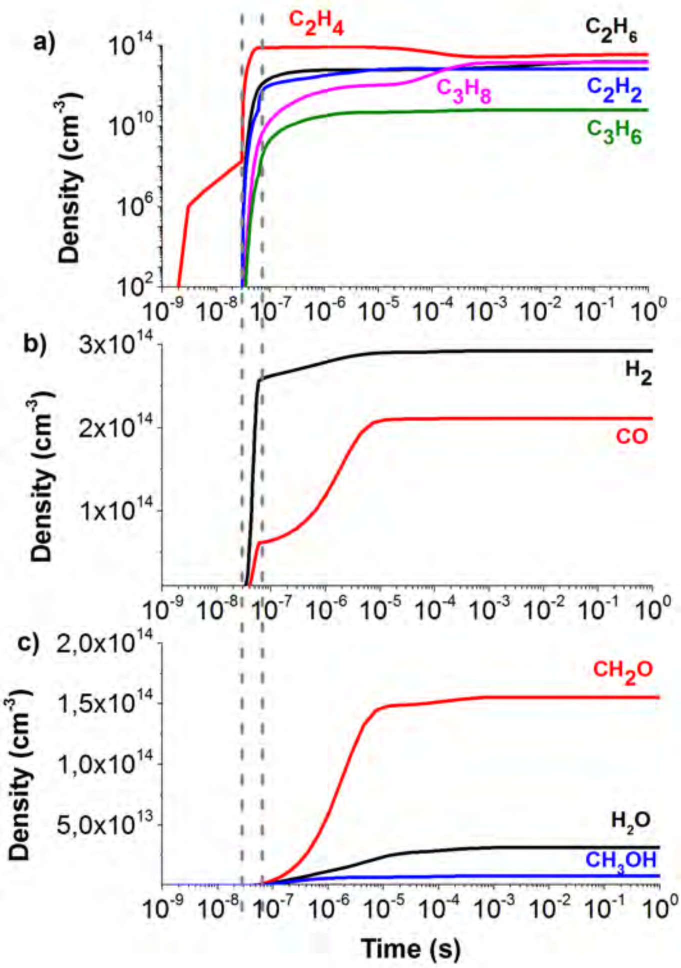

Figure 3-4. Calculated densities of the most important molecules formed in the plasma, i.e., higher hydrocarbons (a), syngas components (b), and H_2O and oxygenated products (c), as a function of time during one pulse and afterglow. The grey dashed lines indicates the start and the end of the micro-discharge pulse.

Finally, **Figure 3-4(c)** illustrates the densities of H_2O and of the two most important oxygenated products, i.e., formaldehyde (CH_2O) and methanol (CH_3OH). The latter two molecules are even more important than syngas for the chemical industry, as they are bulk chemicals that are largely consumed worldwide for a large number of industrial syntheses.[35] Hence it would be beneficial if they could be produced directly from the CH_4/CO_2 gas mixture. It is clear that these species are mainly formed in the afterglow, and not by electron impact reactions during the pulse. The formaldehyde density is only a factor of two lower than the densities of the syngas components, whereas the methanol density is still one order of magnitude lower. The most important production process for formaldehyde is the reaction:

$CH_2 + CO_2 \rightarrow CH_2O + CO$,

Whereas methanol is mainly formed by:

$OH^- + CH_3 \rightarrow CH_3OH + e^-$.

These molecules only reach steady state densities after ca. 1 ms.

The time evolution of the most important radical and ion densities is illustrated in **Figure 3-5**. In general, the radicals (see **Figure 3-5(a)**) reach clearly higher densities than the ions, because they are more efficiently formed during the pulse (see also **Figure 3-2** above), but their densities drop significantly in the afterglow due to recombination reactions. The most important radicals are CH_3 and H, because they are both formed directly from electron impact dissociation of CH_4. Contrary to many common assumptions (see section 2.3.3. below), the OH radicals are found to play a quite minor role, with a density of 10^{10} cm^{-3} during the pulse, increasing to 4×10^{11} cm^{-3} during the afterglow, and then followed by a strong decline, due to the loss process $CO + OH \rightarrow CO_2 + H$.

The ions are depicted in **Figure 3-5(b,c)** and can be divided in two groups: CH_5^+, $C_2H_5^+$, H_3O^+ and OH^- (**Figure 3-5(b)**) are formed during the pulse, but have also a considerable lifetime in the afterglow, whereas CH_4^+, CH_3^+, CO_2^+ and O^- (**Figure 3-5(c)**) are only present during the pulse. The CH_5^+, $C_2H_5^+$ and OH^- ions are formed immediately and their densities reach a steady state already during the pulse. This is due to a competition of formation and loss processes, i.e.,

- For CH_5^+, there is an equilibrium between $CH_4^+ + CH_4 \rightarrow CH_5^+ + CH_3$ as formation process, and $e^- + CH_5^+ \rightarrow CH_3 + H + H$ as loss process.

- For $C_2H_5^+$, the two most important production processes (i.e., $CH_5^+ + C_2H_4 \rightarrow C_2H_5^+ + CH_4$, and $CH_3^+ + CH_4 \rightarrow C_2H_5^+ + H_2$) are in equilibrium with the two dominant loss processes (i.e., $e^- + C_2H_5^+ \rightarrow C_2H_3 + H + H$, and $e^- + C_2H_5^+ \rightarrow C_2H_2 + H_2 + H$).

- Finally, for OH^-, the dominant production processes (i.e., $O^- + CH_4 \rightarrow OH^- + CH_3$, and $e^- + H_2O \rightarrow OH^- + H$) are compensated by the loss process $OH^- + CH_3 \rightarrow CH_3OH + e^-$.

The formation of H_3O^+ ions occurs at a lower rate, but continues in the afterglow, because it is formed out of $C_2H_5^+$ ions, through:

$C_2H_5^+ + H_2O \rightarrow H_3O^+ + C_2H_4$.

However, when all $C_2H_5^+$ has reacted away, the loss processes of H_3O^+ become more important than the production process, leading also to a drop in H_3O^+ density.

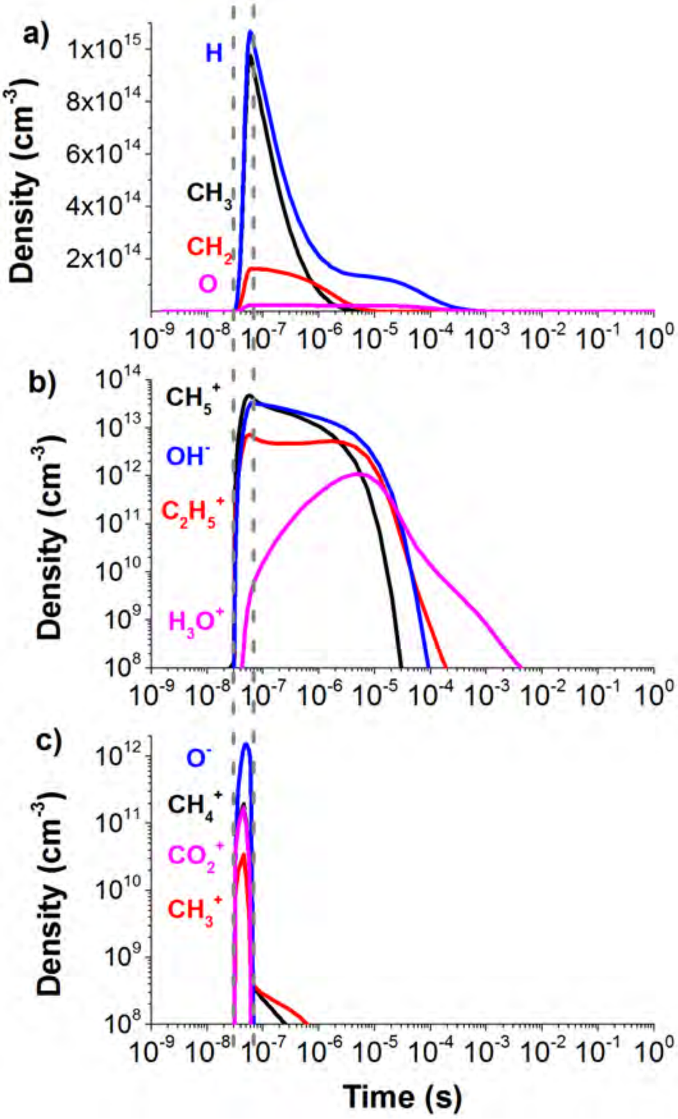

Figure 3-5. Calculated densities of the most important radicals (a) and ions (b,c) formed in the plasma, as a function of time during one pulse and afterglow. The grey dashed lines indicate the start and the end of the micro-discharge pulse.

c) *Reaction path analysis for loss and production of CH_4 and CO_2*

Table 3-2. Overview of the most important loss and formation reactions for CH_4, during the pulse and afterglow.

Loss processes:	
During the pulse	**During the afterglow**
(1) $e^- + CH_4 \rightarrow CH_3 + H + e^-$	(4) $CH + CH_4 \rightarrow C_2H_4 + H$
(2) $e^- + CH_4 \rightarrow CH_2 + H_2 + e^-$	(9) $OH + CH_4 \rightarrow CH_3 + H_2O$
(3) $e^- + CH_4 \rightarrow CH + H_2 + H + e^-$	(10) $CH_3^+ + CH_4 \rightarrow C_2H_5^+ + H_2$
(4) $CH + CH_4 \rightarrow C_2H_4 + H$	(5) $CH_4^+ + CH_4 \rightarrow CH_5^+ + CH_3$
(5) $CH_4^+ + CH_4 \rightarrow CH_5^+ + CH_3$	
(6) $e^- + CH_4 \rightarrow CH_4^+ + e^- + e^-$	
(7) $O^- + CH_4 \rightarrow CH_3 + OH^-$	
(8) $CO_2^+ + CH_4 \rightarrow CH_4^+ + CO_2$	
Formation processes:	
During the pulse	**During the afterglow**
(11) $CH_3 + H + M \rightarrow CH_4 + M$	(11) $CH_3 + H + M \rightarrow CH_4 + M$
	(12) $CH_5^+ + C_2H_4 \rightarrow CH_4 + C_2H_5^+$
	(13) $CH_5^+ + CH_2 \rightarrow CH_4 + CH_3^+$
	(14) $CH_5^+ + H_2O \rightarrow CH_4 + H_3O^+$

Note: M can be any plasma species (but typically CH_4 or CO_2, as they have the highest densities)

Table 3-2 lists the most important loss and formation processes for CH_4 in order of decreasing importance, during the pulse and afterglow. During the pulse, the electron impact reactions are by far the most important loss mechanisms, and especially electron impact dissociation with the formation of CH_3 and H (reaction 1 of **Table 3-2**). This explains why the CH_3 and H radical densities are higher than the other radical and ion densities (see **Figure 3-5** above). However, immediately after pulse termination, the rates of these electron impact reactions drop to nearly zero, due to the drop in electron temperature (see **Figure 3-1** above), and in the afterglow, the chemical reactions with radicals and ions are the most important loss processes (especially reactions 4 and 9 of **Table 3-2**). Integrated over one pulse and afterglow, the electron impact reactions contribute for 77% to the loss of CH_4, in spite of the fact that they only occur during the pulse, while the ion and radical reactions account for 23% (see **Table 3-3**).

Table 3-3. Contributions of the most important loss and formation processes for CH_4, integrated over the time of one pulse (30 ns), the afterglow (30ns–1s) and the total pulse + afterglow.

Loss processes	**Pulse**	**Afterglow**	**Pulse and afterglow**
Electron impact (1-3, 6)	80 %	0 %	77 %
Chemical reactions (4-5, 7-10)	20 %	100 %	23 %
Formation processes	**Pulse**	**Afterglow**	**Pulse and afterglow**
Reaction 11	100 %	99 %	99 %
Reactions 12-14	0 %	1 %	1 %

The formation processes of CH_4 are not so relevant, because CH_4 is mainly lost (dissociated), but nevertheless, they are briefly discussed here, as they have a negative contribution to the conversion of CH_4. During the pulse, the three-body recombination reaction between CH_3 and H radicals, with a gas molecule as third body (reaction 11 of **Table 3-2**), is the only production mechanism for CH_4, and this reaction is also dominant in the afterglow. Integrated over pulse and afterglow, it contributes for 99 % to the production of CH_4 (see **Table 3-3**), whereas the remaining 1 % is attributed to other chemical reactions (i.e. reactions 12–14 of **Table 3-2**).

Figure 3-6(a,b) illustrates the absolute reaction rates of the loss and production processes, respectively, as a function of time. It is clear that during the pulse the rate of the electron impact reactions yielding loss of CH_4 (reactions 1–3 and 6 of **Table 3-2**) is one order of magnitude higher than the rate of reaction 11, which is the major production process (i.e., ca. 10^{23} cm^{-3} s^{-1} vs. ca. 10^{22} cm^{-3} s^{-1}), so that during the pulse mainly dissociation of CH_4 takes place. In the afterglow, however, the electron impact reactions do not play a role anymore, and the loss is mainly attributed to reactions 4–5 and 9–10, with an overall reaction rate of ca. 10^{15}–10^{19} cm^{-3} s^{-1} (see **Figure 3-6(a)**). The formation processes (reaction 11–14), on the other hand, are characterized by an overall rate of ca. 10^{18}–10^{20} cm^{-3} s^{-1} in the afterglow (see **Figure 3-6(b)**), so that the formation of CH_4 is now much larger than the loss, explaining why the CH_4 density rises again in the afterglow (see **Figure 3-3** above).

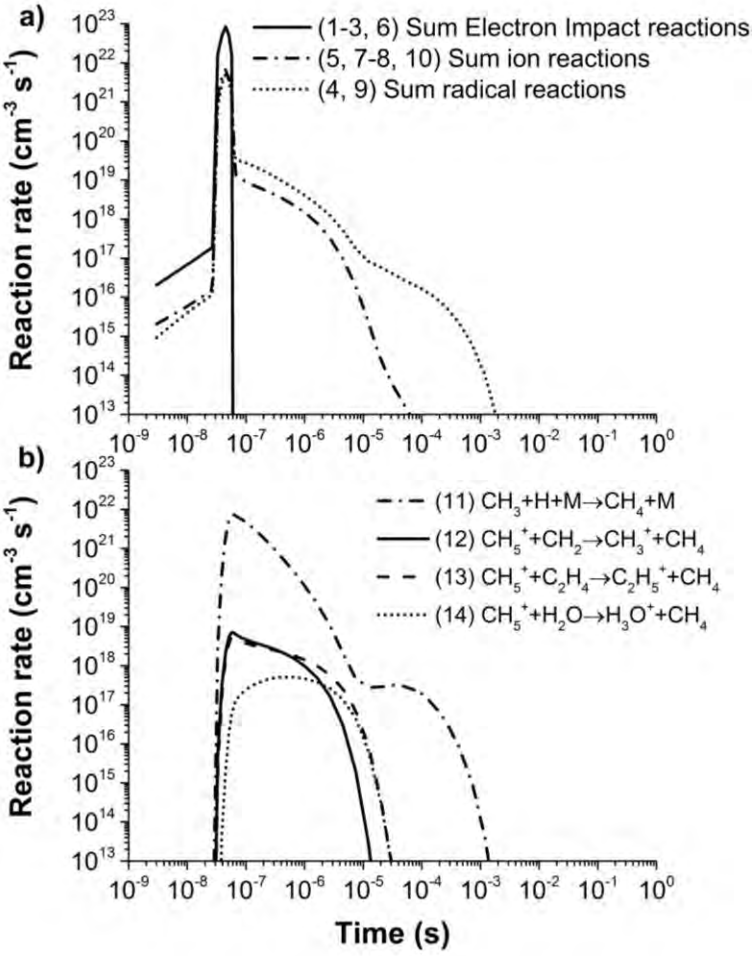

Figure 3-6. Rates of the most important loss (a) and formation (b) processes of CH_4, as a function of time during one pulse and afterglow. The numbers of the reactions correspond to the numbers of Table 3-2.

Table 3-4. Overview of the most important loss and formation reactions for CO_2, during the pulse and afterglow.

Loss processes:

During the pulse	**During the afterglow**
(15) $e^- + CO_2 \rightarrow CO + O^-$	(18) $CH_2 + CO_2 \rightarrow CH_2O + CO$
(16) $e^- + CO_2 \rightarrow CO + O + e^-$	
(17) $e^- + CO_2 \rightarrow CO_2^+ + e^- + e^-$	

Formation processes:

During the pulse	**During the afterglow**
(8) $CO_2^+ + CH_4 \rightarrow CH_4^+ + CO_2$	(19) $O + CHO \rightarrow CO_2 + H$
	(20) $O + CH_3CO \rightarrow CO_2 + CH_3$
	(21) $CO + OH \rightarrow CO_2 + H$

The most important loss and formation processes for CO_2 are listed in **Table 3-4**. During the pulse, the electron impact (dissociation and ionization) processes (i.e., reactions 15–17 of **Table 3-4**) are again dominant. In contrast to CH_4, the dissociation and ionization reactions of CO_2 are equally important, which can be explained by their cross sections.[36] Note that the dissociation reactions (reactions 15–16) both produce CO, whereas only reaction 16 produces O. This explains partly why the CO density during the pulse is about a factor of 2 higher than the O density (cf. **Figure 3-4(b)** and **Figure 3-5(a)** above). Similar to CH_4, the electron impact reaction rates drop to zero in the afterglow, and the chemical reactions with radicals become responsible for the loss of CO_2. Especially reaction 18 of **Table 3-4** is important, which explains the strong increase in CH_2O density in the afterglow (see **Figure 3-4(c)** above). As CO is also formed in this reaction, this explains why also the CO density increases further in the afterglow, as was clear from **Figure 3-4(b)** above. Integrated over one pulse and afterglow, the electron impact reactions (i.e., reactions 15–17) contribute for 33% to the loss of CO_2, as is summarized in **Table 3-5**, whereas the chemical reactions with radicals contribute for 67%. This is in contrast to CH_4, where the electron impact reactions were clearly dominant (see above).

Table 3-5. Contributions of the most important loss and formation processes for CO_2, integrated over the time of one pulse (30 ns), the afterglow (30ns–1s) and the total pulse + afterglow.

Loss processes	Pulse	Afterglow	Pulse and afterglow
Electron impact (15-17)	98 %	0 %	33 %
Reaction 18	2 %	100 %	67 %

Formation processes	Pulse	Afterglow	Pulse and afterglow
Reaction 8	100 %	0 %	99.7 %
Reactions 19-21	0 %	100 %	0.3 %

During the pulse, the dominant formation reaction is the charge transfer between CO_2^+ and CH_4 (reaction 8 of **Table 3-4**), with a rate of ca. $2x10^{21}$ cm^{-3} s^{-1}. In the afterglow, this reaction becomes negligible, and some radical reactions (especially reactions 19–21 of **Table 3-4**) become important.

When looking again at the reaction rates of the different loss and formation processes as a function of time (see **Figure 3-7(a,b)**), it is obvious that during the pulse again mainly loss of CO_2 takes place, i.e., the total loss rate of reactions 15–17 is with a value of ca. 10^{22} cm^{-3} s^{-1} nearly one order of magnitude higher than the rate of the most important formation process (i.e., reaction 8, ca. $3x10^{21}$ cm^{-3} s^{-1}). Nevertheless, this difference is smaller than in the case of CH_4, which explains why the conversion of CO_2 is less pronounced during the pulse than for CH_4 (see **Figure 3-3** above). This is an immediate consequence of the much higher binding energy of C=O vs. C-H (i.e. 8.3 eV/molecule vs. 4.3 eV/molecule), so that electron impact dissociation of CO_2 is somewhat more difficult. Furthermore, this higher stability causes the CO_2 conversion to occur predominantly by electron impact during the pulse (see **Table 3-5**), while CH_4 loss is initiated by both electrons and radicals (see **Table 3-3**), thus explaining again the higher conversion of CH_4 versus CO_2 during the discharge pulse.

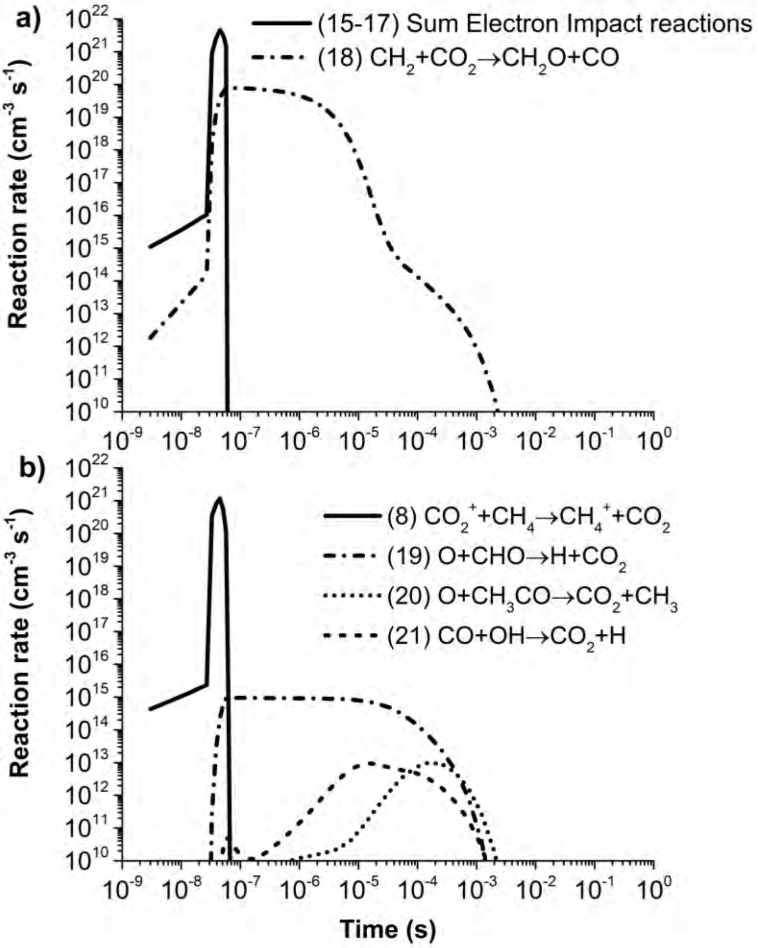

Figure 3-7. Rates of the most important loss (a) and formation (b) processes of CO_2, as a function of time during one pulse and afterglow. The numbers of the reactions correspond to the numbers of Table 3-4.

In contrast to CH_4, where the formation mechanisms became more important than the loss processes in the afterglow, for CO_2 the chemical loss processes (more specifically reaction 18) are still far more important than the formation processes (reactions 19–21), i.e., with rates of 10^{20} cm^{-3} s^{-1} vs. 10^{15} cm^{-3} s^{-1} (see **Figure 3-7**). Hence, CO_2 will continue to be lost in the afterglow, explaining why its density drops further (see **Figure 3-3** above).

2.3.2. Five consecutive discharge pulses: Study of the accumulation effect

a) Power deposition, electron density, and temperature

In **Figure 3-8**, the applied power deposition and calculated electron density and temperature are plotted as a function of time, for five consecutive discharge pulses, with an interpulse period of 1 μs. This corresponds to a typical interpulse period of a filamentary DBD regime, as is observed in **Figure 2-2**. However, in reality, not all filaments take place at the same position; they are spatially distributed, and thus most probably not all molecules pass through all filaments. As mentioned above, in the next section, we will show results of several calculations, with different assumptions about the number of filaments per half cycle. However, as we don't know the real number of filaments that each molecule passes, we will assume a much higher pulse repetition frequency in this section compared to section 2.3.3. for the real time-scale simulations. We use this method to find out whether some accumulation effects might occur experimentally in case some molecules would pass more pulses in a short time period, because of their statistical distribution.

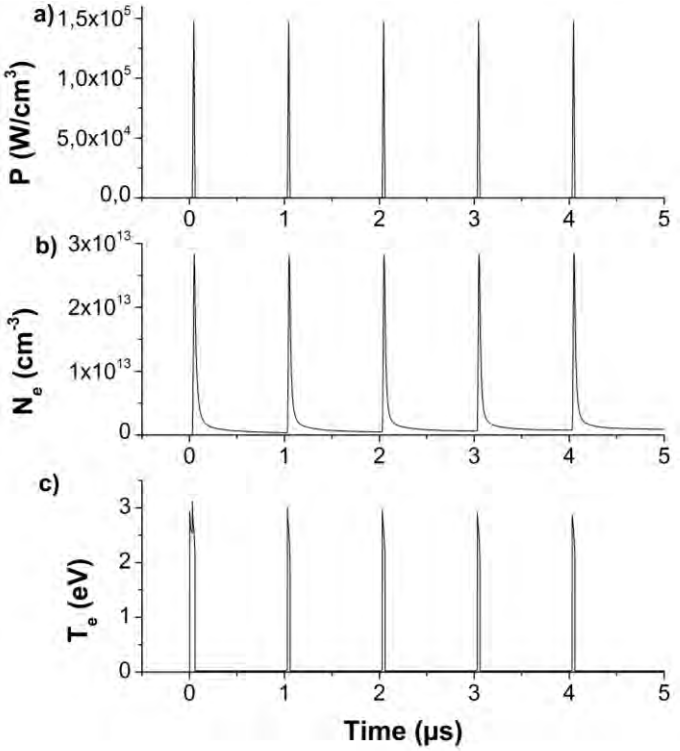

Figure 3-8. Applied power deposition (a), and calculated electron density (b) and electron temperature (c), as a function of time for five consecutive pulses with an interpulse period of 1 μs.

As is clear from **Figure 3-8**, the same triangular pulse as in previous section, with the same power density, is applied, and therefore, the calculated electron density and temperature reach the same values as in **Figure 3-1** above. This indicates that the plasma nearly extinguishes in the afterglow between two micro-discharge pulses, even when we assume a very high pulse repetition frequency of 1 MHz.

b) Densities of the plasma species

Figure 3-9 illustrates the overall densities of the molecules, radicals and positive and negative ions, as a function of time, for the five consecutive discharge pulses. In spite of the fact that the plasma nearly extinguishes between two pulses (see **Figure 3-8** above), the consecutive pulses still lead to some accumulation of the radicals and ions, as is clear from **Figure 3-9**. Indeed, each separate pulse exhibits the same effect on the species densities, but because the formed radicals and ions do not fully recombine at a timescale of 1 μs, i.e. the interpulse period, some accumulation in the densities is observed in **Figure 3-9**.

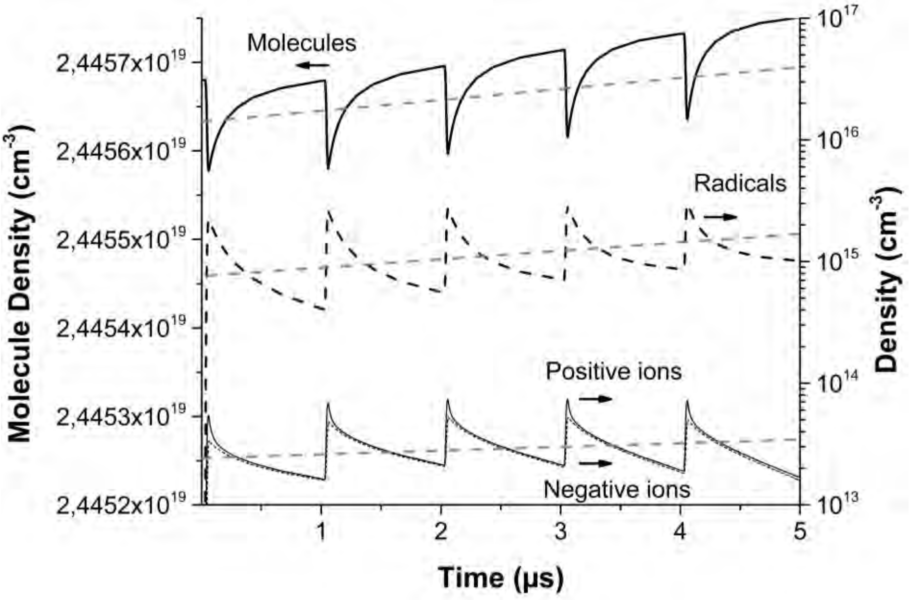

Figure 3-9. Calculated densities of all the molecules (left axis) and all the radicals, positive and negative ions (right axis), as a function of time for five consecutive pulses with an interpulse period of 1 μs. The dashed lines indicate the (slightly) increasing trend of the densities as a function of time.

It appears that also the molecule density shows a slightly increasing trend. This is because the number of molecules increases during the conversion process. This can be explained by reactions 2 and 18 from **Table 3-2** and **Table 3-4**, respectively, which are important loss mechanisms for CH_4 and CO_2, respectively:

Reaction 2: $e^- + CH_4 \rightarrow CH_2 + H_2 + e^-$

Reaction 18: $CH_2 + CO_2 \rightarrow CH_2O + CO$

Hence the combination of both reactions gives: $e^- + CH_4 + CO_2 \rightarrow CH_2O + CO + H_2 + e^-$. It is indeed clear that the number of molecules in this reaction increases from two to three. However, the rise in molecule density is very minor, as appears from the left y-axis of **Figure 3-9**.

When related to the actual density values, the radical density increases by 28% per pulse, whereas the positive and negative ion densities rise by 4% and 3%, respectively, and the molecule density remains virtually constant. This indicates that, even in case each molecule passes through every micro-discharge (filament), the accumulation effect on the molecule densities, and hence on the conversion of CH_4 and CO_2 and the selectivities of the formed products, will be very limited. On the other hand, the number of discharge pulses per half cycle will have a great influence on the electron density, and the latter will affect the calculated conversion and selectivities, as will be illustrated below.

The densities of the individual species are not plotted here for the five consecutive pulses, as the results are very similar as for one pulse, presented in section 2.3.1. above, combined with the accumulation effect illustrated in **Figure 3-9**.

2.3.3. Real time-scale simulations

Finally, in this section, we apply the model to real time-scales, corresponding to typical residence times of the gas molecules in the plasma, in order to obtain a first estimate of the obtained conversions, selectivities and energy efficiency, to be compared with experimental data as a validation of the model. It should be emphasized, however, that it is not yet the focus of the present study to optimize the obtained conversions, selectivities and energy efficiency. The latter will be elaborated in section 3.

a) Considerations about residence time and specific energy input

We still consider triangular micro-discharge pulses of 30 ns, but with a repetition frequency of 70 kHz. This correlates to an applied frequency of 35 kHz, as used in the experiments,[37] assuming that each molecule passes through only one micro-discharge per half cycle. The residence time for the experimental data used to validate our model is 6.8 s, 13.7 s and 27.4 s, as calculated from the gas flow rate and the length of the reactor. This corresponds to simulating ca. 500,000–2,000,000 consecutive micro-discharge pulses. Furthermore, the maximum power deposition per pulse is adapted, so that the total SEI (see eq.2-4 to eq.2.7) corresponds to the typical experimental values [26] (i.e. in the order of 18-144 J/cm^3; see below).

We performed simulations for residence times of 6.8, 13.7 and 27.4 s, exactly as used in the experiments. This corresponds to flow rates of 100, 50 and 25 ml/min, respectively, for a reactor with a plasma volume of 11.4 cm^3 as used in the work of Gallon et al.[37] In order to obtain the same SEI as in the experiments, the maximum power deposition per discharge pulse was adapted accordingly with the different applied powers used experimentally (30, 40, 50 and 60 W) for a constant simulated micro-discharge pulse frequency of 70 kHz (corresponding to the experimentally applied frequency of 35 kHz). These values of the power deposition per pulse gave again rise to calculated electron temperature values during the pulse of ~3 eV, which corresponds to typical experimental values. The resulting calculated maximum values for N_e, however, were rather on the lower limit of typical experimental values (~10^{12} cm^{-3}). Furthermore, the conversions were slightly overestimated. Therefore, additional simulations were performed yielding the same values of T_e, but calculated values for N_e of ~10^{14} cm^{-3}. To achieve this, the pulse frequency was lowered to 0.7 kHz, corresponding to the assumption that each molecule passes one micro-discharge every 100 half cycles instead of every half cycle. This assumption does not only provide better agreement with experiment, but also makes more sense intuitively, since we have spatially divided filaments, which only occupy a low volume in comparison to the total reactor volume. As will be illustrated below, these simulations still resulted in an overestimation of the conversions. However, in our calculations we assumed the same plasma power as in the experiments, whereas it is generally known that not all the plasma power goes into chemical reaction processes. Indeed, part of it is lost by reflection in the reactor and to gas heating. Furthermore, not all excitation processes of all species are taken into account, but they also “consume” part of the plasma power. Hence, we have to take these “power loss processes” into account in the simulations, by using a factor which we will call the “plasma power transfer efficiency”. That is why we performed two more sets of simulations, assuming that only 75 % and 50 % of the plasma power is effectively transferred to the chemical reaction processes, while maintaining a T_e of ~3 eV and a N_e in the order of ~10^{14} cm^{-3}. The results of all four sets of simulations will be presented in the following figures, to investigate the impact of these assumptions. It will be demonstrated that the simulations assuming N_e of ~10^{14} cm^{-3} with 50 % plasma power transfer efficiency show the best agreement with the experiments, hence these results will be discussed in the points below.

b) Conversion of CH_4 and CO_2

The parameters of interest to define whether plasma technology has enough perspectives for the dry reforming of methane are, as already mentioned, the conversion of CO_2 and CH_4 (eq.2-8), the selectivity of the reaction products (eq.2-15–eq.2-18), and the energy cost (eq.2-13–eq.2-14) and energy efficiency (eq.2-11) of the process. The calculated selectivity, energy cost and energy efficiency will be presented in the next sections. Here we will present the calculated conversion, and compare with experimental data.

The calculated conversions of CH_4 and CO_2, as obtained with the assumption of N_e ~10^{14} cm^{-3} with 50 % plasma power transfer efficiency (see above), are plotted in **Figure 3-10** as a function of time, for a SEI of 18 J/cm^3. It is clear that the conversion of CH_4 and CO_2 increases with time, and the conversion of CH_4 is about a factor of 2 higher than the conversion of CO_2, as was anticipated from the short time-scale simulations presented in section 2.3.1. The conversion of both gases increases more or less linearly with time, but it will saturate after a certain time, due to the competition of production and loss processes.

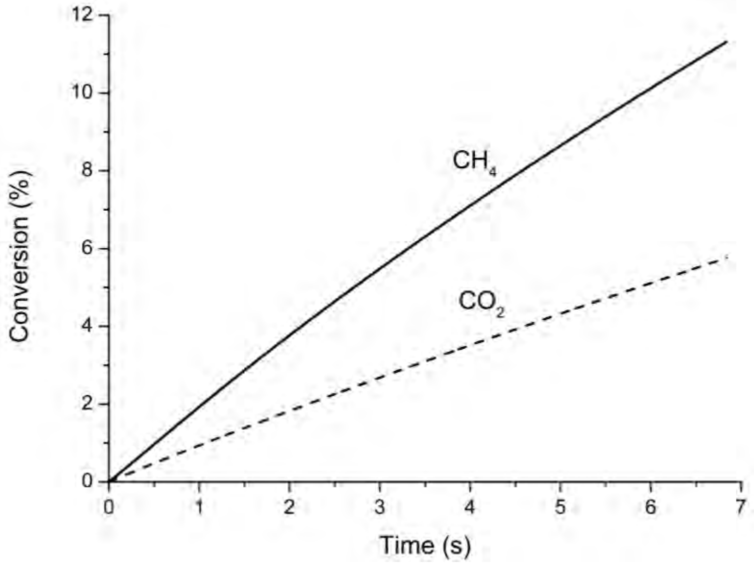

Figure 3-10. Calculated conversion of CH_4 and CO_2, as a function of time, for a simulated residence time of 6.84 s, with a SEI of 18 J/cm^3.

Figure 3-11 illustrates the calculated conversions of CH_4 and CO_2 as a function of discharge power (open symbols), for different gas flow rates, in comparison with experimental values obtained from Tu et al.[32] (black symbols and trend lines). As explained above, four sets of simulation results are illustrated. It is clear that the results obtained with N_e ~10^{12} cm^{-3} and N_e ~10^{14} cm^{-3}, assuming 100 % plasma power transfer efficiency (red and orange open symbols, respectively) are systematically higher than the experimental data. The agreement is still reasonable for the data obtained with N_e ~10^{12} cm^{-3}, but the data obtained with N_e ~10^{14} cm^{-3} are significantly higher. Therefore, we also performed simulations with N_e ~10^{14} cm^{-3}, assuming a plasma power transfer efficiency of only 75 % and 50 % (dark and light green symbols, respectively), and this yields lower conversions, as expected. In general, the latter assumption (i.e., 50 % plasma power transfer efficiency) yields an almost perfect agreement with the experimental data.

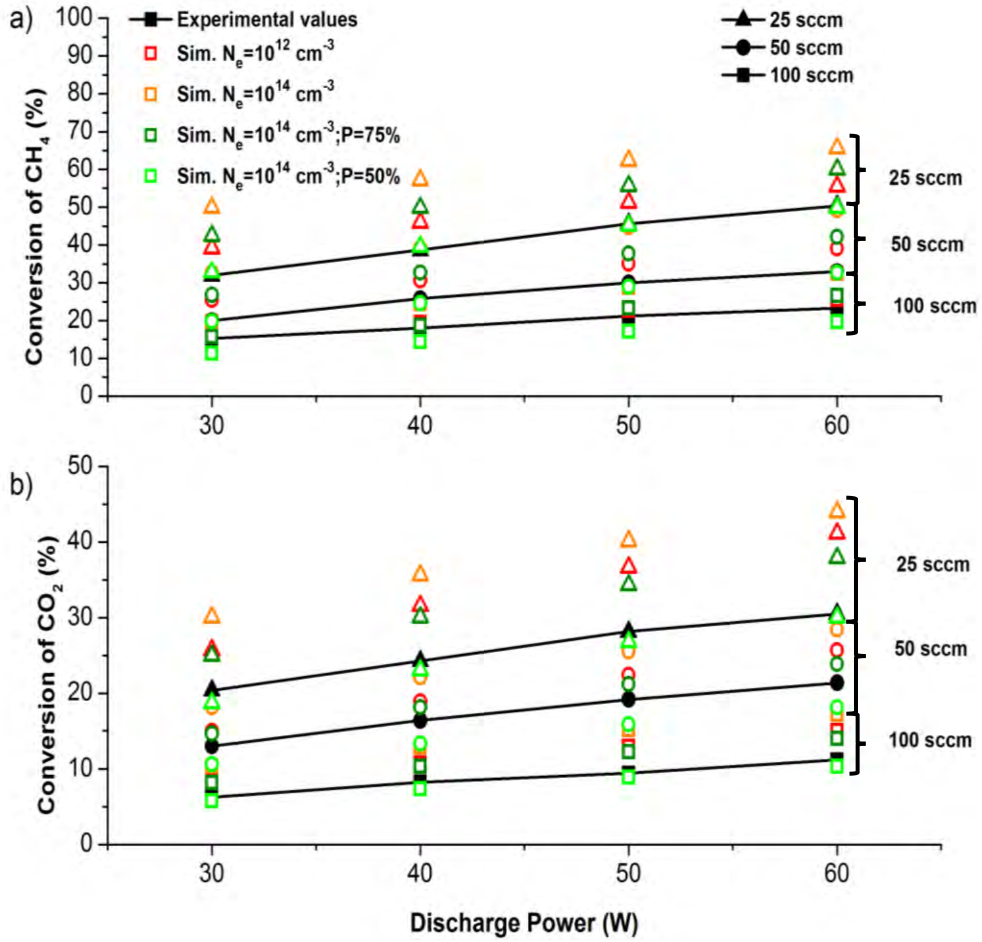

Figure 3-11. Comparison of the calculated (open symbols) and experimentally measured (full black symbols + trend lines) conversions of CH_4 (a) and CO_2 (b), as a function of discharge power for various flow rates (see legend).

It needs to be mentioned that a relative error of 5–10% due to plasma instability should be taken into account for the experimental values obtained by GC measurement, on top of the already mentioned unknown uncertainty for the 'real' experimental plasma power input. Moreover, also the calculated values are subject to some uncertainties, mainly due to uncertainties (i.e. unknown error bars) in the reaction rate coefficients, used as input in the model. Therefore, the present comparison can be considered to be fairly good for both CH_4 and CO_2, because the difference between calculated and experimental values is probably within the error bars. Moreover, all the simulations show exactly the same rising trend as the experiments. In general, this reasonable agreement between calculated and experimental conversions, in this range of power and gas flow rates, is a very important validation of the model, and it indicates that our model gives a quite realistic description of the plasma chemistry.

In **Figure 3-12**, the same data are plotted as a function of SEI, as calculated from the power values and flow rates. Again, the best agreement is reached for the simulations with $N_e \sim 10^{14}$ cm^{-3}, assuming 50 % plasma power transfer efficiency. It is apparent from this figure that the conversion increases more or less linearly with the SEI values, which seems logical. However, a higher SEI value implies a higher energy cost, and it has therefore a negative impact on the energy efficiency (see below). There will probably be an optimum between conversion, selectivity and energy cost and efficiency, which we will further investigate in section 3 below.

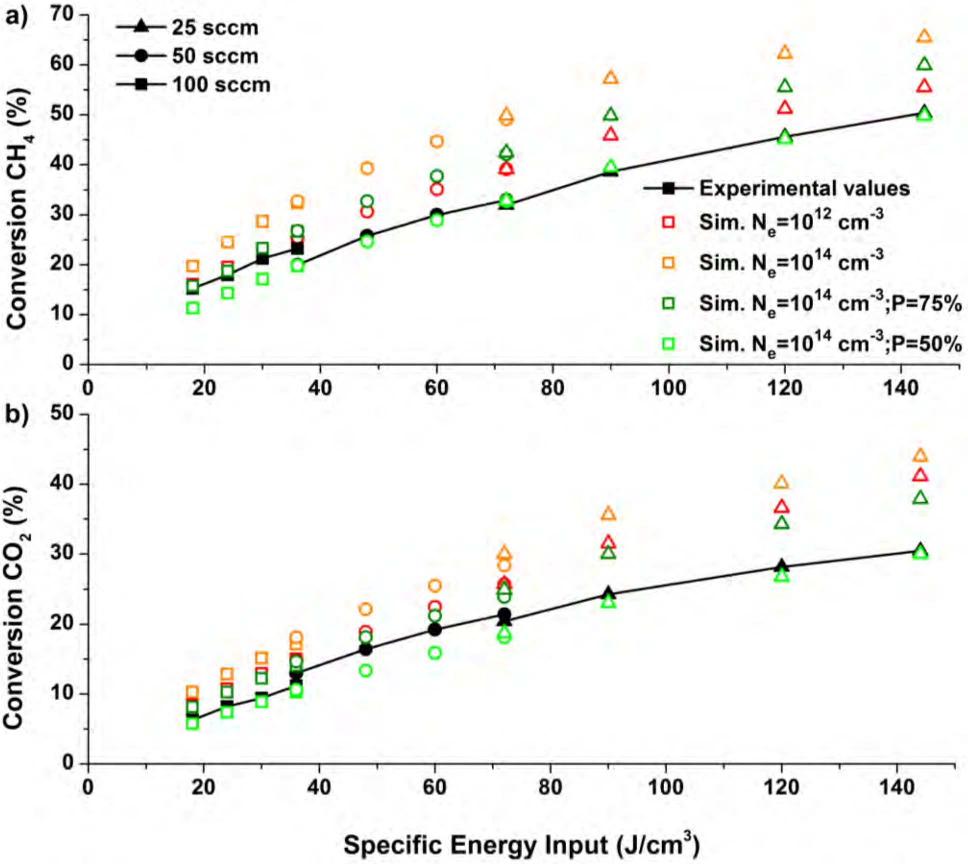

Figure 3-12. Calculated (open symbols) and experimentally measured (full black symbols + trend line) conversions of CH_4 (a) and CO_2 (b), as a function of SEI.

Furthermore, comparing **Figure 3-12(a,b)** tells us that the CH_4 conversion is systematically higher than the CO_2 conversion, for the same SEI and residence time. This behaviour was also found experimentally,[13] but was considered to be surprising, as for the separate gases, the conversion of CO_2 is typically higher than for CH_4.[16] A possible explanation suggested in literature,[35] is the reaction: CO + OH → CO_2 + H. According to Yao et al.[38] this reaction would reduce the conversion of CO_2 in the CH_4/CO_2 mixture. However, our reaction path analysis, presented in section 3.2.1. above, revealed that this reaction (i.e., reaction 21 in **Table 3-4** above) accounts only for 0.02 % of the CO_2 production, whereas reaction 8 of **Table 3-4**, i.e., $CO_2^+ + CH_4 \rightarrow CH_4^+ + CO_2$, contributes for 99 % to the CO_2 production. Hence, our calculations predict that the latter reaction accounts for the reduced CO_2 conversion in the presence of CH_4. This high contribution is the result of the high reaction rate coefficient for this charge transfer process (5.50×10^{-10} cm^3 s^{-1}) in combination with the high density of the second reactant CH_4 (1.22×10^{19} cm^{-3}). This results in a high reaction rate ($\sim 2 \times 10^{21}$ cm^{-3} s^{-1}) during the pulse, as is clear from **Figure 3-7(b)**, where the reaction rates are plotted for the reactions that have the largest (time integrated) contribution to the formation of CO_2. This example illustrates that numerical simulations can be very useful for obtaining a better insight in the underlying physical and chemical processes, as they are based on real quantitative data (i.e. reaction rate coefficients and calculated densities). Moreover, simulations can be very useful to optimize experiments, e.g. by choosing plasma conditions which suppress reaction 8, to enhance the CO_2 conversion.

c) Selectivities of the formed products

The selectivity of the formed products (eq.2-15–eq.2-18) is an even more important quantity than the conversion, as we target the formation of value-added chemicals or new fuels.

The calculated selectivities for the most important reaction products are plotted as a function of time in **Figure 3-13**, again for a fixed SEI of 18 J/cm^3 and obtained with N_e $\sim 10^{14}$ cm^{-3}, assuming 50 % plasma power transfer efficiency. It is clear that H_2 and CO are formed with the highest selectivities, followed by the sum of C_3H_8 and C_3H_6 (noted as sum C_3), CH_2O, the sum of C_2H_6, C_2H_4 and C_2H_2 hydrocarbons (noted as sum C_2) and CH_3OH. Note that the sum of these selectivities is above 100 %, which is due to the definitions given in **Chapter 2**, where the H_2 selectivity is a H-based selectivity and the other selectivities are C-based.

It is also clear from **Figure 3-13** that the selectivities change drastically on a very short time-scale in the beginning of the simulations. This information is of interest, as it indicates that we could tune the process by varying the reaction conditions. In this respect, microplasma reactors could offer an interesting perspective, to stimulate the production of the desired components, yielding higher selectivities.

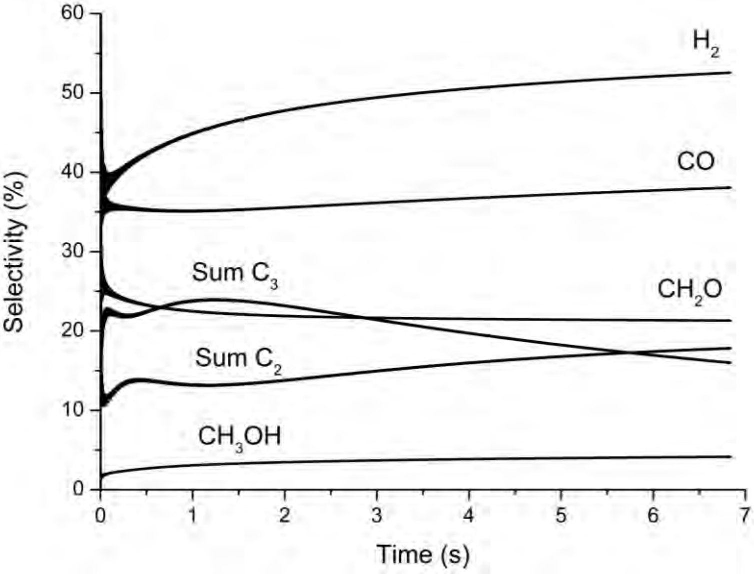

Figure 3-13. Calculated selectivities of the most important products, as a function of time, for a simulated residence time of 6.84 s, with a SEI of 18 J/cm^3.

The calculated selectivities are in reasonable agreement with experimental data from literature,[13,32,39] as illustrated in **Table 3-6**. It needs to be mentioned that it is difficult to identify experimentally the C_2H_y-product selectivities separately and also determining the H_2 selectivity with gas chromatography is quite challenging. Finally, it should be mentioned that the selectivities of the oxygenated products (CH_2O and CH_3OH) could not be compared, as they were not quantitatively measured. However, it is reported in literature that they were indeed observed,[13,20,21,40] which is at least some qualitative validation of our model.

Table 3-6. Calculated selectivities of the most important products and comparison with the experimental data of Tu,[32] Gallon[13] and Wang[39] for a SEI of 18 J/cm^3 and a 1:1 CH_4/CO_2 mixture.

	Conversion		**Selectivity**					
	CH_4	**CO_2**	**H_2**	**CO**	**Sum C_2**	**Sum C_3**	**CH_2O**	**CH_3OH**
Simulation	***16***	***8***	***55***	***48***	***6***	***30***	***13***	***3***
Tu[32]	***15***	***6***	***22***	***35***	***30***	***12***	***-***	***-***
Gallon[13]	10	8	23	42	18	23	-	-
Wang[39]	14	-	57	-	-	-	-	-

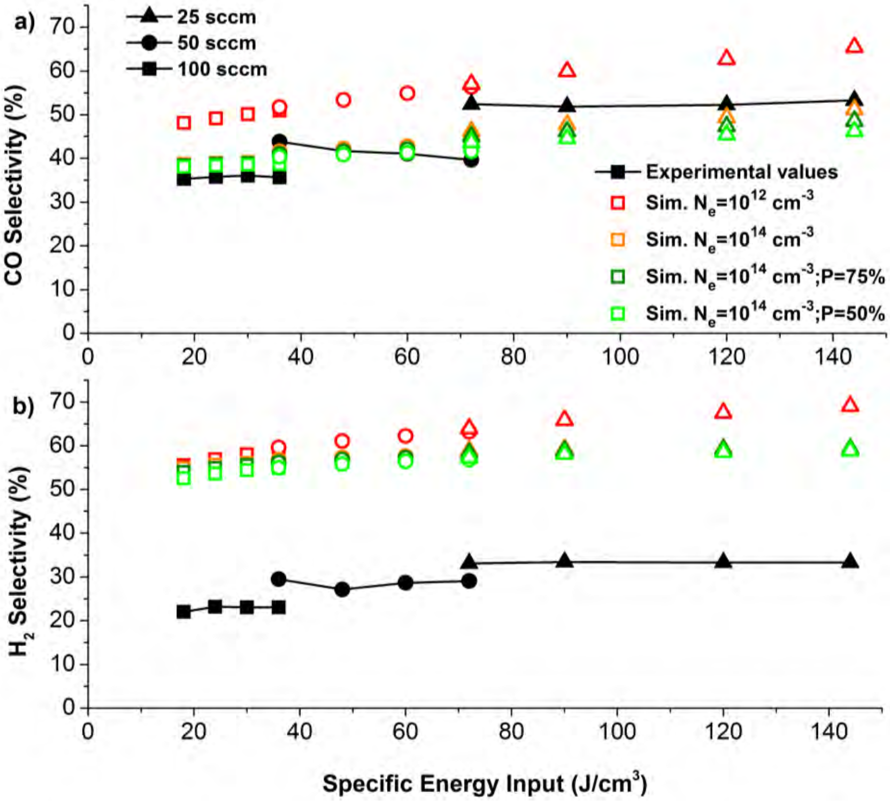

Figure 3-14. Calculated (open symbols) and experimentally measured (full black symbols + trend lines) selectivities of the syngas components CO (a) and H_2 (b), as a function of SEI.

The calculated and experimentally measured selectivities of the two major products, i.e. H_2 and CO, are plotted against SEI values in **Figure 3-14**. Again, the four sets of simulation results are illustrated. They all exhibit a rising trend with SEI. When comparing the calculated and experimental data, it appears that the calculated H_2 selectivity is overestimated by about a factor 2, while the deviations in CO selectivities are only minor, and very similar to the deviation of the CO_2 conversion, presented in **Figure 3-11** and **Figure 3-12** above. However, our results are in reasonable qualitative agreement with the experiments of Gallon et al.[13] Tu et al.[32] and Wang et al.[39] where a similar rising trend with SEI is also observed. In section 3 below, we will carry out a more extensive comparison with experiments to validate our modelling results. It should be stressed that our model contains a large number of chemical reactions, and by changing the reaction kinetics (e.g., rate coefficients) of the model, we can always obtain "a better" fit with experiments. However, we don't want to tune our rate coefficient data, simply to obtain a better agreement with experiment, without physical grounds. The present differences between calculated and measured selectivities illustrate that some chemistry, probably related to the formation or loss of H_2, is not yet fully accounted for in the model, but at present we don't know which loss reaction would be missing or underestimated, or which production reaction would be overestimated in the model. In general, we are already very satisfied with the good qualitative trends. Indeed, the focus of the present section is rather on the detailed investigation of the plasma chemistry during one micro-discharge pulse and afterglow, to mimic the filamentary behaviour.

In any case, it is clear that the syngas components (H_2 and CO) are the main products formed in the dry reforming process, with a syngas ratio (H_2/CO) of ~1.5. This ratio is of considerable interest for the chemical industry, as already discussed above. Also the selectivity of CH_3OH and especially CH_2O are already reasonable, and of great importance, because our simulations predict that these products can be formed directly, without the usual intermediate syngas step.

d) Energy cost and energy efficiency of the process

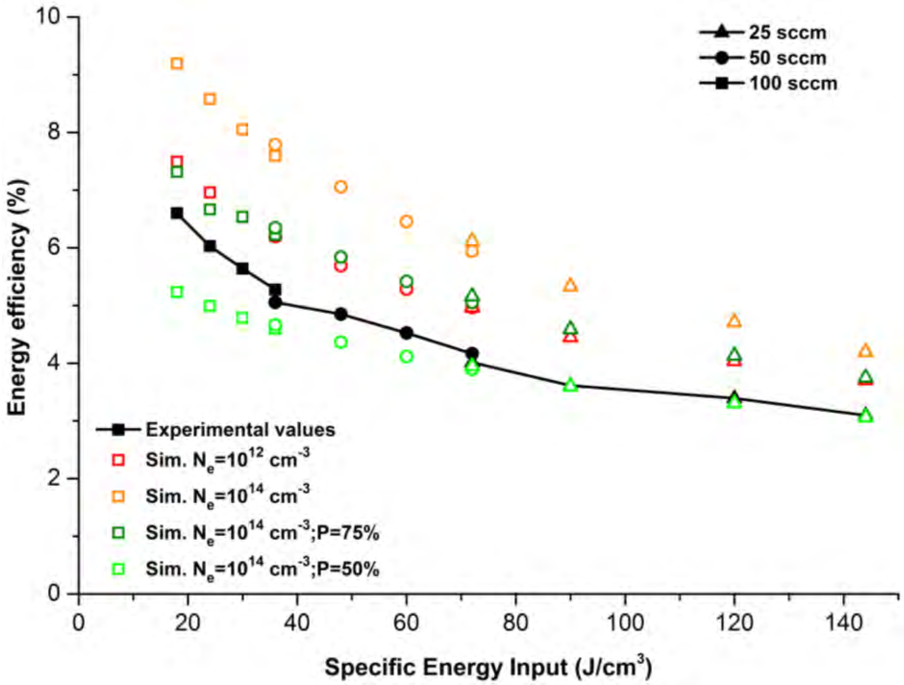

Figure 3-15. Calculated (open symbols) and experimentally measured (full black symbols + trend line) energy efficiency as a function of SEI.

As mentioned above, the energy cost (eq. 2-13–eq.2-14) and energy efficiency (eq.2-11) are probably the most important criteria for the dry reforming process. In **Figure 3-15** the calculated energy efficiency is plotted as a function of SEI for the four sets of simulations (open symbols), in comparison with the experimental data (black symbols + trend lines). It is clear that the higher conversion with increasing SEI (see **Figure 3-12** above) does not compensate for the higher energy input with regard to the energy efficiency. Indeed, the highest energy efficiency is obtained for the lowest SEI value considered in this work, i.e. 18 J/cm^3. For this condition the calculated CH_4 and CO_2 conversions were 11 % and 6 %, respectively, yielding an overall conversion of 8.5 %. This gives rise to an energy cost of 49 eV/converted molecule, and an energy efficiency of 5.2 %. Note that this is still a factor of 10 lower than the classical dry reforming process. However, the latter is not unexpected, as the plasma-based dry reforming process in this section is not yet optimized, which was indeed not the focus of the present section, but rather of section 3 below. Moreover, it is well possible that a pure DBD reactor will never be competitive with the classical dry forming. Therefore, in future work, we should also investigate the combination with catalysis, in so-called plasma catalysis, as well as the performance of other types of plasma reactors, which are stated in literature to be more energy efficient (see also **Chapter 1**).[28,41–43]

2.4. Conclusion

The goal of this section was to obtain a better understanding of the plasma chemistry in a DBD reactor used for the dry reforming of CH_4 and CO_2. For this purpose, a 0D chemical kinetics model, called "Global_kin", developed by Kushner and co-workers, was applied. The filamentary behaviour of a DBD reactor was simulated by describing a large number of consecutive micro-discharge pulses. We investigated in detail the plasma behaviour and the reaction chemistry in one discharge pulse and its afterglow, and we made a reaction path analysis for the two gases to be converted, i.e., CH_4 and CO_2. During the pulse, the electron impact reactions were found to be dominant, whereas chemical reactions with radicals were of primary importance in the afterglow.

We also investigated the accumulation effect of five consecutive micro-discharge pulses, and performed simulations for real time-scales, following a large number of discharge pulses, to calculate the conversion of the gases, the selectivity of the products and the energy cost and energy efficiency of the process. The calculated conversion for a range of different SEI values was found in good agreement with experiments, but a more extensive validation of the model, with respect to the selectivity of the formed products, needs to be carried out in future work. The main reaction products are syngas (in a H_2/CO ratio of ~1.5), as well as, to a lower extent, formaldehyde and methanol, which are all important for the chemical industry. Finally, the energy cost and energy efficiency of the process were calculated, but were found to be not yet competitive with the existing classical dry reforming process. However, it should be mentioned that the process under study is far from optimized yet. Indeed, the main focus of the current section was on understanding the underlying chemical processes. A more extensive study of conversion and especially energy cost and energy efficiency, will be the focus of the next section.

3. Improving the conversion and energy efficiency in a dielectric barrier discharge

3.1. Description of the chemical model

The same model and plasma chemistry were applied as in previous section. Here, we only explain in more detail the physical meaning of the parameters varied in this study.

The parameters varied in this study are as follows:

- CH_4/CO_2 gas composition (%): 90-10, 75-25, 50-50, 25-75, 10-90;
- SEI (J/cm^3): 0.01, 0.1, 1, 10, 100;
- Residence time (s): 0.001, 0.01, 0.1, 1, 10, 100;
- Frequency (kHz): 0.01, 0.1, 1, 10, 100.

Hence, it is clear that for every gas composition 150 different combinations are possible, bringing the total number of numerically investigated cases to 750.

Note that the values of these parameters are chosen based on typical values reported in literature, i.e., a residence time ranging from 1 till 100 s, a SEI going from 1 till 100 J/cm^3 and a frequency in the order of 1 to 100 kHz are commonly reported.[18,32,39,44–48] However, besides these typical values, we also want to explore new regions of these parameters, which are to date not yet reported, e.g. a residence time of 0.001 s, coupled with an SEI of 0.1 J/cm^3, which might be pursued for micro-reactors.[49,50] This is exactly the strength of computer simulations to go beyond the classical conditions and to predict whether new conditions could be more promising, and thus whether experimentally the construction of new reactor types or power set-ups should be pursued.

For the interpretation of the calculation results it is important to understand how the variation of these parameters relates to experiments. The gas composition, SEI and residence time can be directly compared to experiments (through the experimental gas flow rate, reactor volume and power). However, the variation of the “frequency” is a more complex story, which can be looked at from two different angles. (a) On one hand, if we assume that the average number of filaments that occur during each half cycle of the applied voltage is constant, varying the frequency is a way to control the total number of filaments that occur during a certain residence time of the gas, and thus the energy deposited in each filament (keeping the total applied power constant). In this case, the “frequency” directly corresponds to the experimental frequency of the applied voltage. (b) Another way to interpret the “frequency” is when the number of filaments that occur during each half cycle is not constant but varies with the operating conditions. Then, a higher (or lower) “frequency” corresponds to a larger (or smaller) number of filaments during each half cycle, with a lower (or higher) energy deposition per filament. To our knowledge, it is not yet known from literature whether (and how) the number of filaments per half cycle changes for a CH_4/CO_2 gas mixture, depending on the operating conditions. It is well possible that for certain conditions or experimental set-ups assumption (a) is valid, while for other conditions, case (b) is valid, or even a combination of both. This meaning of the "frequency" should thus be kept in mind in the following sections, but in any case, the frequency is directly proportional to the total number of filaments for a fixed gas residence time.

To identify the most energy efficient operating conditions, we varied the following parameters in a wide range: gas composition, specific energy input (SEI), gas residence time and "frequency" (see below). The critical calculation output in this assessment will be the total conversion and the energy efficiency of the process.

3.2. Description of the experiments

3.2.1. Plasma reactor and product analysis

The experiments were carried out by Y.X. Zeng at the University of Liverpool, in a coaxial DBD reactor. A stainless steel mesh (ground electrode) is wrapped over the outside of a quartz tube with an outer and inner diameter of 22 and 19 mm, respectively, while a stainless steel rod with an outer diameter of 14 mm is placed in the centre of the quartz tube and used as high voltage electrode. The length of the discharge region is 90 mm with a discharge gap of 2.5 mm. CH_4 and CO_2 are used as feed gases with a variable total flow rate of 25-200 mL min^{-1} and a CH_4/CO_2 molar ratio from 1:9 to 9:1. The DBD reactor is supplied by a high voltage AC power supply with peak-to-peak voltage of 10 kV and frequency of 50 Hz. The *Q-U* Lissajous method is used to calculate the discharge power.

The feed and product gases are analysed by a two-channel gas chromatograph (Shimadzu GC-2014) equipped with a flame ionization detector (FID) and a thermal conductivity detector (TCD). The GC is calibrated for a wide range of gases using reference gas mixtures (Air Liquid).

3.2.2. Experimental parameter range

Although our model was validated before (see section 2), several additional experiments were performed for this work, to assure that the model, and especially the chemistry set, behave in a realistic manner for conditions beyond the previously validated range (see section 2). However, as the total parameter range under investigation is quite large, still only a small part of it could be probed experimentally. This is exactly the aim of our simulations, i.e., by identifying the effects of the above mentioned parameters and subsequently searching for the optimal conditions, we can save a lot of work on expensive and time consuming experiments.

The experimental parameters selected for this additional model validation are listed in **Table 3-7** for a fixed applied frequency of 50 Hz. This parameter selection is limited, because it is based on one experimental set-up, i.e., reactor (volume), power supply, mass flow controllers, and this of course restricts the experimental range that is possible. The range could have been made wider if experiments would have been performed with different set-ups, but this would have introduced more unknown variables and effects, which we want to avoid. To allow a one-to-one comparison between model and experiments, we performed additional simulations besides the parameter range already mentioned, to mimic the exact experimental conditions.

Table 3-7. Experimental parameters selected for the model validation. The applied frequency was equal to the 50 Hz of the power supply.

Gas mixture CH_4/CO_2 (%)	Residence time (s)	Power (W)	SEI (J/cm^3)
90-10	32.57	15	36
		7.5	18
75-25	32.57	15	36
		7.5	18
50-50	32.57	15	36
		7.5	18
	16.29	15	18
		7.5	9
	10.86	15	12
		7.5	6
	8.14	15	9
		7.5	4.5
	4.07	15	4.5
		7.5	2.25
25-75	32.57	15	36
		7.5	18
10-90	32.57	15	36
		7.5	18

3.3. Results and discussion

First, we will show the comparison between the model and experimental results, explaining the effect of the various parameters on the conversion and energy efficiency. Subsequently, the general influence of these parameters will be discussed in more detail, as observed for the entire simulation range, to reveal the optimum conditions. Finally, we will compare our model predictions with literature and we will identify the limitations as well as the benefits and future possibilities.

In this study, we focus only on the total conversion and resulting energy efficiency, and not on the selectivity of the formed products. However, in general, the following trends regarding the product distributions were observed. At high CO_2 contents, the main products are the molecules typically formed in CO_2 splitting (i.e. CO and O_2), and also a fair amount of H_2O. The reason of its formation was explained in our previous work.[51] Upon increasing the CH_4 content, on the other hand, the concentration of the classical dry reforming products (i.e. H_2, C_2H_2, C_2H_4, C_2H_6, C_3H_6, C_3H_8) starts to increase, at the expense of the CO_2 splitting products. Changing the frequency or residence time only had a small effect on the absolute concentrations of the formed products, but no significant effect on the product distributions.

3.3.1. Comparison between model and experiments

a) *Effect of the gas ratio*

The total conversion and energy efficiency are plotted in **Figure 3-16** as a function of the CO_2 fraction in the mixture, for a SEI of 18 and 36 J/cm³, for both the experimental (black symbols) and modelling results (open red symbols). The total conversion and energy efficiency increase slightly upon addition of more CO_2 in the mixture, followed by a decrease for the highest values. The total conversion is about a factor two higher at 36 than at 18 J/cm³, whereas the energy efficiency is slightly lower. The modelling results only slightly overestimate the total conversion for low CO_2 contents (by 13 and 7 % for the SEI of 18 and 36 J/cm³) and slightly underestimate the total conversion for high CO_2 contents (by 11 and 22 % for the SEI of 18 and 36 J/cm³). This deviation can be explained by the fact that our chemistry does not take into account the vibrational levels of CO_2, which are of lower importance for a DBD,[52,53] and that the chemistry set was primarily validated for a 1:1 mixture.[9] However, the absolute values of both conversion and energy efficiency, as predicted by the model, are generally in good agreement with the experiments, indicating that our model includes the correct plasma chemistry.

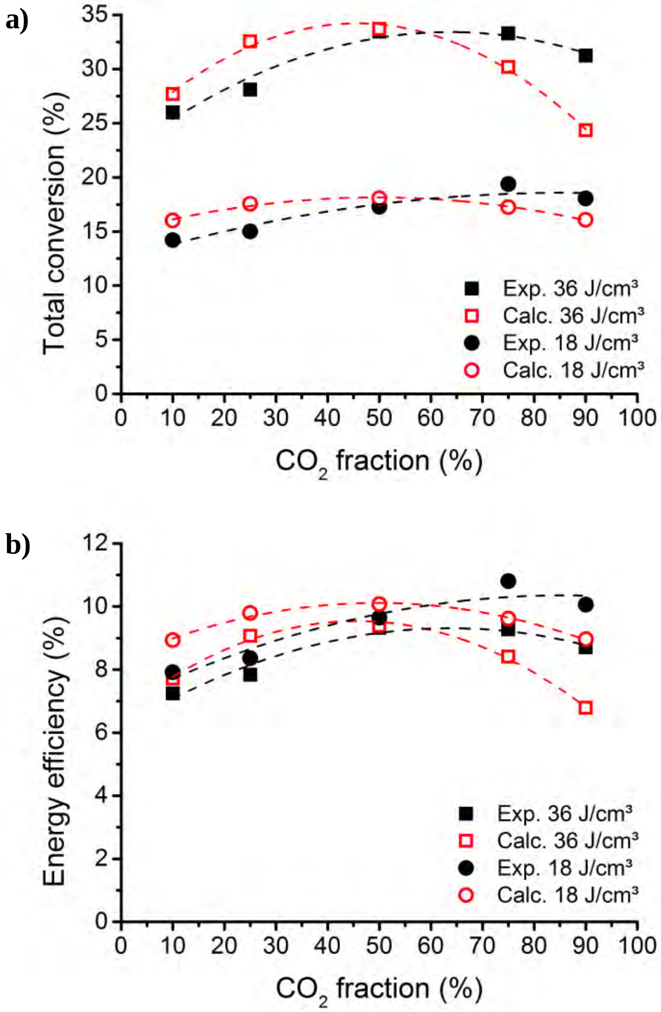

Figure 3-16. Calculated and experimental total conversion (a) and energy efficiency (b) as a function of CO_2 fraction, for a SEI of 18 and 36 J/cm³.

b) Effect of the power, residence time and SEI

In **Figure 3-17**, the total conversion and energy efficiency are plotted as a function of the residence time, for a 1:1 CH_4/CO_2 mixture, at a plasma power of 7.5 and 15 W, for both the experimental (black symbols) and modelling results (open red symbols). The experiments were limited to a residence time between 4 and 33 s, but the model was applied to a residence time of 1 and 100 s, for both power values.

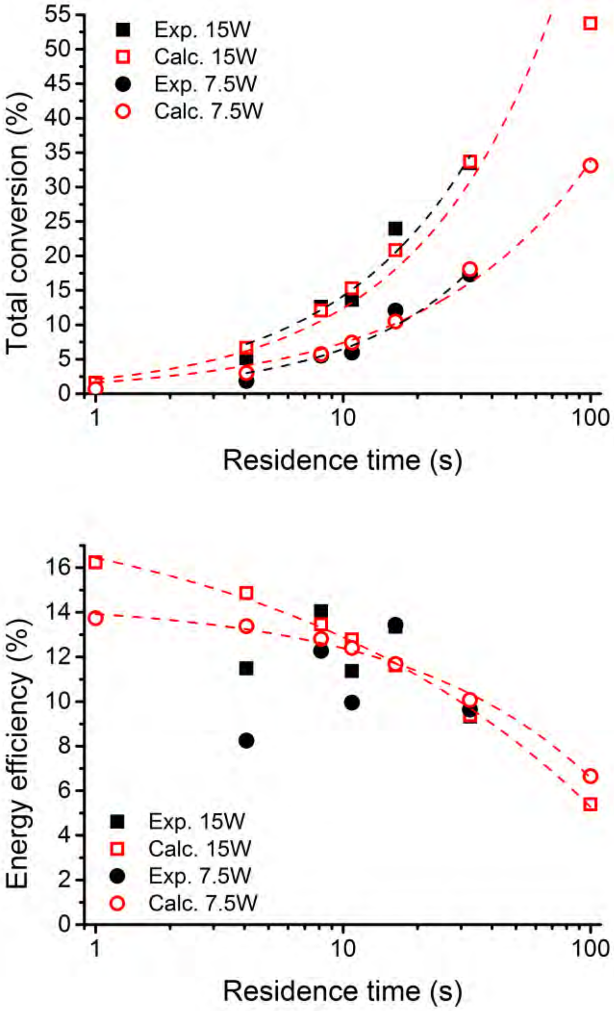

Figure 3-17. Calculated and experimental total conversion (a) and energy efficiency (b) as a function of residence time, for a 1:1 CH_4/CO_2 mixture, and a plasma power of 7.5 and 15 W.

It is clear that both in the experiments and the simulations the total conversion is about a factor two higher for a power of 15 W compared to 7.5 W, at the same residence time, which is logical because a higher power yields more (and higher energy) electrons, which can activate the gas and thus initiate the conversion. For the energy efficiency, the trend is less clear. For a residence time $\leq$ 10 s a higher power yields a slightly higher energy efficiency, whereas for a higher residence time the effect is opposite, but not significant.

Furthermore, when the power is kept constant, the total conversion increases with increasing residence time (which is also straightforward) and the energy efficiency shows the opposite decreasing trend. The latter is most obvious in the calculation results. It follows directly from (eq.2-11) and (eq.2-4): a higher residence time corresponds to a lower flow rate, and thus a higher SEI, at constant power (cf. (eq.2-4)). If the SEI increases more than the conversion, upon increasing residence time, this results in a drop in the energy efficiency (cf. (eq.2-11)).

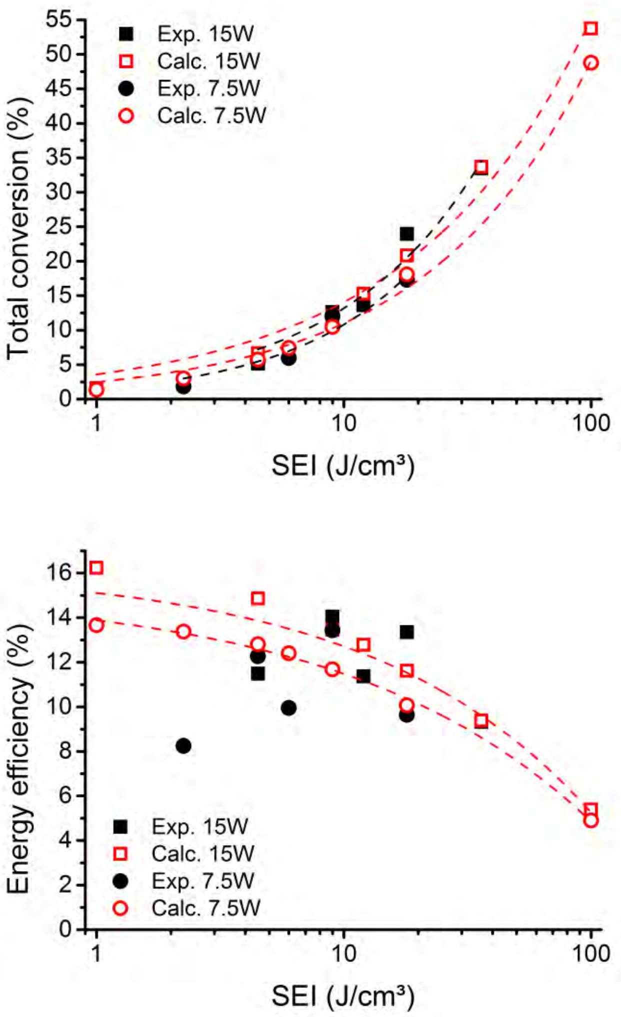

Figure 3-18. Calculated and experimental total conversion (a) and energy efficiency (b) as a function of SEI, for a 1:1 CH_4/CO_2 mixture, and a plasma power of 7.5 and 15 W.

The effect of the residence time and power can also be combined by plotting the total conversion and energy efficiency as a function of the SEI, as shown in **Figure 3-18**, for a plasma power of 7.5 and 15 W and corresponding residence times as reported in

Table 3-7. Note that the model is again applied in a broader range than could be investigated in the experiments, i.e., four extra points were added for an SEI of 1 and 100 J/cm^3, for both power values.

It is clear that the SEI is the major determining factor for the conversion and energy efficiency, as it combines the effect of power and residence time (see (eq.2-4)). Indeed, at the same SEI, increasing the power (thus lowering the residence time) does not affect the total conversion, which remains practically the same at constant SEI. The energy efficiency shows somewhat more variations, when varying the power or residence time, at constant SEI, but these variations are still within a few %.

In general, we may conclude that the calculation and experimental results are again in reasonable agreement, so that we can be confident about the predictive nature of our model, and use it to investigate the effect of the operating conditions in a wider range, beyond what is typically accessible for (standard) experiments.

3.3.2. Model predictions in a wider parameter range

We have systematically studied the effect of all individual parameters, by means of 750 simulations (see above), of which the detailed graphs can be found in **Appendix IV**. In this section, we will show the combined effects, and summarize the general results by means of a few graphs, to elucidate the optimum conditions both in terms of conversion and energy efficiency.

a) Effect of the gas ratio

Figure 3-19 illustrates the calculated energy efficiency plotted as a function of the total conversion, for the best results (solid lines, full symbols) and worst results (dashed lines, open symbols), obtained with the model for all (750) conditions under study. The different gas mixtures are represented by the different coloured symbols (see legend) and the different SEI values are also indicated. The conditions at which the maximum and minimum values of conversion and energy efficiency were reached for each CH_4/CO_2 mixture can be found in Table A IV-3 and A IV-4 of **Appendix IV**.

It is clear that a larger amount of CO_2 leads to a higher total conversion and energy efficiency. This trend is certainly true for the best conditions (solid lines, full symbols). For example, with increasing CO_2 content, the maximum achieved energy efficiency goes from 11.4 to 15.1 %. For the worst conditions, the same trend can be observed for the low SEI values, but for the higher SEI values (10 and 100 J/cm^3), the frequency and residence time start to play a role, and depending on the product of both, a slightly different trend can be observed. These trends are elaborated in detail in **Appendix IV** (see Figures A IV-1–A IV-10).[54] Summarized, in general, the higher total conversion and energy efficiency at larger CO_2 contents is attributed to the O atoms formed by electron impact dissociation of CO_2, which react very effectively with the H atoms originating from electron impact dissociation of CH_4. As shown in our kinetic analysis in section 2,[44] the conversion of CH_4 is normally limited by the fast backward reaction, $CH_3 + H \rightarrow CH_4$, but when more O atoms are available, this reaction is of minor importance compared to the reaction $O + H \rightarrow OH$. Thus, by limiting the backward reaction, the conversion of CH_4 rises dramatically with increasing CO_2 content, leading to a higher total conversion.

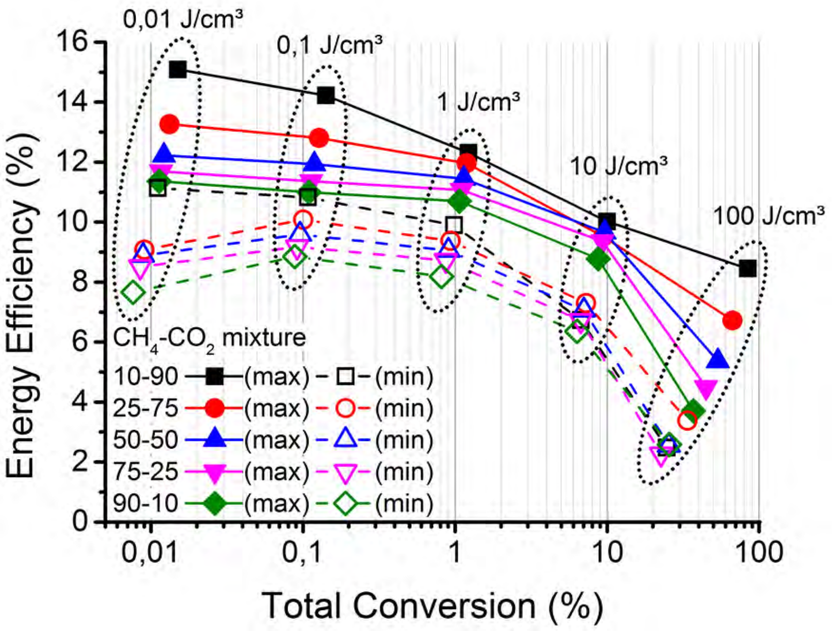

Figure 3-19. Maximum and minimum achieved values of energy efficiency vs total conversion, as obtained from the calculations, for all conditions investigated. The different SEI values are identified with the labels above the curves.

b) Effect of the power, residence time and SEI

Since the residence time and power are coupled through the SEI (see (eq.2.4) above), the same trends are observed when increasing either the power or the residence time. Therefore, we will describe their effect simultaneously, by means of the variation in SEI. At all conditions investigated, increasing the SEI at a constant gas ratio and frequency, results in a higher total conversion, as is clear from **Figure 3-19**. This is logical, and was explained above. However, the increase in conversion is not entirely proportional to the rise in SEI, resulting in somewhat lower energy efficiencies with increasing SEI (cf. (eq.2.4)). The highest energy efficiency (i.e., at the lowest SEI of 0.01 J/cm³ and a 10-90 CH_4/CO_2 mixture) is 15.1 %, but this corresponds to very low values for the total conversion (i.e., 0.015 %). On the other hand, the highest total conversion (i.e., 84.2 %, at the highest SEI value of 100 J/cm³ and again a 10-90 CH_4/CO_2 mixture) corresponds to an energy efficiency of 8.5 %. The same trade-off between conversion and energy efficiency was illustrated in section 2 above, and has also been reported in previous studies.[45,46] The obtained values will be discussed in more detail, and compared with literature values below.

c) *Effect of the frequency*

As described above, the interpretation of the frequency is the most difficult to grasp, but it is in any case linked to the number of micro-discharge filaments that occur in the reactor within a certain residence time. At first sight the calculated conversion as a function of frequency did not show a comprehensible trend or coherency. However, it is observed that all of the maximum achieved conversions and energy efficiencies, for all gas mixtures in **Figure 3-19**, are obtained at either a residence time of 100 s and a frequency of 10 kHz, or a residence time of 10 s and a frequency of 100 kHz, except for an SEI of 10 and 100 J/cm³ for the 10-90 CH_4/CO_2 mixture and at 100 J/cm³ for the 25-75 mixture, where a residence time of 0.001 s and a frequency of 0.1 kHz gave the best results. Furthermore, all simulations with a frequency of 100 kHz and a residence time of 100 seconds resulted in a steep decrease in total conversion (see Figures A IV-1–A IV-10 in **Appendix IV**). This led us to believe that the critical factors are not the frequency (f) and residence time (τ), but rather the product of both ($\tau \cdot f$), i.e., the total number of micro-discharge filaments, which the gas molecules experience when passing through the reactor.

Therefore, in **Figure 3-20** the conversion and energy efficiency are plotted as a function of the total number of micro-discharge filaments experienced by the gas molecules, for a 50-50 gas mixture and for the different values of SEI investigated (see legend). The graphs for the other gas mixtures can be found in **Appendix IV** (see Figures A IV-11–A IV-15).

Keeping in mind that for every gas mixture 150 different simulations are performed (see above), this means that **Figure 3-20** contains 30 data points per SEI value (i.e. per colour symbol). As there are only 7 different combinations of the product $\tau \cdot f$, it means that several data points (more or less) coincide with each other. Hence, as anticipated above, all cases with different values of frequency and residence time, but with the same product $\tau \cdot f$, yield almost identical values for conversion and energy efficiency, at a fixed SEI. Thus, it becomes clear that, for a given gas mixture, both the product $\tau \cdot f$ and the SEI are the main underlying factors determining the plasma chemistry and linking the SEI, residence time and frequency all together.

It is clear from **Figure 3-20** that, at fixed SEI, increasing the number of micro-discharge filaments leads to a slightly higher conversion and energy efficiency, except for the highest number (200,000), where the opposite trend is seen, and for the highest SEI values of 10 and 100 J/cm³, where an initial decrease is observed for a low number of filaments. As mentioned above, all gas mixtures show the same general trends, except in the case of 90 % CO_2 for the highest SEI values of 10 and 100 J/cm³ and for 75 % for an SEI of 100 J/cm³, where a lower number of filaments leads to a higher total conversion.[54]

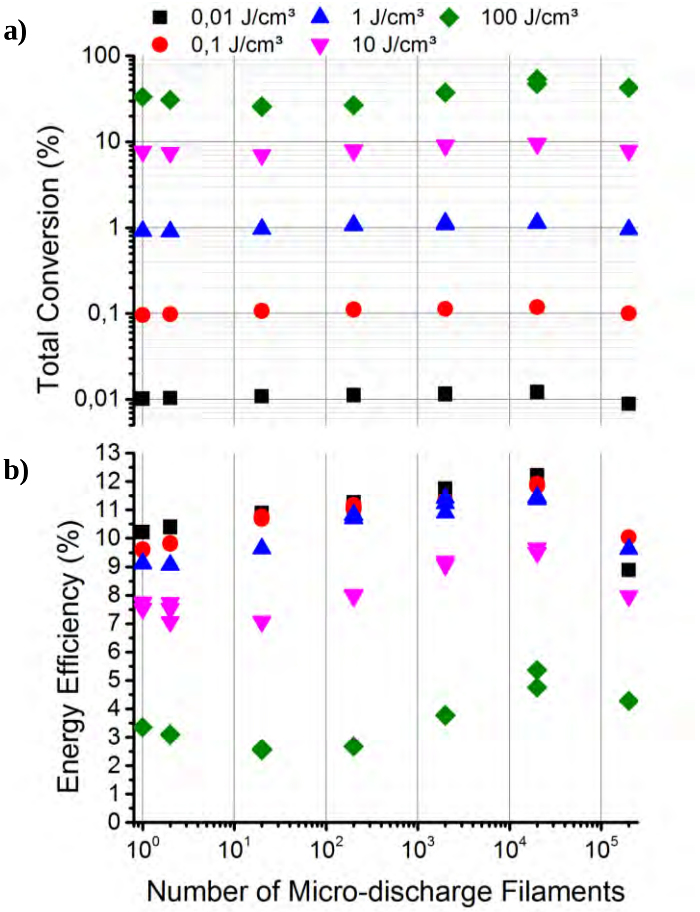

Figure 3-20. Calculated conversion (a) and energy efficiency (b) as a function of the total number of micro-discharge filaments for all the different residence times, frequencies and SEI values investigated, for a 1:1 CH_4/CO_2 mixture.

Since in the model the energy is divided equally over all micro-discharge filaments, increasing the number of filaments results in a lower energy deposited per filament. It seems that for most cases (except the ones mentioned before) a higher number of filaments, but with lower energy, yields higher values for conversion and energy efficiency, compared to a lower number of filaments, but with more energy deposited per filament. In general, the effect of the total number of filaments seems more important for the energy efficiency than the SEI (except between 10 and 100 J/cm³), while the total conversion seems less affected by the number of filaments than by the SEI, which was explained above.

3.3.3. Comparison with literature and critical analysis of the limitations and possibilities of plasma technology

As mentioned above, the highest total conversion (84.2 %) is obtained at the highest SEI (100 J/cm^3), and a CO_2 content of 90 %, yielding an energy efficiency of 8.5 %. The highest energy efficiency (15.1 %), on the other hand, is found for the lowest SEI (0.01 J/cm^3) and again a CO_2 content of 90 %, but this corresponds to a total conversion of only 0.015 %. Furthermore, both the total conversion and energy efficiency increase with increasing CO_2 content, while increasing the SEI results in a higher total conversion but a lower energy efficiency, illustrating the trade-off between both. Considering all operating conditions investigated, it is clear that the best overall results (i.e. combination of conversion and energy efficiency) are obtained for the highest SEI and typically for a large total number of filaments, obtained through a residence time of 10–100 s, combined with a frequency of 100–10 kHz, respectively, except for 90 and 75 % CO_2, where a lower number of filaments (obtained through a short residence time of 0.001–0.01 s independent of the frequency), or a higher residence time, combined with a low frequency of 0.1 kHz, led to the best results. **Table 3-8** summarizes the best results obtained for the different gas mixtures.

Table 3-8. Overview of the best results (i.e., combination of conversion and energy efficiency) obtained with the model, for the different gas mixtures.

CH_4/CO_2 gas mixture	Conversion	Energy efficiency
90-10	36.9 %	3.7 %
75-25	44.7 %	4.5 %
50-50	53.5 %	5.4 %
25-75	67.0 %	6.7 %
10-90	84.2 %	8.5 %

To compare our results with the current state-of-the-art from literature, **Figure 3-21** illustrates the various experimental data for energy efficiency vs total conversion, obtained from literature,[32,39,47,48,55,56] in comparison with our simulation results, for all conditions investigated. The experimental conditions from literature, and their corresponding results for conversion and energy efficiency, are summarized in **Table 3-9**.

Table 3-9. Experimental conversions and energy efficiencies collected from literature, for DRM in a DBD, illustrating the current state-of-the-art. When different operating conditions were investigated, the values for the conversion and energy efficiency corresponding to the lower and upper SEI values, are listed. A comparison is also made with values reported for a packed bed DBD, a microwave and a gliding arc plasma.

SEI (J/cm^3)	Frequency (kHz)	CH$_4$/CO$_2$ (%)	Conversion (%)		Energy Efficiency (%)		ref
			Lower	*Upper*	*Lower*	*Upper*	
7 - 23	2.5	50-50	2.8	8.1	4.2	3.5	[48]
7 - 48	Pulsed	60-40[a]	1.1	17.2	1.5	3.6	[47]
15 - 40	19.5	50-50[b]	4.4	11.1	2.9	2.8	[56]
18 - 144	30-40	50-50	10.8	40.5	6.0	2.8	[32]
64 - 532	15.67	50-50	27.2	64.6	4.3	1.2	[39]
22.5	19.5	80-20[b]	8.9	-	4	-	[56]
		20-80[b]	-	18.4	-	8.2	
25 - 40	Pulsed	60-40[a]	7.26	19.7	2.5	4.6	[47]
		40-60[a]	10.1	24	5.6	7.5	
100	25	83-17	-	62	-	6.2	[55]
		34-66	29.3	-	2.9	-	
143	15.67	83-17	-	46	-	3.2	[39]
		17-83	36.3	-	2.6	-	
Packed bed DBD			27		22.6		[23]
12	1-100	50-50					
Microwave at atm. pressure			70		39.0		[18]
18	Pulsed	60-40					
Gliding arc			35.5		31.2		[25]
11.4	10-20	50-50					
Gliding arc			9.8	13.9	74.6	35.2	[26]
1.32 - 3.96	0.05	50-50					

[a] Experiments diluted in N$_2$ [b] Experiments diluted in Ar

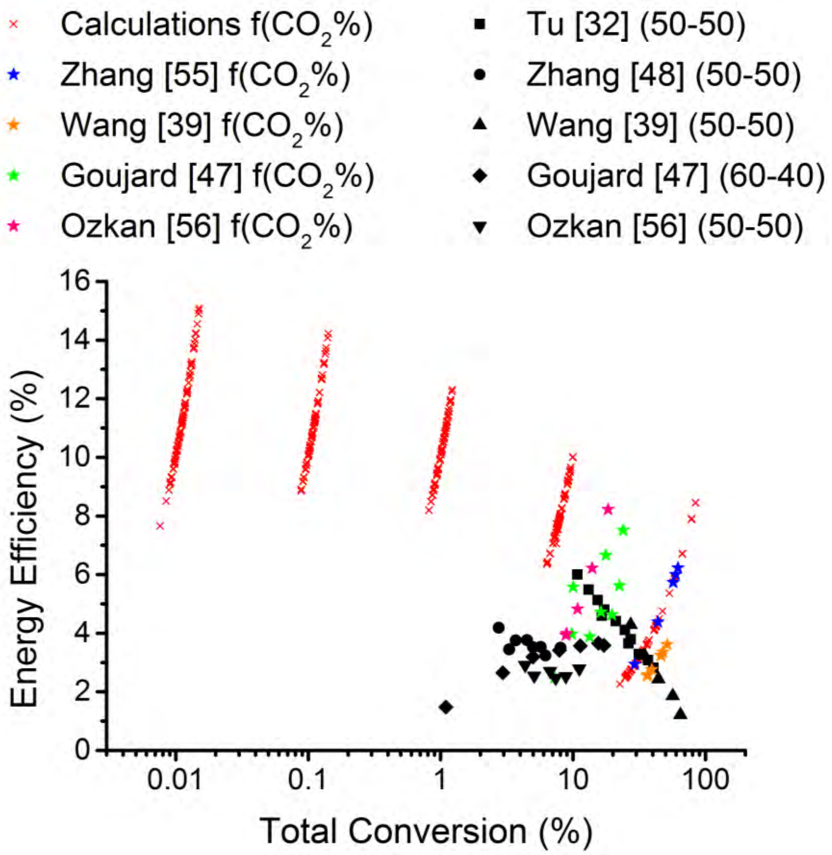

Figure 3-21. Comparison between our calculated values of energy efficiency vs total conversion, for all conditions investigated, with experimental data collected from literature, as indicated in the legend.

It is clear from **Figure 3-21** and **Table 3-9** that the operating conditions, especially the SEI values, have a large influence on the obtained conversion and energy efficiency. Most experiments are performed for SEI values between 10 and 100 J/cm³, and they give rise to conversions and energy efficiencies in the same order as predicted by our simulations. Especially the agreement with experimental results obtained for different CH_4/CO_2 mixtures (denoted by the coloured stars) is remarkable. The results of Goujard et al.[47] and Ozkan et al.[56] show exactly the same trend for the effect of gas mixture (i.e. higher conversion and energy efficiency at higher CO_2 content). Furthermore, for a SEI of 100 J/cm³ our calculations perfectly match with the results of Zhang et al.[55] Finally, the results of Wang et al.[39] indicate a maximum conversion and energy efficiency at 50 % CO_2, which can also be explained by our model, because for the high SEI under consideration, the applied frequency (15.67 kHz) yields good results for low CO_2 content, but at high CO_2 content, lower frequencies would be required.

Besides the good correlation between our model predictions and the literature results, it is also obvious from **Figure 3-21** that by careful selection of the operating conditions, higher values of energy efficiency (at fixed conversion) or higher conversions (for a given energy efficiency) could be achieved in our model than the values currently reported in literature. Indeed, at a conversion of 10%, the best energy efficiencies found in literature are about 5 %, whereas our calculations predict values up to 10 %, by careful selection of the frequency, residence time and gas mixture. Furthermore, a conversion of 84.2 % with 8.5 % energy efficiency, as obtained for 90% CO_2 content (see circle in **Figure 3-21**) is also significantly better than the available experimental data. Also for the other gas mixing ratios, our "best results" (in terms of combination of conversion and energy efficiency; cf. **Table 3-8**) are better than the results reported to date in literature (see **Table 3-9**).

As mentioned above, in general a compromise needs to be made between the energy efficiency and the total conversion, since the conversion increases but the energy efficiency drops with higher SEI. Nevertheless, this trade-off is less severe than expected. Increasing the SEI over five orders of magnitude results in almost the same rise in conversion, while the energy efficiency drops only by 44–67 % (depending on the gas mixture). This clearly demonstrates that it is not interesting to work at low SEI values to optimize the energy efficiency, since the gain in energy efficiency is negligible compared to the enormous loss in conversion.

In order to be competitive with current technologies and to reduce end-of-pipe gas separation costs, a conversion of 50–80 %, comparable with current DRM plants, would be preferred. This is achievable with a DBD, as is clear from Figure 6, but it requires an SEI in the order of 100 J/cm³, resulting in energy efficiencies of 8.5 to 3.7 %, depending on the gas mixture.

3.4. Conclusions

In this section we have studied the influence of the operating parameters (gas mixture, power, residence time and "frequency") of a DBD plasma on the conversion and energy efficiency, to investigate which of these parameters lead to the most promising results and whether these are eventually sufficient for industrial implementation.

The obtained conversion of 84 % with an energy efficiency of 8.5 % can be considered as the best results in terms of both energy efficiency and conversion. The parameters leading to this result were an SEI of 100 J/cm³, a 10-90 CH_4/CO_2 mixture, 10 Hz, a residence time of 1 ms. In general we found that increasing the amount of CO_2 in the mixture led to an increase in conversion and energy efficiency, while increasing the SEI, which couples the effect of the power and residence time, only resulted in an increased conversion, but saw a slight decrease in energy efficiency. The most complicated effect was that of the frequency; in the end it was unravelled that it was rather the product of frequency (f) and residence time (τ), i.e. the total number of micro-discharge filaments which the gas molecules experience when passing through the reactor, which was critical here. For most cases, passing a higher number of filaments (with less energy per filament) yielded higher values for conversion and energy efficiency.

Furthermore, the maximum (theoretical) energy efficiency predicted in this study lies between 11.4 and 15.1 %, depending on the CH_4/CO_2 mixture, which clearly demonstrates that there is still room for improvement for the experiments reported to date, by careful selection of the operating conditions. However, when comparing this maximum theoretical value with the maximum theoretical energy efficiency obtained for classical thermal DRM, i.e. around 60 %, it is clear that when the energy efficiency is the "key performance indicator", a classical DBD is not competitive. On the other hand, its ease of use (incl. its fast start-up and switch-off, which can save a lot of energy when DRM is combined with other technologies such as fuel cells), its scale-up possibilities as demonstrated for ozone generation and gas cleaning,[33] and its capability to convert peak currents from renewable energy sources, will probably still give it an advantage over the classical DRM process. Nevertheless, keeping in mind that other alternative techniques can also take advantage of the same peak renewable energy,[6] it is clearly more interesting from a combined economic and ecologic point of view to focus on other plasma reactor types, for which already higher energy efficiencies have been obtained (see **Table 3-9**). This includes microwave discharges,[18] gliding arcs,[18,25,26] and packed bed DBDs.[23] In the latter case, a DBD is filled with a packing, yielding higher energy efficiencies, i.e. up to a factor 12, as demonstrated already for air pollution control,[57] although for CO_2 conversion only enhancements up to a factor 2 were reported.[58] Moreover, this packing can be made of catalytic material, yielding plasma-catalysis.[24,59,60] This has the additional advantage that the selectivity towards value-added chemicals and fuels (such as methanol, formaldehyde, formic acid, etc.) can greatly be improved, making plasma technology very promising for the dry reforming of methane.

4. References

1 S. Solomon, D. Qin, M. Manning, M. Marquis, K. Averyt, M. M. B. Tignor, H. L. Miller and Z. Chen, Eds., *Climate Change 2007: The Physical Science Basis. Contribution of Working Group I to the Fourth Assesment Report of the Intergovernmental Panel on Climate Change*, Cambridge University Press, New York, 2007.

2 J. H. Lunsford, *Catal. Today*, 2000, **63**, 165–174.

3 A. T. Ashcroft, A. K. Cheetham, M. L. H. Green and P. D. F. Vernon, *Nature*, 1991, **352**, 225–226.

4 M. C. J. Bradford and M. A. Vannice, *Catal. Rev. Eng.*, 1999, **41**, 1–42.

5 J. R. H. Ross, *Catal. Today*, 2005, **100**, 151–158.

6 M. Mikkelsen, M. Jørgensen and F. C. Krebs, *Energy Environ. Sci.*, 2010, **3**, 43–81.

7 I. Omae, *Catal. Today*, 2006, **115**, 33–52.

8 C. De Bie, B. Verheyde, T. Martens, J. van Dijk, S. Paulussen and A. Bogaerts, *Plasma Process. Polym.*, 2011, **8**, 1033–1058.

9 A. S. K. Raju, C. S. Park and J. M. Norbeck, *Fuel Process. Technol.*, 2009, **90**, 330–336.

10 D. Treacy and J. R. H. Ross, *Stud. Surf. Sci. Catal.*, 2004, **147**, 193–198.

11 A. P. E. York, J. B. Claridge, C. Márquez-Alvarez, A. J. Brungs, S. C. Tsang and M. L. H. Green, *Stud. Surf. Sci. Catal.*, 1997, **110**, 711–720.

12 R. Labrecque and J. M. Lavoie, *Bioresour. Technol.*, 2011, **102**, 11244–11248.

13 H. J. Gallon, University of Manchester, 2010.

14 G. Petitpas, J. Rollier, A. Darmon, J. Gonzalez-Aguilar, R. Metkemeijer and L. Fulcheri, *Int. J. Hydrogen Energy*, 2007, **32**, 2848–2867.

15 L. Bromberg, D. R. Cohn, A. Rabinovich and N. Alexeev, *Int. J. Hydrogen Energy*, 1999, **24**, 1131–1137.

16 L. Bromberg, D. R. Cohn, A. Rabinovich, N. Alexeev, A. Samokhin, R. Ramprasad and S. Tamhankar, *Int. J. Hydrogen Energy*, 2000, **25**, 1157–1161.

17 L. Bromberg, D. R. Cohn, A. Rabinovich and J. Heywood, *Int. J. Hydrogen Energy*, 2001, **26**, 1115–1121.

18 X. Tao, M. Bai, X. Li, H. Long, S. Shang, Y. Yin and X. Dai, *Prog. Energy Combust. Sci.*, 2011, **37**, 113–124.

19 I. Istadi and N. A. S. Amin, *Chem. Eng. Sci.*, 2007, **62**, 6568–6581.

20 C.-J. Liu, Y. Li, Y.-P. Zhang, Y. Wang, J. Zou, B. Eliasson and B. Xue, *Chem. Lett.*, 2001, **30**, 1304–1305.

21 S. A. Nair, T. Nozaki and K. Okazaki, *Chem. Eng. J.*, 2007, **132**, 85–95.

22 M. Kraus, W. Egli, K. Haffner, B. Eliasson, U. Kogelschatz and A. Wokaun, *Phys. Chem. Chem. Phys.*, 2002, **4**, 668–675.

23 Q. Wang, Y. Cheng and Y. Jin, *Catal. Today*, 2009, **148**, 275–282.

24 S. Samukawa, M. Hori, S. Rauf, K. Tachibana, P. Bruggeman, G. Kroesen, J. C. Whitehead, A. B. Murphy, A. F. Gutsol, S. Starikovskaia, U. Kortshagen, J.-P. Boeuf, T. J. Sommerer, M. J. Kushner, U. Czarnetzki and N. Mason, *J. Phys. D. Appl. Phys.*, 2012, **45**, 253001.

25 A. Indarto, J. Choi, H. Lee and H. Song, *Energy*, 2006, **31**, 2986–2995.

26 X. Tu and J. C. Whitehead, *Int. J. Hydrogen Energy*, 2014, **39**, 9658–9669.

27 A. Fridman, *Plasma chemistry*, Cambridge University Press, New York, 2008.

28 A. Gutsol, A. Rabinovich and A. Fridman, *J. Phys. D. Appl. Phys.*, 2011, **44**, 274001.

29 R. Dorai and M. J. Kushner, *J. Phys. D. Appl. Phys.*, 2003, **36**, 1075–1083.

30 D. S. Stafford and M. J. Kushner, *J. Appl. Phys.*, 2004, **96**, 2451–2465.

31 A. Bogaerts, C. De Bie, R. Snoeckx and T. Kozák, *Plasma Process. Polym.*, 2016, 1–21.

32 X. Tu and J. C. Whitehead, *Appl. Catal. B Environ.*, 2012, **125**, 439–448.

33 U. Kogelschatz, *Plasma Chem. plasma Process.*, 2003, **23**, 1–46.

34 P. Gangadharan, K. C. Kanchi and H. H. Lou, *Chem. Eng. Res. Des.*, 2012, **90**, 1956–1968.

35 C. De Bie, T. Martens, J. van Dijk, S. Paulussen, B. Verheyde, S. Corthals and A. Bogaerts, *Plasma Sources Sci. Technol.*, 2011, **20**, 24008.

36 Y. Itikawa, *J. Phys. Chem. Ref. Data*, 2002, **31**, 749–767.

37 H. J. Gallon, X. Tu, M. V. Twigg and J. C. Whitehead, *Appl. Catal. B Environ.*, 2011, **106**, 616–620.

38 S. L. Yao, M. Okumoto, A. Nakayama and E. Suzuki, *Energy and Fuels*, 2001, **15**, 1295–1299.

39 Q. Wang, B.-H. Yan, Y. Jin and Y. Cheng, *Plasma Chem. Plasma Process.*, 2009,

29, 217–228.

40 C. J. Liu, B. Xue, B. Eliasson, F. He, Y. Li and G. H. Xu, *Plasma Chem. Plasma Process.*, 2001, **21**, 301–310.

41 Z. Bo, J. Yan, X. Li, Y. Chi and K. Cen, *Int. J. Hydrogen Energy*, 2008, **33**, 5545–5553.

42 B. Fidalgo, A. Domínguez, J. Pis and J. Menéndez, *Int. J. Hydrogen Energy*, 2008, **33**, 4337–4344.

43 J. Q. Zhang, Y. J. Yang, J. S. Zhang and Q. Liu, *Acta Chim. Sin.*, 2002, **60**, 1973–1980.

44 R. Snoeckx, R. Aerts, X. Tu and A. Bogaerts, *J. Phys. Chem. C*, 2013, **117**, 4957–4970.

45 C. Xu and X. Tu, *J. Energy Chem.*, 2013, **22**, 420–425.

46 R. Aerts, W. Somers and A. Bogaerts, *ChemSusChem*, 2015, **8**, 702–716.

47 V. Goujard, J.-M. Tatibouët and C. Batiot-Dupeyrat, *Appl. Catal. A Gen.*, 2009, **353**, 228–235.

48 X. Zhang and M. S. Cha, *J. Phys. D. Appl. Phys.*, 2013, **46**, 415205.

49 J. H. Lozano-Parada and W. B. Zimmerman, *Chem. Eng. Sci.*, 2010, **65**, 4925–4930.

50 U. Kogelschatz, *Contrib. to Plasma Phys.*, 2007, **47**, 80–88.

51 R. Aerts, R. Snoeckx and A. Bogaerts, *Plasma Process. Polym.*, 2014, **11**, 985–992.

52 T. Kozák and A. Bogaerts, *Plasma Sources Sci. Technol.*, 2014, **23**, 45004.

53 R. Aerts, T. Martens and A. Bogaerts, *J. Phys. Chem. C*, 2012, **116**, 23257–23273.

54 R. Snoeckx, Y. X. Zeng, X. Tu and A. Bogaerts, *RSC Adv.*, 2015, **5**, 29799–29808.

55 Y. Zhang, Y. Li, Y. Wang, C. Liu and B. Eliasson, *Fuel Process. Technol.*, 2003, **83**, 101–109.

56 A. Ozkan, T. Dufour, G. Arnoult, P. De Keyzer, A. Bogaerts and F. Reniers, *J. CO2 Util.*, 2015, **9**, 78–81.

57 H. L. Chen, H. M. Lee, S. H. Chen and M. B. Chang, *Ind. Eng. Chem. Res.*, 2008, **47**, 2122–2130.

58 K. Van Laer and A. Bogaerts, *Energy Technol.*, 2015, **3**, 1038–1044.

59 E. C. Neyts and A. Bogaerts, *J. Phys. D. Appl. Phys.*, 2014, **47**, 224010.

60 E. C. Neyts, K. Ostrikov, M. K. Sunkara and A. Bogaerts, *Chem. Rev.*, 2015, **115**, 13408–13446.

CHAPTER 4

$CO_2 + H_2O$: Artificial photosynthesis

This chapter is published as:

R Snoeckx, A Ozkan, F Reniers and A Bogaerts, The Quest For Value-Added Products From CO_2 And H_2O In A Dielectric Barrier Discharge: A Chemical Kinetics Study, ChemSusChem 10 (2017) 409-424 (16p).

1. Aim of the work

An interesting co-reactant to pursue the utilization of CO_2 and converting it into a new feedstock is water. It is not only the most ubiquitous and cheapest hydrogen source, compared to CH_4 and H_2, but in addition, converting CO_2 in combination with H_2O to produce value-added products using renewable energy, would successfully mimic the natural photosynthetic process.[1] Indeed, the successful development of artificial photosynthesis technology is no longer a fairy tale. Furthermore, water is always present in industrial effluent gas streams (fumes). As such, technologies that aim to convert CO_2 immediately at the exit of industrial installations, could take advantage of this major and unavoidable "contaminant". Several routes for the combined conversion of CO_2 and H_2O have already reported promising results, e.g. thermochemical, electrochemical, and photochemical, either with or without catalysts, and all their possible combinations,[2–8] as outlined in **Chapter 1**. In recent years, plasma technology is also considered to have potential in this area.

The reactions of greatest interest are the conversion of CO_2 and H_2O to syngas, hydrocarbons, short-chain olefins (ethylene and propylene) and oxygenated products (i.e. methanol, formaldehyde, dimethyl ether, formic acid, hydrogen peroxide, etc.). Other products of interest that can in principle be formed starting from CO_2 and H_2O are peroxides. Hydrogen peroxide (H_2O_2) has been shown to be a microbicidal active agent and its ability to sterilize is widely used and well-studied.[9–11] As such, the production of H_2O_2 by plasma technology is gaining a lot of interest for biomedical and (bio-)decontamination applications.[12–14] In a recent extensive review by Lu et al., which focuses on the generation, transport and biological effects of the reactive plasma species, H_2O_2 is even considered to be one of the most important reactive oxygen species that acts as signalling molecule, together with O_2^-.[15]

Because of its advantages over conventional reforming technologies, a lot of research was already devoted to the plasma-based conversion of greenhouse gases into value-added products. Most research was based on pure CO_2 splitting,[16–25] or dry reforming of methane.[26–41] Pure H_2O plasmas for the production of hydrogen have also been extensively studied.[42–46] However, the research on the simultaneous conversion of CO_2 and H_2O into syngas or oxygenated products by plasma is very limited. Ihara et al.[47,48] were the first to investigate the conversion of CO_2 and H_2O, by means of a microwave plasma set-up. Other researchers have considered a ferroelectric packed-bed reactor,[49] a dielectric barrier discharge (DBD),[49] a DBD packed with Ni/γ-Al_2O_3 catalyst,[50] a surface discharge,[51] a negative DC corona discharge,[52] and a surface-wave microwave discharge.[53] More details about these studies can be found in **Chapter 6** below.

In general, five main trends can be distinguished from the above literature: (i) the CO_2 conversion increases with increasing energy input, (ii) the H_2/CO ratio decreases with increasing energy input, (iii) the CO_2 conversion decreases with increasing water content, (iv) the H_2/CO ratio increases with increasing water content, and (v) the main products formed are H_2, CO and O_2, but some papers also report the production of hydrogen peroxide (H_2O_2),[47] oxalic acid ($C_2H_2O_4$),[47] formic acid (CH_2O_2),[51] methane (CH_4),[50,51] dimethyl ether (C_2H_6O, DME),[51] methanol (CH_3OH)[48,50,52] and ethanol (C_2H_5OH).[52] Unfortunately, most data on the formation of these products are only qualitative and incomplete, making it impossible to deduce a general trend on product yields or selectivities.

It becomes clear that not much is known about the simultaneous conversion of CO_2 and H_2O into value-added products, and specifically not about the underlying mechanisms. In this chapter, we study the combined plasma-based conversion of CO_2 and H_2O for a DBD plasma reactor, by means of experiments and computer simulations, based on a zero-dimensional (0D) chemical kinetics model.

The main aim of this study is to evaluate whether the combined conversion of CO_2 and H_2O using plasma can become a viable route to produce value-added chemicals, by identifying and analysing the underlying plasma chemical kinetic behaviour. For this analysis, first a plasma chemical kinetics model for CO_2/H_2O and its interactions needs to be developed. The investigation will then be performed in a step-wise manner, by first determining the influence of the water content and the SEI on the conversion and product formation in a combined effort of experiments and computations. The latter also allows to validate the model. Subsequently, a detailed chemical kinetics analysis will be performed to elucidate the mechanisms behind the observed trends. This approach enables us to investigate the current and future possibilities and limitations in more detail. Furthermore, based on this analysis we can also suggest possible solutions to enhance the formation of the desired products, and as such, make an initial evaluation towards the industrial viability of plasma technology for this process.

2. Description of the chemical model

2.1. 0D chemical kinetics model

The same 0D kinetic model, called Global_kin,[54,55] is used as in **Chapter 3**, and more details about this model can be found in the work of Kushner et al.[54,55] and in **Chapter 2**, Section 2.

The experimental gas flow rate is used, i.e. 600 mL min^{-1} at 323 K and atmospheric pressure, with a DBD reactor volume of 15.1 cm^3, thus corresponding to a residence time of 1.66 s. The model was run at constant temperature of 323 K. In reality, the temperature might change due to the chemical reactions taking place (either exo- or endotherm). Indeed, a considerable fraction of the energy delivered to the plasma will be lost in reaction pathways that eventually lead to the re-formation of the reactants (cf. reactions 1–7, in section 4.1.4.), which means that the energy supplied by the electrons to the chemical species will be eventually transformed into other forms of energy (e.g. thermal energy). This energy might lead to a local rise of the temperature, probably limited to the micro-discharge volume, which might affect the chemical reactivity of the system. However, we believe that our assumption of constant temperature is in first instance justified, for the following reasons. (i) There are both exothermic and endothermic reactions in the overall reaction chemistry, and the energy released by the exothermic reactions will be balanced by the endothermic reactions. (ii) In similar work on dry reforming of methane (see previous chapter)³³ it was demonstrated that the conversion is mainly determined by the (gas temperature independent) electron impact reactions during (and shortly after) the micro-discharge filaments, whereas most of the product formation (and hence the selectivities) are determined by the afterglow reactions. Furthermore, it was observed during temperature-controlled experiments that conversions and selectivity did not change significantly when increasing the temperature from 297 K to 473 K.[33] Nevertheless, to check the validity of the assumption of constant temperature, we have run our model for two additional temperatures, i.e., 373 and 423 K (instead of the standard calculations of 323 K). At 373 K the relative changes in CO_2 conversion compared to the standard calculations are about + 2–4 %, and the relative changes in the H_2O conversion are about + 2 %. At 423 K the relative changes in CO_2 conversion compared to the standard calculations are about + 6–10 %, and the relative changes in the H_2O conversion are about - 10–13 %. The selectivities remained almost unchanged, with only a significant + 20–30 % increase in the O_3 and H_2O_2 concentrations. However, we believe that such heating of the gas temperature in the reactor up to 423 K does not occur, as it was not observed experimentally, mainly due to the small micro-discharge volumes and the cooling due to the continuous gas flow.

2.2. Plasma chemistry included in the model

The data to compile the necessary plasma chemistry, was taken from different sources and expanded with additional CO_2/H_2O interactions. The CO_2 chemistry and the H_2O/O_2 chemistry used in this study are mainly adopted from Aerts et al.[56] and van Gaens et al.,[57] respectively, while the hydrocarbon chemistry, necessary to describe the reactions between CO_2 and H_2O species, and thus for the product formation, was partially taken from our chemistry for DRM (see previous Chapter). The total chemistry set considers 75 different species (listed in **Table 4-1**), which react with each other in 187 electron impact reactions, 346 ion reactions and 369 neutral reactions. Their corresponding rate coefficients and the references where these data were adopted from can be found in Appendix II.

From **Table 4-1** it is evident that several high-value oxygenates, like oxalic acid, formic acid, DME or ethanol, are not included in our model, because of lack of complete data on the specific reaction rate coefficients in literature, needed to describe their formation and loss processes. Of course, we could have incorporated these species, but due to the scarcity of coherent input data, their densities would be subject to such large uncertainties that the predictive character of the model would have less to no value, as also mentioned in **Chapter 3**. Furthermore, these oxygenates were not detected in the experiments. In literature, some of them were detected, but this was in a microwave plasma set-up, which operates at significantly different conditions than the DBD plasma under study here. Last but not least, as will be illustrated in section 4.1.4 below, the oxygenates that are included in the model, such as methanol and formaldehyde, are barely formed (not in the calculations, nor in the experiments), and as the other high value oxygenates (not included in the model) are likely to be formed from the same precursors, one can expect their formation to be of minor importance at the plasma conditions under study, as also supported by their experimental absence. Nevertheless, we hope that rate coefficients for these molecules will become available in literature in the near future, which would allow us to build an even more complete model, and more importantly, to investigate under which other circumstances these oxygenates might be formed.

Table 4-1. Species included in the model

C-O compounds	CO_2, CO, C_2O, CO_2^+, CO^+, CO_4^+, CO_4^-, CO_3^-, $C_2O_4^+$, $C_2O_3^+$, $C_2O_2^+$
C compounds	C, C_2, C_2^+, C^+
O compounds	O_3, O_2, O, O_4^-, O_3^-, O_2^-, O^-, O_4^+, O_2^+, O^+
C-H compounds	CH_4, CH_3, CH_2, CH, CH_5^+, CH_4^+, CH_3^+, CH_2^+, CH^+
C_2-H compounds	C_2H_6, C_2H_5, C_2H_4, C_2H_3, C_2H_2, C_2H, $C_2H_6^+$, $C_2H_5^+$, $C_2H_4^+$, $C_2H_3^+$, $C_2H_2^+$
C_3-H and C_4-H compounds	C_3H_8, C_3H_7, C_3H_6, C_4H_2
H compounds	H_2, H, H_3^+, H_2^+, H^+, H^-
H-O compounds	H_2O, OH, HO_2, H_2O_2, OH^-, H_3O^+, H_2O^+, OH^+
C-H-O compounds	CHO, CH_2O, CH_3O, CH_2OH, CH_3OH, CHCO, CH_2CO, CH_3CO, CH_2CHO, CH_3CHO, $C_2H_5O_2$
Electrons	e^-

3. Description of the experiments

The experiments were carried out by A. Ozkan at Université Libre de Bruxelles, in a coaxial DBD reactor (see **Figure 4-1**). A stainless steel mesh (ground electrode) is wrapped over the outside of a borosilicate (Pyrex) tube with an outer and inner diameter of 30 and 26 mm, respectively (dielectric thickness = 2 mm). A copper rod with a diameter of 22 mm is placed in the centre of the borosilicate tube and used as high voltage electrode. The length of the discharge region is 100 mm with a discharge gap of 2 mm, giving rise to a discharge volume of 15.1 cm^3. The DBD is supplied with an AFS generator G10S-V for a maximum power of 1000 W, with a maximum peak-to-peak voltage of 5 kV and frequency of 28.06 kHz. The Q-U Lissajous method[17,58] is used to calculate the discharge power. The energy input is defined as the SEI (see eq.2-4).

Note that the SEI is used here as parameter for the energy input. Normally, it is rather the energy selectivity which is most important, since it defines the fraction of input energy used to drive the reactions, compared to the energy being lost to heating. However, in a DBD there is only local heating due to the discharge filaments. The latter only accounts for a very small fraction of the reactor volume for several nanoseconds, with a repetition in the microseconds scale, yielding a volume-corrected filament frequency of about 0.01 % per discharge cycle.[59] Thus overall, the gas heating is very limited, and we can assume that all the energy, as defined by the SEI, goes into driving the reactions. Of course, there are energy losses when converting the (low voltage) outlet power to (high voltage) applied power to discharge power. To date those may vary greatly depending on the power supply used, but this is independent from the plasma process under study. As such, a lot of (successful) research progress is still being made in minimizing the electrical conversion from outlet power to discharge power.

CO_2 and water vapour are used as feed gases with a continuous total flow rate of 600 mL min^{-1} at 323 K, varying the H_2O content in the mixture between 0 and 8 %, resulting in a CO_2 content between 100 and 92 %. The individual CO_2 and water flow rates are controlled via a mass flow controller (Bronkhorst) and a liquid flow controller (Bronkhorst), respectively. Subsequently, both flows are mixed using a controlled evaporator mixer (CEM, Bronkhorst), where both the liquid and the gas flow are heated up in a controlled manner for total evaporation. Finally, this liquid delivery system with vapour control is connected to the DBD reactor. Additionally, the entire system (tubing and reactor) is heated up to 323 K to minimize condensation and to promote total evaporation of the water throughout the discharge, as much as possible.

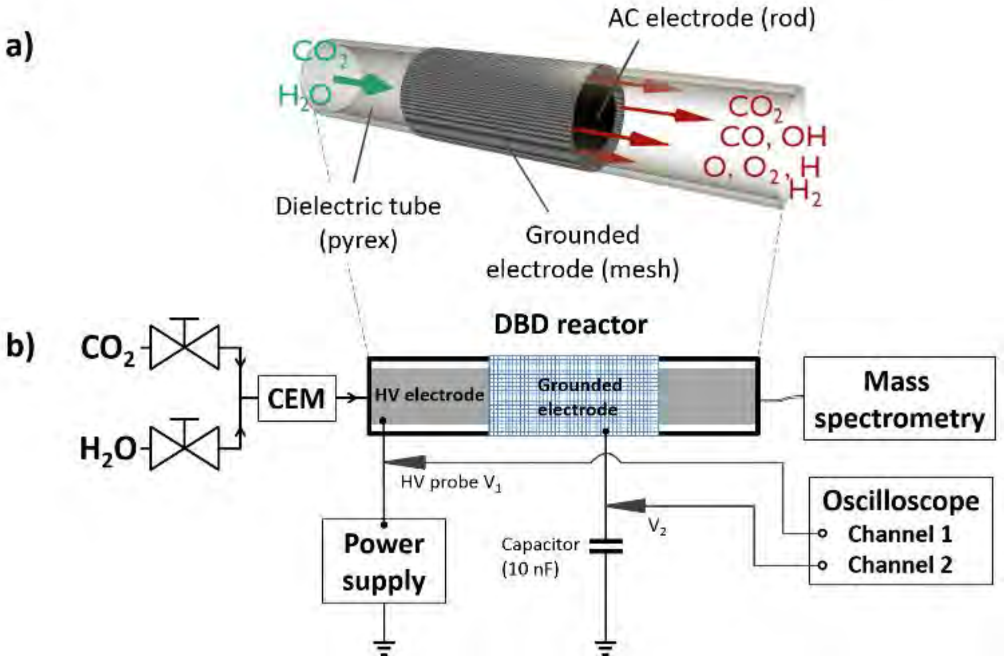

Figure 4-1. Schematic of the experimental DBD reactor (a) and the experimental set-up (b), figure courtesy of A. Ozkan (ULB).

The CO_2 and H_2O conversion is studied using mass spectrometry operating at atmospheric pressure (Hiden Analytical QGA MS, Warrington, UK). The multi-level software package MASsoft7 Professional used, allows having a simple control of mass spectrometer parameters. This software also permits to set the electron energy in the ionization chamber at 35 eV or lower for soft ionization in case of complex mixtures, in order to have a reduced spectral fragmentation and simplified data interpretation, for example in case of the presence of more than one reactive component in the discharge. In our case the electron energy in the ionization chamber is set at 35 eV, the detector is a secondary electron multiplier (SEM) and the MASsoft7 software is used to simultaneously monitor the partial pressure variations with specific *m/z* ratios as a function of time. The electrical measurements are performed by means of an oscilloscope (Tektronix DPO 3032) and a high-voltage probe (Tektronix P6015A) in order to evaluate the properties of the discharge. As indicated in **Figure 4-1**, the potential V_2 is measured through a capacitor of 10 nF (placed in series with the DBD) to evaluate the power absorbed by the plasma (P_{abs}) via the Lissajous method. This power is used as input in our simulations. Each experiment is repeated three times and the standard deviation is used to express the experimental uncertainties for the presented results.

4. Results and discussion

First we will compare the calculated conversion of CO_2 and H_2O (and the product selectivities with the experimentally measured values. We will also discuss in detail the underlying chemistry for the obtained results, based on the model predictions, to explain the observed trends. Subsequently, we will briefly discuss additional simulations for a broader range of conditions, to predict the CO_2 and H_2O conversion, and the product selectivities, at larger values of SEI and water contents. Finally, based on this plasma chemical kinetic analysis, we will summarize the current potential and limitations of plasma technology for combined CO_2 and H_2O conversion into value-added chemicals, and propose some solutions on how to move forward in this field.

4.1. Conversion and selectivity: A comparison between model calculations and experiments

4.1.1. CO_2 and H_2O conversion

In **Figure 4-2** the calculated and experimental absolute CO_2 and H_2O conversions (eq.2-8) are plotted as a function of water vapour content for a total gas flow rate of 600 mL min^{-1} at 323 K, for three different SEI values, i.e. 3.2, 4.0 and 4.8 J/cm^3. As to be expected, the absolute CO_2 and H_2O conversions increase when more energy is supplied, i.e. at higher SEI values. Regardless of the SEI, both the calculated and experimental absolute CO_2 conversion is the highest for pure CO_2, when no water vapour is added to the discharge. The experimental conversions in this case are 4.3, 3.3 and 2.6 % for the three different SEI values investigated, and the calculated values are very similar.

The drop in CO_2 conversion with increasing water content may result from the destabilization of the discharge induced by the presence of water. Indeed, our calculations reveal a ~40 % drop of the maximum electron density with increasing water content from 0 to 8 %. Furthermore, our chemical analysis pathway also allows us to identify a chemical reason for the drop in CO_2 conversion, as will be explained in the underlying mechanism section below. Adding 2 % water vapour yields a drop in the CO_2 conversion by about 25 % for all SEI values investigated. When increasing the water content up to 8 %, the CO_2 conversion continues to drop slightly by an additional 15–25 %, compared to the conversion at 2 % water, and depending on the SEI. As the CO_2 content in the gas flow drops upon increasing H_2O fraction, the effective CO_2 conversion (eq.2-9) will drop even more than the absolute CO_2 conversion, i.e. from 4.3–2.6 % (depending on the SEI, see above) for pure CO_2, till 2.5–1.4 %, for 8 % H_2O addition.

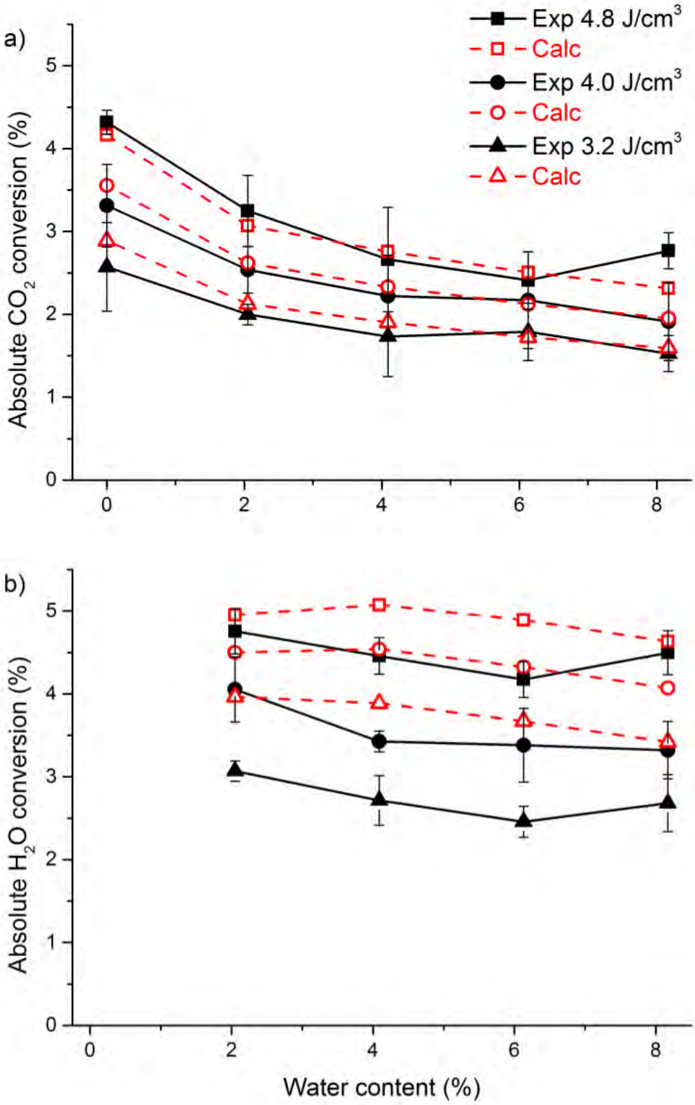

Figure 4-2. Calculated and experimental values of absolute CO_2 (a) and H_2O (b) conversion as a function of water vapour content for the different values of SEI and a total flow rate of 600 mL min^{-1} at 323 K.

The absolute H_2O conversion shows a slightly decreasing trend of about 10 % with increasing water content from 2 to 8 %. At a water content of 2 % the absolute experimental H_2O conversions are 4.8, 4.1 and 3.1 %, for an SEI of 4.8, 4.0 and 3.2 J/cm^3, respectively, while these values amount to 4.5, 3.3 and 2.7 % at a water content of 8 %. As the drop in absolute H_2O conversion is limited, the effective H_2O conversion obviously rises upon higher water content (from 2 to 8 %), i.e. from 0.10 to 0.37 %, from 0.08 to 0.27 % and from 0.06 to 0.22 %, for an SEI of 4.8, 4.0 and 3.2 J/cm^3, respectively.

The calculated H_2O conversions are overestimated, on average by about 9.5, 23.5 and 37.3 % in the entire range of water addition, for the SEI values of 4.8, 4.0 and 3.2 J/cm^3, respectively, compared to the experimental values. This overestimation is probably due to some more complex processes taking place in the experiments as a result of the water vapour, which could not be easily accounted for in the 0D plasma chemistry model. Indeed, the model describes all chemical processes, but does not take into account some physical effects, such as condensation and nebulization. It is well possible that the evaporation in reality is not complete, leading to small droplets (nebulization) of water spread throughout the discharge zone, despite the fact that the entire plasma system is heated starting from the CEM. This would lead to a lower concentration of gaseous H_2O that can undergo reactions in the plasma, but nevertheless this H_2O will also reach the MS capillary and thus will be accounted for when calculating the conversion (cf. eq.2-8). Hence, this results in a lower experimental conversion. Upon increasing the SEI, more energy is supplied to the gas and slightly more heat is locally generated in the discharge filaments, which might reduce the probability of condensation, and this may explain the lower deviation between calculated and measured conversion with increasing SEI values.

4.1.2. Product selectivity

CO_2 splitting typically yields CO and O_2 molecules, the latter being formed by the recombination of O atoms. Besides, also some O_3 can be created.[17] Upon addition of a H-source, such as CH_4 or H_2O, we target the production of small oxygenated hydrocarbons, such as formaldehyde, methanol and formic acid. In the case of CH_4 addition in the plasma, we mainly form syngas, as demonstrated in **Chapter 3**.[60] In the present chapter, we investigate whether H_2O addition to a DBD plasma can result in some oxygenated molecules, like reported for microwave, atmospheric surface and negative DC corona discharge plasmas;[47,48,51,52] see section 1 above and **Chapter 6** below. Unfortunately, for all investigated cases in both the experiments and calculations, the main products formed are O_2, and the syngas components CO and H_2. We do form some hydrogen peroxide (H_2O_2) and trace amounts of ozone (O_3), but no oxygenated hydrocarbons were detected in the experiments, and the calculated concentrations of methanol and formaldehyde were only in the ppb range (hence far below the experimental detection level). The reason for this will be discussed in more detail in the next section, by elucidating the underlying chemistry.

Figure 4-3 represents the calculated number densities of the most important molecules present or formed in the plasma, as a function of time for an SEI of 4 J/cm^3 and a water content of 4 %. The total residence time of the gas in the plasma reactor corresponds to 1.66 s, as indicated above. The CO_2 and H_2O density show a slightly decreasing trend, in line with their conversion. As a consequence, the main products formed, i.e. CO, O_2, H_2 (and O_3), exhibit the opposite increasing trend, with final concentrations in the percentage range (see also below). H_2O_2 is characterized by a slightly different, more flat trend, with final concentration in the ppm range. Finally, the oxygenated products (CH_2O and CH_3OH), together with CH_4, reach concentrations well below the ppm range.

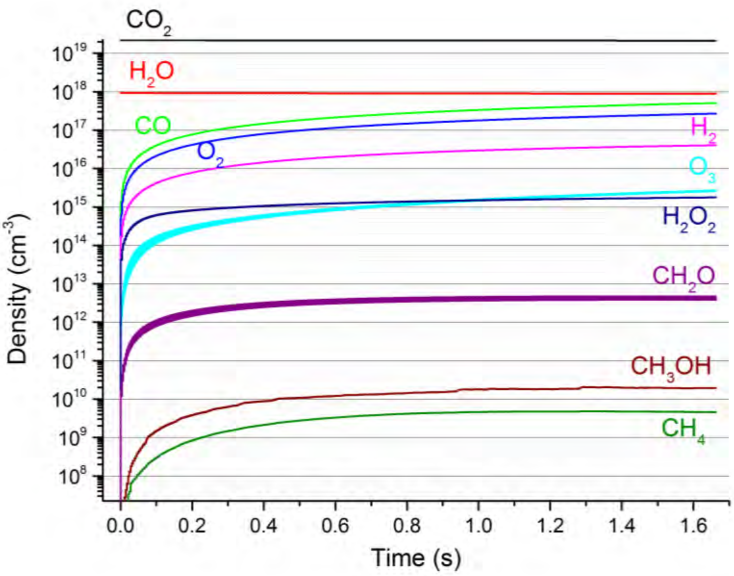

Figure 4-3. Calculated species densities of the most important molecules present or formed in the plasma, as a function of time for an SEI of 4 J/cm^3 and a water content of 4 %.

The agreement between measured and calculated gas composition is very good. CO is the main product, as expected (due to the higher CO_2 content in the mixture), but its fraction obviously drops upon increasing H_2O content, as is also the case for the O_2 and O_3 fraction. The H_2 and H_2O_2 fractions, on the other hand, rise upon addition of more H_2O, which is also logical. The O_3 and H_2O_2 contents could—although detected—not be quantified, due to their low signal-to-noise ratio, so only an order of magnitude could be given for the experimental data in **Table 4-2**. The measured and calculated concentrations of O_2, CO, H_2, H_2O_2 and O_3 are listed in **Table 4-2**, for the different water vapour contents investigated, and for an SEI of 4.0 J/cm^3.

Table 4-2. Calculated and measured gas composition after plasma treatment for an SEI of 4.0 J/cm^3, and for the different water vapour contents investigated, with the remainder being unconverted CO_2 and H_2O.

Water content (%)	**O_2 (%)**	**CO (%)**	**H_2 (%)**	**H_2O_2 (ppm)**	**O_3 (ppm)**
2.05 (Exp)	1.27 ± 0.11	2.46 ± 0.32	0.081 ± 0.006	ca. 10–100	ca. 10
2.05 (Calc)	1.28	2.53	0.09	47	193
4.09 (Exp)	1.12 ± 0.18	2.11 ± 0.53	0.138 ± 0.015	ca. 10–100	ca. 10
4.09 (Calc)	1.17	2.21	0.18	77	118
6.13 (Exp)	1.11 ± 0.13	2.02 ± 0.27	0.205 ± 0.005	ca. 10–100	ca. 10
6.13 (Calc)	1.09	1.97	0.25	106	96
8.17 (Exp)	1.00 ± 0.08	1.74 ± 0.14	0.269 ± 0.003	ca. 10–100	ca. 10
8.17 (Calc)	1.03	1.77	0.32	135	81

If we take a look at the calculated and experimental H_2/CO ratio (also known as syngas ratio) in **Figure 4-4**, we can draw the following conclusions. First of all, the calculated ratios are higher than the experimental values. This is of course a direct result of the above mentioned overestimation of the H_2O conversion, which leads to a higher concentration of H_2.

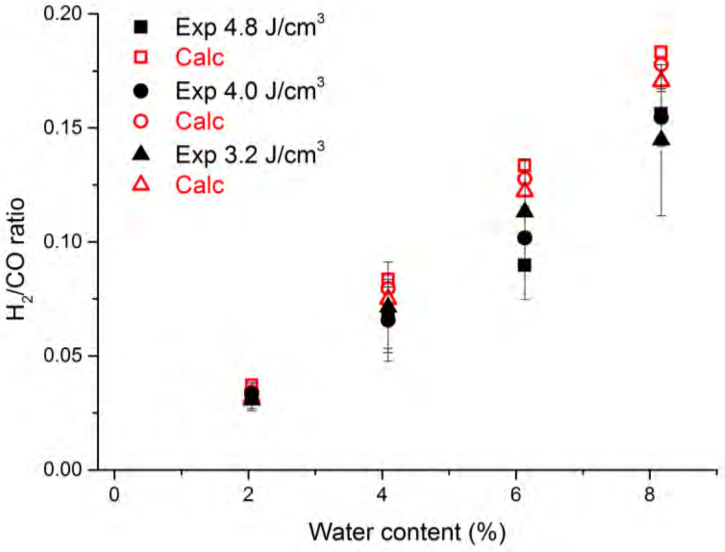

Figure 4-4. Calculated and experimental values of H_2/CO ratio as a function of water vapour content for the different values of SEI and a total flow rate of 600 mL min^{-1} at 323 K.

Secondly, the SEI has only a minor effect on the syngas ratio in the investigated range. Finally, and most importantly, the H_2/CO ratio increases linearly with increasing water content. This is logical because the absolute H_2O and CO_2 conversions only decrease slightly upon increasing water content (see above), so a higher water content (and thus a lower CO_2 content) leads to an increase in the effective production of H_2 (being formed out of H_2O) and a drop in CO production (being formed out of CO_2). As such, although no detectable amounts of oxygenated hydrocarbons are produced, this type of combined CO_2 and H_2O plasma conversion could still be of significant interest, because changing the water content in the gas mixture allows for a process with an easily controllable H_2/CO ratio. This is very important, since several post-processes require a different syngas ratio depending on the targeted products.[61] For example, Fischer Tropsch synthesis needs a ratio of 1.7 or 2.15, depending on the catalyst used, while for methanol synthesis a ratio of 3 is needed. The values obtained here, i.e., for water vapour contents up to 8 %, lead to syngas ratios clearly below 1, and thus they will need hydrogen enrichment for most practical applications. However, further in this paper we will investigate the conversion process in a wider range of water vapour contents and SEI values, yielding significantly larger syngas ratios up to 8.6 (see below).

Figure 4-5 illustrates the calculated and measured O-based selectivity of CO (eq.2.19) and O_2 (eq.2.20) and H-based selectivity of H_2 (eq.2.22) and H_2O_2 (eq.2.23) as a function of the water vapour content. The results are only shown for an SEI of 3.2 J/cm^3, since the absolute values and especially the trends of the selectivities appear to be almost independent from the used SEI.

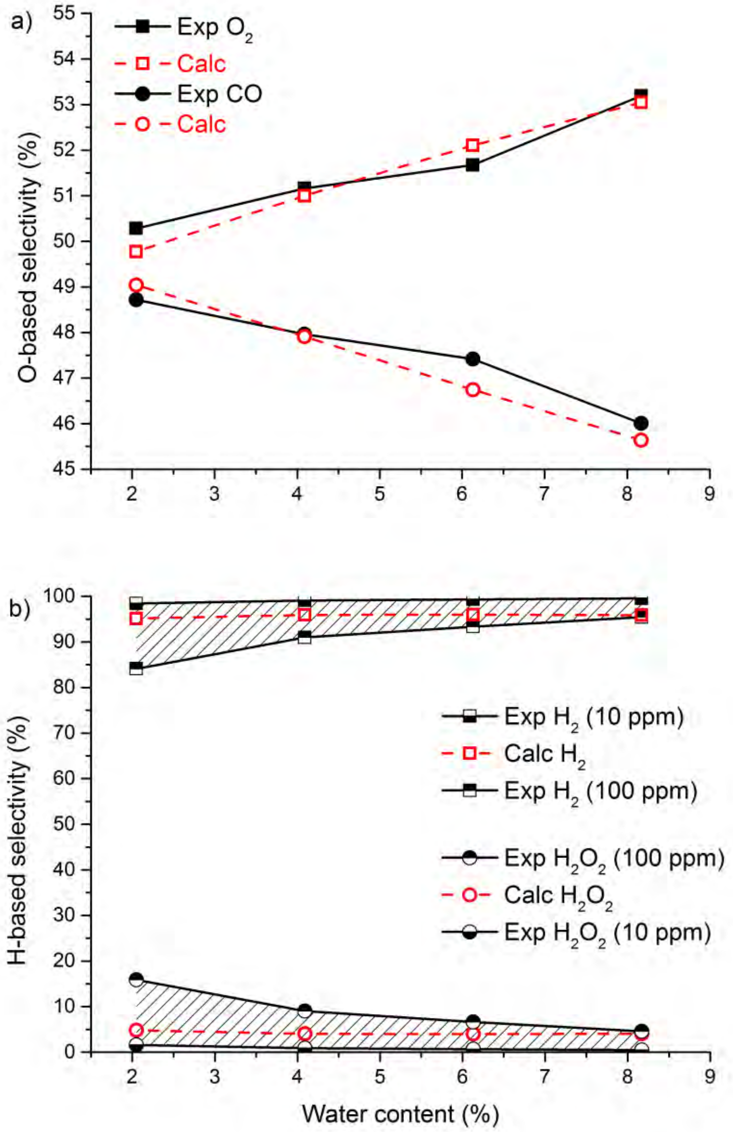

Figure 4-5. Calculated and experimental values of O-based (a) and H-based (b) selectivity of the major products as a function of water vapour content for a SEI value of 3.2 J/cm^3 and a total flow rate of 600 mL min^{-1} at 323 K. Note that although H_2O_2 was detected during the measurements (ca. 10–100 ppm), it could not be exactly quantified due to its low signal-to-noise ratio; therefore, a selectivity range is presented for the experimental H-based selectivities.

The O-based selectivity in **Figure 4-5(a)** indicates that with increasing water content from 2 to 8 %, the experimental O_2 selectivity increases from 50.3 to 53.2 % and the CO selectivity decreases from 48.7 to 46 %. The calculated values are in excellent agreement with the measured values (note the detailed Y-axis). The rise in O_2 selectivity upon increasing water content can easily be explained by the conversion of H_2O which leads to the additional formation of O_2 and thus increased selectivity for O_2 and decreased selectivity for CO. The sum of the CO and O_2 selectivity is about 99 %. The remaining 1 % selectivity in both the calculated and experimental results is accounted for by O_3 and H_2O_2.

Figure 4-5(b) shows the H-based selectivity versus the water content. The calculated H_2 selectivity is about 95–96 % and the remaining 4–5 % is due to the selectivity towards H_2O_2, independent of the water content within the investigated range. Although it is clear from the MS spectra that H_2O_2 is present in the mixture, its signal-to-noise ratio is too low to exactly quantify its effective amount and hence to calculate its selectivity directly. Nevertheless, from the spectra it was possible to estimate its concentration to be in the order of 10–100 ppm. Since the calculated selectivity for H_2O_2 corresponds to a concentration between 47 and 135 ppm (cf. **Table 4-2** above), this is indeed in the same range as the measured values. We calculated the experimental selectivity for H_2 and H_2O_2 for this range of 10–100 ppm, taking these values as lower and upper limit, respectively; see shaded area in **Figure 5-4(b)**. As to be expected, for low water contents the calculated results are closer to the values for 10 ppm, while at higher water contents the values are closer to the values of 100 ppm, since our calculations predict an increase of H_2O_2 with increasing water content. From these results we may conclude that all calculated selectivity results are in good agreement with the experiments.

4.1.3. Energy efficiency

The values for the energy efficiencies obtained through equation 2.12 are presented in **Table 4-3**, for both the calculations and the experiments.

For pure CO_2 splitting the thermal equilibrium dissociation limit lies at about 45–50 % energy efficiency and the same target is assumed for dry reforming of methane, see **Chapter 1**.[60,62,63] At the same time the energy efficiency of water splitting by electrolysis lies in the same 60–70 % range. Therefore, we believe that the same 60 % energy efficiency should be the target for the combined process under study here (for more details see **Chapter 1 and 6**). If we do not take the energy into account required for evaporating the water and heating the system, the highest (measured) energy efficiency achieved in our study is 7.3 %, for an SEI of 4.8 J/cm^3 and a water content of 2.05 %. As such, it becomes clear that from an energetic point of view, the process needs to be improved by at least a factor 8 to be considered competitive. It should be realized, however, that by adding a catalyst, which we believe is necessary to target the production of value-added compounds like methanol, the energy efficiency of a DBD plasma reactor typically also improves. In most cases, the catalyst is added as beads or pellets in a DBD reactor, yielding a so-called packed-bed DBD, which gives rise to electric field enhancements near the contact points of the beads or pellets,[64] leading to higher electron energies, and thus more pronounced electron impact dissociation of the gas molecules for the same applied power, resulting in a better energy efficiency. The latter was indeed demonstrated in several papers for pure CO_2 splitting,[65–67] and we believe that similar improvements in energy efficiency would also be possible for the combined CO_2/H_2O conversion.

Table 4-3. Calculated and measured energy efficiencies based on the standard reaction enthalpy, for the different specific energy inputs and water vapour contents investigated.

SEI (J/cm³)	Water content (%)	η (exp) (%)	η (calc) (%)
3.2	2.05	6.7	7.2
	4.09	5.9	6.5
	6.13	6.0	6.0
	8.17	5.3	5.7
4.0	2.05	6.8	7.1
	4.09	6.0	6.4
	6.13	5.9	5.9
	8.17	5.3	5.5
4.08	2.05	7.3	6.9
	4.09	6.0	6.3
	6.13	5.5	5.8
	8.17	6.4	5.5

4.1.4. Underlying mechanisms for the observed trends

As shown above, the experiments and computer simulations reveal exactly the same trends for the absolute conversion of CO_2 and H_2O and for the selectivity towards CO, H_2 and O_2. This justifies using the plasma chemistry model for the most important—and chemically most interesting part—of this work, i.e. analysing the main reactions taking place, to describe and explain the observed macroscopic trends, and eventually to compile a general reaction scheme, which illustrates the overall underlying chemical reaction mechanisms. This allows us in the end to draw important conclusions, regarding the applicability of this process.

a) Limited CO_2 (and H_2O) conversion upon water addition

There are two main reasons why the CO_2 conversion decreases when adding water: a physical reason and a chemical reason. The physical reason was already mentioned above, namely the drop in maximum electron density, which leads to a lower rate of the electron impact dissociation reactions. The chemical reason behind the drop in CO_2 conversion upon rising water vapour content is revealed by the kinetic analysis. One of the crucial reactions for this process is the reaction between CO and OH:

$CO + OH \rightarrow CO_2 + H$

$k = 5.4\text{x}10^{-14}\ [\text{cm}^3/\text{molecule s}]\ (T/298\ \text{K})^{1.50}\ e^{250\ [K]/T}$

This is a fast reaction and plays a pivotal role in the ratio between the conversion of CO_2 and H_2O. We can explain this in a very simple way by means of the following reaction paths that take place:

$$
\begin{array}{lcll}
e^- + CO_2 & \rightarrow & CO + O + e^- & (1) \\
e^- + H_2O & \rightarrow & OH + H + e^- & (2) \\
CO + OH & \rightarrow & CO_2 + H & (3) \\
H + O_2 + M & \rightarrow & HO_2 + M & (4) \\
HO_2 + O & \rightarrow & OH + O_2 & (5) \\
OH + H + M & \rightarrow & H_2O + M & (6) \\
\hline
2e^- + CO_2 + H_2O & \rightarrow & CO_2 + H_2O + 2e^- & (7)
\end{array}
$$

Reactions (1) and (2) lead to the (electron impact) dissociation of CO_2 and H_2O, yielding the products CO and OH (as well as O and H atoms). However, due to the large reaction rate constant of reaction (3), CO and OH will quickly recombine to form again CO_2. In these three reactions, two H atoms and one O atom are formed, but they recombine quickly as well, first into OH through the subsequent reactions (4) and (5), and subsequently OH reacts even faster with H back into H_2O through reaction (6). In the end, this leaves us exactly where we started (see overall reaction (7)). Of course, this does not mean that there will be no net conversion of CO_2 and H_2O. Indeed, this is not the only pathway taking place for the conversion of CO_2 and H_2O, but this pathway highlights the interaction between the CO_2 and H_2O dissociation products, which limits their conversion. The overall CO_2 and H_2O loss rates, however, are higher than their formation rates, effectively leading to the observed conversions. Nevertheless, reactions (2) and (3) illustrate why the absolute conversion of CO_2 decreases upon addition of H_2O, while in general an increasing trend is found for the absolute CO_2 conversion in admixtures, i.e. upon addition of N_2,[68] He[69,70] and Ar.[70]

b) Absence of methanol production

The above reaction scheme can also explain why no production of methanol is observed. Indeed, in 1988 Eliasson et al.[71] investigated the production of methanol in a CO_2/H_2 DBD reactor. When using the plasma only set-up, the CO_2 conversion reached 12.4 % and the major products were CO (with a selectivity of 96 %) and H_2O, while very small yields of CH_4 and methanol were detected, with selectivities of 3.2 and 0.4 %, respectively. The authors proposed the following radical reaction mechanism for the formation of methanol:

$$CO_2 \xrightarrow{+e^-} CO \xrightarrow{+H} CHO \xrightarrow{+H} CH_2O \xrightarrow{+H} CH_3O \xrightarrow{+H} CH_3OH$$

These reactions are also included in our model, but they seem to be of minor importance when using H_2O as a co-reactant, because the H atoms are quickly consumed by O_2 and OH, according to the scheme presented above (reactions (4) and (6)). Our plasma chemistry model elucidates that in the case of a CO_2/H_2O mixture another pathway to methanol is more important (note that the reactant "+H" above the arrows does not only designate H atoms but can also be replaced by other H-containing species such as H_2, HO_2, H_2O, …):

$$CO_2\ (\xrightarrow{+e^-} CO\ ) \xrightarrow{+e^-} C \xrightarrow{+H} CH \xrightarrow{+H} CH_2 \xrightarrow{+H} CH_3 \xrightarrow{+OH} CH_3OH$$

Nevertheless, both these pathways turn out to be unimportant in our case, because the H atoms that are needed to start forming CHO and CH fragments from CO and C, respectively, are being steered to OH and subsequently to H_2O again (see reactions (4–6) above), leaving no room for the production of oxygenated hydrocarbons, such as methanol. This chemical analysis reveals that H_2O might not be a suitable H-source for the formation of methanol (as well as other oxygenated hydrocarbons) after all, because of the abundance of O atoms, O_2 molecules and OH radicals, trapping the H atoms. This important new insight will allow us to propose solutions on how the production of methanol might still be pursued in a CO_2/H_2O plasma and/or which other options might be more attractive, as will be elaborated in the Summary below.

c) Formation of H_2O_2

Both our experiments and calculations illustrate that a mixture of CO_2 and H_2O can yield non-negligible amounts of H_2O_2, which is also of great value, more specifically for decontamination purposes, as explained in section 1. The main pathways for the production of H_2O_2, as revealed by our chemical kinetics analysis, are:

2x ($e^- + H_2O \rightarrow OH + H + e^-$) (2)

$OH + OH + M \rightarrow H_2O_2 + M$ (8)

$2\ e^- + 2\ H_2O \rightarrow H_2O_2 + 2\ H + 2\ e^-$ (9)

Reaction (2) leads to the (electron impact) dissociation of H_2O into H and OH. Subsequently, 2 OH radicals react with each other in the presence of a third body, to form H_2O_2 (reaction (8)). For the operating conditions investigated here, i.e. water contents up to 8 % and SEI values up to 4.8 J/cm³, this pathway is responsible for 90 % of the H_2O_2 production. The remaining 10 % follows a slightly more complicated pathway:

3x ($e^- + CO_2 \rightarrow CO + O + e^-$) (1)

$e^- + H_2O \rightarrow OH + H + e^-$ (2)

$OH + O \rightarrow H + O_2$ (10)

$H + O_2 + M \rightarrow HO_2 + M$ (4)

$HO_2 + O \rightarrow OH + O_2$ (5)

$OH + O \rightarrow H + O_2$ (10)

2x ($H + O_2 + M \rightarrow HO_2 + M$) (4)

$HO_2 + HO_2 + M \rightarrow H_2O_2 + O_2 + M$ (11)

$4\ e^- + H_2O + 3\ CO_2 \rightarrow H_2O_2 + 3\ CO + O_2 + 4\ e^-$ (12)

Reactions (1) and (2) again lead to the (electron impact) dissociation of CO_2 and H_2O, producing CO, O, OH and H. OH and O subsequently form H and O_2 (reaction (10)), which then react further with a third body to HO_2 (reaction (4)). HO_2 turns out to be the main production source for O_2 and the second most important source for OH (reaction (5)). Next, reactions (11) and (4) can repeat themselves, finally yielding two HO_2 radicals, which react with each other in a three-body reaction, producing H_2O_2 and O_2 (11). Thus, the overall reaction is given by reaction (12).

d) General reaction overview

A general reaction overview is illustrated in **Figure 4-6**, which is composed of the time-integrated formation and loss rates of the most important species in our model for explaining the chemical pathways taking place. The results are presented for an SEI of

3.2 J/cm³ and 8 % water content. A higher SEI yields higher integrated rates, but does not change the reaction paths significantly. A lower water content only decreases the reaction rates of the H_2O chemistry but again, it does not change the reaction paths significantly.

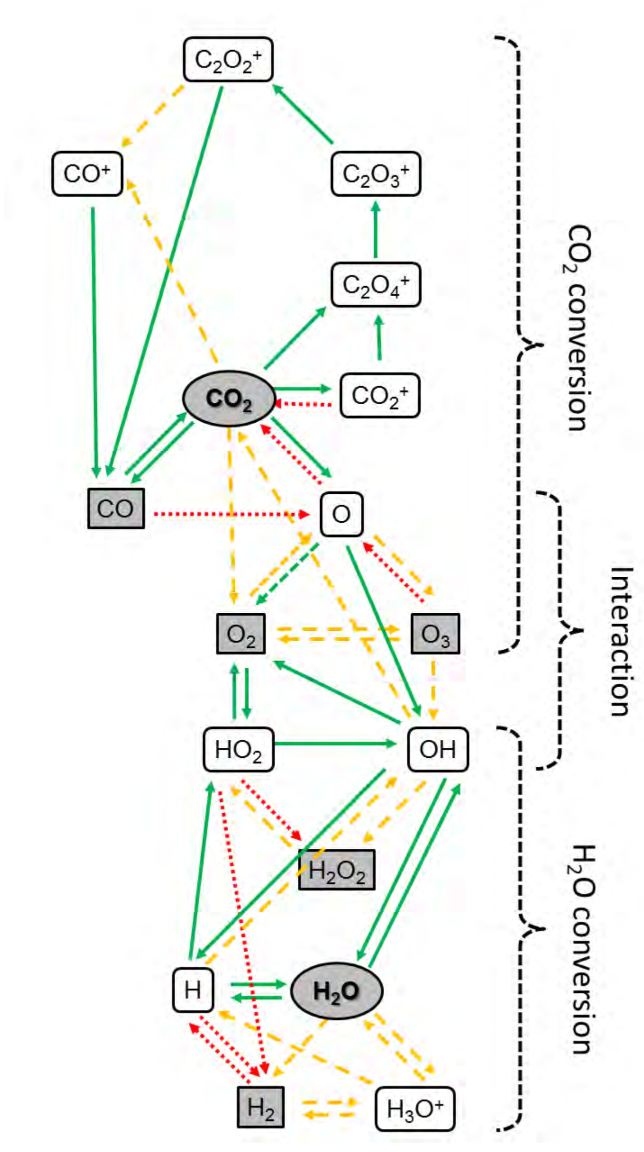

Figure 4-6. Reaction scheme to illustrate the main pathways for CO_2 and H_2O conversion and their interactions. The arrow lines represent the formation rates of the species, with full green lines being formation rates over 10^{17} $cm^{-3}\cdot s^{-1}$, orange dashed lines between 10^{17} and 10^{16} $cm^{-3}\cdot s^{-1}$ and red dotted lines between 10^{16} and 10^{15} $cm^{-3}\cdot s^{-1}$.

The reaction scheme can be divided in three main parts: the top part describes the CO_2 conversion, the bottom part deals with the H_2O conversion and the middle part explains the interaction between both. The arrow lines represent the formation rates of the species they point to, with full green lines being formation rates over 10^{17} $cm^{-3}\cdot s^{-1}$, orange dashed lines between 10^{17} and 10^{16} $cm^{-3}\cdot s^{-1}$ and red dotted lines between 10^{16} and 10^{15} $cm^{-3}\cdot s^{-1}$.

Starting from CO_2 the main reactions are electron impact dissociation towards CO and O, and electron impact ionization towards CO_2^+. Once ionization takes place, the main reaction path becomes $CO_2^+ + CO_2 + M \rightarrow C_2O_4^+ + M$ (reaction (14) below). The $C_2O_4^+$ ions convert further into $C_2O_3^+$ and $C_2O_2^+$ ions (reactions (15) and (16) below), and the latter ions split into two CO molecules or into CO and CO^+ (reactions (17) and (18) below). The CO molecules are mainly consumed in these ion conversion processes, forming again CO_2. Thus, a circular pathway interaction between CO and CO_2 takes place, as illustrated by reactions (13)–(19) below, with no net conversion. The only net conversion is due to electron impact dissociation (reaction (1)). This can be summarized as follows:

$$e^- + CO_2 \rightarrow CO + O + e^- \tag{1}$$

$$e^- + CO_2 \rightarrow CO_2^+ + e^- + e^- \tag{13}$$

$$2x\ (\ CO_2^+ + CO_2 + M \rightarrow C_2O_4^+ + M\ ) \tag{14}$$

$$2x\ (\ C_2O_4^+ + CO + M \rightarrow C_2O_3^+ + CO_2 + M\ ) \tag{15}$$

$$2x\ (\ C_2O_3^+ + CO + M \rightarrow C_2O_2^+ + CO_2 + M\ ) \tag{16}$$

$$e^- + C_2O_2^+ \rightarrow CO + CO \tag{17}$$

$$C_2O_2^+ + M \rightarrow CO + CO^+ + M \tag{18}$$

$$CO^+ + CO_2 \rightarrow CO + CO_2^+ \tag{19}$$

$$3\ e^- + CO_2 \rightarrow CO + O + 3\ e^- \tag{20}$$

Furthermore, the O atoms formed by the CO_2 splitting are also involved in a triangular interaction with O_2 and O_3, as already described in our earlier work,[17,68] with the main product being O_2. Thus, the two main products of CO_2 splitting are CO and O_2.

The interaction between CO_2 and H_2O takes place through the intermediate water products (H, OH and HO_2) with O, O_2, O_3 and CO, through the following main reactions:

$$H + O_2 + M \rightarrow HO_2 + M \qquad (4)$$

$$H + O_3 \rightarrow OH + O_2 \qquad (21)$$

$$OH + O \rightarrow H + O_2 \qquad (10)$$

$$OH + CO \rightarrow H + CO_2 \qquad (3)$$

$$HO_2 + O \rightarrow O_2 + OH \qquad (5)$$

$$HO_2 + OH \rightarrow H_2O + O_2 \qquad (22)$$

Starting from H_2O the main reaction is also electron impact dissociation into OH and H (see reaction (2)). Other products formed are H_2 (mainly through reactions (23) and (24) below) and intermediate ions such as H_3O^+ (not included in the reactions below). Although the formation rates of H_2 are only moderate, its loss rates are even lower, explaining why it is still one of the main reaction products. The main reaction for OH and H radicals is their recombination into H_2O (see reaction (6) below). Moreover, part of the OH radicals also recombine into H_2O_2 through a third body reaction (see reaction (8)). This reaction is indeed the main production pathway for hydrogen peroxide, as explained above. In turn, H_2O_2 can be destroyed upon reaction with an additional OH radical (see reaction (27)). Just like for O, O_2 and O_3, an interaction is taking place between OH, HO_2 and H_2O_2, which can be summarized as follows: HO_2, mainly formed from H and O_2 (reaction (4)), reacts with O to form OH (reaction (5)). As explained above, HO_2 can also recombine to form H_2O_2 (reaction (11)) and again part of this H_2O_2 is converted back into HO_2 (reaction (27)).

If we combine the net reactions (26) and (28), we get the overall reaction (29), which is one of the most important reaction paths of the conversion of CO_2 and H_2O in the main observed products O_2, CO, H_2 and H_2O_2.

$$e^- + H_2O \rightarrow OH + H + e^- \qquad (2)$$

$$e^- + H_2O \rightarrow OH + H^- \qquad (23)$$

$$H^- + H_2O \rightarrow OH^- + H_2 \qquad (24)$$

$$H + OH^- \rightarrow H_2O + e^- \qquad (25)$$

$$OH + OH + M \rightarrow H_2O_2 + M \qquad (8)$$

$$2\,e^- + 2\,H_2O \rightarrow H_2 + H_2O_2 + 2\,e^- \qquad (26)$$

$$2x \quad (\quad e^- + CO_2 \rightarrow CO + O + e^- \quad) \qquad (1)$$

$$3x \quad (\quad e^- + H_2O \rightarrow OH + H + e^- \quad) \qquad (2)$$

$$OH + H + M \rightarrow H_2O + M \qquad (6)$$

$$OH + OH + M \rightarrow H_2O_2 + M \qquad (8)$$

$$H_2O_2 + OH \rightarrow H_2O + HO_2 \qquad (27)$$

$$2x \quad (\quad H + O_2 + M \rightarrow HO_2 + M \quad) \qquad (4)$$

$$HO_2 + O \rightarrow OH + O_2 \qquad (5)$$

$$HO_2 + HO_2 + M \rightarrow H_2O_2 + O_2 + M \qquad (11)$$

$$H_2O_2 + OH \rightarrow H_2O + HO_2 \qquad (27)$$

$$HO_2 + O \rightarrow OH + O_2 \qquad (5)$$

$$2\,e^- + 2\,CO_2 \rightarrow 2\,CO + O_2 + 2\,e^- \qquad (28)$$

$$4\,e^- + 2\,H_2O + 2\,CO_2 \rightarrow 2\,CO + O_2 + H_2 + H_2O_2 + 4\,e^- \qquad (29)$$

4.2. Model predictions in a wider range

So far our modelling calculations and experiments are perfectly in line with four of the five main observations from literature (see end Section 1): (i) the CO_2 conversion increases with increasing energy input; (ii) the CO_2 conversion drops with increasing water content; (iii) the H_2/CO ratio increases with increasing water content; and (iv) the main products formed are H_2, CO, O_2 and (ppm amounts of) H_2O_2.

Nevertheless, the above study could only be carried out for a small range of experimental conditions, based on the available set-up. To analyse this process for a wider range of conditions and especially to reveal whether the latter can yield certain products in larger amounts, we have performed additional model calculations, beyond what is typically accessible for one experimental set-up. More specifically, we have varied the SEI from 5 to 250 J/cm^3 for water contents from 10 to 90 %.

Since this newly developed chemistry model was not validated in this wider range of conditions, caution is advised with its interpretation and predictive value. Another critical note is that the experimental conditions required to achieve the highest water contents under study might not be straightforward to realize, due to the condensation issues already observed at low concentrations. One solution might, therefore, be to dilute the entire mixture with an inert gas, such as argon or helium. Nitrogen is probably less suited, since it gives rise to NO_X formation.[68] This approach would also solve possible safety issues, but on the other hand, increase the energy cost, as discussed in the Summary section 4.3 below.

Although caution is advised when extrapolating models outside their validated range, our previous modelling studies[17,26,60,68,72] for several different mixtures have already shown that in general the plasma chemistry behaviour is almost independent on the SEI, showing a steadily increasing trend of conversion and production. The same studies with admixtures have also shown that in general the plasma chemistry follows a stable and logic trend when changing the mixture ratios. Furthermore, we performed a sensitivity analysis for the most important reactions, which showed that when taking the uncertainties of the reaction rate constants into account, the average deviation on the calculation results is indeed independent of the SEI and only ca. 2 % on average. Hence, extrapolation of the model to a wider range of conditions would give us the opportunity to investigate whether the same results can be expected in this wider range, and/or whether certain products can be formed in larger amounts, and thus, give an indication whether it would be worth pursuing these other conditions experimentally.

4.2.1. CO_2 and H_2O Conversion

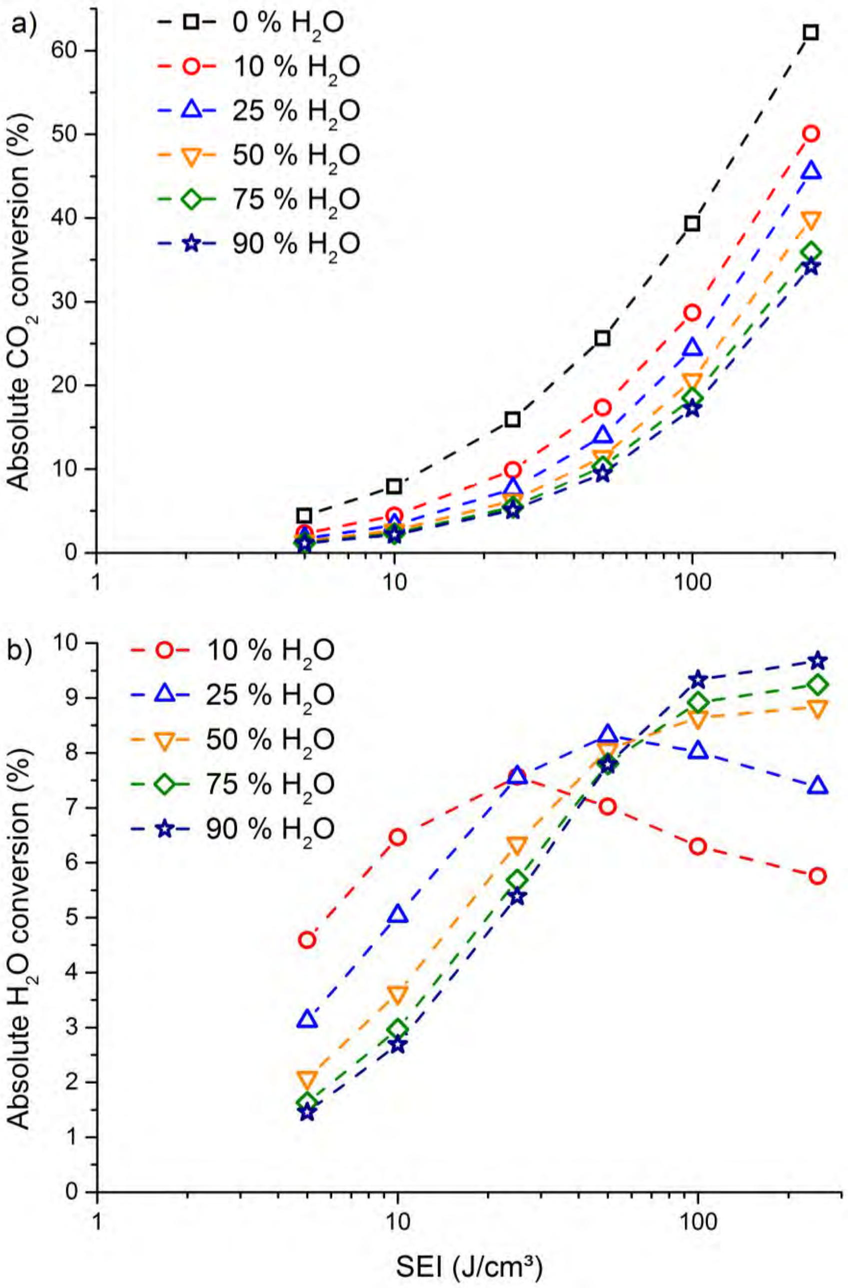

Figure 4-7. Calculated values of absolute CO_2 (a) and H_2O (b) conversion as a function of water vapour content for the different values of SEI.

In **Figure 4-7** the calculated absolute CO_2 (a) and H_2O (b) conversions are plotted as a function of the SEI values for the various water vapour contents in this wider range.

Note that we opted to plot the conversion as a function of the SEI instead of the water vapour content, which allows for an easier interpretation of the results. The absolute CO_2 conversion shows the same trends as observed before: it increases with increasing SEI, and regardless of the SEI, it is the highest for pure CO_2, and it drops with increasing water content over the entire range, with the initial drop being most pronounced. As already mentioned, this drop in absolute CO_2 conversion upon addition of water in the mixture is opposite to the trend previously observed for CO_2 admixtures with N_2,[68] He[69,70] and Ar.[70]

The absolute H_2O conversion, on the other hand, shows different trends depending on the SEI. For an SEI of 5 and 10 J/cm³ the H_2O conversion increases with increasing SEI and decreases with increasing water content, while for an SEI of 100 and 250 J/cm³ the H_2O conversion increases with increasing water content. Furthermore, at the low water contents, the H_2O conversion now drops with increasing SEI. The results at 25 and 50 J/cm³ show an intermediate behaviour.

We also take a look at the effective conversions as a function of SEI for different water contents, as plotted in **Figure 4-8**. The effective CO_2 conversion again rises with SEI and drops with increasing water content. This is logical, because of the lower absolute CO_2 conversion and the lower CO_2 content in the gas mixture. However, the influence of the water content seems to depend on the SEI. The higher the SEI, the lower is the influence of the water content on the CO_2 conversion, at least for low enough water contents. Indeed, at an SEI of 5 J/cm³, adding 10 % water leads to a decrease in effective CO_2 conversion by 53 % (i.e. from 4.4 to 2.1 %). On the other hand, at a SEI of 250 J/cm³ the initial drop in effective CO_2 conversion is only 27 % (i.e. from 62.2 % in pure CO_2 to 45.1 % upon addition of 10 % water). Upon further increasing the water content, the drop in CO_2 conversion becomes, however, similar in the entire SEI range. Indeed, at 90 % water content, the effective CO_2 conversion decreases by 97 % and 94 % with respect to pure CO_2 for an SEI of 5 and 250 J/cm³, respectively. Thus, a higher SEI reduces the negative influence of H_2O on the effective CO_2 conversion, but only for relatively low water contents (i.e. up to 50 %).

The effective H_2O conversion for different SEI values and H_2O contents (**Figure 4-8(b)**) reveals a much easier to understand trend than the absolute conversion plotted in **Figure 4-7(b)**. First of all, the effective H_2O conversion increases with increasing water content for all SEI values. The behaviour as a function of the SEI clearly depends on the water content in the mixture. For a water content of 10 %, the effective H_2O conversion shows a parabolic trend, reaching a maximum at a SEI of 25 J/cm³. For 25 % water content, a maximum is reached at an SEI of 50 J/cm³, while for higher water contents, the conversion rises more clearly with SEI, but seems to saturate at a SEI of 100 J/cm³. In other words, depending on the amount of water present in the mixture, increasing the SEI will lead to a higher effective H_2O conversion until an equilibrium in the chemistry is reached, when the backward reactions (e.g., the recombination of OH and H into H_2O) start to become equally important as the forward reactions (e.g., the splitting of H_2O into OH and H). This means that the conversion stops increasing and even starts decreasing slightly upon a further rising SEI.

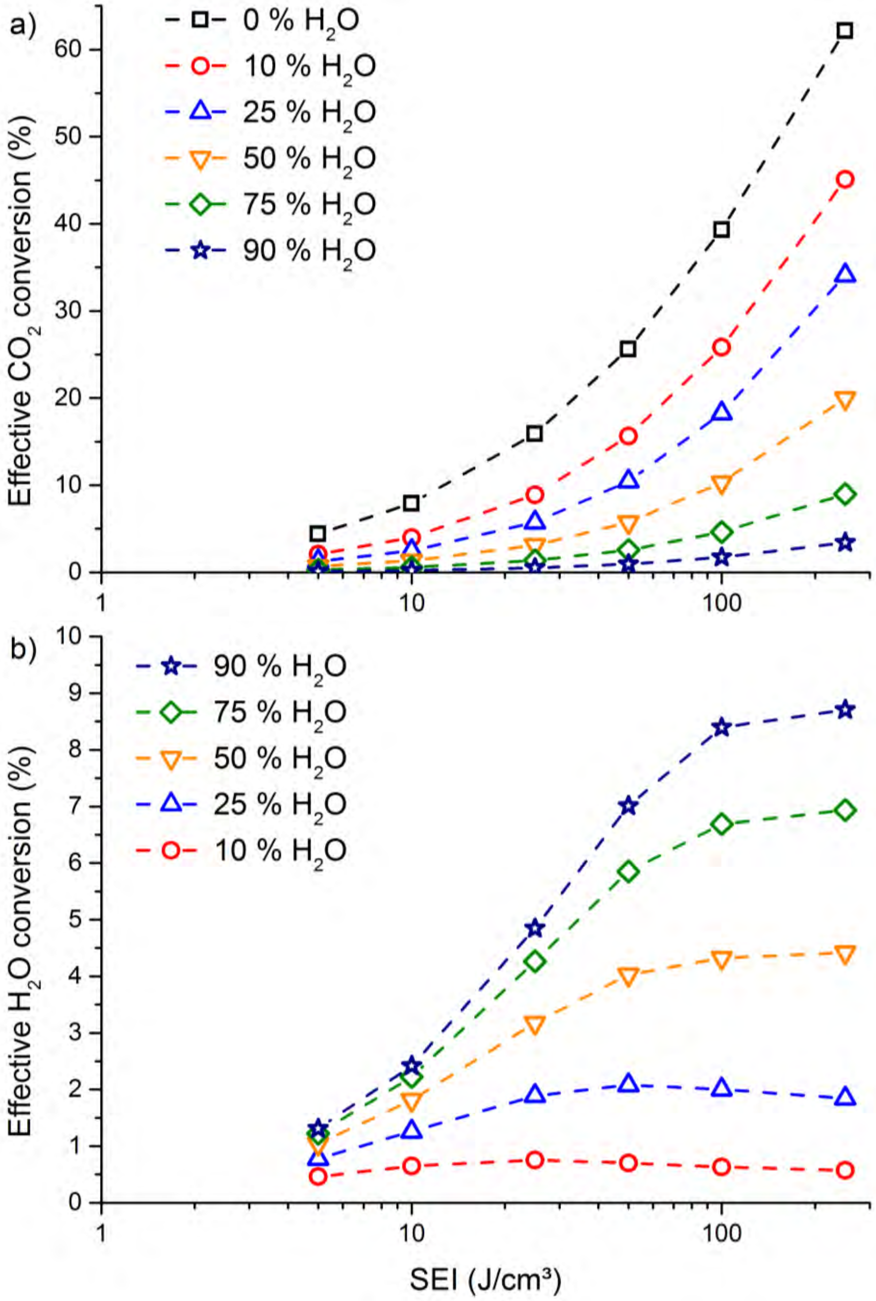

Figure 4-8. Calculated values of effective CO_2 (a) and H_2O (b) conversion as a function of SEI for the different water vapour contents.

These results clearly indicate that the CO_2 chemistry shows mainly the same behaviour as presented for the smaller range of water contents and SEI values, while the H_2O chemistry undergoes more changes with increasing SEI and water content, which has an influence on the effective CO_2 conversion. This will also become clear from the product selectivity, presented below.

4.2.2. Product selectivity

In this wide range of energy inputs and water contents, O_2 and the syngas components CO and H_2 are still the main products formed. Again, no oxygenated hydrocarbons are formed, at least not in concentrations above 20 ppm. However, the production of hydrogen peroxide (H_2O_2) increases significantly with increasing SEI and rising water content, and concentrations in the percentage range are achieved. The calculated concentrations of O_2, CO, H_2, H_2O_2 and O_3 are listed in **Table 4.4** for the different water vapour contents and SEI values investigated. Note that at higher SEI values high concentrations of H_2O_2 can be reached, i.e. up to 2.1–2.2 % at a SEI of 100–250 J/cm³ and 90 % water, but this will be at the expense of the energy cost and the H_2/CO ratio (see below), and therefore, these higher SEI values might not be interesting in practice, depending of their intended use.

Table 4-4. Calculated and measured gas composition after plasma treatment for an SEI of 5 (a), 10 (b), 25 (c), 50 (d), 100 (e), and 250 (f) J/cm³, and for the different water vapour contents investigated, with the remainder being unconverted CO_2 and H_2O.

(a) SEI 5 J/cm³

CO_2 (%)	H_2O (%)	χ CO_2 (%)	χ H_2O (%)	O_2 (%)	CO (%)	H_2 (%)	H_2O_2 (ppm)	O_3 (ppm)	CH_3OH (ppb)
100	0	4.41	-	1.37	4.33	-	-	5259.42	-
90	10	2.32	4.59	1.22	2.06	0.43	0.02	102.48	4.61
75	25	1.69	3.12	0.95	1.26	0.72	0.05	59.59	12.16
50	50	1.36	2.08	0.69	0.68	0.87	0.16	34.98	24.68
25	75	1.18	1.63	0.47	0.29	0.93	0.28	18.79	31.91
10	90	1.12	1.45	0.35	0.11	0.95	0.35	13.61	24.43

(b) SEI 10 J/cm³

CO_2 (%)	H_2O (%)	χ CO_2 (%)	χ H_2O (%)	O_2 (%)	CO (%)	H_2 (%)	H_2O_2 (ppm)	O_3 (ppm)	CH_3OH (ppb)
100	0	7.91	-	2.44	7.65	-	-	9245.04	-
90	10	4.43	6.46	2.20	3.90	0.60	0.03	231.37	9.94
75	25	3.30	5.03	1.73	2.43	1.15	0.08	140.34	31.36
50	50	2.65	3.62	1.28	1.31	1.53	0.26	75.88	68.99
25	75	2.31	2.96	0.87	0.57	1.69	0.51	38.84	86.85
10	90	2.16	2.69	0.65	0.21	1.75	0.65	27.82	56.96

(c) SEI 25 J/cm³

CO_2 (%)	H_2O (%)	χ CO_2 (%)	χ H_2O (%)	O_2 (%)	CO (%)	H_2 (%)	H_2O_2 (ppm)	O_3 (ppm)	CH_3OH (ppb)
100	0	15.91	-	4.91	14.86	-	-	16819.43	-
90	10	9.90	7.56	4.46	8.51	0.66	0.06	652.49	15.58
75	25	7.66	7.56	3.47	5.54	1.68	0.15	418.09	82.58
50	50	6.21	6.35	2.62	3.02	2.68	0.41	218.48	202.49
25	75	5.46	5.68	1.80	1.34	3.23	0.95	101.76	284.77
10	90	5.09	5.39	1.32	0.50	3.47	1.31	66.89	185.43

(d) SEI 50 J/cm³

CO_2 (%)	H_2O (%)	χ CO_2 (%)	χ H_2O (%)	O_2 (%)	CO (%)	H_2 (%)	H_2O_2 (ppm)	O_3 (ppm)	CH_3OH (ppb)
100	0	25.62	-	7.39	23.03	-	-	27480.12	-
90	10	17.36	7.02	7.25	14.47	0.56	0.09	1444.21	13.13
75	25	13.94	8.32	5.55	9.86	1.74	0.22	919.55	124.11
50	50	11.44	8.06	4.09	5.48	3.35	0.51	508.19	384.66
25	75	10.31	7.80	2.83	2.50	4.46	1.23	214.66	667.44
10	90	9.47	7.79	1.99	0.93	4.98	1.89	120.27	443.34

(e) SEI 100 J/cm³

CO_2 (%)	H_2O (%)	χ CO_2 (%)	χ H_2O (%)	O_2 (%)	CO (%)	H_2 (%)	H_2O_2 (ppm)	O_3 (ppm)	CH_3OH (ppb)
100	0	39.33	-	10.70	33.53	-	-	40463.39	-
90	10	28.69	6.30	11.11	22.87	0.42	0.13	3124.34	8.42
75	25	24.35	8.02	8.60	16.65	1.50	0.33	2068.42	135.66
50	50	20.64	8.64	6.02	9.68	3.39	0.67	1220.40	1015.51
25	75	18.50	8.92	4.05	4.43	5.11	1.30	474.22	1309.11
10	90	17.25	9.33	2.71	1.68	5.99	2.18	220.25	988.41

(f) SEI 250 J/cm^3

CO_2 (%)	H_2O (%)	χ CO_2 (%)	χ H_2O (%)	O_2 (%)	CO (%)	H_2 (%)	H_2O_2 (ppm)	O_3 (ppm)	CH_3OH (ppb)
100	0	62.18	-	15.35	48.87	-	-	60579.05	-
90	10	50.09	5.75	17.40	36.91	0.28	0.19	7290.70	4.28
75	25	45.48	7.38	14.05	29.13	1.08	0.49	5403.69	112.57
50	50	39.97	8.84	9.52	18.02	2.98	1.00	3246.65	1046.46
25	75	35.93	9.25	5.65	8.38	4.85	1.55	1252.43	1601.53
10	90	34.22	9.68	3.70	3.29	6.33	2.05	579.34	1811.43

From these tables the same logical trends upon increasing water content as in **Table 4-3** are observed here, i.e. a decreasing trend for the O_2, CO and O_3 concentrations and an increasing trend for the H_2 and H_2O_2 concentrations. Our calculations reveal that H_2O_2 is produced with concentrations in the range of 300 ppm to 2.2 %, depending on the SEI and water content, which is high enough for the effluent mixture to be suitable as disinfectant.[12–14]

Moreover, it is obvious that the H_2 concentration increases significantly upon addition of more water, and becomes clearly larger than CO for the highest water contents. This will have a beneficial effect for the H_2/CO ratio, as is shown in **Figure 4-9**. When comparing the calculated H_2/CO ratio in **Figure 4-9** with the results from **Figure 4-5**, the same increasing trend with increasing water content is observed. For a SEI of 5 and 10 J/cm^3 the trend is still more or less linear, like in **Figure 4-5**, but it starts deviating with increasing SEI. Furthermore, the effect of the SEI is now clearly visible, with a decreasing H_2/CO ratio upon increasing the SEI. This behaviour is in line with the fifth observation reported in literature, which did not yet follow from our experimental and calculation results in the limited range of conditions. This drop in H_2/CO ratio upon increasing SEI can be explained by the effective H_2O conversion, which starts to saturate with increasing SEI, while the effective CO_2 conversion keeps on rising (see **Figure 4-8(a,b)** above).

Finally, and most importantly, the maximum H_2/CO ratio appears to be around 8.6 and is obtained for SEI values between 5 and 25 J/cm^3 and for a water content of 90 %. As such, our earlier claim that plasma technology allows for a process with an easily controllable H_2/CO ratio is confirmed even in this wider range of water contents and SEI values, and **Figure 4-9** demonstrates that it can even be controlled in two ways, i.e.

by the water content and the SEI value. Thus, our calculations reveal that a CO_2/H_2O plasma is able to supply a hydrogen rich syngas ratio for direct Fischer Tropsch synthesis and would only need to be enriched with small amounts of additional H_2 to be suitable for methanol synthesis.

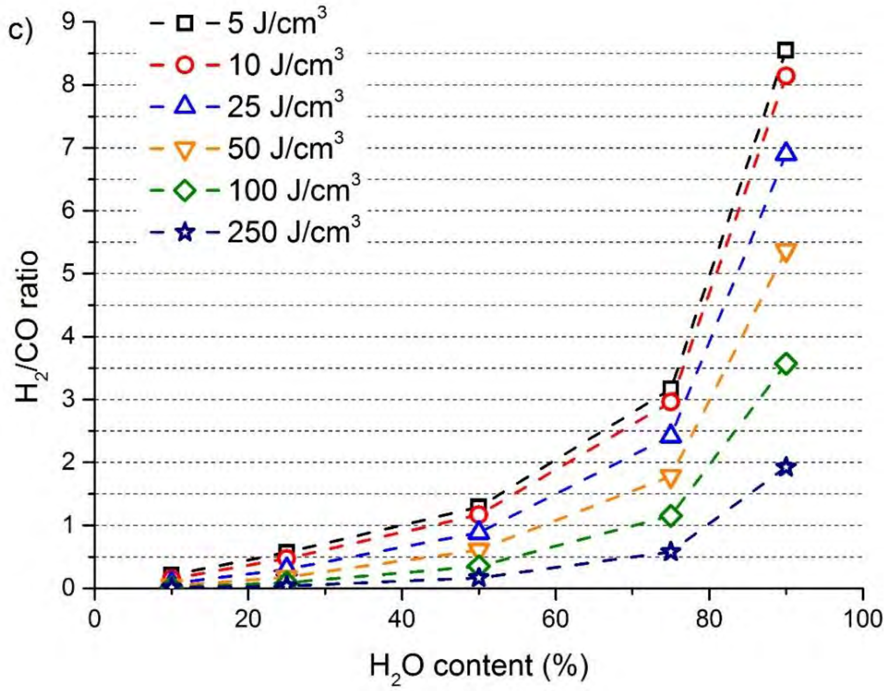

Figure 4-9. Calculated values of H_2/CO ratio as a function of water vapour content for the different values of SEI.

Figures 4-10 to 4-15 illustrate the (O-based and H-based) selectivity of the major products as a function of water vapour content, for the different SEI values. As to be expected from the conversion results, the O-based selectivity is almost independent from the SEI. The H-based selectivity, however, shows a significant shift from H_2 to H_2O_2 depending on the SEI and the water content, which is a direct result of the saturation of the effective H_2O conversion, illustrated in **Figure 4-8(b)** above.

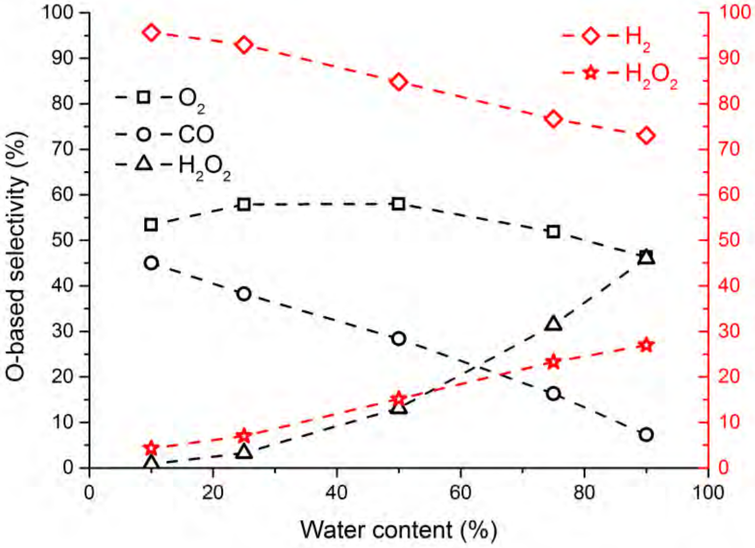

Figure 4-10. Calculated values of O-based (black symbols, left axis) and H-based (red symbols, right axis) selectivity of the major products as a function of water vapour content for a SEI value of 5 J/cm^3.

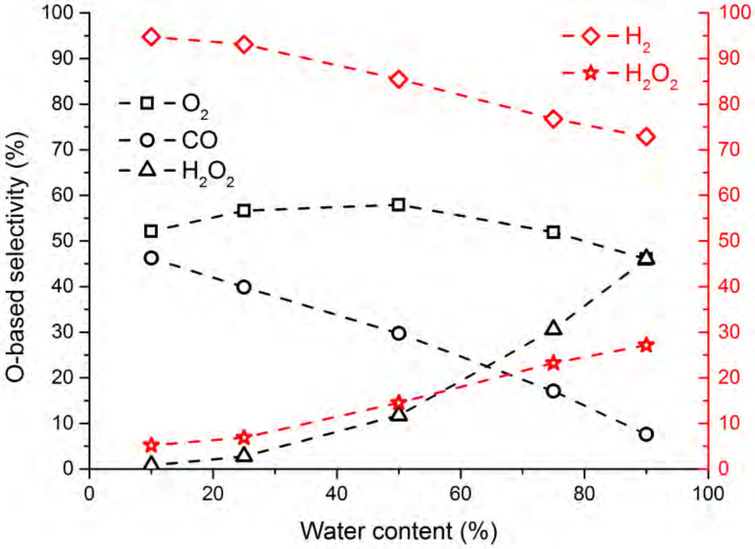

Figure 4-11. Calculated values of O-based (black symbols, left axis) and H-based (red symbols, right axis) selectivity of the major products as a function of water vapour content for a SEI value of 10 J/cm^3.

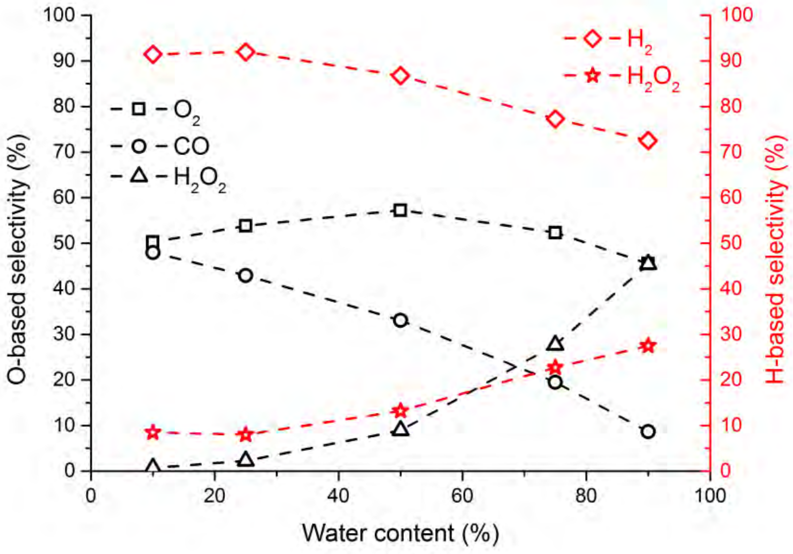

Figure 4-12. Calculated values of O-based (black symbols, left axis) and H-based (red symbols, right axis) selectivity of the major products as a function of water vapour content for a SEI value of 25 J/cm^3.

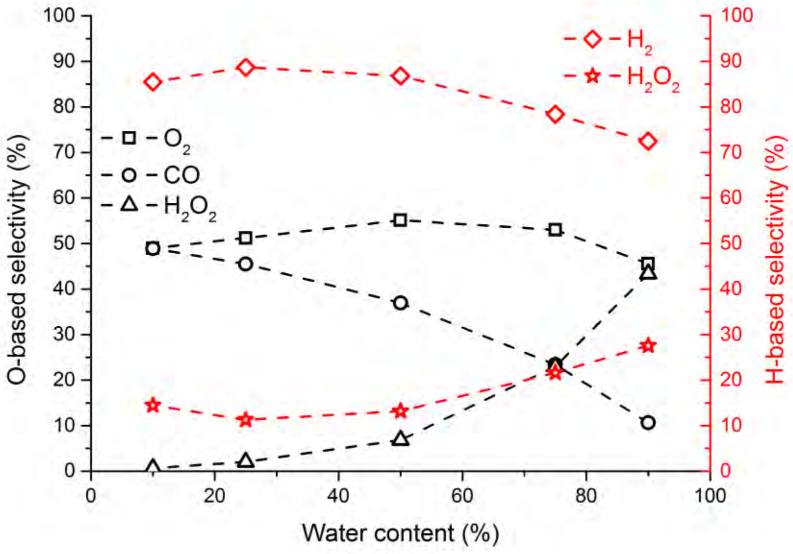

Figure 4-13. Calculated values of O-based (black symbols, left axis) and H-based (red symbols, right axis) selectivity of the major products as a function of water vapour content for a SEI value of 50 J/cm^3.

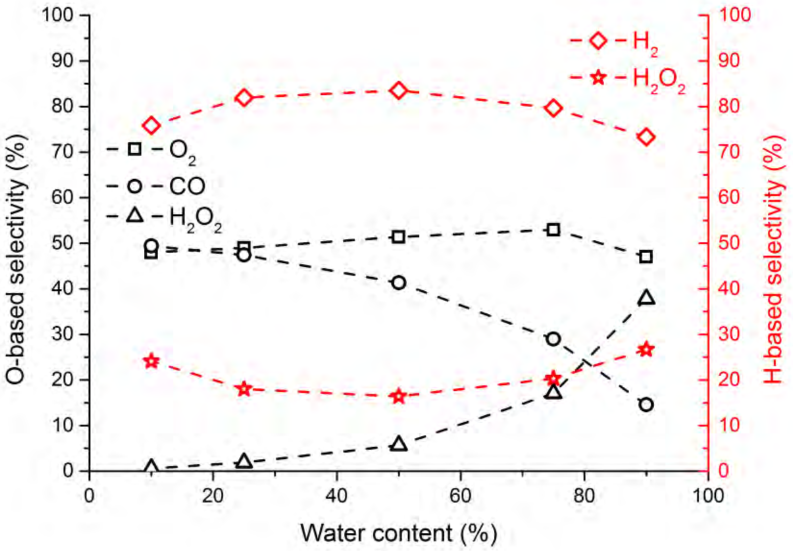

Figure 4-14. Calculated values of O-based (black symbols, left axis) and H-based (red symbols, right axis) selectivity of the major products as a function of water vapour content for a SEI value of 100 J/cm^3.

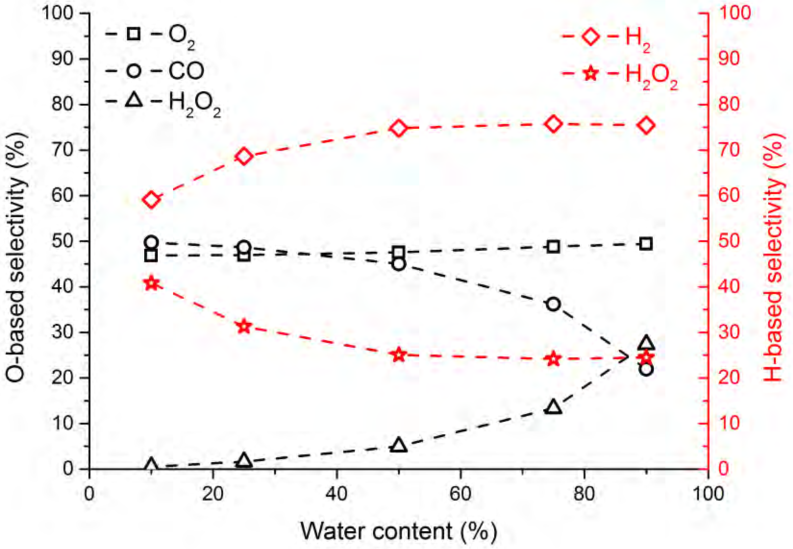

Figure 4-15. Calculated values of O-based (black symbols, left axis) and H-based (red symbols, right axis) selectivity of the major products as a function of water vapour content for a SEI value of 250 J/cm^3.

If we look to the results for an SEI of 25 J/cm^3 in **Figure 4-12**, the O-based selectivity indicates that upon increasing water content the O_2 selectivity increases slightly from 50 to 57 % when adding up to 50 % water and then decreases slightly again to 46 %. The CO selectivity, on the other hand, exhibits a continuous drop from 48 to 9 %, which is logical due to the lower CO_2 content in the gas mixture. This drop in CO selectivity is balanced by the H_2O_2 selectivity, which increases at the same time from 1 to 45 %, for water contents between 10 and 90 % and a SEI value of 25 J/cm^3, which is again logical. At the other SEI values investigated, a similar rise in H_2O_2 selectivity is observed, from 1 % (at 10 % water content) to 46 % (at 5 and 10 J/cm^3), to 43 % (at 50 J/cm^3), and to 38 % and 27 %, (at 100 and 250 J/cm^3, respectively) upon 90 % water addition (**Figure 4-10 to 4-15**). Combined with the conversions, this clearly demonstrates that significant yields of H_2O_2 can be formed at sufficiently high water vapour contents and SEI values.

The H-based selectivity for H_2O_2 also generally rises with increasing water content, although the effect is not so pronounced as for the O-based selectivity, with an initial drop from 9 to 8 % (up to 25 % water content), followed by a rise to 27 %, at a SEI of 25 J/cm^3 (see **Figure 4-12**). The reason that the effect is less pronounced is because the other product (H_2) also arises from the H_2O splitting. Indeed, the behaviour of the H-based selectivity towards H_2O_2 is mirrored by the selectivity towards H_2, which first increases from 91 to 92 %, followed by a drop to 73 %. At low water contents (10-50 %) the H_2O_2 selectivity increases with SEI, while at higher water contents (75-90 %) it is quite independent of the SEI. This leads to a slow shift from a continuously increasing trend upon higher water contents at 5 J/cm^3, to a parabolic trend at 50–100 J/cm^3, and even a decreasing trend as a function of water content at 250 J/cm^3, with the H_2 selectivity showing the opposite trends. This again indicates that the CO_2 chemistry shows the same behaviour as presented in the smaller range of conditions (see above), while the H_2O chemistry undergoes more drastic changes with increasing SEI, which will be discussed in more detail in the following section.

4.2.3. Underlying mechanism for the observed trends

The entire chemical behaviour leading to the (effective) CO_2 and H_2O conversions shown above can easily be explained with the chemistry outlined in Section 4.1.4. Indeed, from **Figure 4-8(b)** it became clear that the effective H_2O conversion increases with increasing water content, which is due to the growing importance of electron impact dissociation of H_2O into OH and H. The latter in turn results in a higher OH concentration, subsequently stimulating the H_2O_2 production (see reactions (11) and (12)). At the same time, however, the higher OH concentration will limit the absolute H_2O conversion at too high SEI values and water contents (see **Figure 4-7(b)**, through the recombination with H into H_2O (see reaction (6)). Moreover, it will also limit the absolute CO_2 conversion upon higher water contents, through the recombination with CO into CO_2 and H (see reaction (3)).

Increasing the SEI has almost the same effect as the higher water content, with the difference being that depending on the water content, the H_2O production and loss rates reach an equilibrium at high SEI values, as explained above, and the effective H_2O conversion reaches a plateau or even goes over a maximum at a certain SEI (see **Figure 4-8(b)** above). The reason that this occurs for H_2O and not for CO_2 can be deduced from the reaction scheme in **Figure 4-6**. CO_2 is split into CO and O, which will subsequently form O_2. From O_2 there is no "fast" pathway back to CO_2; it reaches a "stable end product" and thus, the CO_2 molecules that are converted into O_2 will not form CO_2 again. H_2O, on the other hand, is split into OH and H, which are both reactive products, and the "fastest" pathway for both is the recombination reaction back to H_2O. Hence, due to Le Chatelier's principle, upon increasing SEI, the CO_2 conversion will keep on rising, since its dissociation products (O in this case) react away, or are stable molecules (O_2 and O_3) that do not quickly react back to CO_2, and thus the overall reaction equilibrium favours the conversion. On the other hand, for H_2O, an equilibrium between conversion and formation will be reached at a certain point, explaining why the H_2O conversion reaches a maximum or saturation at a certain SEI value. Even the production of H_2O_2 cannot prevent this, since it is also easily split into OH radicals, leading again to the formation of H_2O.

As shown in **Figures 4-10 to 4-15**, the O-based product selectivities do not change much with changing conditions, since the CO_2 chemistry almost does not change. The shift in H-based selectivities can be explained based on the effective H_2O conversion. For low water contents (10–50 %), increasing the SEI leads to a saturation of the H_2O conversion. At this point, the concentration of OH radicals is very high and thus the reactions leading to H_2O_2 are stimulated and a rise in the H_2O_2 selectivity is observed. For high water contents, however, the saturation point is not reached for the investigated range, hence the H_2O_2 selectivity remains quite constant.

This is also obvious when looking at the H_2O_2 production pathway. The first pathway, through OH recombination (reaction (10)), remains dominant for all cases. However, upon decreasing SEI from 250 to 5 J/cm³, the second pathway, involving HO_2 recombination (reaction (13)), becomes gradually more important, with a relative contribution rising from 5 to 34 %, for a water content of 50 %. At the same time, this second pathway also becomes more important with increasing water content. Its relative contribution increases from 5 to 40 %, for water contents rising from 10 to 90 %, at an SEI of 50 J/cm³. This can be explained by reaction (28). Indeed, upon increasing water content, the amount of H_2O_2 increases, and as a result, its loss rate increases as well, leading to a higher HO_2 production through reaction (28), explaining why the second pathway, i.e., through HO_2 recombination, becomes more important for the formation of H_2O_2.

The higher syngas ratio with higher water content is of course a direct result of the increasing effective H_2O conversion and the decreasing CO_2 conversion upon adding more water. On the other hand, the lower syngas ratio upon rising SEI can be explained by the faster rise in the effective CO_2 conversion vs. the effective H_2O conversion, with the latter being explained due to the back reaction of water dissociation products.

4.3. Summary: potential and limitations of CO_2/H_2O plasma conversion

From the above reaction schemes and chemical kinetics analysis, we can draw a number of conclusions. The bad news is that CO_2 and H_2O seem to be unsuitable to create methanol (or other oxygenated hydrocarbons) in a one-step process by means of a DBD plasma. There are too many steps involved in generating CH_3OH in an efficient way, and all of them involve H atoms, which will in our case more quickly recombine with OH into H_2O or with O_2 into HO_2, which also reacts further with O into OH. This means that we would need to inhibit these two reactions (i.e. both with OH and with O_2). However, even then, the H atoms would more quickly recombine with O atoms into OH. The problem at hand is thus that the interactions of H atoms with oxygen species (either OH, O_3, O_2 or O atoms) are too fast and their tendency to form H_2O is too strong. This is of course not unexpected since water is one of the end products of total combustion. Although this fast reaction between H and O atoms has already been proven useful in other plasma-based applications (more specifically for O-trapping in the case of CO_2 conversion, providing a solution for the separation of the CO_2 splitting products),[73] here it plays against us.

On the other hand, our calculations do reveal that a CO_2/H_2O DBD plasma can deliver an easily controllable H_2/CO ratio with a rich hydrogen content, when sufficient amounts of water can be added to the CO_2 plasma. Hence, at first sight it appears suitable to create value-added chemicals, including methanol, in a two-step process, which is good news. However, our calculations also show that the interaction between H_2O and CO_2 dissociation products, i.e. the recombination between OH and CO into CO_2, and the recombination of H and OH into H_2O, limit the CO_2 and H_2O conversion, and thus the formation of useful products.

Besides syngas, the direct production of sufficient amounts of hydrogen peroxide, which can be used as a disinfectant or for biomedical purposes, seems possible. However, the formation rate of H_2O_2, is also partially limited by the destruction reaction of OH + H_2O_2 towards H_2O and HO_2. Therefore, again, the rapid removal of the formed product (i.e. H_2O_2), e.g., by means of a membrane, would be an important aspect for further improving this process.

Based on the reaction pathways outlined above, we believe that, in order to produce value-added chemicals, the plasma should be combined with a catalyst (so-called plasma-catalysis).[62,74] This catalyst should selectively let the plasma-generated CO and H_2 react into methanol and subsequently separate the methanol from the mixture. For example, Eliasson et al.[71] used a $CuO/ZnO/Al_2O_3$ catalyst in a CO_2/H_2 discharge, which led to an increase in methanol yield and selectivity by more than a factor 10. Several other reported catalysts used for the conversion of CO_2 with H_2 might also be interesting to investigate for their suitability in plasma-catalysis, such as Ni-zeolite catalysts for which methanation is reported,[75] a Rh_{10}/Se catalyst yielding an ethanol selectivity up to 83 %,[76] and a Ni-Ga catalyst for the conversion into methanol.[77] Furthermore, a lot of research into the catalytic CO_2 hydrogenation is showing promising results for $CuO/ZnO/ZrO_2$, Cu/ZnO-based catalysts promoted with Pd and Ga, Pd/ZnO and Pd/SiO_2 with the addition of Ga.[78] In general, multicomponent systems ($Cu/ZnO/ZrO_2/Al_2O_3/SiO_2$) have reported good performances for the formation of methanol starting from $CO/CO_2/H_2$ mixtures,[76] making them potentially very interesting for plasma-catalysis, since this is the in-situ generated mixture during plasma-based conversion, as demonstrated in our paper. The additional advantage is that adding a catalyst should also enhance the conversions, due to Le Chatelier‘s principle. However, it is important to realize that the catalyst affects the discharge and vice versa (see **Chapter 1**),[62,74] so it is recommended to use tailored catalysts for the plasma process rather than simply relying on classical catalysts. As explained in **Chapter 1** it is important to distinguish between physical and chemical effects when introducing a catalyst in a plasma. In this case we are mainly interested in improving the selectivity towards targeted (value-added) products, therefore the focus should be mainly on the chemical effects. This could be done by replacing the stainless steel inner electrode by another metal (e.g., Cu or Ni),[79] although care should be taken that the contact time between plasma species and catalyst is long enough. For this purpose, adding catalyst pellets in the entire reactor volume, like in a packed bed reactor, might be more suitable. Keeping the reaction scheme and reactive species as predicted by our model in mind, two pathways might be interesting and realistic to achieve: promoting the recombination of OH radicals to H_2O_2 or promoting the reduction of CO to methanol. In both cases the thermodynamic aspects at the nanoscale will become very important, especially since plasma catalysis is a far-from-equilibrium process.[74] The critical point will be the arrival and binding (e.g., physi- or chemisorption) of the reactants to the catalyst surface. To be successful, this process will have to be faster than the recombination rate of OH with H. Of course, these suggestions are only speculations, and further research will be needed to investigate this in practice.

Note, however, that we need to be cautious about the explosive mixture that might be formed during this process, due to the presence of O_2, together with CO, H_2 and an ignition source in such a set-up. At the research level this will probably never be a problem due to the low volumes and conversions. However, when going to a pilot or industrial scale, with larger volumes and conversions, the risk will increase significantly. Consequently, both the capital and operating costs will increase drastically to ensure safe operations. One way to circumvent this problem is by diluting this mixture with an inert gas, such as argon or helium. In this case, however, an additional separation (for the products) and recuperation (for the inert gas) step will need to be included, which will also increase the cost. Furthermore, part of the input energy will be lost due to the electron impact excitation and ionization of these gases. Therefore, this will reduce the energy efficiency and increase the operating cost, but it ensures safe operations.

Finally, the energy efficiency in a classical DBD reactor is quite limited, i.e. in the order of maximum 10 % for pure CO_2 splitting,[17] and it will be even lower in the CO_2/H_2O mixture, due to the lower conversion, as indicated in this study. This again limits the industrial applicability of CO_2/H_2O conversion in a DBD reactor. On the other hand, different plasma reactors, such as microwave or gliding arc plasmas, are characterized by higher energy efficiencies, i.e. in the order of 50 %, due to the importance of the CO_2 vibrational kinetics at these conditions.[22,42] Moreover, they operate at somewhat higher temperatures, i.e. in the order of 1000 K, which enables the addition of more H_2O. Nevertheless, it has been suggested[24,25] that H_2O might quench the vibrational levels of CO_2, thus reducing the good energy efficiency, characteristic for this type of plasma reactors.

5. Conclusions

The purpose of this work was to evaluate the viability of plasma technology for the combined conversion of CO_2 and H_2O into value-added products, by obtaining a better understanding of the plasma chemistry, based on a combined experimental and computational study. First a novel plasma chemistry set was developed, based on available data in literature. More importantly, this model was then used to identify and analyse the underlying plasma chemical kinetic behaviour, and this allowed us to evaluate whether the combined conversion of CO_2 and H_2O using plasma can become a viable route to produce value-added chemicals. We focused on the effects of the water content and SEI on the H_2O and CO_2 conversion as well as on the formation of products, such as H_2, CO, O_2, H_2O_2 and oxygenated hydrocarbons (i.e. methanol).

We demonstrated that adding a few % of water to a CO_2 plasma in a DBD leads to a steep drop in the CO_2 conversion, and when adding even more water, both the CO_2 and H_2O conversion keep decreasing slightly. Furthermore, as also observed in pure CO_2 and CO_2/CH_4 or CO_2/N_2 mixtures, both the CO_2 and H_2O conversion increase with increasing SEI, resulting from a lower flow rate (or higher residence time) or a higher power. The main products formed are CO, H_2 and O_2, as well as H_2O_2, up to 2 % for high SEI values and water contents.

A detailed kinetic analysis by our model indeed revealed (i) why the CO_2 conversion decreases upon adding water, (ii) why the H_2O conversion is limited, (iii) why no methanol (or other oxygenated hydrocarbons) formation was observed, and (iv) how H_2O_2 is formed. In general, the main reactive species created in the plasma are OH, CO, O and H. The OH radicals will quickly recombine with CO into CO_2, thereby limiting the CO_2 conversion upon addition of water, while the O and H atoms will undergo reactions to form H_2O again, explaining why the H_2O conversion is also limited. Furthermore, the fast reaction between O/OH and H atoms also explains why no oxygenated products are formed, because it occurs much faster than the possible pathways that might lead to oxygenates.

Since we can elucidate the underlying mechanisms of the limited CO_2 and H_2O conversion and the absence of methanol formation based on our kinetic analysis, this allows us to look for possible solutions to overcome these limitations. However, due to its inherent nature, this mixture seems unsuitable to directly produce methanol in a one-step process using a DBD plasma, unless a suitable catalyst can be found. Furthermore, although plasma technology would allow for a process with an easily steerable syngas ratio—even up to 8.6 according to the extended calculations—making it suitable for Fischer Tropsch synthesis and a two-step process for methanol synthesis, the presence of a highly flammable/explosive mixture makes it doubtful that plasma technology will be the most suitable process for the combined conversion of CO_2 and H_2O on a large industrial scale. One way to solve this problem is to dilute the gas mixture with inert gases, such as argon or helium. The downside, however, is that part of the energy input will be lost to excite and ionize these gases, and an additional separation and recuperation step will need to be added, thus leading to a significant drop in overall energy efficiency.

6. References

1 J. Barber, *Chem. Soc. Rev.*, 2009, **38**, 185–196.

2 E. E. Benson, C. P. Kubiak, A. J. Sathrum and J. M. Smieja, *Chem. Soc. Rev.*, 2009, **38**, 89–99.

3 M. Aresta, A. Dibenedetto and A. Angelini, *Chem. Rev.*, 2014, **114**, 1709–1742.

4 J. R. Scheffe and A. Steinfeld, *Mater. Today*, 2014, **17**, 341–348.

5 E. V. Kondratenko, G. Mul, J. Baltrusaitis, G. O. Larrazabal, J. Perez-Ramirez, G. O. Larrazábal and J. Pérez-Ramírez, *Energy Environ. Sci.*, 2013, **6**, 3112–3135.

6 A. H. McDaniel, E. C. Miller, D. Arifin, A. Ambrosini, E. N. Coker, R. O'Hayre, W. C. Chueh and J. Tong, *Energy Environ. Sci.*, 2013, **6**, 2424–2428.

7 J. Albo, M. Alvarez-Guerra, P. Castaño and A. Irabien, *Green Chem.*, 2015, **17**, 2304–2324.

8 A. Goeppert, M. Czaun, J.-P. Jones, G. K. Surya Prakash and G. A. Olah, *Chem. Soc. Rev.*, 2014, **43**, 7995–8048.

9 E. Linley, S. P. Denyer, G. McDonnell, C. Simons and J. Y. Maillard, *J. Antimicrob. Chemother.*, 2012, **67**, 1589–1596.

10 G. McDonnell, in *New Biocides Development*, 2007, pp. 292–308.

11 M. Finnegan, E. Linley, S. P. Denyer, G. McDonnell, C. Simons and J. Y. Maillard, *J. Antimicrob. Chemother.*, 2010, **65**, 2108–2115.

12 D. Dobrynin, G. Fridman, G. Friedman and A. Fridman, *New J. Phys.*, 2009, **11**, 115020.

13 J. Ehlbeck, U. Schnabel, M. Polak, J. Winter, T. von Woedtke, R. Brandenburg, T. von dem Hagen and K.-D. Weltmann, *J. Phys. D. Appl. Phys.*, 2011, **44**, 13002.

14 J. Winter, H. Tresp, M. U. Hammer, S. Iseni, S. Kupsch, a Schmidt-Bleker, K. Wende, M. Dünnbier, K. Masur, K.-D. Weltmann and S. Reuter, *J. Phys. D. Appl. Phys.*, 2014, **47**, 285401.

15 X. Lu, G. V. Naidis, M. Laroussi, S. Reuter, D. B. Graves and K. Ostrikov, *Phys. Rep.*, 2016, **630**, 1–84.

16 A. Bogaerts, T. Kozák, K. van Laer and R. Snoeckx, *Faraday Discuss.*, 2015, **183**, 217–232.

17 R. Aerts, W. Somers and A. Bogaerts, *ChemSusChem*, 2015, **8**, 702–716.

18 S. Heijkers, R. Snoeckx, T. Kozák, T. Silva, T. Godfroid, N. Britun, R. Snyders and

A. Bogaerts, *J. Phys. Chem. C*, 2015, **119**, 12815–12828.

19 T. Silva, N. Britun, T. Godfroid and R. Snyders, *Plasma Sources Sci. Technol.*, 2014, **23**, 25009.

20 A. P. H. Goede, W. A. Bongers, M. F. Graswinckel, R. M. C. M. Van De Sanden, M. Leins, J. Kopecki, A. Schulz and M. Walker, *EPJ Web Conf.*, 2014, **79**, 1005.

21 F. Brehmer, S. Welzel, R. M. C. M. Van De Sanden and R. Engeln, *J. Appl. Phys.*, 2014, **116**, 123303.

22 T. Kozák and A. Bogaerts, *Plasma Sources Sci. Technol.*, 2014, **23**, 45004.

23 L. F. Spencer and A. D. Gallimore, *Plasma Sources Sci. Technol.*, 2013, **22**, 15019.

24 A. Indarto, D. R. Yang, J.-W. Choi, H. Lee and H. K. Song, *J. Hazard. Mater.*, 2007, **146**, 309–15.

25 T. Nunnally, K. Gutsol, A. Rabinovich, A. Fridman, A. Gutsol and A. Kemoun, *J. Phys. D. Appl. Phys.*, 2011, **44**, 274009.

26 R. Snoeckx, Y. X. Zeng, X. Tu and A. Bogaerts, *RSC Adv.*, 2015, **5**, 29799–29808.

27 X. Tao, M. Bai, X. Li, H. Long, S. Shang, Y. Yin and X. Dai, *Prog. Energy Combust. Sci.*, 2011, **37**, 113–124.

28 G. Petitpas, J. Rollier, A. Darmon, J. Gonzalez-Aguilar, R. Metkemeijer and L. Fulcheri, *Int. J. Hydrogen Energy*, 2007, **32**, 2848–2867.

29 C. Liu, G. Xu and T. Wang, *Fuel Process. Technol.*, 1999, **58**, 119–134.

30 A. Janeco, N. R. Pinhao and V. Guerra, *J. Phys. Chem. C*, 2015, **119**, 109–120.

31 G. Scarduelli, G. Guella, D. Ascenzi and P. Tosi, *Plasma Process. Polym.*, 2011, **8**, 25–31.

32 Y. Zhang, Y. Li, Y. Wang, C. Liu and B. Eliasson, *Fuel Process. Technol.*, 2003, **83**, 101–109.

33 X. Zhang and M. S. Cha, *J. Phys. D. Appl. Phys.*, 2013, **46**, 415205.

34 L. M. Martini, G. Dilecce, G. Guella, A. Maranzana, G. Tonachini and P. Tosi, *Chem. Phys. Lett.*, 2014, **593**, 55–60.

35 D. Li, X. Li, M. Bai, X. Tao, S. Shang, X. Dai and Y. Yin, *Int. J. Hydrogen Energy*, 2009, **34**, 308–313.

36 B. Eliasson, C. Liu and U. Kogelschatz, *Ind. Eng. Chem. Res.*, 2000, **39**, 1221–1227.

37 V. J. Rico, J. L. Hueso, J. Cotrino and A. R. González-Elipe, *J. Phys. Chem. A*,

2010, **114**, 4009–4016.

38 X. Tu and J. C. Whitehead, *Appl. Catal. B Environ.*, 2012, **125**, 439–448.

39 Q. Wang, Y. Cheng and Y. Jin, *Catal. Today*, 2009, **148**, 275–282.

40 B. Fidalgo, A. Domínguez, J. Pis and J. Menéndez, *Int. J. Hydrogen Energy*, 2008, **33**, 4337–4344.

41 A. Ozkan, T. Dufour, G. Arnoult, P. De Keyzer, A. Bogaerts and F. Reniers, *J. CO2 Util.*, 2015, **9**, 78–81.

42 A. Fridman, *Plasma chemistry*, Cambridge University Press, New York, 2008.

43 P. Bruggeman and C. Leys, *J. Phys. D. Appl. Phys.*, 2009, **42**, 53001.

44 M. A. Malik, A. Ghaffar and S. A. Malik, *Plasma Sources Sci. Technol.*, 2001, **10**, 82–91.

45 P. Sunka, V. Babický, M. Clupek, P. Lukes, M. Simek, J. Schmidt and M. Cernák, *Plasma Sources Sci. Technol.*, 1999, **8**, 258–265.

46 B. R. Locke and S. M. Thagard, *Plasma Chem. Plasma Process.*, 2012, **32**, 875–917.

47 T. Ihara, M. Kiboku and Y. Iriyama, *Bull. Chem. Soc. Jpn.*, 1994, **67**, 312–314.

48 T. Ihara, T. Ouro, T. Ochiai, M. Kiboku and Y. Iriyama, *Bull. Chem. Soc. Jpn.*, 1996, **69**, 241–244.

49 S. Futamura and H. Kabashima, *Stud. Surf. Sci. Catal.*, 2004, **153**, 119–124.

50 S. Mahammadunnisa, E. L. Reddy, D. Ray, C. Subrahmanyam and J. C. Whitehead, *Int. J. Greenh. Gas Control*, 2013, **16**, 361–363.

51 N. Hayashi, T. Yamakawa and S. Baba, *Vacuum*, 2006, **80**, 1299–1304.

52 L. Guo, X. Ma, Y. Xia, X. Xiang and X. Wu, *Fuel*, 2015, **158**, 843–847.

53 G. Chen, T. Silva, V. Georgieva, T. Godfroid, N. Britun, R. Snyders and M. P. Delplancke-Ogletree, *Int. J. Hydrogen Energy*, 2015, **40**, 3789–3796.

54 R. Dorai and M. J. Kushner, *J. Phys. D. Appl. Phys.*, 2003, **36**, 1075–1083.

55 D. S. Stafford and M. J. Kushner, *J. Appl. Phys.*, 2004, **96**, 2451–2465.

56 R. Aerts, T. Martens and A. Bogaerts, *J. Phys. Chem. C*, 2012, **116**, 23257–23273.

57 W. Van Gaens and A. Bogaerts, *J. Phys. D. Appl. Phys.*, 2013, **46**, 275201.

58 S. Paulussen, B. Verheyde, X. Tu, C. De Bie, T. Martens, D. Petrovic, A.

Bogaerts and B. Sels, *Plasma Sources Sci. Technol.*, 2010, **19**, 34015.

59 A. Bogaerts, W. Wang, A. Berthelot and V. Guerra, *Plasma Sources Sci. Technol.*, 2016, **25**, 55016.

60 R. Snoeckx, R. Aerts, X. Tu and A. Bogaerts, *J. Phys. Chem. C*, 2013, **117**, 4957–4970.

61 P. L. Spath and D. C. Dayton, *Natl. Renew. Energy Lab.*, 2003, **December**, 1–160.

62 E. C. Neyts, K. Ostrikov, M. K. Sunkara and A. Bogaerts, *Chem. Rev.*, 2015, **115**, 13408–13446.

63 W. Bongers, H. Bouwmeester, B. Wolf, F. Peeters, S. Welzel, D. van den Bekerom, N. den Harder, A. Goede, M. Graswinckel, P. W. Groen, J. Kopecki, M. Leins, G. van Rooij, A. Schulz, M. Walker and R. van de Sanden, *Plasma Process. Polym.*, 2016, DOI 10.1002/ppap.201600126.

64 L. Koen Van and B. Annemie, *Plasma Sources Sci. Technol.*, 2016, **25**, 15002.

65 Q. Yu, M. Kong, T. Liu, J. Fei and X. Zheng, *Plasma Chem. Plasma Process.*, 2012, **32**, 153–163.

66 D. Mei, X. Zhu, Y.-L. He, J. D. Yan and X. Tu, *Plasma Sources Sci. Technol.*, 2014, **24**, 15011.

67 K. Van Laer and A. Bogaerts, *Energy Technol.*, 2015, **3**, 1038–1044.

68 R. Snoeckx, S. Heijkers, K. Van Wesenbeeck, S. Lenaerts and A. Bogaerts, *Energy Environ. Sci.*, 2016, **9**, 30–39.

69 N. R. Pinhão, a. Janeco and J. B. Branco, *Plasma Chem. Plasma Process.*, 2011, **31**, 427–439.

70 M. Ramakers, I. Michielsen, R. Aerts, V. Meynen and A. Bogaerts, *Plasma Process. Polym.*, 2015, **12**, 755–763.

71 B. Eliasson, U. Kogelschatz, B. Xue and L.-M. Zhou, *Ind. Eng. Chem. Res.*, 1998, **37**, 3350–3357.

72 R. Snoeckx, M. Setareh, R. Aerts, P. Simon, A. Maghari and A. Bogaerts, *Int. J. Hydrogen Energy*, 2013, **38**, 16098–16120.

73 R. Aerts, R. Snoeckx and A. Bogaerts, *Plasma Process. Polym.*, 2014, **11**, 985–992.

74 E. C. Neyts and K. Ostrikov, *Catal. Today*, 2015, **256**, 23–28.

75 E. Jwa, S. B. Lee, H. W. Lee and Y. S. Mok, *Fuel Process. Technol.*, 2013, **108**, 89–93.

76 G. Centi and S. Perathoner, *Catal. Today*, 2009, **148**, 191–205.

77 F. Studt, I. Sharafutdinov, F. Abild-Pedersen, C. F. Elkjær, J. S. Hummelshøj, S. Dahl, I. Chorkendorff and J. K. Nørskov, *Nat. Chem.*, 2014, **6**, 320–324.

78 S. G. Jadhav, P. D. Vaidya, B. M. Bhanage and J. B. Joshi, *Chem. Eng. Res. Des.*, 2014, **92**, 2557–2567.

79 M. Scapinello, L. M. Martini and P. Tosi, *Plasma Process. Polym.*, 2014, **11**, 624–628.

CHAPTER 5

N_2 influence on CO_2 and CH_4 conversion :

First steps towards realistic gas mixtures

This chapter is published as:

- R Snoeckx, M Setareh, R Aerts, P Simon, A Maghari and A Bogaerts, Influence of N_2 concentration in a CH_4/N_2 dielectric barrier discharge used for CH4 conversion into H_2, International Journal of Hydrogen Energy 38 (2013) 16098-16120 (23p).
- R Snoeckx, S Heijkers, K Van Wesenbeeck, S Lenaerts and A Bogaerts, CO_2 conversion in a dielectric barrier discharge plasma: N_2 in the mix as helping hand or problematic impurity? Energy & Environmental Science 9 (2016) 999-1011 (13p).

1. Aim of the work

Most research studies focus on “clean” gas flows, while in reality most gas flows contain impurities, for which it is often economically unfeasible to be further purified. In most cases nitrogen is the main impurity.[1] Therefore, it is of the uttermost importance to study the effect of N_2 impurities on the plasma chemistry. The questions that come to mind are: how do these impurities affect the conversion and energy efficiency, and more importantly, which by-products (useful or harmful compounds) would be formed. This allows to find out whether pre- or post-purification steps would be needed and which one is to be preferred.

In section 2 we will first take a look at the effect of N_2 on a CH_4 plasma. Natural gas is a mixture of several hydrocarbons belonging to the paraffin series (at least 95 %) and non-hydrocarbon gases such as nitrogen (up to 5 %), carbon dioxide and hydrogen sulphide. Methane is the principal component (between 70 and 90 %) of most natural gas reserves.[2] The composition of natural gas varies significantly depending on the geographical source, time of year, and treatments applied during production or transportation.[3] In many respects methane is an attractive fuel for heating and electrical power generation. However, this makes methane an underutilized source for the production of valuable and useful chemicals and liquid fuels, such as hydrogen gas, higher hydrocarbons, syngas (a mixture of CO and H_2), methanol (CH_3OH) and formaldehyde (CH_2O). In section 2 we thus focus on the conversion of methane by means of a non-thermal DBD. More specifically, we will investigate the effect of N_2 on the CH_4 conversion and H_2 yield, both in the ppm range, as N_2 is typically present as impurity in natural gas, as well as in the % range (1–99 %), to investigate whether nitrogenated compounds can be formed, which could be of interest for the chemical industry.

Plasmas produced in N_2-hydrocarbon gas mixtures and the resulting chemical reactions between the various plasma species have attracted the attention of several researchers.[4–12] This is the result of various applications under study, such as cleaning of polluted air streams, plasma assisted ignition and combustion, nitrocarburizing, production of hydrogen and higher order hydrocarbon molecules and studying the atmospheric chemistry of Titan. Furthermore, a mixture with N_2 also offers more stable plasma conditions, as reported in literature.[9] In our own experiments, we also observed the discharge to be more homogenous and we were able to ignite it at lower power inputs. Especially, the influence of N_2 on the plasma chemistry and discharge characteristics is being studied,[5,7–10] since the metastable states of N_2 play an important role in the dissociation of hydrocarbon molecules.[4–6,9,13]

We present a combined study of experiments and computer simulations to investigate the CH_4 conversion and resulting product yields, i.e. with focus on H_2, for several

CH_4/N_2 mixtures in a DBD set-up. Furthermore, by means of a kinetic analysis, based on the simulation results, we will elucidate the role of various plasma species, and especially of the N_2 metastable states, in the CH_4 conversion process. As mentioned above, both the effect of N_2 impurities (1 to 50,000 ppm) in a CH_4 discharge, as well as a CH_4/N_2 discharge with N_2 content ranging from 1 to 99 %, will be studied.

In section 3 we continue with investigating the influence of N_2 on a CO_2 plasma. This is crucial, since its presence influences the plasma properties as well as the chemical pathways and thus the chemicals formed, which can have detrimental effects on air quality and human health, for example NO_X. However, from another point of view if N_2O and other NO_x compounds are produced, it is important to know whether maybe high enough concentrations might be obtained, to be considered relevant for nitrogen fixation.[14]

To provide answers to these important questions, we have performed experiments, supported by chemical reaction simulations, to increase the general understanding of the underlying mechanisms and pathways. We focus again on a DBD as it has a very simple design and operates at atmospheric pressure, which is beneficial for up-scaling for industrial applications.[15] Again, both the effect of N_2 as impurity (1 to 10 %) as well as the effect of N_2 as admixture or as dilutant (10 to 98 %) was studied. To our knowledge, only a few papers have reported on the effect of N_2 on CO_2 conversion, and only for a GA[16] and MW plasma,[17,18] while no papers have addressed the second question, i.e. which by-products are formed in the mix and what are their consequences. The influence of N_2 on the CO_2 conversion as well as the NO_x production pathways are revealed for the first time, and the observed trends are explained, based on a kinetic analysis of the reaction chemistry.

2. $CH_4 + N_2$

2.1. Description of the chemical model

2.1.1. 0D chemical kinetics model

We use again the 0D kinetic model, called Global_kin,[19,20] and more details about this model can be found in the work of Kushner et al.[19,20] and in Chapter 2, Section 2.

For the experiments an applied frequency of 23.5 kHz is used and a residence time of 2.2 s, as calculated from the gas flow rate and the length of the reactor. To mimic these conditions, we again simulated triangular micro-discharge pulses of 30 ns, with a repetition frequency of 0.47 kHz, assuming that each molecule passes through only one micro-discharge every 100 half cycles (see detailed discussion in **Chapter 2 and 3**).[21] Furthermore, the maximum power deposition per pulse is defined in such a way that the total specific energy input (SEI) corresponds to the experimental values (i.e. in the order of 6 $J{\cdot}cm^{-3}$; see below).

Figure 5-1 illustrates the calculated electron density (N_e) and electron temperature (T_e) for one pulse as a function of time. The calculated maximum E_0/n is in the order of 200 Td. This results in a maximum N_e of ~$5.5\cdot10^{13}$ cm^{-3} and a maximum T_e of ~3 eV during the pulse. At the start of the pulse, T_e reaches its maximum of ~3 eV, as the electrons are heated by the electric field, whereas upon pulse termination, T_e drops significantly. N_e on the other hand increases with time during the pulse and reaches its maximum of 5.5×10^{13} cm^{-3} at the end of the pulse, as shown in **Figure 5-1**. This is logical, as the power leads to the electron heating and subsequently it gives rise to electron impact ionization, creating electrons during the pulse. However, the electron density decays very slowly upon termination of the pulse, indicating low recombination rates and/or the fact that electrons might still be created in the early afterglow by heavy particle reactions. For all investigated CH_4/N_2 mixtures the maximum T_e was around ~3 eV, while the maximum N_e was in the order of 10^{12}–10^{14}, which are typical conditions for a DBD.[22,23]

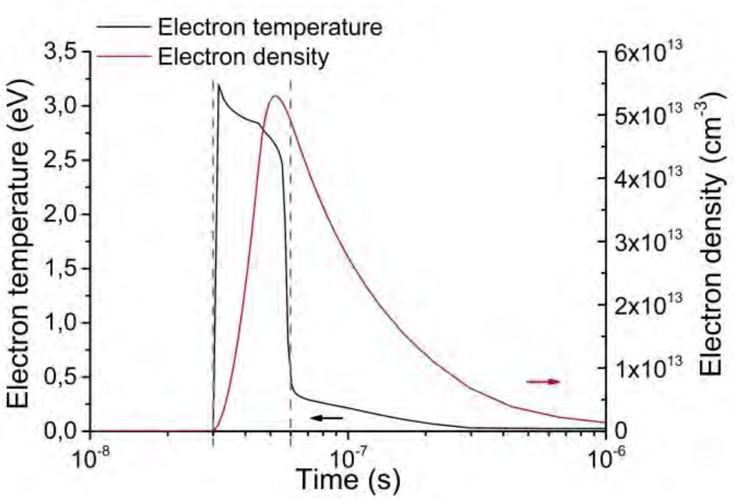

Figure 5-1. Calculated electron density (red line, right axis) and electron temperature (black line, left axis) during one triangular discharge pulse of 30 ns for a 95:5 CH_4/N_2 mixture. The grey dashed lines indicate the start and the end of the micro discharge pulse.

2.1.2. Plasma chemistry included in the model

The plasma chemistry used in the model is based on several chemistry sets. The hydrocarbon chemistry was developed in Chapter 3,[21] and the N_2 chemistry was adopted from Van Gaens et al.[24] Finally, these reactions were expanded with hydrocarbon-N_2 coupling reactions from literature.[5,10,25] The model considers 68 different species, including the electrons, various molecules, radicals, ions and excited species. Two types of (electronically excited) metastable N_2 species are included in the model, i.e. $N_2(A^3\,\Sigma_u^+)$ and $N_2(a'^1\,\Sigma_u^-)$. All these species are listed in **Table 5-1**. They react with each other in 598 reactions: 194 electron impact reactions, 194 ion reactions and 210 neutral reactions, which are listed in Appendix III, together with the corresponding rate coefficients and the references where these data are adopted from.

The carbon balance in the experiments, dropped from 97 % to 89 % upon rising N_2 concentration from 1 % to 87 %, which is in agreement with the "visual" observation that more soot/polymer was deposited on the reactor walls when increasing the N_2 content. In the simulations, carbon formation reactions are also included, but as the model is zero-dimensional, it is not possible to predict the carbon balance in an accurate way, because carbon formation and especially diffusion/deposition/accumulation appears to be most important on the reactor walls, which needs at least a one-dimensional model.

Table 5-1. List of species included in the model for the CH_4/N_2 gas mixture.

Molecules	**Charged species**	**Radicals**	**Excited species**
CH_4	CH_5^+, CH_4^+, CH_3^+, CH_2^+, CH^+, C^+	CH_3, CH_2, CH, C	
C_2H_6, C_2H_4, C_2H_2	$C_2H_6^+$, $C_2H_5^+$, $C_2H_4^+$, $C_2H_3^+$, $C_2H_2^+$, C_2H^+, C_2^+	C_2H_5, C_2H_3, C_2H, C_2	
C_3H_8, C_3H_6		C_3H_7, C_3H_5	
C_4H_2			
H_2	H_3^+, H_2^+, H^+, H^-	H	$H_2(R)$, $H_2(V)$, H_2^*, H^*
N_2	N_4^+, N_3^+, N_2^+, N^+	N	$N_2(R)$, $N_2(V)$, $N_2(A^3\,\Sigma_u^+)$, $N_2(a'^1\,\Sigma_u^-)$, N^*
HCN	HCN^+	H_2CN, CN	
NH_3	NH_4^+, NH_3^+, NH_2^+, NH^+	NH_2, NH	NH_3^*
N_2H_4, N_2H_2		N_2H_3, N_2H	
	electrons		

2.2. Description of the experiments

A schematic diagram of the experimental set-up, as well as a more detailed description, was given in **Chapter 2** (Figure 2-4). The length of the discharge region is 90 mm and the discharge gap is fixed at 1.5 mm, resulting in a discharge volume of 21.9 cm^3. CH_4 and N_2 are used as feed gases with a constant total flow rate of 605 mL min^{-1} and N_2 content of 1, 10, 19, 29, 39, 48, 58, 67, 77 and 87 %, controlled with mass flow controllers (Bronkhorst).

The feed and product gases are analysed by a three-channel compact-gas chromatograph (CGC) (Interscience), equipped with two thermal conductivity detectors (TCD) and a flame ionization detector (FID). The first TCD channel contains a Molecular Sieve 5A column for the segregation of H_2, CH_4 and N_2, while the second TCD channel is equipped with a Rt-Q-BOND column for the measurement of C_2-C_4 hydrocarbons and nitrogen containing compounds. The FID is equipped with a Rtx-5 column for the measurement of C_1-C_{10} and nitrogen containing compounds. It should be noted that there is also some soot and polymer deposition on the reactor walls so that the carbon and hydrogen balance is not completely 100 %.

2.3. Results and discussion

2.3.1. Effect of N_2 as impurity on CH_4 conversion and H_2 yield

As mentioned above, there are always impurities present in natural gas, of which N_2 is the most important one, and these can influence the plasma chemistry and thus the conversion of CH_4 as well as the product yields. Therefore, the influence of N_2 as impurity in the range of 1–50,000 ppm on a CH_4 plasma is computationally investigated in this section. In **Figure 5-2**, the calculated conversion of CH_4 (eq.2-8) and the yield of H_2 (eq.2-24) are plotted versus the N_2 concentration, for a residence time of 2.2 s and a SEI of 6 $J\cdot cm^{-3}$. The results indicate that the conversion decreases slightly from 3.4 % to 2.9 % (equals -15 %) upon increase of the N_2 impurity. This decreasing trend is the result of the decreasing electron density, as will be discussed more thoroughly below. The H_2 yield shows the same decreasing trend from 2.1 % to 1.8 % (equals -17 %) upon increase of the N_2 impurity. This is logical since the H_2 yield is related to the CH_4 conversion, which is the only source of H atoms. The most abundant N containing reaction product is hydrogen cyanide (HCN), however, its density is three orders of magnitude lower than the N_2 concentration. Thus, this indicates that N_2 does almost not chemically react in the plasma under study, and the N_2 impurities only have a small indirect (i.e. electron density) influence on the conversion of CH_4 and the yield of H_2 and do not result in a significant production of nitrogen containing species.

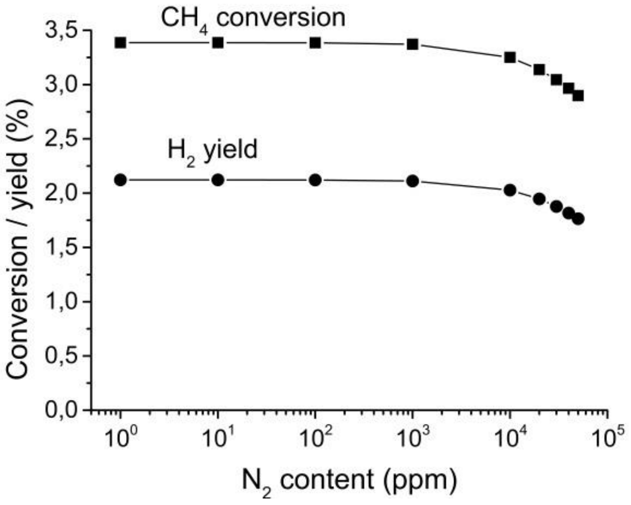

Figure 5-2. Calculated CH_4 conversion and H_2 yield as a function of N_2 content (ppm) for a residence time of 2.2 s and a SEI of 6 J·cm^{-3}.

2.3.2. Effect of N_2 as additive gas

a) Effect on CH_4 conversion and product yields

Aside from studying the effect of N_2 as an impurity, it is also interesting to study the effect of N_2 as additive gas. The purpose is not only to study the effect on the conversion of CH_4 and the yield of H_2, but also to investigate whether nitrogenated compounds could be formed, which could be of interest as a feedstock for the chemical industry. Therefore, we performed both experiments and simulations for different mixtures of CH_4/N_2. We carried out experiments with a N_2 content of 1, 10, 19, 29, 39, 48, 58, 67, 77 and 87 %. The same N_2 contents were also investigated in the simulations, as well as all (other) values in the range of 1 to 99 % with a 2.5 % interval. These simulations were performed for exactly the same operating conditions as in the experiments, i.e. a residence time of 2.2 s, a SEI of 6 J·cm^{-3}, a gas temperature of 300 K and atmospheric pressure for all mixing ratios.

The calculated and measured values for the conversion of CH_4 are plotted *vs* N_2 content in **Figure 5-3**. **Figure 5-3(a)** shows the results for the N_2 content in the entire range from 1 to 99 %, while **Figure 5-3(b)** presents the more detailed results for a N_2 content ranging only till 88 %. It is clear that excellent agreement is reached between calculated and measured results.

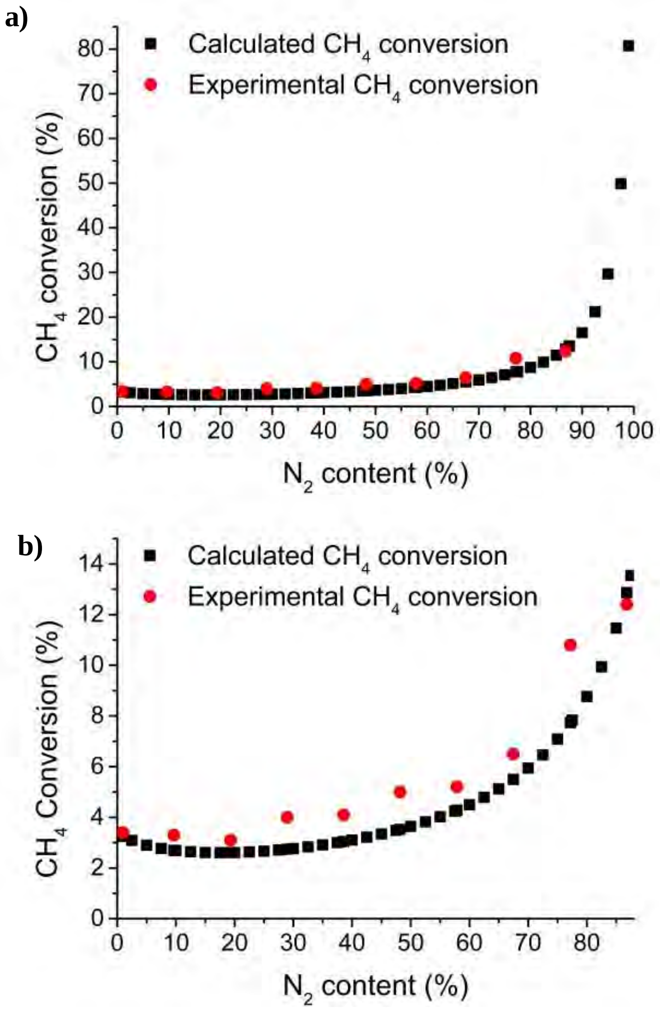

Figure 5-3. Calculated and experimental values of CH_4 conversion as a function of N_2 content in the entire range from 1 to 99 % (a), and more detailed comparison from 1 to 88 % (b), for a residence time of 2.2 s and a SEI of 6 $J\cdot cm^{-3}$.

From the simulation results in **Figure 5-3(a)** it appears that the CH_4 conversion is increasing exponentially with increasing N_2 content, however, if we take a closer look to **Figure 5-3(b)**, we notice that for low N_2 content the conversion slightly decreases first, as was also observed in the ppm range (see previous section). Indeed, the calculated conversion decreases slightly from 3.4 % to 2.6 % for a N_2 content ranging from 0 to 17.5 %. Subsequently, it starts increasing slightly, reaching 3.4 % again for a N_2 content of 45 %. It continues increasing and for a N_2 content above ~70 % the increasing trend starts to become more significant. This trend is the result of the interplay of several effects, i.e. the decreasing electron density with increasing N_2 content, the lower reaction rate constants for several three-body reactions with N_2

compared to CH_4 as third body, and the increasing role of the N_2 metastable states with increasing N_2 content. These effects will be discussed more thoroughly below.

Although the absolute conversion increases with rising N_2 content, it does not compensate for the inherent drop of CH_4 content in the mixture, resulting in a lower effective CH_4 conversion (eq.2-9), as shown in **Figure 5-4**.

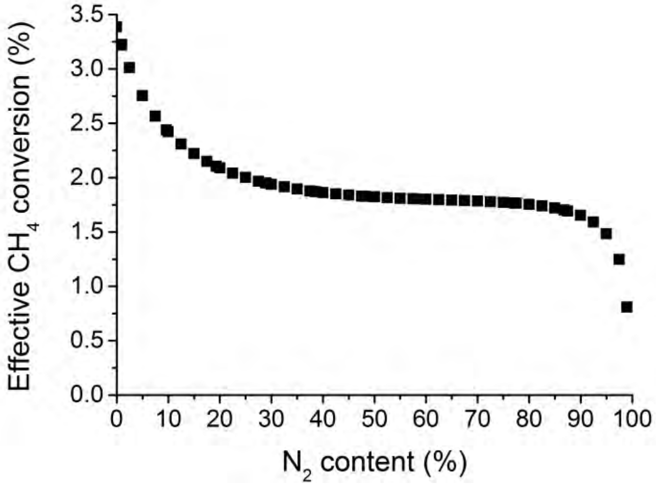

Figure 5-4. Calculated effective CH_4 conversion as a function of N_2 content, for a residence time of 2.2 s and a SEI of 6 J·cm^{-3}.

It is clear that the CH_4 conversion obtained both in the experiments and calculations is in the order of several %, increasing only to 80 % for very high N_2 contents. This reflects the high stability of the CH_4 molecule. Note that these values are in agreement with experimental results, at least for pure CH_4 conversion in a DBD.[26–28]

The calculated and measured values for the H_2 yield are presented in **Figure 5-5**. Again, **Figure 5-5(a)** shows the results for a N_2 content ranging from 1 to 99 %, while **Figure 5-5(b)** presents the results in more detail for a N_2 content up to 88 %. We only present the yields of H_2, since it is the most important reaction product. Its density is almost one order of magnitude higher than the second most import reaction product (i.e. C_2H_6); other hydrocarbons detected with the GC are C_2H_2, C_2H_4, C_3H_x and C_4H_y, but they have an even lower density. The H_2 selectivity is calculated to be around 40–60 % for all CH_4/N_2 gas mixing ratios investigated. This means that for every mole CH_4 converted one mole H_2 is produced; the remaining H atoms are “lost” in the formation of higher hydrocarbons.

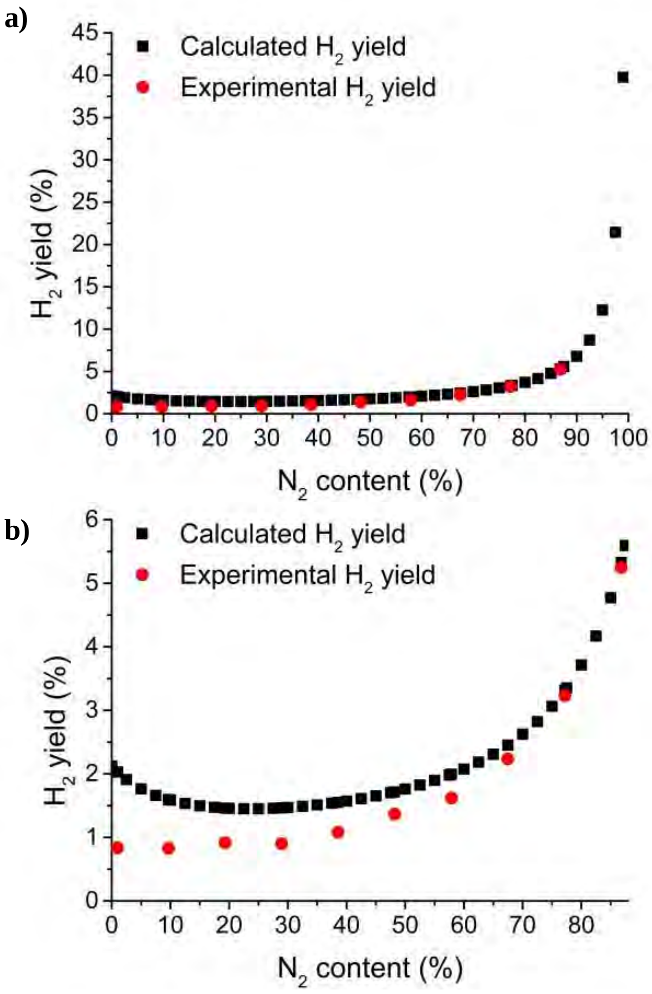

Figure 5-5. Calculated and experimental H_2 yield as a function of N_2 content in the entire range from 1 to 99 % (a), and more detailed comparison from 1 to 88 % (b), for a residence time of 2.2 s and a SEI of 6 J·cm^{-3}.

The H_2 yield is in the order of 1–2 % up to 50 % N_2 content, and increases to 40 % at a N_2 content of 99 %. These values are again in agreement with literature results, at least for pure CH_4 conversion in a DBD.[26–28] Moreover, the H_2 yield shows the same trend upon increasing N_2 content as the CH_4 conversion, as was also observed in the previous section, since CH_4 is the main source of H atoms. The somewhat lower experimental values for the H_2 yield are probably attributed to polymerization on the reactor walls, a phenomenon which is also observed in Horvath et al.[7] Indeed a same polymer like deposition (which is not accounted for in the simulations) was visible in our set-up, resulting in a loss in the hydrogen and carbon balance after reaction. This can explain the difference between the calculated and experimental values. Furthermore, it should also be mentioned that determining the H_2 selectivity, and thus by extension the H_2 yield, with gas chromatography is quite challenging. However, overall, a satisfactory agreement between calculations and experiments is reached.

Again, the higher yield upon increasing N_2 content does not compensate for the inherent drop of CH_4 content in the mixture, resulting in a lower effective H_2 yield upon increasing N_2 content, as shown in **Figure 5-6**.

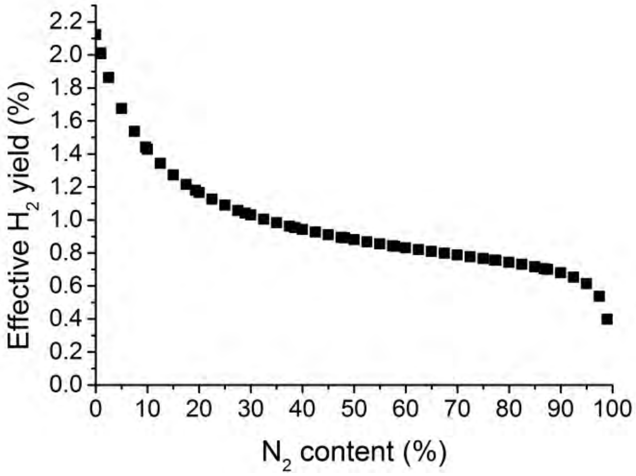

Figure 5-6. Calculated effective H_2 yield as a function of N_2 content, for a residence time of 2.2 s and a SEI of 6 J·cm^{-3}.

Figure 5-7 illustrates the calculated number densities of the main components present (or formed) in the plasma. CH_4, N_2 and H_2 have the highest density, as expected. The CH_4 density drops whereas the N_2 density rises with increasing N_2 content, as is logical. The H_2 density is around one order of magnitude lower than the CH_4 density, which is like expected from the conversion values (in the order of a few %) seen in **Figure 5-3** above. Only at high N_2 contents (i.e. above 90 %), the H_2 density becomes larger than the CH_4 density, which corresponds to the high conversion, illustrated in **Figure 5-3** above. The densities of the higher hydrocarbon molecules (grouped as C_2H_x and C_3H_y) are at least an order of magnitude lower than the H_2 density.

As mentioned above, one of the reasons why we are interested in studying the effect of higher N_2 contents in the gas mixture is because of the possibility of forming N-containing products, which can be of interest for the chemical industry. The simulations indicate that some N-containing species are formed, such as HCN and NH_3, and that their densities increase with rising N_2 content, as shown in **Figure 5-7**. However, their densities are always several orders of magnitude lower than the N_2 density. The most abundant N-containing species is HCN, which increases from 6x10^{14}

cm^{-3} (i.e. 25 ppm with respect to the density corresponding to atmospheric pressure) at 1 % N_2, to 2.4x10^{16} cm^{-3} (i.e., 1000 ppm) at 99 % N_2 content. NH_3 is still of lower importance, with a density around 10^{9} cm^{-3}, or a concentration in the order of only 0.1 ppb. This is in qualitative agreement with our experiments, since no N-containing species were detected. It should be mentioned that the production of HCN and NH_3 in CH_4/N_2 mixtures was reported for packed bed DBD and other discharges in literature,[29–34] and it was mainly attributed to ionization of N_2 molecules. However, the latter process occurs at higher electron energy than is reached for our operating conditions, explaining why our calculations predict only negligible amounts of HCN and NH_3 formed.

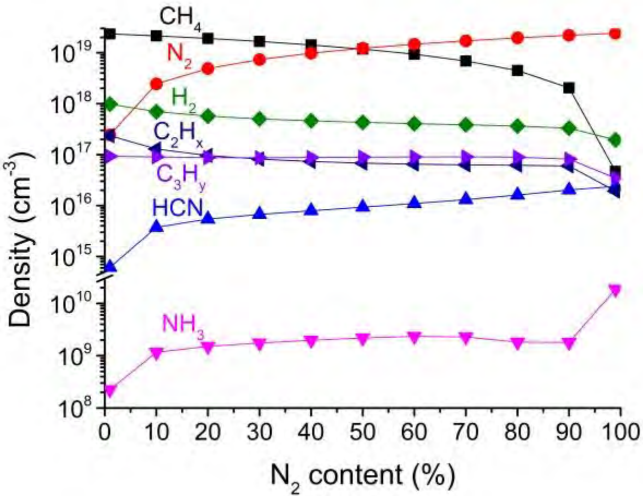

Figure 5-7. Calculated density of CH_4, N_2, H_2, C_2H_x, C_3H_y, HCN and NH_3 as a function of N_2 content (%) for a residence time of 2.2 s and a SEI of 6 J·cm^{-3}.

As the calculated and experimental results for the CH_4 conversion and the H_2 yield are in good agreement in the entire range of CH_4/N_2 gas mixing ratios (see **Figure 5-3** and **Figure 5-5**), the plasma chemistry in the model can be used to describe and explain the observed trends, as will be done in the next two sections.

b) Effect on the electron density

To explain the effect of the N_2 content on the CH_4 conversion, we should first take a look at the effect of the N_2 content on the electron density. The maximum electron density for each CH_4/N_2 mixture is illustrated in **Figure 5-8**.

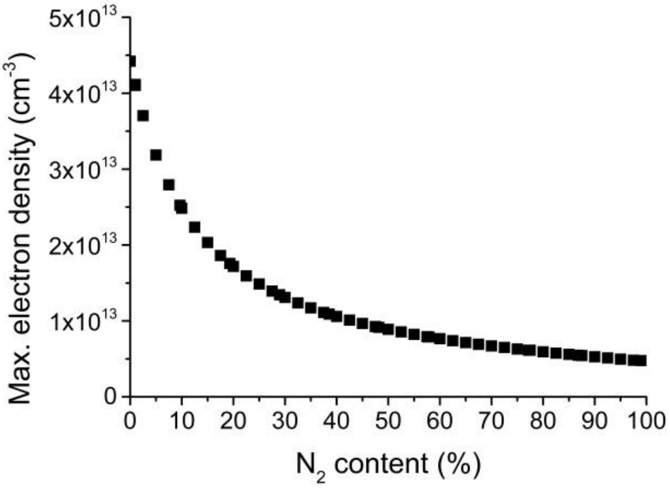

Figure 5-8. Calculated maximum electron density as a function of N_2 content (ranging from 1 to 99 %) for a residence time of 2.2 s and a SEI of 6 J·cm^{-3}.

The maximum electron density drops significantly upon increasing the N_2 content: it decreases almost exponentially from 4.1×10^{13} cm^{-3} at 1 % N_2 content to 4.8×10^{12} cm^{-3} at 99 % N_2 content. This is explained by the lower electron production rate, which is dependent on electron impact ionization reactions. The most important electron production reactions are:

$$e^- + CH_4 \rightarrow CH_4^+ + 2e^- \quad (1)$$

$$e^- + CH_4 \rightarrow CH_3^+ + H + 2e^- \quad (2)$$

$$e^- + N_2 \rightarrow N_2^+ + 2e^- \quad (3)$$

For a N_2 content up to ~88 %, reactions 1 and 2 are the main contributors for electron production, whereas reaction 3 becomes the dominant electron production process for N_2 contents above 88 %. As the ionization potential of N_2 (i.e. 15.6 eV for reaction 3) is higher than for CH_4 (i.e., 12.6 eV and 14.3 eV for reactions 1 and 2), the electron production by electron impact ionization of N_2 is less efficient than by electron impact ionization of CH_4, explaining the lower electron production rate upon increasing N_2 content.

c) *Kinetic analysis*

As illustrated in **Figure 5-3** and **Figure 5-5**, the CH_4 conversion and H_2 yield increase with increasing N_2 content, and this is attributed to collisions of CH_4 with singlet and triplet N_2 metastable states (i.e. $N_2(a'^1\Sigma_u^-)$ and $N_2(A^3\Sigma_u^+)$), as will be shown below.

Therefore, it is interesting to start our kinetic analysis with looking at the production and loss processes of these N_2 metastable states.

The densities of the two N_2 metastable states included in the model, i.e. the singlet $N_2(\boldsymbol{a'^1\,\Sigma_u^-})$ and triplet $N_2(\boldsymbol{A^3\,\Sigma_u^+})$) states, are plotted in **Figure 5-9**, during one pulse and afterglow for a N_2 content of 50 % and a SEI of 6 J·cm^{-3}. It is clear that their densities, at the maximum of their profile, are several orders of magnitude lower than the N_2 ground state density, as shown in **Figure 5-7**. The triplet $N_2(\boldsymbol{A^3\,\Sigma_u^+})$) state has the highest density (which is three orders of magnitude lower than the N_2 ground state density) and it occurs during the pulse and afterglow, while the singlet $N_2(\boldsymbol{a'^1\,\Sigma_u^-})$ state has a density which is still three orders of magnitude lower, and it only occurs during the pulse. These trends will be explained below based on the reaction rates.

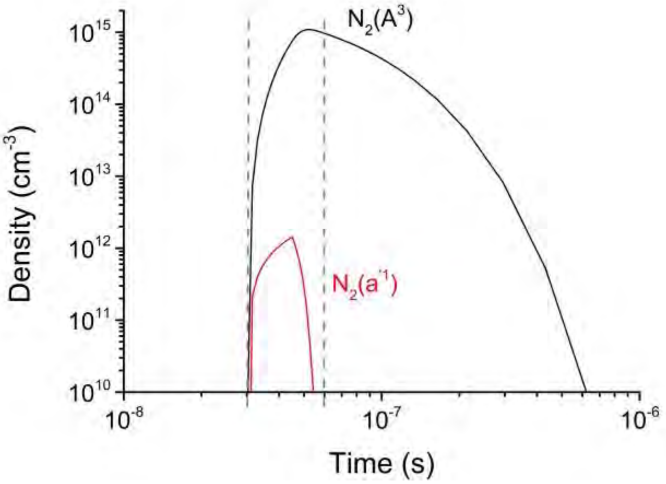

Figure 5-9. Calculated density of the $N_2(\boldsymbol{a'^1\,\Sigma_u^-})$ and $N_2(\boldsymbol{A^3\,\Sigma_u^+})$ states during one pulse and afterglow for a N_2 content of 50 % and a SEI of 6 J·cm^{-3}. The grey dashed lines indicate the start and the end of the micro discharge pulse.

The production of $N_2(a'^1\,\Sigma_u^-)$ and $N_2(A^3\,\Sigma_u^+)$ takes place during the discharge pulse and is caused by electron impact excitation:

$$e^- + N_2 \rightarrow e^- + N_2(a'^1\,\Sigma_u^-) \quad (4)$$

$$e^- + N_2 \rightarrow e^- + N_2(A^3\,\Sigma_u^+) \quad (5)$$

The production rate of these metastable states increases with increasing N_2 content, which is logical. Furthermore, the production rate of the triplet state is found to be one order of magnitude higher than for the singlet state, due to the lower excitation threshold, i.e. 6.17 eV for the triplet state compared to 8.4 eV for the singlet state.[6]

For the singlet state, the most important loss channels are the Penning dissociation reactions with CH_4, which only take place during the pulse:

$$N_2(a'^1\Sigma_u^-) + CH_4 \rightarrow CH_3 + H + N_2 \quad (6)$$

$$N_2(a'^1\Sigma_u^-) + CH_4 \rightarrow C + 2\,H_2 + N_2 \quad (7)$$

For the triplet state, the most important loss channel is the quenching reaction with H_2, followed by the Penning dissociation reaction with CH_4:

$$N_2\,(A^3\Sigma_u^+) + H_2 \rightarrow H_2 + N_2 \quad (8)$$

$$N_2\,(A^3\Sigma_u^+) + CH_4 \rightarrow CH_3 + H + N_2 \quad (9)$$

The quenching reaction takes place during the pulse as well as during the afterglow. For low N_2 contents, the quenching during the pulse appears to be dominant, but with increasing N_2 content, quenching in the afterglow becomes more important. Indeed, a higher N_2 content results in a higher density of the metastable triplet state, and a lower CH_4 and hence also lower H_2 density. As a result, not all the metastable states are quenched during the pulse, so the quenching continues in the afterglow and the latter becomes more and more important with increasing N_2 content.

Overall, the singlet state is found to be quenched more significantly than the triplet state, in agreement with literature.[6] The combination of higher production rate for the triplet state and higher quenching rate of the singlet state, explains why the triplet state has a higher density than the singlet state, as is indeed apparent from **Figure 5-9** above.

As the triplet state has a higher density than the singlet state, it will be the more important for the conversion of CH_4. On the other hand, the singlet state appears to be more important for the production of H_2, as will be shown below. This is explained because the triplet state is mainly quenched by H_2, and dissociation of CH_4 into CH_3 and H (i.e. reaction 9 above), whereas the singlet state is also quenched by the decomposition of CH_4 into C and 2 H_2 molecules (i.e. reaction 7 above). The reason that this decomposition can occur with the singlet state and not with the triplet state is the higher energy content of the former (as explained at the beginning of this section).

In order to better understand the influence of the N_2 content on the CH_4 conversion, we investigated the dominant reaction pathways for the loss and formation of CH_4 for several N_2 contents (i.e., 1, 10, 20, 30, 40, 50, 60, 70, 80, 90 and 99 %). This kinetic analysis was performed by looking at the time integrated rates of the various processes during the pulse(s), the afterglow(s), as well as for the total time of 2.2 s, including many pulses and afterglows.

Table 5-2. Overview of the most important loss and formation reactions for CH_4.

Loss processes		**Formation processes**	
L1	$e^- + CH_4 \rightarrow e^- + CH_3 + H$	F1	$CH_3 + H + CH_4 \rightarrow CH_4 + CH_4$
L2	$e^- + CH_4 \rightarrow e^- + CH_2 + H_2$	F2	$CH_3 + H + N_2 \rightarrow CH_4 + N_2$
L3	$N_2(A^3\,\Sigma_u^+) + CH_4 \rightarrow N_2 + CH_3 + H$	F3	$e^- + C_3H_8 \rightarrow CH_4 + C_2H_4 + e^-$
L4	$N_2(a'^1\,\Sigma_u^-) + CH_4 \rightarrow N_2 + CH_3 + H$	F4	$e^- + C_3H_6 \rightarrow CH_4 + C_2H_2 + e^-$
L5	$N_2(a'^1\,\Sigma_u^-) + CH_4 \rightarrow N_2 + C + 2\,H_2$		
L6	$CH + CH_4 \rightarrow C_2H_4 + H$		
L7	$C_2H + CH_4 \rightarrow C_2H_2 + CH_3$		

Table 5-2 lists the most important loss (L1-L7) and formation (F1-F4) processes for CH_4 and in **Figure 5-10** the time integrated rates, as well as the relative contributions of these processes are plotted as a function of N_2 content, for the total time of 2.2 s, as well as for the pulse(s) and the afterglow(s). It is clear from this figure that CH_4 is mainly decomposed during the pulse (see **Figure 5-10(a2)**), whereas its formation occurs more in the afterglow (see **Figure 5-10(a1)**). The same behaviour was seen in our previous work about dry reforming.[21] Furthermore, it is also clear that the dominant reaction pathways change with increasing N_2 content.

If we take a look at the loss processes first, we see a clear shift in dominant loss processes when going from low to high N_2 content. At low N_2 contents, the direct decomposition of CH_4 by electron impact reactions (i.e. mainly reaction L1) is the dominant loss process. However, with increasing N_2 content the role of the N_2 metastable singlet and triplet states becomes more important and especially reaction L3 (so-called Penning dissociation by the triplet state) becomes the dominant loss process. Only at 99 % N_2 content, reactions L4 and L5 (i.e. Penning dissociation by the singlet state) become the dominant loss processes.

If we take a look at the formation processes, it appears that the three-body recombination of CH_3 radicals with H atoms, with either CH_4 or N_2 molecules as third body (i.e. reactions F1 and F2), is the dominant formation process, but we can again notice a clear shift upon increasing N_2 content: up to a N_2 content of 90 %, the three-body recombination with CH_4 as third body (i.e. reaction F1) is dominant, while above 90 % the three-body recombination with N_2 (i.e. reaction F2) becomes most important. This is logical, since the amount of CH_4 in the mixture decreases and the amount of N_2 increases. The reason why the relative contributions of both processes do not change symmetric with N_2 content is because the recombination with CH_4 as third body is 3 times more efficient than with N_2 as third body.[35]

From this analysis we can draw the following conclusions: with increasing N_2 content the electron density drops, especially in the lower N_2 content range (up to about 20 %), leading to lower rates for the electron impact dissociation reactions of CH_4 (i.e. reaction L1). Since this reaction is the prime source of CH_3, this results in a lower CH_3 density, which in turn results in lower rates for the recombination reactions (i.e. reactions F1 and F2; note that this cannot be seen in the plots of the relative contributions, but it can be deduced from **Figure 5-10(a1)**). So the lower loss rate is partially countered by lower formation rates, which explains why there is only a very small drop in CH_4 conversion (as shown in **Figure 5-3** between 1 and 20 % N_2) compared to the significant drop in electron density. At the same time the role of the N_2 metastable states for the conversion of CH_4 increases (see L3–L5 in **Figure 5-10(b2)**), explaining why the loss rate in **Figure 5-10(a2)** drops less dramatically above 20 % N_2 content, in spite of the fact that the electron density keeps decreasing (cf. **Figure 5-8** above). Furthermore, by comparing **Figures 5-11(a1-a2)**, it is clear that the total loss rate drops less than the total formation rate of CH_4 upon increasing N_2 content, so there will be a higher "absolute" conversion of CH_4. This explains why the CH_4 conversion starts increasing rapidly above 20 % N_2 content, as seen in **Figure 5-3** above, due to dissociation upon collision with the N_2 metastable states.

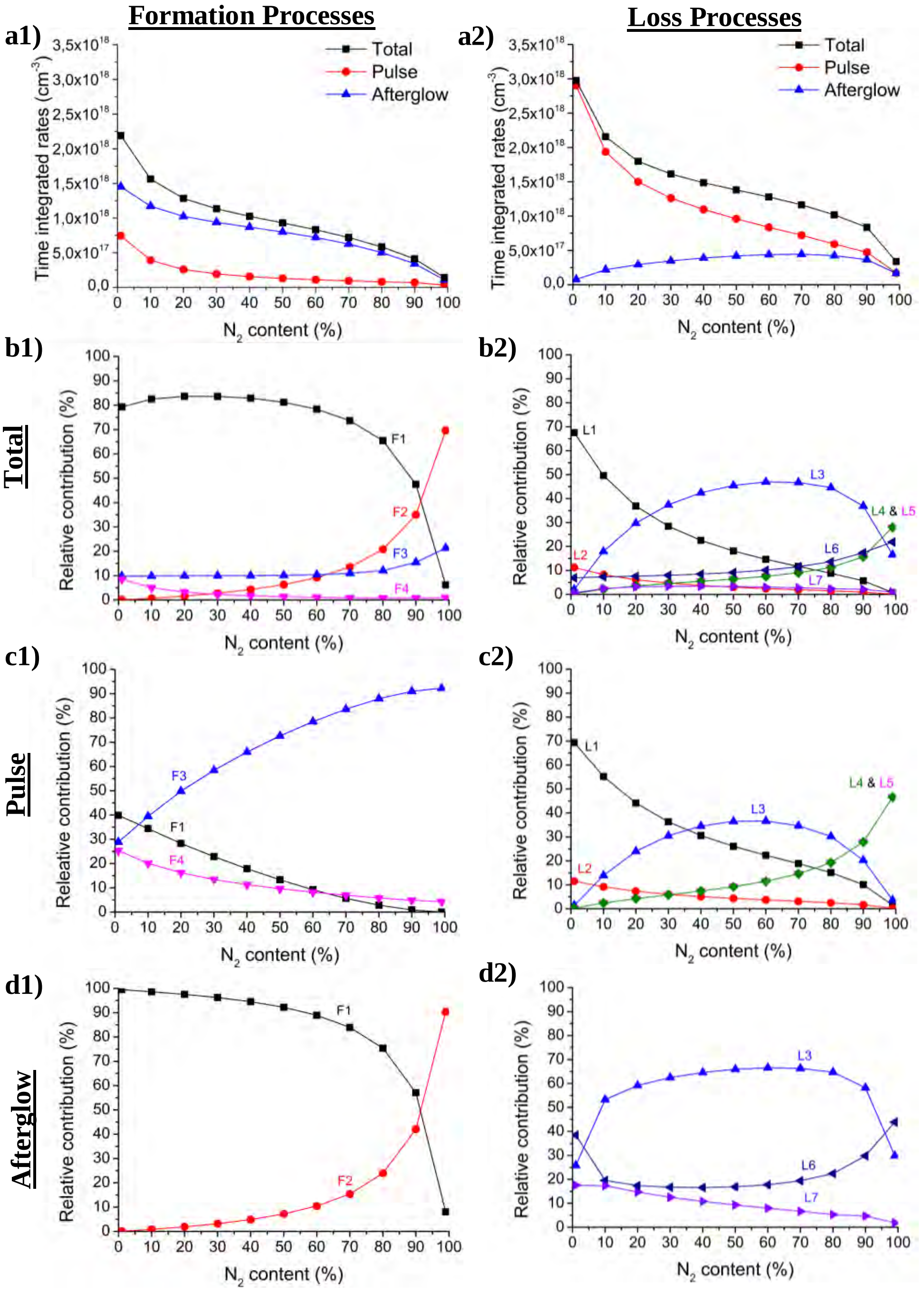

Figure 5-10. Time integrated rates of formation (a1) and loss (a2) of CH_4, and relative contributions of the various formation and loss processes for the total time (b1-2), the pulse(s) (c1-2) and the afterglow(s) (d1-2), as a function of N_2 content for a residence time of 2.2 s and a SEI of 6 J·cm^{-3}. The numbers of the reactions correspond to the numbers of **Table 5-2**.

As H_2 is the prime product of the CH_4 conversion, with a selectivity of about 40–60 % (see above), it is also of interest to take a look at the dominant reaction pathways for the formation and loss of H_2 for several N_2 contents (i.e., 1, 10, 20, 30, 40, 50, 60, 70, 80, 90 and 99 %) to obtain a better understanding of the influence of the N_2 content on the H_2 yield. This kinetic analysis will be performed again by looking at the time integrated rates for the total time, the pulse(s) and the afterglow(s) of the simulations.

Table 5-3. Overview of the most important loss and formation reactions for H_2.

Loss processes		**Formation processes**	
L1	$e^- + H_2 \rightarrow e^- + H + H$	F1	$e^- + CH_4 \rightarrow H_2 + CH_2 + e^-$
L2	$CH_2 + H_2 \rightarrow CH_3 + H$	F2	$e^- + CH_4 \rightarrow H_2 + H + CH + e^-$
L3	$C + H_2 \rightarrow CH + H$	F3	$e^- + C_3H_8 \rightarrow H_2 + C_3H_6 + e^-$
		F4	$e^- + C_2H_6 \rightarrow H_2 + C_2H_4 + e^-$
		F5	$CH_2 + CH_2 \rightarrow H_2 + C_2H_2$
		F6	$CH_2 + H \rightarrow H_2 + CH$
		F7	$N_2(a'^1\,\Sigma_u^-) + CH_4 \rightarrow 2\,H_2 + C + N_2$
		F8	$N_2(A^3\,\Sigma_u^+) + CH_4 \rightarrow H_2 + CH_2 + N_2$

Table 5-3 lists the most important loss (L1-L3) and formation (F1-F8) processes for H_2 and **Figure 5-11** illustrates the time integrated rates as well as the relative contributions of these processes, for the above mentioned N_2 contents for the total time, the pulse(s) and the afterglow(s). From this figure it is clear that H_2 is almost exclusively formed during the pulse, whereas it can be decomposed both in the pulse and afterglow. However, when comparing **Figures 5-12(a1-a2)**, it is obvious that the formation rate is clearly higher than the loss rate, so there will be a net formation of H_2, for all N_2 contents, although it will drop slightly upon increasing N_2 content, in agreement with **Figure 5-6** above.

It also appears from **Figure 5-11** that the dominant reaction pathways again change drastically with increasing N_2 content. If we take a look at the production processes first, at low N_2 contents, the direct decomposition of CH_4 and higher hydrocarbons by electron impact reactions (i.e. reactions F1–F4) is the dominant formation process for H_2. However, with increasing N_2 content, the role of the N_2 metastable singlet state becomes increasingly important and reaction F7 becomes the dominant formation process for 30 % N_2 content and above. As far as the loss processes are concerned, at very low N_2 content, electron impact dissociation of H_2 (i.e. reaction L1) is dominant, while with increasing N_2 content, reaction L3 rapidly becomes the most important loss process.

If we take a look at the relative contributions of formation and loss during pulse and afterglow (i.e., **Figures 5-12(c1-c2-d1-d2)**, we see that even during the pulse the loss reaction L3 becomes more important as a loss process above 10 % N_2 content, compared to electron impact dissociation (L1). During the afterglow, reaction L3 is dominant at all N_2 contents. Since the formation almost exclusively takes place during the pulse, **Figure 5-11(c1)** looks exactly like **Figure 5-11(b1)**, except for the radical recombination reactions F5 and F6, which only occur during the afterglow, see **Figure 5-11(d1)**.

From these results it can be concluded that with increasing N_2 content the electron density drops, leading to lower rates for the electron impact dissociation reactions of CH_4 and higher hydrocarbons which produce H_2 (i.e. reaction F1–F4). At the same time, the rate of the dominant loss process L1, drops for the same reason. Furthermore, the rates of processes L2, F5 and F6 also drop because the prime source of CH_2 is electron impact dissociation of CH_4 (process F1). Quickly the role of the N_2 metastable singlet state increases (i.e. reaction F7), and becomes the dominant production process of H_2 above 30 % N_2 content. Moreover, this reaction also leads to an increase in the production of C atoms, which was also observed experimentally by an increased amount of soot deposition in the plasma reactor. This higher C production in its turn leads to a higher rate of L3. Overall, the total H_2 formation rate is much higher than the total loss rate, so that there is a net formation of H_2 at all N_2 contents, although this overall formation drops upon increasing N_2 content, as was also shown in **Figure 5-6**.

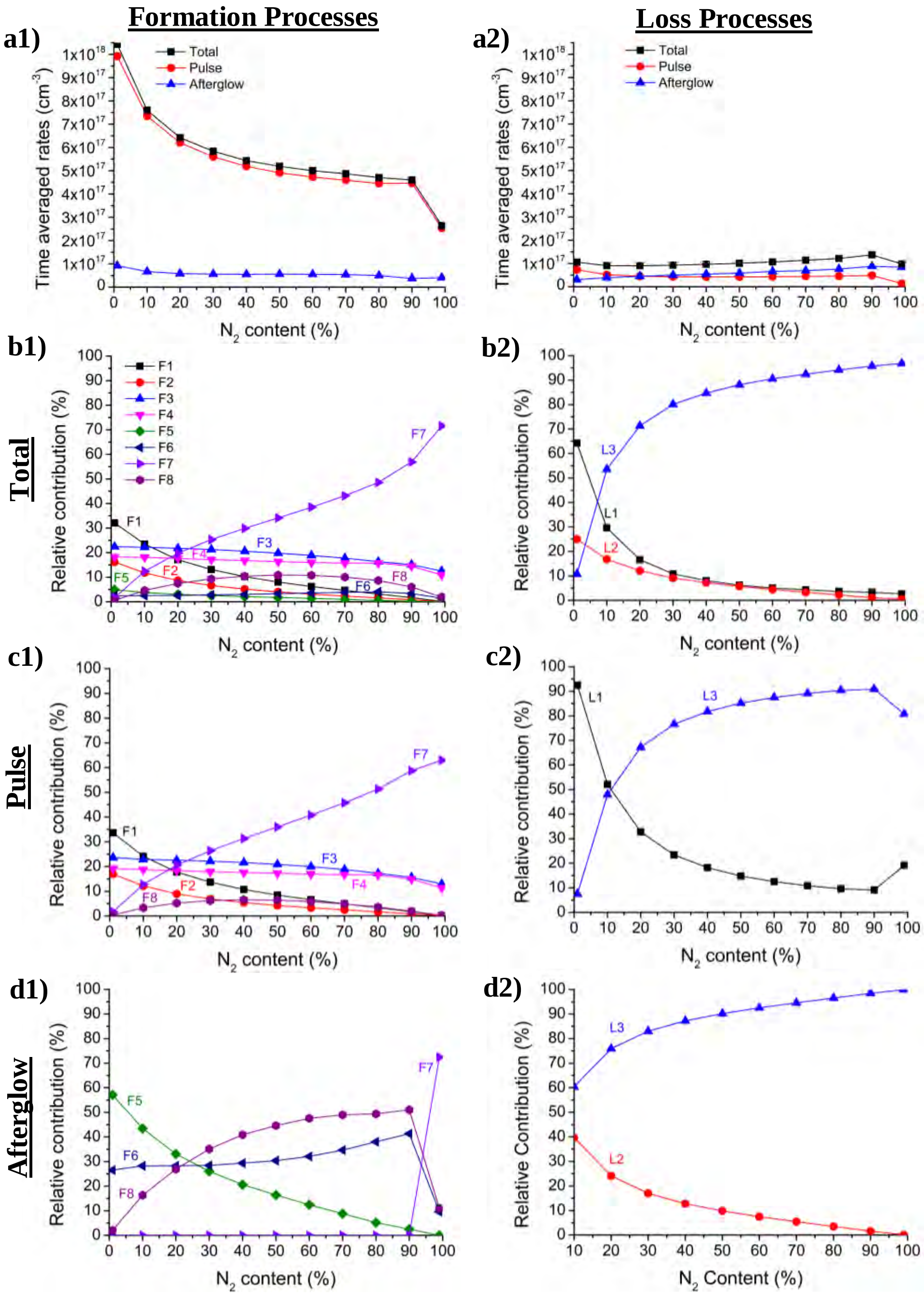

Figure 5-11. Time integrated rates of formation (a1) and loss (a2) of H_2, and relative contributions of the various formation and loss processes for the total time (b1-2), the pulse(s) (c1-2) and the afterglow(s) (d1-2), as a function of N_2 content for a residence time of 2.2 s and a SEI of 6 $J{\cdot}cm^{-3}$. The numbers of the reactions correspond to the numbers of **Table 5-3**.

2.4. Conclusions

The goal of this section was to investigate the effect of N_2 impurities (in the range of 1-50,000 ppm) as well as the effect of N_2 as additive gas (in the range of 1-99 %) on the CH_4 conversion and on the H_2 yield, and to find out whether nitrogenated compounds could be formed. For this purpose a combined experimental and computational study was performed: a 0D chemical kinetics model, called "Global_kin" was applied to our experimental DBD set-up.

The simulation results showed that the presence of N_2 impurities in the ppm range only has a minor indirect influence on the CH_4 conversion and H_2 yield, as a result of the decreasing electron density with increasing N_2 impurity content.

The experiments and simulations for the effect of N_2 as additive were in good agreement, for both CH_4 conversion and H_2 yield, in the entire range of CH_4/N_2 gas mixing ratios, allowing us to perform a kinetic analysis based on the modelling results.

The combined experimental and computational study revealed that increasing the N_2 content has a large influence on the CH_4 conversion and H_2 yield, since both clearly increase with N_2 content. These trends are the result of the interplay of several effects: (a) the decreasing electron density with increasing N_2 content lowers the contribution of the electron impact reactions for both the CH_4 loss and H_2 production; (b) the lower reaction rate constants for several three body reactions with N_2 as third body compared to CH_4 lowers the recombination of species into CH_4, partly counteracting the lower CH_4 loss rates of the electron impact loss reactions; and (c) with increasing N_2 content the role of the N_2 metastable states becomes more important and Penning dissociation reactions with CH_4 become the dominant loss processes for CH_4 and the most important formation processes for H_2.

However, although the CH_4 conversion and H_2 yield increase upon rising N_2 content, this is not sufficient to counteract the inherent lower CH_4 content in the gas mixture with increasing N_2 content, thus the effective CH_4 conversion and H_2 yield drop upon increasing N_2 content. Finally, our calculations predict that only very low yields (in the ppm and ppb level) of nitrogenated compounds (e.g., HCN and NH_3) were produced, because the electron energy appears to be too low for efficient ionization of N_2, which was reported in literature to be the dominant precursor process for the formation of these nitrogenated compounds.

3. $CO_2 + N_2$

3.1. Description of the model

3.1.1. 0D chemical kinetics model

In this section, another zero-dimensional (0D) chemical kinetics model was used, called ZDPlaskin.[36] In this model, again the time-evolution of the species densities is calculated by balance equations, taking into account the various production and loss terms by chemical reactions. The rate coefficients for the electron impact reactions are calculated with a Boltzmann solver, BOLSIG+,[37] which is integrated into ZDPlaskin. For a more detailed description of the model, we refer to the work of Panchesniy et al.[36]

We assume the same gas flow rate as used experimentally, i.e. 611 ml min^{-1} at atmospheric pressure, and the same DBD reactor volume of 7.4 cm^3 (see section 2.1 above), which corresponds to a total residence time of 0.73 s. The temperature is assumed to remain constant at 300 K, as predicted by Aerts et al.[15]

3.1.2. Plasma chemistry included in the model

Table 5-4. Species included in the model, besides the electrons. The symbols 'V' and 'E' stand for various vibrational and electronically excited levels of the various species, as explained in detail in the work of Heijkers et al.[17]

Molecules	Radicals	Charged species	Excited species
CO_2	C_2O, C_2, C	CO_2^+, $C_2O_2^+$, $C_2O_3^+$, $C_2O_4^+$, C_2^+, C^+	CO_2(Va), CO_2(Vb), CO_2(Vc), CO_2(Vd), CO_2(V1-V21), CO_2(E1), CO_2(E2)
CO		CO^+, CO_3^-, CO_4^-, CO_4^+	CO(V1-V10), CO(E1), CO(E2), CO(E3), CO(E4)
O_2, O_3	O	O_2^+, O_2^-, O^+, O^-, O_4^-, O_4^+, O_3^-	O_2(V1), O_2(V2), O_2(V3), O_2(V4), O_2(E1), O_2(E2)
N_2	N	N^+,, N_2^+, N_3^+, N_4^+	N_2(V1-V14), N_2($C^3\Pi_u$), N_2($A^3\Sigma_u^+$), N_2($a'^1\Sigma_u^-$), N_2($B^3\Pi_g$), N(2D), N(2P)
N_2O, N_2O_3, N_2O_4, N_2O_5	NO, NO_2, NO_3	NO^+, N_2O^+, NO_2^+, NO^-, N_2O^-, NO_2^-, NO_3^-, $N_2O_2^+$	
ONCN, C_2N_2, NCN	CN, NCO		

The chemistry set used in this model was recently developed and validated for a microwave discharge.[17] In short, it considers 119 different species (see **Table 5-4**), which react with each other in 339 electron impact reactions, 804 ion reactions and 2795 neutral reactions. Their corresponding rate coefficients, and the references where these data were adopted from, are listed in the ESI of the work of Heijkers et al.[17] Some minor adjustments were made (see **Table 5-5**).

Table 5-5. List of the minor changes in rate constant made to the kinetic model of Heijkers et al.[17]

Reaction	**Rate Constant (cm^3*$molecule^{-1}$*s^{-1} or cm^6*$molecule^{-2}$*s^{-1})**	**Reference**
$N + O_3 \rightarrow NO + O_2$	$5.0*10^{-12}*exp(-650/Tgas)$	38
$NO + NO_2 + M \rightarrow N_2O_3 + M$	$9.1*10^{-33}$	39
$N_2O_3 + M \rightarrow NO + NO_2 + M$	$1.9*10^{-7}*(Tgas/300)^{-8.7}-exp(-4880/Tgas)$	40
$2NO_2 + M \rightarrow N_2O_4 + M$	$1.4*10^{-33}*(Tgas/300)^{-3.8}$	41
$N_2O_4 + M \rightarrow 2NO_2 + M$	$1.3*10^{-5}*(Tgas/300)^{-3.8}*exp(-6460/Tgas)$	40
$N + O + M \rightarrow NO + M$	$1.0*10^{-32}*(300/Tgas)^{0.5}$	40
$NO_2 + NO_3 + M \rightarrow N_2O_5 + M$	$3.6*10^{-30}*(300/Tgas)^{4.1}$	41
$N_2O_5 + M \rightarrow NO_2 + NO_3 + M$	$1.3*10^{-3}*(Tgas/300)^{-3.5}*exp(-11000/Tgas)$	40,41
$N_2(A^3\Sigma_u^+) + CO_2 \rightarrow CO + O$	$6.25*10^{-14}$	42

3.2. Description of the experiments

The experiments are again carried out in a coaxial DBD reactor, illustrated in Chapter 2 (**Figure 2-4**). A stainless steel mesh (ground electrode) is wrapped over the outside of a quartz tube with an outer and inner diameter of 22 and 16.5 mm, respectively, while a stainless steel rod with an outer diameter of 13 mm is placed in the centre of the quartz tube and used as high voltage electrode. The length of the discharge region is 90 mm, with a discharge gap of 1.75 mm, resulting in a discharge volume of 7.4 cm^3. CO_2 and N_2 are used as feed gases with a total flow rate of 611 mL min^{-1}. The N_2 content is controlled with mass flow controllers (Bronkhorst), and varied between 0 and 98 %, in steps of 1 % (in the regions of 0–10 % and 90–98 % N_2), while steps of 10 % are used in the region between 10 and 90 % N_2. The DBD reactor is powered by an AC high-voltage power supply (AFS), providing a maximum peak-to-peak voltage of 40 kV and a variable frequency of 1–90 kHz. The total current is recorded by a Rogowski-type current monitor (Pearson 4100), while a high voltage probe is used to measure the applied voltage. Furthermore, to obtain the charge generated in the discharge, the voltage on the external capacitor (10 nF) is measured. Finally, all the electrical signals are sampled by a four-channel digital oscilloscope (Picotech PicoScope 64201) and the discharge power is obtained by a control system used to calculate the area of the Q-U Lissajous Figures.[15]

3.2.1. Product analysis: molecular gases

The feed and product gases are analysed by a three-channel compact-gas chromatograph (CGC) (Interscience), equipped with two thermal conductivity detectors (TCD) and a flame ionization detector (FID). The first TCD channel is equipped with a Molecular Sieve 5A column for the separation of the molecular gases O_2, CO and N_2, while the second TCD channel contains an Rt-Q-BOND column for the measurement of CO_2, C_2–C_4 hydrocarbons and nitrogen containing compounds. The FID is equipped with an Rtx-5 column for the measurement of C_1–C_{10} and nitrogen containing compounds.

3.2.2. Gas expansion factor

The moles of CO_2 and N_2, written in (eq.2.9), are as mentioned above, obtained with gas chromatography by sampling a small volume of the gas stream. Subsequently, the concentrations are deduced from a calibration curve, which is obtained for a constant gas flow. However, in a DBD the number of molecules and thus the volumetric flux, increases along the reactor, as CO_2 is gradually converted into CO and O_2 molecules. More specifically, two CO_2 molecules are split into three molecules which increase the volume by 50 %:

$$2\ CO_2 \rightarrow 2\ CO + \ O_2 \qquad (1)$$

As will be shown in section 3.3.1 below, N_2 is almost not converted and thus its contribution to the change in volume is minimal. However, it does act as a dilutant: when adding more N_2, the volume expansion due to CO_2 splitting becomes less pronounced, since the share of CO_2 in the total gas mixture decreases.

This so-called gas expansion effect is clearly not taken into account in the gas chromatography approach above, which up till now is used by almost all authors. However, depending on the gas mixture it can be quite significant, as stated by Pinhão et al.[43] Therefore, in the present study, we have accounted for this effect. When neglecting this effect, the N_2 conversion would be overestimated by an order of magnitude. This is the result of the very low conversion for N_2, as shown below. Pinhão et al.[43] also reported that the relative error, and thus the overestimation, indeed increases significantly for lower values of the conversion. The CO_2 conversion, on the other hand, would be overestimated by a factor 1.5 for pure CO_2, a factor 1.2 for a mixture with 50 % CO_2 and a factor 1.04 in case of 10 % CO_2 in the mixture. Indeed, as mentioned above, the volume expansion becomes less pronounced when more N_2 is present in the mixture. It is thus clear that when studying the effect of different gas mixing ratios, as in the present paper, the gas expansion effect will vary, depending on the gas mixing ratio, which further complicates the situation, and stresses the importance of taking this effect properly into account.

In this work the corrected results are obtained by performing an iterative back calculation, with the following assumptions: (i) CO_2 is split into CO and ½ O_2, so every converted CO_2 molecule gives rise to an expansion of the volume by a factor 1.5. (ii) On the other hand, for N_2, due to its low conversion, we assume that the conversion of N_2 does not contribute to the gas expansion.

Based on these two assumptions we start from the "faulty" conversions obtained from our GC measurements. We know that the gas expanded and since we have a sample loop with a fixed volume, this means that the pressure increases. However, since our GC samples at atmospheric pressure, part of the gas is lost due to the depressurization in the GC system before injection, leaving less molecules in the sample volume than originally present in the outlet flow. Since there are now less (CO_2 and N_2) molecules in the sample, the (CO_2 and N_2) conversion will appear higher. To correct for this, we calculate X_{GC} by solving the equation below for different values of X_{Real} until X_{GC} matches the (CO_2 or N_2) conversion measured by the GC.

$$X_{GC} = 1 - \left(\frac{1-X_{Real}}{1+\alpha\left(\frac{X_{Real}}{2}\right)}\right) \qquad \text{(eq.5-1)}$$

This formula is used for both the CO_2 and N_2 conversion. The derivation of it, in case of CO_2, is explained below. In this formula X_{GC} is the calculated conversion, which we expect to be measured by the GC due to the gas expansion for a certain value of X_{Real}, which is the real conversion.

This equation is derived, on one hand, from the expression to calculate the remaining fraction of (CO_2 or N_2) in the output:

$$Fraction\ (output) = (1 - X_{Real}) \qquad \text{(eq.5-2)}$$

And on the other hand, from the expression for the gas expansion due to the CO_2 conversion:

$$Gas\ expansion = 1 + \alpha\left(\frac{X_{Real}}{2}\right) \qquad \text{(eq.5-3)}$$

In the latter expression, according to our first assumption, $\alpha(X_{Real}/2)$ accounts for the gas expansion due to the CO_2 conversion, as this corresponds to the O_2 formed for a certain CO_2 conversion (X_{Real}), where α is the fraction of CO_2 in the initial (CO_2/N_2) gas mixture. Furthermore, according to the second assumption, the N_2 conversion does not give rise to further volume expansion.

Dividing (eq.5-2) by (eq.5-3) tells us how the output is normalized due to the depressurization in the CGC system, and subtracting this value from one, ultimately gives us the "faulty" conversion as obtained in the CGC under influence of the gas expansion. Thus by doing this calculation for a range of different X_{Real} values and matching X_{GC} to the measured "faulty" conversion by the GC, we can determine the "real" CO_2 conversion, X_{Real}.

After calculating X_{Real} for CO_2, we can calculate the "real" conversion for N_2 following the same procedure. In this case, X_{Real} in (eq.5-2) stands for the N_2 conversion, while X_{Real} in (eq.5-3) is the already calculated "real" conversion of CO_2.

3.2.3. Product analysis N_2O and NO_x compounds

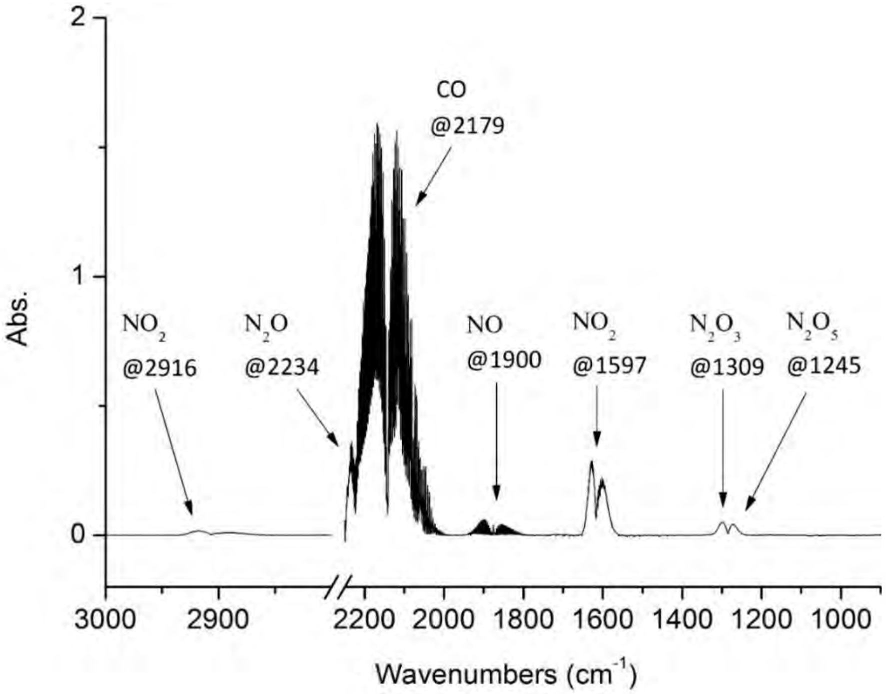

Figure 5-12. FTIR spectrum for a 1:1 mixture CO_2/N_2, indicating the different NO_x (and N_2O and CO) logging bands.

Gas chromatography is not a suitable technique to study the formation of O_3, N_2O and NO_x compounds (e.g., NO, NO_2, N_2O_3 and N_2O_5). Therefore, we applied Fourier transform infrared spectroscopy (FTIR; Thermo Fischer Scientific, Waltham, MA). By inserting a 2-m IR gas cell in the FTIR spectrometer, we obtain an IR absorption spectrum showing all IR active vibrations. During the experiments, an FTIR resolution of 1 cm^{-1} is used, which results in a spectrum being taken every 15 s. For basic qualitative measurements, this technique provides nearly real-time information on gas phase production of the N-containing compounds. **Figure 5-12** shows the spectrum for a 1:1 mixture CO_2/N_2 with the different bands indicated.

3.3. Results and discussion

First, we will show the experimental results and compare them with the model predictions, for the conversion of CO_2 and N_2, the energy efficiency of CO_2 conversion and the formation of N_2O and NO_x compounds, upon addition of N_2 in the gas mixture. Subsequently, the underlying plasma chemistry for the CO_2 and N_2 conversion and the formation of the various compounds will be discussed in more detail, based on the modelling results.

3.3.1. Effect of N_2 on plasma splitting of CO_2

a) Effect on conversion and energy efficiency

Figure 5-13(a) illustrates the experimental and calculated absolute CO_2 and N_2 conversion as a function of the N_2 content. The absolute CO_2 conversion increases more or less exponentially with rising N_2 fraction, both in the experimental data and the calculations. This indicates that N_2 has a beneficial effect on the CO_2 splitting, as will be explained below. The N_2 conversion, on the other hand, is very low, i.e. in the order of 0.1–1 % for both the experiments and the model, showing again a good agreement. The reason for the low N_2 conversion is that it mainly occurs through electron impact ionization of N_2 molecules, followed by the reaction of the produced ions with other species, as we explained above for a CH_4/N_2 mixture.[44] However, this electron impact ionization occurs at high electron energy (above 15.5 eV), which is higher than the values typically reached for our operating conditions, and this explains the low N_2 conversion.

Figure 5-13(b) illustrates the experimental and calculated effective (or overall) CO_2 and N_2 conversion as a function of the N_2 content. The effective CO_2 conversion remains relatively constant around 4 % when adding up to 40–50 % N_2. This can be explained because the absolute conversion increases (cf. **Figure 5-13(a)**), but at the same time the fraction of CO_2 in the gas mixture decreases, and both effects compensate each other. In other words, the increase in absolute conversion upon adding N_2 is high enough to counteract the lower CO_2 concentration in the gas mixture. When reaching 50 % N_2, the effective conversion starts decreasing exponentially. This means that the increase in absolute conversion is no longer high enough to compensate for the lower CO_2 concentration in the mixture. This behaviour can be explained from the kinetic analysis presented in section "Underlying Chemistry" below. When adding up to 50 % N_2, the energy put into the plasma goes to CO_2 splitting, both directly through electron impact dissociation and indirectly through electron impact excitation of N_2, which aids in the dissociation of CO_2 (see below). Above 50 % N_2, more energy goes into N_2 excitations and it is no longer efficiently transferred to the reactions leading to CO_2 dissociation (see section 3.3.2 below).

Again, excellent agreement is obtained between the experimental and calculated data, except in the region between 0 and 1 % N_2, where a significant rise in CO_2 conversion is seen in the experiments, being absent in the model predictions. This is attributed to a change in the physical properties of the discharge when comparing a pure CO_2 plasma with a CO_2/N_2 plasma. Indeed, it is known that a DBD plasma in CO_2 has a filamentary character,[15,23] while adding N_2 leads to a more homogeneous and stable discharge.[9,44] This effect cannot be completely captured in the 0D model, explaining the slight discrepancy between experiments and model predictions.

The effective N_2 conversion rises slightly (from 0.01 to 0.3 % in the experiment, and from 0.005 to 0.1 % in the model predictions) when adding up to 90 % N_2, followed by a drop to zero for pure N_2. This behaviour can again be explained by the fact that the N_2 conversion occurs through ionization and the subsequent reaction of the formed ions with other species (see above), which are absent for pure N_2. The small difference in experimental and calculated values comes from the large uncertainties in the experiment, resulting from the low values and thus the large effect of the gas expansion factor, as discussed in the experimental section above.

The energy efficiency for CO_2 conversion (see **Figure 5-13(c)**) shows exactly the same trend as the effective CO_2 conversion, where it is calculated from (see (eq.2-12)). Thus, the energy efficiency remains quite constant around 4 % in the experiments (and slightly lower in the model predictions) until about 50 % N_2 and then it starts decreasing rapidly, because of the lower effective CO_2 conversion and the fact that more energy is consumed by the N_2 molecules upon increasing N_2 content in the mixture, and cannot be used anymore for the CO_2 conversion.

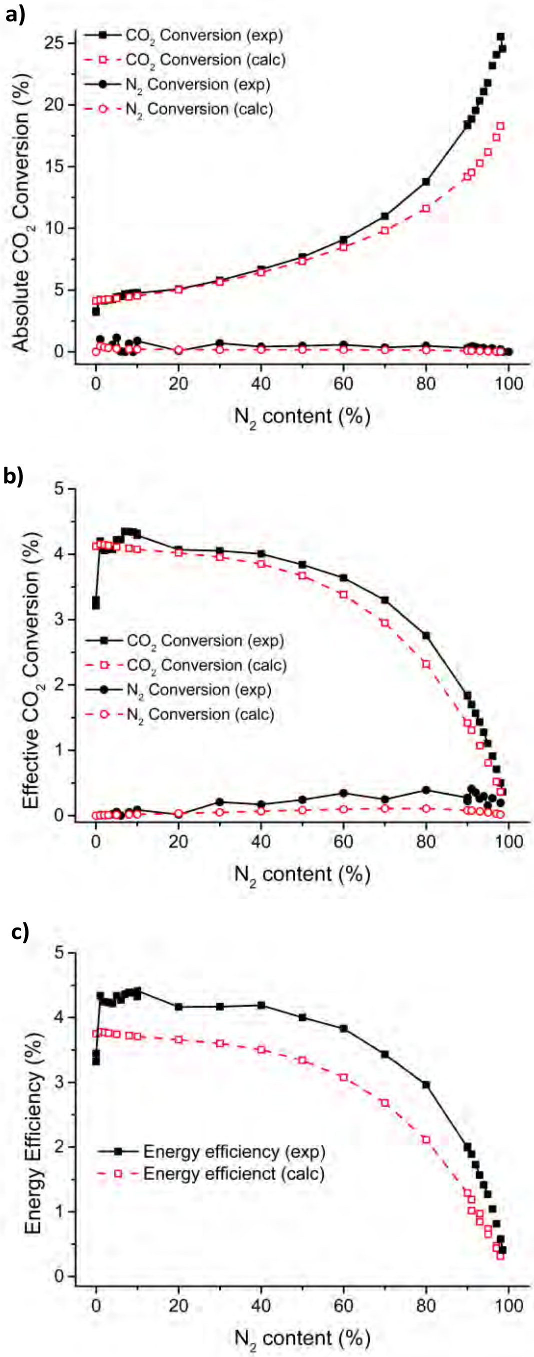

Figure 5-13. Experimental and calculated values of absolute CO_2 and N_2 conversion (a), effective CO_2 and N_2 conversion (b) and energy efficiency of CO_2 conversion (c) as a function of N_2 content, for a residence time of 0.73 s and a SEI of approx. 12 J cm^{-3}.

b) Effect on product formation

CO_2 splitting typically yields CO and O_2 molecules; the latter being formed by the recombination of O atoms. Besides, also some O_3 can be created.[45] This product distribution does not change when adding N_2, as revealed by our experiments and model predictions. However, the N_2 addition leads to the formation of some N_2O and NO_x compounds, which will be discussed in more detail in this section. This is very important because the production of N_2O and certain NO_x might be beneficial when formed in very high concentrations, as this would indicate that the process could be effective for nitrogen fixation.[14] However, in low concentrations (i.e. below 1 %), it has no economic value, and even worse, it gives a high environmental cost, since N_2O and NO_x have a severe negative impact on air quality, leading to a restriction of their emissions and the need of denox installations.[46,47] Therefore, it is of crucial importance to analyse the product formation in the CO_2/N_2 plasma, to know which of the two scenarios take place.

For NO and NO_2 a calibration curve is available, which allows to express the measurement results in absolute concentrations (ppm). For N_2O, N_2O_3 and N_2O_5, however, this is not the case and the formation of these compounds can thus only be expressed in arbitrary units (a.u.) of the measured absorbance. To maintain consistency throughout the discussion here, all experimental results will be presented in arbitrary units (a.u.) as measured absorbance with the FTIR-cell, while the calculation results will be given in ppm. For NO and NO_2, we will briefly report about the absolute concentrations in the text below and the detailed concentrations can be found in **Table 5-6**. Furthermore, to allow a detailed comparison between the experimental and calculated trends, the two y-axes (representing the experimental and calculated data, respectively) will be constructed so that they vary over the same range.

The measured and calculated NO and NO_2 concentrations are plotted as a function of N_2 content in the gas mixture in **Figure 5-14(a)** and **Figure 5-14(b)**, respectively. Experimentally both compounds follow the same parabolic trend with a maximum at 50 % N_2. As will be illustrated in section “N_2O and NO_x formation” below, the NO_x species are formed out of N (or $N_2(A^3\Sigma_u^+)$) and O atoms, which originate from N_2 and CO_2, respectively. Thus, it is not unexpected that the maximum of the NO_x concentration is achieved when both reactants are present in approximately equal concentrations. The calculated results follow more or less the same trend for NO_2 but a left-skewed trend for NO with respect to the experimental values. Nevertheless, in both cases, the profiles first rise and then drop with increasing N_2 content, so we believe that the model can be used to explain the observed trends (see section “N_2O and NO_x formation” below). Furthermore, even the absolute values of the concentrations are in reasonable agreement.

Table 5-6. Measured concentration (ppm) of NO and NO_2 as function of the CO_2/N_2 mixture.

CO_2 (%)	N_2 (%)	NO 1900 cm^{-1} (a.u.)	NO 1900 cm^{-1} (ppm)	NO_2 1597 cm^{-1} (a.u.)	NO_2 1597 cm^{-1} (ppm)
99	1	0.0122	39.96	0.0316	9.97
98	2	0.0215	70.46	0.0398	12.54
97	3	0.0298	97.35	0.0455	14.37
96	4	0.0340	111.36	0.0491	15.48
95	5	0.0416	136.14	0.0569	17.94
94	6	0.0473	154.64	0.0610	19.25
92	8	0.0606	198.45	0.0714	22.53
91	9	0.0662	216.78	0.0756	23.84
90	10	0.0666	217.90	0.0798	25.18
80	20	0.119	389.43	0.1249	39.41
70	30	0.1302	426.15	0.1363	43.00
60	40	0.1668	545.73	0.1602	50.54
50	50	0.1695	554.70	0.1696	53.51
40	60	0.1543	504.86	0.1498	47.27
30	70	0.1349	441.26	0.1241	39.14
20	80	0.1211	396.38	0.0953	30.06
10	90	0.0610	199.55	0.0417	13.15
9	91	0.0392	128.46	0.0271	8.54
8	92	0.0291	95.22	0.0210	6.61
7	93	0.0258	84.32	0.0179	5.65
6	94	0.0121	39.68	0.0133	4.18
5	95	0.00051	1.68	0.00059	0.19
4	96	0.00045	1.48	0.00084	0.26
3	97	0.00027	0.90	0.00059	0.19
2	98	0.00029	0.96	0.00057	0.18

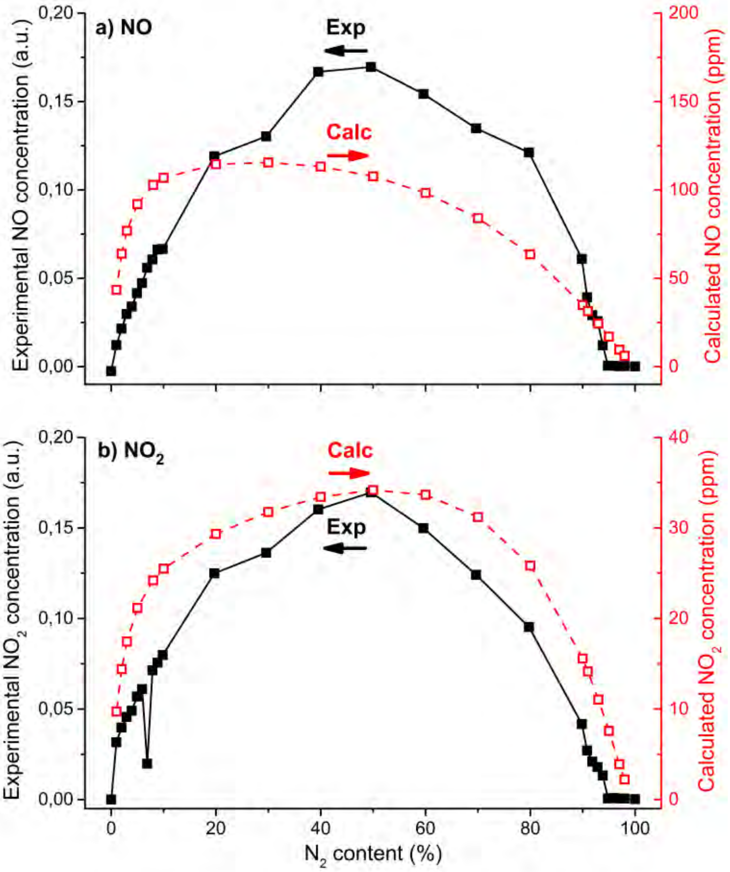

Figure 5-14. Experimental and calculated concentrations of NO (a) and NO_2 (b) as a function of N_2 content, for a residence time of 0.73 s and a SEI of approx. 12 J cm^{-3}.

Experimentally, the obtained NO concentration is about an order of magnitude higher than the NO_2 concentration, with maximum values of 550 and 54 ppm, respectively. Even at 1 % N_2 the measured concentrations are already 40 and 10 ppm, respectively. To put these values in perspective, when converting them to emissions in the common units of g/km in the automobile sector,[48] they are ~3000 times higher than currently allowed under European emission standards for passenger cars (EURO 6 norm, 80 mg/km).[49] Compared with industrial emissions, when converting them to the industrially used units of mg/m^3, they are in the order of 10–20 times higher than the current BAT-AELs (Best Available Technique Associated Emission Levels) for coal fired power plants with a capacity of >300 MW in Europe, which allow NO_x emissions of 50–200 mg/m^3.[50] The calculated NO and NO_2 concentrations are somewhat lower, but in the same order of magnitude, with a maximum of 115 and 34 ppm, respectively.

These NO_x compounds react in the air, resulting in smog formation and acid rain. Thus, these high concentrations will have a negative effect on air quality and the environment.[51] At the same time, however, the concentrations are too low to be considered useful for nitrogen fixation.[14] Indeed, the current industrial processes for nitrogen fixation, i.e. the Haber-Bosch process (for making ammonia) and the Ostwald process (for making nitric acid starting from ammonia) can achieve overall yields of 99 %.[52]

The other NO_x compounds detected in the experiments are N_2O_3 and N_2O_5, for which the concentrations (again in a.u.) are plotted in **Figure 5-15(a)** and **Figure 5-15(b)**, along with the model predictions (in ppm). Again, a reasonable agreement is obtained in the experimental and calculated trends, especially for N_2O_5 (note the same variation in the orders of magnitude of both y-axes).

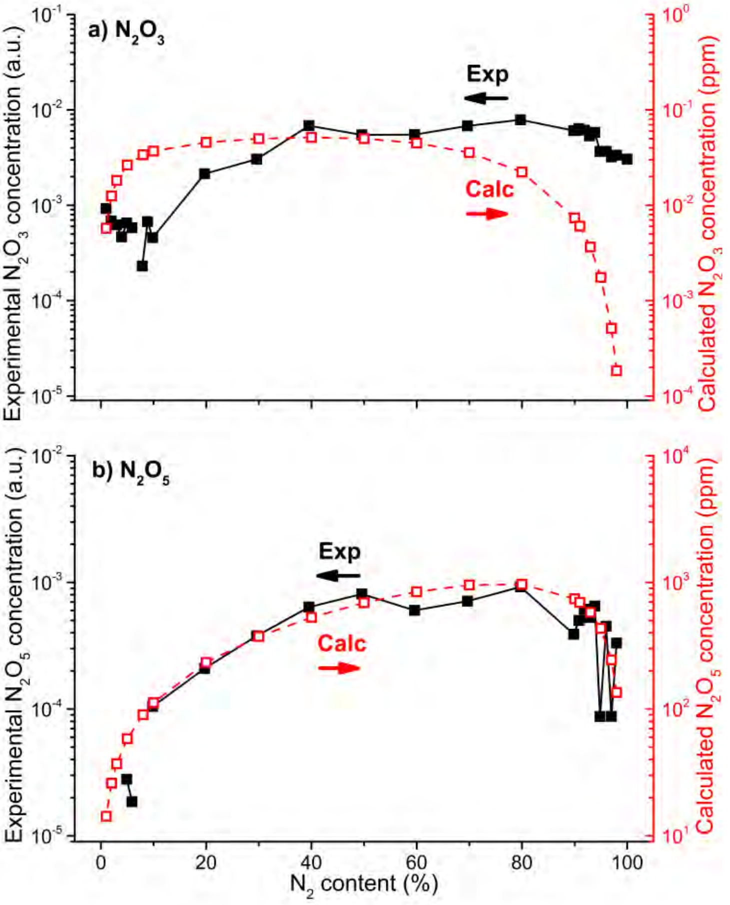

Figure 5-15. Experimental and calculated concentrations of N_2O_3 (a) and N_2O_5 (b) as a function of N_2 content, for a residence time of 0.73 s and a SEI of approx. 12 J cm^{-3}.

The N_2O_3 and N_2O_5 concentrations vary over two and three orders of magnitude, respectively, within the entire range of N_2 contents in the gas mixture. According to our calculations, concentrations up to 1000 ppm are found for N_2O_5, while the calculated N_2O_3 concentrations do not exceed 0.05 ppm. Unfortunately, we were not able to deduce the absolute values for the experimental concentrations, because of lack of suitable detectors to create a calibration curve. Since N_2O_5 can be considered as the anhydride of nitric acid, this would indicate that if the calculated concentrations are realistic, these concentrations would contribute heavily to the formation of acid rain if emitted to the atmosphere. Regarding the N_2O_3 emission, this appears not to be a problem, since the calculations predict negligible amounts to be formed. This is in agreement with the fact that at room temperature the dissociation into the constituent gases NO and NO_2 is favoured over the formation of N_2O_3.[41]

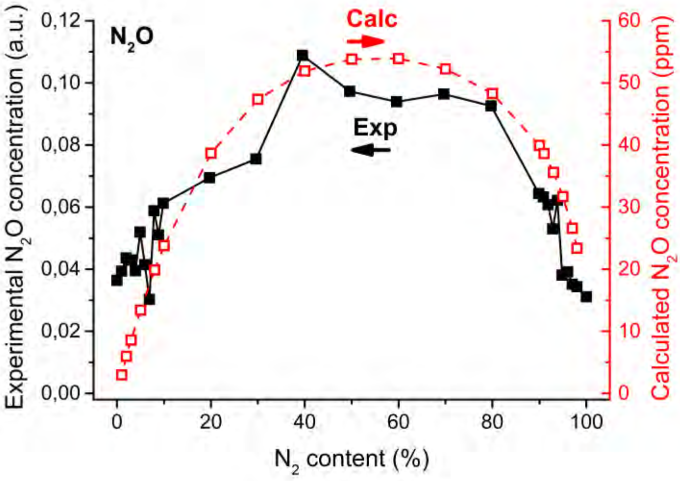

Figure 5-16. Experimental and calculated concentrations of N_2O as a function of N_2 content, for a residence time of 0.73 s and a SEI of approx. 12 J cm^{-3}.

Finally, the measured and calculated N_2O concentrations are presented in **Figure 5-16**. Again the same parabolic trend as a function of the N_2 content in the gas mixture is observed as for the NO_x compounds, with a maximum at 50–60 % N_2. The calculated maximum concentration is about 55 ppm, but experimentally it was again not possible to obtain absolute values of the concentration. Nitrous oxide is a very potent greenhouse gas, with a global warming potential (GWP) of 298 $CO_{2,equivalent}$. Keeping in mind that for the conditions under study, we effectively convert about 4 % CO_2 (see **Figure 5-13(b)** above), this means that if the N_2O concentration would exceed 130 ppm, the reduction in GWP would be equal to zero. Hence, the production of nitrous oxide is voiding the greenhouse gas mitigation potential of our technology (by up to 40 % for N_2O concentrations up to 55 ppm) if we do not add a denox purification step afterwards. Denox technology mainly includes Selective non-Catalytic Reduction (SNCR), Selective Catalytic Reduction (SCR) and a combination of both. Although these are already mature technologies with high NOx reduction efficiencies (70–95%), they are also prone to high operational costs.[53,54] This is no surprise since in general, end-of-pipe clean-up technology is always more expensive.

It becomes clear from both the measurements and the calculations that N_2O and several NO_x compounds are produced. Although their concentrations remain in the ppm range, this is certainly not negligible, since they give rise to several environmental problems. Hence, it appears to be crucial to separate the CO_2 gas from N_2 impurities (or gas fractions) before plasma treatment, to avoid the formation of NO_x compounds and thus the need to install expensive denox installations afterwards.

3.3.2. Underlying chemistry

In the following sections, the underlying plasma chemistry, as predicted by the model, will be discussed in more detail, for the CO_2 conversion in the presence of N_2, as well as for the formation of NO_x compounds and N_2O. Indeed, a better insight in the underlying chemical reactions might help to steer the process, to improve the CO_2 conversion and energy efficiency, and to reduce the NO_x and N_2O formation.

a) CO_2 conversion

The reactions responsible for the CO_2 conversion are presented in **Figure 5-17**, as a function of the N_2 content in the gas mixture. At low N_2 contents, the most important reaction is electron impact dissociation of CO_2 into CO and O, while at high N_2 contents, the reaction with metastable $N_2(A^3\Sigma_u^+)$ molecules, yielding the same splitting products (CO and O) and leaving N_2 in its ground state, is mainly responsible for the CO_2 conversion. Indeed, upon higher N_2 contents, the electron energy is gradually being used for N_2 excitation instead of CO_2 dissociation, explaining the drop in electron impact dissociation rate and the corresponding increase in the dissociation rate by N_2 metastable molecules. The former reaction is dominant during the micro discharge filaments of the DBD, while the latter reaction is more important in the time between the filaments, i.e. the so-called afterglows. Other reactions that play a minor role towards CO_2 dissociation (~5 %) are electron impact ionization of CO_2 and electron impact dissociation from vibrationally excited CO_2 (i.e. CO_2 (V)) (see **Figure 5-17**).

Up to 60–70 % N_2, the sum of the rates due to electron impact dissociation and dissociation by N_2 metastable molecules drops only slightly upon increasing N_2 content, explaining why the effective CO_2 conversion drops only slightly, as shown in **Figure 5-13(b)**. In other words, upon adding N_2, the N_2 metastable molecules provide an extra dissociation mechanism for CO_2, explaining why the absolute CO_2 conversion rises (**Figure 5-13(a)**), but this is compensated by the lower CO_2 content in the mixture, leading to a slight drop in effective CO_2 conversion. Above 70 % N_2, however, both rates start decreasing due to the lower CO_2 concentration, which is not compensated by the higher N_2 concentration (and thus higher dissociation by N_2 metastable molecules), leading to a drop in the effective CO_2 conversion.

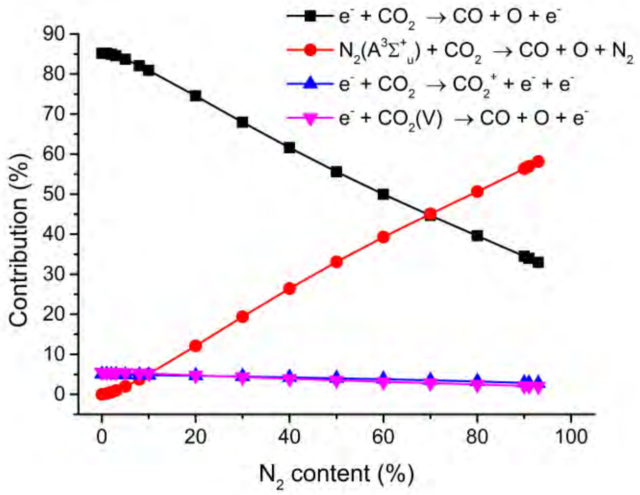

Figure 5-17. Relative contribution of the main processes leading to CO_2 conversion as a function of N_2 content, for a residence time of 0.73 s and a SEI of approx. 12 J cm^{-3}.

b) N_2O and NO_x formation

The most important formation and destruction processes for NO, NO_2 and N_2O are resp. presented in **Figure 5-18**, **Figure 5-19** and **Figure 5-20**, respectively.

Our calculations predict that NO is mainly formed during the afterglows, i.e. in between the micro discharge filaments, because it is dictated by heavy particle reactions. The dominant formation mechanism of NO is the reaction between O radicals and NO_2 molecules, forming NO and O_2 molecules.

This reaction is by far the most important for N_2 fractions below 95 % (see **Figure 5-18(a)**). Above 95 %, the reaction between N radicals and ozone, yielding the same products, becomes slightly more important. The dominant NO loss mechanism is the recombination with O atoms into NO_2 through a three-body reaction. This third body can be either CO_2 (mainly important for N_2 contents below 40 %) or N_2 (for N_2 contents between 40 and 90 %). For N_2 contents above 95 % the reaction with N atoms, yielding the formation of O and N_2, becomes most important. Other loss mechanisms are the formation of N_2O_3 (mainly at N_2 fractions below 70 %) and the reaction with electronically excited $N_2(a'^1\Sigma_u^-)$, forming N_2, N and O (at higher N_2 fractions). However, these reactions do not contribute for more than ~5–20 %.

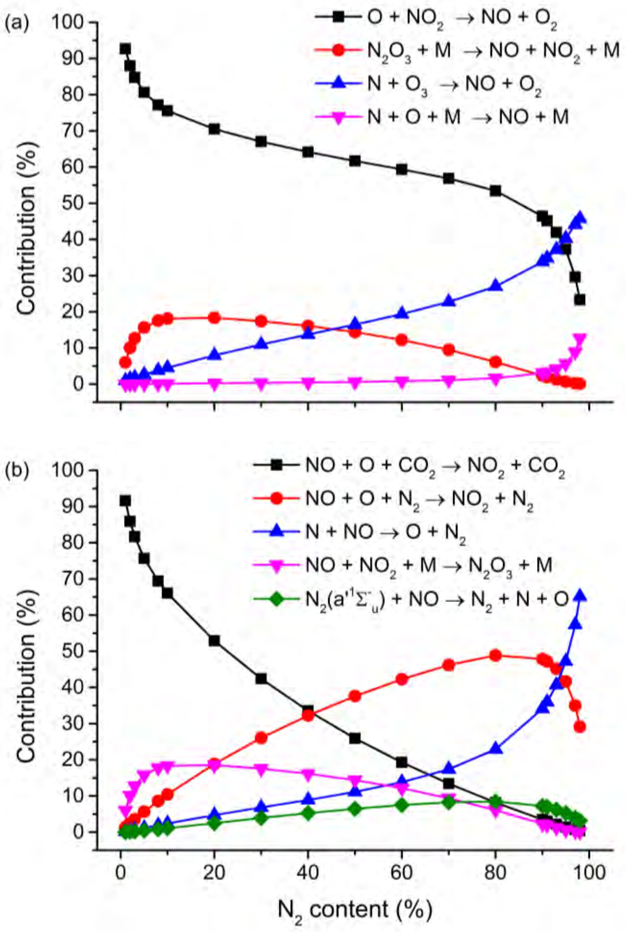

Figure 5-18. Relative contributions of the main formation (a) and loss (b) mechanisms of NO as a function of N_2 content, for a residence time of 0.73 s and a SEI of approx. 12 J cm^{-3}.

It is thus clear that there is an interplay between NO and NO_2, as was also observed in other modelling work, albeit for other conditions (i.e. a plasma jet expanding in humid air).[55] NO_2 is the main source of NO production and vice versa, as will be shown in **Figure 5-19**. This will also become clear from the reaction scheme in **Figure 5-21** below.

The NO_2 production also occurs mainly in between the filaments, attributed to heavy particle reactions. The only important process for NO_2 production is the three-body recombination between NO and O, with either CO_2 or N_2 as third body (at N_2 contents below and above 40 %, respectively; see **Figure 5-19(a)**). These are also the main loss mechanisms of NO, as was illustrated in **Figure 5-18(b)**. Some other processes, like the dissociation of N_2O_3 into NO and NO_2, the reaction between NO_3 and NO, forming two NO_2 molecules, or between NO_3 and O, forming NO_2 and O_2, also play a minor role (~5–20%) in the production of NO_2.

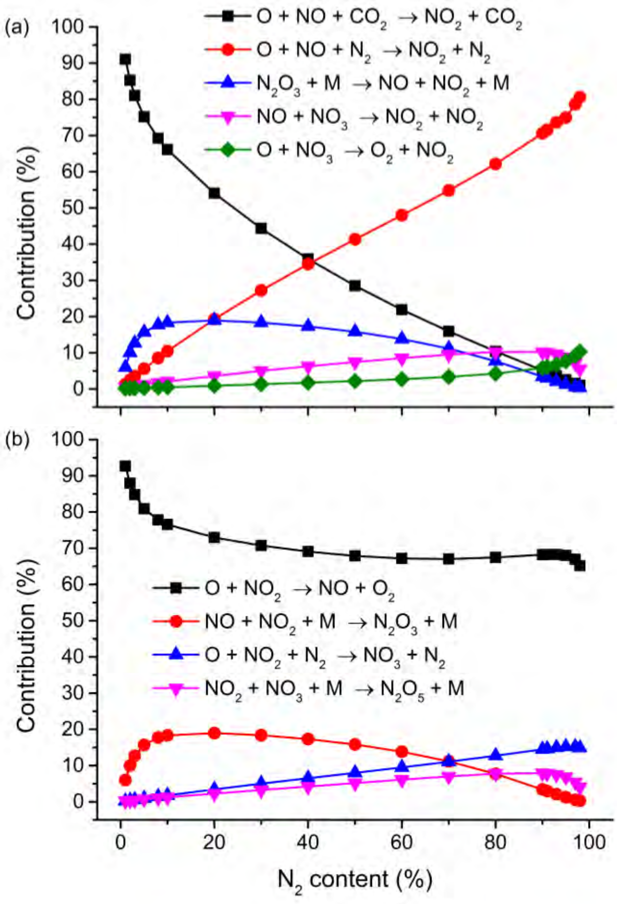

Figure 5-19. Relative contributions of the main formation (a) and loss (b) mechanisms of NO_2 as a function of N_2 content, for a residence time of 0.73 s and a SEI of approx. 12 J cm^{-3}.

As is clear from **Figure 5-19(b)**, the dominant loss mechanism of NO_2, for all N_2 fractions, is the reaction with O atoms, forming NO and O_2, which is also the most important formation mechanism of NO, see **Figure 5-18(a)** above. Some other loss mechanisms are the formation of N_2O_3 through three-body recombination with NO, the formation of NO_3 through three-body recombination with O (and N_2 as a third body), and the formation of N_2O_5 through three-body recombination with NO_3, but they clearly play a minor role, as appears from **Figure 5-19(b)**. Note that the rates of formation of N_2O_5 (by the three-body recombination reaction between NO_2 and NO_3; pink curve in **Figure 5-19(b)**) and its dissociation into NO_2 and NO_3 (upon collision with a neutral particle; blue curve in **Figure 5-19(a)**) are almost equal to each other. This indicates that these molecules are equally converted into each other, as will also be visible from the reaction scheme in **Figure 5-21** below.

Finally, in **Figure 5-20(a)** and **Figure 5-20(b)** we show the main N_2O formation and loss processes, respectively. The dominant formation mechanism of N_2O is the reaction between N and NO_2, forming N_2O and O. Only at N_2 fractions below 5 %, N_2O is mainly formed by the reaction between NCO and NO, forming N_2O and CO. Finally, the reaction between the metastable $N_2(A^3\Sigma_u^+)$ molecules and O_2, forming N_2O and O, also makes a minor contribution (~5–20%).

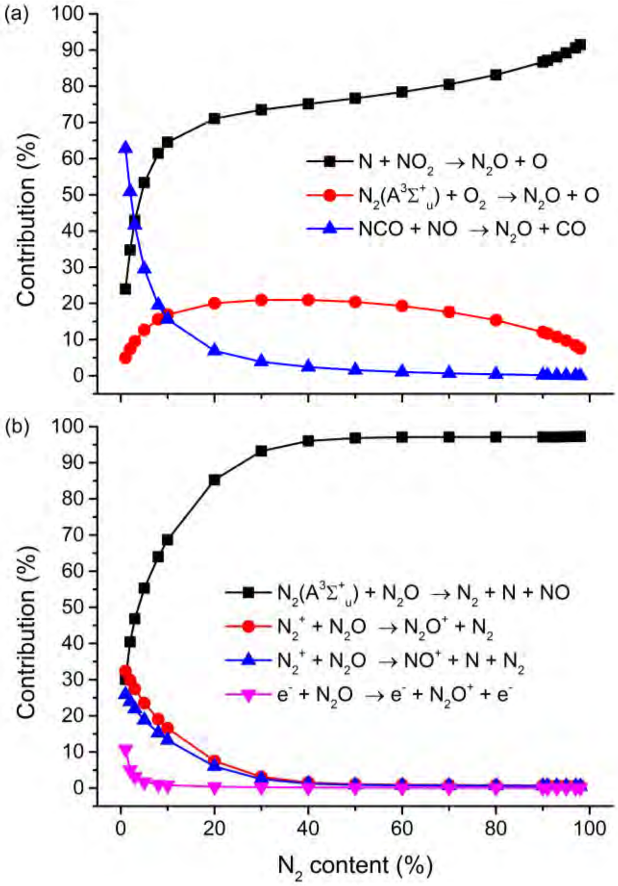

Figure 5-20. Relative contributions of the main formation (a) and loss (b) mechanisms of N_2O as a function of N_2 content, for a residence time of 0.73 s and a SEI of approx. 12 J cm^{-3}.

The main loss mechanism of N_2O is the reaction with $N_2(A^3\Sigma_u^+)$, forming N_2, N and NO. Only at low N_2 fractions, the charge transfer reactions with N_2^+ ions, forming either N_2O^+ and N_2, or NO^+, N and N_2, play a minor role (up to 30 % at 1 % N_2 fraction), while electron impact ionization also has a small, yet non-negligible contribution towards the destruction of N_2O (~5–10 % at 1 % N_2 fraction).

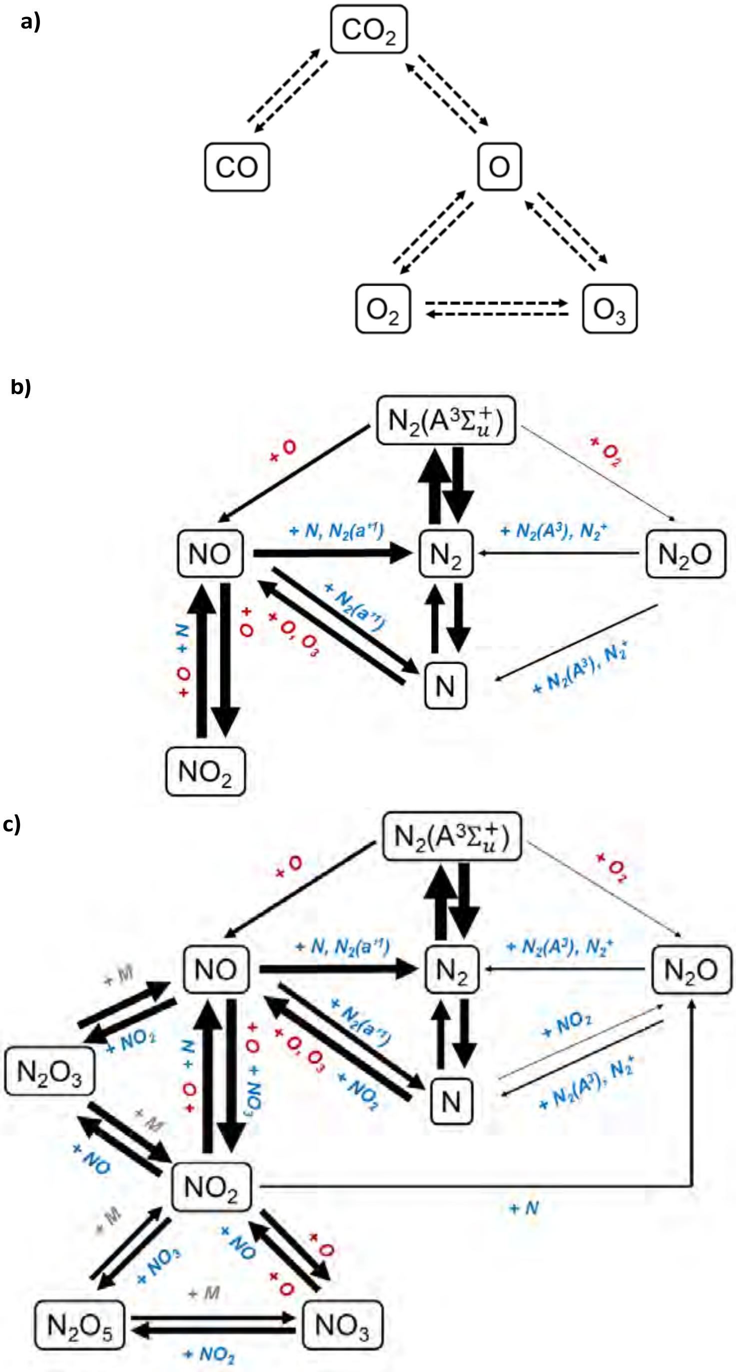

Figure 5-21. Reaction scheme to illustrate the main pathways of the N_2O and NO_x chemistry as predicted by the model. Reaction paths starting from CO_2 (a), initiation of the NO_x chemistry (b), complete overview of the N_2O and NO_x chemistry (c). The thickness of the arrows corresponds to the importance of the reactions.

With these data, we can compose an overall reaction scheme, as presented in **Figure 5-21**. The width of the full arrows is scaled according to the values of the time integrated reaction rates. **Figure 5-21(a)** illustrates the main products arising from CO_2, which will subsequently react with the N-compounds presented in **Figure 5-21(b)** and **Figure 5-21(c)**. Below the most important processes will be described. Initially, N_2 will be excited to its metastable state $N_2(A^3\Sigma_u^+)$, which will react with O atoms into the formation of NO, or with O_2 creating N_2O. Upon electron impact dissociation, N_2 will also be split in N atoms, which can react with both O and O_3 yielding NO. Subsequently, NO can be converted into NO_2 through a reaction with O, but NO_2 will also react back into NO upon reaction with O. This makes NO_2 the main source of NO production and vice versa, as is clear from **Figure 5-21(b)**. Furthermore, the N atoms, which are directly formed from N_2 dissociation, also play a role in the conversion between NO and NO_2. From NO there is also a pathway back to N_2 upon reaction with N or $N_2(a'^1\Sigma_u^-)$, and a pathway back to N upon reaction with $N_2(a'^1\Sigma_u^-)$. Furthermore, N_2O can also react back to N_2 and N upon reaction with $N_2(A^3\Sigma_u^+)$ and N_2^+. NO_2, on the other hand, has no significant pathway back to N_2 or N. This is all illustrated in **Figure 5-21(b)**, which represents the start of the different chemical pathways. This will be important to keep in mind in the further discussion below, as it will allow us to see whether we can intervene in the chemistry taking place.

Subsequently, a loop between NO, NO_2 and N_2O_3, as well as a loop between NO_2, NO_3 and N_2O_5, is created, as presented in **Figure 5-21(c)**. Furthermore, some of the NO_2 is also lost to N_2O through reaction with N radicals. The only way out of these loops, as mentioned above, is through the reaction of NO with N or $N_2(a'^1\Sigma_u^-)$, yielding either N or N_2 and an O atom, or through the reaction of N_2O with $N_2(A^3\Sigma_u^+)$ or N_2^+, leading to N_2, NO and a N atom, or to NO^+, N_2 and N or N_2O^+ and N_2, respectively.

From these reaction schemes it becomes obvious that, with respect to the plasma chemistry, there are two possibilities to prevent the formation of N_2O and NO_x compounds. The first one is to prevent the formation of the N-species involved in these reactions, i.e. metastable $N_2(A^3\Sigma_u^+)$ and N. This would only be possible in a plasma set-up in which all the electrons have an energy lower than 6.2 eV, which is the excitation threshold energy for the formation of $N_2(A^3\Sigma_u^+)$ through electron impact, while the dissociation threshold of N_2 into N lies at 9.75 eV. These conditions are not possible with a classic DBD. Set-ups which operate at lower average electron energies than a DBD are gliding arcs and microwave discharges. Indeed, in the model for the CO_2/N_2 microwave plasma by Heijkers et al.[17] it was shown that metastable $N_2(A^3\Sigma_u^+)$ is of minor importance. Nevertheless, the formation of NO_x was also observed, albeit through a different mechanism. Indeed, in a microwave plasma, the lower energy of the electrons causes vibrational excitation to become more important than electronic excitation and dissociation, and the vibrationally excited N_2 molecules react with O atoms to form N and NO, instead of the electronically excited N_2 in a DBD.

The second, more realistic option is to prevent the reaction between the N-species ($N_2(A^3\Sigma_u^+)$ and N) and the O-species (O, O_2 or O_3), which is the initial pathway for the formation of NO and N_2O (cf. **Figure 5-21(b)** above). In order to achieve this, one should look for quenching mechanisms of the $N_2(A^3\Sigma_u^+)$ metastable molecules, or possible scavengers, catalyst interactions or separation membranes for the N atoms and the O-species. Quenching of metastable molecules can be realized upon collision with other molecules. Although possible in theory, this will not be easy to realize in practice. Moreover, it is even not advisable, because exactly these metastable $N_2(A^3\Sigma_u^+)$ molecules aid in the conversion of CO_2 upon increasing N_2 content, as shown in **Figure 5-17**. With respect to the O-species, it is important to notice that in a DBD plasma operating in CO_2 all O_2 and O_3 is originating from O (cf. **Figure 5-21(a)**). Thus, when eliminating O, we automatically eliminate O_2 and O_3. Furthermore, from **Figure 5-21(c)** it becomes clear that if we only succeed in eliminating O_2 and O_3, but not the O atoms, there is still a pathway from NO_2 to N_2O upon reaction with N atoms. This stresses the importance of trying to eliminate especially the O atoms.

In the three cases suggested above to eliminate the O-species, the main idea is the same, i.e. to find an interaction which makes the O atoms or O_2 and O_3 molecules no longer available as reactant, and most importantly, this interaction has to be significantly faster than the reaction between $N_2(A^3\Sigma_u^+)$ and O or O_2; and between N and O or O_3. An example of a scavenger in the case of O is H, which reacts very fast with O to form OH and subsequently to H_2O. This effectively traps the O atoms, as was proven to be possible by a combined experimental and computational study of Aerts et al.[56] Another well-known scavenger of O is O_2, reacting to O_3. However, since the latter product reacts again to form O and O_2, and furthermore O_3 is also unwanted, it is not a suitable choice in this case. Furthermore, the advantage of H as a scavenger is that the scavenged product, H_2O, can be easily separated from the gas mixture. For the second option, i.e. catalyst interactions, the idea of using a catalyst with a high surface interaction with O atoms, allowing the recombination reaction to O_2 on its surface,[57] is not a good choice. Indeed, in this way the O_2 would be released in the plasma and it could undergo reactions again. A more advanced catalytic process that could be an option is an alternative form of chemical looping,[58,59] in which the O (or O_2) is captured in the plasma set-up and then used as oxidizing agent in a second set-up. The third method, based on separation membrane technology, could be considered as similar to the catalyst, but instead of recombining the O to O_2 on the surface, the O atoms (or O_2 molecules) would be transported away from the reaction mixture. A last option could be the combination of a solid oxide electrolyser cell with a plasma set-up.[60] It should be realized, however, that the options mentioned above for catalysts, membranes and electrolyser cells, have only been applied up to now to separate O_2 from the gas mixture, and not the O atoms, while it is clear, as mentioned above, that in order to avoid the formation of all NO_x compounds, we need to be one step ahead and thus, we need to be able to trap already the O atoms, which is still a challenge.

If one of these concepts could be realized, it would eliminate the need for a pre-purification (N_2) or post-purification (denox) step, and thus reduce the cost of the overall process. Indeed, besides the N_2O and NO_x formation, the presence of N_2 in the gas mixture has no detrimental effect, as the effective CO_2 conversion remains more or less constant up to a N_2 fraction of 50 %, as shown in **Figure 5-13(b)**, because the lower CO_2 fraction in the mixture is compensated for by the higher absolute CO_2 conversion due to the $N_2(A^3\Sigma_u^+)$ metastable molecules.

Future work should also address other impurities such as noble gases (e.g. He and Ar) or molecular gases such as H_2 and hydrocarbons. The presence of He and Ar should not affect the chemical pathways and products. They will mainly influence the electrical characteristics of the plasma. More specifically, their presence will lower the breakdown voltage. This was demonstrated in previous work from our own group and others.[61,62] Only for very high concentrations, the addition of noble gases would lead to a diluting effect.[63]

H_2 and hydrocarbons, on the other hand, will have an important influence on the chemical pathways and products. For example, we expect H_2 and CH_4 to have the same influence as reported in our previous work.[56] Both will be split in H atoms upon electron impact reactions, and the latter will react very fast with the O atoms present, leading to OH and subsequently to H_2O. As mentioned above, this might eliminate the production of NO_x compounds. Furthermore, this might lead to a slightly increased CO_2 conversion, since the O atoms are being directed to a liquid product.

3.4. Conclusions

The purpose of this study was to obtain a better understanding of the effect of N_2 (in the range between 1 and 98 %) on the CO_2 splitting in a DBD plasma, by means of an extensive combined experimental and computational study. We focused on the effect on the CO_2 conversion, both absolute and effective, and the energy efficiency, as well as on the formation of N-containing by-products, like N_2O and NO_x compounds.

We made a comparison between the measured CO_2 and N_2 conversions and the energy efficiency for CO_2 conversion, and the corresponding values calculated by means of a 0D chemical kinetics model, for the entire range of N_2 fractions. A good agreement was reached between the experimental data and the model predictions, indicating that the model includes the correct plasma chemistry and can be used to describe the main production and loss pathways for the various compounds. This allows us to gain sufficient insight in the entire process, and to propose solutions for improving the process in the future.

Our study clearly reveals that the presence of N_2 in the gas mixture up to 50 % barely influences the effective CO_2 conversion and the corresponding energy efficiency, in spite of the lower CO_2 fraction in the mixture (and thus the lower CO_2 amount available for conversion). The reason is that N_2 enhances the absolute CO_2 conversion, due to the dissociation of CO_2 upon collision with $N_2(A^3\Sigma_u^+)$ metastable molecules, and both effects compensate each other. On the other hand, N_2 admixtures above 50 % result in an exponential drop in the effective CO_2 conversion and energy efficiency, because more and more energy is consumed by N_2 molecules, and not used anymore for CO_2 conversion. This means that, for mixtures containing up to 50 % N_2, no pre-separation steps are necessary with respect to the effective conversion and energy efficiency.

On the other hand, the presence of N_2 in the mixture leads to the formation of N_2O and several NO_x compounds, with concentrations in the range of several 100 ppm. While these concentrations are too low to be considered useful for nitrogen fixation, they will give rise to several environmental problems. N_2O is an even more potent greenhouse gas than CO_2, with a GWP of 298 $CO_{2,equivalent}$, while NO and NO_2 are responsible for acid rain and the formation of ozone and a wide variety of toxic products. Thus, from the point of view of by-product formation, it would be necessary to use either a pre-purification (N_2) or post-purification (denox) step.

Our detailed chemical kinetics analysis tells us that the production of these N_2O and NO_x compounds starts through a reaction between metastable $N_2(A^3\Sigma_u^+)$ molecules and either O or O_2 and between N atoms and either O or O_3; yielding the formation of NO or N_2O. Subsequently, the N is trapped in three reaction loops between the various NO_x compounds and N_2O, and the only way out is through the reaction of NO or N_2O with either N or $N_2(A^3\Sigma_u^+)$, yielding the formation of either N or N_2 and O atoms. On the plasma chemistry level, we believe that the only option to prevent the formation of N_2O and NO_x compounds is by inhibiting the reaction between the N-species ($N_2(A^3\Sigma_u^+)$ and N) and the O species (O, O_2 or O_3). To realize this, we should search for possible scavengers, catalyst interactions or separation membranes, especially for the O atoms, since this would also inhibit the formation of O_2 and O_3. If this could be successful, it would effectively eliminate the need for a pre-purification (N_2) or post-purification (denox) step.

4. References

1 M. Aresta, A. Dibenedetto and A. Angelini, *Chem. Rev.*, 2014, **114**, 1709–1742.

2 L. F. Khilyuk, G. V. Chilingar, J. O. Robertson and B. Endres, in *Gas Migration Events Preceding Earthquakes*, Gulf Professional Publishing, 2000, pp. 238–247.

3 G. Karavalakis, M. Hajbabaei, T. D. Durbin, K. C. Johnson, Z. Zheng and W. J. Miller, *Energy*, 2013, **50**, 280–291.

4 A. Indarto, J. Choi, H. Lee and H. Song, *Energy*, 2006, **31**, 2986–2995.

5 N. Moreau, S. Pasquiers, N. Blin-Simiand, L. Magne, F. Jorand, C. Postel and J.-R. Vacher, *J. Phys. D. Appl. Phys.*, 2010, **43**, 285201.

6 O. Koeta, N. Blin-Simiand, W. Faider, S. Pasquiers, A. Bary and F. Jorand, *Plasma Chem. Plasma Process.*, 2012, **32**, 991–1023.

7 G. Horvath, N. J. Mason, L. Polachova, M. Zahoran, L. Moravsky and S. Matejcik, *Plasma Chem. Plasma Process.*, 2010, **30**, 565–577.

8 J. Legrand, A. Diamy, R. Hrach and V. Hrachova, *Vacuum*, 1997, **48**, 671–675.

9 A. Majumdar, J. F. Behnke, R. Hippler, K. Matyash and R. Schneider, *J. Phys. Chem. A*, 2005, **109**, 9371–7.

10 C. D. Pintassilgo, C. Jaoul, J. Loureiro, T. Belmonte and T. Czerwiec, *J. Phys. D. Appl. Phys.*, 2007, **40**, 3620–3632.

11 J. L. Jauberteau, I. Jauberteau, M. J. Cinelli and J. Aubreton, *New J. Phys.*, 2002, **4**, 1–13.

12 S. Y. Savinov, H. Lee, H. Keun and B. Na, *Plasma Chem. plasma Process.*, 2003, **23**, 159–173.

13 J. Legrand, A. Diamy, R. Hrach and V. Hrachova, *Contrib. to Plasma …*, 1997, **37**, 521–537.

14 B. S. Patil, Q. Wang, V. Hessel and J. Lang, *Catal. Today*, 2015, **256**, 49–66.

15 R. Aerts, W. Somers and A. Bogaerts, *ChemSusChem*, 2015, **8**, 702–716.

16 A. Indarto, D. R. Yang, J.-W. Choi, H. Lee and H. K. Song, *J. Hazard. Mater.*, 2007, **146**, 309–15.

17 S. Heijkers, R. Snoeckx, T. Kozák, T. Silva, T. Godfroid, N. Britun, R. Snyders and A. Bogaerts, *J. Phys. Chem. C*, 2015, **119**, 12815–12828.

18 T. Silva, N. Britun, T. Godfroid and R. Snyders, *Plasma Sources Sci. Technol.*, 2014, **23**, 25009.

19 R. Dorai and M. J. Kushner, *J. Phys. D. Appl. Phys.*, 2003, **36**, 1075–1083.

20 D. S. Stafford and M. J. Kushner, *J. Appl. Phys.*, 2004, **96**, 2451–2465.

21 R. Snoeckx, R. Aerts, X. Tu and A. Bogaerts, *J. Phys. Chem. C*, 2013, **117**, 4957–4970.

22 A. Fridman, *Plasma chemistry*, Cambridge University Press, New York, 2008.

23 U. Kogelschatz, *Plasma Chem. plasma Process.*, 2003, **23**, 1–46.

24 W. Van Gaens and A. Bogaerts, *J. Phys. D. Appl. Phys.*, 2014, **47**, 79502.

25 R. a Arakoni, A. N. Bhoj and M. J. Kushner, *J. Phys. D. Appl. Phys.*, 2007, **40**, 2476–2490.

26 H. J. Gallon, University of Manchester, 2010.

27 A. Indarto, N. Coowanitwong, J.-W. Choi, H. Lee and H. K. Song, *Fuel Process. Technol.*, 2008, **89**, 214–219.

28 K. Thanyachotpaiboon, S. Chavadej, T. A. Caldwell, L. L. Lobban and R. G. Mallinson, *AIChE J.*, 1998, **44**, 2252–2257.

29 G. Scarduelli, G. Guella, D. Ascenzi and P. Tosi, *Plasma Process. Polym.*, 2011, **8**, 25–31.

30 B. Fidalgo, A. Domínguez, J. Pis and J. Menéndez, *Int. J. Hydrogen Energy*, 2008, **33**, 4337–4344.

31 T.-S. Kim, S. Song, K.-M. Chun and S. H. Lee, *Energy*, 2010, **35**, 2734–2743.

32 D. Li, X. Li, M. Bai, X. Tao, S. Shang, X. Dai and Y. Yin, *Int. J. Hydrogen Energy*, 2009, **34**, 308–313.

33 A. Beloqui Redondo, E. Troussard and J. a. van Bokhoven, *Fuel Process. Technol.*, 2012, **104**, 265–270.

34 A. E. E. Putra, S. Nomura, S. Mukasa and H. Toyota, *Int. J. Hydrogen Energy*, 2012, **37**, 16000–16005.

35 *http://www.me.berkeley.edu/gri_mech/index.html*.

36 S. Pancheshnyi, B. Eismann, G. J. M. Hagelaar and L. C. Pitchford, 2008.

37 G. J. M. Hagelaar and L. C. Pitchford, *Plasma Sources Sci. Technol.*, 2005, **14**, 722–733.

38 I. Stefanovic, N. ~K. Bibinov, A. ~a. Deryugin, I. ~P. Vinogradov, A. ~P. Napartovich and K. Wiesemann, *Plasma Sour. Sci. Technol.*, 2001, **10**, 406.

39 I. W. M. Smith and G. Yarwood, *Faraday Discuss. Chem. Soc.*, 1987, **84**, 205–

220.

40 S. Teodoru, Y. Kusano and A. Bogaerts, *Plasma Process. Polym.*, 2012, **9**, 652–689.

41 R. Atkinson, D. L. Baulch, R. a. Cox, J. N. Crowley, R. F. Hampson, R. G. Hynes, M. E. Jenkin, M. J. Rossi and J. Troe, *Atmos. Chem. Phys. Discuss.*, 2003, **3**, 6179–6699.

42 G. Black, T. G. Slanger, G. a S. T. John and R. a Youngt, *Chem. Phys.*, 1969, **51**, 116–121.

43 N. Pinhão, A. Moura, J. B. Branco and J. Neves, *Int. J. Hydrogen Energy*, 2016, **41**, 9245–9255.

44 R. Snoeckx, M. Setareh, R. Aerts, P. Simon, A. Maghari and A. Bogaerts, *Int. J. Hydrogen Energy*, 2013, **38**, 16098–16120.

45 R. Aerts, T. Martens and A. Bogaerts, *J. Phys. Chem. C*, 2012, **116**, 23257–23273.

46 *Convention on Long-Range Transboundary Air Pollution*, 1979.

47 N. Fontaine and A. Neyts-Uytterbroeck, *Off. J. Eur. Communities*, 2001, **309**, 22–30.

48 T. J. Pilusa, *Aerosol Air Qual. Res.*, 2012, 994–1006.

49 H.-G. Pöttering and G. Gloser, *Off. J. Eur. Communities*, 2007, **171**, 1–16.

50 *Integrated Pollution Prevention and Control: Reference Document on Best Available Techniques for Large Combustion Plants*, European Commision, 2006.

51 C. Baird and M. Cann, *Environmental Chemistry Fourth Edition*, W. H. Freeman and company, New York, 2008.

52 V. Smil, *Enriching the earth: Fritz Haber, Carl Bosch, and the transformation of world food production.*, MIT press, 2004.

53 K. Skalska, J. S. Miller and S. Ledakowicz, *Sci. Total Environ.*, 2010, **408**, 3976–3989.

54 S. Roy, M. S. Hegde and G. Madras, *Appl. Energy*, 2009, **86**, 2283–2297.

55 W. Van Gaens and a Bogaerts, *Plasma Sources Sci. Technol.*, 2014, **23**, 35015.

56 R. Aerts, R. Snoeckx and A. Bogaerts, *Plasma Process. Polym.*, 2014, **11**, 985–992.

57 Y. C. Kim and M. Boudart, *Langmuir*, 1991, **7**, 2999–3005.

58 J. Adanez, A. Abad, F. Garcia-Labiano, P. Gayan and L. F. de Diego, *Prog. Energy Combust. Sci.*, 2012, **38**, 215–282.

59 M. M. Hossain and H. I. de Lasa, *Chem. Eng. Sci.*, 2008, **63**, 4433–4451.

60 Y. Tagawa, S. Mori, M. Suzuki, I. Yamanaka, T. Obara, J. Ryu and Y. Kato, *Kagaku Kogaku Ronbunshu*, 2011, **37**, 114–119.

61 M. Ramakers, I. Michielsen, R. Aerts, V. Meynen and A. Bogaerts, *Plasma Process. Polym.*, 2015, **12**, 755–763.

62 N. R. Pinhão, a. Janeco and J. B. Branco, *Plasma Chem. Plasma Process.*, 2011, **31**, 427–439.

63 V. Goujard, J.-M. Tatibouët and C. Batiot-Dupeyrat, *Plasma Chem. Plasma Process.*, 2011, **31**, 315–325.

CHAPTER 6

Critical assessment of plasma-based CO_2 conversion

1. Summary of literature and results of this thesis

In this chapter, the present state-of-the-art with respect to plasma-based CO_2 conversion is addressed, focusing on a critical assessment of the advantages and disadvantages of the various set-ups described in **Chapter 1**. The aim is to unveil their future challenges, risks and opportunities for successful implementation. Several options are being investigated, including both pure CO_2 splitting into CO and O_2, as well as the reaction with other gases, like CH_4 (dry reforming of methane), H_2O (artificial photosynthesis) and H_2 (hydrogenation). By adding a hydrogen source, the main aim is to produce value-added chemicals and/or fuels, i.e. syngas, hydrocarbons and valuable oxygenates, such as methanol, formaldehyde and formic acid. As mentioned in **Chapter 1**, most research on plasma-based CO_2 conversion is performed with dielectric barrier discharges (DBD), microwave (MW) plasmas and gliding arc (GA) discharges, with a main focus on improving the energy efficiency of the conversion, as well as the selectivity towards value-added chemicals, in combination with catalysis.

In order for plasma technology to be competitive with traditional and novel technologies, as described in Chapter 1, we can define two main goals. First of all, plasma technology will have to be competitive with electrolysis, which is its main competitor, having the same advantage to rely on all sorts of renewable electricity. For electrochemical water splitting, commercial energy efficiencies of 65–75 % are obtained, hence, the goal of plasma technology should be at least to aim for an energy efficiency comparable to this, and better than the thermal equilibrium energy efficiencies of ~ 45–60 % (see **Chapter 1**). Secondly, when comparing with other novel technologies which can make use of direct solar energy, such as solar thermochemical conversion, we should look at the solar-to-fuel conversion efficiency. As such, for novel technologies, a solar-to-fuel conversion efficiency of approximately 20 % is considered industrially competitive, when looking at the production of syngas,[1] as will be elaborated in section 2.3 below. When relying on solar energy, taking a solar panel efficiency of 25 %,[2] and a plasma conversion energy efficiency of 60–80 % towards the syngas components CO and H_2, this would yield a competitive solar-to-fuel efficiency of 15–20 %. Hence, in the following critical assessment of plasma-based CO_2 conversion technology, we should keep in mind that—from an energy efficiency point of view—to be considered as a competitive and worthy alternative, plasma technology should aspire an energy efficiency of at least 60 %, at least when focussing on the production of syngas.

On the other hand, the conversion of syngas into more suitable fuels and chemicals through the Fischer-Tropsch process or for methanol synthesis (and subsequently methanol or ethanol to olefin) is a very energy intensive process. As a result, the energy efficiency requirements for the direct production of these compounds is highly dependent on the formed products and the target energy cost to be competitive can be significantly lower for a direct one-step process. For example a solar-to-methanol conversion efficiency of 7.1 % is already economically feasible.[1] In this case, a plasma conversion energy efficiency of 30 % (instead of the above 60 %) would already suffice. This is very important and it shows that, in contrast to the indirect approach through syngas, for the direct oxidative pathway—which aims to synthesize oxygenated liquid products in one step—the energy efficiency target is much lower, depending on the products formed, due to the circumvention of the energy intensive conversion step of syngas into the desired liquids. The possibility to proceed through this direct oxidative pathway is one of the key-benefits of plasma technology, and in theory this pathway is the most promising. For now, however, a lot of research is still needed to understand the underlying processes, in order to improve the yield of the desired (oxygenated) liquid products.[3] Hence, the analysis in this chapter will be based on the production of the syngas components CO and H_2 using plasma technology, based on the energy efficiency target of 60 %. Nevertheless, it is important to keep in mind that this 60 % energy efficiency target applies to syngas production, but the target thus changes completely—it decreases by a factor two to three—when the direct oxidative pathway towards liquids can be successfully realized using plasma technology.

1.1. CO_2 splitting

As outlined in **Chapter 1**, in the case of pure CO_2 splitting, the dominant products are CO and O_2 in a 2-to-1 ratio. Hence, this is a simple chemical process and there are no concerns regarding the complexity and wide variety of products that can be formed—as in the case with an added H-source—and one does not have to contemplate about how to steer the different selectivities. As such, the research can solely focus on optimizing the CO_2 conversion and the energy efficiencies, and be judged on those indicators.

1.1.1. DBD plasmas

Although many papers are already published on CO_2 conversion by DBD, detailed systematic studies presenting values for both conversion and energy efficiency in a DBD appear to be very scarce. The most detailed studies focusing on a wide range of conditions have been performed by Aerts et al.,[4] Paulussen et al.,[5] Yu et al.[6] and Ozkan et al.[7] We will combine the most important observations from these works and complement them with various other findings in literature, to sketch a complete image with the data available to date.

The most commonly used geometry to study CO_2 conversion uses a coaxial DBD reactor,[4–7] while parallel plate reactors[8] (see **Chapter 1; Figure 1-13**) are mainly used to study the system with advanced optical diagnostics.[9] To achieve higher values of CO_2 conversion and energy efficiency, several approaches have already been investigated, including changing the applied frequency, applied power, gas flow rate, discharge length, discharge gap, reactor temperature, dielectric material, electrode material, mixing with gases, i.e. Ar, He, N_2, and introducing (catalytic) packing materials. Furthermore, extensive modelling has also been performed to obtain a more fundamental insight in the plasma chemistry in a DBD and in turn aid in the improvement of future experiments. **Figure 6-1** summarizes most of the data available in literature. From this figure several main trends become clear. First of all, the conversion increases with increasing specific energy input (SEI), while the energy efficiency generally decreases with increasing SEI, especially above an SEI of 10 eV/molecule. When plotting the energy efficiency as a function of the conversion, it is clear that most of the results are situated below an energy efficiency of 15 % and a conversion of 40 %, with some exceptions. The highest conversions of 42 % are obtained for packed bed DBDs and the highest energy efficiency of 23 % with a pulsed power DBD. It is important to note that some of the data in this figure has been recalculated to represent coherent values of conversions and energy efficiencies. For instance, in plasma research the mixture is sometimes diluted with He, Ar or N_2 to obtain an easier ignitable and more stable discharge, but as will be mentioned below, this influences the results—an effect which was among others not always taken into account in the original data. A more detailed influence of the different parameters is discussed below.

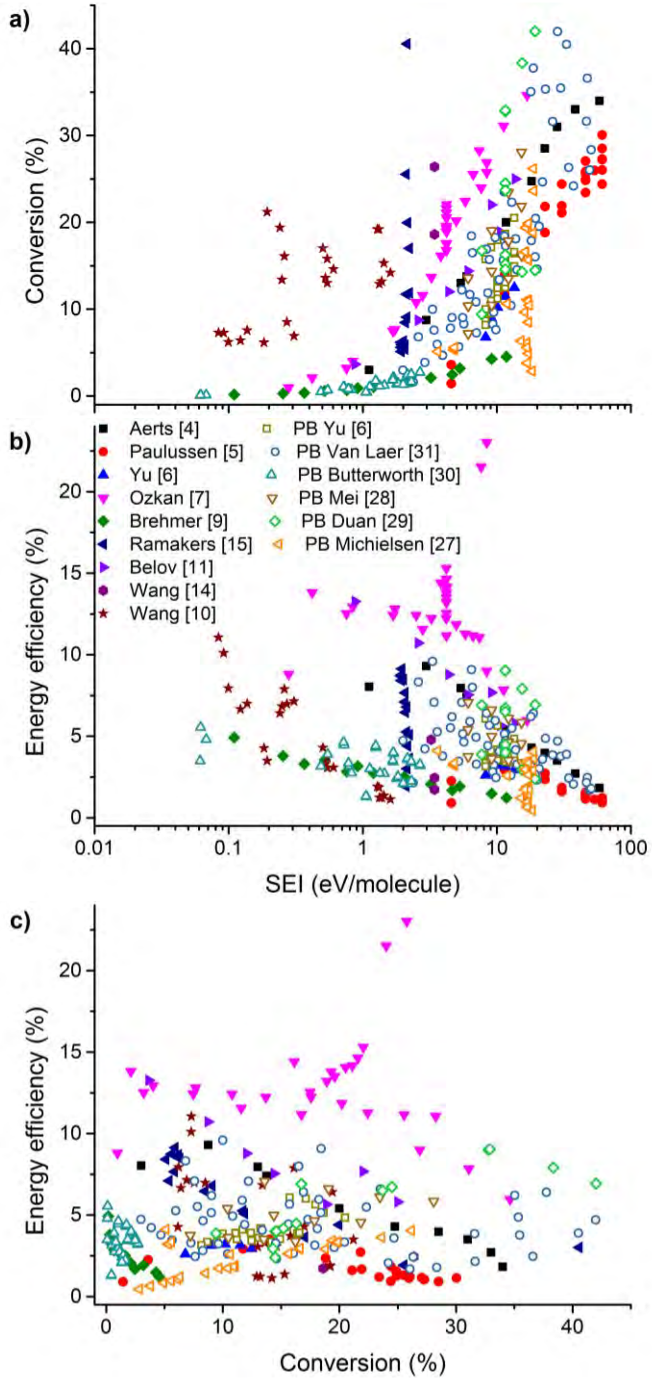

Figure 6-1. Experimental data collected from literature for CO_2 splitting in a DBD, showing the conversion (a) and energy efficiency (b) as a function of the SEI, as well as the energy efficiency as a function of the conversion (c). The open symbols represents the data with a packed bed (PB). Note, some of the data has been recalculated from the original references to take, among others, dilution effects into account.

It is well known that the specific energy input (SEI), which is defined as the plasma power divided by the gas flow rate (see **Chapter 2**; eq.2-4), is the dominant determining factor for the conversion and energy efficiency.[4,6,7,10] It has also been observed that the same values of SEI defined by different combinations of plasma power and gas flow rate can result in different conversions. It is the gas flow rate, and hence the residence time, which has the most important effect, while the effect of the power is less significant. As such, a lower power with lower gas flow rate results in a higher conversion and energy efficiency than a higher power with higher gas flow rate for the same SEI.[4,7]

Possible geometry modifications are the discharge length and discharge gap. Yu et al.[6] found that varying the discharge length for a fixed SEI has no significant effect on the discharge characteristics, the conversion and energy efficiency. On the other hand, the discharge gap appears to affect the discharge behaviour, and thus also the CO_2 conversion. Aerts et al.[4] found that above a certain gap width (3.3 mm in their case) less streamer formation occurs, leading to a decrease in effective plasma volume and hence lower conversions and efficiencies.

Furthermore, Aerts et al.[4] also reported that the applied frequency seems to have a negligible effect on the conversion and energy efficiency. However, the plasma appears more filamentary at high frequency (75 kHz) compared to a low frequency (6 kHz). Ozkan et al.[7], however, found that both the conversion and energy efficiency decrease slightly upon increasing the frequency from 15 to 30 kHz. This could be explained by Paulussen et al.[5] who suggested that the optimum discharge frequency depends on the power input, and as such it cannot be unambiguously stated that higher or lower frequencies give rise to an increased CO_2 conversion and energy efficiency.

In thermochemical reactions, the gas temperature is one of the most important parameters governing the reaction rates. For the plasma-based conversion in a DBD, however, the effect of temperature is not that clear. Paulussen et al.[5] observed a slight and linear increase in the conversion from 26 to 28.5 % when the inlet gas is heated from 303 K to 443 K. Ozkan et al.[7] on the other hand reported that the wall and gas temperature should remain as low as possible. In addition, Wang et al.[10] detected an increase in conversion of 0.5–3 % when using an external fan to cool the reactor, and they suggested that higher flow rates are preferred, since the latter remove large amounts of heat from the reactor. Brehmer et al.[9] noted a big effect of the wall temperature on the O_3 density and suggested that recombination of CO and O on the wall would also increase with rising wall temperatures.

The effect of the dielectric material used in the DBD reactor is another topic of debate. By studying the formation of a conductive coating, Belov et al.[11] observed that the conductivity of the dielectric might be the most crucial parameter affecting the discharge properties. Aerts et al.[4] reported no significant effect between quartz or alumina under a wide range of conditions, although it was concluded that alumina has several advantages in terms of reactor stability. Ozkan et al.[7] found that alumina and quartz perform better than mullite and Pyrex, and that a thicker dielectric leads to a higher conversion and energy efficiency.[7] More sophisticated dielectrics materials were created and tested by Li et al.[12,13] and Wang et al.[14] The former investigated the influence of $Ca_{0.8}Sr_{0.2}TiO_3$ (CST) with 0.5 wt% $Li_2Si_2O_5$ as the dielectric barrier and achieved an improvement of the conversion by up to a factor 9, compared to silica glass. Wang et al.[14] investigated the performance of CST ceramics with various amounts of CaO-B_2O_3-SiO_2 (CBS) glass addition (0.5–5 wt%). The addition of 5.0 wt% CBS resulted in an increase of the conversion by a factor of 2.6 and the energy efficiency almost tripled compared to that at 0.5 wt% CBS. However, from the calculation of the plasma power in both studies, it appears that the more sophisticated dielectrics mainly increase the efficiency between input power and plasma power, and not the effective plasma conversion energy efficiency. Nevertheless, these dielectrics allow to operate under lower voltages, which could be beneficial for certain processes. Summarized, different dielectrics may allow for easier igniting and streamer formation, but not necessary more energy efficient plasma conversion chemistry.

Besides the dielectric material also the electrode material can be varied. Wang et al.[10] studied the effect of changing—or coating—the high voltage electrode and obtained an order of activity of Cu>Au>Rh>Fe~Pt~Pd. The Cu and Au electrodes yielded a relative increase in the conversion of a factor 1.5 compared to an Fe electrode. Furthermore, the maximum energy efficiency of the Au electrode was almost three times higher than the energy efficiency for the Rh electrode under the same conditions. However, besides the fact that some of these electrodes or coatings are more expensive—compared to the inert stainless steel electrode—they also are susceptible to chemical erosion (i.e. oxidation) and plasma sputtering (as observed for Au).

As mentioned above, some researchers have also added inert gases, such as N_2, Ar and He, to ignite the plasma more easily. This also has several effects on the discharge characteristics, conversion, energy efficiency and even by-product formation in the case of N_2. The addition of He and Ar leads to an increase of the CO_2 conversion, but the effective conversion decreases, since there is less CO_2 present in the mixture and the increased conversion is not sufficient to counteract this drop in CO_2 fraction. As a result, the energy efficiency decreases as well.[10,15,16] The addition of N_2, on the other hand, shows a completely different behaviour. Snoeckx et al.[17] discovered that the presence of N_2 in the gas mixture up to 50 % barely influences the effective CO_2 conversion and the corresponding energy efficiency. Indeed, N_2 enhances the absolute CO_2 conversion, due to the dissociation of CO_2 upon collision with N_2 metastable molecules, and this effect is strong enough to compensate for the lower CO_2 content in the mixture. However, the presence of N_2 in the mixture leads to the formation of unwanted by-products, i.e., N_2O and several NO_x compounds, with concentrations in the range of several 100 ppm, which will give rise to severe air pollution problems.

Other modifications being investigated to improve the CO_2 conversion in a DBD reactor are the use of micro plasma reactors,[18] a hybrid DBD reactor on the surface of a SOEC,[19] and a pulsed power supply.[7] A micro plasma reactor provides a stronger electric field and a higher concentration of reactive species, while offering better control of the processing parameters.[18] The DBD plasma on the surface of an SOEC allows the in situ exclusion of O_2 during CO_2 splitting, resulting in an increase of a factor 4 for the conversion.[19] Finally, the use of a power supply in pulsed or so-called burst mode, instead of injecting the power in a continuous AC mode, is reported to give an increase of conversion and energy efficiency by a factor 1.5 for a duty cycle of 50 %.[7]

Besides all the experimental work, great advances have also been made in modelling the plasma chemistry for CO_2 conversion in a DBD.[4,16,20–24] The main findings are that the splitting of CO_2 is dominated by electron impact reactions with ground state molecules, and predominantly by electron impact excitation followed by dissociation. Electron impact ionization is also important, but is compensated by the fact that a large fraction of the formed ions will eventually recombine, resulting in the formation of CO_2. Splitting from the vibrationally excited states is found to be of minor importance in a DBD.[4,20] A reduced chemistry model, consisting of only 9 species and 17 reactions was presented by Aerts et al.,[4] which allowed to identify the main dissociation mechanisms. A 1D fluid model, with roughly the same chemistry, was developed by Ponduri et al.[22] Furthermore, recently a thorough examination of the cross sectional data was performed,[25,26] as well as a careful examination of all rate coefficients and a comparison of the performance of different models.[21]

Finally, as mentioned in **Chapter 1**, a packing can be added to the DBD reactor to enhance the conversion and energy efficiency. In the case of pure CO_2 splitting, the addition of a packing will not influence the formation of products, since no hydrogen source is available. Hence, most of the work focuses on increasing the conversion and energy efficiency by physical effects. Generally, when tested, the CO_2 conversion in packed bed DBD reactors is always higher than in the corresponding empty reactors, but **Figure 6-1** obviously illustrates that the highest efficiencies found to date are for regular DBD reactors—varying the different parameters discussed above. Nevertheless, at high conversions we see that the packed bed reactors are generally more efficient. As such, in general, adding a packing seems to allow to operate at the same energy efficiency, but significantly increasing the conversion. Several materials have already been investigated, more specifically, glass wool,[27] glass beads,[28] silica gel,[6] quartz,[6] quartz wool,[27,29] quartz sand,[29] Al_2O_3,[6,27,29,30] $CaTiO_3$,[6] ZrO_2,[27,31] SiO_2,[27]

$BaTiO_3$,[27,28,30] MgO,[29] and CaO.[29] The best results have been obtained for ZrO_2[31] and CaO,[29] with conversions in the range of 30–45 % and energy efficiencies in the 5–10 % range (see **Figure 6-1**). One of the more recent and interesting works is from Butterworth et al.[30] The authors stated that the testing of different materials should be performed according to a more predefined protocol, since the packing particle size affects the discharge phenomena and the chemistry within the packed bed. More specifically, the efficacy of CO_2 conversion is strongly affected by the particle size, and small particle sizes (180–300 µm) increase the CO_2 conversion up to 70 %. However, they also increase the reactor breakdown voltage and they lead to partial discharging, i.e. a drop in the fraction of the reactor where plasma formation occurs. Comparison with the work of other researchers shows that quite often, insufficient electric field strengths are applied for complete reactor discharging to occur. Hence, packing materials for plasma catalysis should be tested with equivalent reactor operating conditions. It is therefore important to ensure that either (a) complete discharging occurs in the reactor, or (b) the partial reactor discharging is quantified.[30] A similar message, regarding the need to compare material performances with similar reactor set ups, is given in the recent work of Michielsen et al.[27]

From all these data in literature we can conclude that a DBD reactor can provide reasonable conversions up to 40 %, but the energy efficiency is still at least a factor 3–4 away from the necessary 60 % mark. DBDs have the advantage to be very scalable and easy to operate, but their current energy efficiency makes it doubtful that they will be the most suitable technology for pure CO_2 splitting.

1.1.2. MW and RF plasmas

Dissociation of CO_2 using MW and RF discharges was already extensively studied both theoretically and experimentally in the 1970–80s,[32] and gained renewed interest with the current global challenges regarding CO_2 emissions. Already back in the 1970–80s, it was concluded that these MW discharges were ideal for obtaining high energy efficiencies for CO_2 conversion, due to a combination of relatively high electron density and low reduced electric field (see **Chapter 1**). These conditions favour the excitation of the asymmetric mode vibrational levels of CO_2.[33] This efficient dissociation channel is a combination of several reaction steps—excitation of the lower vibrational levels by electrons, followed by collision between vibrational levels, gradually populating the higher levels, and dissociation of the excited vibrational levels stimulated by collisions with other molecules—covering a whole spectrum of vibrational levels.[34]

The main set-ups used for CO_2 conversion are the (surfaguide) MW discharge (2.45 GHz and 915 GHz), as well as RF discharges (13.56 MHz). More details about these set-ups can be found in **Chapter 1**. To obtain the best values for conversion and energy efficiency, several approaches have already been proposed, including changing the applied power, gas flow rate, flow type, reactor geometry, gas temperature, admixture gases, introducing (catalytic) packing materials, as well as extensive plasma chemistry modelling to gain a better insight in the underlying mechanisms. **Figure 6-2** summarizes all data available in literature. The highest energy efficiencies reported in the 1970–80s were up to 80 % for subsonic flow conditions, and up to 90 % for supersonic flows.[32,35,36] Recently, several attempts are made to reproduce these high energy efficiencies.[37–40] To date, maximum energy efficiencies of 50 % have already been successfully achieved, with both MW and RF discharges.[37–39] The results obtained by Bongers et al.[38] are near the thermal dissociation limit, indicating that the thermal dissociation mechanism is predominant. The authors concluded that the applied values of reduced electric field, i.e. 70–80 Td, are too high, and future experiments should be directed towards values of 20–50 Td, while keeping the temperature in the discharge as low as possible. It should be noted that all the experiments reporting such high energy efficiencies were performed at reduced pressures, which might not be beneficial for high-throughput industrial implementation—despite the high flow rates of up to 75 SLPM.[38] Indeed, increasing the pressure leads to a significant decrease in energy efficiency.[36] For atmospheric pressure, Spencer et al.[40] obtained a maximum energy efficiency of 20 %, which is nevertheless still a factor two better than obtained for a DBD (see previous section).

Figure 6-2 also demonstrates that in general the surfaguide MWs achieve the highest energy efficiencies (up to 90 %). Furthermore, just like for the DBD results, the conversion increases with increasing SEI, while the energy efficiency decreases above an SEI of 0.1–1 eV/molecule. When plotting the energy efficiency as a function of the conversion, it is clear that the more recent results typically have an energy efficiency of 10–50 % in the entire range of conversions up to 95 %. Again, like for the DBD results above, it is important to note that some of the data has been recalculated to represent coherent values of conversions and energy efficiencies. A more detailed influence of the different parameters is discussed below.

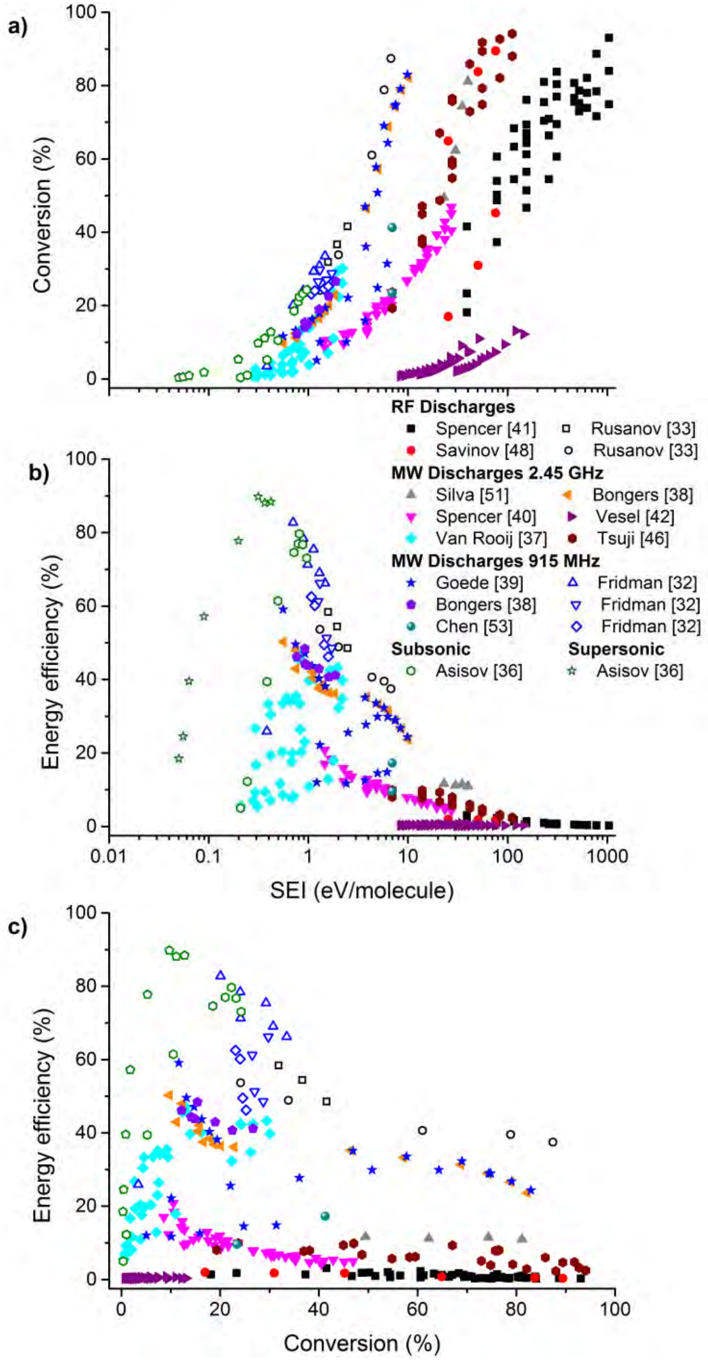

Figure 6-2. Experimental data collected from literature for CO_2 splitting in MW and RF discharges, showing the conversion (a) and energy efficiency (b) as a function of the SEI, as well as the energy efficiency as a function of the conversion (c). The open symbols represent the data from the 1970–80s. Note, some of the data has been recalculated from the original references to take, among others, dilution effects into account.

For the MW discharges, the same trade-off as described for the DBD between energy efficiency and conversion as a function of SEI is present.[37,38,40–42] Hence, to successfully increase the energy efficiency, one must be able to increase the conversion degree without increasing the specific energy input of the system, which essentially requires using techniques other than increasing the input power.[41] It is also clear that the highest energy efficiencies are obtained for low SEI values (0.1–1 eV/molecule), while the conversion is low at these conditions, hence conflicting requirements are encountered.[39]

As already mentioned, pressure has one of the most important influences on the MW discharge and on its performance for CO_2 conversion, and most studies are carried out at reduced pressure. One of the reasons is that at low pressure the three-body recombination reaction $CO + O + M \rightarrow CO_2 + M$—which is the most important reaction limiting the effective CO_2 conversion in the gas phase—becomes negligible.[42] An optimum operation pressure seems to exist around 150 mbar (at 5 SLPM), but the latter depends on other operating conditions, such as the gas flow rate.[37] Furthermore, the pressure plays an important role in which mode—contracted, diffuse or combined—the plasma is operating.[37]

Several more complex flow types and geometries have already been studied to optimize the MW discharge performance for CO_2 conversion. Supersonic flows in MW discharges have proven to reduce losses of vibrational levels upon collision with ground state molecules (i.e., so-called VT relaxation), which occurs mainly at higher temperature, and allowed to achieve an energy efficiency of up to 90 %,[36] in agreement with theoretical calculations.[35] Bongers et al.[38] observed an energy efficiency of only 15 % for a supersonic flow, but by additionally quenching the plasma, an energy efficiency up to 47 % was observed, as predicted for plasmas in the thermal regime (see **Chapter 1; Figure 1-2**). Similarly, the addition of a vortex gas flow, more specifically a reverse vortex, led to a significant improvement in CO_2 conversion and energy efficiency compared to a forward vortex flow.[38]

For MW discharges, the effect of gas temperature is quite complicated. A signature of the desired non-equilibrium conditions in a MW plasma is a low (or moderate) gas temperature (order of 1000–2000 K), while vibrational and electron temperatures are higher (i.e., 3000 up to 8000 K and 1–5 eV, respectively).[37,43] For low pressures and reduced electric fields (E/n), gas temperatures around 2000 K are observed. However, with increasing pressure at an SEI of about 0.5 eV/molecule, the discharge undergoes a transition from diffuse to contracted regime, and the temperature rises steeply to 14,000 K.[37] When this transition occurs and the vibrational and rotational gas temperature are in thermal equilibrium, low values of energy efficiency are observed.[40] Recent modelling studies suggest that keeping the temperatures under control, is beneficial for the vibrational excitation, and is a key parameter for more efficient CO_2 conversion.[24,43,44] Bongers et al.[38] noted that the E/n in their MW plasma set-up was too high to achieve VT non-equilibrium conditions and that the high temperatures in the plasma core may account for the observed high values of E/n. It is thus clear that the gas temperature should be kept as low as possible to reduce vibrational energy losses via VT relaxation.[44]

Just like for the DBD plasma, some papers also reported on the addition of other gases to CO_2 in the MW plasma, i.e. Ar,[40,45,46] He[46] and N_2.[47] For Ar, Spencer et al.[45] observed no effect on CO production, suggesting it does not affect the collisional processes benefiting dissociation, but depending on the set-up it might be necessary as an electron source to ignite the discharge.[40] Tsuji et al.[46] observed higher CO_2 conversions when diluted in Ar compared to He, and furthermore, the conversion increased but the energy efficiency decreased when adding more Ar or He. In contrast, just like for the DBD, N_2 can play a very important role in the CO_2 conversion, but the mechanism in the MW plasma is different than in the DBD plasma. Indeed, while in the DBD the metastable electronically excited N_2 molecules give rise to enhanced CO_2 conversion (see previous section),[17] in the MW plasma the improvement is due to the vibrationally excited N_2 molecules.[47] The energy difference between the first vibrational level of N_2 and CO_2 is very small, making the fast resonance transfer of vibrational energy from N_2 to CO_2 possible.[48] As such, N_2 can help with the vibrational pumping of the asymmetric mode of CO_2 and thus enhance the CO_2 conversion. On the other hand, the vibrationally excited N_2 molecules can also react with O atoms, leading to the production of NO_x in undesirable concentrations, as was also observed for a DBD (see previous section).[47]

Just like for DBDs, big leaps forward have been made in the past few years regarding modelling the plasma chemistry to better understand and improve CO_2 conversion in MW discharges.[23–25,34,43,44,49,50] The added complexity for MW plasmas compared to the plasma chemistry in DBDs stems from the very effective excitation to vibrational states, which can lead to the so-called ladder climbing effect and eventually very efficient dissociation of the vibrationally excited CO_2 molecule (as discussed in **Chapter 1**). This means that all the vibrational levels up to the dissociation limit need to be taken into account in accurate models for a CO_2 MW plasma, as well as all reactions with these different vibrationally excited levels. The models predict that besides electron impact dissociation of the vibrationally excited levels, also collisions with neutrals will become important as dissociation mechanisms, as was also suggested by an optical characterisation study,[51] and this is the key to achieve maximum energy efficiency of the CO_2 splitting process.[34] It is also shown that at low E/n values,[49] and in post discharge conditions,[50] the rates from the vibrational dissociation mechanism overcome the electron impact dissociation. To be able to perform multidimensional modelling investigations for these type of discharges where the vibrational levels play an important role, a reduced chemistry set has been developed in which, among others, the vibrational levels are lumped into a limited number of groups, to avoid the need of solving equations for all individual CO_2 vibrational levels.[52]

Finally, in contrast to the DBD research, no work has been performed on adding a (catalyst) packing in the MW discharge zone, and only a few papers report on adding a post-discharge (catalytic) packing.[40,53] Of course, as mentioned in **Chapter 1**, this is due to the high temperature in a MW discharge. Spencer et al.[40] added a monolith structure with and without a Rh/TiO_2 catalytic coating in the post-discharge zone. For both cases, a slight energy efficiency loss was observed and the Rh/TiO_2 was deemed inappropriate due to the possible stimulation of the backward reaction of $CO + O_2 \rightarrow CO_2 + O$. On the other hand, Chen et al.[53] reported that the use of plasma pre-treated TiO_2 supported NiO catalysts in the post-discharge zone led to an energy efficiency of 17 %, which was an increase of a factor two compared to the plasma only case. However, this increase is suggested to come from dissociation of CO_2 at the catalyst surface with oxygen vacancies through dissociative electron attachment, which is an inherent less-efficient dissociation process than the step-wise vibrational excitation (as shown in **Chapter 1**; **Figure 1-12**). We believe that the addition of a catalyst to a MW discharge for pure CO_2 splitting will only be beneficial if it is capable of either effectively lowering the E/n value of the discharge due to its physical effects, and/or stimulating the dissociation of vibrationally excited CO_2 molecules on the surface. Furthermore, the development of MW discharges operating at lower temperatures (≤ 1000 K) would allow the implementation of thermal catalysts in the discharge zone, rather than the current post-discharge packings.

From all these data, it should be clear that MW discharges are more than capable of crossing the 60 % efficiency mark for pure CO_2 splitting. However, the best results of this earlier work[32,35,36] have not yet been reproduced to-date, while the best energy efficiency in the more recent work appears to be around the thermodynamic equilibrium value of 45–50 %. This observation, together with the reported gas temperatures, makes it questionable whether vibrational excitation plays the major role here. Nonetheless, from modelling insights[43,44] it is evident that when the set-up can be tailored to achieve the correct strong non-equilibrium conditions,[37] vibrational excitations can lead to energy efficiencies up to 90 %. The main disadvantage of MW discharges is, however, their current requirement to operate at low pressures, in order to reach this strong non-equilibrium, and thus these high energy efficiencies.

1.1.3. GA plasmas

It is evident that both DBD and MW discharges have their distinctive advantages and disadvantages. DBDs operate at atmospheric pressure, but can’t make use of the most energy efficient dissociation process by vibrational interactions, while MW discharges can, but the vibrational pathways are only fully exploited when they operate at reduced pressure. The gliding arc tries to combine the best of both worlds, offering the possibility to operate at atmospheric pressure and at the same time trying to reach a strong enough non-equilibrium to stimulate the most efficient dissociation process through vibrational excitation.[54]

As explained in **Chapter 1**, there are two main GA reactor geometries used for CO_2 conversion. The first one relies on simple two-dimensional electrode blades. However, this configuration has a few disadvantages: the residence time in the plasma is quite short, flow rates are more limited, and due to its geometry only a limited fraction of the gas flow is processed by the discharge (e.g., about 20 % depending on the actual geometry).[55–57] As a result, this limits the theoretical maximum possible conversion to ~ 20 %.[55] The GAP configuration, on the other hand, is based on cylindrical electrodes, and the gas follows a vortex flow pattern. The gas in the reverse (inner) vortex flow passes exactly through the arc in the longitudinal direction, which ensures longer residence times in the discharge zone, even at high flow rates. Based on gas flow calculations, about 40 % of the gas flow can be processed by the discharge,[58] doubling the theoretical maximum conversion compared to the classical 2D electrode configuration.

Beside these geometry variations, other work has focused on changing the applied power, gas flow rate, flow type, inter-electrode gap, admixture gases and plasma chemistry modelling. Again, all the data available in literature is plotted in **Figure 6-3**. Most experiments report a maximum energy efficiency around 40–50 %,[54,55,59] with the highest experimentally reported and also calculated energy efficiency being 65 %.[55,60] Most of the conversion results, however, remain below 15 %, for both the regular GA and the GAP set-up. The only exception is the work of Indarto et al.[61] (35 % conversion) where the mixture was diluted with N_2, but at the expense of the energy efficiency (< 5 %). As such, compared to DBDs, which also work at atmospheric pressures, GA plasmas deliver about the same conversion, but the energy efficiency is in general 3–4 times higher. A more detailed discussion on the influence of the different parameters is given below.

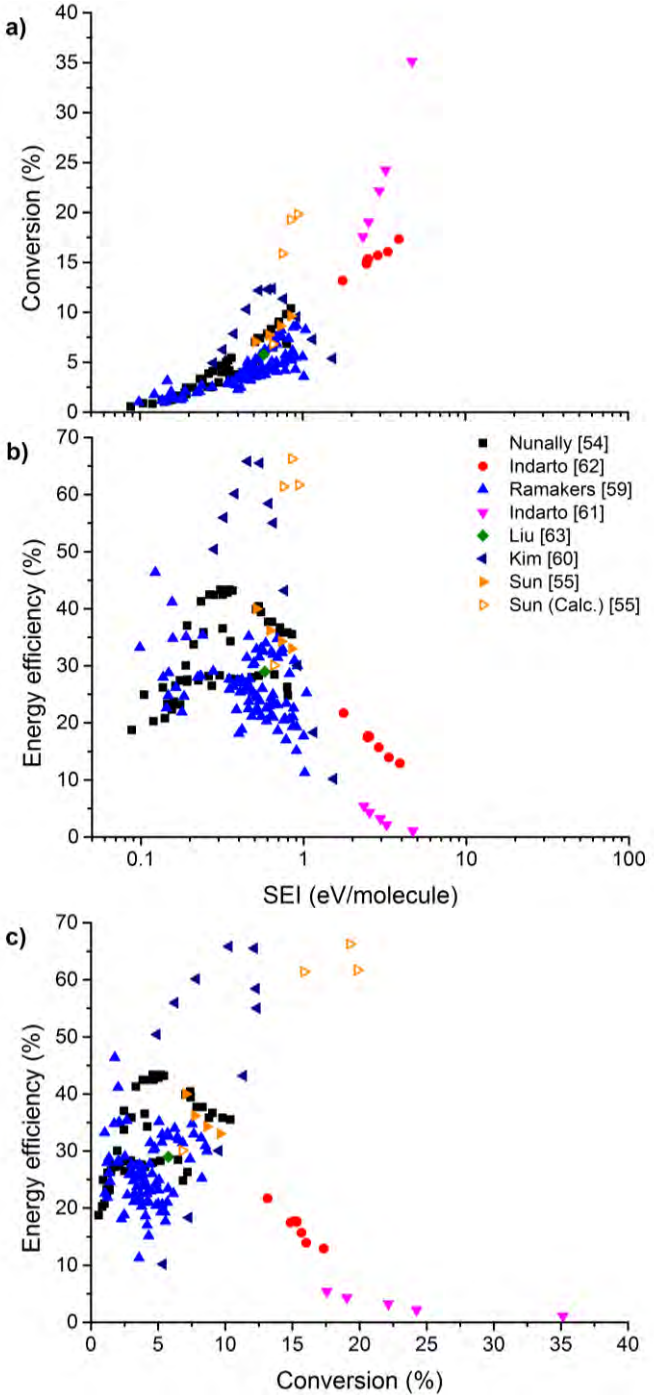

Figure 6-3. Experimental data collected from literature for CO_2 splitting in a GA, showing the conversion (a) and energy efficiency (b) as a function of the SEI, as well as the energy efficiency as a function of the conversion (c). Note, some of the data has been recalculated from the original references to take, among others, dilution effects into account.

It should be no surprise that again a trade-off between energy efficiency and conversion as function of SEI is observed.[54,55,59,61,62] In general, the conversion increases and the energy efficiency decreases with increasing SEI, as can be seen in **Figure 6-3**, and the same optimal SEI range of 0.1–1 eV/molecule, in terms of energy efficiency, is observed as for the MW discharges. For a regular GA, the conversion clearly increases and the energy efficiency decreases, when more power is supplied.[55] The GAP geometry, on the other hand, can operate in two regimes depending on the power input, i.e. a low and a high current regime, with the highest energy efficiency but lowest conversion observed for the former and the opposite for the latter.[59] Furthermore, it is reported that the lower the gas flow rate, the higher is the conversion, both in the low and high current regime, which is a direct result of the longer residence time of the gas in the discharge.[59] The same, albeit slightly less pronounced effect was observed for the regular GA.[61] Kim et al.[60], however, observed an optimum conversion while varying the gas flow rate. This is probably the result of reaching an optimum SEI (0.45 eV/molecule), since this value is in the same order as the SEI range at which Nunnally et al. reported a peak energy efficiency (0.30–0.37 eV/molecule).[54]

Besides the gas flow rate, an important parameter for the GAP is the vortex flow type, which can be modulated by adjusting the reactor geometry.[54,59,63] Operating in a reversed vortex flow (RVF) compared to a forward vortex flow (FVF), provides an increase in residence time and thermal insulation of the discharge from the reactor walls. As a result, the RVF delivers higher energy efficiencies at higher SEI values, leading to an improved conversion.[54,59] It is also this vortex flow, which allows for higher gas flow rates to be processed compared to a regular GA, and theoretically also to obtain higher maximum conversions because the gas passes through the arc in the longitudinal direction, yielding a longer residence time.

For the regular GA, the interelectrode gap can be varied to improve the CO_2 conversion, and the best result was observed for the smallest interelectrode distance. Indeed, increasing this distance leads to a larger arc volume and a corresponding drop in plasma power and electron density, and consequently also in the CO_2 conversion.[55]

Only one research group reports the use of additive gases—other than CH_4, H_2O or H_2, more specifically the addition of N_2, O_2 and air.[61] The experiments revealed that adding N_2 has a positive effect on the conversion (up to a factor 2 upon addition of 95 % N_2), but due to the dilution, a detrimental effect on the energy efficiency was observed (down by a factor 10–20). Furthermore, the presence of N_2 will again lead to the unwanted production of NO_X. The addition of O_2 and air showed a decrease in the conversion, indicating the possible strong negative effect of the presence of O_2 (impurities)—presumably due to Le Chatelier's principle.

Due to the more complex behaviour of the gas flow and of the arc movement, and the relationship between both in a GA, modelling work is more limited in literature. For the regular GA, a simple plasma kinetic model has been developed,[61] but recently a more detailed 0D chemical kinetic model,[55] and a 1D quasi-gliding arc mode[64] were presented. The results from these modelling studies show that electron impact dissociation of vibrationally excited CO_2 is predominant for an arc temperature of 1200 K and the recombination between CO and O atoms is the main conversion limiting reaction.[55] Reducing the arc temperature to 1000 K would significantly increase the conversion and energy efficiency, because it limits the recombination reaction rate and it enhances the importance of the higher vibrational levels in CO_2 dissociation.[55] Just like for the MW chemistry, lumping of the vibrational levels into a limited number of groups has been successfully performed, opening future perspectives for 2D and 3D GA modelling.[64] A successful first attempt at modelling the more complex GAP with a 0D chemical kinetics model supported by 3D gas flow modelling has also been reported, and it confirms the assumption, in line with the regular GA, that the vibrational levels play an important role for the energy efficient conversion of CO_2.[59]

In summary, the data in literature shows that GA discharges succeed in exploiting the most energy efficient CO_2 dissociation channel based on vibrational excitation, while operating at atmospheric pressure. Energy efficiencies of 45 % are no exception and results above the target value of 60 % have already been reported. On the other hand, model calculations reveal that the non-equilibrium character of the GA—making full potential of the vibrational excitation/dissociation pathway—could be further exploited to improve the energy efficiency. Just like for MW discharges, operating GA plasmas at lower gas temperatures might be the key. At this time, the main limiting factor compared to MW discharges appears to be the conversion, due to the limited fraction of the gas flow that is currently processed by the discharge. Smart reactor design—enhancing the processed gas fraction—should lead to the necessary advancements to overcome this limitation in the future.

1.1.4. Other plasma types

Beside the three most common plasma types discussed above, a number of other non-thermal plasmas have been used for CO_2 conversion, including corona discharges,[65–70] glow discharges,[71–74] non-self-sustained discharges,[74] capillary discharges,[75] and nanosecond pulsed discharges.[76] For more details and background regarding these different discharges, we refer to the respective references. When available, the relevant data has been extracted from literature and the results are presented in **Figure 6-4.** In general, the performance of all these different discharges is similar to that observed for a DBD, with maximum conversions up to 40 % and energy efficiencies below 15 %. The main exception is the non-self-sustained discharge investigated by Andreev et al.,[74] reaching a conversion of 50 % with a corresponding energy efficiency of almost 30 %. The advantage of this discharge type is its ability to control the mean electron energy by changing the E/N. The higher energy efficiency is reached when operating at values around 20 Td, which favours the vibrational excitation mechanism, as shown in **Chapter 1** (**Figures 1-11 and 1-12)**. However, just like for the MW plasmas, this discharge operates at reduced pressures (1550 Pa).

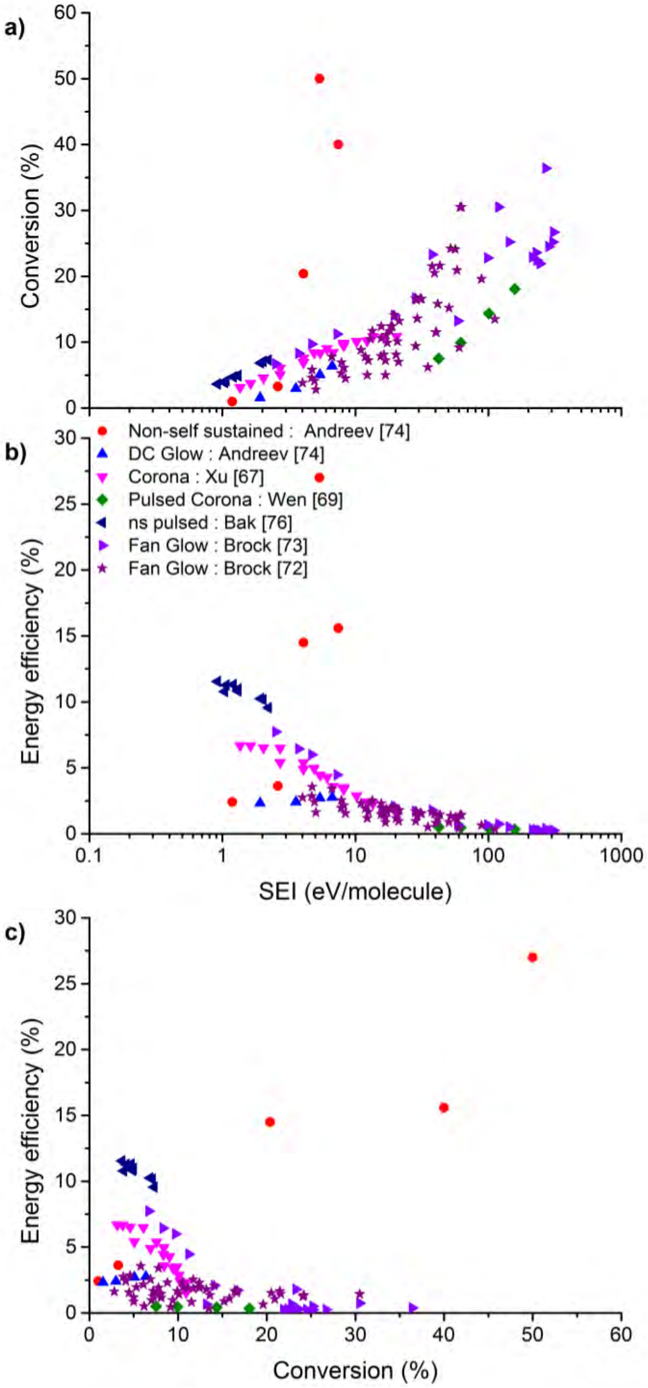

Figure 6-4. Experimental data collected from literature for CO_2 splitting in other plasmas, besides DBD, MW/RF and GA, showing the conversion (a) and energy efficiency (b) as a function of the SEI, as well as the energy efficiency as a function of the conversion (c). Note, some of the data has been recalculated from the original references to take, among others, dilution effects into account.

1.1.5. Summary

To summarize, in **Figure 6-5** we plot the energy efficiency as a function of the CO_2 conversion, grouped per discharge type, for all the data discussed above. Furthermore, both the thermal equilibrium limit (see **Chapter 1; Figure 1-2**) and the target energy efficiency of 60 % (see beginning of this Chapter) are displayed. This figure allows to draw the following conclusions.

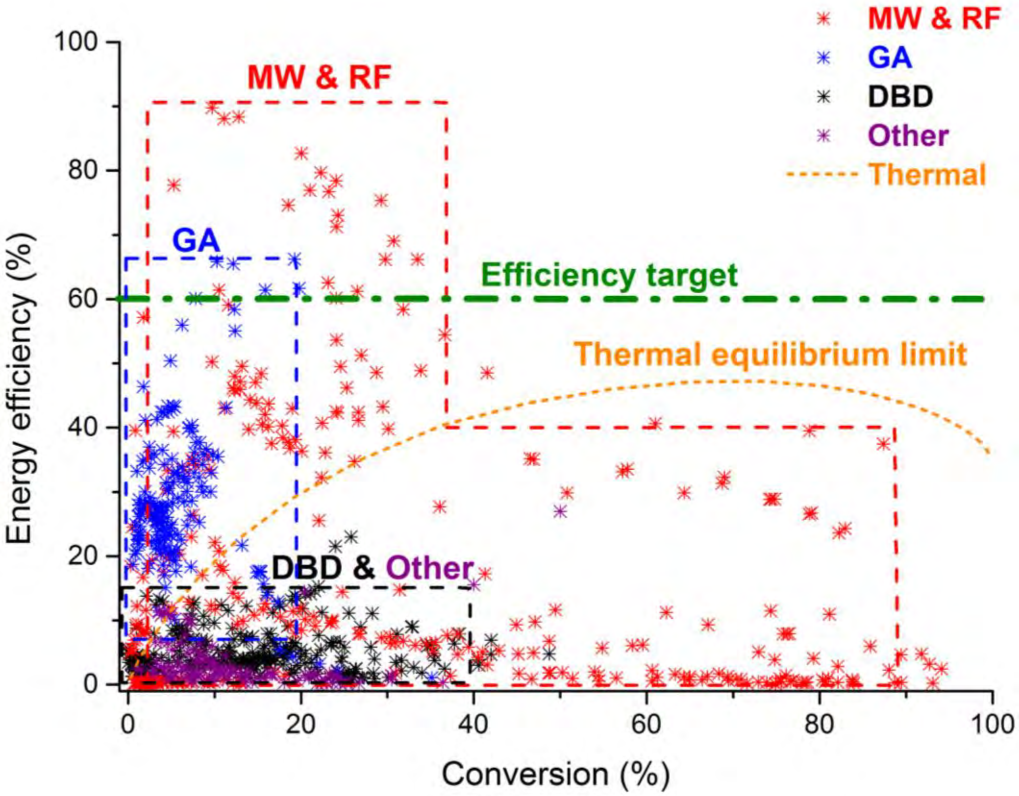

Figure 6-5. Comparison of all the data collected from literature for CO_2 splitting in the different plasma types, showing the energy efficiency as a function of the conversion. The thermal equilibrium limit and the 60 % efficiency target are also indicated.

First of all, it becomes clear that, although DBDs are among the most extensively studied for CO_2 conversion—and already successfully applied[77] for commercial O_3 production and VOC removal—they appear unsuitable for the efficient conversion of CO_2. Their energy efficiency remains a factor 4 too low, even when combined with a packing, in order to be industrially competitive. The same applies to most of the other plasma types listed in section 1.1.4 above.

Second, the best results for GA plasmas are capable of reaching the set energy efficiency target. Moreover, almost all the results obtained are far above the thermal equilibrium limit, which is especially interesting, keeping in mind that the GA plasmas operate at atmospheric pressure. This demonstrates the non-equilibrium character of this type of plasma, even at atmospheric pressure, and the benefits of being able to exploit this behaviour through the energy efficient dissociation of the CO_2 vibrational levels. Moreover, modelling reveals that this non-equilibrium character could (and should) be further exploited, to further enhance the energy efficiency. To date, the main challenge is the limited conversion, which remains below 20 % because only a limited fraction of the gas passes through the active arc plasma.

Finally, if—for now—we ignore the fact that most MW discharges used for CO_2 conversion operate at reduced pressure, in contrast to the commercially more interesting atmospheric pressure of GA plasmas, it is clear that MW discharges offer a wide variety of possibilities. Even up to conversions of 40 %, the energy efficiency target is easily crossed and they clearly operate in a non-equilibrium regime, favouring the step-wise vibrational dissociation mechanism. Conversions in the range of 40–90 % are also possible, albeit with maximum energy efficiencies of 40 %. Under these conditions, the MW discharges most probably operate in the thermal regime. Nevertheless, this shows the wide variety for both conversion and energy efficiency that is achievable with MW discharges for the conversion of pure CO_2.

1.2. CO_2 + CH_4 : Dry reforming of methane

Contrary to pure CO_2 splitting, DRM can yield a wide variety of products. This has several implications for the evaluation and comparison of the various studies in literature, mainly because it affects the definition of the energy efficiency. To determine the true energy efficiency of the process, we would need to take all the formed products into account—both gaseous and liquids—to determine the theoretical reaction enthalpy. Another possibility would be to determine the thermal energy efficiency, based on the higher (or lower) heating value of the output, i.e. the products, relative to that of the input, i.e. reactants and power input. However, typically only the selectivity (or yield) towards the syngas components, CO and H_2, and light hydrocarbons is given for most studies in literature. Thus, at the moment these strategies are impossible to pursue, when presenting an overview of the available literature results in the sections below. Therefore, in this section we will use the energy cost, in units of eV per converted molecule, to compare the different discharges—together with their total conversion. As energy efficiency target for syngas production we will consider the same 60 % for the general stoichiometric DRM process, which equals an energy cost of 4.27 eV/molecule converted. Indeed, 100 % energy efficiency would yield an energy cost equal to the standard reaction enthalpy of 2.56 eV/molecule (as outlined in **Chapter 1**). In our opinion this is the best representation to compare the results in literature, considering the fact that in most of the studies the higher hydrocarbons and the valuable liquid fraction containing oxygenates (e.g., formaldehyde, methanol, ethanol, formic acid, acetic acid) are neglected. However, as explained in **Chapter 1,** this 60 % energy efficiency target is only valid for the comparison towards syngas production. When liquids (such as methanol) are formed through the direct oxidative pathway—which has already been demonstrated using the plasmachemical conversion of CO_2 with a co-reactant—the energy efficiency requirements are drastically lowered by a factor two to three. This is a direct result of circumventing the energy intensive step of further processing the syngas into the desired liquid products.

Plasma-based DRM has received a lot of attention in recent years. Some overviews can be found in literature.[32,78–81] In a recent review on the liquefaction of methane,[3] DRM is considered as oxidative plasma-based CH_4 liquefaction. It can be performed in two ways: either as two-step process, yielding mainly syngas, which can then be further processed into Fischer-Tropsch liquids or methanol, or as one-step process, to aim for the direct formation of value-added oxygenated products, such as formaldehyde, methanol, ethanol, dimethyl ether, formic acid, etc. These two options are therefore called the indirect and direct oxidative plasma liquefaction approaches, respectively. An overview of the progress in the field on plasma-based DRM will be given below, starting again with DBD, MW and GA plasmas. However, in contrast to CO_2 splitting, a vast amount of research has been performed with some other discharges as well for DRM, so these have been given their separate sections below.

First some general trends applicable for all discharges will be summarized. We start off with the SEI, because for all discharges studied it is clear that for DRM—just like for pure CO_2 splitting—the SEI is the major determining factor for the conversion and energy cost, as it combines the effect of power and residence time. Typically, a higher SEI leads to a higher conversion, but also energy cost. The conversions of CH_4 and CO_2 increase almost linearly when a higher voltage or input power is applied, as observed for DBD,[82–93] MW,[94] GA,[95–97] corona,[98–101] spark,[102–108] APGD[109,110] and nanosecond pulsed discharges.[111–115] Generally, this is accompanied by an increase in energy cost. Regarding product selectivity, some different trends are reported as a function of power, for the different discharge types. In general, in DBDs, higher H_2 and CO yields are reported, with the ratio of H_2 to CO remaining constant,[86,89,90] as well as a sharp drop in the selectivity of the light hydrocarbons.[88,92,93] Furthermore, some studies observed no significant changes in the selectivities in a DBD, except for an increase in carbon deposition,[86] while other studies report an increase in CO and H_2 selectivity,[88,89,93] or even the opposite trend.[90] For corona discharges, the H_2 selectivity seems to decrease, while the CO selectivity exhibits the opposite trend,[98,99] and as a result, the H_2/CO ratio greatly depends on the discharge power.[100] In spark discharges, more pronounced carbon deposition at higher input power,[105] as well as an increased selectivity for H_2 and CO and a drop in C_2H_2 selectivity is reported, pointing to an enhancement of reforming reactions over coupling reactions.[105,106] APGD discharges exhibit a higher CO selectivity and coke deposition at higher input voltages and these conditions favour the production of unsaturated hydrocarbons, such as C_2H_2.[109] On the other hand, for nanosecond pulsed discharges, upon higher SEI the mass balance points to a loss of oxygen and carbon, which are converted into water and carbon powder or deposition, respectively.[111] Finally, for MW and GA plasmas, no specific trends are reported yet for the effect of power on the product selectivities. Thus we can conclude that—with some exceptions—a higher discharge power generally improves the conversion, but does not change the reaction pathways significantly.

A higher total flow rate has the opposite effect as the power, and leads to lower conversions and energy costs, for DBD,[82,85,87,88,90–92,116] GA,[97] corona,[99–101,117] spark,[102,105] APGD[109,110] and nanosecond pulsed discharges.[112] No results are reported yet for MW plasmas. On the other hand, the flow seems to have almost no effect on the selectivity towards the syngas components CO and H_2 and hence also not on the syngas ratio itself, for DBD,[85,87,92,116] GA[97] and APGD.[109,110] At higher flow rates, some researchers also report a decrease in H_2 and CO selectivity in DBDs,[88,90] while the selectivity towards hydrocarbons increases.[82,85,88,90,116] For corona discharges, a slightly higher H_2 and CO selectivity is observed, but the syngas ratio remains almost unchanged.[99–101,117] For spark discharges, it is reported that the H_2 selectivity rises and the CO selectivity drops, at higher flow rates.[102] Finally, for MW and nanosecond pulsed discharges, again no specific data are reported yet for the effect of flow rate on the product selectivities. Nevertheless, in general we may again conclude that the dissociation and formation mechanisms are—with some exceptions—not significantly influenced by a change in the flow rate, although the selectivities can be altered.

Besides the SEI (or power and gas flow rate), the CH_4/CO_2 mixing ratio has a tremendous influence on the CH_4 and CO_2 conversions, as well as on the product selectivities. In general, when adding more CH_4 to the mixture, the effective CH_4 conversion rises, while the effective CO_2 conversion drops. Note that we talk about the effective conversions (as defined in **Chapter 2**; eq.2-9) and not about the (absolute) conversion itself, to take the effect of the change in gas mixture into account. At the same time, the selectivity towards (light) hydrocarbons increases, as well as the selectivity towards H_2, while the CO selectivity decreases, when more CH_4 is present in the mixture. This inevitably leads to an increase of the syngas ratio. Thus, the H_2/CO ratio is highly dependent on the inlet feed, which makes the ratio easily adjustable in a wide range to fit the Fischer-Tropsch or methanol synthesis requirements. This was found for all discharges, i.e. DBD,[84,85,88–90,92,93] GA,[95–97,118] MW,[94] corona,[100,117,119–121] spark,[103,105,107,108] APGD[110,120,122,123] and nanosecond pulsed discharges.[112,114,124] The formation of carbon black and its deposition on the electrode and reactor walls for mixtures seems to occur with a high CH_4/CO_2 ratio (> 1), and this deposition can highly influence the discharge operation.[11] For lower CH_4/CO_2 ratios, this is not observed, neither in DBD,[84,92,93] GA,[95–97,118] corona,[98–100] spark,[103,108] APGD[110,120,122,123] and nanosecond pulsed discharges,[112] as CO_2 prevents carbon formation. For APGDs, a higher CH_4/CO_2 ratio is reported to increase the water formation. In contrast, for a DBD[89] and spark discharge[105] a higher water production is observed at low CH_4/CO_2 feed ratios, presumably due to the occurrence of the reverse water gas shift reaction.

These trends can be explained by the following reactions: Increasing the CH_4/CO_2 ratio leads to a more pronounced H_2 formation and at the same time it reduces the amount of O species in the mixture. Hence, the reaction $C + O \rightarrow CO$ is reduced, leading to a lower CO selectivity, and increased carbon deposition. On the other hand, the reaction $H_2 + O \rightarrow H_2O$ becomes more important, giving rise to the higher H_2O production, but it is not important enough to balance the higher H_2 production, explaining the increased H_2 selectivity. This also means that the deposited C is still an active species in the reactions and it is suggested that the addition of O_2[110] and/or H_2O[120] can prevent carbon deposition. Finally, it is reported that the rate of CO production is always higher than the rate of CO_2 reduction, proving that CO is formed by both the reduction of CO_2 and the oxidation of CH_4.[117]

The effect of the CH_4/CO_2 mixing ratio on the total conversion and hence on the energy cost is less straightforward. For nanosecond pulsed discharges, depending on the setup, different optimum values for this mixing ratio for achieving the lowest energy cost are reported. Ghorbanzadeh et al.[112,115] report a considerable increase in the energy cost when methane becomes predominant in the mixture, while Zhang et al.[114] report an energy cost which is cut in half when going from a 1:3 to a 3:1 CH_4/CO_2 ratio. For a DBD, the effect of the mixing ratio on the total conversion also appears to depend on the specific set-up, since both an increase [84,88,125,126] and decrease[85,90,91] are widely reported upon addition of more CH_4. Snoeckx et al.,[83] Zheng et al.,[116] and Pinhão et al.[127] report an initial increase in total conversion upon adding CH_4 when the CH_4/CO_2 ratio is < 1 and a decrease when the ratio becomes > 1. These trends suggest that the CH_4 conversion is strongly affected by the CO_2 conversion, especially when the ratio is < 1 and CO_2 is thus the main component in the mixture. For the other plasma types, no specific data are reported in literature on the effect of CH_4/CO_2 mixing ratio on the total conversion. Finally, as the energy cost is inversely proportional to the obtained conversion (cf. **Chapter 2**; equation 2-13), the effect of the CH_4/CO_2 mixing ratio on the energy cost is opposite to the effects described above for the total conversion.

Besides these general trends for the effect of SEI and CH_4/CO_2 mixing ratio, which are very similar for the various discharge types, some specific trends, characteristic for each plasma reactor, are reported for DRM. They will be summarized in the next sections, along with a summary of all values for conversion and energy cost, reported in literature.

1.2.1. DBD plasmas

Due to its simple design and ease of use—also in combination with packing materials—again most of the research to date has been performed with DBDs, with the coaxial reactor (see **Chapter 1; Figure 1-13**) being the main geometry. To improve the conversion and energy costs, and to tune the product distribution, several approaches have been investigated, including changing the SEI, applying pulsed power, changing the gas flow rate or feed ratio, the reaction temperature or pressure, applying multi-electrode configurations or different electrode materials, mixing with other gases, i.e. Ar, He, N_2, as well as introducing (catalytic) packing materials. Some of these effects have already been described above, but the others will be explained in more detail below. Furthermore, extensive modelling work has also been performed to obtain a more fundamental insight in the plasma chemistry and in turn aid in the improvement of future experiments. For all the experiments reported in literature, the syngas components H_2 and CO are the major reaction products, with smaller amounts of C_2 and C_3 hydrocarbons also detected, in the order C_2H_6 >>> C_3H_8 > C_2H_4 > C_2H_2. In even lower quantities, hydrocarbons up to C_5 have been detected, where the selectivities of unsaturated hydrocarbons are again much lower than those of paraffins. The major products that are detected when the condensate is analysed,[85,125,128,129] are C_4–C_{10} hydrocarbons as well as oxygenates, including methanol, ethanol, 1-propanol, acetic acid and other e.g., tertiary alcohols, ketones, esters, and carboxylic acids.

Figure 6-6 summarizes most of the results, in terms of both conversion and energy cost, available in literature. Due to the large amount of data available for packed bed reactors, those data is discussed and presented further below in **Figure 6-7**. The conversion and energy cost increase again upon rising SEI. When plotting the energy cost as a function of the conversion, it is clear that most of the results are situated above an energy cost of 20 eV/molecule and below a conversion of 60 %, with only some exceptions. The highest experimental conversion reported is 66 %,[88] and the lowest experimentally observed energy cost is 18 eV/molecule.[83] This is more than a factor 4 higher than the set efficiency target of 4.27 eV/molecule (see beginning of section 1.2). Model calculations predict that higher values of conversion and lower energy costs should be achievable by a careful selection of the operating conditions, as will be outlined below.[83] It is important to note that some of the data in this figure has again been recalculated to represent coherent values of conversions and energy costs. For instance, as also explained for pure CO_2 splitting, the mixture is sometimes diluted with He, Ar or N_2 to obtain an easier ignitable and more stable discharge, but this influences the results—an effect that was not always taken into account in the original data. A more detailed influence of the different parameters is discussed below.

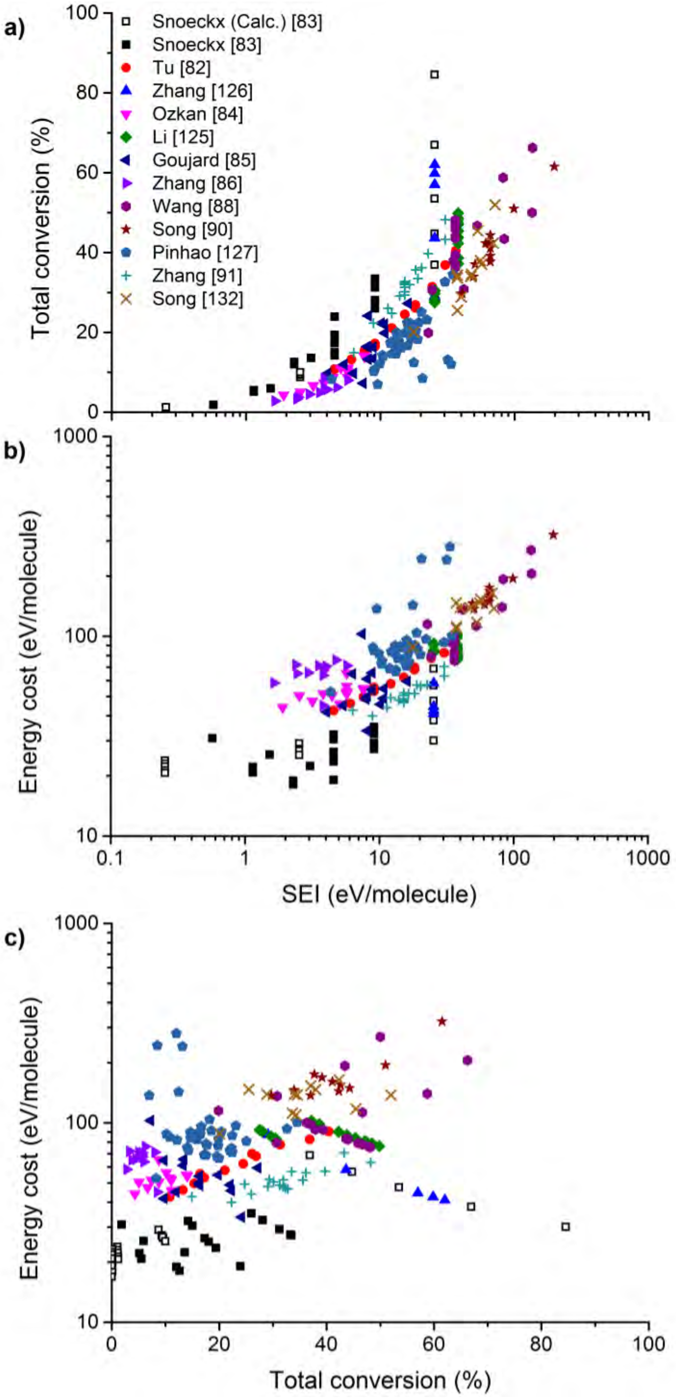

Figure 6-6. Experimental data collected from literature for DRM in a DBD, showing the conversion (a) and energy cost (b) as a function of the SEI, as well as the energy cost as a function of the conversion (c). Note, some of the data has been recalculated from the original references to take, among others, dilution effects into account.

The effect of the temperature and pressure on DRM in a DBD has been investigated by several authors. Low pressures seem to favour the reactant conversion, while the syngas ratio does not show any pressure dependence.[89] On the other hand, the selectivity of both CO and light hydrocarbons is reported to increase with rising pressure.[93] For a wall temperature range of 353–523 K, Zhou et al.[89] observed slightly higher conversions and product yields upon increasing temperature, with the syngas ratio being independent of the temperature. Zhang et al.[86] and Goujard et al.[85] investigated the temperature effect in the range of 297–773 K and 298–873 K, respectively. Both the conversions and the hydrocarbon selectivity are reported to increase with temperature, while the H_2 and CO selectivity decrease. However, Zhang et al.[86] found an increase in syngas ratio, while Goujard et al.[85] observed the opposite. When the temperature reaches 773 K, the CO_2 conversion appears to increase more rapidly than the CH_4 conversion, indicating a shift in dominant reforming processes around 673 K.[85] These results indicate that while the electron-impact dissociation reactions govern the reactant conversions, thermo-chemistry can be used to control the consecutive product reaction pathways.

Several changes with respect to the electrode configuration and materials have been reported as well. Wang et al.[88] found little influence of the discharge gap on the reactions, while Li et al.[125] observed higher conversions upon reducing the discharge gap. At the same time, Wang et al.[88] reported a significant influence on the conversions using multi-stage ionization (i.e. multiple DBD and “afterglow” zones in one reactor by placing several electrodes in series), while only small effects were observed by Li et al.[125] Both groups, however, found a significant positive influence on the syngas product selectivities when applying multi-stage ionization. Rico et al.[87] reported better conversions with porous electrodes, while the (catalytic) effect of different inner electrodes only showed very little influence on the conversions,[130,131] but a significant increase in oxygenate synthesis for nickel and copper, suggesting a catalytic role of the metallic surface.[131] Finally, applyng a pulsed power also seems to have a beneficial effect on the conversion.[132]

As mentioned above, some researchers have also added inert gases, such as N_2, Ar and He, to ignite the plasma more easily. This has several effects on the discharge characteristics, conversion and energy cost. Ozkan et al.[84] investigated the effect of Ar and He dilution, but did not compare the results with pure CH_4/CO_2 mixtures. The CH_4 conversion was higher for He than for Ar addition, while the opposite was found for the CO_2 conversion. This could be related to a change from filamentary to glow discharge when switching from Ar to He, which significantly influences the shape of the EEDF and thus the electron impact reactions. Zhang et al.[91] indicated that, although the conversion increases when adding Ar, the latter is not sufficient to counteract the lower CH_4/CO_2 feed content, since the conversion rates are lower compared to a mixture without Ar. On the other hand, they observed a positive effect towards the syngas component selectivities. Pinhão et al.[127] reported a positive effect on the breakdown voltage with increasing He content, resulting in a rise of the conversion rates with increasing He content up to 80 %. A still higher He content showed detrimental effects on both conversion and selectivity, but again no comparison for the mixture without He was made. In a follow-up modelling study by Janeco et al.[133] a shift in the electron velocity distribution function due to the addition of He was observed.

Kolb et al. studied the addition of the molecular gases O_2 and H_2O on the performance of DRM in a DBD.[134,135] O_2 aids in the conversion of CH_4 but also produces CO_2,[135] which is not beneficial. H_2O, on the other hand, only has a small negative influence on the conversion of CO_2, but significantly enhances the conversion of CH_4 and more importantly, the production of valuable oxygenates such as formaldehyde and methanol.[134] This study shows that a tri- or more general multi-reforming process, using a mixture of $CO_2/CH_4/H_2O$ or a combination of different reforming processes in series, could be a very interesting next step to pursue using plasma technology.

Due to the historical interest into thermo-catalytic DRM and the ease of implementing a (catalytic) packing in the discharge zone of a DBD, as explained in **Chapter 1**, a lot of research has already been performed towards plasma-catalytic DRM and hybrid reactors. A complete but brief overview will be given below, while for more detailed information on the effects and mechanisms behind plasma catalysis, we refer to the existing excellent literature on this topic.[136–138] Most of the work to date has been performed with packed bed reactors, but some research also exists on fluidized bed reactors.[139,140] Contrary to pure CO_2 splitting, for DRM the addition of a packing can greatly influence the formation of products, due to the availability of CH_4 as a hydrogen source. Hence, the work focuses both on increasing the conversion and lowering the energy cost by physical effects, as well as on chemical effects to steer the product distribution towards more value-added chemicals, such as light hydrocarbons and oxygenates. Packed bed DBD reactors generally yield similar conversions and energy costs as the corresponding empty reactors, as can be seen when comparing **Figures 6-6 and 6-7**. Nevertheless, the use of a catalytic packing can drastically alter the chemical pathways and thus the selectivity and product distributions, which would be beneficial to exploit the direct oxidative pathway of DRM, instead of the indirect process through syngas production.

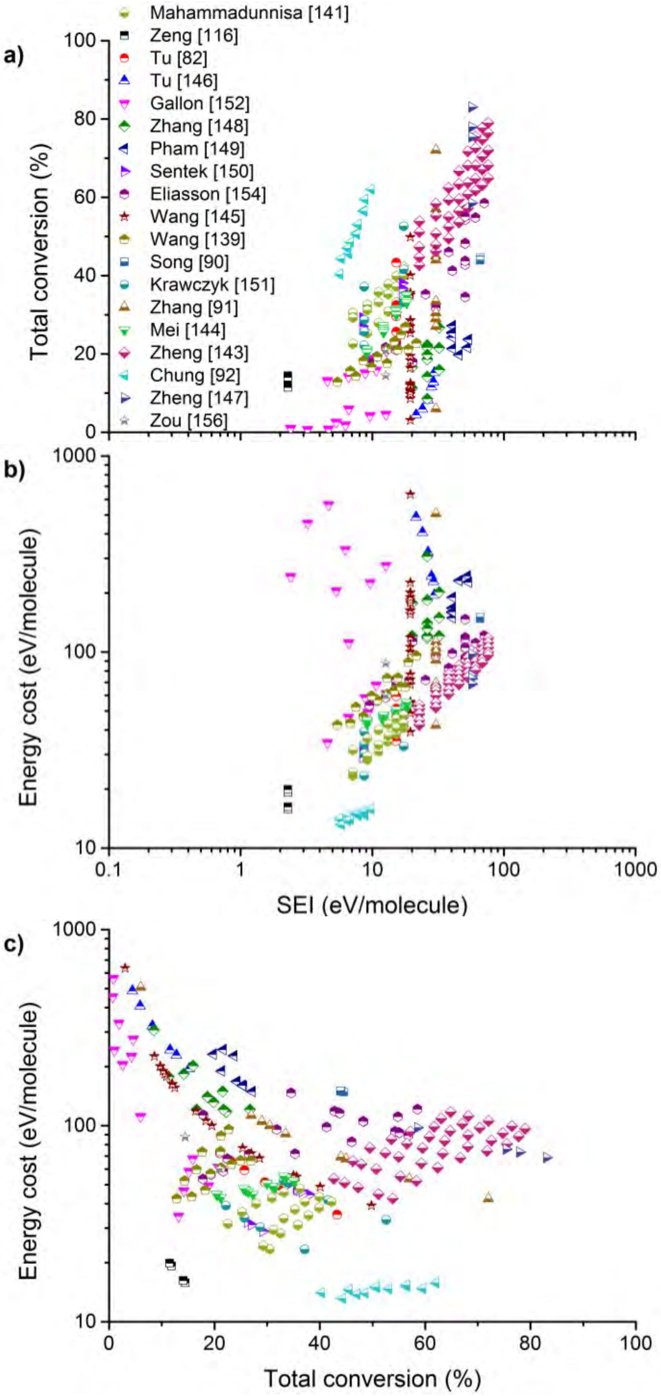

Figure 6-7. Experimental data collected from literature for DRM in a packed bed DBD, showing the conversion (a) and energy cost (b) as a function of the SEI, as well as the energy cost as a function of the conversion (c). Note, some of the data has been recalculated from the original references to take, among others, dilution effects into account.

A broad spectrum of materials have already been investigated for the plasma-catalytic DRM, of which Ni is by far the most commonly used active phase, such as in Ni/γ-Al_2O_3,[82,90,91,116,139,141–146] Ni/SiO_2,[144,147,148] Ni-Fe/γ-Al_2O_3,[143] Ni-Fe/SiO_2,[143,148] Ni-Cu/γ-Al_2O_3,[91] Ni^0/La_2O_3,[85] Ni/MgO,[144] Ni/TiO_2,[144] $NiFe_2O_4$,[143] $NiFe_2O_4$#SiO_2,[143] $LaNiO_3$/SiO_2,[147] $LaNiO_3$,[147] $LaNiO_3$@SiO_2.[147] Furthermore, alumina is the most commonly used support, i.e., Ni/γ-Al_2O_3,[82,90,91,116,139,141–146] Ni-Fe/γ-Al_2O_3,[143] Mn/γ-Al_2O_3,[116] Cu/γ-Al_2O_3,[91,116,140] Co/γ-Al_2O_3,[116] La_2O_3/γ-Al_2O_3,[149] Ag/γ-Al_2O_3,[150] Pd/γ-Al_2O_3,[140,150] Fe/γ-Al_2O_3,[151] Cu-Ni/γ-Al_2O_3,[91] or even in its pure form.[87,90,150,152] Other catalytic systems are based on zeolites, e.g., 3A,[152] A4,[153] NaX,[154] NaY,[151] Na-ZSM-5.[151] Besides, studies were also conducted using $BaTiO_3$,[87,148] a mixture of $BaTiO_3$ and $NiSiO_2$,[148] ceramic foams (92 % Al_2O_3, 8 % SiO_2) coated with Rh, Ni or NiCa,[155] quartz wool,[152] glass beads,[92] a stainless steel mesh,[148] starch,[156] BZT ($BaZr_{0.75}T_{0.25}O_3$) and BFN ($BaFe_{0.5}Nb_{0.5}O_3$).[92] For a regular AC packed DBD, the best result was obtained for the Zeolite Na-ZSM-5 with a total conversion of 37 % and an energy cost of 24 eV/converted molecule (see **Figure 6-7**).[151] Just like for pure CO_2 splitting, the addition of a catalyst does not seem to make the process more energy efficient, but it yields higher conversions at the same energy costs. The best overall results in a packed bed DBD have been obtained for a quasi-pulsed DBD packed with BFN and BZN, with total conversions in the range of 45–60 % and an energy cost in the range of 13–16 eV/converted molecule (see **Figure 6-7**),[92] which is lower than for a DBD without packing, but this might also be due to the pulsed operation.

Besides the experimental work, major insights have been obtained in recent years based on modelling of the DRM process for a DBD. Different kind of models and computational techniques have been successfully developed, e.g., semi-empirical kinetic models,[89,157,158] zero-dimensional chemical kinetic models with both simplified[159] and extensive chemistry sets,[23,83,160] a one-dimensional fluid model,[161] a so-called 3D "Incompressible Navier−Stokes" model combined with a convection−diffusion model,[162] a hybrid artificial neural network-genetic algorithm,[163] a model focusing on a more accurate description of the electron kinetics,[133] and density functional theory (DFT) studies to investigate reaction mechanisms.[129,164] Due to the complex chemistry taking place in DRM, the development of accurate multi-dimensional models with extensive chemistry is currently restricted by computational limits.

Some key findings of these models will be given here. Snoeckx et al. [83] performed an extensive modelling study, with detailed plasma chemistry, spanning a wide range of experimentally accessible conditions. The model predicted that increasing the SEI at a constant gas ratio and frequency results in a higher total conversion. However, the increase in conversion is not entirely proportional to the rise in SEI, resulting in somewhat higher energy costs with increasing SEI. The lowest energy cost was predicted to be 16.9 eV/molecule, but this corresponds to very low values for the total conversion, i.e. 0.015 %. On the other hand, the highest total conversion predicted by the model, i.e. 84.2 %, corresponds to an energy cost of 30.1 eV/molecule. A larger amount of CO_2 was observed to lead to a higher total conversion and lower energy cost. This is attributed to the O atoms formed by electron impact dissociation of CO_2, which react very effectively with the H atoms originating from electron impact dissociation of CH_4. As shown in the kinetic analysis of Snoeckx et al.[160] the conversion of CH_4 is normally limited by the fast backward reaction, i.e. $CH_3 + H \rightarrow CH_4$, but when more O atoms are available, this reaction is of minor importance compared to the reactions $O + H/OH \rightarrow OH/H_2O$. Thus, by limiting the backward reaction, the conversion of CH_4 rises dramatically with increasing CO_2 content, leading to a higher total conversion.[83] Another important effect is the total number of micro-discharge filaments, which the gas molecules experience when passing through the DBD reactor. It seems that for most cases a larger number of filaments, but with lower energy, yields higher values for conversion and lower energy costs, compared to a smaller number of filaments, but with more energy deposited per filament.[83] In some other models by Janeco et al.[133] and Goujard et al.[159] the effect of adding He to the CH_4/CO_2 mixture was investigated. Both groups reported that He, as well as all other species that may result from the electron collisions in the gas mixture, can significantly change the electron velocity distribution function, the electron reaction rates, and the energy losses, which can affect the energy cost when taken into account in the model.

Summarizing all data in literature, we can conclude that a DBD reactor can provide reasonable conversions up to 60 % and 80 %, for empty (i.e. non-packed) and packed bed DBDs, respectively. However, the energy cost lies in the range of 20–100 eV/molecule, which would correspond to an energy efficiency of 12.8–2.6 %, assuming that only syngas is formed. This is at least a factor 5 away from the necessary 4.27 eV/molecule benchmark for the energy cost (or the 60 % benchmark for energy efficiency), as defined in the beginning of this section, with no positive outlook on the horizon. Indeed, even extensive modelling studies predicted that the lowest achievable energy cost, obtained after careful selection of the operating conditions, would be 16.9 eV/molecule (see above).[83] Hence, despite the simple reactor design for scalability, the ease of implementing a wide variety of packings, and its industrial success for ozone generation (and possibly VOC abatement), at this point, the high energy cost—and hence low energy efficiency—makes it doubtful that DBDs will be the most suitable technology for DRM into syngas. Nevertheless, due to its ease of use, research with DBDs still can yield valuable insights and knowledge, which is transferable to other more efficient discharges. On the other hand, when suitable catalysts can be found for the production of valuable oxygenates with high yields through direct (plasma-catalytic) oxidative liquefaction,[3] the energy efficiency target will be a significantly lower (a factor 2–3 in the case of methanol), so this could change the analysis drastically. Although still many challenges for this pathway remain–such as finding suitable catalysts–and advances in energy efficiency will still be required.

1.2.2. MW plasmas

Compared to the extensive work available on pure CO_2 splitting in MW plasmas, almost no work exists yet for DRM using a MW plasma. This is in great contrast to the extensive work performed for DRM in DBD reactors (see above). We are aware of only one study for a pulsed MW plasma,[165] and one for a continuous MW plasma, where the comparison is made with the introduction of a Ni catalyst.[94] The pulsed setup achieved a CH_4 and CO_2 conversion of 71 % and 69 %, respectively, at an energy cost of 6.5 eV/molecule for a CH_4/CO_2 ratio of 1.5. Syngas was again the major product, but also C_2H_2 and C_2H_4 were detected.[165] Furthermore, no coking was observed. The data will be presented together with the results for the GA plasma, in **Figure 6-8**.

Cho et al.[94] obtained conversions in the continuous MW plasma in the same range as in the pulsed MW plasma of Zhang et al.,[165] but at much high powers—up to 1.5 kW compared to 120 W—and at low flow rates (100 mL/min vs. 200 mL/min), so their energy costs were unacceptably high, i.e. between 93 and 343 eV/molecule. Adding a Ni catalyst to the discharge is reported to lead to a higher conversion by 10 % for CH_4 and by 15 % for CO_2. Furthermore, the H_2/CO ratio changed drastically from 1.7 for the plasma-only case to 1.2 when combined with the catalyst. As additional products only C_2H_4 was detected, with increasing selectivity when more CH_4 was added to the feed.[94]

In **Chapter 1**, we also discussed catalysis based on MW heating (section 3.5). Fidalgo et al.[166] observed the formation of microplasmas in their so-called microwave receptor/catalyst set-up. However, the MW source was simply used in that case to heat the gas, while the creation of microplasmas at the catalyst surface was only a side effect of the strong electric fields at the sharp edges.

In general, the few studies reported in literature for DRM by MW plasmas show high conversions, as well as a high selectivity toward CO and H_2. Furthermore, based on the pure CO_2 splitting results presented in previous section, we may expect that a large treatment capacity is in principle possible, as well as high energy efficiencies. Nevertheless, experimental evidence remains extremely scarce. One of the major unanswered questions is related to the role played by the vibrational levels of CH_4 in the CO_2 dissociation, and more specifically in the ladder climbing effect, explained in **Chapter 1** (cf. **Figure 1-12**). In particular, it is not clear whether they will affect (i.e., stimulate or inhibit) this process or not, as well as how the dissociation of CH_4 itself will be influenced.

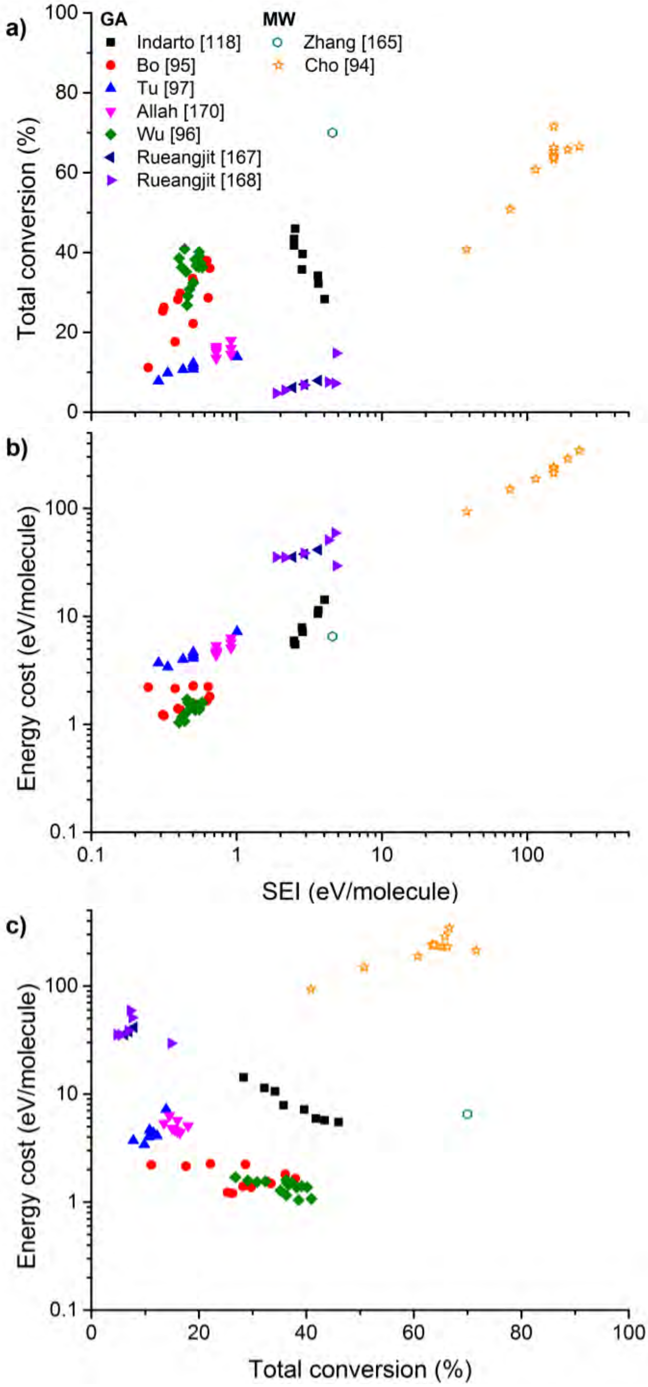

Figure 6-8. Experimental data collected from literature for DRM in a MW (open symbols) and GA plasma (closed symbols), showing the conversion (a) and energy cost (b) as a function of the SEI, as well as the energy cost as a function of the conversion (c). Note, some of the data has been recalculated from the original references to take, among others, dilution effects into account.

1.2.3. GA plasmas

Most of the research for DRM with GA plasmas is based upon the 2D bladed electrodes,[95,97,118,167–170] while only some studies reported the use of a rotating GA discharge,[96,171–173] and mostly for biogas instead of a pure CH_4/CO_2 mixture.[171–173] All the data available in literature is plotted in **Figure 6-8**. Conversions in the 30–50 % range for both CH_4 and CO_2 have been reached, with energy costs as low as 1–2 eV per converted molecule. The best result achieved a total conversion of 39 % with an energy cost of only 1 eV/molecule.[96] The main products formed seem to be the syngas components, unsaturated C_2 hydrocarbons (i.e. C_2H_2 and C_2H_4) and solid carbon.[95–97,118] Hence, compared to a DBD, the distribution of C_2 hydrocarbons seems to be shifted from C_2H_6 to C_2H_2 and C_2H_4, and there is no formation of C_3 hydrocarbons reported.[97] This shift is commonly observed for discharges where the gas temperature is higher. Furthermore, compared to a DBD, which also operates at atmospheric pressure, GA plasmas deliver about the same conversion, but the energy cost is in general 20 times lower. This follows directly from **Figure 6-8**, because the energy input is also an order of magnitude lower. A more detailed discussion on the influence of the different parameters is given below.

For GA discharges, the addition of inert gases has not yet been studied in literature for DRM, but some studies have reported mixtures with reactive gases. Rueangjit et al.[167,168] investigated the dry reforming of simulated natural gas with a high CO_2 content, represented by CH_4:C_2H_6:C_3H_8:CO_2 in a molar ratio of 70:5:5:20. Only a comparison with mixtures without CO_2 was made, and it was concluded that CO_2 considerably enhances the conversion of the hydrocarbons in the feed.[167] In addition, very high syngas ratios, i.e. around 10–20, could be obtained by adding these small amounts of hydrocarbons in the feed, due to their lower C-H bond-energy.[167,168]

Furthermore, some research has also been performed on the combination of dry reforming with O_2 and steam using GA plasmas, to mimic biogas feeds as input source.[168,169,171–173] However, in this case CO_2 is not only converted but also being produced from the reaction of the CH_4 dissociation products with O atoms,[168,171,172] and in the case of H_2O addition, even a net CO_2 formation can be observed.[169,173] It is suggested that when adding O_2 the main process becomes the partial oxidation of methane, while the main involvement of CO_2 is in the reverse water gas shift reaction.[171] The positive effect of adding O_2 is the minimization of carbon deposit.[168] When adding steam, it seems again possible to obtain high syngas ratios, i.e. around 7.[169,173]

For DRM, the addition of a catalytic bed after the GA discharge zone has been investigated.[169,170] In both studies, a NiO/Al_2O_3 catalyst was used. The CO_2 and CH_4 conversion increased by 24 and 16 %, respectively. The selectivity of the syngas components, on the other hand, was found to drop slightly and the unsaturated hydrocarbons, C_2H_2 and C_2H_4, were formed with selectivities ranging from 16 to 19 %. Lower NiO loading and smaller particle sizes appeared to be beneficial. Finally, it is suggested that there is scope for further development and optimisation using a fluidised bed for maximising the plasma–catalyst interactions.[170]

It is clear that the obtained energy costs for DRM using a GA plasma are much lower than those obtained for DBDs, while at the same time achieving much higher feed processing capacities. Furthermore, the energy costs achieved already, i.e. around 1 eV/molecule, are already a factor 4 better than the required target for syngas production. No data is available yet for DRM of the GAP setup, but we may expect even further improvements, as already demonstrated for pure CO_2 splitting (see section 1.1.3 above). Finally, the use of a catalytic spouted bed might be able to influence the product distributions, as already reported for pure CH_4 reforming.[174]

1.2.4. Corona discharges

As described in **Chapter 1**, corona discharges can operate in both negative and positive mode, and both modes can be used to perform DRM, although positive coronas seem to exhibit slightly higher conversions, while the H_2/CO ratio is slightly higher for negative coronas.[100] This effect can be attributed to the different characteristics and generation mechanisms between both operation modes. Nevertheless, most research on DRM is performed with positive coronas. **Figure 6-9** summarizes the available data from literature. Both the conversion and energy cost increase with the SEI. Conversion values in the entire range up to 90 % are achieved, with energy costs around 20 eV/molecule. The best result comprises a total conversion of 44 % with an energy cost of 5.2 eV/molecule.[99] The main products formed are the syngas components, as well as C_2H_2, with some minor production of C_2H_6 and C_2H_4.[119]

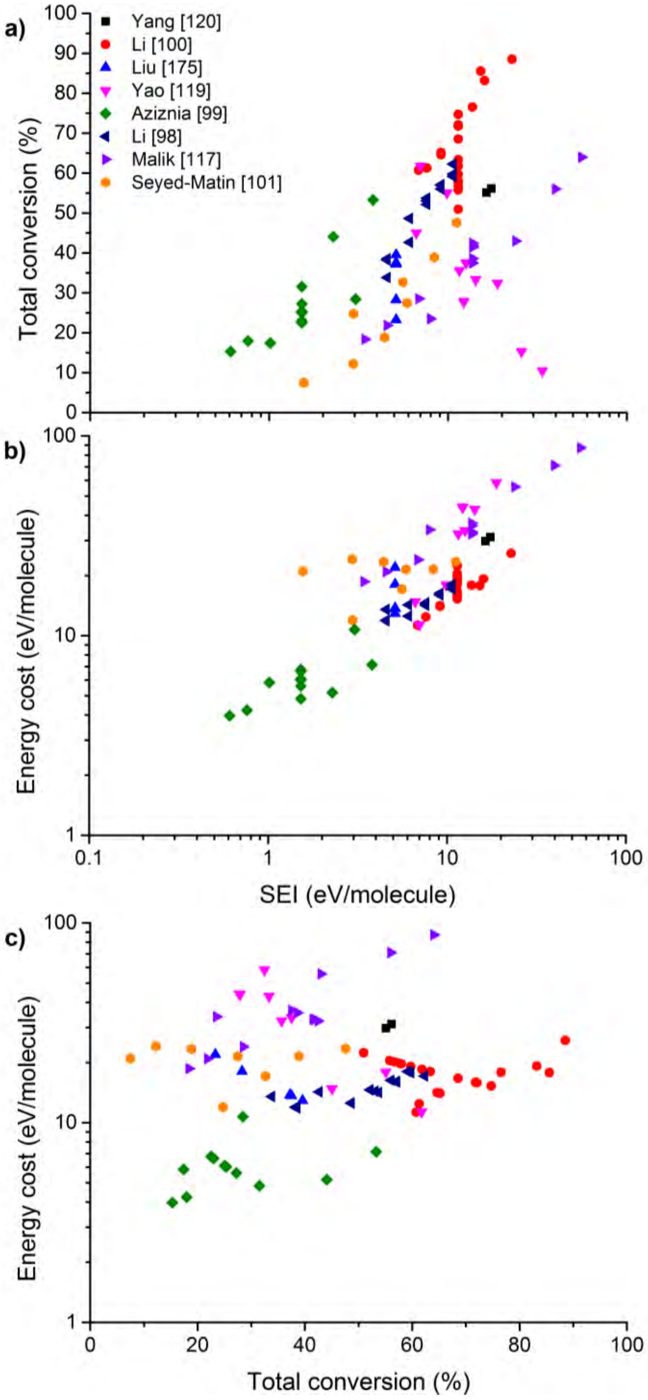

Figure 6-9. Experimental data collected from literature for DRM in a corona discharge, showing the conversion (a) and energy cost (b) as a function of the SEI, as well as the energy cost as a function of the conversion (c). Note, some of the data has been recalculated from the original references to take, among others, dilution effects into account.

A pulsed corona was investigated by Yao et al.[119], and it is reported that the conversions and CO selectivity increase with rising frequency, while the hydrocarbon selectivities showed the opposite trend.

Some experiments were also perfomed by placing catalysts in the corona discharge. Liu et al.[175] observed a significant conversion of CH_4 and CO_2 over NaOH treated Y zeolite placed in the discharge zone. The selectivity shifted towards higher hydrocarbons, e.g., propane, n-butane, isobutane, 1-butene, n-pentane. Aziznia et al.[99] investigated the effect of Ni/Al_2O_3 in the discharge zone. Upon addition of Al_2O_3, the conversions decreased slightly, the CO selectivity also decreased but the H_2 selectively increased remarkably. When adding up to 20 wt% Ni, the CH_4 and CO_2 conversions increased from 18 % and 25 %, to 23 % and 36 %, respectively. Furthermore, the selectivity towards CO was favoured over other carbon-containing compounds, and as a result, the H_2/CO ratio decreases, i.e. from 0.7 to 0.6 for Ni 20 wt%. It is suggested that CO_2 molecules are readily chemisorbed and dissociated into CO on the surface of Ni-based catalysts, and in a high electric field the Ni sites become active and affect the conversion and selectivity. Finally, Li et al.[98] used both Ni/Al_2O_3 and HZSM-5 zeolite (SiO_2/Al_2O_3=38) as catalysts. No significant effect on the conversions was observed, but the catalysts do affect the selectivities. Again, a higher CO and lower H_2 selectivity was observed for Ni/Al_2O_3, while higher H_2 and lower CO selectivities were measured for HZSM-5 zeolite as catalyst.

It is clear that corona discharges exhibit several similarities with DBDs, with an energy cost in the range of 4–100 eV/molecule and conversions up to 60 % (with exceptions up to 80 %). Thus, much work would still be required to lower the energy cost by a factor 2–3, before corona plasmas can become a competitive alternative. In addition, it is difficult to achieve a high treatment capacity due to a corona's localized breakdown.[78] This leads us to believe that at this point corona discharges have the same negative outlook as DBDs.

1.2.5. Spark discharges

Spark discharges are also being explored for DRM, but the developments are rather new and limited to date.[102–108,176–180] The available data is presented in **Figure 6-10**, showing a pronounced increase of total conversion with SEI. Furthermore, the energy cost is between 3 and 10 eV/molecule, with the best results achieving a total conversion of 85 % at an energy cost of barely 3.2 eV/molecule.[102] In addition to H_2 and CO, C_2H_2 is formed with selectivities up to 40 % and minor quantities of C_2H_4 and C_2H_6 are detected.[105]

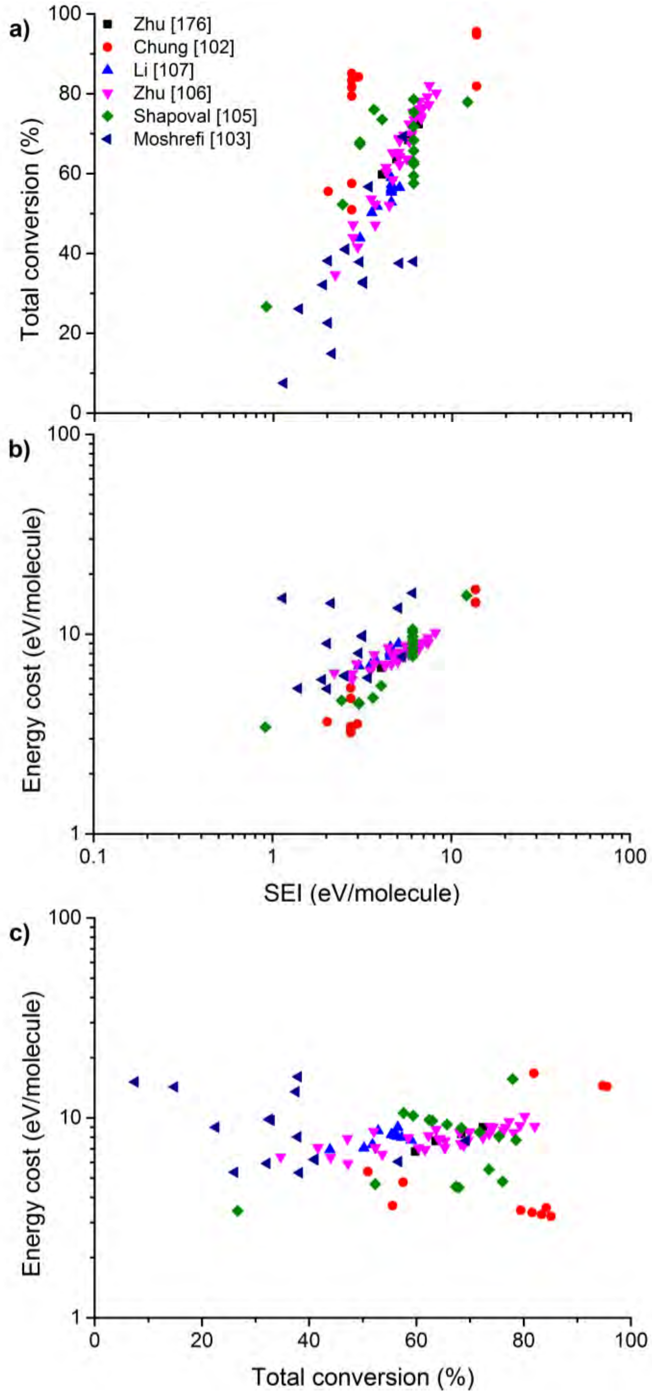

Figure 6-10. Experimental data collected from literature for DRM in a spark discharge, showing the conversion (a) and energy cost (b) as a function of the SEI, as well as the energy cost as a function of the conversion (c). Note, some of the data has been recalculated from the original references to take, among others, dilution effects into account.

A spark discharge with different interelectrode distances, varying pressure and frequency was investigated by Zhu et al.[106] With rising interelectrode distance from 3 to 9 mm a higher conversion was observed, followed by a slight decrease for even larger gap widths, while the selectivities are only slight affected. At increased pressures, i.e. up to 2.5 bar, higher conversions are reported for the same SEI.[106,176] The selectivities again appeared unaffected. When increasing the frequency from 5 to 80 kHz at the same SEI, an increase in the conversions of CH_4 and CO_2 from 67 % and 58 % to 74 % and 63 %, respectively, was observed. This might be explained by the relatively higher density of active species at higher frequencies. The product selectivities, on the other hand, showed only a minor dependence on the frequency.

Just like mentioned for the GA discharge above, for spark discharges a lot of research has already been performed for the addition of O_2 to the mixture to simulate biogas reforming.[107,177–180] The same observations were made regarding a shift from DRM to partial oxidation reactions,[107,177–179] with the suggestion that the water gas shift reaction is the major or even only effective contributor to the CO_2 conversion.[178,179]

Finally, some experiments were also performed for the implementation of catalysts in spark discharges. Chung et al.[102] used $BaZr_{0.05}Ti_{0.95}O_3$ (BZT) with a perovskite structure and ferroelectric properties as packing material inside the spark discharge zone. Compared to the empty reactor, the CH_4 and CO_2 conversions increased from 53 and 49 % to 84 and 77 %, respectively. This indicates that the combination induces synergistic effects and reduces the specific energy cost. Two types of packing were tested, i.e., coarse (C-BZT) and fine (F-BZT) particles. C-BZT showed a better performance than C-BZT, possibly because the void space is larger in the former, leading to a higher electron density.

In summary, spark discharges allow a high conversion, up to 85 %, while demonstrating low energy costs, i.e. 3–10 eV/molecule. At the same time they achieve high selectivities towards syngas, which is interesting for the indirect oxidative liquefaction. The direct formation of oxygenates was, however, not observed up to this point.

1.2.6. Atmospheric pressure glow discharges (APGDs)

The APGD shows quite some similarities with DBD and corona discharges. However, to date, the application of this discharge type for DRM is rather limited.[109,110,120,122,123] Nevertheless, it has some distinctive properties, which makes it more suitable than its two companions, e.g., its high electron density, as well as its proper plasma temperature for vibrational excitation. The highest obtained conversion of CH_4 and CO_2 is 99 % and 90 %, while the main products are H_2 and CO, with a ratio that can easily be modulated with the CH_4/CO_2 ratio.[122] **Figure 6-11** summarizes the data available in literature, with the best result achieving a total conversion of 89 % at an energy cost of only 1.2 eV/molecule.[122] Both the conversion and energy cost show a clear increasing trend with SEI.

Long et al.[123] added N_2 to the CH_4/CO_2 mixture to generate a stable discharge, but increasing the N_2 flow rate leads to a decrease of the CH_4 and CO_2 conversions from 46 % and 34 % to 37 % and 22 %, respectively, while the H_2 and CO selectivity only changed slightly.

Furthermore, Long et al.[123] combined the APGD plasma jet with a post discharge catalyst bed. A γ-Al_2O_3 carrier and 12 wt.% Ni/γ-Al_2O_3 catalyst were used. The performance for the γ-Al_2O_3 was similar to the plasma-only results, while the Ni/γ-Al_2O_3 catalyst significantly enhanced the process. The conversion of CH_4 and CO_2 increased by 14 % and 6 %, respectively, while the yields of H_2 and CO increased by 18 % and 11 %, respectively. The single pass conversion was, however, too low and N_2 was needed to maintain a stable discharge.[123]

In summary, the APGD seems to be promising for DRM, based on its proper plasma temperature for vibrational excitation and its high electron density, as it has a higher conversion ability compared to DBD and corona discharges, i.e. conversions up to 90 % are reported for energy costs as low as 1 eV/molecule. More research will be needed to fully demonstrate its capabilities. One of the major challenges remains a further enlargement of the process to treat large volumes.

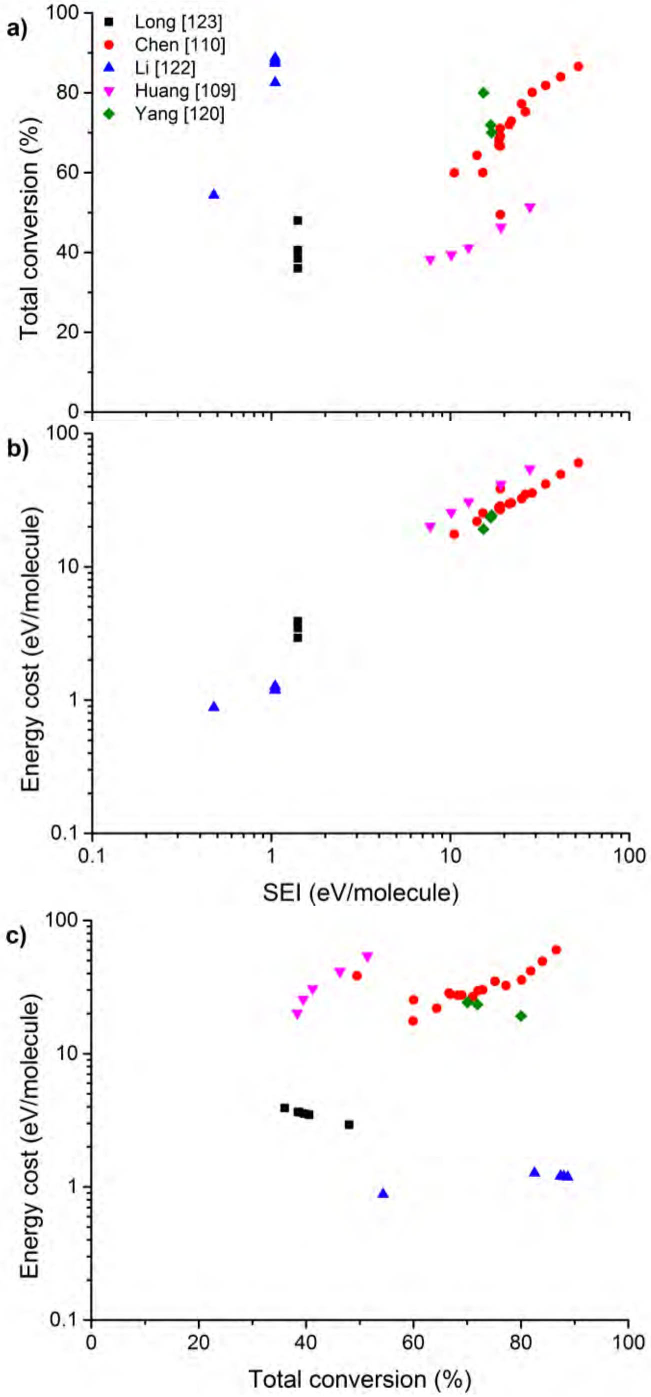

Figure 6-11. Experimental data collected from literature for DRM in an APGD, showing the conversion (a) and energy cost (b) as a function of the SEI, as well as the energy cost as a function of the conversion (c). Note, some of the data has been recalculated from the original references to take, among others, dilution effects into account.

1.2.7. Nanosecond pulsed discharges

Nanosecond pulsed discharges are another relatively new alternative used for DRM, for which relatively high energy efficiencies, or low energy costs, have been reported, compared to other discharge types. All the data available in literature is plotted in **Figure 6-12**. Total conversions in the 40–60 % range have been achieved, with energy costs around 3–10 eV per converted molecule.[111,115] The best results comprise an energy cost of only 5.3 eV/molecule for a total conversion of 56 %,[115] and 47 %.[111] The most abundant hydrocarbons formed are C_2H_2 (and C_2H_4). This is different from the results for DBD where C_2H_6 is mostly formed. Hence, the product distribution—with a prevalence for unsaturated hydrocarbons—in nanosecond pulsed discharges seems to be more similar to GA or spark discharges.[111] Work in this area has been performed for pulsed coronas with a pulse width of both 100 ns,[181] and 330 ns,[114,124] and pulsed glow-arc discharges with a typical pulse width in the range of 20–70 ns.[111–113,115]

In this type of discharges, the amount of power dissipated in the plasma is determined by the pulse voltage and pulse frequency.[112–115] A higher pulse voltage or repetition frequency leads to a higher power and hence increases the SEI and conversions. The influence of the pulse voltage seems to be stronger than that of the pulse frequency.[114] Regarding product selectivity, increasing the pulse frequency gives rise to a higher C_2H_4 selectivity and a decrease in C_2H_2 selectivity.[113,114]

Zhang et al.[124] investigated the effect of adding various catalysts to the discharge and observed significant effects. Pure γ-Al_2O_3 significantly increases the CH_4 conversion, while both the CO_2 conversion and C_2 selectivity decrease. La_2O_3/γ-Al_2O_3 catalysts, in contrast, give lower CH_4 conversions and higher C_2 selectivities, i.e. more than 60 %. Pd/γ-Al_2O_3 and Pd-La_2O_3/γ-Al_2O_3 catalysts show the same results as pure γ-Al_2O_3 and La_2O_3/γ-Al_2O_3, respectively, but the C_2 product distribution shifts from C_2H_2 to C_2H_4.[124]

In summary, these nanosecond pulsed discharges allow a high conversion, up to 50–60 %, while demonstrating relatively low energy costs, i.e. 3–10 eV/molecule. In previous sections, pulsed power DBD and corona discharges were mentioned, operating in the microsecond pulse regime, but it is clear that the latter does not attain the high conversions and energy efficiencies of nanosecond pulsed discharges. This leads us to believe that the nanosecond timescale is essential to create the necessary strong non-equilibrium,[112] as is also the case in the filaments of a DBD.

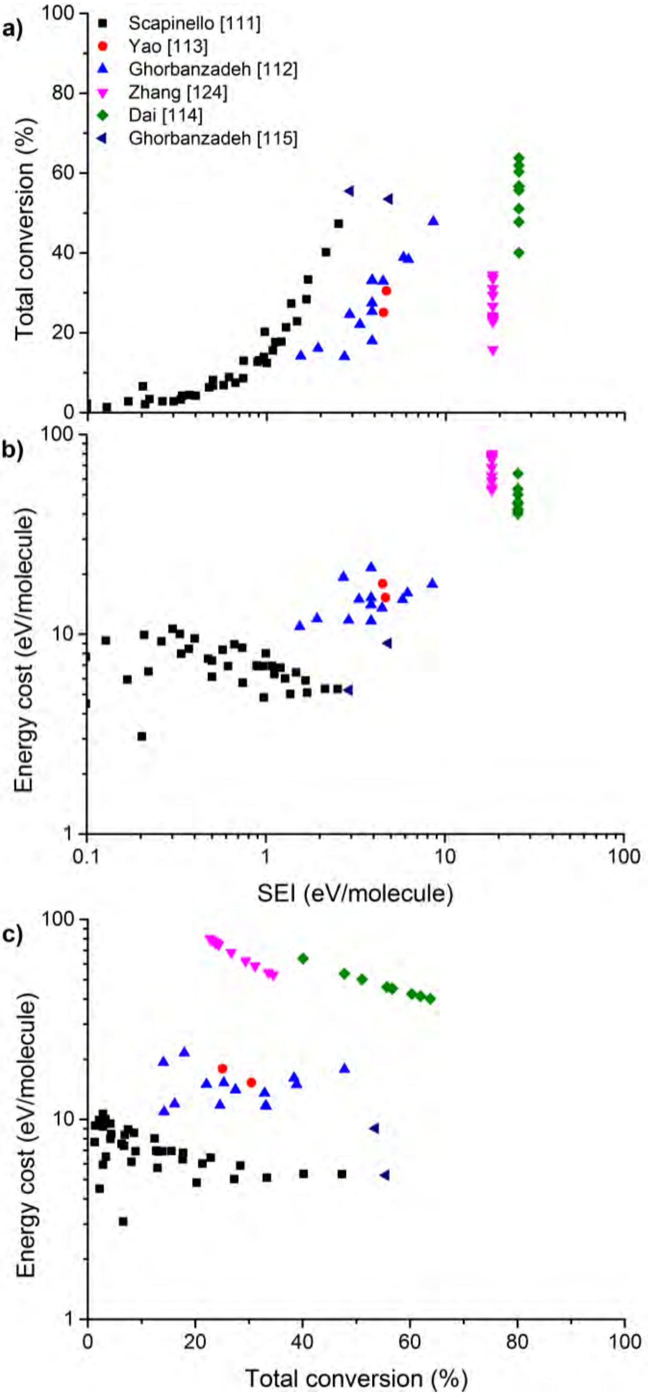

Figure 6-12. Experimental data collected from literature for DRM in nanosecond pulsed discharges, showing the conversion (a) and energy cost (b) as a function of the SEI, as well as the energy cost as a function of the conversion (c). Note, some of the data has been recalculated from the original references to take, among others, dilution effects into account.

1.2.8. Summary

It is clear that DRM has already been explored more extensively than pure CO_2 splitting, and several promising results have already been obtained for various types of plasmas. On the other hand, the DRM process is clearly more complex than pure CO_2 splitting. The CH_4/CO_2 ratio plays an extremely important role, not only in the conversion rates and energy cost, but even more importantly in the product distributions and syngas ratio. A balance appears to be required, since at high CH_4/CO_2 ratios carbon deposition can cause detrimental effects, while at low ratios the H atoms are being lost to H_2O, next to H_2 formation. Several discharges also exhibit high selectivities towards syngas, which is beneficial for the indirect oxidative process, while others might be more interesting in the long run due to their suitability for a direct oxidative process, in combination with catalysts.[3]

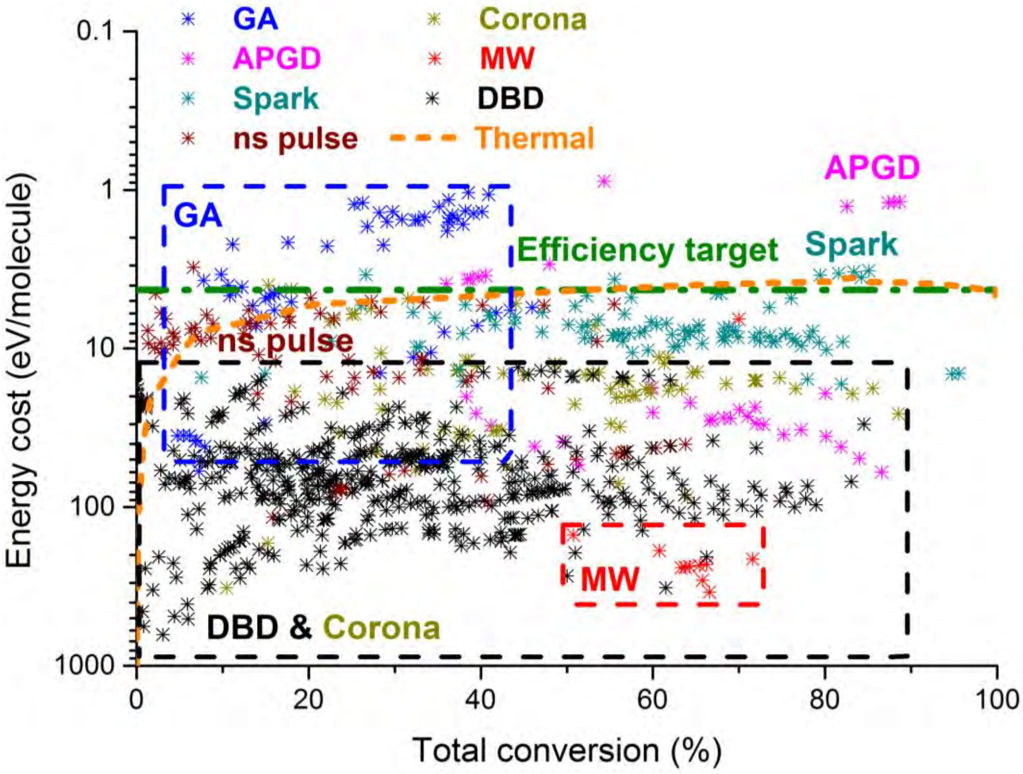

Figure 6-13. Comparison of all the data collected from literature for DRM in the different plasma types, showing the energy cost as a function of the conversion. The thermal equilibrium limit and the 60 % efficiency target for the production of syngas are also indicated. Note that the y-axis has been reversed to be more comparable with **Figure 6-5**.

To summarize, we plot in **Figure 6-13** the energy cost as a function of the total conversion, grouped per discharge type, for all the data discussed above. Furthermore, both the thermal equilibrium limit (see **Chapter 1; Figure 1-3**) and the target energy cost of 4.27 eV/molecule for the production of syngas (see beginning of the section on DRM; indicated as “Efficiency target”) are displayed. Note that the y-axis is reversed, to allow better comparison with **Figure 6-5** for pure CO_2 splitting, where we have plotted the energy efficiency. This figure allows to draw the following conclusions.

First of all, it is clear that for DRM—just like for CO_2 splitting—although DBDs are by far the most extensively studied, they do not allow energy-efficient conversion of CO_2 and CH_4 into syngas. Their energy cost currently remains a factor 5 too high, even when combined with a packing, and we do not expect this to be sufficiently improved in the near future, to become industrially competitive. On the other hand, when suitable catalysts can be found, allowing the direct high yield production of valuable oxygenates, this changes the analysis drastically, due to the more favourable energy requirements for the one-step process, as explained above. The same conclusion applies to most studies on corona discharges and several studies on APGDs, with some exceptions as mentioned below.

Second, the lack of data with MW plasmas on DRM compared to pure CO_2 splitting is slightly stunning. Research in this area is highly recommended to evaluate whether the potential of MW discharges for DRM can be as high as for pure CO_2 splitting.

Third, the best results for GA plasmas are easily capable of surpassing the energy efficiency (or energy cost) target set for DRM. Even for conversions up to 40 %, the energy efficiency target is easily crossed and they clearly operate in a strong non-equilibrium regime, as evidenced when compared to the thermal equilibrium limit. Moreover, further improvements are still to be expected from this discharge type, as the capabilities of the novel type of GAP, which has many advantages compared to classical GA discharges (see **Chapter 1** and section 1.1.3 above), have not yet been explored for DRM.

Fourth, although the use of spark discharges and nanosecond pulsed discharges is relatively new and studies are more scarce, energy costs in the range of 10 eV/molecule are reported —even as low as 3 eV/molecule, thus already reaching the efficiency target, even with the limited amount of research performed to date. For the nanosecond pulsed discharges, conversions are currently limited to 40–50 % at these energy costs, while for spark discharges conversions up to 85–95 % are already achieved. This clearly shows the potential for this type of discharges, and more research should be performed to further exploit their possibilities.

Finally, as mentioned above, for APGDs, some results obtained in literature seem to be very promising. Indeed, as appears from **Figure 6-13**, the best overall results are clearly achieved for APGDs, reaching a high conversion like for the spark discharge, i.e. 88 %, in combination with low energy costs, like for the GA discharges, i.e. 1.2 eV/molecule. Thus, at this stage, APGDs together with GA discharges, seem to be the most powerful, providing significant conversions at high energy efficiencies for DRM into syngas.

1.3. CO_2 + H_2O : Artificial photosynthesis

As is clear from the sections above, to date a lot of research is based on both pure CO_2 splitting and dry reforming of methane. There has also been some research on pure H_2O splitting with plasmas, for the production of hydrogen.[32,182–186] However, the research on the simultaneous conversion of CO_2 and H_2O—or so-called artificial photosynthesis—into syngas or oxygenated products by plasma is rather limited. The different plasma set-ups used to date for the combined CO_2/H_2O conversion are a a regular DBD,[187,188] a ferroelectric packed bed DBD,[187] a DBD packed with Ni/γAl_2O_3,[189] a MW discharge,[190–193] a GA,[54,62] a surface discharge,[194] and a negative DC corona discharge.[195]

1.3.1. DBD plasmas

Futamura et al.[187] investigated two different plasma reactor types, a ferroelectric packed bed reactor (using $BaTiO_3$ pellets) and a silent discharge reactor, a.k.a. a DBD. For both reactors the CO_2/H_2O mixture was diluted to 0.5–2.5 % in N_2. For the DBD reactor a CO_2 conversion of only 0.5 % was obtained with product yields of 0.7 % for H_2, 0.5 % for CO and 0 % for O_2, but no oxygenated compounds are mentioned. The packed bed reactor was much more successful and a CO_2 conversion of 12.3 % was reached with product yields of 12.4 % for H_2, 11.8 % for CO and 2.8 % for O_2, but again, nothing is mentioned on the formation of oxygenates.

Mahammadunnisa et al.[189] investigated the effect of a DBD reactor packed with a Ni/γ-Al_2O_3 catalyst, in both its unreduced and partially reduced forms, on the combined CO_2/H_2O conversion. For the measurements without a catalyst, a CO_2 conversion of 12–25 % was obtained, depending on the SEI. The higher the power or the longer the residence time, the higher was the conversion. The reported selectivity was 18–14 % for H_2 and 97–99 % for CO, leading to a syngas ratio of 0.55–0.18. When adding the catalysts, the conversion and syngas ratio increased, to 18–28 % and 0.95–0.45, respectively, for the unreduced catalyst (NiO/γ-Al_2O_3), and to 24–36 % and 0.66–0.35, respectively, for the partially reduced catalyst (Ni/γ-Al_2O_3). In this case, the added catalyst leads to a combination of physical and chemical effects, since beside the enhanced conversion, the NiO catalyst is responsible for a further reduction of the produced CO to CH_4 (and CH_3OH), as well as other compounds that were detected, i.e., C_2H_2, propadiene, as well as carbon nanofibers for the partially reduced catalyst.

Furthermore, it was concluded that higher flow rates lead to a higher H_2/CO ratio, and thus to economical syngas production.

Snoeckx et al.[188] recently performed a combined experimental and computational study for CO_2/H_2O conversion in a DBD. CO_2 and water vapour were used as feed gases, varying the H_2O content in the mixture between 0 and 8 % for three different SEI values. It was demonstrated that adding a few % of water to a CO_2 plasma leads to a steep drop in the CO_2 conversion, and both the CO_2 and H_2O conversion keep decreasing slightly when adding more water. The main products formed were CO, H_2 and O_2, as well as H_2O_2—up to 2 % for high SEI values and water contents. The combination of experiments with a computational chemical kinetics study allowed to analyse the chemical kinetics and to construct and investigate the different chemical pathways to clarify the experimental results. In general, it was concluded that for a DBD the main reactive species created are OH, CO, O and H, of which the OH radicals will quickly recombine with CO into CO_2, thereby limiting the CO_2 conversion upon addition of water. At the same time, the O and H atoms will undergo subsequent reactions to form H_2O again, explaining why the H_2O conversion is also limited. Furthermore, the fast reaction between O/OH and H atoms also explains why no oxygenated products were formed, because it occurs much faster than the possible pathways that might lead to oxygenates.[188]

1.3.2. MW plasmas

Ihara et al.[190,191] were the first to investigate the combined CO_2 and H_2O conversion. In their first study[190] a 1:1 mixture of CO_2/H_2O was investigated for a MW plasma. They detected low yields of oxalic acid and H_2O_2 in the cold trap condensate by reversed-phase chromatography using UV and conductivity detectors. The H_2O_2 production was very dependent on the discharge power and a maximum yield of 0.024 % was obtained. Furthermore, they assumed that H_2 and O_2 are generated, but these products were not measured. Interestingly, they also found the deposition of a transparent solid crystal film on the reactor walls, corresponding to oxalic acid.

In their follow-up study[191] they used the same MW set-up, but alternative detection techniques, i.e. steam chromatography and gas chromatography-mass spectrometry (GC-MS). The CO_2/H_2O gas mixture was varied from a 1:4 to 1:1 ratio but the conditions for the presented results were not mentioned. This time, methanol formation, instead of H_2O_2 and oxalic acid, is reported, albeit in very low concentrations < 0.01 %, both in the effluent stream as in the transparent solid crystal film that was deposited on the reactor walls. Therefore, the authors concluded that two pathways for methanol formation could be considered, i.e., the direct formation from CO_2 and H_2O in the plasma and the reformation of deposited polymeric material on the walls during the plasma reaction with H_2O. Most importantly, they observed that the methanol yield increased by a factor 3.5 when increasing the pressure from 240 to 400 Pa, stating that the system pressure is one of the most important parameters.

Chen et al.[192] applied a surface-wave MW discharge for the simultaneous dissociation of CO_2 and H_2O. The formation of syngas and O_2 was observed, but no hydrocarbons or oxygenates were detected. The influence of the gas mixing ratio, the SEI, and the feed flow rate on the H_2 and CO production is studied. It is found that syngas with a ratio close to 1 can be produced when the CO_2/H_2O ratio in the gas mixture is 1:1.

In a follow-up study[193], the authors combined their MW setup with NiO/TiO_2 catalysts. In this work they report an increase in CO_2 conversion from 23 to 31 %, along with a lower energy cost from 30.2 to 22.4 eV/molecule, when adding 10 % H_2O for the plasma-only conditions. At the same time, a lower gas temperature was observed, which might be due to the higher heat capacity of water and the induced endothermic reactions. In turn, this lower temperature might be responsible for the higher conversion, since a lower gas temperature in MW plasmas is beneficial for energy efficient CO_2 conversion, due to lower vibrational losses by V-T relaxation (see also **Chapter 1** and section 1.1.2 above) and a reduced backward reaction rate, i.e. recombination of CO back into CO_2.[43,44] When adding a NiO/TiO_2 catalyst treated with an Ar plasma, the CO_2 conversion further increased to 48 %, with an energy cost of 14.5 eV/molecule. Still, no oxygenated products were detected. It is suggested that CO_2 is adsorbed at an oxygen vacancy on the catalyst surface, reducing the threshold for the dissociative electron attachment process to 2 eV, creating CO, an adsorbed O atom at the vacancy and an electron. Subsequently, the adsorbed O atoms interact with OH to form O_2 and H, as well as with gas phase O atoms to recombine to O_2. As such, this seems to be some evidence that the reactions and species limiting the CO_2 and H_2O conversion, as described in the chemical reaction pathways for a pure DBD plasma,[188] (see previous section) can indeed—as suggested—be hijacked by the implementation of a catalyst.

1.3.3. GA plasmas

As mentioned in section 1.1 on pure CO_2 splitting, Indarto et al.[62] and Nunnally et al.[54] applied a GA to investigate the conversion and energy efficiency of CO_2. The former investigated the addition of water vapour in the range of 5 to 31 % for a classical GA. A decrease in CO_2 conversion (from 7.1 to 3.0 %) and an increase in energy cost (from 89 to 189 eV/molecule) was observed over this range compared to 13.4 % and 53 eV/molecule for pure CO_2. One of the suggested reasons was the increased instability of the GA with increasing water vapour concentration. Nunnally et al.[54] investigated the effect of adding 1 % water vapour for a GAP, which showed an increase in energy cost from 9.5 to 14.8 eV/molecule. While Indarto et al.[62] attributed this to arc instabilities, no instabilities were observed for the GAP. Therefore, it was concluded that this higher energy cost is due to vibrational energy losses through V-T relaxation. This process is relatively slow for CO_2 molecules,[32,54] leading to the high energy efficiency of pure CO_2 splitting in a GA and MW plasma. However, for H_2O this V-T relaxation is much faster,[32,54] hence it is believed that water will absorb part of the vibrational excitation energy of CO_2 and subsequently lose this energy quickly through V-T relaxation, leading to the observed drop in energy efficiency, or vice versa, the rise in energy cost.[32,54]

1.3.4. Other plasma types

Another discharge type, the surface discharge, was applied for both a 1:1 mixture of CO_2/H_2 and CO_2/H_2O in a comparative study by Hayashi et al.[194] The CO_2 conversions were 15 and 5 %, respectively. In both cases the major products were the same, i.e., CO, CH_4, dimethyl ether (DME) and formic acid, and in the case of H_2 as co-reactant, water formation was also observed.

Guo et al.[195] reported the use of a negative DC corona discharge for the reaction between CO_2 and H_2O, varying the water vapour content between 10 and 43 %, and the pressure between 1 and 4 bar. They observed a drop in CO_2 conversion with increasing gas flow rates (hence decreasing SEI) and increasing water content. The main products formed were ethanol and methanol, in roughly a 3:1 ratio, with a total molar yield up to 4.7 % and the CO_2 conversion reached a maximum of 16 % at 1 bar, 50 mL/min and 23 % water vapour. Other compounds detected were H_2 and CO. Increasing the pressure had a beneficial effect on the methanol and ethanol yields. For example, when going from 1 to 4 bar, the ethanol yield increased from 3.2 to 11.9 %. Unfortunately, some of the reported results seem to be contradictory/inconsistent, making it difficult to interpret the obtained results.

1.3.5. Summary

In general, from all the data presented in the available literature, we may conclude that for plasma-only cases the addition of even small amounts of water (1–2 %) leads to a significantly lower CO_2 conversion. The declining trend continues upon addition of even more water, albeit less severe. As a result the addition of water also leads to higher energy costs. For a classical DBD reactor the energy cost was already quite limited, making it unsuitable for the combined CO_2/H_2O conversion. As shown in sections 1.1 and 1.2 above MW and GA plasmas are far more efficient. Moreover, they operate at somewhat higher temperatures, i.e. in the order of 1000 K or more, which enables the addition of more H_2O vapour. Nevertheless, it has been suggested that H_2O might quench the vibrational levels of CO_2,[54,62] thus reducing the most energy efficient conversion process, and therefore raising the energy cost. Both GA studies reported in literature, by Nunnally et al.[54] and Indarto et al.,[62] seem to confirm this hypothesis, while the MW results from Chen et al.[193] seem to contradict it. However, their MW set-up might be less prone to this quenching mechanism, since it operates at low pressures (30–60 Torr). Furthermore, the presence of water in the low pressure MW case seems also to lead to a cooling effect, resulting in a higher energy efficiency. Nevertheless, the low pressure operation is still less ideal for industrial implementation. **Figure 6-14** summarizes the energy cost per converted CO_2 molecule as a function of the conversion, for those discharges where data was available.

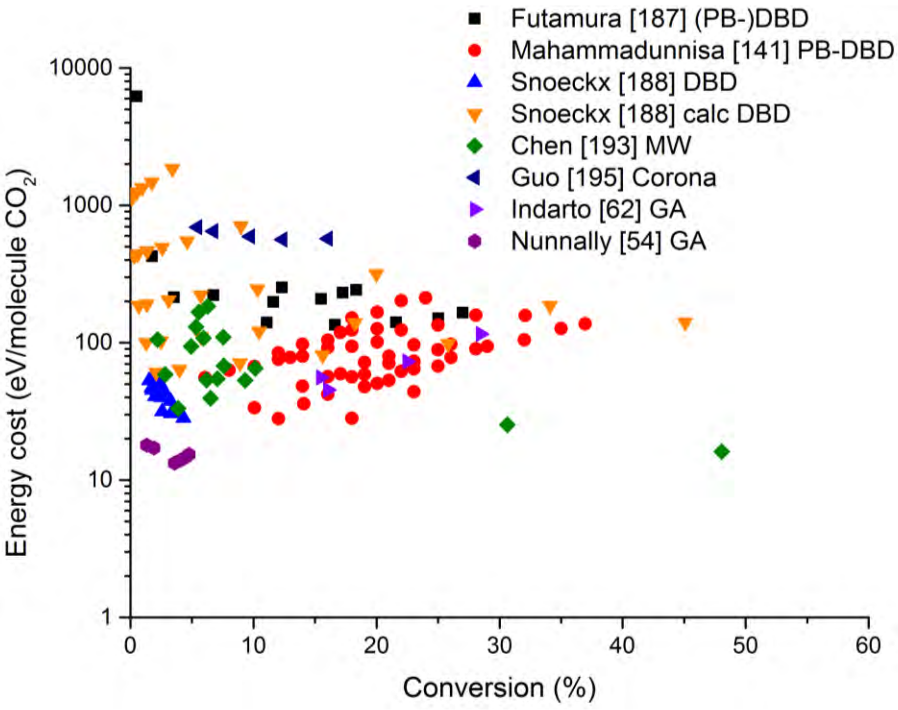

Figure 6-14. Comparison of all the data collected from literature for the artificial photosynthesis ($CO_2 + H_2O$) in the different plasma types, showing the energy cost per converted CO_2 molecule as a function of the conversion. Note, some of the data has been recalculated from the original references to take, among others, dilution effects into account.

The main products formed are again H_2, CO, like in the case of DRM (see previous section), as well as O_2, but some papers also report the production of hydrogen peroxide (H_2O_2),[188,190] oxalic acid ($C_2H_2O_4$),[190] formic acid (CH_2O_2),[194] methane (CH_4),[189,194] dimethyl ether (C_2H_6O, DME),[194] methanol (CH_3OH),[189,191,195] ethanol (C_2H_5OH),[195] acetylene (C_2H_2),[189] propadiene (C_3H_4)[189] and carbon nanofibres (CNF).[189] Unfortunately, most data on the formation of these products are only qualitative and mainly incomplete, making it impossible to deduce a general trend on product yields or selectivities. Although, research on this process is more limited than for DRM—and hence the road ahead is longer—this clearly indicates that, just like for DRM above, the plasmachemical conversion of CO_2 with H_2O as co-reactant allows for the development of the highly desirable direct oxidative pathway.

It is clear from the results obtained in literature that CO_2 and H_2O seem to be unsuitable to create oxygenated hydrocarbons in a one-step process by means of a pure non-thermal plasma, i.e. in the absence of a catalyst, with the exception of a negative DC corona discharge. There are too many steps involved in generating these oxygenates, such as CH_3OH, in an efficient way, and all of them involve H atoms, which will have the tendency to quickly recombine with OH into H_2O or with O_2 into HO_2, which also reacts further with O into OH—and hence H_2O. The problem at hand is thus that the interactions of H atoms with oxygen species (either OH, O_3, O_2 or O atoms) are too fast and their tendency to form H_2O is too strong.

On the other hand, CO_2/H_2O plasmas can deliver an easily controllable H_2/CO ratio with a rich hydrogen content—even up to 8.6—when sufficient amounts of water can be added to the CO_2 plasma, as was demonstrated in the computational study of Snoeckx et al.[188] Hence, they might be suitable to create value-added chemicals, such as oxygenates, in a two-step process, which is good news. However, the interaction between H_2O and CO_2 dissociation products, i.e., the recombination between OH and CO into CO_2, and the recombination of H and OH into H_2O, limit the CO_2 and H_2O conversion, and thus the formation of useful products. Besides syngas, the direct production of sufficient amounts of hydrogen peroxide, which can be used as a disinfectant or for biomedical purposes, seems possible. However, the formation rate of H_2O_2, is also partially limited by the destruction reaction of OH + H_2O_2 towards H_2O and HO_2. Therefore, the rapid removal of the formed product (i.e., H_2O_2), e.g., by means of a membrane, would be an important aspect for further improving this process. Based on these findings, and the work by Mahammadunnisa et al.[189] it is evident that a CO_2/H_2O plasma should be combined with a catalyst in order to produce value-added chemicals.[136,196]

As such, it appears that due to the inherent nature of this mixture and the plasma set-ups, the future for the combined CO_2 and H_2O conversion by pure plasma technology does not looks so bright at the moment. Nevertheless, we believe that a possible promising way forward is by its combination with specific tailored catalysts to produce value-added chemicals.

This catalyst should be able to selectively let the plasma-generated CO and H_2 react into oxygenates, such as methanol, and subsequently separate the methanol from the mixture. As mentioned in the next section, Eliasson et al.[197] applied a $CuO/ZnO/Al_2O_3$ catalyst in a CO_2/H_2 discharge, resulting in an increase in methanol yield and selectivity by more than a factor 10. Several other reported catalysts used already for CO_2 conversion with H_2 in traditional thermal catalysis might also be interesting to investigate for their suitability in plasma-catalysis in a CO_2/H_2O mixture, such as Ni-zeolite catalysts for which methanation is reported,[198] a Rh_{10}/Se catalyst yielding an ethanol selectivity up to 83 %,[199] and a Ni-Ga catalyst for the conversion into methanol.[200] Moreover, a lot of research into the catalytic CO_2 hydrogenation is showing promising results for $CuO/ZnO/ZrO_2$, Cu/ZnO-based catalysts promoted with Pd and Ga, as well as Pd/ZnO and Pd/SiO_2 with the addition of Ga.[201] In general, multicomponent systems ($Cu/ZnO/ZrO_2/Al_2O_3/SiO_2$) have reported good performances for the formation of methanol starting from $CO/CO_2/H_2$ mixtures,[199] making them potentially also very interesting for plasma-catalysis of a CO_2/H_2O mixture (as well as for DRM), because the $CO/CO_2/H_2$ mixture is anyway generated during plasma-based conversion.

Based on the chemical kinetics pathway analysis presented by Snoeckx et al.[188] (see section 1.3.1 above), two pathways might be interesting and realistic to achieve: (i) promoting the recombination of OH radicals to H_2O_2 or (ii) promoting the reduction of CO to methanol. In both cases, the thermodynamic aspects at the nanoscale will become very important, especially since plasma catalysis is a far-from-equilibrium process.[196] The critical point will be the arrival and binding (e.g., physi- or chemisorption) of the reactants to the catalyst surface. To be successful, this process should be faster than the recombination rate of OH with H into H_2O. Of course, these suggestions are only speculations, and further research will be needed to investigate these possibilities in practice.

We need to make a final critical note concerning safety. We need to be cautious about the explosive mixture that can be formed during this process—which could of course also occur for some of the other novel technologies discussed in **Chapter 1** when O_2 and H_2 are not produced separately—due to the presence of O_2, together with CO, H_2 and an ignition source in a plasma set-up. At the research level this will probably never be a problem due to the low volumes and conversions. However, when going to a pilot or industrial scale, with larger volumes and conversions, the risk will increase significantly. Consequently, both the capital and operating costs will increase drastically to ensure safe operations. One way to circumvent this problem is by diluting this mixture with an inert gas, such as argon or helium. In this case, however, an additional separation (for the products) and recuperation (for the inert gas) step will need to be included, which will also increase the cost. Furthermore, part of the input energy will be lost due to the electron impact excitation and ionization of these gases. Therefore, this option will reduce the energy efficiency and increase the operating cost, but it ensures safe operations.

1.4. $CO_2 + H_2$: Hydrogenation of CO_2

Research on the plasma-based hydrogenation of CO_2—using H_2 as co-reactant—is as limited as the combined conversion of CO_2 and H_2O. Historically, this is in part due to the high cost of hydrogen. Like for multiple other novel technologies discussed in **Chapter 1**, the sustainable and economically viable production of H_2 is indispensable for pathways relying on the use of H_2 as co-reactant. Although interest into the plasma-based hydrogenation of CO_2 emerged around the same time as the use of H_2O as co-reactant, most of the work performed is very recent. The different plasma set-ups used to date are a DBD,[197,202] , a packed bed DBD,[197,203] a MW discharge,[193,204,205] an RF discharge,[206] and a surface discharge.[194]

1.4.1. DBD plasmas

Eliasson et al.[197] investigated the hydrogenation of CO_2 to methanol in a DBD, both with and without the presence of a $CuO/ZnO/Al_2O_3$ catalyst. The experiments were performed at a gas pressure of 8 bar and a H_2/CO ratio of 3:1. For the plasma-only case, the major products found were CO and H_2O, which is not surprising keeping the results of CO_2/H_2O in mind (see previous section). Other components detected were CH_4 and methanol, with a selectivity of only 3–4 % and 0.4–0.5 %, respectively. By adding the catalyst, the methanol yield increased about 10 times and the selectivity was 10–20 times higher. Furthermore, by optimizing the system to use low power and high pressure, it became possible to further enhance the methanol selectivity over the CH_4 selectivity. The results indicate that the discharge shifts the region of maximum catalyst activity from 220 °C to 100 °C. Nevertheless, the electric power used is considered to be prohibitive for methanol production on an industrial scale, due to the low yield, ~1 %.

The methanation of CO_2 in a DBD packed with Ni/zeolite pellets was investigated by Jwa et al.[198] Conventional and plasma-assisted catalytic hydrogenation were compared with a varying nickel loading for a temperature range of 180–360 °C for the stoichiometric 4:1 ratio of H_2/CO_2. For the conventional catalytic hydrogenation case, a conversion of 96 % was observed at 360 °C, while for the plasma-assisted hydrogenation, the same conversion was already reached at 260 °C. It is assumed that reactive species generated in the plasma reactor can speed up the rate determining step of the catalytic hydrogenation. The hydrogenation of CO_2 involves the dissociation of CO_2 to CO and O on the active site of Ni/zeolite ($CO_{2,ads} \rightarrow CO_{ads} + O_{ads}$). The rate determining step in the CO_2 conversion into CH_4 would be the same as for CO conversion ($CO_{ads} \rightarrow C_{ads} + O_{ads}$). Subsequently, the dissociated species react with hydrogen to produce CH_4. This increased methanation rate is believed to arise from an increase in the surface concentration of carbon. The plasma can help to dissociate the adsorbed molecules, hence surface carbon can be produced by both thermal activation and plasma activation, eventually resulting in a higher methanation rate. Without Ni (bare zeolite), the conversion of CO and CO_2 was found to be less than 1 %, implying that the zeolite support together with the plasma cannot efficiently convert CO_2 into CH_4.[198]

Nizio et al.[203] investigated the effect of a packed bed DBD with Ni-$Ce_xZr_{1-x}O_2$ catalysts on the hydrogenation of CO_2 for the stoichiometric H_2/CO_2 ratio of 4:1. At 90 °C without catalyst, the CO_2 conversion was around 5 %, without any methanation taking place. For the same conditions, 78 % CO_2 conversion and methanation with a selectivity of 99 % and energy cost < 3 eV/molecule CH_4 was achieved, when adding a catalyst. This demonstrates the activity of plasma catalytic systems at low temperature ($T_g < 260$ °C) and the possibility of enhancing both the conversion and selectivity of the process under study, by combining plasma with catalysts. Furthermore, the plasma-catalytic system showed almost no difference in activity for the different ceria-zirconia supports, while in absence of plasma this was the case. The latter clearly indicates that it is indeed the plasma which initiates the methanation process by dissociating adsorbed CO_2 molecules—a reaction which does not take place catalytically below 250 °C.

Recently, Zeng et al.[202] investigated the performance of CO_2 hydrogenation in a DBD at atmospheric pressure and low temperature, both with and without catalyst, i.e. Cu/γ-Al_2O_3, Mn/γ-Al_2O_3 and Cu-Mn/γ-Al_2O_3. Some plasma-only results are also presented. The CO_2 conversion was found to be 7.5 %, and the main products were CO, H_2O and CH_4. The CO and CH_4 selectivity were 46 % and 8 %, respectively. No methanol production is reported, although this might be due to the inability to detect this compound by the GC set-up used. Adding the catalysts enhanced the process: the CO_2 conversion increased to 8–10 %; the CH_4 selectivity remained around 6.9–8.6 %, but the CO selectivity and yield were enhanced to 76–80 and 6.4–7.9 %, respectively.

Finally, de Bie et al.[207] performed an extensive computational study on the hydrogenation of CO_2 in a DBD, using a one-dimensional fluid model. The H_2/CO_2 mixing ratio was varied in the entire range from 1:9 to 9:1. The most abundant products predicted by the model were CO, H_2O and CH_4, and to a lower extent also formaldehyde, C_2H_6, O_2 and methanol. The CO_2 conversion was found to be rather low (2–7 % in the entire gas mixing ratio), especially when compared to typical values found for DRM (3–20 %) at comparable conditions. This is thought to be the result of the lack of high enough concentrations of CH_2 and CH_3 radicals, which aid in the CO_2 conversion. Moreover, a very similar chemical behaviour as described above for the CO_2/H_2O mixture[188] is reported. Indeed, the CO_2 conversion was limited due to the formation of CHO ($CO + H + M \rightarrow CHO + M$), which reacts back to CO_2 ($CHO + O \rightarrow CO_2 + H$). Furthermore, a lot of subsequent reactions are needed to form the desired hydrocarbons or oxygenates, such as CH_4 and methanol, making their overall production rates negligible. Hence, it was concluded that a CO_2/H_2 mixture in a DBD-only set-up is not suitable for the production of value-added chemicals.

1.4.2. MW and RF plasmas

Maya[204] employed a MW discharge to explore the possibility of obtaining formic acid from a H_2/CO_2 mixture. The pressure in the reactor was, however, very low, i.e. about 1–2 Torr. The main products observed were CO and water, with some secondary products when the H_2/CO_2 ratio exceeded 1:1, including acetylene, methane, methanol, ethylene, formaldehyde and formic acid.

A so-called RF impulse discharge was used by Kano et al.[206] to study the combined H_2/CO_2 conversion into CH_4 and methanol at low gas pressures (1–10 Torr). For a CO_2/H_2 mixing ratio of 4:1, the main products detected were CO and H_2O, as well as CH_4 and to a lesser extent—one order of magnitude lower—methanol. Formaldehyde and formic acid were not observed. When the repetition frequency was lowered from 60 to 10 kHz, the formation of products decreased as well, and the CH_4 production almost disappeared. The maximum CO_2 conversion and CH_4 selectivity obtained were 26 and 21 %, respectively. The most efficient production of CH_4 took place for a mixing ratio of 6:1 H_2/CO_2, which is larger than the stoichiometric ratio (4:1).

De la Fuente et al.[205] recently used a surface-wave MW plasma reactor without catalyst, to study the effect of gas flow rate, H_2/CO_2 mixing ratio and SEI on the performance for CO_2 hydrogenation. The main products found were CO and H_2O, as well as 200 ppm C_2H_4 and 10–20 ppm methanol, but remarkably no CH_4 was detected. The best performance was obtained for a H_2/CO_2 mixture of 3:1, obtaining a CO_2 conversion of 82 % and an energy cost of 28 eV per converted CO_2 molecule, which are the best values reported in literature for plasma-only operation. The CO_2 conversion was even higher than for pure CO_2 splitting, which was 65 %, with an energy cost of 35 ev/molecule. It was predicted by means of a zero-dimensional reactor model that the dominant intermediate species are H and O, which was also found by OES measurements. The higher conversion of CO_2 when adding H_2 is thought to be the result of the slightly lower ionization energy of H atoms, resulting in higher electron densities. Furthermore, as these atoms cannot be excited vibrationally and/or rotationally, it might lead to higher electron temperatures.[205]

Chen et al.[193] added a Ni/TiO_2 catalyst to a surface-wave MW plasma, to not only investigate a CO_2/H_2O mixture (see previous section), but also a H_2/CO_2 mixture in a ratio of 1:9. For the plasma-only case, a reduction in the CO_2 conversion from 23 to 14 % occurred. When adding the catalyst, the conversion was enhanced by a factor 2, up to 28 %, which was however still lower than for the pure CO_2 case (41 %) and no methanol or CH_4 formation was observed.

1.4.3. Other plasma types

As also mentioned in section 1.3 above, Hayashi et al.[194] investigated both the effect of H_2O and H_2 as additive gas for the plasma-based conversion of CO_2 using a surface discharge. A 1:1 mixing ratio was used at atmospheric pressure. The products observed were again CO and H_2O as main components and additionally CH_4, DME and formic acid. For the highest SEI conditions, the maximum CO_2 conversion was approximately 15 %. Although higher than for the CO_2/H_2O case, these conversions and yields are considered to be too low.

1.4.4. Summary

It is clear from the above results that the conversions in CO_2 hydrogenation are about a factor 2–3 lower (and the energy costs the same factor higher) than for DRM and pure CO_2 splitting. Therefore, we may conclude from the limited data available in literature that the hydrogenation of CO_2 for plasma-only cases is not successful. **Figure 6-15** summarizes the energy cost per converted CO_2 molecule as a function of the conversion for those discharges where data was available.

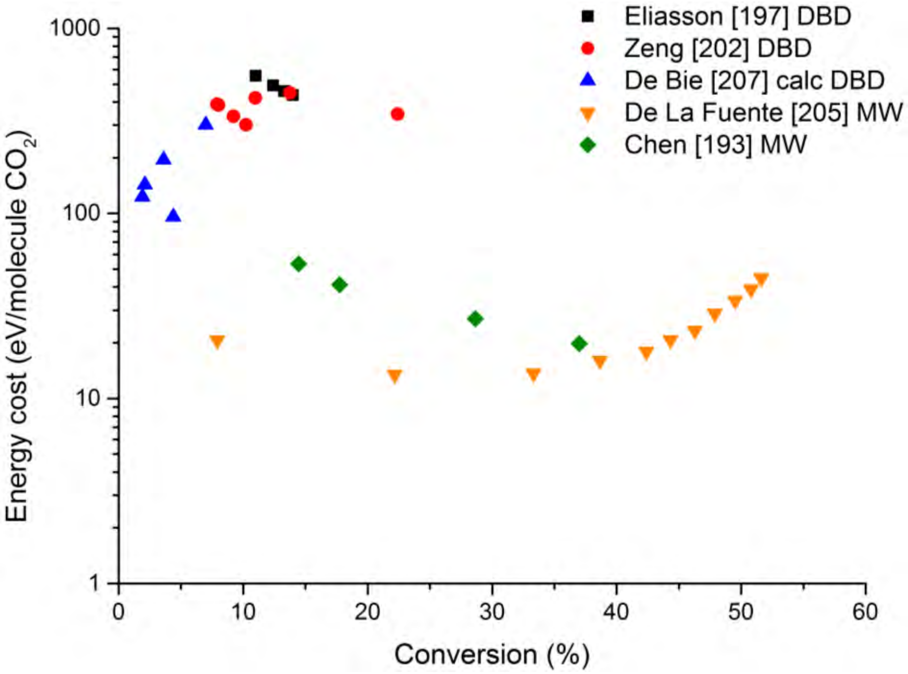

Figure 6-15. Comparison of all the data collected from literature for CO_2 hydrogenation in the different plasma types, showing the energy cost per converted CO_2 molecule as a function of the conversion. Note, some of the data has been recalculated from the original references to take, among others, dilution effects into account.

From all the data presented in the available literature, the main products formed are clearly CO and H_2O. Some secondary products are reported, but always in much smaller—sometimes negligible—amounts, with the most important ones being CH_4[194,197,202,204,206,207] and methanol,[197,204–207] although some papers also report the production of formaldehyde (CH_2O),[204,207] formic acid (CH_2O_2),[194,204] dimethyl ether (C_2H_6O, DME),[194] acetylene(C_2H_2),[204] ethylene (C_2H_4)[204,205] and ethane (C_2H_6).[207] In spite of these low amounts, the fact that these products can be formed is an indication that the plasmachemical conversion process has the potential for the development of the highly desirable direct oxidative pathway when suitable catalysts can be found.

Thus, CO_2 conversion using H_2 as an additive, without a catalytic packing, shows high resemblance with the use of H_2O, which is of course not surprising, since the same reactive intermediate species and hence reactions are responsible for the plasma chemistry taking place. In accordance with that observation, in a pure plasma set-up the combination of CO_2 and H_2 also seems to be unsuitable to create methane and/or methanol (or other oxygenated hydrocarbons) in a one-step process. The same number of steps—still too many—are involved in generating these value-added hydrocarbons or oxygenates in an efficient way. All these steps involve H atoms, which will have the same tendency to quickly recombine into OH and subsequently H_2O.

Nevertheless, from the limited studies available, it appears that the combination with a catalytic packing is a viable option to produce value-added chemicals in an efficient way. We would like to make the same suggestions as in the previous section, namely the catalyst should be able to selectively let the plasma-generated C (or CO) and H_2 react into methane (or oxygenates). Multicomponent systems ($Cu/ZnO/ZrO_2/Al_2O_3/SiO_2$) which show good performance for $CO/CO_2/H_2$ mixtures,[199] are potentially very interesting, since this mixture is anyway generated during plasma-based conversion of CO_2/H_2. Additionally, based on the work of Jwa et al.[198] and Nizio et al.,[203] the most effective and efficient pathway seems to be a low power Ni-based plasma-catalytic set-up, in which the plasma takes care of the rate determining step—namely dissociating the adsorbed CO into C—allowing for the catalyst to reduce the C with H to CH_4.

2. Benchmarking of plasma-based CO_2 conversion against the other (traditional and novel) technologies

In this section, we will compare plasma technology with the traditional catalytic approach and with the other novel approaches for CO_2 conversion, based on all aspects explained in the previous sections as well as **Chapter 1** and the other chapters of this dissertation. Furthermore, we will identify the advantages and limitations of plasma-based CO_2 conversion with respect to the other technologies, which will help us to define future priorities for the development of plasma-based CO_2 conversion systems.

2.1. Process versatility

A first comparison is made based on the versatility of the different CO_2 conversion technologies. **Table 6-1** shows the different technologies and the four different CO_2 conversion approaches that were discussed in this chapter. Traditional thermal catalysis, as discussed in **Chapter 1**, can be successfully applied for DRM and hydrogenation of CO_2, but seems unsuccessful at this point for pure CO_2 splitting, and data for the combined conversion of CO_2 and H_2O is unavailable. The novel technologies, discussed in **Chapter 1**, are all applicable to converting CO_2 together with H_2O. Furthermore, the electrochemical and solar thermochemical based technologies are also capable of pure CO_2 splitting. The combinations with CH_4 and H_2 are not generally reported in literature. Plasmachemical conversion, on the other hand, currently is the only technology reporting successful application for all four processes, i.e., pure CO_2 splitting, DRM, hydrogenation of CO_2, and the combined conversion of CO_2 and H_2O. As discussed in detail in section 1 of this chapter, plasma-based pure CO_2 splitting and DRM are obviously the two most successful processes today, with some types of plasmas already surpassing the posed 60 % energy efficiency target for syngas production and achieving conversions up to 90–95 %, even without the combination with catalysis. Furthermore, the production of liquids in a one step process, through a direct oxidative pathway (in combination with catalysts), has already proven successful and further research is in full progress. In this case, avoiding the intermediate syngas step and thus circumventing the need for an additional Fischer-Tropsch or methanol synthesis and subsequently methanol/ethanol to olefins synthesis would reduce the energy efficiency target to be competitive significantly (i.e. with at least a factor 2–3 in the case of methanol). Studies regarding the hydrogenation of CO_2 using plasmas in combination with catalysis are very promising as well, but more research is required. Although technically possible, the combined conversion of CO_2 and H_2O—so-called artificial photosynthesis—with plasma technology seems the least promising with the data available to date. Nonetheless, here as well the combination with catalysis could prove beneficial, if a suitable catalyst can be found, as discussed in section 1.3.5 above, but to date, research in this area is very scarce.

This high process versatility makes the plasmachemical conversion of CO_2 very interesting as a CCU technique. It allows the process to be used on a wide variety of locations, independent of the available product feed, and even adjustable to a variable product feed at a specific location by the easily adaptable process. This process versatility gives the plasmachemical conversion a substantial benefit over the other technologies.

Table 6-1. Overview of traditional thermal catalysis and the different emerging technologies, indicating their suitability for the four different CO_2 conversion processes discussed in previous section. The colour coding gives an additional visual sense for how efficient this process can be applied when it is achievable, as discussed in more detail in the text: inefficient (red), to be proven (orange) or efficient (green).

	CO_2 splitting	**CO_2/CH_4**	**CO_2/H_2**	**CO_2/H_2O**
Catalysis	🟥 **X**	🟩 **X**	🟩 **X**	NA
Electrochemical	🟩 **X**	NA	NA	🟩 **X**
Solar thermochemical	🟩 **X**	NA	NA	🟩 **X**[a]
Photochemical	NA	NA	NA	🟩 **X**
Biochemical	NA	NA	NA	🟩 **X**[b]
Plasmachemical	🟩 **X**	🟩 **X**	🟩 **X**[c]	🟧 **X**[c]

[a] CO_2 and H_2O are not converted at the same time, see discussion in **Chapter 1**.
[b] H_2O is a vital nutrient for the growth of the algae, see discussion in **Chapter 1**.
[c] When used in combination with catalysts (plasma catalysis), see sections 1.3 and 1.4.

2.2. Advantages/disadvantages

It is clear that, although all technologies—regardless of their maturity—have specific or even unique advantages, there is always a flip side to the coin. **Table 6-2** provides a visual overview of the different technologies discussed in **Chapter 1**, as well as plasmachemical conversion, with some of their key distinctive advantages and disadvantages.

From an economical and sustainable point of view, the use of rare earth metals is one of the key-disadvantages of most technologies at this point, except for the biochemical and plasmachemical conversion. As mentioned before, the grand challenge for the other emerging technologies to be successful (as well as for traditional catalysis) is switching to inexpensive earth-abundant metals. It cannot be stressed enough that this is a critical make or break point, which is not an issue for the plasmachemical conversion.

Table 6-2. Overview of traditional thermal catalysis and the different emerging technologies, indicating their distinctive key advantages and disadvantages. The colour coding gives an additional visual sense for the impact of the feature, as discussed in more detail in the text: negative (red), undesirable/neutral (orange) or positive (green).

	Use of rare earth metals	Renewable energy	Key-turn process	Conversion and yield	Separation step needed	Oxygenated products (e.g. alcohols, acids)	Investment cost	Operating cost	Overall flexibility
Traditional catalysis	*Yes*	-	*No*	*High*	*Yes*	*Yes*	*Low*	*High*	*Low*
Catalysis by MW-heating		*Indirect*						*Low*	*Low*
Electro-chemical	*Yes*	*Indirect*	*No*[b]	*High*	*Yes*[c]	*Yes*	*Low*	*Low*	*Low*
Solar thermo-chemical	*Yes*	*Direct*	*NA*	*High*	*No*	*No*	*High*	*Low*	*Low*
Photo-chemical	*Yes*	*Direct*[a]	*Yes*	*Low*	*Yes*	*Yes*	*Low*	*Low*	*Low*
Bio-chemical	*No*	*Direct*[a]	*No*	*Medium*	*Yes*[d]	*Yes*	*High /low*	*High*	*Low*
Plasma-chemical	*No*	*Indirect*	*Yes*	*High*	*Yes*[e]	*Yes*	*Low*	*Low*	*High*

[a] Bio- and photochemical processes can also rely on indirect renewable energy when they are coupled with artificial lighting, see **Chapter 1**.

[b] Electrochemical cells are key-turn, but generally the cells need to operate at elevated temperatures and the cells are sensitive to on/off fluctuations, see **Chapter 1**.

[c] The need for post-reaction separation for the electrochemical conversion highly depends on the process and cell type used, see **Chapter 1**.

[d] Biochemical CO_2 conversion requires very energy intensive post-reaction separation and processing steps, see **Chapter 1**.

[e] The need for post-reaction separation for plasma technology highly depends on the process, see section 1 of this chapter.

The discussion regarding the reliance on renewable energy in a direct or indirect manner (see **Chapter 1**) is more nuanced. The possibility of solar thermochemical, photochemical and biochemical conversion to rely directly on renewable energy—solar radiation—can be considered to be an edge over the other novel technologies, i.e., catalysis by MW-heating, electrochemical and plasmachemical conversion, which rely on electricity—hence indirect renewable energy. The former have the advantage of skipping an energy conversion step, which always leads to energy losses, hence the energy efficiency of the latter is intrinsically determined by the efficiency of the renewable electricity generation. On the other hand, this also means that the MW-heating, electrochemical and plasmachemical processes can rely on other renewable energy sources as well, e.g. wind, hydro, wave and tidal power, significantly increasing their versatility and employability, since they can be installed and operated independent of the availability of solar light. This significantly increases the application flexibility of MW-heating, electrochemical, as well as plasmachemical conversion. Note that bio- and photochemical technologies could also rely on indirect renewable energy, when used in combination with artificial lighting.

The wide scale adoption of these renewable energy sources, and their intermittent character, poses a challenge for the efficient storage and easy transport of the electricity produced. Not only is there a need for peak shaving, but more importantly a need for grid stabilisation, which requires technologies to follow the irregular and at times intermittent supply of renewable electricity in a flexible manner. Technologies which would be able to harness this energy and convert it into carbon neutral fuels could play an important role for the energy infrastructure industry. Due to the intermittent character of the renewable energies, a flexible storage process, which can easily be switched on and off to follow the supply, i.e. a so-called key-turn process, would be most ideal. Photochemical and plasmachemical conversion are the only two processes which truly meet this condition. They can be turned on with the flick of a button, since no pre-heating or long stabilization times (< 30 minutes) are required—like is the case for traditional catalysis. Likewise, they can be turned off with the flick of a button, since no sensitive cool down times are required and there is no risk in damaging the reactors with repeated on-off cycles. The problem with electrochemical cells is that they do not only operate at elevated temperatures, but they are not designed—they suffer—for repeatedly being turned on and off, while biochemical processes need to be looked after on a continuous basis, e.g. regarding nutrients, light, temperature, mixing.

From an industrial point of view, high conversions and yields are required, and most technologies are already capable of delivering on these requirements, with the exception of the photo- and biochemical conversion. A closely related key parameter is the solar-to-fuel efficiency, which will be discussed separately in the next section.

Furthermore, when assuming that all or most of the feed is converted, the question arises whether an additional post-reaction separation step is required for the products. The solar thermochemical and electrochemical conversion (depending on the process and cell type) are the only two technologies capable of generating separated product streams, i.e. separated CO and O_2 streams in the case of pure CO_2 splitting. This is an important advantage, since the separation of CO and O_2 is rather energy intensive at this point, but in the future, membranes might bring a convenient solution to this problem. Currently, this is probably the main disadvantage of plasma technology, as the products are all in one feed, i.e. for pure CO_2 splitting, a mixture of CO and O_2 is produced, and for DRM a mixture of (mainly) CO and H_2, with—highly depending on the discharge type—some (minor) side-products, like hydrocarbons and oxygenates. Of course, a mixture of CO and H_2 should not be a big problem, if it will be immediately processed further through Fischer-Tropsch or methanol synthesis, since the plasmachemical conversion is able to deliver any desired syngas ratio, mainly depending on the gas mixing ratio in the feed. Nevertheless, research on the in-situ trapping of species[208] or the combination with other technologies[209] is highly valuable, and requires more attention.

At the same time, this problem can also become less significant when focusing on the direct conversion of CO_2 into value-added liquid oxygenated products by means of plasma catalysis,[136,138] including alcohols, aldehydes and acids, which are easier to separate. In the long run, as already mentioned before, this direct method to produce more value-added products is highly preferred rather than the current indirect method, by first producing CO and H_2, which is then to be further processed. At the moment, except for solar thermochemical conversion, all technologies are already able to produce more value-added chemicals in a direct fashion, although the yields are still extremely low and most research is in its early stages.

The investment and operating costs are in general considered to be low for most technologies. The main exceptions are solar thermochemical conversion, which has a high investment cost for concentrating the solar energy, and biochemical conversion, where both investment and operating costs can be high, depending on the bioreactor type. Furthermore, the plasmachemical conversion is a highly modular technology, which is not dependent on an economy of scale and thus allows for local on-demand production capabilities.

Finally, one of the key-features for CCU techniques is their overall flexibility. This is actually a combination of many of the features discussed above. The plasmachemical conversion has a tremendous advantage here, due to its feed flexibility (CO_2, CO_2/CH_4, CO_2/H_2 and CO_2/H_2O), its energy source flexibility (solar, wind, hydro, nuclear power), its operation flexibility (instant on/off, power scalability) and its flexibility of scale.

None of the other technologies possess this unique combination of features required for the successful worldwide implementation as a CCU technique.

In conclusion, plasma technology fares very well in this comparison, with its main disadvantage being its current need for post-reaction separation processes, additionally the energy efficiency is dependent on the reactor type and the combination with catalysis is required to steer the product yield and selectivity.

2.3. Solar-to-fuel efficiency

In our opinion, the most interesting measure to compare the different technologies is based on how well solar energy is converted into chemical energy, known as the solar-to-fuel energy conversion efficiency ($\eta_{\text{solar-to-fuel}}$). First we will calculate this value for the various plasma-based technologies, based on the data presented above. Subsequently, we will compare these solar-to-fuel efficiencies with the values for the other emerging technologies.

Where possible (see the discussion in section 2.4 below) we calculated the solar-to-fuel conversion efficiency for all the pure CO_2 splitting data, based upon:

$$\eta_{\text{solar-to-fuel}}(\%) = \frac{E_{out}}{E_{in}} = \frac{\Delta H_{c,fuel}\left(\frac{kJ}{mol}\right)}{SEI\left(\frac{kJ}{mol}\right)} \cdot \eta_{\text{PV}}(\%) \qquad \text{(eq.6-1)}$$

where $\Delta H_{c,fuel}$ is the standard enthalpy of combustion of the fuel, based on the high heating value (HHV) of all the products—so basically this is the energy output. Furthermore, the SEI is the specific energy input based on the plasma power, which is thus the energy input. Finally, η_{PV} is the photovoltaic efficiency for electricity production, to be able to compare the technologies relying on direct and indirect solar energy. Of course, as discussed in section 2.2 above, one of the key-benefits of plasma technology is its energy source flexibility. Hence, when (renewable) electricity from other sources is used, this term can be removed from the equation (just like for the electrochemical conversion). As mentioned above, it is added here for the easy comparison of all the different novel technologies. However, in the overall comparison, it is important to keep this note in mind.

For the simple case of CO_2 splitting, $\Delta H_{c,fuel}$ equals:

$$\Delta H_{c,fuel}\left(\frac{kJ}{mol}\right) = \left(\chi_{CO_2} \cdot S_{C,CO} \cdot 283\left(\frac{kJ}{mol}\right)\right) + \left(\chi_{CO_2} \cdot S_{O,O_2} \cdot 0\left(\frac{kJ}{mol}\right)\right)$$

$$\Rightarrow \Delta H_{c,fuel}\left(\frac{kJ}{mol}\right) = \frac{\dot{n}_{CO,out}}{\dot{n}_{CO_2,inlet}} \cdot 283\left(\frac{kJ}{mol}\right) = Y_{C,CO} \cdot 283\left(\frac{kJ}{mol}\right) \qquad \text{(eq.6-2)}$$

where χ stands for the conversion, S and Y are the selectivity and yield, respectively, which are here expressed with respect to C (for CO) and to O (for O_2), and $\dot{n}$ stands for the molar flow rate.

Thus, since the C-based selectivity for CO in case of pure CO_2 splitting in most cases is 100 %, the equation for the solar-to-fuel efficiency equals here the definition for energy efficiency (eq.2-11; defined in **Chapter 2**)—as well as the thermal energy efficiency (based on the HHV)—multiplied with the photovoltaic efficiency:

$$\eta_{\text{solar-to-fuel}}(\%) = \frac{\Delta H_{c,fuel}\left(\frac{kJ}{mol}\right)}{SEI\left(\frac{kJ}{mol}\right)} \cdot \eta_{\text{PV}}(\%) = \frac{\chi_{CO_2} \cdot 283\left(\frac{kJ}{mol}\right)}{SEI\left(\frac{kJ}{mol}\right)} \cdot \eta_{\text{PV}}(\%)$$

$$= \eta(\%) \cdot \eta_{\text{PV}}(\%) = \eta_{Thermal,HHV}(\%) \cdot \eta_{\text{PV}}(\%) \qquad \text{(eq.6-3)}$$

For the DRM data, the equation becomes a bit more delicate. First of all we need to take the HHV of the converted CH_4 in the feed into account as part of the denominator—since this counts as an energy input.

$$\eta_{\text{solar-to-fuel}}(\%) = \frac{E_{out}}{E_{in}} = \frac{\Delta H_{c,fuel}\left(\frac{kJ}{mol}\right)}{SEI\left(\frac{kJ}{mol}\right) + \Delta H_{c,conv\,CH_4}\left(\frac{kJ}{mol}\right)} \times \eta_{\text{PV}}(\%) \qquad \text{(eq.6-4)}$$

Second, as mentioned in the sections above, a wide variety of products is formed, which all need to be taken into account. Hence, for DRM the solar-to-fuel efficiency would only equal the definition for energy efficiency (eq.2-11) multiplied with the photovoltaic efficiency, when the stoichiometric reaction as defined **in Chapter 1** occurs, i.e. $CO_2 + CH_4 \rightarrow 2\ CO + 2\ H_2$.

Note that since the SEI is based on the plasma power, this efficiency does not take the energy losses into account, which occur at the level of the power supply and power coupling with the plasma. The data regarding these energy losses is generally not reported, since those may vary greatly, depending on the plasma type and power supply used, but they are independent from the plasma process under study. Furthermore, a lot of (successful) research progress is still being made in minimizing these electrical losses when going from outlet power to plasma power.

It should be noted that the solar-to-fuel conversion efficiency could only be calculated based upon the available data in literature. If certain reaction products were not measured, their contribution to the enthalpy of combustion could not be taken into account. Due to the scarcity of information regarding CO_2/H_2O and CO_2/H_2 mixtures, we only consider CO_2 splitting and DRM in the following analysis.

For the following discussions, we consider a PV efficiency value of 25 % based on the efficiencies of current commercial PV systems at cell level.[2] It is important to keep in mind that advancements in PV efficiency have a direct positive influence on the solar-to-fuel efficiency of plasma technology. For example, PV efficiencies up to 45 % have already been reported on a lab scale,[210] a value which would almost double the solar-to-fuel efficiency of plasma technology as reported below.

It is reported in literature that—on a pure economic basis—for the various novel technologies to be cost competitive with existing chemical and fuel processes, a solar-to-fuel conversion efficiency of 20 % is likely needed for the production of syngas.[1,211] Nonetheless, as already indicated above, all of these emerging technologies have additional advantages compared to the traditional catalytic technologies currently used. Furthermore, when the intermediate syngas step can be circumvented, due to the production of liquids through a direct oxidative pathway, this solar-to-fuel conversion efficiency target decreases drastically, e.g. for methanol a solar-to-methanol efficiency of 7.1 % would already be feasible.[1] This is the greatest advantage of the plasmachemical conversion (in combination with catalysis), namely its already proven capability of producing a wide variety of liquid chemicals in a direct manner.

Table 6-3 presents the best data obtained in literature on solar-to-fuel efficiencies, together with the obtained conversions, for the different plasma types discussed in section 1 of this chapter. It should be no surprise that the plasma setups which showed the best performance also have the highest solar-to-fuel efficiency. For pure CO_2 splitting, MW and GA plasmas are the two most promising discharge types, with maximum achieved solar-to-fuel efficiencies to date of 22.5 and 16.4 %, respectively. For DRM, APGDs and GA plasmas have obtained the highest solar-to-fuel efficiencies up to now of 23.0 and 22.1 %, respectively. However, most other discharges, except for DBDs, already reach efficiencies between 11 and 15 %. This means that chemicals and fuels produced by plasmachemical conversion of CO_2 into syngas could already be cost-competitive, depending on the critical notes made above on product separation costs and power supply efficiencies. Finally, it is important to realise that this is only a screen shot for the current production of syngas. When a successful shift is made towards the direct oxidative production of liquids, the performance of the different plasma types could change drastically. Especially, since certain plasma types (i.e. DBDs) allow for the easier implementation of catalytic materials, which will play an important role for the selective production of these value-added compounds through the direct oxidative pathway. Furthermore, by circumventing the energy intensive conversion of syngas to the desired liquids through the Fischer-Tropsch or methanol synthesis, the required solar-to-fuel conversion efficiency to be competitive decreases by a factor two to three.

Table 6-3. Overview of the best solar-to-fuel efficiencies, along with the obtained conversions, calculated from the data in literature for the different plasma types discussed in sections 1.1 and 1.2, and presented in **Figures 6-5 and 6-13**. For some plasma types, two or three "best values" are listed, as some conditions lead to the best conversion, while others lead to the best efficiency; cf. the trade-off between both, as discussed in previous sections. Processes reaching efficiencies below 10 % are considered inefficient (red), between 10–15 % are considered promising (orange), above 15 % very promising (green) and values above 20 % might already be cost competitive (green, underline, bold). Note that this analysis applies to the production of the syngas components CO and H_2; when considering the direct oxidative pathway to produce liquid fuels, lower values will already be cost competitive (see text).

	CO_2 splitting		Dry reforming of methane	
	χ_{CO_2}	$\eta_{solar-to-fuel}{}^{a}$	χ_{CH_4}/χ_{CO_2}	$\eta_{solar-to-fuel}{}^{b}$
DBD	25.8 %[7]	5.8 %	7 / 3 %[83]	4.2 %
	42.0 %[29]	1.7 %	88 / 78 %[147]	1.8 %
MW (1980s)	9.7 %[36]	**22.5 %**		
	35.9 %[33]	17.1 %		
	87.4 %[32]	9.4 %		
MW (2010s)	9.7 %[38]	12.6 %		
	29.5 %[37]	10.8 %		
	82.9 %[39]	6.1 %	71 / 69 %[165]	11.6 %
GA	12.2 %[60]	16.4 %	13 / 9 %[95]	**22.1 %**
			41 / 36 %[95]	15.5 %
			45 / 34 %[118]	11.1 %
APGD	50.0 %[74]	6.75 %	94 / 77 %[122]	**23.0 %**
Ns-pulsed	7.1 %[76]	2.5 %	61 / 50 %[115]	14.5 %
Corona	6.1 %[67]	1.6 %	23 / 36 %[99]	12.2 %
Spark			87 / 83 %[102]	14.7 %

[a] Based on equation 6-1 above, using a PV efficiency of 25 %.

[b] Based on equation 6-4 above, using a PV efficiency of 25 %.

Finally, in **Table 6-4**, we compare the reported solar-to-fuel conversion efficiencies obtained to date, as well as the theoretical maximum values, of plasmachemical conversion with the other novel technologies. As mentioned in **Chapter 1**, water electrolysis powered by renewable energy is already a more mature technology, so we have added it here to the comparison.

Water electrolysis yields efficiencies in the range of 16–19 % for a PV efficiency of 25 % and an electricity-to-hydrogen efficiency of 65–75 %.[212] Despite this success, electrochemical CO_2 splitting, on the other hand, faces large efficiency losses due to overpotentials, and the theoretical efficiency is expected below 15 %.[212] For the solar thermochemical approach, theoretical efficiencies of 16–19 % or 35–50 % are assumed,[211–213] depending on the heat recovery (see details in the cited references). Nevertheless, efficiencies above 10 % are still pending experimental demonstration with robust and scalable solar reactors.[1,211,213,214] For the photochemical conversion, the efficiency is theoretically limited to a maximum below 5 %[212] or 17 %[215] depending on the band gap energy of the photocatalysts. However, the solar-to-fuel conversion efficiencies obtained to date are generally much lower (< 2 %),[212,215] with some exceptions when coupled with an electrolytic cell (10.9 %).[215] For the biochemical conversion a maximum efficiency for the conversion of light to stored chemical energy of about 4.5% has been calculated.[216] However, this value is rarely achieved. Only in exceptional cases will dry matter yield exceed 1 or 2 %.[216]

Finally, it is clear from **Table 6-4** that the highest value obtained to date on lab scale for the plasmachemical conversion of CO_2, i.e. 23 % (see **Table 6-3** above), already appears to be competitive with the current most mature technology (i.e. water electrolysis) to transform renewable energy into chemicals and fuels through the intermediate production of the syngas components CO and H_2. Furthermore, the theoretical maximum energy efficiency is 90–95 %, multiplied with the power supply efficiency and the PV efficiency. This is based on the theoretical—and experimentally proven—most energy efficient CO_2 dissociation process through vibrational excitation (see **Chapter 1**). Hence, the construction, use and matching of efficient power supplies for generating the plasma is very critical. Nonetheless, we should not forget the critical note made above on product separation. Additional—and substantial—research is needed to provide an answer to this issue—just like is the case with all other emerging technologies and their specific concerns. Due to its emerging character, interdisciplinary research towards plasma technology, especially in combination with other fields, such as catalysis will—undoubtedly—lead to further advancement and breakthroughs in this field.

Table 6-4. Overview of the currently obtained and theoretical maximum solar-to-fuel conversion efficiency to the syngas components CO and H_2 for the different emerging technologies described in Chapter 1, as well as plasma technology.

Solar-to-fuel efficiency:	**Currently obtained**	**Theoretical maximum**
Water electrolysis	16–19 %[a]	65–75 %[212] (x PV efficiency)
Electrochemical conversion	NA	< 15 %[212]
Solar thermochemical conversion	0.4–0.8 %[211,213]	16–19 %[211,213]
	1.7–3.5 %[214]	
	7.1 %[1]	
	NA	35–50 %[212]
Photochemical conversion	< 2 %[212]	< 5 %[212]
	0.01–10.9 %[215]	~17 %[215]
Biochemical conversion	NA	4.5 %[216] x harvesting efficiency
Plasmachemical conversion	23 %[a]	90–95 % x power supply efficiency (x PV efficiency)

[a] Based on a PV efficiency of 25 %.

2.4. Research recommendations

To conclude, we would like to provide some research recommendations for plasma technology, based on all the collected data from literature, to further advance the field of plasma-based CO_2 conversion. The first recommendation is related to the need for a more standardised framework in reporting data, to allow easier comparison of data within and outside the field of plasma technology. The most important criterion here is to be able to compare the conversions and energy cost/efficiency. Regarding the conversions, this requires a clear reporting on the presence of diluting agents (i.e., N_2, He, Ar) when used, since these agents can significantly influence the plasma process, as discussed in section 1 of this chapter. Furthermore, Pinhão et al.[217] elaborately described the effect of gas expansion during plasma processing, which is to date often neglected, but which can have a tremendous influence on data accuracy, for example on the conversions obtained through GC measurements.[4,17,133] Concerning the energy cost/efficiency, first of all there should be no room for interpretation whether the reported power is the applied input power or the measured plasma power and through which electrical techniques, such as Lissajous plots, this power is obtained. Secondly, one should aim to identify all the important products and their selectivities, to be able to determine the energy efficiency based on the enthalpy of the reaction, as well as the so-called fuel production efficiencies. In general, as also discussed by Butterworth et al.[30] for the testing of materials for plasma catalysis, general frameworks on performing experiments and reporting data are becoming essential for a transparent further development of plasma research, both within the plasma community as within the larger CO_2 conversion community.

Finally, we also have some more personal recommendations. From the plots in the sections above, showing the energy cost/efficiency as a function of the SEI, it becomes more than clear that most applied SEIs are far too high, especially for combinations with catalysis. An SEI range of 0.1–5 eV per reactant molecule (taking possible dilutions into account) should be the target to achieve energy efficient conversions, as also recommended by Fridman.[32] Furthermore, since plasma processes are very susceptible to the effect of impurities in the feed, more research and insight is needed towards the effect of real life gas compositions on both the physical side (e.g. discharge stability) as on the chemical side (e.g., product distributions, harmful by-products, etc.).

3. Conclusions and outlook

The main aim of this dissertation was to provide a significant contribution to the question whether, in the long run, plasma technology is suitable for the efficient conversion of CO_2 into value-added products, by providing the necessary chemical insight using extensive combined experimental and modelling studies.

Conversion of CO_2—preferably into value-added products—is considered one of the great challenges of our century. In the past decade, substantial progress with several novel technologies has been made. The last chapter of this dissertation intended to provide the reader with the state-of-the art and critical assessment of an—up till now—rather underexposed emerging technology: the plasmachemical conversion of CO_2. To achieve this, we provided an introduction in the basic concepts of plasma, and we demonstrated its viability as gas conversion technology, finally putting it in the broader context of its peers.

From the advances in the area of CO_2 conversion discussed in this dissertation, one outcome stands without doubt. The question is not "if" one of these novel technologies will be industrially competitive, but rather "when" and "which one(s) will play the leading role". To shine a brighter light on—the final burning question—whether plasma technology could be the answer—or at least be part of the equation—we briefly summarize the arising opportunities and challenges for plasma technology in the field of CO_2 conversion.

Plasmas possess some important advantages over certain other (novel) technologies; (i) they can operate at room temperature using any source of (renewable) electricity, (ii) they have a large flexibility towards the feed that needs to be processed, (iii) they provide an extremely flexible "key-turn" process, which allows for the efficient storage of energy, peak shaving and grid stabilisation, (iv) the reactors have low investment and operating costs, (v) they have a simple scalability both in size and applicability, and (vi) last but not least, the technology does not rely on rare-earth materials—making it rather unique at this point. This unprecedented combination of features gives the plasmachemical conversion a very high overall flexibility, making it an extremely grateful and valuable technology for CCU.

The flip side of the coin is that the reliance of plasma technology on indirect solar energy in the form of electricity is—at the same time—a limiting factor for the solar-to-fuel conversion efficiency, especially compared to technologies which can directly harvest solar energy. Nonetheless, this also allows plasma technology to rely on other renewable energy sources, and more importantly, it adds to its overall—location and process—flexibility, since it is not dependent on the availability of sunlight. More urgent, however, is the issue of product separation. From all data available in literature, it becomes clear that converting CO_2—with or without an additional hydrogen source—always yields a mixture of products after reaction. This implies the need for an—often expensive—post-processing separation step.

From the benchmarking discussion, it becomes clear that plasma technology can definitely play an important role in the field of CO_2 conversion and it is not beyond our grasp to think about its eventual commercial implementation—be it on a large or small scale. Nevertheless, as always, only a few candidates seem suitable for the specific task at hand, as we will outline here.

Two main CO_2 conversion strategies were discussed, i.e., (i) pure CO_2 splitting and (ii) CO_2 conversion in combination with a co-reactant serving as hydrogen source, i.e. CH_4, H_2 and H_2O, yielding processes named dry reforming of methane (DRM), hydrogenation of CO_2 and artificial photosynthesis, respectively. At this time, the conversion of CO_2 through the latter two processes is—although possible—inefficient in a plasma-only set-up, not to mention industrially undesirable, due to the formation of possibly dangerous mixtures to handle. In the future, the combination of plasma with other technologies, such as catalysis or electrolysis, could solve these issues. On the contrary, for both pure CO_2 splitting and DRM the proposed energy efficiency target of 60 % is already surpassed with several types of plasma reactors, resulting in a solar-to-fuel conversion efficiency for the production of syngas above—the required—20 % mark.

In the short run, pure CO_2 splitting using the most energy-efficient set-ups, i.e. MW and GA discharges, appears to have a high potential. In this case, pure CO and O_2 could be produced, after a separation step, or a pure CO stream when in-situ trapping of the O_2 can be successfully implemented—by combination with other technologies or through the addition of scavengers.

In the long run, it seems evident that CO_2 conversion in combination with a hydrogen containing co-reactant has the highest potential for the efficient production of value-added products, such as alcohols, aldehydes, esters and acids. Especially the direct oxidative pathway, in which the intermediate syngas step is being circumvented, has great potential. For now, however, a lot of research in this area is still needed to increase the selectivity towards these valuable bulk chemicals over the currently produced syngas. This will most probably need to be achieved in combination with catalysts. However, even today, APGD and GA discharges already provide an energy-efficient alternative to produce syngas in any desired ratio through DRM.

By all means, plasma technology is not just an overlooked unicorn—although its combination of features does make it quite unique for CCU—and as mentioned several times throughout this work, several important challenges remain—just like for all other emerging technologies in this field. General challenges comprise the need for further fundamental research, concerning (i) the plasmachemical processes taking place in warm discharges, such as MW and GA, which stimulate vibrational excitation; the latter—most energy efficient dissociation pathway—should be further exploited by enhancing the non-equilibrium character of these plasmas, to further improve the energy efficiency, (ii) the combination of plasma with catalysis and the possibility towards synergetic effects and the selective production of value-added compounds, (iii) in-situ O/O_2 trapping by using scavengers, or combinations with other technologies, such as catalysis or SOEC, to further enhance the conversions and yield towards desired value-added compounds, (iv) the demonstration of successful scale-up for other discharges than DBDs, and (v) the production and tuning of efficient power supplies for generating and sustaining the plasma.

Moreover, some important discharge-specific research challenges can also be identified. For MW plasmas, the ultimate goal should be to achieve the same energy efficiency at atmospheric pressure as currently obtained at reduced pressure for CO_2 splitting, while more research towards DRM is essential. For GA plasmas, the limited amount of gas that passes through the active arc region, and thus that can be converted by the plasma, is currently limiting the overall CO_2 conversion, and more research in this direction is needed, e.g. by improved reactor design. Furthermore, some other plasma reactors show good performance, but the available data and insights are still limited, requiring more research to explore their full potential. Of course, inherent to every review, the above analysis represents the current state-of-the-art. Plasma technology based CO_2 conversion is relatively new and it is clearly a fast advancing field with—just like for any emerging technology—ample room for improvement and new (interdisciplinary) developments.

Future research towards the direct oxidative production of oxygenates, as well as multi-reforming processes with a combination of gases (e.g., CO_2, CH_4 and H_2O or O_2) or several reforming processes in series, using plasma technology appears very promising and should be pursued. Furthermore, more interdisciplinary research for the combination of plasmas with other novel technologies is highly desirable. For catalysis the combination is already proving alluring, and it is our opinion that combinations with electrolysis—although even more challenging—could also lead to synergetic effects. As is the case for many important issues brought forward in the current age, with a high probability the future will rely on a true amalgam of technologies and solutions, each for its specific tasks, rather than the—more brute—one solution (or technology) fits all mentality of the old age.

From the current analysis it becomes evident that pure CO_2 splitting can reach industrial implementation at a faster pace. Nevertheless, the CO_2 conversion using a hydrogen source as co-reactant should certainly be further pursued, since—when successful—on the long run it offers us the possibility of producing a wide variety of value-added chemicals and fuels, starting from the same building block and allowing the flexibility to tune the output depending on the market's needs. On that account, we believe plasmas could be—at least part of—the bright light that shines on our horizon.

4. References

1 J. Kim, C. A. Henao, T. A. Johnson, D. E. Dedrick, J. E. Miller, E. B. Stechel and C. T. Maravelias, *Energy Environ. Sci.*, 2011, **4**, 3122.

2 K. Yoshikawa, H. Kawasaki, W. Yoshida, T. Irie, K. Konishi, K. Nakano, T. Uto, D. Adachi, M. Kanematsu, H. Uzu and K. Yamamoto, *Nat. Energy*, 2017, **2**, 17032.

3 R. Snoeckx, A. Rabinovich, D. Dobrynin, A. Bogaerts and A. Fridman, *Plasma Process. Polym.*, 2016, DOI: 10.1002/ppap.201600115.

4 R. Aerts, W. Somers and A. Bogaerts, *ChemSusChem*, 2015, **8**, 702–716.

5 S. Paulussen, B. Verheyde, X. Tu, C. De Bie, T. Martens, D. Petrovic, A. Bogaerts and B. Sels, *Plasma Sources Sci. Technol.*, 2010, **19**, 34015.

6 Q. Yu, M. Kong, T. Liu, J. Fei and X. Zheng, *Plasma Chem. Plasma Process.*, 2012, **32**, 153–163.

7 A. Ozkan, A. Bogaerts and F. Reniers, *J. Phys. D. Appl. Phys.*, 2017, **50**, 84004.

8 M. Schiorlin, R. Klink and R. Brandenburg, *Eur. Phys. J. Appl. Phys.*, 2016, **75**, 1–7.

9 F. Brehmer, S. Welzel, R. M. C. M. Van De Sanden and R. Engeln, *J. Appl. Phys.*, 2014, **116**, 123303.

10 J. Wang, G. Xia, A. Huang, S. L. Suib, Y. Hayashi and H. Matsumoto, *J. Catal.*, 1999, **185**, 152–159.

11 I. Belov, S. Paulussen and A. Bogaerts, *Plasma Sources Sci. Technol.*, 2016, **25**, 15023.

12 R. Li, Q. Tang, S. Yin and T. Sato, *Appl. Phys. Lett.*, 2007, **90**, 3–5.

13 R. Li, Q. Tang, S. Yin and T. Sato, *Fuel Process. Technol.*, 2006, **87**, 617–622.

14 S. Wang, Y. Zhang, X. Liu and X. Wang, *Plasma Chem. Plasma Process.*, 2012, **32**, 979–989.

15 M. Ramakers, I. Michielsen, R. Aerts, V. Meynen and A. Bogaerts, *Plasma Process. Polym.*, 2015, **12**, 755–763.

16 M. A. Lindon and E. E. Scime, *Front. Phys.*, 2014, **2**, 1–13.

17 R. Snoeckx, S. Heijkers, K. Van Wesenbeeck, S. Lenaerts and A. Bogaerts, *Energy Environ. Sci.*, 2016, **9**, 30–39.

18 X. Duan, Y. Li, W. Ge and B. Wang, *Greenh. Gases Sci. Technol.*, 2015, **5**, 131–140.

19 Y. Tagawa, S. Mori, M. Suzuki, I. Yamanaka, T. Obara, J. Ryu and Y. Kato, *Kagaku Kogaku Ronbunshu*, 2011, **37**, 114–119.

20 R. Aerts, T. Martens and A. Bogaerts, *J. Phys. Chem. C*, 2012, **116**, 23257–23273.

21 P. Koelman, S. Heijkers, S. Tadayon Mousavi, W. Graef, D. Mihailova, T. Kozak, A. Bogaerts and J. van Dijk, *Plasma Process. Polym.*, 2016.

22 S. Ponduri, M. M. Becker, S. Welzel, M. C. M. Van De Sanden, D. Loffhagen and R. Engeln, *J. Appl. Phys.*, 2016, **119**.

23 A. Bogaerts, C. De Bie, R. Snoeckx and T. Kozák, *Plasma Process. Polym.*, 2016, 1–21.

24 A. Bogaerts, A. Berthelot, S. Heijkers, S. Kolev, R. Snoeckx, S. R. Sun, G. Trenchev, K. van Laer and W. Wang, *Plasma Sources Sci. Technol.*, 2017, in press.

25 A. Bogaerts, W. Wang, A. Berthelot and V. Guerra, *Plasma Sources Sci. Technol.*, 2016, **25**, 55016.

26 M. Grofulovic, L. L. Alves and V. Guerra, *J. Phys. D Appl. Phys.*, 2016, **49**, 395207.

27 I. Michielsen, Y. Uytdenhouwen, J. Pype, B. Michielsen, J. Mertens, F. Reniers, V. Meynen and A. Bogaerts, *Chem. Eng. J.*, 2017, submitted.

28 D. Mei, X. Zhu, Y.-L. He, J. D. Yan and X. Tu, *Plasma Sources Sci. Technol.*, 2014, **24**, 15011.

29 X. Duan, Z. Hu, Y. Li and B. Wang, *AIChE J.*, 2015, **61**, 898–903.

30 T. Butterworth, R. Elder and R. Allen, *Chem. Eng. J.*, 2016, **293**, 55–67.

31 K. Van Laer and A. Bogaerts, *Energy Technol.*, 2015, **3**, 1038–1044.

32 A. Fridman, *Plasma chemistry*, Cambridge University Press, New York, 2008.

33 V. D. Rusanov, a. a. Fridman and G. V. Sholin, *Uspekhi Fiz. Nauk*, 1981, **134**, 185–235.

34 T. Kozák and A. Bogaerts, *Plasma Sources Sci. Technol.*, 2014, **23**, 45004.

35 R. I. Asisov, A. A. Fridman, V. K. Givotov, E. G. Krasheninnikov, B. I. Patrushev, B. V. Potapkin, V. D. Rusanov and M. F. Krotov, in *5th International Symposium on Plasma Chemistry*, 1983, vol. 1, p. 52.

36 R. I. Asisov, A. K. Vakar, V. K. Jivotov, M. F. Krotov, O. A. Zinoviev, B. V Potapkin, A. A. Rusanov, V. D. Rusanov and A. A. Fridman, *Proc. USSR Acad. Sci.*, 1983, **271**.

37 G. J. van Rooij, D. C. M. van den Bekerom, N. den Harder, T. Minea, G. Berden, W. A. Bongers, R. Engeln, M. F. Graswinckel, E. Zoethout and M. C. M. van de Sanden, *Faraday Discuss.*, 2015, **183**, 233–248.

38 W. Bongers, H. Bouwmeester, B. Wolf, F. Peeters, S. Welzel, D. van den Bekerom, N. den Harder, A. Goede, M. Graswinckel, P. W. Groen, J. Kopecki, M. Leins, G. van Rooij, A. Schulz, M. Walker and R. van de Sanden, *Plasma Process. Polym.*, 2016, DOI 10.1002/ppap.201600126.

39 A. P. H. Goede, W. A. Bongers, M. F. Graswinckel, R. M. C. M. Van De Sanden, M. Leins, J. Kopecki, A. Schulz and M. Walker, *EPJ Web Conf.*, 2014, **79**, 1005.

40 L. F. Spencer and A. D. Gallimore, *Plasma Sources Sci. Technol.*, 2013, **22**, 15019.

41 L. F. Spencer and A. D. Gallimore, *Plasma Chem. Plasma Process.*, 2010, **31**, 79–89.

42 A. Vesel, M. Mozetic, A. Drenik and M. Balat-Pichelin, *Chem. Phys.*, 2011, **382**, 127–131.

43 A. Berthelot and A. Bogaerts, *J. Phys. Chem. C*, 2017, in press.

44 T. Kozák and A. Bogaerts, *Plasma Sources Sci. Technol.*, 2015, **24**, 15024.

45 L. F. Spencer, The University of Michigan, 2012.

46 M. Tsuji, T. Tanoue, K. Nakano and Y. Nishimura, *Chem. Lett.*, 2001, **30**, 22–23.

47 S. Heijkers, R. Snoeckx, T. Kozák, T. Silva, T. Godfroid, N. Britun, R. Snyders and A. Bogaerts, *J. Phys. Chem. C*, 2015, **119**, 12815–12828.

48 S. Y. Savinov, H. Lee, H. K. Song and B.-K. Na, *Korean J. Chem. Eng.*, 2002, **19**, 564–566.

49 L. D. Pietanza, G. Colonna, G. D'Ammando, a Laricchiuta and M. Capitelli, *Plasma Sources Sci. Technol.*, 2015, **24**, 42002.

50 L. D. Pietanza, G. Colonna, G. D'Ammando, A. Laricchiuta and M. Capitelli, *Chem. Phys.*, 2016, **468**, 44–52.

51 T. Silva, N. Britun, T. Godfroid and R. Snyders, *Plasma Sources Sci. Technol.*, 2014, **23**, 25009.

52 A. Berthelot and A. Bogaerts, *Plasma Sources Sci. Technol.*, 2016, **25**, 45022.

53 G. Chen, V. Georgieva, T. Godfroid, R. Snyders and M. P. Delplancke-Ogletree, *Appl. Catal. B Environ.*, 2016, **190**, 115–124.

54 T. Nunnally, K. Gutsol, A. Rabinovich, A. Fridman, A. Gutsol and A. Kemoun, *J. Phys. D. Appl. Phys.*, 2011, **44**, 274009.

55 S. R. Sun, H. X. Wang, D. H. Mei, X. Tu and A. Bogaerts, *J. CO2 Util.*, 2017, **17**, 220–234.

56 I. Rusu and J. M. Cormier, *Chem. Eng. J.*, 2003, **91**, 23–31.

57 F. Ouni, A. Khacef and J. M. Cormier, *Chem. Eng. Technol.*, 2006, **29**, 604–609.

58 S. Heijkers and G. Trenchev, 2017, private communication.

59 M. Ramakers, G. Trenchev, S. Heijkers, W. Wang and A. Bogaerts, *Green Chem.*, **submitted**, 1–28.

60 S. C. Kim, M. S. Lim and Y. N. Chun, *Plasma Chem. Plasma Process.*, 2014, **34**, 125–143.

61 A. Indarto, J.-W. Choi, H. Lee and H. K. Song, *Environ. Eng. Sci.*, 2006, **23**, 1033–1043.

62 A. Indarto, D. R. Yang, J.-W. Choi, H. Lee and H. K. Song, *J. Hazard. Mater.*, 2007, **146**, 309–15.

63 J. L. Liu, H. W. Park, W. J. Chung and D. W. Park, *Plasma Chem. Plasma Process.*, 2016, **36**, 437–449.

64 W. Wang, A. Berthelot, S. Kolev, X. Tu and A. Bogaerts, *Plasma Sources Sci. Technol.*, 2016, **25**, 65012.

65 G. Horváth, J. D. Skalný and N. J. Mason, *J. Phys. D. Appl. Phys.*, 2008, **41**, 225207.

66 T. Mikoviny, M. Kocan, S. Matejcik, N. J. Mason and J. D. Skalny, *J. Phys. D. Appl. Phys.*, 2004, **37**, 64–73.

67 W. Xu, M.-W. Li, G.-H. Xu and Y.-L. Tian, *Jpn. J. Appl. Phys.*, 2004, **43**, 8310–8311.

68 M. Morvová, *J. Phys. D. Appl. Phys.*, 1998, **31**, 1865–1874.

69 Y. Wen and X. Jiang, *Plasma Chem. Plasma Process.*, 2001, **21**, 665–678.

70 I. Maezono and J.-S. Chang, *IEEE Trans. Ind. Appl.*, 1990, **26**, 651–655.

71 S. L. Suib, S. L. Brock, M. Marquez, J. Luo, H. Matsumoto and Y. Hayashi, *J. Phys. Chem. B*, 1998, **102**, 9661–9666.

72 S. L. Brock, M. Marquez, S. L. Suib, Y. Hayashi and H. Matsumoto, *J. Catal.*, 1998, **180**, 225–233.

73 S. L. Brock, T. Shimojo, M. Marquez, C. Marun, S. L. Suib, H. Matsumoto and Y. Hayashi, *J. Catal.*, 1999, **184**, 123–133.

74 S. N. Andreev, V. V. Zakharov, V. N. Ochkin and S. Y. Savinov, *Spectrochim.*

Acta - Part A Mol. Biomol. Spectrosc., 2004, **60**, 3361–3369.

75 S. Mori, A. Yamamoto and M. Suzuki, *Plasma Sources Sci. Technol.*, 2006, **15**, 609–613.

76 M. S. Bak, S. K. Im and M. Cappelli, *IEEE Trans. Plasma Sci.*, 2015, **43**, 1002–1007.

77 U. Kogelschatz, *Plasma Chem. plasma Process.*, 2003, **23**, 1–46.

78 X. Tao, M. Bai, X. Li, H. Long, S. Shang, Y. Yin and X. Dai, *Prog. Energy Combust. Sci.*, 2011, **37**, 113–124.

79 A. Lebouvier, S. A. Iwarere, P. D'Argenlieu, D. Ramjugernath and L. Fulcheri, *Energy and Fuels*, 2013, **27**, 2712–2722.

80 I. Istadi and N. A. S. Amin, *Fuel*, 2006, **85**, 577–592.

81 J.-M. Lavoie, *Front. Chem.*, 2014, **2**, 1–17.

82 X. Tu and J. C. Whitehead, *Appl. Catal. B Environ.*, 2012, **125**, 439–448.

83 R. Snoeckx, Y. X. Zeng, X. Tu and A. Bogaerts, *RSC Adv.*, 2015, **5**, 29799–29808.

84 A. Ozkan, T. Dufour, G. Arnoult, P. De Keyzer, A. Bogaerts and F. Reniers, *J. CO2 Util.*, 2015, **9**, 78–81.

85 V. Goujard, J.-M. Tatibouët and C. Batiot-Dupeyrat, *Appl. Catal. A Gen.*, 2009, **353**, 228–235.

86 X. Zhang and M. S. Cha, *J. Phys. D. Appl. Phys.*, 2013, **46**, 415205.

87 V. J. Rico, J. L. Hueso, J. Cotrino and A. R. González-Elipe, *J. Phys. Chem. A*, 2010, **114**, 4009–4016.

88 Q. Wang, B.-H. Yan, Y. Jin and Y. Cheng, *Plasma Chem. Plasma Process.*, 2009, **29**, 217–228.

89 L. M. Zhou, B. Xue, U. Kogelschatz and B. Eliasson, *Energy & Fuels*, 1998, **12**, 1191–1199.

90 H. K. Song, J.-W. Choi, S. H. Yue, H. Lee and B.-K. Na, *Catal. Today*, 2004, **89**, 27–33.

91 A. Zhang, A. Zhu, J. Guo, Y. Xu and C. Shi, *Chem. Eng. J.*, 2010, **156**, 601–606.

92 W. Chung, K. Pan, H. Lee and M. Chang, *Energy & Fuels*, 2014, **28**, 7621–7631.

93 C. J. Liu, B. Xue, B. Eliasson, F. He, Y. Li and G. H. Xu, *Plasma Chem. Plasma Process.*, 2001, **21**, 301–310.

94 W. Cho, W. S. Ju, S. H. Lee, Y. S. Baek and Y. C. Kim, in *Proceedings of 7th*

International Conference on Carbon Dioxide Utilization, 2004, pp. 205–208.

95 Z. Bo, J. Yan, X. Li, Y. Chi and K. Cen, *Int. J. Hydrogen Energy*, 2008, **33**, 5545–5553.

96 A. Wu, J. Yan, H. Zhang, M. Zhang, C. Du and X. Li, *Int. J. Hydrogen Energy*, 2014, **39**, 17656–17670.

97 X. Tu and J. C. Whitehead, *Int. J. Hydrogen Energy*, 2014, **39**, 9658–9669.

98 M. Li, C. Liu, Y. Tian, G. Xu, F. Zhang and Y. Wang, *Energy & Fuels*, 2006, **20**, 1033–1038.

99 A. Aziznia, H. R. Bozorgzadeh, N. Seyed-matin, M. Baghalha and A. Mohamadalizadeh, *J. Nat. Gas Chem.*, 2012, **21**, 466–475.

100 M. Li, G. Xu, Y. Tian, L. Chen and H. Fu, *J. Phys. Chem. A*, 2004, **108**, 1687–1693.

101 N. Seyed-Matin, A. H. Jalili, M. H. Jenab, S. M. Zekordi, A. Afzali, C. Rasouli and A. Zamaniyan, *Plasma Chem. Plasma Process.*, 2010, **30**, 333–347.

102 W. Chung and M. Chang, *Energy Convers. Manag.*, 2016, **124**, 305–314.

103 M. M. Moshrefi, F. Rashidi, H. R. Bozorgzadeh and M. Ehtemam Haghighi, *Plasma Chem. Plasma Process.*, 2013, **33**, 453–466.

104 V. Shapoval, E. Marotta, C. Ceretta, N. Konjevi, M. Ivkovic, M. Schiorlin and C. Paradisi, *Plasma Process. Polym.*, 2014, **11**, 787–797.

105 V. Shapoval and E. Marotta, *Plasma Process. Polym.*, 2015, **12**, 808–816.

106 B. Zhu, X. Li, J. Liu, X. Zhu and A. Zhu, *Chem. Eng. J.*, 2015, **264**, 445–452.

107 X.-S. Li, B. Zhu, C. Shi, Y. Xu and A.-M. Zhu, *AIChE J.*, 2011, **57**, 2854–2860.

108 S. Kado, K. Urasaki, Y. Sekine and K. Fujimoto, *Fuel*, 2003, **82**, 1377–1385.

109 A. Huang, G. Xia, J. Wang, S. L. Suib, Y. Hayashi and H. Matsumoto, *J. Catal.*, 2000, **189**, 349–359.

110 Q. Chen, W. Dai, X. Tao, H. Yu, X. Dai and Y. Yin, *Plasma Sour. Sci. Technol.*, 2006, **8**, 181–184.

111 M. Scapinello, L. M. Martini, G. Dilecce and P. Tosi, *J. Phys. D. Appl. Phys.*, 2016, **49**, 75602.

112 A. M. Ghorbanzadeh, S. Norouzi and T. Mohammadi, *J. Phys. D Appl. Phys. J. Phys. D Appl. Phys*, 2005, **38**, 3804–3811.

113 S. L. Yao, F. Ouyang, A. Nakayama, E. Suzuki, M. Okumoto and A. Mizuno, *Energy and Fuels*, 2000, **14**, 910–914.

114 B. Dai, X. L. Zhang, W. M. Gong and R. He, *Plasma Sci. Technol.*, 2000, **2**, 577–580.

115 A. M. Ghorbanzadeh, R. Lotfalipour and S. Rezaei, *Int. J. Hydrogen Energy*, 2009, **34**, 293–298.

116 Y. Zeng, X. Zhu, D. Mei, B. Ashford and X. Tu, *Catal. Today*, 2015, **256**, 80–87.

117 M. a Malik and X. Z. Jiang, *Plasma Chem. Plasma Proc.*, 1999, **19**, 505–512.

118 A. Indarto, J. Choi, H. Lee and H. Song, *Energy*, 2006, **31**, 2986–2995.

119 S. L. Yao, M. Okumoto, A. Nakayama and E. Suzuki, *Energy and Fuels*, 2001, **15**, 1295–1299.

120 Y. Yang, *Ind. Eng. Chem. Res.*, 2002, **41**, 5918–5926.

121 C. Liu, A. Marafee, R. Mallinson and L. Lobban, *Appl. Catal. A Gen.*, 1997, **164**, 21–33.

122 D. Li, X. Li, M. Bai, X. Tao, S. Shang, X. Dai and Y. Yin, *Int. J. Hydrogen Energy*, 2009, **34**, 308–313.

123 H. Long, S. Shang, X. Tao, Y. Yin and X. Dai, *Int. J. Hydrogen Energy*, 2008, **33**, 5510–5515.

124 X. Zhang, B. Dai, A. Zhu, W. Gong and C. Liu, *Catal. Today*, 2002, **72**, 223–227.

125 Y. Li, C. J. Liu, B. Eliasson and Y. Wang, *Energy and Fuels*, 2002, **16**, 864–870.

126 Y. Zhang, Y. Li, Y. Wang, C. Liu and B. Eliasson, *Fuel Process. Technol.*, 2003, **83**, 101–109.

127 N. R. Pinhão, a. Janeco and J. B. Branco, *Plasma Chem. Plasma Process.*, 2011, **31**, 427–439.

128 G. Scarduelli, G. Guella, D. Ascenzi and P. Tosi, *Plasma Process. Polym.*, 2011, **8**, 25–31.

129 L. M. Martini, G. Dilecce, G. Guella, A. Maranzana, G. Tonachini and P. Tosi, *Chem. Phys. Lett.*, 2014, **593**, 55–60.

130 Y. Li, G. Xu, C. Liu, B. Eliasson and B. Xue, *Energy and Fuels*, 2001, **15**, 299–302.

131 M. Scapinello, L. M. Martini and P. Tosi, *Plasma Process. Polym.*, 2014, **11**, 624–628.

132 H. Song, H. Lee, J.-W. Choi and B. Na, *Plasma Chem. Plasma Process.*, 2004, **24**, 57–72.

133 A. Janeco, N. R. Pinhao and V. Guerra, *J. Phys. Chem. C*, 2015, **119**, 109–120.

134 T. Kolb, T. Kroker, J. H. Voigt and K. H. Gericke, *Plasma Chem. Plasma Process.*, 2012, **32**, 1139–1155.

135 T. Kolb, J. H. Voigt and K.-H. Gericke, *Plasma Chem. Plasma Process.*, 2013, **33**, 631–646.

136 E. C. Neyts, K. Ostrikov, M. K. Sunkara and A. Bogaerts, *Chem. Rev.*, 2015, **115**, 13408–13446.

137 W. C. Chung and M. B. Chang, *Renew. Sustain. Energy Rev.*, 2016, **62**, 13–31.

138 J. C. Whitehead, *J. Phys. D. Appl. Phys.*, 2016, **49**, 243001.

139 Q. Wang, Y. Cheng and Y. Jin, *Catal. Today*, 2009, **148**, 275–282.

140 T. Kroker, T. Kolb, A. Schenk, K. Krawczyk, M. Młotek and K.-H. Gericke, *Plasma Chem. Plasma Process.*, 2012, **32**, 565–582.

141 S. Mahammadunnisa, P. M. K. Reddy, B. Ramaraju and C. Subrahmanyam, 2013.

142 S. Kameshima, K. Tamura, Y. Ishibashi and T. Nozaki, *Catal. Today*, 2015, **256**, 67–75.

143 X. Zheng, S. Tan, L. Dong, S. Li and H. Chen, *J. Power Sources*, 2015, **274**, 286–294.

144 D. Mei, X. Zhu, C. Wu, B. Ashford, P. T. Williams and X. Tu, *Appl. Catal. B Environ.*, 2016, **182**, 525–532.

145 Q. Wang, B. H. Yan, Y. Jin and Y. Cheng, *Energy and Fuels*, 2009, **23**, 4196–4201.

146 X. Tu, H. J. Gallon, M. V Twigg, P. a Gorry and J. C. Whitehead, *J. Phys. D. Appl. Phys.*, 2011, **44**, 274007.

147 X. Zheng, S. Tan, L. Dong, S. Li and H. Chen, *Int. J. Hydrogen Energy*, 2014, **39**, 11360–11367.

148 K. Zhang, T. Mukhriza, X. Liu, P. P. Greco and E. Chiremba, *Appl. Catal. A Gen.*, 2015, **502**, 138–149.

149 M. H. Pham, V. Goujard, J. M. Tatibouët and C. Batiot-Dupeyrat, *Catal. Today*, 2011, **171**, 67–71.

150 J. Sentek, K. Krawczyk, M. Młotek, M. Kalczewska, T. Kroker, T. Kolb, A. Schenk, K. H. Gericke and K. Schmidt-Szałowski, *Appl. Catal. B Environ.*, 2010, **94**, 19–26.

151 K. Krawczyk, M. Młotek and B. Ulejczyk, *Fuel*, 2014, **117**, 608–617.

152 H. J. Gallon, X. Tu and J. C. Whitehead, *Plasma Process. Polym.*, 2012, **9**, 90–97.

153 H. H. Nguyen and K. Kim, *Catal. Today*, 2015, **256**, 88–95.

154 B. Eliasson, C. Liu and U. Kogelschatz, *Ind. Eng. Chem. Res.*, 2000, **39**, 1221–1227.

155 M. Kraus, B. Eliasson and A. Wokaun, *Phys. Chem. Chem. Phys.*, 2001, **3**, 294–300.

156 J. J. Zou, Y. P. Zhang, C. J. Liu, Y. Li and B. Eliasson, *Plasma Chem. Plasma Process.*, 2003, **23**, 69–82.

157 M. Kraus, W. Egli, K. Haffner, B. Eliasson, U. Kogelschatz and A. Wokaun, *Phys. Chem. Chem. Phys.*, 2002, **4**, 668–675.

158 B. B. Hwang, Y. K. Yeo and B. K. Na, *Korean J. Chem. Eng.*, 2003, **20**, 631–634.

159 V. Goujard, J.-M. Tatibouët and C. Batiot-Dupeyrat, *Plasma Chem. Plasma Process.*, 2011, **31**, 315–325.

160 R. Snoeckx, R. Aerts, X. Tu and A. Bogaerts, *J. Phys. Chem. C*, 2013, **117**, 4957–4970.

161 C. De Bie, J. van Dijk and A. Bogaerts, *J. Phys. Chem. C*, 2015, **119**, 22331–22350.

162 H. Machrafi, S. Cavadias and J. Amouroux, *J. Phys. Conf. Ser.*, 2011, **275**, 12016.

163 I. Istadi and N. A. S. Amin, *Chem. Eng. Sci.*, 2007, **62**, 6568–6581.

164 J. Wang, C. Liu and B. Eliassion, *Energy*, 2004, **153**, 148–153.

165 J. Q. Zhang, Y. J. Yang, J. S. Zhang and Q. Liu, *Acta Chim. Sin.*, 2002, **60**, 1973–1980.

166 B. Fidalgo, A. Domínguez, J. Pis and J. Menéndez, *Int. J. Hydrogen Energy*, 2008, **33**, 4337–4344.

167 N. Rueangjitt, C. Akarawitoo, T. Sreethawong and S. Chavadej, *Plasma Chem. Plasma Process.*, 2007, **27**, 559–576.

168 N. Rueangjitt, T. Sreethawong and S. Chavadej, *Plasma Chem. Plasma Process.*, 2008, **28**, 49–67.

169 Y. N. Chun, Y. C. Yang and K. Yoshikawa, *Catal. Today*, 2009, **148**, 283–289.

170 Z. A. Allah and J. C. Whitehead, *Catal. Today*, 2015, **256**, 76–79.

171 J. L. Liu, H. W. Park, W. J. Chung, W. S. Ahn and D. W. Park, *Chem. Eng. J.*,

2016, **285**, 243–251.

172 K. Li, J. Liu, X. Li, X. Zhu and A. Zhu, *Chem. Eng. J.*, 2016, **288**, 671–679.

173 Y. N. Chun, H. W. Song, S. C. Kim and M. S. Lim, *Energy and Fuels*, 2008, **22**, 123–127.

174 H. Lee and H. Sekiguchi, *J. Phys. D. Appl. Phys.*, 2011, **44**, 274008.

175 C.-J. Liu, R. G. Mallinson and L. L. Lobban, *Appl. Catal. A Gen.*, 1999, **178**, 17–27.

176 B. Zhu, X. S. Li, C. Shi, J. L. Liu, T. L. Zhao and A. M. Zhu, *Int. J. Hydrogen Energy*, 2012, **37**, 4945–4954.

177 B. Zhu, X. Li, J. Liu and A. Zhu, *Int. J. Hydrogen Energy*, 2012, **37**, 16916–16924.

178 X. Zhu, K. Li, J. Liu and X. Li, *Int. J. Hydrogen Energy*, 2014, **39**, 13902–13908.

179 J. Liu, X. Li, X. Zhu, K. Li, C. Shi and A. Zhu, *Chem. Eng. J.*, 2013, **234**, 240–246.

180 K. Li, J. Liu, X. Li, X. Zhu and A. Zhu, *Catal. Today*, 2015, **256**, 96–101.

181 O. Mutaf-yardimci, A. Saveliev, A. A. Fridman and L. A. Kennedy, *Int. J. Hydrogen Energy*, 1998, **23**, 1109–1111.

182 P. Bruggeman and C. Leys, *J. Phys. D. Appl. Phys.*, 2009, **42**, 53001.

183 B. R. Locke and K.-Y. Shih, *Plasma Sources Sci. Technol.*, 2011, **20**, 34006.

184 M. A. Malik, A. Ghaffar and S. A. Malik, *Plasma Sources Sci. Technol.*, 2001, **10**, 82–91.

185 P. Sunka, V. Babický, M. Clupek, P. Lukes, M. Simek, J. Schmidt and M. Cernák, *Plasma Sources Sci. Technol.*, 1999, **8**, 258–265.

186 B. R. Locke and S. M. Thagard, *Plasma Chem. Plasma Process.*, 2012, **32**, 875–917.

187 S. Futamura and H. Kabashima, *Stud. Surf. Sci. Catal.*, 2004, **153**, 119–124.

188 R. Snoeckx, A. Ozkan, F. Reniers and A. Bogaerts, *ChemSusChem*, 2017, **10**, 409–424.

189 S. Mahammadunnisa, E. L. Reddy, D. Ray, C. Subrahmanyam and J. C. Whitehead, *Int. J. Greenh. Gas Control*, 2013, **16**, 361–363.

190 T. Ihara, M. Kiboku and Y. Iriyama, *Bull. Chem. Soc. Jpn.*, 1994, **67**, 312–314.

191 T. Ihara, T. Ouro, T. Ochiai, M. Kiboku and Y. Iriyama, *Bull. Chem. Soc. Jpn.*, 1996, **69**, 241–244.

192 G. Chen, T. Silva, V. Georgieva, T. Godfroid, N. Britun, R. Snyders and M. P. Delplancke-Ogletree, *Int. J. Hydrogen Energy*, 2015, **40**, 3789–3796.

193 G. Chen, N. Britun, T. Godfroid, V. Georgieva, R. Snyders and M.-P. Delplancke-Ogletree, *J. Phys. D. Appl. Phys.*, 2017, **50**, 84001.

194 N. Hayashi, T. Yamakawa and S. Baba, *Vacuum*, 2006, **80**, 1299–1304.

195 L. Guo, X. Ma, Y. Xia, X. Xiang and X. Wu, *Fuel*, 2015, **158**, 843–847.

196 E. C. Neyts and K. Ostrikov, *Catal. Today*, 2015, **256**, 23–28.

197 B. Eliasson, U. Kogelschatz, B. Xue and L.-M. Zhou, *Ind. Eng. Chem. Res.*, 1998, **37**, 3350–3357.

198 E. Jwa, S. B. Lee, H. W. Lee and Y. S. Mok, *Fuel Process. Technol.*, 2013, **108**, 89–93.

199 G. Centi and S. Perathoner, *Catal. Today*, 2009, **148**, 191–205.

200 F. Studt, I. Sharafutdinov, F. Abild-Pedersen, C. F. Elkjær, J. S. Hummelshøj, S. Dahl, I. Chorkendorff and J. K. Nørskov, *Nat. Chem.*, 2014, **6**, 320–324.

201 S. G. Jadhav, P. D. Vaidya, B. M. Bhanage and J. B. Joshi, *Chem. Eng. Res. Des.*, 2014, **92**, 2557–2567.

202 Y. Zeng and X. Tu, *IEEE Trans. Plasma Sci.*, 2015, **44**, 1–7.

203 M. Nizio, A. Albarazi, S. Cavadias, J. Amouroux, M. E. Galvez and P. Da Costa, *Int. J. Hydrogen Energy*, 2016, **41**, 11584–11592.

204 L. Maya, *J. Vac. Sci. Technol. A Vacuum, Surfaces, Film.*, 2000, **18**, 285–287.

205 J. F. de la Fuente, S. H. Moreno, A. I. Stankiewicz and G. D. Stefanidis, *Int. J. Hydrogen Energy*, 2016, 1–11.

206 M. Kano, G. Satoh and S. Iizuka, *Plasma Chem. Plasma Process.*, 2012, **32**, 177–185.

207 C. De Bie, J. van Dijk and A. Bogaerts, *J. Phys. Chem. C*, 2016, **120**, 25210–25224.

208 R. Aerts, R. Snoeckx and A. Bogaerts, *Plasma Process. Polym.*, 2014, **11**, 985–992.

209 S. Mori, N. Matsuura, L. L. Tun and M. Suzuki, *Plasma Chem. Plasma Process.*, 2016, **36**, 231–239.

210 F. Dimroth, M. Grave, P. Beutel, U. Fiedeler, C. Karcher, T. N. D. Tibbits, E. Oliva, G. Siefer, M. Schachtner, A. Wekkeli, A. W. Bett, R. Krause, M. Piccin, N. Blanc, C. Drazek, E. Guiot, B. Ghyselen, T. Salvetat, A. Tauzin, T.

Signamarcheix, A. Dobrich, T. Hannappel and K. Schwarzburg, *Prog. Photovoltaics Res. Appl.*, 2014, **22**, 277–282.

211 P. Furler, J. R. Scheffe and A. Steinfeld, *Energy Environ. Sci.*, 2012, **5**, 6098–6103.

212 G. P. Smestad and A. Steinfeld, *Ind. Eng. Chem. Res.*, 2012, **51**, 11828–11840.

213 W. C. Chueh, C. Falter, M. Abbott, D. Scipio, P. Furler, S. M. Haile and A. Steinfeld, *Science (80-.).*, 2010, **330**, 1797–1801.

214 J. R. Scheffe and A. Steinfeld, *Mater. Today*, 2014, **17**, 341–348.

215 S. C. Roy, O. K. Varghese, M. Paulose and C. a Grimes, *ACS Nano*, 2010, **4**, 1259–1278.

216 J. Barber, *Chem. Soc. Rev.*, 2009, **38**, 185–196.

217 N. Pinhão, A. Moura, J. B. Branco and J. Neves, *Int. J. Hydrogen Energy*, 2016, **41**, 9245–9255.

Summary

The steadily rising atmospheric concentration of CO_2—in the past century—has a growing detrimental effect on our climate and environment, and is considered as a threat for our society in general. This results in a booming interest for technologies which can convert CO_2 into value-added products like chemicals and fuels, as they can effectively convert waste into new feedstock—following the cradle-to-cradle principle. Several alternative (non-conventional) technologies are being investigated, such as photochemical, electrochemical and thermochemical pathways, either with or without catalysts, and all their possible combinations. Another new technology considered to have great potential in recent years is based on (non-thermal) plasma. The worldwide transition to renewable energy gives plasma processes a clean electricity source, and due to their high operation flexibility, plasmas are very suitable for storing this intermittent sustainable energy in chemicals. Several options are being investigated, including both pure CO_2 splitting into CO and O_2, as well as the reaction with other gases, like CH_4 (dry reforming of methane), H_2 (hydrogenation of CO_2) or H_2O (artificial photosynthesis), aiming for the production of syngas and valuable oxygenates, such as methanol, formaldehyde and formic acid. Most research on plasma-based CO_2 conversion is performed with dielectric barrier discharges (DBD), microwave (MW) plasmas and gliding arc (GA) discharges, with a main focus on improving the energy efficiency of the conversion, as well as the selectivity towards value-added chemicals, in combination with catalysis. To-date, the highest energy efficiencies have been achieved with the GA and MW set-up, with values up to 43 % for the GA and up to 90 % for the MW plasma being reported. The energy efficiency of a DBD is more limited (typically up to 10 %), but can be improved by inserting a packing inside the plasma, and the latter also easily allows the integration of a catalyst for the selective production of value-added chemicals. This background is thoroughly reviewed in **Chapter 1**. By using computer simulations in combination with experiments, this dissertation contributes to the development of several reaction chemistry sets used for a better understanding of the complex plasma chemistry taking place in a DBD and unravelling the underlying chemical reaction pathways. Both the model and the experiments are outlined in **Chapter 2**, while all the relevant reaction chemistry data can be found in **Appendices I, II and III**.

Chapter 3 covers the combined conversion of CO_2 and CH_4, i.e. dry reforming of methane, in a DBD. In the first half of this chapter, an extensive study of the reaction chemistry mimicking the filamentary discharge regime is carried out. A zero-dimensional chemical kinetics model is applied to study the plasma chemistry in a 1:1 CH_4/CO_2 mixture. The calculations are first performed for one microdischarge pulse

and its afterglow, to study the chemical pathways of the conversion in detail. Subsequently, long timescale simulations are carried out, corresponding to real residence times in the plasma, assuming a large number of consecutive microdischarge pulses, to mimic the conditions of the filamentary discharge regime in a DBD reactor. The conversion of CH_4 and CO_2 as well as the selectivity of the formed products and the energy cost and energy efficiency of the process are calculated and compared to experiments for a range of different powers and gas flows, and reasonable agreement is reached.

In the second half of **Chapter 3** an extensive computational study is carried out, supported by experiments, aiming to identify the influence of the operating parameters (gas mixture, power, residence time and "frequency") of a DBD plasma on the conversion and energy efficiency, and to investigate which of these parameters lead to the most promising results and whether these are eventually sufficient for industrial implementation. Supporting data is presented in **Appendix IV**. The best results, in terms of both energy efficiency and conversion, are obtained at a specific energy input (SEI) of 100 J cm^3, a 10:90 CH_4/CO_2 ratio, 10 Hz, a residence time of 1 ms, resulting in a total conversion of 84 % and an energy efficiency of 8.5 %. In general, increasing the CO_2 content in the gas mixture leads to a higher conversion and energy efficiency. The SEI couples the effect of the power and residence time, and increasing the SEI always results in a higher conversion, but somewhat lower energy efficiencies. The effect of the frequency is more complicated: we observed that the product of frequency (f) and residence time (s), being a measure for the total number of microdischarge filaments which the gas molecules experience when passing through the reactor, was critical. For most cases, a higher number of filaments yields higher values for conversion and energy efficiency. To benchmark our model predictions, we also give an overview of measured conversions and energy efficiencies reported in the literature, to indicate the potential for improvement compared to the state-of the art. Finally, we identify the limitations as well as the benefits and future possibilities of plasma technology for DRM.

The second process that is studied for a DBD is the combined conversion of CO_2 and H_2O, i.e. artificial photosynthesis, in **Chapter 4**. To investigate whether plasma technology is promising for this application, we performed a series of experiments and developed a chemical kinetics plasma chemistry model for a deeper understanding of the process. The main products formed were the syngas components CO and H_2, as well as O_2 and H_2O_2, whereas methanol formation was only observed in the parts-per-billion to parts-per-million range. The syngas ratio, on the other hand, could easily be controlled by varying both the water content and/or energy input. On the basis of the model, which was validated with experimental results, a chemical kinetics analysis was performed, which allowed the construction and investigation of the different pathways leading to the observed experimental results and which helped to clarify these results. This approach allowed us to evaluate this technology on the basis of its underlying chemistry and to propose solutions on how to further improve the formation of value-added products by using plasma technology.

Quite some research has already been performed on plasma-based CO_2 and CH_4 conversion, but mostly on pure gases. In reality, N_2 will always be an important impurity in effluent gases. Therefore, we performed two studies on the effect of N_2 in **Chapter 5**. In the first half we present a combined study of experimental and computational work for a DBD used for CH_4 conversion into H_2. More specifically, we investigated the influence of N_2 as an impurity (1–50,000 ppm) and as additive gas (1–99 %) on the CH_4 conversion and H_2 yield. For this purpose, a zero-dimensional chemical kinetics model is applied to study the plasma chemistry. The calculated conversions and yields for various gas mixing ratios are compared to the obtained experimental values, and good agreement is achieved. The study reveals the significance of the $\mathrm{N_2}(A^3\sum_u^+)$ and $\mathrm{N_2}(a'^1\sum_u^-)$ metastable states for the CH_4 conversion into H_2, based on a kinetic analysis of the reaction chemistry.

In the second part of **Chapter 5** an extensive combined experimental and computational study on the effect of N_2 in the range of 1–98 % on CO_2 splitting in DBD plasma is performed. The presence of up to 50 % N_2 in the mixture barely influences the effective (or overall) CO_2 conversion and energy efficiency, because the N_2 metastable molecules enhance the absolute CO_2 conversion, and this compensates for the lower CO_2 fraction in the mixture. Higher N_2 fractions, however, cause a drop in the CO_2 conversion and energy efficiency. Moreover, in the entire CO_2/N_2 mixing ratio, several harmful compounds, i.e. N_2O and NO_x compounds, are produced in the range of several 100 ppm. The reaction pathways for the formation of these compounds are explained based on a kinetic analysis, which allows proposing solutions on how to prevent the formation of these harmful compounds.

Finally, **Chapter 6** delivers an overview of the present state-of-the-art with respect to plasma-based CO_2 conversion, focusing on a critical assessment of the advantages and disadvantages of the various set-ups, also in comparison to other novel conversion technologies, and it provides an outlook and conclusions regarding their future challenges, risks and opportunities for successful implementation.

Samenvatting

De gestaag stijgende atmosferische CO_2 concentratie in de afgelopen eeuw heeft een groeiend nadelig effect op ons klimaat en milieu, en is een bedreiging voor onze samenleving in het algemeen. Dit resulteert in een sterk groeiende belangstelling voor technologieën die CO_2 kunnen omzetten in meer waardevolle producten, zoals chemicaliën en/of brandstoffen. Op deze manier kan een afvalstof worden omgezet in een nieuwe grondstof volgens het cradle-to-cradle principe. Verschillende alternatieve (niet-conventionele) technieken worden momenteel onderzocht, o.a. fotochemische, elektrochemische en thermochemische paden, met of zonder katalysator, en alle mogelijke combinaties. Een andere nieuwe technologie met een groot potentieel is gebaseerd op (niet-thermisch) plasma. De wereldwijde transitie naar duurzame energie geeft plasmaprocessen een schone elektriciteitsbron, en vanwege hun hoge flexibiliteit zijn plasma's zeer geschikt voor het opslaan van intermitterende hernieuwbare energie in chemicaliën. Verschillende opties worden onderzocht, met inbegrip van zowel zuivere CO_2 splitsing in CO en O_2, evenals de reactie met andere gassen, zoals CH_4 (droog reformen van methaan), H_2 (hydrogenatie van CO_2) en H_2O (artificiële fotosynthese) die streven naar de productie van syngas en waardevolle oxygenaten, zoals methanol, formaldehyde en mierenzuur. Het meeste onderzoek naar plasma-gebaseerde CO_2-conversie wordt uitgevoerd met behulp van diëlektrische barrière-ontladingen (DBD), magnetron (MW) plasma's en glijdende boog (GA) ontladingen, met als voornaamste focus het verbeteren van de energie-efficiëntie van de omzetting, evenals de selectiviteit naar waardevolle producten, in combinatie met een katalysator. Tot op heden werd de hoogste energie-efficiëntie bereikt met de GA en MW set-up, met waarden tot 43 % voor de GA en 90 % voor een MW plasma. De energie-efficiëntie van een DBD is beperkter (gewoonlijk tot 10 %), maar dit kan worden verbeterd door het toevoegen van een pakking in de reactor, wat eveneens toelaat om een katalysator te integreren voor de selectieve productie van waardevolle chemicaliën. Deze achtergrond wordt beschreven in **Hoofdstuk 1**. Door gebruik te maken van computersimulaties in combinatie met experimenten draagt dit proefschrift bij aan de ontwikkeling van verschillende reactiechemie sets, gebruikt voor een beter inzicht in de complexe plasmachemie voor een DBD, en bij het ontrafelen van de onderliggende chemische reactiepaden. Zowel het computationeel model als de experimenten worden beschreven in **Hoofdstuk 2**. De reactie kinetiek data kan teruggevonden worden in de **Appendices I, II en III**.

Hoofdstuk 3 behandelt de gecombineerde omzetting van CO_2 en CH_4, droog reformeren van methaan, in een DBD. In de eerste helft van dit hoofdstuk wordt een uitgebreide studie van de reactiechemie uitgevoerd die het filamentvormige ontladingsregime nabootst. Een nuldimensionaal chemisch kinetiek model wordt toegepast om de plasmachemie in een 1:1 CH_4/CO_2 mengsel te onderzoeken. De berekeningen worden eerst uitgevoerd voor één micro-ontladingspuls en zijn afterglow, om zo de chemische conversiepaden te bestuderen. Vervolgens worden simulaties uitgevoerd op lange tijdschaal, d.w.z. werkelijke verblijftijden in het plasma, uitgaande van een groot aantal opeenvolgende micro-ontladingspulsen, om zo het filamentair regime van een DBD reactor na te bootsen. Zowel de conversie van CH_4 en CO_2 als de selectiviteit van de gevormde producten en de energiekosten/energie-efficiëntie worden berekend en redelijke overeenstemming wordt bereikt bij vergelijking met experimenten voor een reeks van verschillende vermogens en gasstromen.

In de tweede helft van **Hoofdstuk 3** wordt een uitgebreide computationele studie, ondersteund door experimenten uitgevoerd, gericht op het identificeren van de invloed van de reactieparameters (gasmengsel, vermogen, verblijftijd en "frequentie") op de conversie en energie-efficiëntie voor een DBD plasma, en om te onderzoeken welke van deze parameters leiden tot de meest veelbelovende resultaten, om na te gaan of deze uiteindelijk voldoende zijn voor een industriële implementatie. Extra ondersteunende data is terug te vinden in **Appendix IV**. De beste resultaten, zowel op vlak van energie-efficiëntie als conversie, worden verkregen bij een specifieke energie-invoer (SEI) van 100 J cm^3, een 10:90 verhouding CH_4/CO_2, 10 Hz, een verblijftijd van 1 ms, resulterend in een totale conversie van 84 % en een energie-efficiëntie van 8,5 %. In het algemeen leidt het verhogen van de CO_2 concentratie in het gasmengsel tot een hogere conversie en energie-efficiëntie. De SEI combineert het effect van het vermogen en de verblijftijd, en het verhogen van de SEI resulteert altijd in een hogere conversie, maar iets lager energie-efficiëntie. Het effect van de frequentie is ingewikkelder: we konden vaststellen dat het product van de frequentie (f) en verblijftijd (s) een kritische factor is, zijnde een maat voor het totale aantal micro-ontladingsfilamenten die de gasmoleculen ervaren bij het passeren van de reactor. Voor de meeste gevallen, leverde een groter aantal filamenten hogere waarden voor de conversie en energie-efficiëntie. Om onze modelresultaten te benchmarken, geven we ook een overzicht van de gemeten conversies en energie-efficiënties in de literatuur, om de mogelijkheden voor verbetering ten opzichte van de huidige stand van de techniek aan te geven. Tenslotte identificeren we zowel de beperkingen als de voordelen en toekomstige mogelijkheden van plasmatechnologie.

Het tweede proces dat is onderzocht voor een DBD is de gecombineerde omzetting van CO_2 en H_2O, artificiële fotosynthese, in **Hoofdstuk 4**. Om na te gaan of plasmatechnologie beloftevol is voor deze toepassing is voerde A. Ozkan (ULB) een serie experimenten uit en ontwikkelden we een chemisch kinetiek plasmachemie model voor een dieper inzicht in het proces. De belangrijkste gevormde producten zijn de syngas componenten CO en H_2, en O_2 en H_2O_2, terwijl methanol vorming alleen waarneembaar is in het ppm bereik. De syngas verhouding kan gemakkelijk worden geregeld door het variëren van zowel het watergehalte als de energietoevoer. Op basis van het computationeel model gevalideerd met experimentele resultaten is een chemische kinetiek analyse uitgevoerd. Deze analyse laat toe om de verschillende reactiepaden te construeren en onderzoeken die aanleiding geven tot de waargenomen experimentele resultaten en deze zo helpen te verduidelijken. Deze aanpak laat toe om deze technologie te beoordelen op basis van zijn onderliggende chemie en om oplossingen aan te reiken om de vorming van waardevolle producten te verbeteren.

Er is al tamelijk veel onderzoek uitgevoerd naar plasma-gebaseerde CO_2 en CH_4 conversie, maar vooral op zuivere gassen. In werkelijkheid zal N_2 altijd een belangrijke onzuiverheid zijn in gasstromen. Daarom voerden we in **Hoofdstuk 5** twee studies uit naar het effect van N_2. In het eerste deel presenteren we een gezamenlijke studie van experimenteel en computationeel werk voor een DBD gebruikt voor de omzetting van CH_4 in H_2. Meer specifiek werd de invloed van N_2 als onzuiverheid (1–50,000 ppm) en als additief gas (1–99 %) nagegaan op de conversie van CH_4 en opbrengst van H_2. Hiervoor wordt een nuldimensionaal chemisch kinetiek model gebruikt om de plasmachemie te bestuderen. De berekende conversies en opbrengsten voor verschillende gasmengselverhoudingen worden vergeleken met de experimentele waarden en goede overeenstemming wordt bereikt. De studie toont het belang van de $\mathrm{N_2}(A^3\sum_u^+)$ en $\mathrm{N_2}(a'^1\sum_u^-)$ metastabiele toestanden voor de omzetting van CH_4 naar H_2, gebaseerd op de kinetische analyse van de reactiechemie.

In het tweede deel van **Hoofdstuk 5** wordt een uitgebreide gecombineerde experimentele en computationele studie uitgevoerd naar het effect van N_2 in het bereik van 1–98 % op CO_2-splitsing in een DBD plasma. De aanwezigheid tot 50 % N_2 in het mengsel heeft nauwelijks een invloed op de effectieve (of totale) CO_2 conversie en energie efficiëntie, omdat de N_2 metastabiele moleculen de absolute CO_2 conversie verbeteren, en dit effect compenseert de lagere CO_2 fractie in het mengsel. Hogere N_2 fracties leiden echter tot een daling van de CO_2-conversie en energie-efficiëntie. Bovendien worden voor alle CO_2/N_2 mengverhoudingen verschillende schadelijke stoffen, N_2O en NO_x verbindingen geproduceerd in een hoeveelheid van enkele 100 ppm. De reactiepaden voor de vorming van deze verbindingen worden uitgelegd gebaseerd op een kinetische analyse die toelaat om oplossingen voor te stellen om de vorming van deze schadelijke verbindingen te voorkomen.

Tot slot geeft **Hoofdstuk 6** een overzicht van de huidige stand van zaken met betrekking tot plasma gebaseerde CO_2-conversie, met een focus op de kritische beoordeling van de voor- en nadelen van de verschillende set-ups, ook in vergelijking met andere nieuwe technologieën die ontwikkeld worden, en om een vooruitblik en conclusies te bieden met betrekking tot hun toekomstige uitdagingen, risico's en kansen tot een succesvolle implementatie.

List of publications

1. **R Snoeckx** and A Bogaerts, *Plasma technology – a novel solution for CO_2 conversion?*, Chemical Society Reviews (2017) proposal accepted, manuscript in peer review.
2. A Bogaerts, A Berthelot, S Heijkers, S Kolev, **R Snoeckx**, S Song, K Van Laer and W Wang, *CO_2 conversion by plasma technology: Insights from modeling the plasma chemistry and plasma reactor design*, Plasma Sources Science and Technology (2017) invited topical review, in press.
3. **R Snoeckx**, A Rabinovich, D Dobrynin, A Bogaerts and A Fridman, *Plasma based liquefaction of methane: the road from hydrogen production to direct methane liquefaction*, Plasma Processes and Polymers (2017) invited review for special issue on "Plasma Conversion", DOI: 10.1002/ppap.201600115.
4. A Bogaerts, C De Bie, **R Snoeckx** and T Kozak, *Plasma based CO_2 and CH_4 conversion: a modeling perspective*, Plasma Processes and Polymers (2017) invited review for special issue on "Plasma Conversion" and cover paper, DOI: 10.1002/ppap.201600070.
5. **R Snoeckx**, A Ozkan, F Reniers and A Bogaerts, *The Quest For Value-Added Products From CO_2 And H_2O In A Dielectric Barrier Discharge: A Chemical Kinetics Study*, ChemSusChem 10 (2017) 409-424 (16p).
6. **R Snoeckx**, S Heijkers, K Van Wesenbeeck, S Lenaerts and A Bogaerts, *CO_2 conversion in a dielectric barrier discharge plasma: N_2 in the mix as helping hand or problematic impurity?* Energy & Environmental Science 9 (2016) 999-1011 (13p).
7. A Bogaerts, T Kozak, K Van Laer and **R Snoeckx**, *FDCDU15 – Carbon dioxide utilization: Plasma-based conversion of CO_2: current status and future challenges*, Faraday Discussions 183 (2015) 217-232 (16p).
8. S Heijkers, **R Snoeckx**, T Kozak, T silva, T Godfroid, N Britun, R Snyders and A Bogaerts, *CO_2 conversion in a microwave plasma reactor in the presence of N_2: elucidating the role of vibrational levels*, The Journal of Physical Chemistry C 119 (2015) 12815-12828 (14p).
9. **R Snoeckx**, Y X Zeng, X Tu and A Bogaerts, *Plasma-Based Dry Reforming: improving the conversion and energy efficiency in a dielectric barrier discharge*, RSC Advances 5 (2015) 29799-29808 (10p).

10. R Aerts, **R Snoeckx** and A Bogaerts, *In-situ chemical trapping of oxygen after the splitting of carbon dioxide by plasma*, Plasma Processes and Polymers 11 (2014) 985-992 *[back cover]*.
11. M Yusupov, E Neyts, P Simon, G Berdiyorov, **R Snoeckx**, A C T van Duin and A Bogaerts, *Reactive molecular dynamics simulations of oxygen species in a liquid water layer of interest for plasma medicine*, Journal of Physics D: Applied Physics 47 (2014) 025205 (9p).
12. **R Snoeckx**, M Setareh, R Aerts, P Simon, A Maghari and A Bogaerts, *Influence of N_2 concentration in a CH_4/N_2 dielectric barrier discharge used for CH_4 conversion into H_2*, International Journal of Hydrogen Energy 38 (2013) 16098-16120 (23p).
13. M Yusupov, A Bogaerts, S Huygh, **R Snoeckx**, A C T van Duin and E C Neyts, *Plasma-Induced Destruction of Bacterial Cell Wall Components: A Reactive Molecular Dynamics Simulation*, The Journal of Physical Chemistry C 117 (2013) 5993-5998 (6p).
14. **R Snoeckx**, R Aerts, X Tu and A Bogaerts, *Plasma-Based Dry Reforming: A Computational Study Ranging from the Nanoseconds to Seconds Time Scale*, The Journal of Physical Chemistry C 117 (2013) 4957-4970 (41p).
15. A Bogaerts, R Aerts, **R Snoeckx**, W Somers, W Van Gaens, M Yusupov and E Neyts, *Modeling of plasma and plasma-surface interactions for medical, environmental and nano applications*, Journal of Physics: Conference Series 399 (2012) 012011 (12p).
16. M Yusupov, E C Neyts, U Khalilov, **R Snoeckx**, A C T van Duin and A Bogaerts, *Atomic-scale simulations of reactive oxygen plasma species interacting with bacterial cell walls*, New Journal of Physics 14 (2012) 093043 (18p) *[Selected for IOP Select]*.

List of conference contributions

A. Conference contributions: presenting author

1. 63rd International Symposium of the American Vacuum Society (**AVS 63**): Invited oral presentation "Plasma-based CO_2 Conversion: Experiments and Modeling", USA, Nashville, November 6-11, 2016. *[received a travel grant from the Research Foundation Flanders (FWO)].*
2. 14th International Conference on Carbon Dioxide Utilization (**ICCDU 14**): Flash presentation and poster presentation "Plasma-based CO_2 conversion: a chemical kinetics story", UK, Sheffield, September 11-15, 2016.
3. 10th International Symposium on Non-Thermal/Thermal Plasma Pollution Control Technology and Sustainable Energy (**ISNTP 10**): Oral presentation "Unwanted NO_x production during the conversion of CO2 in a dielectric barrier discharge in the presence of N_2 and how to prevent it", Brasil, Florianopolis, August 1-5, 2016. *[received a travel grant from the Royal Society of Chemistry (RSC)]*.
4. 10th International Symposium on Non-Thermal/Thermal Plasma Pollution Control Technology and Sustainable Energy (**ISNTP 10**): Oral presentation "How does N_2 influence the dry reforming of methane in a dielectric barrier discharge: a combined experimental and computational study", C Brasil, Florianopolis, August 1-5, 2016. *[received a travel grant from the Royal Society of Chemistry (RSC)]*.
5. 10th International Symposium on Non-Thermal/Thermal Plasma Pollution Control Technology and Sustainable Energy (**ISNTP 10**): Poster presentation "Non-Equilibrium Gliding Arc and Dielectric Barrier Discharge Treatment of Liquids for Pathogen Removal from Food and Food-Contacting Surface", Brasil, Florianopolis, August 1-5, 2016. *[received a travel grant from the Royal Society of Chemistry (RSC)]*.
6. 22nd International Symposium on Plasma Chemistry (**ISPC 22**): Oral presentation and Full paper "Plasma-based dry reforming: can we improve the dielectric barrier discharge process", Belgium, Antwerp, July 5-10, 2015.
7. 22nd International Symposium on Plasma Chemistry (**ISPC 22**): Poster presentation and Full paper "A combined study for turning CO_2 and H_2O into value-added products in a dielectric barrier discharge", Belgium, Antwerp, July 5-10, 2015.

8. 22nd International Symposium on Plasma Chemistry (**ISPC 22**): Poster presentation and Full paper “How does N2 influence the CO2 conversion and energy efficiency in a dielectric barrier discharge and microwave plasma?”, Belgium, Antwerp, July 5-10, 2015.
9. 9th International Symposium on Non-Thermal/Thermal Plasma Pollution Control Technology and Sustainable Energy (**ISNTP 9**): Poster Presentation “Paschen curves and analytical expressions for the electron collision rate coefficients in CH_4/CO_2 and CH_4/O_2 mixtures”, China, Dalian, June 16-20, 2014.
10. 9th International Symposium on Non-Thermal/Thermal Plasma Pollution Control Technology and Sustainable Energy (**ISNTP 9**): Oral Presentation “The influence of N_2 on CH_4 reforming and CO_2 splitting by plasmas: A combined computational and experimental study”, China, Dalian, June 16-20, 2014. *[received a travel grant from the Research Foundation Flanders (FWO)]*.
11. 21st International Symposium on Plasma Chemistry (**ISPC 21**): Poster presentation and Full paper “Plasma-based Dry Reforming in a Dielectric Barrier Discharge: a Computational Study”, Australia, Cairns, August 4-9, 2013.
12. 65th Gaseous and Electronics Conference (**GEC 65**): Oral presentation “Numerical simulations for plasma-based dry reforming”, USA, Texas, October 22-26, 2012. *[received a student travel assistance grant from the American Physical Society (APS)]*.

B. Invited talks: co-author

13. Chemical Research in Flanders – (**CRF**): Invited lecture “CO_2 conversion into value-added chemicals by plasma and plasma catalysis.” A. Bogaerts, R. Aerts, S. Heijkers, ***R. Snoeckx***, T. Kozák, K. Van Laer. Belgium, Blankenberge, October 24-26, 2016.
14. Seventh International Symposium on Plasma Nanoscience and Nanotechnology (**iPlasmaNano-VII**): Invited lecture “Plasma-based CO_2 conversion: Better insights by modeling.” A. Bogaerts, R. Aerts, S. Heijkers, ***R. Snoeckx***, T. Kozák, K. Van Laer. Greece, Attica, October 16 – 20, 2016.
15. Workshop on Plasma Catalysis: Invited lecture “Plasma catalysis: a better insight by computer modeling” A. Bogaerts, ***R. Snoeckx***, C. De Bie, K. Van Laer, Y-R. Zhang, E. Neyts. France, Lille, October 13, 2016.

16. International Symposium on High Pressure Low Temperature Plasma Chemistry" (**HAKONE**): Invited lecture "Plasma-based CO_2 conversion: A combined modeling and experimental study." A. Bogaerts, R. Aerts, S. Heijkers, ***R. Snoeckx***, T. Kozák, K. Van Laer. Czech Republic, Brno, September 11 -16, 2016.

17. International Workshop on Plasmas for Energy and Environmental Applications: Invited lecture "Plasma chemistry modeling for CO_2 conversion: A better understanding of energy efficiency and product formation." A. Bogaerts, R. Aerts, A. Berthelot, S. Heijkers, St. Kolev, T. Kozák, ***R. Snoeckx***, G. Trenchev, K. Van Laer, Y-R. Zhang. UK, Liverpool, August 21-24, 2016.

18. Conference: Quo vadis Complex Plasmas: Invited lecture "Modeling plasma and plasma catalysis for CO_2 conversion." A. Bogaerts, R. Aerts, A. Berthelot, S. Heijkers, St. Kolev, T. Kozák, ***R. Snoeckx***, G. Trenchev, K. Van Laer, Y-R. Zhang, E. Neyts. Germany, Hamburg, August 1-4, 2016.

19. Eurosectional Conference on Atomic and Molecular Physics of Ionized Gases" (**ESCAMPIG**): Invited plenary lecture "Modeling of CO_2 plasmas." A. Bogaerts, R. Aerts, A. Berthelot, S. Heijkers, St. Kolev, T. Kozák, ***R. Snoeckx***, G. Trenchev, K. Van Laer, Y-R. Zhang. Slovakia, Bratislava, July 12-16, 2016.

20. Fifth International Symposium on Plasma Nanoscience (**iPlasmaNano-V**): Invited lecture "Plasma conversion of greenhouse gases in value-added chemicals: a modeling point of view." A. Bogaerts, R. Aerts, S. Kolev, T. Kozak, E. Neyts, ***R. Snoeckx***, W. Somers, K. Van Laer. Spain, Torremolinos, September 28 – October 2, 2014.

21. 17th International Congress on Plasma Physics (**ICPP**): Invited lecture "Combined Plasma Chemistry and Plasma-Surface Interactions Modeling for CO_2 conversion by Gas Discharge Plasmas." A. Bogaerts, R. Aerts, S. Kolev, T. Kozak, E. Neyts, ***R. Snoeckx***, W. Somers, K. Van Laer. Portugal, Lisbon, September 15-19, 2014.

22. 5th Central European Symposium on Plasma Chemistry: Invited lecture "Improving environmental, medical and materials science applications by a combination of plasma chemistry and plasma-surface interactions modeling." A. Bogaerts, E. Neyts, ***R. Snoeckx***, W. Somers, J. van der Paal, W. Van Gaens and M. Yusupov. Hungary, Balatonkenese, August 25-29, 2013.

C. Other scientific contributions

23. Scientific research visit, Drexel University – Drexel Plasma Institute (DPI), Supervisor: Prof. Dr. Greg Fridman and Prof. Dr. Alexander Rabinovich, February 15 – August 31, 2016. *[received a travel grant for a long stay abroad from the Research Foundation Flanders (FWO) and from the Antwerp Doctoral School (ADS)]*
24. Scientific research visit, King Abdullah University of Science and Technology (KAUST) – Clean Combustion Research Center (CCRC), Supervisor: Prof. Dr. Min Suk Cha, January 6 – February 9, 2016.
25. 4th Enmix workshop, "Nanoporous Materials for Advanced Applications", Invited talk, Slovenia, Bled, September 17-20, 2014.
26. Solvay Workshop "Plasmas for Environmental Applications", Poster presentation, Belgium, Brussels, March 31 – April 2, 2014.
27. BASF "Research Forum Europe" (Knowledge carrier, co-creation workshop: Energy storage possibilities for the future), Poster presentation, Belgium, Antwerp, March 25-26, 2014.
28. E3C3 CO2 Workshop "CO2 Dissociation – Reactive Plasma for Building Molecules", Invited talk, France, Normandy, Island of Tatihou, March 2-5, 2014
29. Scientific research visit, Technical University of Lisbon - Campus Technológico e Nuclear - Institute for Plasma Research and Nuclear Fusion (IPFN), Supervisor: Prof. Dr. Nuno Pinhão, January 15 – February 15, 2014.
30. IAP workshop "Fundamentals of Plasma-Surface Interactions", Poster presentation, Belgium, Antwerp, November 8, 2013.
31. CO2Chem Event "Applications of cold plasma to CO2 chemistry - 'Chemical Transformations Cluster' meeting", Oral presentation, United Kingdom, York, November 13, 2013.

APPENDIX I

Data chemistry set $CO_2 + CH_4$

1. Overview of the reactions included in the model.

Table A I-1. Electron impact reactions with the various molecules and radicals, included in the model. These reactions are treated by energy-dependent cross sections, and the references where these cross sections were adopted from, are also included. For the vibrational and electronic excitations, several individual excitations are included, as indicated by the number between brackets.

Momentum Transfer	$e^- + CH_4$	$\rightarrow$	$e^- + CH_4$		[1]
Vibrational Excitation	$e^- + CH_4$	$\rightarrow$	$e^- + CH_4^*$	(2)	[1]
Ionization	$e^- + CH_4$	$\rightarrow$	$2e^- + CH_4^+$		[2]
Dissociative Ionization	$e^- + CH_4$	$\rightarrow$	$2e^- + CH_3^+ + H$		[2]
	$e^- + CH_4$	$\rightarrow$	$2e^- + CH_2^+ + H_2$		[2]
Dissociation	$e^- + CH_4$	$\rightarrow$	$e^- + CH_3 + H$		[3, 4]
	$e^- + CH_4$	$\rightarrow$	$e^- + CH_2 + H_2$		[3, 4]
	$e^- + CH_4$	$\rightarrow$	$e^- + CH + H_2 + H$		[3, 4]
	$e^- + CH_4$	$\rightarrow$	$e^- + C + 2H_2$		[3, 4]
Ionization	$e^- + CH_3$	$\rightarrow$	$2e^- + CH_3^+$		[2]
Dissociative Ionization	$e^- + CH_3$	$\rightarrow$	$2e^- + CH_2^+ + H$		[2]
	$e^- + CH_3$	$\rightarrow$	$2e^- + CH^+ + H_2$		[2]
Dissociation	$e^- + CH_3$	$\rightarrow$	$e^- + CH_2 + H$		[3, 4]
	$e^- + CH_3$	$\rightarrow$	$e^- + CH + H_2$		[3, 4]
Ionization	$e^- + CH_2$	$\rightarrow$	$2e^- + CH_2^+$		[2]
Dissociation	$e^- + CH_2$	$\rightarrow$	$e^- + CH + H$		[3, 4]
Ionization	$e^- + CH$	$\rightarrow$	$2e^- + CH^+$		[2]
Dissociation	$e^- + CH$	$\rightarrow$	$e^- + C + H$		[3, 4]
Momentum Transfer	$e^- + C_2H_6$	$\rightarrow$	$e^- + C_2H_6$		[1]
Vibrational Excitation	$e^- + C_2H_6$	$\rightarrow$	$e^- + C_2H_6^*$	(3)	[1]
Ionization	$e^- + C_2H_6$	$\rightarrow$	$2e^- + C_2H_6^+$		[2]
Dissociative Ionization	$e^- + C_2H_6$	$\rightarrow$	$2e^- + C_2H_5^+ + H$		[2]
	$e^- + C_2H_6$	$\rightarrow$	$2e^- + C_2H_4^+ + H_2$		[2]

	$e^- + C_2H_6 \rightarrow 2e^- + C_2H_3^+ + H_2 + H$		2
	$e^- + C_2H_6 \rightarrow 2e^- + C_2H_2^+ + 2H_2$		2
	$e^- + C_2H_6 \rightarrow 2e^- + CH_3^+ + CH_3$		2
Dissociation	$e^- + C_2H_6 \rightarrow e^- + C_2H_5 + H$		5, 6
	$e^- + C_2H_6 \rightarrow e^- + C_2H_4 + H_2$		5, 6
Ionization	$e^- + C_2H_5 \rightarrow 2e^- + C_2H_5^+$		2
Dissociative Ionization	$e^- + C_2H_5 \rightarrow 2e^- + C_2H_4^+ + H$		2
	$e^- + C_2H_5 \rightarrow 2e^- + C_2H_3^+ + H_2$		2
	$e^- + C_2H_5 \rightarrow 2e^- + C_2H_2^+ + H_2 + H$		2
Dissociation	$e^- + C_2H_5 \rightarrow e^- + C_2H_4 + H$		5, 6
	$e^- + C_2H_5 \rightarrow e^- + C_2H_3 + H_2$		5, 6
Momentum Transfer	$e^- + C_2H_4 \rightarrow e^- + C_2H_4$		1
Vibrational Excitation	$e^- + C_2H_4 \rightarrow e^- + C_2H_4^*$	(2)	1
Ionization	$e^- + C_2H_4 \rightarrow 2e^- + C_2H_4^+$		2
Dissociative Ionization	$e^- + C_2H_4 \rightarrow 2e^- + C_2H_3^+ + H$		2
	$e^- + C_2H_4 \rightarrow 2e^- + C_2H_2^+ + H_2$		2
Dissociation	$e^- + C_2H_4 \rightarrow e^- + C_2H_3 + H$		5, 6
	$e^- + C_2H_4 \rightarrow e^- + C_2H_2 + H_2$		5, 6
Ionization	$e^- + C_2H_3 \rightarrow 2e^- + C_2H_3^+$		2
Dissociative Ionization	$e^- + C_2H_3 \rightarrow 2e^- + C_2H_2^+ + H$		2
Dissociation	$e^- + C_2H_3 \rightarrow e^- + C_2H_2 + H$		5, 6
	$e^- + C_2H_3 \rightarrow e^- + C_2H + H_2$		5, 6
Momentum Transfer	$e^- + C_2H_2 \rightarrow e^- + C_2H_2$		1
Vibrational Excitation	$e^- + C_2H_2 \rightarrow e^- + C_2H_2^*$	(3)	1
Ionization	$e^- + C_2H_2 \rightarrow 2e^- + C_2H_2^+$		2
Dissociation	$e^- + C_2H_2 \rightarrow e^- + C_2H + H$		5, 6
Dissociation	$e^- + C_2H \rightarrow e^- + C + CH$		5, 6

Momentum Transfer	e^-	+	C_3H_8	→	e^-	+	C_3H_8				1
Vibrational Excitation	e^-	+	C_3H_8	→	e^-	+	$C_3H_8^*$			(2)	1
Dissociative Ionization	e^-	+	C_3H_8	→	$2e^-$	+	$C_2H_5^+$	+	CH_3		2
	e^-	+	C_3H_8	→	$2e^-$	+	$C_2H_4^+$	+	CH_4		2
Dissociation	e^-	+	C_3H_8	→	e^-	+	C_3H_7	+	H		5, 6
	e^-	+	C_3H_8	→	e^-	+	C_3H_6	+	H_2		5, 6
	e^-	+	C_3H_8	→	e^-	+	C_2H_4	+	CH_4		5, 6
Dissociative Ionization	e^-	+	C_3H_7	→	$2e^-$	+	$C_2H_5^+$	+	CH_2		5, 6
	e^-	+	C_3H_7	→	$2e^-$	+	$C_2H_4^+$	+	CH_3		5, 6
	e^-	+	C_3H_7	→	$2e^-$	+	$C_2H_3^+$	+	CH_4		5, 6
	e^-	+	C_3H_7	→	$2e^-$	+	CH_3^+	+	C_2H_4		5, 6
Dissociation	e^-	+	C_3H_7	→	e^-	+	C_3H_6	+	H		5, 6
	e^-	+	C_3H_7	→	e^-	+	C_2H_4	+	CH_3		5, 6
	e^-	+	C_3H_7	→	e^-	+	C_2H_3	+	CH_4		5, 6
Dissociative Ionization	e^-	+	C_3H_6	→	$2e^-$	+	$C_2H_5^+$	+	CH		5, 6
	e^-	+	C_3H_6	→	$2e^-$	+	$C_2H_4^+$	+	CH_2		5, 6
	e^-	+	C_3H_6	→	$2e^-$	+	$C_2H_3^+$	+	CH_3		5, 6
	e^-	+	C_3H_6	→	$2e^-$	+	$C_2H_2^+$	+	CH_4		5, 6
	e^-	+	C_3H_6	→	$2e^-$	+	CH_3^+	+	C_2H_3		5, 6
Dissociation	e^-	+	C_3H_6	→	e^-	+	C_2H_2	+	CH_4		5, 6
Momentum Transfer	e^-	+	H_2	→	e^-	+	H_2				7
Vibrational Excitation	e^-	+	H_2	→	e^-	+	H_2^*			(3)	8
Dissociation	e^-	+	H_2	→	e^-	+	$2H$				9
Momentum Transfer	e^-	+	O_2	→	e^-	+	O_2				10
Ionization	e^-	+	O_2	→	$2e^-$	+	O_2^+				11
Dissociative Attachment	e^-	+	O_2	→	O^-	+	O				10
Dissociation	e^-	+	O_2	→	e^-	+	$2O$			(2)	10

Momentum Transfer	$e^- + O \rightarrow e^- + O$		12
Electronic Excitation	$e^- + O \rightarrow e^- + O^*$	**(2)**	13
Attachment	$e^- + O + O_2 \rightarrow O^- + O_2$		10
Momentum Transfer	$e^- + CO_2 \rightarrow e^- + CO_2$		14
Vibrational Excitation	$e^- + CO_2 \rightarrow e^- + CO_2^*$	**(3)**	14
Electronic Excitation	$e^- + CO_2 \rightarrow e^- + CO_2^*$	**(2)**	15
Ionization	$e^- + CO_2 \rightarrow 2e^- + CO_2^+$		14
Dissociative Attachment	$e^- + CO_2 \rightarrow O^- + CO$		14
Dissociation	$e^- + CO_2 \rightarrow e^- + CO + O$		14
Momentum Transfer	$e^- + CO \rightarrow e^- + CO$		8
Vibrational Excitation	$e^- + CO \rightarrow e^- + CO^*$	**(1)**	8
Electronic Excitation	$e^- + CO \rightarrow e^- + CO^*$	**(5)**	15
Dissociative Attachment	$e^- + CO \rightarrow O^- + C$		16
Dissociation	$e^- + CO \rightarrow e^- + C + O$		17
Momentum Transfer	$e^- + H_2O \rightarrow e^- + H_2O$		18
Vibrational Excitation	$e^- + H_2O \rightarrow e^- + H_2O^*$	**(2)**	18
Dissociative Attachment	$e^- + H_2O \rightarrow O^- + H_2$		18
	$e^- + H_2O \rightarrow OH^- + H$		18
Dissociation	$e^- + H_2O \rightarrow e^- + OH + H$		18
	$e^- + H_2O \rightarrow e^- + O + H_2$		18
Dissociation	$e^- + OH \rightarrow e^- + O + H$		19

Table A I-2. Electron-ion recombination reactions included in the model, as well as the corresponding rate coefficients for 300 K and the references where these data were adopted from.

e^-	+	CH_5^+	→	CH_3	+	2H			2.57 x 10^{-07}	$cm^3\ s^{-1}$	3, 20
e^-	+	CH_5^+	→	CH_2	+	H_2	+	H	6.10 x 10^{-08}	$cm^3\ s^{-1}$	3, 20
e^-	+	CH_4^+	→	CH_3	+	H			1.18 x 10^{-08}	$cm^3\ s^{-1}$	3, 20
e^-	+	CH_4^+	→	CH_2	+	2H			2.42 x 10^{-08}	$cm^3\ s^{-1}$	3, 20
e^-	+	CH_4^+	→	CH	+	H_2	+	H	1.41 x 10^{-08}	$cm^3\ s^{-1}$	3, 20
e^-	+	CH_3^+	→	CH_2	+	H			2.25 x 10^{-08}	$cm^3\ s^{-1}$	3, 20
e^-	+	CH_3^+	→	CH	+	H_2			7.88 x 10^{-09}	$cm^3\ s^{-1}$	3, 20
e^-	+	CH_3^+	→	CH	+	2H			9.00 x 10^{-09}	$cm^3\ s^{-1}$	3, 20
e^-	+	CH_3^+	→	C	+	H_2	+	H	1.69 x 10^{-08}	$cm^3\ s^{-1}$	3, 20
e^-	+	CH_2^+	→	CH	+	H			1.00 x 10^{-08}	$cm^3\ s^{-1}$	3, 20
e^-	+	CH_2^+	→	C	+	H_2			4.82 x 10^{-09}	$cm^3\ s^{-1}$	3, 20
e^-	+	CH_2^+	→	C	+	2H			2.53 x 10^{-08}	$cm^3\ s^{-1}$	3, 20
e^-	+	CH^+	→	C	+	H			3.23 x 10^{-08}	$cm^3\ s^{-1}$	3, 20
e^-	+	$C_2H_6^+$	→	C_2H_5	+	H			2.19 x 10^{-08}	$cm^3\ s^{-1}$	6
e^-	+	$C_2H_6^+$	→	C_2H_4	+	2H			3.36 x 10^{-08}	$cm^3\ s^{-1}$	6
e^-	+	$C_2H_5^+$	→	C_2H_4	+	H			7.70 x 10^{-09}	$cm^3\ s^{-1}$	6
e^-	+	$C_2H_5^+$	→	C_2H_3	+	2H			1.92 x 10^{-08}	$cm^3\ s^{-1}$	6
e^-	+	$C_2H_5^+$	→	C_2H_2	+	H_2	+	H	1.9 x 10^{-08}	$cm^3\ s^{-1}$	6
e^-	+	$C_2H_5^+$	→	C_2H_2	+	3H			8.98 x 10^{-09}	$cm^3\ s^{-1}$	6
e^-	+	$C_2H_5^+$	→	CH_3	+	CH_2			9.62 x 10^{-09}	$cm^3\ s^{-1}$	6
e^-	+	$C_2H_4^+$	→	C_2H_3	+	H			8.29 x 10^{-09}	$cm^3\ s^{-1}$	6
e^-	+	$C_2H_4^+$	→	C_2H_2	+	2H			3.43 x 10^{-08}	$cm^3\ s^{-1}$	6

e^-	+	$C_2H_4^+$	→	C_2H	+	H_2	+	H	5.53×10^{-09}	$cm^3\ s^{-1}$	6
e^-	+	$C_2H_3^+$	→	C_2H_2	+	H			1.34×10^{-08}	$cm^3\ s^{-1}$	6
e^-	+	$C_2H_3^+$	→	C_2H	+	2H			2.74×10^{-08}	$cm^3\ s^{-1}$	6
e^-	+	$C_2H_2^+$	→	C_2H	+	H			1.87×10^{-08}	$cm^3\ s^{-1}$	6
e^-	+	$C_2H_2^+$	→	2CH					4.87×10^{-09}	$cm^3\ s^{-1}$	6
e^-	+	O_2^+	→	O	+	O			1.94×10^{-20}	$cm^3\ s^{-1}$	21
e^-	+	$O_2^+ + O_2$	→	O_2	+	O_2			1.00×10^{-26}	$cm^3\ s^{-1}$	21
e^-	+	CO_2^+	→	CO	+	O			2.71×10^{-07}	$cm^3\ s^{-1}$	20
e^-	+	H_3O^+	→	H_2O	+	H			2.45×10^{-08}	$cm^3\ s^{-1}$	20
e^-	+	H_3O^+	→	OH	+	H_2			6.58×10^{-09}	$cm^3\ s^{-1}$	20
e^-	+	H_3O^+	→	OH	+	2H			4.02×10^{-09}	$cm^3\ s^{-1}$	20

Table A I-3. Neutral-neutral reactions included in the model, as well as the corresponding rate coefficients for 300 K and the references where these data were adopted from. Note a means that this value is an estimated value; note b means that the rate coefficient is adjusted in the model for a three-body collision by dividing by 2.446 x 10^{19} cm^{-3}, i.e., the density of the background gas.

CH_4	+ CH_2		→	CH_3	+ CH_3	3.01 x 10^{-19}	$cm^3\ s^{-1}$	22
CH_4	+ CH		→	C_2H_4	+ H	9.74 x 10^{-11}	$cm^3\ s^{-1}$	23
CH_4	+ C_2H_5		→	C_2H_6	+ CH_3	1.83 x 10^{-24}	$cm^3\ s^{-1}$	22
CH_4	+ C_2H_3		→	C_2H_4	+ CH_3	2.28 x 10^{-18}	$cm^3\ s^{-1}$	22
CH_4	+ C_2H		→	C_2H_2	+ CH_3	1.31 x 10^{-12}	$cm^3\ s^{-1}$	22
CH_4	+ C_3H_7		→	C_3H_8	+ CH_3	4.38 x 10^{-24}	$cm^3\ s^{-1}$	24
CH_4	+ H		→	CH_3	+ H_2	8.43 x 10^{-19}	$cm^3\ s^{-1}$	23
CH_3	+ CH_3		→	C_2H_5	+ H	2.71 x 10^{-19}	$cm^3\ s^{-1}$	25
CH_3	+ CH_3	+ M	→	C_2H_6	+ M	1.56 x 10^{-26}	$cm^6\ s^{-1}$	23
CH_3	+ CH_2		→	C_2H_4	+ H	7.01 x 10^{-11}	$cm^3\ s^{-1}$	23
CH_3	+ C_2H_6		→	C_2H_5	+ CH_4	7.21 x 10^{-21}	$cm^3\ s^{-1}$	23
CH_3	+ C_2H_5		→	C_2H_4	+ CH_4	1.91 x 10^{-12}	$cm^3\ s^{-1}$	23
CH_3	+ C_2H_5	+ M	→	C_3H_8	+ M	1.00 x 10^{-28}	$cm^6\ s^{-1}$	a
CH_3	+ C_2H_4		→	C_2H_3	+ CH_4	1.94 x 10^{-21}	$cm^3\ s^{-1}$	22
CH_3	+ C_2H_3		→	C_2H_2	+ CH_4	6.51 x 10^{-13}	$cm^3\ s^{-1}$	22
CH_3	+ C_2H_3	+ M	→	C_3H_6	+ M	1.20 x 10^{-10}	$cm^3\ s^{-1}$	26
						4.91 x 10^{-30}	$cm^6\ s^{-1}$	b
CH_3	+ C_2H_2		→	CH_4	+ C_2H	7.65 x 10^{-26}	$cm^3\ s^{-1}$	22
CH_3	+ C_3H_8		→	C_3H_7	+ CH_4	1.02 x 10^{-20}	$cm^3\ s^{-1}$	24
CH_3	+ C_3H_7		→	C_3H_6	+ CH_4	3.07 x 10^{-12}	$cm^3\ s^{-1}$	24
CH_3	+ H_2		→	CH_4	+ H	9.9 x 10^{-21}	$cm^3\ s^{-1}$	23
CH_3	+ H		→	CH_2	+ H_2	9.96 x 10^{-22}	$cm^3\ s^{-1}$	23

CH_3	+	H	+ M	→	CH_4	+	M	2.97×10^{-28}	$cm^6\ s^{-1}$	23
CH_2	+	CH_2		→	C_2H_2	+	2H	5.27×10^{-11}	$cm^3\ s^{-1}$	23
CH_2	+	C_2H_5		→	C_2H_4	+	CH_3	3.01×10^{-11}	$cm^3\ s^{-1}$	22
CH_2	+	C_2H_3		→	C_2H_2	+	CH_3	3.01×10^{-11}	$cm^3\ s^{-1}$	22
CH_2	+	C_2H		→	C_2H_2	+	CH	3.01×10^{-11}	$cm^3\ s^{-1}$	22
CH_2	+	C_3H_8		→	C_3H_7	+	CH_3	1.02×10^{-20}	$cm^3\ s^{-1}$	24
CH_2	+	C_3H_7		→	C_2H_4	+	C_2H_5	3.01×10^{-11}	$cm^3\ s^{-1}$	24
CH_2	+	C_3H_7		→	C_3H_6	+	CH_3	3.01×10^{-12}	$cm^3\ s^{-1}$	24
CH_2	+	H_2		→	CH_3	+	H	5.00×10^{-15}	$cm^3\ s^{-1}$	22
CH_2	+	H		→	CH	+	H_2	2.01×10^{-10}	$cm^3\ s^{-1}$	23
CH	+	C_2H_6	+ M	→	C_3H_7	+	M	2.78×10^{-10}	$cm^3\ s^{-1}$	23
								1.14×10^{-29}	$cm^6\ s^{-1}$	b
CH	+	H_2		→	CH_2	+	H	6.80×10^{-13}	$cm^3\ s^{-1}$	23
CH	+	H		→	C	+	H_2	1.00×10^{-10}	$cm^3\ s^{-1}$	27
C	+	H_2		→	CH	+	H	1.50×10^{-10}	$cm^3\ s^{-1}$	28
C_2H_6	+	C_2H_3		→	C_2H_5	+	C_2H_4	3.39×10^{-21}	$cm^3\ s^{-1}$	22
C_2H_6	+	C_2H		→	C_2H_2	+	C_2H_5	5.99×10^{-12}	$cm^3\ s^{-1}$	22
C_2H_6	+	C_3H_7		→	C_3H_8	+	C_2H_5	3.16×10^{-22}	$cm^3\ s^{-1}$	24
C_2H_6	+	H		→	C_2H_5	+	H_2	4.96×10^{-17}	$cm^3\ s^{-1}$	23
C_2H_5	+	C_2H_5		→	C_2H_6	+	C_2H_4	2.41×10^{-12}	$cm^3\ s^{-1}$	23
C_2H_5	+	C_2H		→	C_2H_4	+	C_2H_2	3.01×10^{-12}	$cm^3\ s^{-1}$	22
C_2H_5	+	C_3H_8		→	C_2H_6	+	C_3H_7	3.62×10^{-22}	$cm^3\ s^{-1}$	24
C_2H_5	+	C_3H_7		→	C_3H_8	+	C_2H_4	1.91×10^{-12}	$cm^3\ s^{-1}$	24
C_2H_5	+	C_3H_7		→	C_3H_6	+	C_2H_6	2.41×10^{-12}	$cm^3\ s^{-1}$	24
C_2H_5	+	H_2		→	C_2H_6	+	H	2.97×10^{-21}	$cm^3\ s^{-1}$	22
C_2H_5	+	H		→	CH_3	+	CH_3	5.99×10^{-11}	$cm^3\ s^{-1}$	23
C_2H_5	+	H		→	C_2H_4	+	H_2	3.01×10^{-12}	$cm^3\ s^{-1}$	22

C_2H_5	+ H	+ M	→	C_2H_6	+ M	2.25×10^{-10}	$cm^3\ s^{-1}$	29
						9.20×10^{-30}	$cm^6\ s^{-1}$	b
C_2H_4	+ C_2H		→	C_2H_2	+ C_2H_3	1.40×10^{-10}	$cm^3\ s^{-1}$	26
C_2H_4	+ H		→	C_2H_3	+ H_2	4.92×10^{-21}	$cm^3\ s^{-1}$	22
C_2H_4	+ H	+ M	→	C_2H_5	+ M	3.66×10^{-30}	$cm^6\ s^{-1}$	23
C_2H_3	+ C_2H_3		→	C_2H_4	+ C_2H_2	1.9×10^{-12}	$cm^3\ s^{-1}$	22
C_2H_3	+ C_2H		→	C_2H_2	+ C_2H_2	1.9×10^{-12}	$cm^3\ s^{-1}$	22
C_2H_3	+ C_3H_8		→	C_2H_4	+ C_3H_7	3.40×10^{-21}	$cm^3\ s^{-1}$	24
C_2H_3	+ C_3H_7		→	C_3H_8	+ C_2H_2	2.01×10^{-12}	$cm^3\ s^{-1}$	24
C_2H_3	+ C_3H_7		→	C_3H_6	+ C_2H_4	2.01×10^{-12}	$cm^3\ s^{-1}$	24
C_2H_3	+ H_2		→	C_2H_4	+ H	9.78×10^{-20}	$cm^3\ s^{-1}$	22
C_2H_3	+ H		→	C_2H_2	+ H_2	2.01×10^{-11}	$cm^3\ s^{-1}$	23
C_2H_3	+ H	+ M	→	C_2H_4	+ M	2.02×10^{-10}	$cm^3\ s^{-1}$	29
						8.26×10^{-30}	$cm^6\ s^{-1}$	b
C_2H_2	+ C_2H		→	C_4H_2	+ H	1.50×10^{-10}	$cm^3\ s^{-1}$	30
C_2H_2	+ H		→	C_2H	+ H_2	6.12×10^{-27}	$cm^3\ s^{-1}$	22
C_2H_2	+ H	+ M	→	C_2H_3	+ M	2.81×10^{-31}	$cm^6\ s^{-1}$	23
C_2H	+ C_3H_8		→	C_2H_2	+ C_3H_7	5.99×10^{-12}	$cm^3\ s^{-1}$	24
C_2H	+ C_3H_7		→	C_3H_6	+ C_2H_2	1.00×10^{-11}	$cm^3\ s^{-1}$	24
C_2H	+ H_2		→	C_2H_2	+ H	1.52×10^{-13}	$cm^3\ s^{-1}$	22
C_2H	+ H	+ M	→	C_2H_2	+ M	2.31×10^{-10}	$cm^3\ s^{-1}$	29
						9.44×10^{-30}	$cm^6\ s^{-1}$	b
C_3H_8	+ H		→	C_3H_7	+ H_2	5.15×10^{-17}	$cm^3\ s^{-1}$	24
C_3H_7	+ C_3H_7		→	C_3H_6	+ C_3H_8	2.81×10^{-12}	$cm^3\ s^{-1}$	24
C_3H_7	+ H_2		→	C_3H_8	+ H	7.12×10^{-21}	$cm^3\ s^{-1}$	24
C_3H_7	+ H		→	C_3H_6	+ H_2	3.01×10^{-12}	$cm^3\ s^{-1}$	24
C_3H_7	+ H	+ M	→	C_3H_8	+ M	9.68×10^{-11}	$cm^3\ s^{-1}$	29

							3.96×10^{-30}	$cm^6\ s^{-1}$	b
C_3H_6	+ H	+ M	→	C_3H_7	+ M		9.26×10^{-14}	$cm^3\ s^{-1}$	31
							3.79×10^{-33}	$cm^6\ s^{-1}$	b
H	+ H	+ M	→	H_2	+ M		6.00×10^{-33}	$cm^6\ s^{-1}$	23
O	+ O	+ O	→	O_2	+ O		5.09×10^{-33}	$cm^6\ s^{-1}$	32
O	+ O	+ M	→	O_2	+ M		7.19×10^{-33}	$cm^6\ s^{-1}$	32
CH4	+ O		→	CH_3	+ OH		5.54×10^{-18}	$cm^3\ s^{-1}$	23
CH3	+ O		→	CH_2O	+ H		1.12×10^{-10}	$cm^3\ s^{-1}$	32
CH3	+ O		→	CO	+ H_2	+ H	2.80×10^{-11}	$cm^3\ s^{-1}$	33
CH_2	+ O		→	CO	+ H_2		5.53×10^{-11}	$cm^3\ s^{-1}$	33
CH_2	+ O		→	CO	+ 2H		8.29×10^{-11}	$cm^3\ s^{-1}$	33
CH_2	+ O_2		→	CO_2	+ H_2		1.42×10^{-12}	$cm^3\ s^{-1}$	23, 34
CH_2	+ O_2		→	CO	+ H_2O		1.42×10^{-12}	$cm^3\ s^{-1}$	23, 34
CH_2	+ O_2		→	CH_2O	+ O		5.39×10^{-13}	$cm^3\ s^{-1}$	23, 34
CH	+ O		→	CO	+ H		6.9×10^{-11}	$cm^3\ s^{-1}$	23
CH	+ O_2		→	CO_2	+ H		1.20×10^{-11}	$cm^3\ s^{-1}$	33
CH	+ O_2		→	CO	+ OH		8.00×10^{-12}	$cm^3\ s^{-1}$	33
CH	+ O_2		→	CHO	+ O		8.00×10^{-12}	$cm^3\ s^{-1}$	33
CH	+ O_2		→	CO	+ H	+ O	1.20×10^{-11}	$cm^3\ s^{-1}$	33
C	+ O_2		→	CO	+ O		2.45×10^{-13}	$cm^3\ s^{-1}$	35
C_2H_6	+ O		→	C_2H_5	+ OH		5.11×10^{-16}	$cm^3\ s^{-1}$	23
C_2H_5	+ O		→	CH_3CHO	+ H		8.80×10^{-11}	$cm^3\ s^{-1}$	33
C_2H_5	+ O		→	CH_2O	+ CH_3		6.9×10^{-11}	$cm^3\ s^{-1}$	33

C_2H_5	+	O			→	C_2H_4	+	OH	4.40×10^{-11}	$cm^3\ s^{-1}$	33
C_2H_5	+	O_2			→	C_2H_4	+	HO_2	3.80×10^{-15}	$cm^3\ s^{-1}$	36
C_2H_5	+	O_2	+	CH_4	→	$C_2H_5O_2$	+	CH_4	5.75×10^{-29}	$cm^6\ s^{-1}$	36
C_2H_4	+	O			→	CH_2CHO	+	H	2.63×10^{-13}	$cm^3\ s^{-1}$	33
C_2H_4	+	O			→	CHO	+	CH_3	4.51×10^{-13}	$cm^3\ s^{-1}$	33
C_2H_3	+	O			→	C_2H_2	+	OH	1.25×10^{-11}	$cm^3\ s^{-1}$	33
C_2H_3	+	O			→	CO	+	CH_3	1.25×10^{-11}	$cm^3\ s^{-1}$	33
C_2H_3	+	O			→	CHO	+	CH_2	1.25×10^{-11}	$cm^3\ s^{-1}$	33
C_2H_3	+	O			→	CH_2CO	+	H	1.25×10^{-11}	$cm^3\ s^{-1}$	33
C_2H_3	+	O_2			→	CH_2O	+	CHO	9.00×10^{-12}	$cm^3\ s^{-1}$	23
C_2H_2	+	O			→	CH_2	+	CO	6.75×10^{-14}	$cm^3\ s^{-1}$	23
C_2H_2	+	O			→	C_2HO	+	H	6.75×10^{-14}	$cm^3\ s^{-1}$	23
C_2H	+	O			→	CH	+	CO	1.70×10^{-11}	$cm^3\ s^{-1}$	23
C_2H	+	O_2			→	CHO	+	CO	3.00×10^{-11}	$cm^3\ s^{-1}$	23
C_2H	+	O_2			→	C_2HO	+	O	1.00×10^{-12}	$cm^3\ s^{-1}$	22
C_3H_8	+	O			→	C_3H_7	+	OH	2.73×10^{-15}	$cm^3\ s^{-1}$	24
H_2	+	O			→	OH	+	H	9.32×10^{-18}	$cm^3\ s^{-1}$	23
H	+	O	+	CH_4	→	OH	+	CH_4	4.33×10^{-32}	$cm^6\ s^{-1}$	22
H	+	O_2			→	OH	+	O	1.87×10^{-22}	$cm^3\ s^{-1}$	23
H	+	O_2	+	CH_4	→	HO_2	+	CH_4	5.40×10^{-32}	$cm^6\ s^{-1}$	37
CH_4	+	OH			→	CH_3	+	H_2O	6.62×10^{-15}	$cm^3\ s^{-1}$	36
CH_4	+	HO_2			→	CH_3	+	H_2O_2	8.76×10^{-27}	$cm^3\ s^{-1}$	22
CH_4	+	CHO			→	CH_3	+	CH_2O	6.07×10^{-30}	$cm^3\ s^{-1}$	22
CH_4	+	CH_3O			→	CH_3OH	+	CH_3	9.42×10^{-20}	$cm^3\ s^{-1}$	22
CH_3	+	CO	+	CH_4	→	CH_3CO	+	CH_4	4.19×10^{-36}	$cm^6\ s^{-1}$	30
CH_3	+	H_2O			→	CH_4	+	OH	1.82×10^{-25}	$cm^3\ s^{-1}$	22
CH_3	+	OH			→	CH_2	+	H_2O	1.13×10^{-12}	$cm^3\ s^{-1}$	30

CH_3	+	OH		→	CH_2OH	+	H	1.31×10^{-11}	$cm^3\ s^{-1}$	38
CH_3	+	OH		→	CH_3O	+	H	1.9×10^{-10}	$cm^3\ s^{-1}$	38
CH_3	+	OH	+ M	→	CH_3OH	+	M	2.30×10^{-27}	$cm^6\ s^{-1}$	30
CH_3	+	HO_2		→	CH_3O	+	OH	3.00×10^{-11}	$cm^3\ s^{-1}$	23
CH_3	+	HO_2		→	CH_4	+	O_2	5.99×10^{-12}	$cm^3\ s^{-1}$	22
CH_3	+	CH_2O		→	CH_4	+	CHO	6.14×10^{-18}	$cm^3\ s^{-1}$	30
CH_3	+	CHO		→	CH_4	+	CO	2.00×10^{-10}	$cm^3\ s^{-1}$	22
CH_3	+	CH_3O		→	CH_4	+	CH_2O	4.00×10^{-11}	$cm^3\ s^{-1}$	22
CH_3	+	CH_3CHO		→	CH_4	+	CH_3CO	4.95×10^{-18}	$cm^3\ s^{-1}$	23
CH_2	+	CO_2		→	CH_2O	+	CO	3.90×10^{-14}	$cm^3\ s^{-1}$	22
CH_2	+	H_2O		→	CH_3	+	OH	1.9×10^{-16}	$cm^3\ s^{-1}$	22
CH_2	+	OH		→	CH_2O	+	H	3.00×10^{-11}	$cm^3\ s^{-1}$	22
CH_2	+	HO_2		→	CH_2O	+	OH	3.00×10^{-11}	$cm^3\ s^{-1}$	22
CH_2	+	CH_2O		→	CH_3	+	CHO	1.00×10^{-14}	$cm^3\ s^{-1}$	22
CH_2	+	CHO		→	CH_3	+	CO	3.00×10^{-11}	$cm^3\ s^{-1}$	22
CH_2	+	CH_3O		→	CH_3	+	CH_2O	3.00×10^{-11}	$cm^3\ s^{-1}$	22
CH	+	CO_2		→	CHO	+	CO	9.68×10^{-13}	$cm^3\ s^{-1}$	33
CH	+	CO_2		→	$2CO$	+	H	9.68×10^{-13}	$cm^3\ s^{-1}$	33
CH	+	CO	+ M	→	C_2HO	+	M	4.04×10^{-30}	$cm^6\ s^{-1}$	33
C_2H_6	+	OH		→	C_2H_5	+	H_2O	2.46×10^{-13}	$cm^3\ s^{-1}$	36
C_2H_6	+	HO_2		→	C_2H_5	+	H_2O_2	6.36×10^{-24}	$cm^3\ s^{-1}$	22
C_2H_6	+	CHO		→	C_2H_5	+	CH_2O	2.19×10^{-26}	$cm^3\ s^{-1}$	22
C_2H_6	+	CH_3O		→	C_2H_5	+	CH_3OH	2.72×10^{-18}	$cm^3\ s^{-1}$	22
C_2H_5	+	OH		→	C_2H_4	+	H_2O	4.00×10^{-11}	$cm^3\ s^{-1}$	22
C_2H_5	+	HO_2		→	C_2H_6	+	O_2	5.00×10^{-13}	$cm^3\ s^{-1}$	22
C_2H_5	+	HO_2		→	C_2H_4	+	H_2O_2	5.00×10^{-13}	$cm^3\ s^{-1}$	22
C_2H_5	+	CH_2O		→	C_2H_6	+	CHO	4.47×10^{-18}	$cm^3\ s^{-1}$	22

C_2H_5	+	CHO		→	C_2H_6	+	CO	2.00×10^{-10}	$cm^3\ s^{-1}$	22
C_2H_5	+	CH_3O		→	C_2H_6	+	CH_2O	4.00×10^{-11}	$cm^3\ s^{-1}$	22
C_2H_4	+	OH		→	C_2H_3	+	H_2O	1.54×10^{-16}	$cm^3\ s^{-1}$	22
C_2H_4	+	HO_2		→	CH_3CHO	+	OH	1.62×10^{-20}	$cm^3\ s^{-1}$	22
C_2H_3	+	H_2O		→	C_2H_4	+	OH	1.82×10^{-25}	$cm^3\ s^{-1}$	22
C_2H_3	+	OH		→	C_2H_2	+	H_2O	5.00×10^{-11}	$cm^3\ s^{-1}$	22
C_2H_3	+	CH_2O		→	C_2H_4	+	CHO	4.41×10^{-18}	$cm^3\ s^{-1}$	22
C_2H_3	+	CHO		→	C_2H_4	+	CO	1.50×10^{-10}	$cm^3\ s^{-1}$	22
C_2H_3	+	CH_3O		→	C_2H_4	+	CH_2O	4.00×10^{-11}	$cm^3\ s^{-1}$	22
C_2H_2	+	OH		→	C_2H	+	H_2O	1.77×10^{-22}	$cm^3\ s^{-1}$	22
C_2H_2	+	HO_2		→	CH_2CO	+	OH	1.62×10^{-20}	$cm^3\ s^{-1}$	22
C_2H	+	OH		→	CH_2	+	CO	3.00×10^{-11}	$cm^3\ s^{-1}$	22
C_2H	+	OH		→	C_2H_2	+	O	3.00×10^{-11}	$cm^3\ s^{-1}$	22
C_2H	+	HO_2		→	C_2H_2	+	O_2	3.00×10^{-11}	$cm^3\ s^{-1}$	22
C_2H	+	HO_2		→	C_2HO	+	OH	3.00×10^{-11}	$cm^3\ s^{-1}$	22
C_2H	+	CHO		→	C_2H_2	+	CO	1.00×10^{-10}	$cm^3\ s^{-1}$	22
C_2H	+	CH_3O		→	C_2H_2	+	CH_2O	4.00×10^{-11}	$cm^3\ s^{-1}$	22
C_3H_8	+	OH		→	C_3H_7	+	H_2O	3.76×10^{-15}	$cm^3\ s^{-1}$	24
C_3H_8	+	CH_3O		→	C_3H_7	+	CH_3OH	1.42×10^{-17}	$cm^3\ s^{-1}$	24
C_3H_7	+	CH_2O		→	C_3H_8	+	CHO	4.10×10^{-18}	$cm^3\ s^{-1}$	24
C_3H_7	+	CHO		→	C_3H_8	+	CO	1.00×10^{-10}	$cm^3\ s^{-1}$	24
C_3H_7	+	CH_3O		→	C_3H_8	+	CH_2O	4.00×10^{-11}	$cm^3\ s^{-1}$	24
H_2	+	OH		→	H	+	H_2O	7.02×10^{-15}	$cm^3\ s^{-1}$	37
H_2	+	CHO		→	H	+	CH_2O	2.78×10^{-26}	$cm^3\ s^{-1}$	22
H	+	CO_2		→	CO	+	OH	1.40×10^{-29}	$cm^3\ s^{-1}$	22
H	+	CO	+ M	→	CHO	+	M	1.54×10^{-34}	$cm^6\ s^{-1}$	30
H	+	H_2O		→	H_2	+	OH	5.86×10^{-26}	$cm^3\ s^{-1}$	23

H	**+**	**OH**		**→**	**H_2**	**+**	**O**	**1.05×10^{-16}**	**$cm^3\ s^{-1}$**	**22**
H	**+**	**OH**	**+ M**	**→**	**H_2O**	**+**	**M**	**4.33×10^{-30}**	**$cm^6\ s^{-1}$**	**23**
H	**+**	**HO_2**		**→**	**H_2**	**+**	**O_2**	**5.9×10^{-12}**	**$cm^3\ s^{-1}$**	**37**
H	**+**	**HO_2**		**→**	**H_2O**	**+**	**O**	**2.40×10^{-12}**	**$cm^3\ s^{-1}$**	**37**
H	**+**	**HO_2**		**→**	**OH**	**+**	**OH**	**7.20×10^{-11}**	**$cm^3\ s^{-1}$**	**37**
H	**+**	**CH_2O**		**→**	**H_2**	**+**	**CHO**	**5.72×10^{-14}**	**$cm^3\ s^{-1}$**	**30**
H	**+**	**CHO**		**→**	**H_2**	**+**	**CO**	**1.50×10^{-10}**	**$cm^3\ s^{-1}$**	**23**
H	**+**	**CH_3O**		**→**	**H_2**	**+**	**CH_2O**	**2.32×10^{-11}**	**$cm^3\ s^{-1}$**	**33**
H	**+**	**CH_3O**		**→**	**CH_3**	**+**	**OH**	**9.93×10^{-12}**	**$cm^3\ s^{-1}$**	**33**
H	**+**	**CH_3CHO**		**→**	**H_2**	**+**	**CH_3CO**	**8.98×10^{-14}**	**$cm^3\ s^{-1}$**	**23**
H	**+**	**CH_2CO**		**→**	**CH_3**	**+**	**CO**	**1.04×10^{-13}**	**$cm^3\ s^{-1}$**	**23**
H	**+**	**C_2HO**		**→**	**CH_2**	**+**	**CO**	**2.50×10^{-10}**	**$cm^3\ s^{-1}$**	**23**
O	**+**	**CO**	**+ M**	**→**	**CO_2**	**+**	**M**	**1.11×10^{-35}**	**$cm^6\ s^{-1}$**	**22**
O	**+**	**H_2O**		**→**	**OH**	**+**	**OH**	**4.48×10^{-24}**	**$cm^3\ s^{-1}$**	**22**
O	**+**	**OH**		**→**	**H**	**+**	**O_2**	**3.46×10^{-11}**	**$cm^3\ s^{-1}$**	**37**
O	**+**	**HO_2**		**→**	**O_2**	**+**	**OH**	**5.70×10^{-11}**	**$cm^3\ s^{-1}$**	**37**
O	**+**	**CH_2O**		**→**	**OH**	**+**	**CHO**	**1.73×10^{-13}**	**$cm^3\ s^{-1}$**	**23**
O	**+**	**CHO**		**→**	**CO**	**+**	**OH**	**5.00×10^{-11}**	**$cm^3\ s^{-1}$**	**23**
O	**+**	**CHO**		**→**	**H**	**+**	**CO_2**	**5.00×10^{-11}**	**$cm^3\ s^{-1}$**	**23**
O	**+**	**CH_3O**		**→**	**CH_3**	**+**	**O_2**	**2.20×10^{-11}**	**$cm^3\ s^{-1}$**	**23**
O	**+**	**CH_3O**		**→**	**OH**	**+**	**CH_2O**	**3.00×10^{-12}**	**$cm^3\ s^{-1}$**	**23**
O	**+**	**CH_3CHO**		**→**	**OH**	**+**	**CH_3CO**	**4.68×10^{-13}**	**$cm^3\ s^{-1}$**	**23**
O	**+**	**CH_2CO**		**→**	**CH_2**	**+**	**CO_2**	**2.29×10^{-13}**	**$cm^3\ s^{-1}$**	**23, 39**
O	**+**	**CH_2CO**		**→**	**CH_2O**	**+**	**CO**	**7.88×10^{-14}**	**$cm^3\ s^{-1}$**	**23, 39**

O	+	CH_2CO			→	CHO	+	CO	+	H	4.33×10^{-14}	$cm^3\ s^{-1}$	23, 39
O	+	CH_2CO			→	CHO	+	CHO			4.33×10^{-14}	$cm^3\ s^{-1}$	23, 39
O	+	C_2HO			→	CO	+	CO	+	H	1.9×10^{-10}	$cm^3\ s^{-1}$	23
O_2	+	CHO			→	CO	+	HO_2			5.10×10^{-12}	$cm^3\ s^{-1}$	36
O_2	+	CH_3O			→	CH_2O	+	HO_2			1.97×10^{-15}	$cm^3\ s^{-1}$	36
O_2	+	CH_2CHO			→	CH_2O	+	CO	+	OH	3.00×10^{-14}	$cm^3\ s^{-1}$	23,40, 41
O_2	+	C_2HO			→	CO	+	CO	+	OH	6.46×10^{-13}	$cm^3\ s^{-1}$	23
CO	+	OH			→	CO_2	+	H			1.25×10^{-13}	$cm^3\ s^{-1}$	23
CO	+	CH_3O			→	CO_2	+	CH_3			6.56×10^{-20}	$cm^3\ s^{-1}$	22
H_2O	+	CH_3O			→	CH_3OH	+	OH			1.67×10^{-14}	$cm^3\ s^{-1}$	42
OH	+	OH			→	H_2O	+	O			1.47×10^{-12}	$cm^3\ s^{-1}$	37
OH	+	OH	+	M	→	H_2O_2	+	M			6.86×10^{-31}	$cm^6\ s^{-1}$	37
OH	+	HO_2			→	O_2	+	H_2O			1.10×10^{-10}	$cm^3\ s^{-1}$	37
OH	+	CH_2O			→	H_2O	+	CHO			8.47×10^{-12}	$cm^3\ s^{-1}$	36
OH	+	CHO			→	CO	+	H_2O			1.70×10^{-10}	$cm^3\ s^{-1}$	23
OH	+	CH_3O			→	CH_2O	+	H_2O			3.00×10^{-11}	$cm^3\ s^{-1}$	22
OH	+	CH_3CHO			→	CH_3CO	+	H_2O			1.49×10^{-11}	$cm^3\ s^{-1}$	36
OH	+	CH_2CO			→	CO	+	CH_2OH			1.14×10^{-11}	$cm^3\ s^{-1}$	23, 43
HO_2	+	HO_2			→	H_2O_2	+	O_2			1.63×10^{-12}	$cm^3\ s^{-1}$	37
HO_2	+	CH_2O			→	CHO	+	H_2O_2			1.05×10^{-20}	$cm^3\ s^{-1}$	22
HO_2	+	CHO			→	OH	+	H	+	CO_2	5.00×10^{-11}	$cm^3\ s^{-1}$	22

HO_2	+	CH_3O	→	CH_2O	+	H_2O_2	5.00×10^{-13}	$cm^3\ s^{-1}$	22
CH_2O	+	CH_3O	→	CH_3OH	+	CHO	1.14×10^{-15}	$cm^3\ s^{-1}$	22
CHO	+	CHO	→	CH_2O	+	CO	5.00×10^{-11}	$cm^3\ s^{-1}$	23
CHO	+	CH_3O	→	CH_3OH	+	CO	1.50×10^{-10}	$cm^3\ s^{-1}$	22
CH_3O	+	CH_3O	→	CH_2O	+	CH_3OH	1.00×10^{-10}	$cm^3\ s^{-1}$	22
CH_4	+	CH_3CO	→	CH_3CHO	+	CH_3	1.14×10^{-29}	$cm^3\ s^{-1}$	22
CH_4	+	CH_2OH	→	CH_3OH	+	CH_3	2.55×10^{-27}	$cm^3\ s^{-1}$	44
CH_3	+	H_2O_2	→	CH_4	+	HO_2	5.46×10^{-14}	$cm^3\ s^{-1}$	22
CH_3	+	CH_3OH	→	CH_4	+	CH_3O	1.01×10^{-20}	$cm^3\ s^{-1}$	44
CH_3	+	CH_3OH	→	CH_4	+	CH_2OH	2.66×10^{-20}	$cm^3\ s^{-1}$	44
CH_3	+	CH_2OH	→	CH_4	+	CH_2O	4.00×10^{-12}	$cm^3\ s^{-1}$	44
CH_2	+	H_2O_2	→	CH_3	+	HO_2	1.00×10^{-14}	$cm^3\ s^{-1}$	22
CH_2	+	CH_3CO	→	CH_2CO	+	CH_3	3.00×10^{-11}	$cm^3\ s^{-1}$	22
CH_2	+	CH_3OH	→	CH_3O	+	CH_3	1.01×10^{-20}	$cm^3\ s^{-1}$	44
CH_2	+	CH_3OH	→	CH_2OH	+	CH_3	2.66×10^{-20}	$cm^3\ s^{-1}$	44
CH_2	+	CH_2OH	→	CH_2O	+	CH_3	2.00×10^{-12}	$cm^3\ s^{-1}$	44
CH_2	+	CH_2OH	→	C_2H_4	+	OH	4.00×10^{-11}	$cm^3\ s^{-1}$	44
C_2H_5	+	H_2O_2	→	C_2H_6	+	HO_2	2.83×10^{-15}	$cm^3\ s^{-1}$	22
C_2H_5	+	CH_3OH	→	C_2H_6	+	CH_3O	3.50×10^{-22}	$cm^3\ s^{-1}$	44
C_2H_5	+	CH_3OH	→	C_2H_6	+	CH_2OH	9.49×10^{-22}	$cm^3\ s^{-1}$	44
C_2H_5	+	CH_2OH	→	C_2H_6	+	CH_2O	4.00×10^{-12}	$cm^3\ s^{-1}$	44
C_2H_5	+	CH_2OH	→	CH_3OH	+	C_2H_4	4.00×10^{-12}	$cm^3\ s^{-1}$	44
C_2H_3	+	H_2O_2	→	C_2H_4	+	HO_2	5.46×10^{-14}	$cm^3\ s^{-1}$	22
C_2H_3	+	CH_3OH	→	C_2H_4	+	CH_3O	1.01×10^{-20}	$cm^3\ s^{-1}$	44
C_2H_3	+	CH_3OH	→	C_2H_4	+	CH_2OH	2.66×10^{-20}	$cm^3\ s^{-1}$	44
C_2H_3	+	CH_2OH	→	C_2H_4	+	CH_2O	5.00×10^{-11}	$cm^3\ s^{-1}$	44
C_2H_2	+	CH_2OH	→	C_2H_3	+	CH_2O	3.32×10^{-19}	$cm^3\ s^{-1}$	44

C_2H	+	CH_3OH			→	C_2H_2	+	CH_3O	2.00×10^{-12}	$cm^3\ s^{-1}$	44
C_2H	+	CH_3OH			→	C_2H_2	+	CH_2OH	1.00×10^{-11}	$cm^3\ s^{-1}$	44
C_2H	+	CH_2OH			→	C_2H_2	+	CH_2O	5.99×10^{-11}	$cm^3\ s^{-1}$	44
C_3H_7	+	OH			→	C_3H_6	+	H_2O	4.00×10^{-11}	$cm^3\ s^{-1}$	24
C_3H_7	+	H_2O_2			→	C_3H_8	+	HO_2	7.08×10^{-17}	$cm^3\ s^{-1}$	24
C_3H_7	+	CH_3OH			→	C_3H_8	+	CH_3O	3.51×10^{-22}	$cm^3\ s^{-1}$	24
C_3H_7	+	CH_3OH			→	C_3H_8	+	CH_2OH	8.45×10^{-22}	$cm^3\ s^{-1}$	24
C_3H_7	+	CH_2OH			→	C_3H_8	+	CH_2O	1.9×10^{-12}	$cm^3\ s^{-1}$	24
C_3H_7	+	CH_2OH			→	C_3H_6	+	CH_3OH	8.00×10^{-13}	$cm^3\ s^{-1}$	24
H	+	H_2O_2			→	H_2O	+	OH	4.20×10^{-14}	$cm^3\ s^{-1}$	23
H	+	H_2O_2			→	H_2	+	HO_2	5.15×10^{-15}	$cm^3\ s^{-1}$	23
H	+	CH_3OH			→	CH_2OH	+	H_2	1.27×10^{-15}	$cm^3\ s^{-1}$	44
H	+	CH_3OH			→	CH_3O	+	H_2	3.18×10^{-16}	$cm^3\ s^{-1}$	44
H	+	CH_2OH			→	CH_2O	+	H_2	1.00×10^{-11}	$cm^3\ s^{-1}$	44
H	+	CH_2OH			→	CH_3	+	OH	1.9×10^{-10}	$cm^3\ s^{-1}$	44
H	+	CH_2OH	+	M	→	CH_3OH	+	M	2.89×10^{-10}	$cm^3\ s^{-1}$	45
									1.18×10^{-29}	$cm^6\ s^{-1}$	b
O	+	H_2O_2			→	HO_2	+	OH	8.91×10^{-16}	$cm^3\ s^{-1}$	33
O	+	H_2O_2			→	O_2	+	H_2O	8.91×10^{-16}	$cm^3\ s^{-1}$	33
O	+	CH_3CO			→	OH	+	CH_2CO	8.75×10^{-11}	$cm^3\ s^{-1}$	33
O	+	CH_3CO			→	CO_2	+	CH_3	2.63×10^{-10}	$cm^3\ s^{-1}$	33
O	+	CH_3OH			→	OH	+	CH_2OH	1.12×10^{-14}	$cm^3\ s^{-1}$	46
O	+	CH_3OH			→	OH	+	CH_3O	1.68×10^{-15}	$cm^3\ s^{-1}$	46
O	+	CH_2OH			→	CH_2O	+	OH	7.00×10^{-11}	$cm^3\ s^{-1}$	44
O_2	+	CH_2OH			→	CH_2O	+	HO_2	9.70×10^{-12}	$cm^3\ s^{-1}$	36
OH	+	H_2O_2			→	HO_2	+	H_2O	1.70×10^{-12}	$cm^3\ s^{-1}$	37
OH	+	CH_3CO			→	CH_2CO	+	H_2O	2.00×10^{-11}	$cm^3\ s^{-1}$	22

OH	+	CH_3CO	→	CH_3	+	CO	+	OH	5.00×10^{-11}	$cm^3\ s^{-1}$	22
OH	+	CH_3OH	→	H_2O	+	CH_2OH			7.67×10^{-13}	$cm^3\ s^{-1}$	36
OH	+	CH_3OH	→	H_2O	+	CH_3O			1.35×10^{-13}	$cm^3\ s^{-1}$	36
OH	+	CH_2OH	→	CH_2O	+	H_2O			4.00×10^{-11}	$cm^3\ s^{-1}$	44
HO_2	+	CH_3CO	→	CH_3	+	CO_2	+	OH	5.00×10^{-11}	$cm^3\ s^{-1}$	22
HO_2	+	CH_3OH	→	CH_2OH	+	H_2O_2			1.10×10^{-22}	$cm^3\ s^{-1}$	44
HO_2	+	CH_2OH	→	CH_2O	+	H_2O_2			2.00×10^{-11}	$cm^3\ s^{-1}$	44
CH_2O	+	CH_3CO	→	CH_3CHO	+	CHO			1.17×10^{-22}	$cm^3\ s^{-1}$	22
CH_2O	+	CH_2OH	→	CH_3OH	+	CHO			4.22×10^{-18}	$cm^3\ s^{-1}$	44
CHO	+	H_2O_2	→	CH_2O	+	HO_2			1.50×10^{-18}	$cm^3\ s^{-1}$	22
CHO	+	CH_3CO	→	CH_3CHO	+	CO			1.50×10^{-11}	$cm^3\ s^{-1}$	22
CHO	+	CH_3OH	→	CH_2O	+	CH_2OH			6.85×10^{-23}	$cm^3\ s^{-1}$	44
CHO	+	CH_2OH	→	CH_2O	+	CH_2O			3.00×10^{-10}	$cm^3\ s^{-1}$	44
CHO	+	CH_2OH	→	CH_3OH	+	CO			2.00×10^{-10}	$cm^3\ s^{-1}$	44
CH_3O	+	CH_3CO	→	CH_3OH	+	CH_2CO			1.00×10^{-11}	$cm^3\ s^{-1}$	22
CH_3O	+	CH_3OH	→	CH_3OH	+	CH_2OH			5.38×10^{-16}	$cm^3\ s^{-1}$	44
CH_3O	+	CH_2OH	→	CH_2O	+	CH_3OH			4.00×10^{-11}	$cm^3\ s^{-1}$	44
H_2O_2	+	CH_3CO	→	CH_3CHO	+	HO_2			3.05×10^{-19}	$cm^3\ s^{-1}$	22
H_2O_2	+	CH_2OH	→	CH_3OH	+	HO_2			6.56×10^{-17}	$cm^3\ s^{-1}$	44
CH_3CO	+	CH_3OH	→	CH_3CHO	+	CH_2OH			2.22×10^{-22}	$cm^3\ s^{-1}$	44
CH_2OH	+	CH_2OH	→	CH_2O	+	CH_3OH			8.00×10^{-12}	$cm^3\ s^{-1}$	44

Table A I-4. Ion-neutral and ion-ion reactions included in the model, as well as the corresponding rate coefficients and the references where these data were adopted from.

CH_5^+	+	CH_2	→	CH_3^+	+	CH_4			9.9 x 10^{-10}	$cm^3\ s^{-1}$	47
CH_5^+	+	CH	→	CH_2^+	+	CH_4			6.90 x 10^{-10}	$cm^3\ s^{-1}$	47
CH_5^+	+	C	→	CH^+	+	CH_4			1.20 x 10^{-09}	$cm^3\ s^{-1}$	47
CH_5^+	+	C_2H_6	→	$C_2H_5^+$	+	H_2	+	CH_4	2.25 x 10^{-10}	$cm^3\ s^{-1}$	48
CH_5^+	+	C_2H_4	→	$C_2H_5^+$	+	CH_4			1.50 x 10^{-09}	$cm^3\ s^{-1}$	47
CH_5^+	+	C_2H_2	→	$C_2H_3^+$	+	CH_4			1.9 x 10^{-09}	$cm^3\ s^{-1}$	47
CH_5^+	+	C_2H	→	$C_2H_2^+$	+	CH_4			9.00 x 10^{-10}	$cm^3\ s^{-1}$	47
CH_5^+	+	H	→	CH_4^+	+	H_2			1.50 x 10^{-10}	$cm^3\ s^{-1}$	47
CH_5^+	+	O	→	H_3O^+	+	CH_2			2.20 x 10^{-10}	$cm^3\ s^{-1}$	47
CH_5^+	+	H_2O	→	H_3O^+	+	CH_4			3.70 x 10^{-09}	$cm^3\ s^{-1}$	47
CH_4^+	+	CH_4	→	CH_5^+	+	CH_3			1.50 x 10^{-09}	$cm^3\ s^{-1}$	47
CH_4^+	+	C_2H_6	→	$C_2H_4^+$	+	CH_4	+	H_2	1.91 x 10^{-09}	$cm^3\ s^{-1}$	48
CH_4^+	+	C_2H_4	→	$C_2H_5^+$	+	CH_3			4.23 x 10^{-10}	$cm^3\ s^{-1}$	47
CH_4^+	+	C_2H_4	→	$C_2H_4^+$	+	CH_4			1.38 x 10^{-09}	$cm^3\ s^{-1}$	47
CH_4^+	+	C_2H_2	→	$C_2H_3^+$	+	CH_3			1.23 x 10^{-09}	$cm^3\ s^{-1}$	47
CH_4^+	+	C_2H_2	→	$C_2H_2^+$	+	CH_4			1.13 x 10^{-09}	$cm^3\ s^{-1}$	47
CH_4^+	+	H_2	→	CH_5^+	+	H			3.30 x 10^{-11}	$cm^3\ s^{-1}$	47
CH_4^+	+	H	→	CH_3^+	+	H_2			1.00 x 10^{-11}	$cm^3\ s^{-1}$	47
CH_4^+	+	O	→	CH_3^+	+	OH			1.00 x 10^{-09}	$cm^3\ s^{-1}$	47
CH_4^+	+	O_2	→	O_2^+	+	CH_4			3.90 x 10^{-10}	$cm^3\ s^{-1}$	47
CH_4^+	+	H_2O	→	H_3O^+	+	CH_3			2.9 x 10^{-09}	$cm^3\ s^{-1}$	47
CH_3^+	+	CH_4	→	CH_4^+	+	CH_3			1.36 x 10^{-10}	$cm^3\ s^{-1}$	49
CH_3^+	+	CH_4	→	$C_2H_5^+$	+	H_2			1.20 x 10^{-09}	$cm^3\ s^{-1}$	47
CH_3^+	+	CH_2	→	$C_2H_3^+$	+	H_2			9.90 x 10^{-10}	$cm^3\ s^{-1}$	47

CH_3^+	+	CH	→	$C_2H_2^+$	+	H_2			7.10×10^{-10}	$cm^3\ s^{-1}$	47
CH_3^+	+	C_2H_6	→	$C_2H_5^+$	+	CH_4			1.48×10^{-09}	$cm^3\ s^{-1}$	47
CH_3^+	+	C_2H_4	→	$C_2H_3^+$	+	CH_4			3.50×10^{-10}	$cm^3\ s^{-1}$	47
CH_3^+	+	C_2H_3	→	$C_2H_3^+$	+	CH_3			3.00×10^{-10}	$cm^3\ s^{-1}$	47
CH_2^+	+	CH_4	→	CH_3^+	+	CH_3			1.38×10^{-10}	$cm^3\ s^{-1}$	50
CH_2^+	+	CH_4	→	$C_2H_5^+$	+	H			3.9×10^{-10}	$cm^3\ s^{-1}$	47
CH_2^+	+	CH_4	→	$C_2H_4^+$	+	H_2			8.40×10^{-10}	$cm^3\ s^{-1}$	47
CH_2^+	+	CH_4	→	$C_2H_3^+$	+	H_2	+	H	2.31×10^{-10}	$cm^3\ s^{-1}$	50
CH_2^+	+	CH_4	→	$C_2H_2^+$	+	$2H_2$			3.97×10^{-10}	$cm^3\ s^{-1}$	50
CH_2^+	+	H_2	→	CH_3^+	+	H			1.9×10^{-09}	$cm^3\ s^{-1}$	47
CH^+	+	CH_4	→	$C_2H_4^+$	+	H			6.50×10^{-11}	$cm^3\ s^{-1}$	47
CH^+	+	CH_4	→	$C_2H_3^+$	+	H_2			1.09×10^{-09}	$cm^3\ s^{-1}$	47
CH^+	+	CH_4	→	$C_2H_2^+$	+	H_2	+	H	1.43×10^{-10}	$cm^3\ s^{-1}$	47
CH^+	+	H_2	→	CH_2^+	+	H			1.20×10^{-09}	$cm^3\ s^{-1}$	47
CH^+	+	H_2O	→	H_3O^+	+	C			5.80×10^{-10}	$cm^3\ s^{-1}$	47
$C_2H_6^+$	+	C_2H_4	→	$C_2H_4^+$	+	C_2H_6			1.15×10^{-09}	$cm^3\ s^{-1}$	47
$C_2H_6^+$	+	C_2H_2	→	$C_2H_5^+$	+	C_2H_3			2.47×10^{-10}	$cm^3\ s^{-1}$	47
$C_2H_6^+$	+	H	→	$C_2H_5^+$	+	H_2			1.00×10^{-10}	$cm^3\ s^{-1}$	47
$C_2H_6^+$	+	H_2O	→	H_3O^+	+	C_2H_5			2.95×10^{-09}	$cm^3\ s^{-1}$	47
$C_2H_5^+$	+	H	→	$C_2H_4^+$	+	H_2			1.00×10^{-11}	$cm^3\ s^{-1}$	47
$C_2H_5^+$	+	H_2O	→	H_3O^+	+	C_2H_4			1.40×10^{-09}	$cm^3\ s^{-1}$	47
$C_2H_4^+$	+	C_2H_3	→	$C_2H_5^+$	+	C_2H_2			5.00×10^{-10}	$cm^3\ s^{-1}$	47
$C_2H_4^+$	+	C_2H_3	→	$C_2H_3^+$	+	C_2H_4			5.00×10^{-10}	$cm^3\ s^{-1}$	47
$C_2H_4^+$	+	H	→	$C_2H_3^+$	+	H_2			3.00×10^{-10}	$cm^3\ s^{-1}$	47
$C_2H_4^+$	+	O	→	CH_3^+	+	CHO			1.08×10^{-10}	$cm^3\ s^{-1}$	47
$C_2H_3^+$	+	C_2H_6	→	$C_2H_5^+$	+	C_2H_4			2.91×10^{-10}	$cm^3\ s^{-1}$	47
$C_2H_3^+$	+	C_2H_4	→	$C_2H_5^+$	+	C_2H_2			8.90×10^{-10}	$cm^3\ s^{-1}$	47

$C_2H_3^+$	+	C_2H_3	→	$C_2H_5^+$	+	C_2H			5.00×10^{-10}	$cm^3\ s^{-1}$	47
$C_2H_3^+$	+	C_2H	→	$C_2H_2^+$	+	C_2H_2			3.30×10^{-10}	$cm^3\ s^{-1}$	47
$C_2H_3^+$	+	H	→	$C_2H_2^+$	+	H_2			6.80×10^{-11}	$cm^3\ s^{-1}$	47
$C_2H_3^+$	+	H_2O	→	H_3O^+	+	C_2H_2			1.11×10^{-09}	$cm^3\ s^{-1}$	47
$C_2H_2^+$	+	CH_4	→	$C_2H_3^+$	+	CH_3			4.10×10^{-09}	$cm^3\ s^{-1}$	50
$C_2H_2^+$	+	C_2H_6	→	$C_2H_5^+$	+	C_2H_3			1.31×10^{-10}	$cm^3\ s^{-1}$	48
$C_2H_2^+$	+	C_2H_6	→	$C_2H_4^+$	+	C_2H_4			2.48×10^{-10}	$cm^3\ s^{-1}$	47
$C_2H_2^+$	+	C_2H_4	→	$C_2H_4^+$	+	C_2H_2			4.14×10^{-10}	$cm^3\ s^{-1}$	47
$C_2H_2^+$	+	C_2H_3	→	$C_2H_3^+$	+	C_2H_2			3.30×10^{-10}	$cm^3\ s^{-1}$	47
$C_2H_2^+$	+	H_2	→	$C_2H_3^+$	+	H			1.00×10^{-11}	$cm^3\ s^{-1}$	47
$C_2H_2^+$	+	H_2O	→	H_3O^+	+	C_2H			2.20×10^{-10}	$cm^3\ s^{-1}$	47
O_2^+	+	CH_2	→	CH_2^+	+	O_2			4.30×10^{-10}	$cm^3\ s^{-1}$	47
O_2^+	+	CH	→	CH^+	+	O_2			3.10×10^{-10}	$cm^3\ s^{-1}$	47
O_2^+	+	C_2H_4	→	$C_2H_4^+$	+	O_2			6.80×10^{-10}	$cm^3\ s^{-1}$	47
O_2^+	+	C_2H_2	→	$C_2H_2^+$	+	O_2			1.11×10^{-09}	$cm^3\ s^{-1}$	47
O_2^+	+	O^-	→	O	+	O_2			2.9×10^{-08}	$cm^3\ s^{-1}$	51
O_2^+	+	O^-	→	O	+	O	+	O	2.9×10^{-08}	$cm^3\ s^{-1}$	51
O^-	+	CH_4	→	OH^-	+	CH_3			1.00×10^{-10}	$cm^3\ s^{-1}$	47
O^-	+	C	→	CO	+	e^-			5.00×10^{-10}	$cm^3\ s^{-1}$	47
O^-	+	H_2	→	H_2O	+	e^-			7.00×10^{-10}	$cm^3\ s^{-1}$	47
O^-	+	H_2	→	OH^-	+	H			3.00×10^{-11}	$cm^3\ s^{-1}$	47
O^-	+	H	→	OH	+	e^-			5.00×10^{-10}	$cm^3\ s^{-1}$	47
O^-	+	O	→	O_2	+	e^-			2.30×10^{-10}	$cm^3\ s^{-1}$	51
O^-	+	O_2	→	O	+	O_2	+	e^-	$k = f(E/N)$		10
O^-	+	CO	→	CO_2	+	e^-			6.50×10^{-10}	$cm^3\ s^{-1}$	47
CO_2^+	+	CH_4	→	CH_4^+	+	CO_2			5.50×10^{-10}	$cm^3\ s^{-1}$	47
CO_2^+	+	C_2H_4	→	$C_2H_4^+$	+	CO_2			1.50×10^{-10}	$cm^3\ s^{-1}$	47

CO_2^+	+	C_2H_2	→	$C_2H_2^+$	+	CO_2	7.30×10^{-10}	$cm^3\ s^{-1}$	[47]
CO_2^+	+	O_2	→	O_2^+	+	CO_2	5.30×10^{-11}	$cm^3\ s^{-1}$	[47]
CO_2^+	+	O	→	O_2^+	+	CO	1.64×10^{-10}	$cm^3\ s^{-1}$	[47]
H_3O^+	+	CH_2	→	CH_3^+	+	H_2O	9.40×10^{-10}	$cm^3\ s^{-1}$	[47]
H_3O^+	+	CH	→	CH_2^+	+	H_2O	6.80×10^{-10}	$cm^3\ s^{-1}$	[47]
H_3O^+	+	C_2H_3	→	$C_2H_4^+$	+	H_2O	2.00×10^{-09}	$cm^3\ s^{-1}$	[47]
OH^-	+	CH_3	→	CH_3OH	+	e^-	1.00×10^{-09}	$cm^3\ s^{-1}$	[47]
OH^-	+	CH	→	CH_2O	+	e^-	5.00×10^{-10}	$cm^3\ s^{-1}$	[47]
OH^-	+	C	→	CHO	+	e^-	5.00×10^{-10}	$cm^3\ s^{-1}$	[47]
OH^-	+	H	→	H_2O	+	e^-	1.40×10^{-09}	$cm^3\ s^{-1}$	[47]

2. References

(1) Janev, R. K. *Atomic and Molecular Processes in Fusion Edge Plasmas*; Plenum Press: New York, 1995.

(2) Janev, R. K.; Wang, J. G.; Murakami, I.; Kato, T. *National Institute for Fusion Science (NIFS) of Japan, Cross Sections and Rate Coefficients for Electron-Impact Ionization of Hydrocarbon Molecules*; Toki: Gifu, 2001.

(3) Janev, R. K.; Reiter, D. Collision Processes of CHy and CHy+ Hydrocarbons with Plasma Electrons and Protons. *Phys. Plasmas* **2002**, *9* (9), 4071-4081.

(4) Janev, R. K.; Reiter, D. Collision Processes of Hydrocarbon Species in Hydrogen Plasmas. Part 2. The Ethane and Propane Families. *ChemInform* **2003**, *34* (37), DOI: 10.1002/chin.200325274.

(5) Janev, R. K.; Reiter, D. Collision Processes of Hydrocarbon Species in Hydrogen Plasmas. Part 2. The Ethane and Propane Families. *ChemInform* **2003**, *34* (37), DOI: 10.1002/chin.20033729.

(6) Janev, R. K.; Reiter, D. Collision Processes of C2,3Hy and C2,3Hy+ Hydrocarbons with Electrons and Protons. *Phys. Plasmas* **2004**, *11* (2), 780-829.

(7) Engelhardt, A. G.; Phelps, A. V. Elastic and Inelastic Collision Cross Sections in Hydrogen and Deuterium from Transport Coefficients. *Phys. Rev.* **1963**, *131* (5), 2115-2128.

(8) Trajmar, S.; Register, D. F.; Chutjian, A. Electron Scattering By Molecules II. Experimental Methods and Data. *Phys. Rep.* **1983**, *97* (5), 219-356.

(9) Corrigan, S. J. B. Dissociation of Molecular Hydrogen by Electron Impact. *J. Chem. Phys.* **1965**, *43* (12), 4381-4386.

(10) Eliasson, B.; Hirth, M.; Kogelschatz, U. Ozone Synthesis From Oxygen in Dielectric Barrier Discharges. *J. Phys. D Appl. Phys.* **1987**, *20* (11), 1421-1437.

(11) Lawton, S. A.; Phelps, A. V. Excitation of the b 1Σ+g State of O2 By Low Energy Electrons. *J. Chem. Phys.* **1978**, *69* (3), 1055-1068.

(12) Joshipura, K. N.; Patel, P. M. Cross Sections of e--O Scattering at Intermediate and High Energies (Ei=8.7—1000 eV). *PhRvA* **1993**, *48* (3), 2464-2467.

(13) Laher, R. R.; Gilmore, F. R. Updated Excitation and Ionization Cross Sections for Electron Impact on Atomic Oxygen. *J. Phys. Chem. Ref. Data* **1990**, *19* (1), 277-305.

(14) Itikawa, Y. Cross Sections for Electron Collisions With Carbon Dioxide, *J. Phys. Chem. Ref. Data* **2002**, *31*, 749-767.

(15) *Lxcat database* Website; http://www.lxcat.laplace.univ-tlse.fr.

(16) Rapp, D.; Briglia, D. D. Total Cross Sections for Ionization and Attachment in Gases by Electron Impact. II. Negative-Ion Formation. *J. Chem. Phys.* **1965**, *43* (5), 1480-1489.

(17) McConkey, J. W.; Malone, C. P.; Johnson, P. V.; Winstead, C.; McKoy, V.; Kanik, I. Electron Impact Dissociation of Oxygen-Containing Molecules–A Critical Review. *Phys. Rep.* **2008**, *466* (1-3), 1103.

(18) Itikawa, Y.; Mason, N. Cross Sections for Electron Collisions with Water Molecules. *J. Phys. Chem. Ref. Data* **2005**, *34* (1), 122.

(19) Riahi, R.; Teulet, P.; Ben Lakhdar, Z.; Gleizes, A. Cross-Section and Rate Coefficient Calculation for Electron Impact Excitation, Ionisation and Dissociation of H and OH Molecules. *EPJD* **2006**, *40* (2), 223-230.

(20) Florescu-Mitchell, A. I.; Mitchell, J. B. A. Dissociative Recombination. *Phys. Rep.* **2006**, *430* (5-6), 277-374.

(21) Kossyi, I. A.; Kostinsky, A. Y.; Matveyev, A. A.; Silakov, V. P. Kinetic Scheme of the Non-Equilibrium Discharge in Nitrogen-Oxygen Mixtures. *Plasma Sources Sci. T.* **1992**, *1* (3), 207-220.

(22) Tsang, W.; Hampson, R. F. Chemical Kinetic Data Base for Combustion Chemistry. Part I. Methane and Related Compounds. *J. Phys. Chem. Ref. Data* **1986**, *15* (3), 1087-1279.

(23) Baulch, D. L.; Cobos, C. J.; Cox, R. A.; Esser, C.; Frank, P.; Just, T.; Kerr, J. A.; Pilling, M. J.; Troe, J.; Walker, R. W.; Warnatz, J. Evaluated Kinetic Data for Combustion Modelling. *J. Phys. Chem. Ref. Data* **1992**, *21* (3), 411-734.

(24) Tsang, W. Chemical Kinetic Data Base for Combustion Chemistry. Part 3: Propane. *J. Phys. Chem. Ref. Data* **1988**, *17* (2), 887-951.

(25) Stewart, P. H.; Larson, C. W.; Golden, D. M. Pressure and Temperature Dependence of Reactions Proceeding Via a Bound Complex. 2. Application to 2CH3 → C2H5 + H. *Combust. Flame* **1989**, *75* (1), 25-31.

(26) Laufer, A. H.; Fahr, A. Reactions and Kinetics of Unsaturated C2 Hydrocarbon Radicals. *Chem. Rev.* **2004**, *104* (6), 2813-2832.

(27) Harding, L. B.; Guadagnini, R.; Schatz, G. C. Theoretical Studies of the Reactions Hydrogen Atom + Methylidyne → carbon + Hydrogen and Carbon + Hydrogen → Methylene Using an Ab Initio Global Ground-State Potential Surface for Methylene. *J. Phys. Chem.* **1993**, *97* (21), 5472-5481.

(28) Lin, S. Y.; Guo, H. Case Study of a Prototypical Elementary Insertion Reaction: C(1D) + H2 → CH + H. *J. Phys. Chem. A* **2004**, *108*, 10066-10071.

(29) Harding, L. B.; Georgievskii, Y.; Klippenstein, S. J. Predictive Theory for Hydrogen Atom – Hydrocarbon Radical Association Kinetics. *J. Phys. Chem. A* **2005**, *109* (21), 4646-4656.

(30) Baulch, D. L.; Cobos, C. J.; Cox, R. A.; Frank, P.; Hayman, G.; Just, T.; Kerr, J. A.; Murrells, T.; Pilling, M. J.; Troe, J.; Walker, R. W.; Warnatz, J. Evaluated Kinetic Data for Combustion Modeling. Supplement I. *J. Phys. Chem. Ref. Data* **1994**, *23*, 847-848.

(31) Tsang, W. Chemical Kinetic Data Base for Combustion Chemistry Part V. Propene. *J. Phys. Chem. Ref. Data* **1991**, *20* (2), 221-273.

(32) Hadj-Ziane, S.; Held, B.; Pignolet, P.; Peyrous, R.; Coste, C. Ozone Generation in an Oxygen-Fed Wire-to-Cylinder Ozonizer at Atmospheric Pressure. *J. Phys. D Appl. Phys.* **1992**, *25* (4), 677-685.

(33) Baulch, D. L.; Bowman, C. T.; Cobos, C. J.; Cox, R. A.; Just, T.; Kerr, J. A.; Pilling, M. J.; Stocker, D.; Troe, J.; Tsang, W.; Walker, R. W.; Warnatz, J. Evaluated Kinetic Data for Combustion Modeling: Supplement II. *J. Phys. Chem. Ref. Data* **2005***, 34*, 757-1397.

(34) Fang, D. C.; Fu, X. Y. CASSCF and CAS+1+2 Studies on the Potential Energy Surface and the Rate Constants for the Reactions between CH2 and O2. *J. Phys. Chem. A* **2002**, *106*, 2988-2993.

(35) Dean, A. J.; Davidson, D. F.; Hanson, R. K. A Shock Tube Study of Reactions of Carbon Atoms with Hydrogen and Oxygen Using Excimer Photolysis of C3O2 and Carbon Atom Atomic Resonance Absorption Spectroscopy. *J. Phys. Chem.* **1991**, *95* (1), 183-191.

(36) Atkinson, R.; Baulch, D. L.; Cox, R. A.; Crowley, J. N.; Hampson, R. F.; Hynes, R. G.; Jenkin, M. E.; Rossi, M. J.; Troe, J. Evaluated Kinetic and Photochemical Data for Atmospheric Chemistry: Volume II – Gas Phase Reactions of Organic Species. *Atmos. Chem. Phys.* **2006**, *6*, 3625-4055.

(37) Atkinson, R.; Baulch, D. L.; Cox, R. A.; Crowley, J. N.; Hampson, R. F.; Hynes, R. G.; Jenkin, M. E.; Rossi, M. J.; Troe, J. Evaluated Kinetic and Photochemical Data for Atmospheric Chemistry: Volume I - Gas Phase Reactions of Ox, HOx, NOx and SOx. *Atmos. Chem. Phys.* **2004**, *4*, 1410-1738.

(38) Pereira, R. D.; Baulch, D. L.; Pilling, M. J.; Robertson, S. H; Zeng, G. Temperature and Pressure Dependence of the Multichannel Rate Coefficients for the CH3+ OH System. *J. Phys. Chem. A* **1997**, *101* (50), 9681-9693.

(39) Sun, H.; Tang, Y. Z.; Wang, Z. L.; Pan, X. M.; Li, Z. S.; Wang, R. S. DFT Investigation of the Mechanism of CH2CO + O(3P) Reaction. *IJQC* **2005**, *105*, 527-532.

(40) Kuwata, K. T.; Hasson, A. S.; Dickinson, R. V.; Petersen, E. B.; Valin, L. C. Quantum Chemical and Master Equation Simulations of the Oxidation and Isomerization of Vinoxy Radicals. *J. Phys. Chem. A* **2005**, *109*, 2514-2524.

(41) Delbos, E.; Fittschen, C.; Hippler, H.; Krasteva, N.; Olzmann, M.; Viskolcz, B. Rate Coefficients and Equilibrium Constant for the CH2CHO + O2 Reaction System *J. Phys. Chem. A* **2006**, *110*, 3238-3245.

(42) Jodkowski, J. T.; Rayez, M. T.; Rayez, J. C.; Berces, T.; Dobe, S. Theoretical Study of the Kinetics of the Hydrogen Abstraction from Methanol. 3. Reaction of Methanol with Hydrogen Atom, Methyl, and Hydroxyl Radicals. *J. Phys. Chem. A* **1999**, *103*, 3750-3765.

(43) Hou, H.; Wang, B. S.; Gu, Y. S. Mechanism of the OH + CH2CO Reaction. *Phys. Chem. Chem. Phys.* **2000**, *2*, 2329-2334.

(44) Tsang, W. Chemical Kinetic Data Base for Combustion Chemistry. Part 2. Methanol. *J. Phys. Chem. Ref. Data* **1987**, *16*, 471-508.

(45) Jasper, A. W.; Klippenstein, S. J.; Harding, L. B.; Ruscic, B. Kinetics of the Reaction of Methyl radical with Hydroxyl Radical and Methanol Decomposition. *J. Phys. Chem. A* **2007**, *111* (19), 3932-3950.

(46) Lu, C. W.; Chou, S. L.; Lee, Y. P.; Xu, S. C.; Xu, Z. F.; Lin, M. C. J. Experimental and Theoretical Studies of Rate Coefficients for the Reaction O(3P)+CH3OH at High Temperatures. *Chem. Phys.* **2005**, *122* (24), 244-314.

(47) Woodall, J.; Agúndez, M.; Markwick-Kemper, A. J.; Millar, T. J. The UMIST Database for Astrochemistry 2006. *Astron. Astrophys.* **2007**, *466* (3), 1197-1204.

(48) Kim, Y. H.; Fox, J. L. The Chemistry of Hydrocarbon Ions in the Jovian Ionosphere. *Icarus* **1994**, *112* (2), 310-325.

(49) Tahara, H.; Minami, K.; Murai, A.; Yasui, T.; Yoshikawa, T. Diagnostic Experiment and Kinetic Model Analysis of Microwave CH4/H2 Plasmas for Deposition of Diamondlike Carbon Films. *Jpn. J. Appl. Phys. 1* **1995**, *34*, 1972-1779.

(50) Tachibana, K.; Nishida, M.; Harima, H.; Urano, Y. Diagnostics and Modeling of a Methane Plasma Used in the Chemical Vapour Deposition of Amorphous Carbon Films. *J. Phys. D Appl. Phys.* **1984**, *17* (8), 1727-1742.

(51) Gudmundsson, J. T.; Thorsteinsson, E. G. Oxygen Discharges Diluted with Argon: Dissociation Processes. *Plasma Sources Sci. T.* **2007**, *16*, 399-412.

APPENDIX II

Data chemistry set CO_2 + H_2O

1. Overview of the reactions included in the model

No.	Reaction	Rate coefficient	Reference
Electron impact reactions: reaction coefficients included in the model and the references where these data were adopted from. Some reactions are treated by energy-dependent cross sections.[1–3]			
1	$e^- + CO_2 \rightarrow CO_2 + e^-$	f(σ)	1
2	$e^- + CO_2 \rightarrow CO_2^+ + e^- + e^-$	f(σ)	1
3	$e^- + CO_2 \rightarrow CO^+ + O + e^- + e^-$	f(σ)	1
4	$e^- + CO_2 \rightarrow C^+ + O_2 + e^- + e^-$	f(σ)	1
5	$e^- + CO_2 \rightarrow CO + O^+ + e^- + e^-$	f(σ)	1
6	$e^- + CO_2 \rightarrow C + O_2^+ + e^- + e^-$	f(σ)	1
7	$e^- + CO_2 \rightarrow CO + O^-$	f(σ)	1
8	$e^- + CO_2 \rightarrow CO + O + e^-$	f(σ)	1
9	$e^- + CO \rightarrow CO + e^-$	f(σ)	1
10	$e^- + CO \rightarrow CO^+ + e^- + e^-$	f(σ)	1
11	$e^- + CO \rightarrow C^+ + O + e^- + e^-$	f(σ)	1
12	$e^- + CO \rightarrow C + O^+ + e^- + e^-$	f(σ)	1
13	$e^- + CO \rightarrow C + O^-$	f(σ)	1
14	$e^- + CO \rightarrow C + O + e^-$	f(σ)	1
15	$e^- + C \rightarrow C + e^-$	f(σ)	1
16	$e^- + C \rightarrow C^+ + e^- + e^-$	f(σ)	1
17	$e^- + C_2 \rightarrow C_2 + e^-$	f(σ)	1
18	$e^- + C_2 \rightarrow C + C + e^-$	f(σ)	1
19	$e^- + C_2 \rightarrow C_2^+ + e^- + e^-$	f(σ)	1
20	$e^- + O_2 \rightarrow O_2 + e^-$	f(σ)	1

21	$e^- + O_2 \rightarrow O + O + e^-$	f(σ)	1
22	$e^- + O_2 \rightarrow O_2^+ + e^- + e^-$	f(σ)	1
23	$e^- + O_2 \rightarrow O + O^+ + e^- + e^-$	f(σ)	1
24	$e^- + O_2 \rightarrow O + O^-$	f(σ)	1
25	$e^- + O_2 + M \rightarrow O_2^- + M$	3.00×10^{-30}	1
26	$e^- + O_3 \rightarrow e^- + O_3$	f(σ)	2
27	$e^- + O_3 \rightarrow O + O_2 + e^-$	f(σ)	2
28	$e^- + O_3 \rightarrow O + O_2^+ + e^- + e^-$	f(σ)	2
29	$e^- + O_3 \rightarrow O^+ + O^- + O + e^-$	f(σ)	2
30	$e^- + O_3 \rightarrow O^- + O_2$	f(σ)	2
31	$e^- + O_3 \rightarrow O + O_2^-$	f(σ)	2
32	$e^- + O_3^- \rightarrow O_3^- + e^-$	f(σ)	2
33	$e^- + O_3 + M \rightarrow O_3^- + M$	2.95×10^{-31}	1
34	$e^- + O \rightarrow O + e^-$	f(σ)	1
35	$e^- + O \rightarrow O^+ + e^- + e^-$	f(σ)	1
36	$e^- + O + M \rightarrow O^- + M$	1.00×10^{-31}	1
37	$e^- + H \rightarrow e^- + H$	1.41×10^{-07}	2
38	$e^- + H \rightarrow e^- + H^+ + e^-$	1.80×10^{-11}	2
39	$e^- + H^+ \rightarrow e^- + H^+$	5.35×10^{-05}	2
40	$e^- + H^- \rightarrow e^- + H^-$	f(σ)	2
41	$e^- + H^- \rightarrow e^- + e^- + H$	f(σ)	2
42	$e^- + H_2 \rightarrow e^- + H_2$	1.04×10^{-07}	2
43	$e^- + H_2 \rightarrow e^- + H + H$	7.53×10^{-10}	2
44	$e^- + H_2 \rightarrow e^- + e^- + H_2^+$	7.67×10^{-12}	2
45	$e^- + H_2^+ \rightarrow e^- + H_2^+$	5.35×10^{-05}	2

46	$e^- + H_2^+ \rightarrow e^- + H^+ + H$	1.09 x 10^{-07}	2
47	$e^- + OH \rightarrow e^- + OH$	f(σ)	2
48	$e^- + OH \rightarrow e^- + O + H$	8.44 x 10^{-09}	2
49	$e^- + OH \rightarrow e^- + e^- + OH^+$	f(σ)	2
50	$e^- + OH^- \rightarrow OH^- + e^-$	f(σ)	2
51	$e^- + OH^- \rightarrow OH + e^- + e^-$	f(σ)	2
52	$e^- + OH^- \rightarrow O + H + e^- + e^-$	1.95 x 10^{-08}	2
53	$e^- + H_2O \rightarrow e^- + H_2O$	f(σ)	2
54	$e^- + H_2O \rightarrow O^- + H_2$	f(σ)	2
55	$e^- + H_2O \rightarrow OH + H^-$	f(σ)	2
56	$e^- + H_2O \rightarrow OH^- + H$	f(σ)	2
57	$e^- + H_2O \rightarrow e^- + OH + H$	f(σ)	2
58	$e^- + H_2O \rightarrow e^- + O + H + H$	f(σ)	2
59	$e^- + H_2O \rightarrow e^- + e^- + H_2O^+$	f(σ)	2
60	$e^- + H_2O^+ \rightarrow e^- + H_2O^+$	f(σ)	2
61	$e^- + H_2O_2 \rightarrow H_2O + O^-$	f(σ)	2
62	$e^- + H_2O_2 \rightarrow OH + OH^-$	f(σ)	2
63	$e^- + H_3^+ \rightarrow e^- + H + H + H^+$	f(σ)	2
64	$e^- + H_3^+ \rightarrow H_3^+ + e^-$	f(σ)	2
65	$e^- + CH_4 \rightarrow C + H_2 + H_2 + e^-$	f(σ)	3
66	$e^- + CH_4 \rightarrow CH_4 + e^-$	f(σ)	3
67	$e^- + CH_4 \rightarrow CH_4^+ + e^- + e^-$	f(σ)	3
68	$e^- + CH_4 \rightarrow CH_3^+ + H + e^- + e^-$	f(σ)	3
69	$e^- + CH_4 \rightarrow CH_2^+ + H_2 + e^- + e^-$	f(σ)	3
70	$e^- + CH_4 \rightarrow CH_3 + H + e^-$	f(σ)	3

71	$e^- + CH_4 \rightarrow CH_2 + H_2 + e^-$	f(σ)	3
72	$e^- + CH_4 \rightarrow CH + H_2 + H + e^-$	f(σ)	3
73	$e^- + CH_3 \rightarrow CH_2^+ + H + e^- + e^-$	f(σ)	3
74	$e^- + CH_3 \rightarrow CH_2 + H + e^-$	f(σ)	3
75	$e^- + CH_3 \rightarrow CH + H_2 + e^-$	f(σ)	3
76	$e^- + CH_3 \rightarrow CH_3^+ + e^- + e^-$	f(σ)	3
77	$e^- + CH_3 \rightarrow CH^+ + H_2 + e^- + e^-$	f(σ)	3
78	$e^- + CH_2 \rightarrow CH^+ + H + e^- + e^-$	f(σ)	3
79	$e^- + CH_2 \rightarrow CH + H + e^-$	f(σ)	3
80	$e^- + CH_2 \rightarrow CH_2^+ + e^- + e^-$	f(σ)	3
81	$e^- + CH \rightarrow C + H + e^-$	f(σ)	3
82	$e^- + CH \rightarrow CH^+ + e^- + e^-$	f(σ)	3
83	$e^- + C_2H_6 \rightarrow C_2H_6 + e^-$	f(σ)	3
84	$e^- + C_2H_6 \rightarrow C_2H_6^+ + e^- + e^-$	f(σ)	3
85	$e^- + C_2H_6 \rightarrow C_2H_5^+ + H + e^- + e^-$	f(σ)	3
86	$e^- + C_2H_6 \rightarrow C_2H_4^+ + H_2 + e^- + e^-$	f(σ)	3
87	$e^- + C_2H_6 \rightarrow C_2H_3^+ + H_2 + H + e^- + e^-$	f(σ)	3
88	$e^- + C_2H_6 \rightarrow C_2H_2^+ + H_2 + H_2 + e^- + e^-$	f(σ)	3
89	$e^- + C_2H_6 \rightarrow CH_3^+ + CH_3 + e^- + e^-$	f(σ)	3
90	$e^- + C_2H_6 \rightarrow C_2H_5 + H + e^-$	f(σ)	3
91	$e^- + C_2H_6 \rightarrow C_2H_4 + H_2 + e^-$	f(σ)	3
92	$e^- + C_2H_5 \rightarrow C_2H_4^+ + H + e^- + e^-$	f(σ)	3
93	$e^- + C_2H_5 \rightarrow C_2H_3^+ + H_2 + e^- + e^-$	f(σ)	3
94	$e^- + C_2H_5 \rightarrow C_2H_2^+ + H_2 + H + e^- + e^-$	f(σ)	3
95	$e^- + C_2H_5 \rightarrow C_2H_4 + H + e^-$	f(σ)	3

96	$e^- + C_2H_5 \rightarrow C_2H_3 + H_2 + e^-$	f(σ)	3
97	$e^- + C_2H_5 \rightarrow C_2H_5^+ + e^- + e^-$	f(σ)	3
98	$e^- + C_2H_4 \rightarrow C_2H_4 + e^-$	f(σ)	3
99	$e^- + C_2H_4 \rightarrow C_2H_4^+ + e^- + e^-$	f(σ)	3
100	$e^- + C_2H_4 \rightarrow C_2H_3^+ + H + e^- + e^-$	f(σ)	3
101	$e^- + C_2H_4 \rightarrow C_2H_2^+ + H_2 + e^- + e^-$	f(σ)	3
102	$e^- + C_2H_4 \rightarrow C_2H_3 + H + e^-$	f(σ)	3
103	$e^- + C_2H_4 \rightarrow C_2H_2 + H_2 + e^-$	f(σ)	3
104	$e^- + C_2H_3 \rightarrow C_2H_2^+ + H + e^- + e^-$	f(σ)	3
105	$e^- + C_2H_3 \rightarrow C_2H_2 + H + e^-$	f(σ)	3
106	$e^- + C_2H_3 \rightarrow C_2H + H_2 + e^-$	f(σ)	3
107	$e^- + C_2H_3 \rightarrow C_2H_3^+ + e^- + e^-$	f(σ)	3
108	$e^- + C_2H_2 \rightarrow C_2H_2 + e^-$	f(σ)	3
109	$e^- + C_2H_2 \rightarrow C_2H_2^+ + e^- + e^-$	f(σ)	3
110	$e^- + C_2H_2 \rightarrow C_2H + H + e^-$	f(σ)	3
111	$e^- + C_2H \rightarrow C + CH + e^-$	f(σ)	3
112	$e^- + C_3H_8 \rightarrow C_3H_8 + e^-$	f(σ)	3
113	$e^- + C_3H_8 \rightarrow C_2H_5^+ + CH_3 + e^- + e^-$	f(σ)	3
114	$e^- + C_3H_8 \rightarrow C_2H_4^+ + CH_4 + e^- + e^-$	f(σ)	3
115	$e^- + C_3H_8 \rightarrow C_3H_7 + H + e^-$	f(σ)	3
116	$e^- + C_3H_8 \rightarrow C_2H_4 + CH_4 + e^-$	f(σ)	3
117	$e^- + C_3H_8 \rightarrow C_3H_6 + H_2 + e^-$	f(σ)	3
118	$e^- + C_3H_7 \rightarrow C_2H_5^+ + CH_2 + e^- + e^-$	f(σ)	3
119	$e^- + C_3H_7 \rightarrow C_2H_4^+ + CH_3 + e^- + e^-$	f(σ)	3
120	$e^- + C_3H_7 \rightarrow C_2H_3^+ + CH_4 + e^- + e^-$	f(σ)	3

121	$e^- + C_3H_7 \rightarrow CH_3^+ + C_2H_4 + e^- + e^-$	f(σ)	3
122	$e^- + C_3H_7 \rightarrow C_2H_4 + CH_3 + e^-$	f(σ)	3
123	$e^- + C_3H_7 \rightarrow C_2H_3 + CH_4 + e^-$	f(σ)	3
124	$e^- + C_3H_7 \rightarrow C_3H_6 + H + e^-$	f(σ)	3
125	$e^- + C_3H_6 \rightarrow C_2H_5^+ + CH + e^- + e^-$	f(σ)	3
126	$e^- + C_3H_6 \rightarrow C_2H_4^+ + CH_2 + e^- + e^-$	f(σ)	3
127	$e^- + C_3H_6 \rightarrow C_2H_3^+ + CH_3 + e^- + e^-$	f(σ)	3
128	$e^- + C_3H_6 \rightarrow C_2H_2^+ + CH_4 + e^- + e^-$	f(σ)	3
129	$e^- + C_3H_6 \rightarrow CH_3^+ + C_2H_3 + e^- + e^-$	f(σ)	3
130	$e^- + C_3H_6 \rightarrow C_2H_2 + CH_4 + e^-$	f(σ)	3
Electron-ion recombination: reaction coefficients included in the model and the references where these data were adopted from. Some reactions are treated by energy-dependent cross sections.			
131	$e^- + CO_2^+ \rightarrow CO + O$	3.94×10^{-08}	1
132	$e^- + CO_2^+ \rightarrow C + O_2$	2.58×10^{-07}	1
133	$e^- + CO_4^+ \rightarrow CO_2 + O_2$	9.50×10^{-08}	1
134	$e^- + CO^+ \rightarrow C + O$	2.06×10^{-08}	1
135	$e^- + C_2O_2^+ \rightarrow CO + CO$	2.79×10^{-07}	1
136	$e^- + C_2O_3^+ \rightarrow CO_2 + CO$	2.58×10^{-08}	1
137	$e^- + C_2O_4^+ \rightarrow CO_2 + CO_2$	3.94×10^{-08}	1
138	$e^- + C_2^+ \rightarrow C + C$	1.06×10^{-08}	1
139	$e^- + O_2^+ + M \rightarrow O_2 + M$	1.00×10^{-26}	1
140	$e^- + O_2^+ \rightarrow O + O$	2.04×10^{-08}	1
141	$e^- + O^+ + M \rightarrow O + M$	1.00×10^{-26}	1
142	$e^- + O_4^+ \rightarrow O_2 + O_2$	1.33×10^{-07}	1
143	$e^- + H^+ \rightarrow H$	3.52×10^{-13}	2

144	$e^- + e^- + H^+ \rightarrow H + e^-$	7.92×10^{-29}	2
145	$e^- + H_2^+ \rightarrow H + H$	2.68×10^{-08}	2
146	$e^- + H_2^+ \rightarrow H^+ + H^-$	f(σ)	2
147	$e^- + e^- + H_2^+ \rightarrow H_2 + e^-$	7.92×10^{-29}	2
148	$e^- + OH^+ \rightarrow O + H$	3.56×10^{-09}	2
149	$e^- + e^- + OH^+ \rightarrow OH + e^-$	7.92×10^{-29}	2
150	$e^- + H_2O^+ \rightarrow O + H_2$	3.70×10^{-09}	2
151	$e^- + H_2O^+ \rightarrow O + H + H$	2.89×10^{-08}	2
152	$e^- + H_2O^+ \rightarrow OH + H$	8.14×10^{-09}	2
153	$e^- + e^- + H_2O^+ \rightarrow H_2O + e^-$	7.92×10^{-29}	2
154	$e^- + H_3O^+ \rightarrow H + H + OH$	2.87×10^{-08}	2
155	$e^- + H_3O^+ \rightarrow H_2O + H$	1.19×10^{-08}	2
156	$e^- + H_3O^+ \rightarrow H_2 + OH$	6.69×10^{-09}	2
157	$e^- + H_3O^+ \rightarrow H_2 + O + H$	6.21×10^{-10}	2
158	$e^- + H_3^+ \rightarrow H_2 + H$	f(σ)	2
159	$e^- + H_3^+ \rightarrow e^- + H_2 + H^+$	f(σ)	2
160	$e^- + H_3^+ \rightarrow H + H + H$	f(σ)	2
161	$e^- + CH_5^+ \rightarrow CH_3 + H + H$	1.87×10^{-07}	3
162	$e^- + CH_5^+ \rightarrow CH_2 + H_2 + H$	4.82×10^{-08}	3
163	$e^- + CH_4^+ \rightarrow CH_3 + H$	6.96×10^{-09}	3
164	$e^- + CH_4^+ \rightarrow CH_2 + H + H$	1.43×10^{-08}	3
165	$e^- + CH_4^+ \rightarrow CH + H_2 + H$	8.32×10^{-09}	3
166	$e^- + CH_3^+ \rightarrow CH_2 + H$	1.33×10^{-08}	3
167	$e^- + CH_3^+ \rightarrow CH + H_2$	4.65×10^{-09}	3
168	$e^- + CH_3^+ \rightarrow CH + H + H$	5.31×10^{-09}	3

169	$e^- + CH_3^+ \rightarrow C + H_2 + H$	9.97 x 10^{-09}	3
170	$e^- + CH_2^+ \rightarrow CH + H$	5.90 x 10^{-09}	3
171	$e^- + CH_2^+ \rightarrow C + H_2$	2.84 x 10^{-09}	3
172	$e^- + CH_2^+ \rightarrow C + H + H$	1.49 x 10^{-08}	3
173	$e^- + CH^+ \rightarrow C + H$	2.07 x 10^{-08}	3
174	$e^- + C_2H_6^+ \rightarrow C_2H_5 + H$	1.04 x 10^{-08}	3
175	$e^- + C_2H_6^+ \rightarrow C_2H_4 + H + H$	1.59 x 10^{-08}	3
176	$e^- + C_2H_5^+ \rightarrow C_2H_4 + H$	3.64 x 10^{-09}	3
177	$e^- + C_2H_5^+ \rightarrow C_2H_3 + H + H$	9.08 x 10^{-09}	3
178	$e^- + C_2H_5^+ \rightarrow C_2H_2 + H_2 + H$	7.57 x 10^{-09}	3
179	$e^- + C_2H_5^+ \rightarrow C_2H_2 + H + H + H$	4.25 x 10^{-09}	3
180	$e^- + C_2H_5^+ \rightarrow CH_3 + CH_2$	4.55 x 10^{-09}	3
181	$e^- + C_2H_4^+ \rightarrow C_2H_3 + H$	3.92 x 10^{-09}	3
182	$e^- + C_2H_4^+ \rightarrow C_2H_2 + H + H$	1.62 x 10^{-08}	3
183	$e^- + C_2H_4^+ \rightarrow C_2H + H_2 + H$	2.61 x 10^{-09}	3
184	$e^- + C_2H_3^+ \rightarrow C_2H_2 + H$	6.34 x 10^{-09}	3
185	$e^- + C_2H_3^+ \rightarrow C_2H + H + H$	1.30 x 10^{-08}	3
186	$e^- + C_2H_2^+ \rightarrow C_2H + H$	8.84 x 10^{-09}	3
187	$e^- + C_2H_2^+ \rightarrow CH + CH$	2.30 x 10^{-09}	3
Neutral-neutral reactions: reaction coefficients included in the model and the references where these data were adopted from.			
188	$O + CO_2 \rightarrow CO + O_2$	6.55 x 10^{-47}	1
189	$C + CO_2 \rightarrow CO + CO$	1.00 x 10^{-15}	1
190	$O + CO + M \rightarrow CO_2 + M$	7.65 x 10^{-36}	1
191	$O_2 + CO \rightarrow CO_2 + O$	2.26 x 10^{-44}	1
192	$O_3 + CO \rightarrow CO_2 + O_2$	4.00 x 10^{-25}	1

193	$C + CO + M \rightarrow C_2O + M$	6.50×10^{-32}	1
194	$O_2 + C \rightarrow CO + O$	3.00×10^{-11}	1
195	$O + C + M \rightarrow CO + M$	2.45×10^{-32}	1
196	$O + C_2O \rightarrow CO + CO$	5.00×10^{-11}	1
197	$O_2 + C_2O \rightarrow CO_2 + CO$	3.30×10^{-13}	1
198	$O + O_2 + CO_2 \rightarrow O_3 + CO_2$	4.62×10^{-34}	2
199	$O + O_2 + CO \rightarrow O_3 + CO$	4.62×10^{-34}	2
200	$O + O_2 + O_2 \rightarrow O_3 + O_2$	4.99×10^{-34}	2
201	$O + O_2 + H_2 \rightarrow O_3 + H_2$	1.01×10^{-33}	2
202	$O + O_2 + O_3 \rightarrow O_3 + O_3$	1.01×10^{-33}	2
203	$O + O_2 + H_2O \rightarrow O_3 + H_2O$	2.49×10^{-33}	2
204	$O_3 + M \rightarrow O_2 + O + M$	1.76×10^{-25}	1
205	$O + O + M \rightarrow O_2 + M$	6.97×10^{-33}	1
206	$O + O_3 \rightarrow O_2 + O_2$	1.36×10^{-14}	2
207	$O_3 + O_3 \rightarrow O_2 + O_2 + O_2$	2.27×10^{-24}	2
208	$H + O + O_3 \rightarrow OH + O_3$	2.79×10^{-32}	2
209	$H + O + H_2O \rightarrow OH + H_2O$	6.97×10^{-32}	2
210	$H + O + CO_2 \rightarrow OH + CO_2$	4.33×10^{-32}	3
211	$H + O + CH_4 \rightarrow OH + CH_4$	4.33×10^{-32}	3
212	$H + O + O_2 \rightarrow OH + O_2$	4.33×10^{-32}	3
213	$H + O + CO \rightarrow OH + CO$	4.33×10^{-32}	3
214	$H + O + H_2 \rightarrow OH + H_2$	1.08×10^{-31}	3
215	$H + O + O \rightarrow OH + O$	1.08×10^{-31}	3
216	$H + O_2 \rightarrow OH + O$	1.46×10^{-20}	2
217	$H + O_2 \rightarrow O + H + O$	3.63×10^{-47}	2

218	$H + O_2 + O_2 \rightarrow HO_2 + O_2$	5.74×10^{-32}	2
219	$H + O_2 + H_2O \rightarrow HO_2 + H_2O$	2.88×10^{-31}	2
220	$H + O_2 + H_2 \rightarrow HO_2 + H_2$	1.44×10^{-31}	2
221	$H + O_2 + O_3 \rightarrow HO_2 + O_3$	1.44×10^{-31}	2
222	$H + O_2 + CO_2 \rightarrow HO_2 + CO_2$	1.40×10^{-32}	2
223	$H + O_3 \rightarrow OH + O_2$	2.86×10^{-11}	2
224	$H + O_3 \rightarrow HO_2 + O$	7.51×10^{-13}	2
225	$H + CO_2 \rightarrow CO + OH$	6.77×10^{-28}	2
226	$H + H + O_2 \rightarrow H_2 + O_2$	1.86×10^{-32}	2
227	$H + H + H_2 \rightarrow H_2 + H_2$	3.72×10^{-32}	2
228	$H + H + H_2O \rightarrow H_2 + H_2O$	8.55×10^{-32}	2
229	$H + H + O_3 \rightarrow H_2 + O_3$	3.72×10^{-32}	2
230	$H + H + CO_2 \rightarrow H_2 + CO_2$	5.61×10^{-33}	2
231	$H + H + CO \rightarrow H_2 + CO$	5.61×10^{-33}	2
232	$H + H_2 \rightarrow H + H + H$	2.63×10^{-45}	2
233	$H + OH \rightarrow H + H + O$	3.63×10^{-47}	2
234	$H + OH \rightarrow H_2 + O$	2.06×10^{-16}	2
235	$H + OH + O_3 \rightarrow H_2O + O_3$	1.49×10^{-30}	2
236	$H + OH + CO_2 \rightarrow H_2O + CO_2$	4.33×10^{-30}	3
237	$H + OH + CH_4 \rightarrow H_2O + CH_4$	4.33×10^{-30}	3
238	$H + OH + CO \rightarrow H_2O + CO$	4.33×10^{-30}	3
239	$H + OH + O_2 \rightarrow H_2O + O_2$	4.33×10^{-30}	3
240	$H + OH + H_2 \rightarrow H_2O + H_2$	1.08×10^{-29}	3
241	$H + OH + O \rightarrow H_2O + O$	1.08×10^{-29}	3
242	$H + OH + H_2O \rightarrow H_2O + H_2O$	2.17×10^{-29}	3

243	$H + HO_2 \rightarrow H_2 + O_2$	9.30×10^{-12}	2
244	$H + HO_2 \rightarrow OH + OH$	4.62×10^{-11}	2
245	$H + HO_2 \rightarrow H_2O + O$	3.42×10^{-12}	2
246	$H + H_2O \rightarrow OH + H + H$	3.51×10^{-47}	2
247	$H + H_2O \rightarrow OH + H_2$	6.61×10^{-25}	2
248	$H + H_2O_2 \rightarrow HO_2 + H_2$	3.35×10^{-16}	2
249	$H + H_2O_2 \rightarrow H_2O + OH$	8.18×10^{-14}	2
250	$H_2 + O \rightarrow OH + H$	1.15×10^{-17}	2
251	$H_2 + O_2 \rightarrow H + HO_2$	1.45×10^{-48}	2
252	$H_2 + O_2 \rightarrow O + O + H_2$	3.63×10^{-47}	2
253	$H_2 + O_2 \rightarrow OH + OH$	1.17×10^{-39}	2
254	$H_2 + OH \rightarrow H_2O + H$	1.10×10^{-14}	2
255	$H_2 + OH \rightarrow H_2 + O + H$	3.63×10^{-47}	2
256	$H_2 + HO_2 \rightarrow H_2O_2 + H$	1.54×10^{-26}	2
257	$H_2 + H_2O \rightarrow OH + H_2 + H$	3.51×10^{-47}	2
258	$OH + O \rightarrow H + O_2$	3.06×10^{-11}	2
259	$OH + O_3 \rightarrow HO_2 + O_2$	9.18×10^{-14}	2
260	$OH + CO \rightarrow CO_2 + H$	2.80×10^{-14}	2
261	$OH + OH \rightarrow H_2O + O$	1.32×10^{-12}	2
262	$OH + OH + O_2 \rightarrow H_2O_2 + O_2$	7.49×10^{-31}	2
263	$OH + OH + H_2 \rightarrow H_2O_2 + H_2$	1.50×10^{-30}	2
264	$OH + OH + H_2O \rightarrow H_2O_2 + H_2O$	3.74×10^{-30}	2
265	$OH + OH + O_3 \rightarrow H_2O_2 + O_3$	1.50×10^{-30}	2
266	$OH + OH + CO_2 \rightarrow H_2O_2 + CO_2$	6.50×10^{-31}	2
267	$OH + OH + CO \rightarrow H_2O_2 + CO$	6.50×10^{-31}	2

268	$OH + HO_2 \rightarrow H_2O + O_2$	1.04×10^{-10}	2
269	$OH + H_2O_2 \rightarrow H_2O + HO_2$	1.85×10^{-12}	2
270	$HO_2 + O \rightarrow OH + O_2$	5.42×10^{-11}	2
271	$HO_2 + O_3 \rightarrow OH + O_2 + O_2$	2.19×10^{-15}	2
272	$HO_2 + CO \rightarrow CO_2 + OH$	2.50×10^{-26}	2
273	$HO_2 + HO_2 \rightarrow H_2O_2 + O_2$	1.41×10^{-12}	2
274	$HO_2 + HO_2 + O_2 \rightarrow H_2O_2 + O_2 + O_2$	3.95×10^{-32}	2
275	$HO_2 + HO_2 + H_2 \rightarrow H_2O_2 + O_2 + H_2$	8.31×10^{-32}	2
276	$HO_2 + HO_2 + H_2O \rightarrow H_2O_2 + O_2 + H_2O$	2.08×10^{-31}	2
277	$HO_2 + HO_2 + O_3 \rightarrow H_2O_2 + O_2 + O_3$	8.31×10^{-32}	2
278	$HO_2 + HO_2 + CO_2 \rightarrow H_2O_2 + O_2 + CO_2$	3.95×10^{-32}	2
279	$HO_2 + HO_2 + CO \rightarrow H_2O_2 + O_2 + CO$	3.95×10^{-32}	2
280	$HO_2 + H_2O \rightarrow H_2O_2 + OH$	3.04×10^{-33}	2
281	$HO_2 + H_2O_2 \rightarrow OH + H_2O + O_2$	1.00×10^{-16}	2
282	$H_2O + O \rightarrow OH + OH$	3.88×10^{-23}	2
283	$H_2O_2 + O \rightarrow HO_2 + OH$	2.97×10^{-15}	2
284	$H_2O_2 + O \rightarrow H_2O + O_2$	1.45×10^{-15}	2
285	$H_2O_2 + O_2 \rightarrow HO_2 + HO_2$	1.16×10^{-37}	2
286	$H + HCO \rightarrow H_2 + CO$	1.50×10^{-10}	2
287	$OH + HCO \rightarrow H_2O + CO$	1.69×10^{-10}	2
288	$HO_2 + HCO \rightarrow H + OH + CO_2$	5.00×10^{-11}	2
289	$O + HCO \rightarrow CO + OH$	5.00×10^{-11}	2
290	$O + HCO \rightarrow H + CO_2$	5.00×10^{-11}	2
291	$O_2 + HCO \rightarrow HO_2 + CO$	5.20×10^{-12}	2
292	$O_2 + HCO \rightarrow OH + CO_2$	2.50×10^{-12}	2

293	$O_3 + HCO \rightarrow H + O_2 + CO_2$	8.30×10^{-13}	2
294	$HCO + HCO \rightarrow H_2 + CO + CO$	3.64×10^{-11}	2
295	$CH_4 + CH_2 \rightarrow CH_3 + CH_3$	3.01×10^{-19}	3
296	$CH_4 + CH \rightarrow C_2H_4 + H$	9.74×10^{-11}	3
297	$CH_4 + C_2H_5 \rightarrow C_2H_6 + CH_3$	1.83×10^{-24}	3
298	$CH_4 + C_2H_3 \rightarrow C_2H_4 + CH_3$	2.28×10^{-18}	3
299	$CH_4 + C_2H \rightarrow C_2H_2 + CH_3$	1.31×10^{-12}	3
300	$CH_4 + C_3H_7 \rightarrow C_3H_8 + CH_3$	4.38×10^{-24}	3
301	$CH_4 + H \rightarrow CH_3 + H_2$	8.43×10^{-19}	3
302	$CH_3 + CH_3 \rightarrow C_2H_5 + H$	2.71×10^{-19}	3
303	$CH_3 + CH_3 \rightarrow C_2H_6$	5.98×10^{-11}	3
304	$CH_3 + CH_2 \rightarrow C_2H_4 + H$	7.01×10^{-11}	3
305	$CH_3 + C_2H_6 \rightarrow C_2H_5 + CH_4$	7.21×10^{-21}	3
306	$CH_3 + C_2H_5 \rightarrow C_2H_4 + CH_4$	1.91×10^{-12}	3
307	$CH_3 + C_2H_5 + M \rightarrow C_3H_8 + M$	1.00×10^{-28}	3
308	$CH_3 + C_2H_4 \rightarrow C_2H_3 + CH_4$	1.94×10^{-21}	3
309	$CH_3 + C_2H_3 \rightarrow C_2H_2 + CH_4$	6.51×10^{-13}	3
310	$CH_3 + C_2H_3 + M \rightarrow C_3H_6 + M$	4.91×10^{-30}	3
311	$CH_3 + C_2H_2 \rightarrow CH_4 + C_2H$	7.65×10^{-26}	3
312	$CH_3 + C_3H_8 \rightarrow C_3H_7 + CH_4$	1.02×10^{-20}	3
313	$CH_3 + C_3H_7 \rightarrow C_3H_6 + CH_4$	3.07×10^{-12}	3
314	$CH_3 + H_2 \rightarrow CH_4 + H$	9.60×10^{-21}	3
315	$CH_3 + H \rightarrow CH_2 + H_2$	9.96×10^{-22}	3
316	$CH_3 + H + M \rightarrow CH_4 + M$	2.97×10^{-28}	3
317	$CH_2 + CH_2 \rightarrow C_2H_2 + H_2$	5.27×10^{-11}	3

318	$CH_2 + C_2H_5 \rightarrow C_2H_4 + CH_3$	3.01×10^{-11}	3
319	$CH_2 + C_2H_3 \rightarrow C_2H_2 + CH_3$	3.01×10^{-11}	3
320	$CH_2 + C_2H \rightarrow C_2H_2 + CH$	3.01×10^{-11}	3
321	$CH_2 + C_3H_8 \rightarrow C_3H_7 + CH_3$	1.02×10^{-20}	3
322	$CH_2 + C_3H_7 \rightarrow C_2H_4 + C_2H_5$	3.01×10^{-11}	3
323	$CH_2 + C_3H_7 \rightarrow C_3H_6 + CH_3$	3.01×10^{-12}	3
324	$CH_2 + H_2 \rightarrow CH_3 + H$	5.00×10^{-15}	3
325	$CH_2 + H \rightarrow CH + H_2$	2.01×10^{-10}	3
326	$CH + C_2H_6 + M \rightarrow C_3H_7 + M$	1.14×10^{-29}	3
327	$CH + H_2 \rightarrow CH_2 + H$	6.80×10^{-13}	3
328	$CH + H \rightarrow C + H_2$	1.00×10^{-10}	3
329	$C + H_2 \rightarrow CH + H$	1.50×10^{-10}	3
330	$C_2H_6 + C_2H_3 \rightarrow C_2H_5 + C_2H_4$	3.39×10^{-21}	3
331	$C_2H_6 + C_2H \rightarrow C_2H_2 + C_2H_5$	5.99×10^{-12}	3
332	$C_2H_6 + C_3H_7 \rightarrow C_3H_8 + C_2H_5$	3.16×10^{-22}	3
333	$C_2H_6 + H \rightarrow C_2H_5 + H_2$	4.96×10^{-17}	3
334	$C_2H_5 + C_2H_5 \rightarrow C_2H_6 + C_2H_4$	2.41×10^{-12}	3
335	$C_2H_5 + C_2H \rightarrow C_2H_4 + C_2H_2$	3.01×10^{-12}	3
336	$C_2H_5 + C_3H_8 \rightarrow C_2H_6 + C_3H_7$	3.62×10^{-22}	3
337	$C_2H_5 + C_3H_7 \rightarrow C_3H_8 + C_2H_4$	1.91×10^{-12}	3
338	$C_2H_5 + C_3H_7 \rightarrow C_3H_6 + C_2H_6$	2.41×10^{-12}	3
339	$C_2H_5 + H_2 \rightarrow C_2H_6 + H$	2.97×10^{-21}	3
340	$C_2H_5 + H \rightarrow CH_3 + CH_3$	5.99×10^{-11}	3
341	$C_2H_5 + H \rightarrow C_2H_4 + H_2$	3.01×10^{-12}	3
342	$C_2H_5 + H \rightarrow C_2H_6$	1.66×10^{-20}	3

343	$C_2H_4 + C_2H \rightarrow C_2H_2 + C_2H_3$	1.40×10^{-10}	3
344	$C_2H_4 + H \rightarrow C_2H_3 + H_2$	4.92×10^{-21}	3
345	$C_2H_4 + H + M \rightarrow C_2H_5 + M$	3.66×10^{-30}	3
346	$C_2H_3 + C_2H_3 \rightarrow C_2H_4 + C_2H_2$	1.60×10^{-12}	3
347	$C_2H_3 + C_2H \rightarrow C_2H_2 + C_2H_2$	1.60×10^{-12}	3
348	$C_2H_3 + C_3H_8 \rightarrow C_2H_4 + C_3H_7$	3.40×10^{-21}	3
349	$C_2H_3 + C_3H_7 \rightarrow C_3H_8 + C_2H_2$	2.01×10^{-12}	3
350	$C_2H_3 + C_3H_7 \rightarrow C_3H_6 + C_2H_4$	2.01×10^{-12}	3
351	$C_2H_3 + H_2 \rightarrow C_2H_4 + H$	9.78×10^{-20}	3
352	$C_2H_3 + H \rightarrow C_2H_2 + H_2$	2.01×10^{-11}	3
353	$C_2H_3 + H + M \rightarrow C_2H_4 + M$	8.26×10^{-30}	3
354	$C_2H_2 + C_2H \rightarrow C_4H_2 + H$	1.50×10^{-10}	3
355	$C_2H_2 + H \rightarrow C_2H + H_2$	6.12×10^{-27}	3
356	$C_2H_2 + H + M \rightarrow C_2H_3 + M$	2.81×10^{-31}	3
357	$C_2H + C_3H_8 \rightarrow C_2H_2 + C_3H_7$	5.99×10^{-12}	3
358	$C_2H + C_3H_7 \rightarrow C_3H_6 + C_2H_2$	1.00×10^{-11}	3
359	$C_2H + H_2 \rightarrow C_2H_2 + H$	1.52×10^{-13}	3
360	$C_2H + H + M \rightarrow C_2H_2 + M$	9.44×10^{-30}	3
361	$C_3H_8 + H \rightarrow C_3H_7 + H_2$	5.15×10^{-17}	3
362	$C_3H_7 + C_3H_7 \rightarrow C_3H_6 + C_3H_8$	2.81×10^{-12}	3
363	$C_3H_7 + H_2 \rightarrow C_3H_8 + H$	7.12×10^{-21}	3
364	$C_3H_7 + H \rightarrow C_3H_6 + H_2$	3.01×10^{-12}	3
365	$C_3H_7 + H + M \rightarrow C_3H_8 + M$	3.96×10^{-30}	3
366	$C_3H_6 + H + M \rightarrow C_3H_7 + M$	3.79×10^{-33}	3
367	$CH_4 + O \rightarrow CH_3 + OH$	5.54×10^{-18}	3

368	$CH_3 + O \rightarrow CH_2O + H$	1.12×10^{-10}	3
369	$CH_3 + O \rightarrow CO + H_2 + H$	2.80×10^{-11}	3
370	$CH_2 + O \rightarrow CO + H_2$	5.33×10^{-11}	3
371	$CH_2 + O \rightarrow CO + H + H$	8.29×10^{-11}	3
372	$CH_2 + O_2 \rightarrow CO_2 + H_2$	1.42×10^{-12}	3
373	$CH_2 + O_2 \rightarrow CO + H_2O$	1.42×10^{-12}	3
374	$CH_2 + O_2 \rightarrow CH_2O + O$	5.39×10^{-13}	3
375	$CH + O \rightarrow CO + H$	6.60×10^{-11}	3
376	$CH + O_2 \rightarrow CO_2 + H$	1.20×10^{-11}	3
377	$CH + O_2 \rightarrow CO + OH$	8.00×10^{-12}	3
378	$CH + O_2 \rightarrow CHO + O$	8.00×10^{-12}	3
379	$CH + O_2 \rightarrow CO + H + O$	1.20×10^{-11}	3
380	$C_2H_6 + O \rightarrow C_2H_5 + OH$	5.11×10^{-16}	3
381	$C_2H_5 + O \rightarrow CH_3CHO + H$	8.80×10^{-11}	3
382	$C_2H_5 + O \rightarrow CH_2O + CH_3$	6.60×10^{-11}	3
383	$C_2H_5 + O \rightarrow C_2H_4 + OH$	4.40×10^{-11}	3
384	$C_2H_5 + O_2 \rightarrow C_2H_4 + HO_2$	3.80×10^{-15}	3
385	$C_2H_5 + O_2 + M \rightarrow C_2H_5O_2 + M$	5.75×10^{-29}	3
386	$C_2H_4 + O \rightarrow CH_2CHO + H$	2.63×10^{-13}	3
387	$C_2H_4 + O \rightarrow CHO + CH_3$	4.51×10^{-13}	3
388	$C_2H_3 + O \rightarrow C_2H_2 + OH$	1.25×10^{-11}	3
389	$C_2H_3 + O \rightarrow CO + CH_3$	1.25×10^{-11}	3
390	$C_2H_3 + O \rightarrow CHO + CH_2$	1.25×10^{-11}	3
391	$C_2H_3 + O \rightarrow CH_2CO + H$	1.25×10^{-11}	3
392	$C_2H_3 + O_2 \rightarrow CH_2O + CHO$	9.00×10^{-12}	3

393	$C_2H_2 + O \rightarrow CH_2 + CO$	6.75×10^{-14}	3
394	$C_2H_2 + O \rightarrow C_2HO + H$	6.75×10^{-14}	3
395	$C_2H + O \rightarrow CH + CO$	1.70×10^{-11}	3
396	$C_2H + O_2 \rightarrow CHO + CO$	3.00×10^{-11}	3
397	$C_2H + O_2 \rightarrow C_2HO + O$	1.00×10^{-12}	3
398	$C_3H_8 + O \rightarrow C_3H_7 + OH$	2.73×10^{-15}	3
399	$CH_4 + OH \rightarrow CH_3 + H_2O$	6.62×10^{-15}	3
400	$CH_4 + HO_2 \rightarrow CH_3 + H_2O_2$	8.76×10^{-27}	3
401	$CH_4 + CHO \rightarrow CH_3 + CH_2O$	6.07×10^{-30}	3
402	$CH_4 + CH_3O \rightarrow CH_3OH + CH_3$	9.42×10^{-20}	3
403	$CH_3 + CO + M \rightarrow CH_3CO + M$	4.19×10^{-36}	3
404	$CH_3 + H_2O \rightarrow CH_4 + OH$	1.82×10^{-25}	3
405	$CH_3 + OH \rightarrow CH_2 + H_2O$	1.13×10^{-12}	3
406	$CH_3 + OH \rightarrow CH_2OH + H$	1.31×10^{-11}	3
407	$CH_3 + OH \rightarrow CH_3O + H$	1.60×10^{-10}	3
408	$CH_3 + OH + M \rightarrow CH_3OH + M$	2.30×10^{-27}	3
409	$CH_3 + HO_2 \rightarrow CH_3O + OH$	3.00×10^{-11}	3
410	$CH_3 + HO_2 \rightarrow CH_4 + O_2$	5.99×10^{-12}	3
411	$CH_3 + CH_2O \rightarrow CH_4 + CHO$	6.14×10^{-18}	3
412	$CH_3 + CHO \rightarrow CH_4 + CO$	2.00×10^{-10}	3
413	$CH_3 + CH_3O \rightarrow CH_4 + CH_2O$	4.00×10^{-11}	3
414	$CH_3 + CH_3CHO \rightarrow CH_4 + CH_3CO$	4.95×10^{-18}	3
415	$CH_2 + CO_2 \rightarrow CH_2O + CO$	3.90×10^{-14}	3
416	$CH_2 + H_2O \rightarrow CH_3 + OH$	1.60×10^{-16}	3
417	$CH_2 + OH \rightarrow CH_2O + H$	3.00×10^{-11}	3

418	$CH_2 + HO_2 \rightarrow CH_2O + OH$	3.00 x 10^{-11}	3
419	$CH_2 + CH_2O \rightarrow CH_3 + CHO$	1.00 x 10^{-14}	3
420	$CH_2 + CHO \rightarrow CH_3 + CO$	3.00 x 10^{-11}	3
421	$CH_2 + CH_3O \rightarrow CH_3 + CH_2O$	3.00 x 10^{-11}	3
422	$CH + CO_2 \rightarrow CHO + CO$	9.68 x 10^{-13}	3
423	$CH + CO_2 \rightarrow CO + CO + H$	9.68 x 10^{-13}	3
424	$CH + CO + M \rightarrow C_2HO + M$	4.04 x 10^{-30}	3
425	$C_2H_6 + OH \rightarrow C_2H_5 + H_2O$	2.46 x 10^{-13}	3
426	$C_2H_6 + HO_2 \rightarrow C_2H_5 + H_2O_2$	6.36 x 10^{-24}	3
427	$C_2H_6 + CHO \rightarrow C_2H_5 + CH_2O$	2.19 x 10^{-26}	3
428	$C_2H_6 + CH_3O \rightarrow C_2H_5 + CH_3OH$	2.72 x 10^{-18}	3
429	$C_2H_5 + OH \rightarrow C_2H_4 + H_2O$	4.00 x 10^{-11}	3
430	$C_2H_5 + HO_2 \rightarrow C_2H_6 + O_2$	5.00 x 10^{-13}	3
431	$C_2H_5 + HO_2 \rightarrow C_2H_4 + H_2O_2$	5.00 x 10^{-13}	3
432	$C_2H_5 + CH_2O \rightarrow C_2H_6 + CHO$	4.47 x 10^{-18}	3
433	$C_2H_5 + CHO \rightarrow C_2H_6 + CO$	2.00 x 10^{-10}	3
434	$C_2H_5 + CH_3O \rightarrow C_2H_6 + CH_2O$	4.00 x 10^{-11}	3
435	$C_2H_4 + OH \rightarrow C_2H_3 + H_2O$	1.54 x 10^{-16}	3
436	$C_2H_4 + HO_2 \rightarrow CH_3CHO + OH$	1.62 x 10^{-20}	3
437	$C_2H_3 + H_2O \rightarrow C_2H_4 + OH$	1.82 x 10^{-25}	3
438	$C_2H_3 + OH \rightarrow C_2H_2 + H_2O$	5.00 x 10^{-11}	3
439	$C_2H_3 + CH_2O \rightarrow C_2H_4 + CHO$	4.41 x 10^{-18}	3
440	$C_2H_3 + CHO \rightarrow C_2H_4 + CO$	1.50 x 10^{-10}	3
441	$C_2H_3 + CH_3O \rightarrow C_2H_4 + CH_2O$	4.00 x 10^{-11}	3
442	$C_2H_2 + OH \rightarrow C_2H + H_2O$	1.77 x 10^{-22}	3

443	$C_2H_2 + HO_2 \rightarrow CH_2CO + OH$	1.62×10^{-20}	3
444	$C_2H + OH \rightarrow CH_2 + CO$	3.00×10^{-11}	3
445	$C_2H + OH \rightarrow C_2H_2 + O$	3.00×10^{-11}	3
446	$C_2H + HO_2 \rightarrow C_2H_2 + O_2$	3.00×10^{-11}	3
447	$C_2H + HO_2 \rightarrow C_2HO + OH$	3.00×10^{-11}	3
448	$C_2H + CHO \rightarrow C_2H_2 + CO$	1.00×10^{-10}	3
449	$C_2H + CH_3O \rightarrow C_2H_2 + CH_2O$	4.00×10^{-11}	3
450	$C_3H_8 + OH \rightarrow C_3H_7 + H_2O$	3.76×10^{-15}	3
451	$C_3H_8 + CH_3O \rightarrow C_3H_7 + CH_3OH$	1.42×10^{-17}	3
452	$C_3H_7 + CH_2O \rightarrow C_3H_8 + CHO$	4.10×10^{-18}	3
453	$C_3H_7 + CHO \rightarrow C_3H_8 + CO$	1.00×10^{-10}	3
454	$C_3H_7 + CH_3O \rightarrow C_3H_8 + CH_2O$	4.00×10^{-11}	3
455	$H_2 + CHO \rightarrow H + CH_2O$	2.78×10^{-26}	3
456	$H + CO + M \rightarrow CHO + M$	1.54×10^{-34}	3
457	$H + CH_2O \rightarrow H_2 + CHO$	5.72×10^{-14}	3
458	$H + CHO \rightarrow H_2 + CO$	1.50×10^{-10}	3
459	$H + CH_3O \rightarrow H_2 + CH_2O$	2.32×10^{-11}	3
460	$H + CH_3O \rightarrow CH_3 + OH$	9.93×10^{-12}	3
461	$H + CH_3CHO \rightarrow H_2 + CH_3CO$	8.98×10^{-14}	3
462	$H + CH_2CO \rightarrow CH_3 + CO$	1.04×10^{-13}	3
463	$H + C_2HO \rightarrow CH_2 + CO$	2.50×10^{-10}	3
464	$O + CH_2O \rightarrow OH + CHO$	1.73×10^{-13}	3
465	$O + CHO \rightarrow CO + OH$	5.00×10^{-11}	3
466	$O + CHO \rightarrow H + CO_2$	5.00×10^{-11}	3
467	$O + CH_3O \rightarrow CH_3 + O_2$	2.20×10^{-11}	3

468	$O + CH_3O \rightarrow OH + CH_2O$	3.00×10^{-12}	3
469	$O + CH_3CHO \rightarrow OH + CH_3CO$	4.68×10^{-13}	3
470	$O + CH_2CO \rightarrow CH_2 + CO_2$	2.29×10^{-13}	3
471	$O + CH_2CO \rightarrow CH_2O + CO$	7.88×10^{-14}	3
472	$O + CH_2CO \rightarrow CHO + CO + H$	4.33×10^{-14}	3
473	$O + CH_2CO \rightarrow CHO + CHO$	4.33×10^{-14}	3
474	$O + C_2HO \rightarrow CO + CO + H$	1.60×10^{-10}	3
475	$O_2 + CHO \rightarrow CO + HO_2$	5.10×10^{-12}	3
476	$O_2 + CH_3O \rightarrow CH_2O + HO_2$	1.97×10^{-15}	3
477	$O_2 + CH_2CHO \rightarrow CH_2O + CO + OH$	3.00×10^{-14}	3
478	$O_2 + C_2HO \rightarrow CO + CO + OH$	6.46×10^{-13}	3
479	$CO + CH_3O \rightarrow CO_2 + CH_3$	6.56×10^{-20}	3
480	$H_2O + CH_3O \rightarrow CH_3OH + OH$	1.67×10^{-14}	3
481	$OH + CH_2O \rightarrow H_2O + CHO$	8.47×10^{-12}	3
482	$OH + CHO \rightarrow CO + H_2O$	1.70×10^{-10}	3
483	$OH + CH_3O \rightarrow CH_2O + H_2O$	3.00×10^{-11}	3
484	$OH + CH_3CHO \rightarrow CH_3CO + H_2O$	1.49×10^{-11}	3
485	$OH + CH_2CO \rightarrow CO + CH_2OH$	1.14×10^{-11}	3
486	$HO_2 + CH_2O \rightarrow CHO + H_2O_2$	1.05×10^{-20}	3
487	$HO_2 + CHO \rightarrow OH + H + CO_2$	5.00×10^{-11}	3
488	$HO_2 + CH_3O \rightarrow CH_2O + H_2O_2$	5.00×10^{-13}	3
489	$CH_2O + CH_3O \rightarrow CH_3OH + CHO$	1.14×10^{-15}	3
490	$CHO + CHO \rightarrow CH_2O + CO$	5.00×10^{-11}	3
491	$CHO + CH_3O \rightarrow CH_3OH + CO$	1.50×10^{-10}	3
492	$CH_3O + CH_3O \rightarrow CH_2O + CH_3OH$	1.00×10^{-10}	3

493	$CH_4 + CH_3CO \rightarrow CH_3CHO + CH_3$	1.14×10^{-29}	3
494	$CH_4 + CH_2OH \rightarrow CH_3OH + CH_3$	2.55×10^{-27}	3
495	$CH_3 + H_2O_2 \rightarrow CH_4 + HO_2$	5.46×10^{-14}	3
496	$CH_3 + CH_3OH \rightarrow CH_4 + CH_3O$	1.01×10^{-20}	3
497	$CH_3 + CH_3OH \rightarrow CH_4 + CH_2OH$	2.66×10^{-20}	3
498	$CH_3 + CH_2OH \rightarrow CH_4 + CH_2O$	4.00×10^{-12}	3
499	$CH_2 + H_2O_2 \rightarrow CH_3 + HO_2$	1.00×10^{-14}	3
500	$CH_2 + CH_3CO \rightarrow CH_2CO + CH_3$	3.00×10^{-11}	3
501	$CH_2 + CH_3OH \rightarrow CH_3O + CH_3$	1.01×10^{-20}	3
502	$CH_2 + CH_3OH \rightarrow CH_2OH + CH_3$	2.66×10^{-20}	3
503	$CH_2 + CH_2OH \rightarrow CH_2O + CH_3$	2.00×10^{-12}	3
504	$CH_2 + CH_2OH \rightarrow C_2H_4 + OH$	4.00×10^{-11}	3
505	$C_2H_5 + H_2O_2 \rightarrow C_2H_6 + HO_2$	2.83×10^{-15}	3
506	$C_2H_5 + CH_3OH \rightarrow C_2H_6 + CH_3O$	3.50×10^{-22}	3
507	$C_2H_5 + CH_3OH \rightarrow C_2H_6 + CH_2OH$	9.49×10^{-22}	3
508	$C_2H_5 + CH_2OH \rightarrow C_2H_6 + CH_2O$	4.00×10^{-12}	3
509	$C_2H_5 + CH_2OH \rightarrow CH_3OH + C_2H_4$	4.00×10^{-12}	3
510	$C_2H_3 + H_2O_2 \rightarrow C_2H_4 + HO_2$	5.46×10^{-14}	3
511	$C_2H_3 + CH_3OH \rightarrow C_2H_4 + CH_3O$	1.01×10^{-20}	3
512	$C_2H_3 + CH_3OH \rightarrow C_2H_4 + CH_2OH$	2.66×10^{-20}	3
513	$C_2H_3 + CH_2OH \rightarrow C_2H_4 + CH_2O$	5.00×10^{-11}	3
514	$C_2H_2 + CH_2OH \rightarrow C_2H_3 + CH_2O$	3.32×10^{-19}	3
515	$C_2H + CH_3OH \rightarrow C_2H_2 + CH_3O$	2.00×10^{-12}	3
516	$C_2H + CH_3OH \rightarrow C_2H_2 + CH_2OH$	1.00×10^{-11}	3
517	$C_2H + CH_2OH \rightarrow C_2H_2 + CH_2O$	5.99×10^{-11}	3

518	$C_3H_7 + OH \rightarrow C_3H_6 + H_2O$	4.00×10^{-11}	3
519	$C_3H_7 + H_2O_2 \rightarrow C_3H_8 + HO_2$	7.08×10^{-17}	3
520	$C_3H_7 + CH_3OH \rightarrow C_3H_8 + CH_3O$	3.51×10^{-22}	3
521	$C_3H_7 + CH_3OH \rightarrow C_3H_8 + CH_2OH$	8.45×10^{-22}	3
522	$C_3H_7 + CH_2OH \rightarrow C_3H_8 + CH_2O$	1.60×10^{-12}	3
523	$C_3H_7 + CH_2OH \rightarrow C_3H_6 + CH_3OH$	8.00×10^{-13}	3
524	$H + CH_3OH \rightarrow CH_2OH + H_2$	1.27×10^{-15}	3
525	$H + CH_3OH \rightarrow CH_3O + H_2$	3.18×10^{-16}	3
526	$H + CH_2OH \rightarrow CH_2O + H_2$	1.00×10^{-11}	3
527	$H + CH_2OH \rightarrow CH_3 + OH$	1.60×10^{-10}	3
528	$H + CH_2OH + M \rightarrow CH_3OH + M$	1.18×10^{-29}	3
529	$O + CH_3CO \rightarrow OH + CH_2CO$	8.75×10^{-11}	3
530	$O + CH_3CO \rightarrow CO_2 + CH_3$	2.63×10^{-10}	3
531	$O + CH_3OH \rightarrow OH + CH_2OH$	1.12×10^{-14}	3
532	$O + CH_3OH \rightarrow OH + CH_3O$	1.68×10^{-15}	3
533	$O + CH_2OH \rightarrow CH_2O + OH$	7.00×10^{-11}	3
534	$O_2 + CH_2OH \rightarrow CH_2O + HO_2$	9.70×10^{-12}	3
535	$OH + CH_3CO \rightarrow CH_2CO + H_2O$	2.00×10^{-11}	3
536	$OH + CH_3CO \rightarrow CH_3 + CO + OH$	5.00×10^{-11}	3
537	$OH + CH_3OH \rightarrow H_2O + CH_2OH$	7.67×10^{-13}	3
538	$OH + CH_3OH \rightarrow H_2O + CH_3O$	1.35×10^{-13}	3
539	$OH + CH_2OH \rightarrow CH_2O + H_2O$	4.00×10^{-11}	3
540	$HO_2 + CH_3CO \rightarrow CH_3 + CO_2 + OH$	5.00×10^{-11}	3
541	$HO_2 + CH_3OH \rightarrow CH_2OH + H_2O_2$	1.10×10^{-22}	3
542	$HO_2 + CH_2OH \rightarrow CH_2O + H_2O_2$	2.00×10^{-11}	3

543	$CH_2O + CH_3CO \rightarrow CH_3CHO + CHO$	1.17×10^{-22}	3
544	$CH_2O + CH_2OH \rightarrow CH_3OH + CHO$	4.22×10^{-18}	3
545	$CHO + H_2O_2 \rightarrow CH_2O + HO_2$	1.50×10^{-18}	3
546	$CHO + CH_3CO \rightarrow CH_3CHO + CO$	1.50×10^{-11}	3
547	$CHO + CH_3OH \rightarrow CH_2O + CH_2OH$	6.85×10^{-23}	3
548	$CHO + CH_2OH \rightarrow CH_2O + CH_2O$	3.00×10^{-10}	3
549	$CHO + CH_2OH \rightarrow CH_3OH + CO$	2.00×10^{-10}	3
550	$CH_3O + CH_3CO \rightarrow CH_3OH + CH_2CO$	1.00×10^{-11}	3
551	$CH_3O + CH_3OH \rightarrow CH_3OH + CH_2OH$	5.38×10^{-16}	3
552	$CH_3O + CH_2OH \rightarrow CH_2O + CH_3OH$	4.00×10^{-11}	3
553	$H_2O_2 + CH_3CO \rightarrow CH_3CHO + HO_2$	3.05×10^{-19}	3
554	$H_2O_2 + CH_2OH \rightarrow CH_3OH + HO_2$	6.56×10^{-17}	3
555	$CH_3CO + CH_3OH \rightarrow CH_3CHO + CH_2OH$	2.22×10^{-22}	3
556	$CH_2OH + CH_2OH \rightarrow CH_2O + CH_3OH$	8.00×10^{-12}	3
Neutral-ion reactions: reaction coefficients included in the model and the references where these data were adopted from.			
557	$O^+ + CO_2 \rightarrow O_2^+ + CO$	9.40×10^{-10}	1
558	$O^+ + CO_2 \rightarrow CO_2^+ + O$	4.50×10^{-10}	1
559	$C^+ + CO_2 \rightarrow CO^+ + CO$	1.10×10^{-09}	1
560	$CO^+ + CO_2 \rightarrow CO_2^+ + CO$	1.00×10^{-09}	1
561	$O^- + CO_2 + M \rightarrow CO_3^- + M$	9.00×10^{-29}	1
562	$O_2^- + CO_2 + M \rightarrow CO_4^- + M$	1.00×10^{-29}	1
563	$O_3^- + CO_2 \rightarrow O_2 + CO_3^-$	5.50×10^{-10}	1
564	$O_4^- + CO_2 \rightarrow CO_4^- + O_2$	4.80×10^{-10}	1
565	$CO_2^+ + CO_2 + M \rightarrow C_2O_4^+ + M$	3.00×10^{-28}	1
566	$O_2^+ + CO_2 + M \rightarrow CO_4^+ + M$	2.30×10^{-29}	1

567	$O^+ + CO \rightarrow CO^+ + O$	3.53×10^{-18}	1
568	$O^- + CO \rightarrow CO_2 + e^-$	5.50×10^{-10}	1
569	$C_2O_3^+ + CO \rightarrow CO_2 + C_2O_2^+$	1.10×10^{-09}	1
570	$C_2O_4^+ + CO \rightarrow C_2O_3^+ + CO_2$	9.00×10^{-10}	1
571	$C_2O_3^+ + CO + M \rightarrow C_2O_2^+ + CO_2 + M$	2.60×10^{-26}	1
572	$C_2O_4^+ + CO + M \rightarrow C_2O_3^+ + CO_2 + M$	4.20×10^{-26}	1
573	$C^+ + CO \rightarrow CO^+ + C$	5.00×10^{-13}	1
574	$CO^+ + C \rightarrow CO + C^+$	1.10×10^{-10}	1
575	$O_2^+ + C \rightarrow CO^+ + O$	5.20×10^{-11}	1
576	$O_2^+ + C \rightarrow C^+ + O_2$	5.20×10^{-11}	1
577	$C_2^+ + C \rightarrow C_2 + C^+$	1.10×10^{-10}	1
578	$O + CO_2^+ \rightarrow O_2^+ + CO$	1.64×10^{-10}	1
579	$O + CO_2^+ \rightarrow O^+ + CO_2$	9.62×10^{-11}	1
580	$O_2 + CO_2^+ \rightarrow O_2^+ + CO_2$	5.30×10^{-11}	1
581	$O + CO^+ \rightarrow CO + O^+$	1.40×10^{-10}	1
582	$O_2 + CO^+ \rightarrow O_2^+ + CO$	1.20×10^{-10}	1
583	$O_2 + C_2O_2^+ \rightarrow CO + CO + O_2^+$	5.00×10^{-12}	1
584	$C_2O_2^+ + M \rightarrow CO^+ + CO + M$	1.00×10^{-12}	1
585	$C_2O_4^+ + M \rightarrow CO_2^+ + CO_2 + M$	1.00×10^{-14}	1
586	$O + CO_3^- \rightarrow CO_2 + O_2^-$	8.00×10^{-11}	1
587	$O + CO_4^- \rightarrow CO_3^- + O_2$	1.10×10^{-10}	1
588	$O + CO_4^- \rightarrow CO_2 + O_2 + O^-$	1.40×10^{-11}	1
589	$O + CO_4^- \rightarrow CO_2 + O_3^-$	1.40×10^{-11}	1
590	$O_2 + C^+ \rightarrow CO + O^+$	6.20×10^{-10}	1
591	$O_2 + C^+ \rightarrow CO^+ + O$	3.80×10^{-10}	1

592	$O^+ + O_2 \rightarrow O_2^+ + O$	1.83×10^{-11}	1
593	$O_2^+ + O_2 + M \rightarrow O_4^+ + M$	2.40×10^{-30}	1
594	$O_2^- + O_2 + M \rightarrow O_4^- + M$	3.50×10^{-31}	1
595	$O^- + O_2 \rightarrow O_3 + e^-$	1.00×10^{-12}	1
596	$O^- + O_2 + M \rightarrow O_3^- + M$	2.79×10^{-28}	1
597	$O^- + O_3 \rightarrow O_3^- + O$	8.00×10^{-10}	1
598	$O_2^- + O_3 \rightarrow O_3^- O_2$	4.00×10^{-10}	1
599	$O_3^- + O_3 \rightarrow O_2 + O_2 + O_2 + e^-$	3.00×10^{-10}	1
600	$O^+ + O_3 \rightarrow O_2^+ + O_2$	1.00×10^{-10}	1
601	$O^+ + O + M \rightarrow O_2^+ + M$	1.00×10^{-29}	1
602	$O_3^- + O \rightarrow O_3 + O^-$	1.00×10^{-13}	1
603	$O_3^- + O \rightarrow O_2 + O_2 + e^-$	1.00×10^{-13}	1
604	$O_3^- + O \rightarrow O_2^- + O_2$	2.50×10^{-10}	1
605	$O_4^- + O \rightarrow O_3^- + O_2$	4.00×10^{-10}	1
606	$O_4^- + O \rightarrow O^- + O_2 + O_2$	3.00×10^{-10}	1
607	$O_4^+ + O \rightarrow O_2^+ + O_3$	3.00×10^{-10}	1
608	$O_2^- + O_2 \rightarrow O_2 + O_2 + e^-$	2.18×10^{-18}	1
609	$O_2^- + M \rightarrow O_2 + M + e^-$	8.54×10^{-18}	1
610	$O_2 + O_3^- \rightarrow O_2 + O_3 + e^-$	2.30×10^{-11}	1
611	$O_3^- + M \rightarrow O_3 + M + e^-$	2.30×10^{-11}	1
612	$O^- + M \rightarrow O + M + e^-$	4.00×10^{-12}	1
613	$O_4^- + M \rightarrow O_2^- + O_2 + M$	3.08×10^{-12}	1
614	$O_4^+ + M \rightarrow O_2^+ + O_2 + M$	1.73×10^{-13}	1
615	$O + O^- \rightarrow O_2 + e^-$	1.50×10^{-10}	2
616	$O + O_2^- \rightarrow O_2 + O^-$	1.56×10^{-10}	2

617	$O + O_2^- \rightarrow O_3 + e^-$	1.50 x 10^{-10}	2
618	$O^- + O_2 \rightarrow O_2^- + O$	1.00 x 10^{-10}	2
619	$O^- + O_3 \rightarrow O_2 + O_2 + e^-$	5.30 x 10^{-10}	2
620	$O^- + O_3 \rightarrow O_2 + O_2^-$	1.04 x 10^{-10}	2
621	$O^+ + CO_2 \rightarrow CO^+ + O_2$	1.00 x 10^{-09}	2
622	$CO + CO_3^- \rightarrow CO_2 + CO_2 + e^-$	1.00 x 10^{-13}	2
623	$H + O^+ \rightarrow H^+ + O$	5.97 x 10^{-10}	2
624	$H + O^- \rightarrow OH + e^-$	5.00 x 10^{-10}	2
625	$H + O_2^- \rightarrow H^- + O_2$	7.00 x 10^{-10}	2
626	$H + O_2^- \rightarrow HO_2 + e^-$	7.00 x 10^{-10}	2
627	$H + CO^+ \rightarrow CO + H^+$	7.50 x 10^{-10}	2
628	$H + CO_2^+ \rightarrow H^+ + CO_2$	1.02 x 10^{-10}	2
629	$H + CO_3^- \rightarrow OH^- + CO_2$	1.70 x 10^{-10}	2
630	$H + CO_4^- \rightarrow OH + CO_3^-$	2.00 x 10^{-10}	2
631	$H + H^- \rightarrow H_2 + e^-$	1.30 x 10^{-09}	2
632	$H + H_2^+ \rightarrow H_2 + H^+$	6.39 x 10^{-10}	2
633	$H + OH^- \rightarrow H_2O + e^-$	1.80 x 10^{-09}	2
634	$H^+ + O \rightarrow H + O^+$	3.26 x 10^{-10}	2
635	$H^+ + O_2 \rightarrow H + O_2^+$	2.00 x 10^{-09}	2
636	$H^+ + OH \rightarrow H + OH^+$	2.10 x 10^{-09}	2
637	$H^+ + H_2O \rightarrow H + H_2O^+$	6.90 x 10^{-09}	2
638	$H^- + O \rightarrow OH + e^-$	1.00 x 10^{-09}	2
639	$H^- + O_2 \rightarrow HO_2 + e^-$	1.20 x 10^{-09}	2
640	$H^- + OH \rightarrow H_2O + e^-$	1.00 x 10^{-10}	2
641	$H^- + H_2O \rightarrow OH^- + H_2$	3.80 x 10^{-09}	2

642	$H_2 + O^+ \rightarrow OH^+ + H$	1.62 x 10^{-09}	2
643	$H_2 + O^- \rightarrow H_2O + e^-$	6.72 x 10^{-10}	2
644	$H_2 + O^- \rightarrow OH^- + H$	2.80 x 10^{-11}	2
645	$H_2 + O_2^- \rightarrow OH^- + OH$	5.00 x 10^{-13}	2
646	$H_2 + O_2^- \rightarrow H^- + HO_2$	5.00 x 10^{-13}	2
647	$H_2 + H_2^+ \rightarrow H_2 + H^+ + H$	6.06 x 10-47	2
648	$H_2 + OH^+ \rightarrow H_2O^+ + H$	1.30 x 10^{-09}	2
649	$H_2 + OH^- \rightarrow H_2O + H^-$	5.00 x 10^{-12}	2
650	$H_2 + H_2O^+ \rightarrow H_3O^+ + H$	1.40 x 10^{-09}	2
651	$H_2^+ + O \rightarrow H + OH^+$	1.50 x 10^{-09}	2
652	$H_2^+ + O_2 \rightarrow H_2 + O_2^+$	8.00 x 10^{-10}	2
653	$H_2^+ + CO \rightarrow CO^+ + H_2$	6.44 x 10^{-10}	2
654	$H_2^+ + OH \rightarrow H_2 + OH^+$	7.60 x 10^{-10}	2
655	$H_2^+ + OH \rightarrow H_2O^+ + H$	7.60 x 10^{-10}	2
656	$H_2^+ + H_2O \rightarrow H_2 + H_2O^+$	3.90 x 10^{-09}	2
657	$H_2^+ + H_2O \rightarrow H_3O^+ + H$	3.40 x 10^{-09}	2
658	$OH + O^+ \rightarrow OH^+ + O$	3.60 x 10^{-10}	2
659	$OH + O^+ \rightarrow O_2^+ + H$	3.60 x 10^{-10}	2
660	$OH + O_2^- \rightarrow OH^- + O_2$	1.00 x 10^{-10}	2
661	$OH + CO^+ \rightarrow CO + OH^+$	2.99 x 10^{-10}	2
662	$OH + CO^+ \rightarrow CO_2^+ + H$	2.10 x 10^{-10}	2
663	$OH + CO_2^+ \rightarrow CO_2 + OH^+$	3.00 x 10^{-10}	2
664	$OH + OH^+ \rightarrow H_2O^+ + O$	7.00 x 10^{-10}	2
665	$OH + H_2O^+ \rightarrow H_3O^+ + O$	6.90 x 10^{-10}	2
666	$OH^+ + O \rightarrow O_2^+ + H$	7.10 x 10^{-10}	2

667	$OH^+ + O_2 \rightarrow OH + O_2^+$	3.80×10^{-10}	2
668	$OH^+ + H_2O \rightarrow H_2O^+ + OH$	1.60×10^{-09}	2
669	$OH^+ + H_2O \rightarrow H_3O^+ + O$	1.30×10^{-09}	2
670	$OH^- + O \rightarrow HO_2 + e^-$	4.15×10^{-10}	2
671	$OH^- + O_3 \rightarrow O_2^- + HO_2$	1.08×10^{-11}	2
672	$H_2O + O^+ \rightarrow H_2O^+ + O$	2.60×10^{-09}	2
673	$H_2O + O^- \rightarrow H_2O_2 + e^-$	6.00×10^{-13}	2
674	$H_2O + CO^+ \rightarrow CO + H_2O^+$	1.66×10^{-09}	2
675	$H_2O + CO_2^+ \rightarrow CO_2 + H_2O^+$	1.97×10^{-09}	2
676	$H_2O + H_2O^+ \rightarrow H_3O^+ + OH$	1.86×10^{-09}	2
677	$H_2O^+ + O \rightarrow H_2 + O_2^+$	5.50×10^{-11}	2
678	$H_2O^+ + O_2 \rightarrow H_2O + O_2^+$	3.30×10^{-10}	2
679	$H^- + CO \rightarrow HCO + e^-$	5.00×10^{-11}	2
680	$H^+ + HCO \rightarrow CO^+ + H_2$	9.06×10^{-10}	2
681	$H^+ + HCO \rightarrow CO + H_2^+$	9.06×10^{-10}	2
682	$OH^+ + HCO \rightarrow H_2O^+ + CO$	2.70×10^{-10}	2
683	$H_2O^+ + HCO \rightarrow CO + H_3O^+$	2.70×10^{-10}	2
684	$O^+ + HCO \rightarrow CO + OH^+$	4.14×10^{-10}	2
685	$H_3^+ + O \rightarrow H_2O^+ + H$	3.60×10^{-10}	2
686	$H_3^+ + O \rightarrow OH^+ + H_2$	8.40×10^{-10}	2
687	$H_3^+ + OH \rightarrow H_2O^+ + H_2$	1.30×10^{-09}	2
688	$H_3^+ + H_2O \rightarrow H_3O^+ + H_2$	5.90×10^{-09}	2
689	$H_2 + H_3O^+ \rightarrow H_2O + H_3^+$	5.00×10^{-10}	2
690	$H_2 + H_2^+ \rightarrow H_3^+ + H$	2.10×10^{-09}	2
691	$H^+ + H_2 + M \rightarrow H_3^+ + M$	1.50×10^{-29}	2

692	$CH_5^+ + CH_2 \rightarrow CH_3^+ + CH_4$	9.60×10^{-10}	3
693	$CH_5^+ + CH \rightarrow CH_2^+ + CH_4$	6.90×10^{-10}	3
694	$CH_5^+ + C \rightarrow CH^+ + CH_4$	1.20×10^{-09}	3
695	$CH_5^+ + C_2H_6 \rightarrow C_2H_5^+ + H_2 + CH_4$	2.25×10^{-10}	3
696	$CH_5^+ + C_2H_4 \rightarrow C_2H_5^+ + CH_4$	1.50×10^{-09}	3
697	$CH_5^+ + C_2H_2 \rightarrow C_2H_3^+ + CH_4$	1.60×10^{-09}	3
698	$CH_5^+ + C_2H \rightarrow C_2H_2^+ + CH_4$	9.00×10^{-10}	3
699	$CH_5^+ + H \rightarrow CH_4^+ + H_2$	1.50×10^{-10}	3
700	$CH_5^+ + O \rightarrow H_3O^+ + CH_2$	2.20×10^{-10}	3
701	$CH_5^+ + H_2O \rightarrow H_3O^+ + CH_4$	3.70×10^{-09}	3
702	$CH_4^+ + CH_4 \rightarrow CH_5^+ + CH_3$	1.50×10^{-09}	3
703	$CH_4^+ + C_2H_6 \rightarrow C_2H_4^+ + CH_4 + H_2$	1.91×10^{-09}	3
704	$CH_4^+ + C_2H_4 \rightarrow C_2H_5^+ + CH_3$	4.23×10^{-10}	3
705	$CH_4^+ + C_2H_4 \rightarrow C_2H_4^+ + CH_4$	1.38×10^{-09}	3
706	$CH_4^+ + C_2H_2 \rightarrow C_2H_3^+ + CH_3$	1.23×10^{-09}	3
707	$CH_4^+ + C_2H_2 \rightarrow C_2H_2^+ + CH_4$	1.13×10^{-09}	3
708	$CH_4^+ + H_2 \rightarrow CH_5^+ + H$	3.30×10^{-11}	3
709	$CH_4^+ + H \rightarrow CH_3^+ + H_2$	1.00×10^{-11}	3
710	$CH_4^+ + O \rightarrow CH_3^+ + OH$	1.00×10^{-09}	3
711	$CH_4^+ + O_2 \rightarrow O_2^+ + CH_4$	3.90×10^{-10}	3
712	$CH_4^+ + H_2O \rightarrow H_3O^+ + CH_3$	2.60×10^{-09}	3
713	$CH_3^+ + CH_4 \rightarrow CH_4^+ + CH_3$	1.36×10^{-10}	3
714	$CH_3^+ + CH_4 \rightarrow C_2H_5^+ + H_2$	1.20×10^{-09}	3
715	$CH_3^+ + CH_2 \rightarrow C_2H_3^+ + H_2$	9.90×10^{-10}	3
716	$CH_3^+ + CH \rightarrow C_2H_2^+ + H_2$	7.10×10^{-10}	3

717	$CH_3^+ + C_2H_6 \rightarrow C_2H_5^+ + CH_4$	1.48×10^{-09}	3
718	$CH_3^+ + C_2H_4 \rightarrow C_2H_3^+ + CH_4$	3.50×10^{-10}	3
719	$CH_3^+ + C_2H_3 \rightarrow C_2H_3^+ + CH_3$	3.00×10^{-10}	3
720	$CH_2^+ + CH_4 \rightarrow CH_3^+ + CH_3$	1.38×10^{-10}	3
721	$CH_2^+ + CH_4 \rightarrow C_2H_5^+ + H$	3.60×10^{-10}	3
722	$CH_2^+ + CH_4 \rightarrow C_2H_4^+ + H_2$	8.40×10^{-10}	3
723	$CH_2^+ + CH_4 \rightarrow C_2H_3^+ + H_2 + H$	2.31×10^{-10}	3
724	$CH_2^+ + CH_4 \rightarrow C_2H_2^+ + H_2 + H_2$	3.97×10^{-10}	3
725	$CH_2^+ + H_2 \rightarrow CH_3^+ + H$	1.60×10^{-09}	3
726	$CH^+ + CH_4 \rightarrow C_2H_4^+ + H$	6.50×10^{-11}	3
727	$CH^+ + CH_4 \rightarrow C_2H_3^+ + H_2$	1.09×10^{-09}	3
728	$CH^+ + CH_4 \rightarrow C_2H_2^+ + H_2 + H$	1.43×10^{-10}	3
729	$CH^+ + H_2 \rightarrow CH_2^+ + H$	1.20×10^{-09}	3
730	$CH^+ + H_2O \rightarrow H_3O^+ + C$	5.50×10^{-10}	3
731	$C_2H_6^+ + C_2H_4 \rightarrow C_2H_4^+ + C_2H_6$	1.15×10^{-09}	3
732	$C_2H_6^+ + C_2H_2 \rightarrow C_2H_5^+ + C_2H_3$	2.47×10^{-10}	3
733	$C_2H_6^+ + H \rightarrow C_2H_5^+ + H_2$	1.00×10^{-10}	3
734	$C_2H_6^+ + H_2O \rightarrow H_3O^+ + C_2H_5$	2.95×10^{-09}	3
735	$C_2H_5^+ + H \rightarrow C_2H_4^+ + H_2$	1.00×10^{-11}	3
736	$C_2H_5^+ + H_2O \rightarrow H_3O^+ + C_2H_4$	1.40×10^{-09}	3
737	$C_2H_4^+ + C_2H_3 \rightarrow C_2H_5^+ + C_2H_2$	5.00×10^{-10}	3
738	$C_2H_4^+ + C_2H_3 \rightarrow C_2H_3^+ + C_2H_4$	5.00×10^{-10}	3
739	$C_2H_4^+ + H \rightarrow C_2H_3^+ + H_2$	3.00×10^{-10}	3
740	$C_2H_4^+ + O \rightarrow CH_3^+ + CHO$	1.08×10^{-10}	3
741	$C_2H_3^+ + C_2H_6 \rightarrow C_2H_5^+ + C_2H_4$	2.91×10^{-10}	3

742	$C_2H_3^+ + C_2H_4 \rightarrow C_2H_5^+ + C_2H_2$	8.90×10^{-10}	3
743	$C_2H_3^+ + C_2H_3 \rightarrow C_2H_5^+ + C_2H$	5.00×10^{-10}	3
744	$C_2H_3^+ + C_2H \rightarrow C_2H_2^+ + C_2H_2$	3.30×10^{-10}	3
745	$C_2H_3^+ + H \rightarrow C_2H_2^+ + H_2$	6.80×10^{-11}	3
746	$C_2H_3^+ + H_2O \rightarrow H_3O^+ + C_2H_2$	1.11×10^{-09}	3
747	$C_2H_2^+ + CH_4 \rightarrow C_2H_3^+ + CH_3$	4.10×10^{-09}	3
748	$C_2H_2^+ + C_2H_6 \rightarrow C_2H_5^+ + C_2H_3$	1.31×10^{-10}	3
749	$C_2H_2^+ + C_2H_6 \rightarrow C_2H_4^+ + C_2H_4$	2.48×10^{-10}	3
750	$C_2H_2^+ + C_2H_4 \rightarrow C_2H_4^+ + C_2H_2$	4.14×10^{-10}	3
751	$C_2H_2^+ + C_2H_3 \rightarrow C_2H_3^+ + C_2H_2$	3.30×10^{-10}	3
752	$C_2H_2^+ + H_2 \rightarrow C_2H_3^+ + H$	1.00×10^{-11}	3
753	$C_2H_2^+ + H_2O \rightarrow H_3O^+ + C_2H$	2.20×10^{-10}	3
754	$O_2^+ + CH_2 \rightarrow CH_2^+ + O_2$	4.30×10^{-10}	3
755	$O_2^+ + CH \rightarrow CH^+ + O_2$	3.10×10^{-10}	3
756	$O_2^+ + C_2H_4 \rightarrow C_2H_4^+ + O_2$	6.80×10^{-10}	3
757	$O_2^+ + C_2H_2 \rightarrow C_2H_2^+ + O_2$	1.11×10^{-09}	3
758	$O^- + CH_4 \rightarrow OH^- + CH_3$	1.00×10^{-10}	3
759	$CO_2^+ + CH_4 \rightarrow CH_4^+ + CO_2$	5.50×10^{-10}	3
760	$CO_2^+ + C_2H_4 \rightarrow C_2H_4^+ + CO_2$	1.50×10^{-10}	3
761	$CO_2^+ + C_2H_2 \rightarrow C_2H_2^+ + CO_2$	7.30×10^{-10}	3
762	$H_3O^+ + CH_2 \rightarrow CH_3^+ + H_2O$	9.40×10^{-10}	3
763	$H_3O^+ + CH \rightarrow CH_2^+ + H_2O$	6.80×10^{-10}	3
764	$H_3O^+ + C_2H_3 \rightarrow C_2H_4^+ + H_2O$	2.00×10^{-09}	3
765	$OH^- + CH_3 \rightarrow CH_3OH + e^-$	1.00×10^{-09}	3
766	$OH^- + CH \rightarrow CH_2O + e^-$	5.00×10^{-10}	3

767	$OH^- + C \rightarrow CHO + e^-$	5.00 x 10^{-10}	3
Ion-ion reactions: reaction coefficients included in the model and the references where these data were adopted from.			
768	$CO_3^- + CO_2^+ \rightarrow CO_2 + CO_2 + O$	5.00 x 10^{-07}	1
769	$CO_4^- + CO_2^+ \rightarrow CO_2 + CO_2 + O_2$	5.00 x 10^{-07}	1
770	$O_2^- + CO_2^+ \rightarrow CO + O_2 + O$	6.00 x 10^{-07}	1
771	$CO_3^- + C_2O_2^+ \rightarrow CO_2 + CO + CO + O$	5.00 x 10^{-07}	1
772	$CO_4^- + C_2O_2^+ \rightarrow CO_2 + CO + CO + O_2$	5.00 x 10^{-07}	1
773	$O_2^- + C_2O_2^+ \rightarrow CO + CO + O_2$	6.00 x 10^{-07}	1
774	$CO_3^- + C_2O_3^+ \rightarrow CO_2 + CO_2 + CO + O$	5.00 x 10^{-07}	1
775	$CO_4^- + C_2O_3^+ \rightarrow CO_2 + CO_2 + CO + O_2$	5.00 x 10^{-07}	1
776	$O_2^- + C_2O_3^+ \rightarrow CO_2 + CO + O_2$	6.00 x 10^{-07}	1
777	$CO_3^- + C_2O_4^+ \rightarrow CO_2 + CO_2 + CO_2 + O$	5.00 x 10^{-07}	1
778	$CO_4^- + C_2O_4^+ \rightarrow CO_2 + CO_2 + CO_2 + O_2$	5.00 x 10^{-07}	1
779	$O_2^- + C_2O_4^+ \rightarrow CO_2 + CO_2 + O_2$	6.00 x 10^{-07}	1
780	$O_2^+ + CO_3^- \rightarrow CO_2 + O_2 + O$	3.00 x 10^{-07}	1
781	$O_2^+ + CO_4^- \rightarrow CO_2 + O_2 + O_2$	3.00 x 10^{-07}	1
782	$O^+ + O_2^- + M \rightarrow O_3 + M$	2.00 x 10^{-25}	1
783	$O_2^+ + O_2^- \rightarrow O_2 + O_2$	2.00 x 10^{-07}	1
784	$O_2^+ + O_2^- \rightarrow O_2 + O + O$	4.20 x 10^{-07}	1
785	$O_2^+ + O_2^- + M \rightarrow O_2 + O_2 + M$	2.00 x 10^{-25}	1
786	$O_2^+ + O_3^- \rightarrow O_2 + O_3$	2.00 x 10^{-07}	1
787	$O_2^+ + O_3^- \rightarrow O + O + O_3$	1.00 x 10^{-07}	1
788	$O^+ + O_3^- \rightarrow O_3 + O$	1.00 x 10^{-07}	1
789	$O^+ + O^- + M \rightarrow O_2 + M$	2.00 x 10^{-25}	1
790	$O_2^+ + O^- + M \rightarrow O_3 + M$	2.00 x 10^{-25}	1

791	$O^+ + O^- \rightarrow O + O$	2.60 x 10^{-07}	2
792	$O^+ + O_2^- \rightarrow O + O_2$	2.60 x 10^{-07}	2
793	$O^+ + O_2^- \rightarrow O + O + O$	1.00 x 10^{-07}	2
794	$O^- + O_2^+ \rightarrow O + O_2$	1.45 x 10^{-07}	2
795	$O^- + O_2^+ \rightarrow O + O + O$	1.00 x 10^{-07}	2
796	$O_2^+ + O_2^- \rightarrow O + O + O + O$	1.00 x 10^{-07}	2
797	$O^+ + CO_3^- \rightarrow O + CO_2 + O$	1.00 x 10^{-07}	2
798	$O^+ + CO_4^- \rightarrow O + CO_2 + O_2$	1.00 x 10^{-07}	2
799	$O^- + CO^+ \rightarrow CO + O$	1.93 x 10^{-07}	2
800	$O^- + CO_2^+ \rightarrow CO_2 + O$	1.93 x 10^{-07}	2
801	$O^- + CO_2^+ \rightarrow CO + O + O$	1.00 x 10^{-07}	2
802	$O_2^+ + CO_3^- \rightarrow O + O + CO_2 + O$	1.00 x 10^{-07}	2
803	$O_2^+ + CO_4^- \rightarrow O + O + CO_2 + O_2$	1.00 x 10^{-07}	2
804	$O_2^- + CO^+ \rightarrow O_2 + CO$	1.93 x 10^{-07}	2
805	$O_2^- + CO^+ \rightarrow O + O + CO$	1.00 x 10^{-07}	2
806	$O_2^- + CO_2^+ \rightarrow O_2 + CO_2$	1.93 x 10^{-07}	2
807	$O_2^- + CO_2^+ \rightarrow O + O + CO_2$	1.00 x 10^{-07}	2
808	$O_2^- + CO_2^+ \rightarrow O + O + CO + O$	1.00 x 10^{-07}	2
809	$CO^+ + CO_3^- \rightarrow CO + CO_2 + O$	1.00 x 10^{-07}	2
810	$CO^+ + CO_4^- \rightarrow CO + CO_2 + O_2$	1.00 x 10^{-07}	2
811	$CO_2^+ + CO_3^- \rightarrow CO + O + CO_2 + O$	1.00 x 10^{-07}	2
812	$CO_2^+ + CO_4^- \rightarrow CO + O + CO_2 + O_2$	1.00 x 10^{-07}	2
813	$H^+ + O^- \rightarrow H + O$	1.93 x 10^{-07}	2
814	$H^+ + O_2^- \rightarrow H + O_2$	1.93 x 10^{-07}	2
815	$H^+ + O_2^- \rightarrow H + O + O$	1.00 x 10^{-07}	2

816	$H^+ + CO_3^- \rightarrow H + CO_2 + O$	1.00×10^{-07}	2
817	$H^+ + CO_4^- \rightarrow H + CO_2 + O_2$	1.00×10^{-07}	2
818	$H^+ + H^- \rightarrow H + H$	1.93×10^{-07}	2
819	$H^+ + OH^- \rightarrow OH + H$	1.93×10^{-07}	2
820	$H^+ + OH^- \rightarrow H + O + H$	1.00×10^{-07}	2
821	$H^- + O^+ \rightarrow H + O$	2.22×10^{-07}	2
822	$H^- + O_2^+ \rightarrow O_2 + H$	1.93×10^{-07}	2
823	$H^- + O_2^+ \rightarrow O + O + H$	1.00×10^{-07}	2
824	$H^- + CO^+ \rightarrow CO + H$	1.93×10^{-07}	2
825	$H^- + CO_2^+ \rightarrow CO_2 + H$	1.93×10^{-07}	2
826	$H^- + CO_2^+ \rightarrow CO + O + H$	1.00×10^{-07}	2
827	$H^- + H_2^+ \rightarrow H + H_2$	1.93×10^{-07}	2
828	$H^- + H_2^+ \rightarrow H + H + H$	1.00×10^{-07}	2
829	$H^- + OH^+ \rightarrow H + OH$	1.93×10^{-07}	2
830	$H^- + OH^+ \rightarrow H + O + H$	1.00×10^{-07}	2
831	$H^- + H_2O^+ \rightarrow H_2O + H$	1.93×10^{-07}	2
832	$H^- + H_2O^+ \rightarrow H + H + OH$	1.00×10^{-07}	2
833	$H^- + H_3O^+ \rightarrow H_2 + H_2O$	2.22×10^{-07}	2
834	$H^- + H_3O^+ \rightarrow H + H_2 + OH$	2.22×10^{-07}	2
835	$H_2^+ + O^- \rightarrow H_2 + O$	1.93×10^{-07}	2
836	$H_2^+ + O^- \rightarrow H + H + O$	1.00×10^{-07}	2
837	$H_2^+ + O_2^- \rightarrow H_2 + O_2$	1.93×10^{-07}	2
838	$H_2^+ + O_2^- \rightarrow H + H + O_2$	1.00×10^{-07}	2
839	$H_2^+ + O_2^- \rightarrow H_2 + O + O$	1.00×10^{-07}	2
840	$H_2^+ + O_2^- \rightarrow H + H + O + O$	1.00×10^{-07}	2

841	$H_2^+ + CO_3^- \rightarrow H_2 + CO_2 + O$	1.93 x 10^{-07}	2
842	$H_2^+ + CO_3^- \rightarrow H + H + CO_2 + O$	1.00 x 10^{-07}	2
843	$H_2^+ + CO_4^- \rightarrow H_2 + CO_2 + O_2$	1.93 x 10^{-07}	2
844	$H_2^+ + CO_4^- \rightarrow H + H + CO_2 + O_2$	1.00 x 10^{-07}	2
845	$H_2^+ + OH^- \rightarrow H_2 + OH$	1.93 x 10^{-07}	2
846	$H_2^+ + OH^- \rightarrow OH + H + H$	1.00 x 10^{-07}	2
847	$H_2^+ + OH^- \rightarrow O + H + H_2$	1.00 x 10^{-07}	2
848	$H_2^+ + OH^- \rightarrow O + H + H + H$	1.00 x 10^{-07}	2
849	$OH^+ + O^- \rightarrow O + OH$	1.93 x 10^{-07}	2
850	$OH^+ + O^- \rightarrow O + H + O$	1.00 x 10^{-07}	2
851	$OH^+ + O_2^- \rightarrow OH + O_2$	1.93 x 10^{-07}	2
852	$OH^+ + O_2^- \rightarrow O + H + O_2$	1.00 x 10^{-07}	2
853	$OH^+ + O_2^- \rightarrow OH + O + O$	1.00 x 10^{-07}	2
854	$OH^+ + O_2^- \rightarrow O + H + O + O$	1.00 x 10^{-07}	2
855	$OH^+ + CO_3^- \rightarrow OH + CO_2 + O$	1.00 x 10^{-07}	2
856	$OH^+ + CO_3^- \rightarrow O + H + CO_2 + O$	1.00 x 10^{-07}	2
857	$OH^+ + CO_4^- \rightarrow OH + CO_2 + O_2$	1.00 x 10^{-07}	2
858	$OH^+ + CO_4^- \rightarrow O + H + CO_2 + O_2$	1.00 x 10^{-07}	2
859	$OH^+ + OH^- \rightarrow OH + OH$	1.93 x 10^{-07}	2
860	$OH^+ + OH^- \rightarrow OH + O + H$	1.00 x 10^{-07}	2
861	$OH^+ + OH^- \rightarrow O + H + O + H$	1.00 x 10^{-07}	2
862	$OH^- + O^+ \rightarrow OH + O$	1.93 x 10^{-07}	2
863	$OH^- + O^+ \rightarrow O + H + O$	1.00 x 10^{-07}	2
864	$OH^- + O_2^+ \rightarrow OH + O_2$	1.93 x 10^{-07}	2
865	$OH^- + O_2^+ \rightarrow O + H + O_2$	1.00 x 10^{-07}	2

866	$OH^- + O_2^+ \rightarrow OH + O + O$	1.00×10^{-07}	2
867	$OH^- + O_2^+ \rightarrow O + H + O + O$	1.00×10^{-07}	2
868	$OH^- + CO^+ \rightarrow CO + OH$	1.93×10^{-07}	2
869	$OH^- + CO^+ \rightarrow CO + O + H$	1.00×10^{-07}	2
870	$OH^- + CO_2^+ \rightarrow CO_2 + OH$	1.93×10^{-07}	2
871	$OH^- + CO_2^+ \rightarrow CO_2 + O + H$	1.00×10^{-07}	2
872	$OH^- + CO_2^+ \rightarrow CO + O + OH$	1.00×10^{-07}	2
873	$OH^- + CO_2^+ \rightarrow CO + O + O + H$	1.00×10^{-07}	2
874	$OH^- + H_2O^+ \rightarrow OH + H_2O$	1.93×10^{-07}	2
875	$OH^- + H_2O^+ \rightarrow O + H + H_2O$	1.00×10^{-07}	2
876	$OH^- + H_2O^+ \rightarrow OH + OH + H$	1.00×10^{-07}	2
877	$OH^- + H_2O^+ \rightarrow O + H + OH + H$	1.00×10^{-07}	2
878	$OH^- + H_3O^+ \rightarrow OH + H_2O + H$	1.00×10^{-07}	2
879	$OH^- + H_3O^+ \rightarrow O + H + H_2O + H$	1.00×10^{-07}	2
880	$H_2O^+ + O^- \rightarrow H_2O + O$	1.93×10^{-07}	2
881	$H_2O^+ + O^- \rightarrow OH + H + O$	1.00×10^{-07}	2
882	$H_2O^+ + O_2^- \rightarrow H_2O + O_2$	1.93×10^{-07}	2
883	$H_2O^+ + O_2^- \rightarrow OH + H + O_2$	1.00×10^{-07}	2
884	$H_2O^+ + O_2^- \rightarrow H_2O + O + O$	1.00×10^{-07}	2
885	$H_2O^+ + O_2^- \rightarrow H + OH + O + O$	1.00×10^{-07}	2
886	$H_2O^+ + CO_3^- \rightarrow H_2O + CO_2 + O$	1.00×10^{-07}	2
887	$H_2O^+ + CO_3^- \rightarrow OH + H + CO_2 + O$	1.00×10^{-07}	2
888	$H_2O^+ + CO_4^- \rightarrow H_2O + CO_2 + O_2$	1.00×10^{-07}	2
889	$H_2O^+ + CO_4^- \rightarrow OH + H + CO_2 + O_2$	1.00×10^{-07}	2
890	$H_3O^+ + O^- \rightarrow H_2O + H + O$	1.00×10^{-07}	2

891	$H_3O^+ + O_2^- \rightarrow H_2O + H + O_2$	1.00×10^{-07}	2
892	$H_3O^+ + O_2^- \rightarrow H_2O + H + O + O$	1.00×10^{-07}	2
893	$H_3O^+ + CO_3^- \rightarrow H_2O + H + CO_2 + O$	1.00×10^{-07}	2
894	$H_3O^+ + CO_4^- \rightarrow H_2O + H + CO_2 + O_2$	1.00×10^{-07}	2
895	$H_3^+ + O^- \rightarrow O + H_2 + H$	1.00×10^{-07}	2
896	$H_3^+ + O_2^- \rightarrow O_2 + H_2 + H$	1.00×10^{-07}	2
897	$H_3^+ + O_3^- \rightarrow H_2 + H + O_3$	1.00×10^{-07}	2
898	$H_3^+ + O_3^- \rightarrow H_2 + H + O_2 + O$	1.00×10^{-07}	2
899	$H_3^+ + O_3^- + M \rightarrow H_2 + H + O_3 + M$	1.66×10^{-25}	2
900	$H_3^+ + OH^- \rightarrow OH + H + H_2$	1.00×10^{-07}	2
901	$H_3^+ + OH^- \rightarrow O + H + H + H_2$	1.00×10^{-07}	2
902	$H^- + H_3^+ \rightarrow H_2 + H + H$	1.00×10^{-07}	2

2. References

(1) Snoeckx, R.; Aerts, R.; Tu, X.; Bogaerts, A. *J. Phys. Chem. C* **2013**, *117* (10), 4957.

(2) Aerts, R.; Martens, T.; Bogaerts, A. *J. Phys. Chem. C* **2012**, *116* (44), 23257.

(3) Van Gaens, W.; Bogaerts, A. *J. Phys. D. Appl. Phys.* **2013**, *46*, 275201.

APPENDIX III

Data chemistry set $CH_4 + N_2$

1. Overview of the reactions included in the model

Table A III-1. Electron impact reactions with the various molecules and radicals, included in the model. These reactions are treated by energy-dependent cross sections, and the references where these cross sections were adopted from, are also included.

No.	Reaction	Rate Coefficient	Ref
1	$e^- + CH_4 \rightarrow C + H_2 + H_2 + e^-$	f(σ)	[1]
2	$e^- + CH_4 \rightarrow CH_4 + e^-$	f(σ)	[1]
3	$e^- + CH_4 \rightarrow CH_4^+ + e^- + e^-$	f(σ)	[1]
4	$e^- + CH_4 \rightarrow CH_3^+ + H + e^- + e^-$	f(σ)	[1]
5	$e^- + CH_4 \rightarrow CH_2^+ + H_2 + e^- + e^-$	f(σ)	[1]
6	$e^- + CH_4 \rightarrow CH_3 + H + e^-$	f(σ)	[1]
7	$e^- + CH_4 \rightarrow CH_2 + H_2 + e^-$	f(σ)	[1]
8	$e^- + CH_4 \rightarrow CH + H_2 + H + e^-$	f(σ)	[1]
9	$e^- + CH_3 \rightarrow CH_2^+ + H + e^- + e^-$	f(σ)	[1]
10	$e^- + CH_3 \rightarrow CH_2 + H + e^-$	f(σ)	[1]
11	$e^- + CH_3 \rightarrow CH + H_2 + e^-$	f(σ)	[1]
12	$e^- + CH_3 \rightarrow CH_3^+ + e^- + e^-$	f(σ)	[1]
13	$e^- + CH_3 \rightarrow CH^+ + H_2 + e^- + e^-$	f(σ)	[1]
14	$e^- + CH_2 \rightarrow CH^+ + H + e^- + e^-$	f(σ)	[1]
15	$e^- + CH_2 \rightarrow CH + H + e^-$	f(σ)	[1]
16	$e^- + CH_2 \rightarrow CH_2^+ + e^- + e^-$	f(σ)	[1]
17	$e^- + CH_2 \rightarrow C^+ + H_2 + e^- + e^-$	f(σ)	[1]
18	$e^- + CH \rightarrow C^+ + H + e^- + e^-$	f(σ)	[1]
19	$e^- + CH \rightarrow C + H + e^-$	f(σ)	[1]
20	$e^- + CH \rightarrow CH^+ + e^- + e^-$	f(σ)	[1]

21	$e^- + C \rightarrow C^+ + e^- + e^-$	f(σ)	[1]
22	$e^- + C_2H_6 \rightarrow C_2H_6 + e^-$	f(σ)	[1]
23	$e^- + C_2H_6 \rightarrow C_2H_6^+ + e^- + e^-$	f(σ)	[1]
24	$e^- + C_2H_6 \rightarrow C_2H_5^+ + H + e^- + e^-$	f(σ)	[1]
25	$e^- + C_2H_6 \rightarrow C_2H_4^+ + H_2 + e^- + e^-$	f(σ)	[1]
26	$e^- + C_2H_6 \rightarrow C_2H_3^+ + H_2 + H + e^- + e^-$	f(σ)	[1]
27	$e^- + C_2H_6 \rightarrow C_2H_2^+ + H_2 + H_2 + e^- + e^-$	f(σ)	[1]
28	$e^- + C_2H_6 \rightarrow CH_3^+ + CH_3 + e^- + e^-$	f(σ)	[1]
29	$e^- + C_2H_6 \rightarrow C_2H_5 + H + e^-$	f(σ)	[1]
30	$e^- + C_2H_6 \rightarrow C_2H_4 + H_2 + e^-$	f(σ)	[1]
31	$e^- + C_2H_5 \rightarrow C_2H_4^+ + H + e^- + e^-$	f(σ)	[1]
32	$e^- + C_2H_5 \rightarrow C_2H_3^+ + H_2 + e^- + e^-$	f(σ)	[1]
33	$e^- + C_2H_5 \rightarrow C_2H_2^+ + H_2 + H + e^- + e^-$	f(σ)	[1]
34	$e^- + C_2H_5 \rightarrow C_2H_4 + H + e^-$	f(σ)	[1]
35	$e^- + C_2H_5 \rightarrow C_2H_3 + H_2 + e^-$	f(σ)	[1]
36	$e^- + C_2H_5 \rightarrow C_2H_5^+ + e^- + e^-$	f(σ)	[1]
37	$e^- + C_2H_4 \rightarrow C_2H_4 + e^-$	f(σ)	[1]
38	$e^- + C_2H_4 \rightarrow C_2H_4^+ + e^- + e^-$	f(σ)	[1]
39	$e^- + C_2H_4 \rightarrow C_2H_3^+ + H + e^- + e^-$	f(σ)	[1]
40	$e^- + C_2H_4 \rightarrow C_2H_2^+ + H_2 + e^- + e^-$	f(σ)	[1]
41	$e^- + C_2H_4 \rightarrow C_2H_3 + H + e^-$	f(σ)	[1]
42	$e^- + C_2H_4 \rightarrow C_2H_2 + H_2 + e^-$	f(σ)	[1]
43	$e^- + C_2H_3 \rightarrow C_2H_2^+ + H + e^- + e^-$	f(σ)	[1]
44	$e^- + C_2H_3 \rightarrow C_2H^+ + H_2 + e^- + e^-$	f(σ)	[1]
45	$e^- + C_2H_3 \rightarrow C_2H_2 + H + e^-$	f(σ)	[1]

46	$e^- + C_2H_3 \rightarrow C_2H + H_2 + e^-$	f(σ)	[1]
47	$e^- + C_2H_3 \rightarrow C_2H_3^+ + e^- + e^-$	f(σ)	[1]
48	$e^- + C_2H_2 \rightarrow C_2H_2 + e^-$	f(σ)	[1]
49	$e^- + C_2H_2 \rightarrow C_2H_2^+ + e^- + e^-$	f(σ)	[1]
50	$e^- + C_2H_2 \rightarrow C_2H + H + e^-$	f(σ)	[1]
51	$e^- + C_2H_2 \rightarrow C_2 + H_2 + e^-$	f(σ)	[1]
52	$e^- + C_2H \rightarrow C_2H^+ + e^- + e^-$	f(σ)	[1]
53	$e^- + C_2H \rightarrow C_2 + H + e^-$	f(σ)	[1]
54	$e^- + C_2H \rightarrow C + CH + e^-$	f(σ)	[1]
55	$e^- + C_2 \rightarrow C_2^+ + e^- + e^-$	f(σ)	[1]
56	$e^- + C_2 \rightarrow C + C + e^-$	f(σ)	[1]
57	$e^- + C_3H_8 \rightarrow C_3H_8 + e^-$	f(σ)	[1]
58	$e^- + C_3H_8 \rightarrow C_2H_5^+ + CH_3 + e^- + e^-$	f(σ)	[1]
59	$e^- + C_3H_8 \rightarrow C_2H_4^+ + CH_4 + e^- + e^-$	f(σ)	[1]
60	$e^- + C_3H_8 \rightarrow C_3H_7 + H + e^-$	f(σ)	[1]
61	$e^- + C_3H_8 \rightarrow C_2H_4 + CH_4 + e^-$	f(σ)	[1]
62	$e^- + C_3H_8 \rightarrow C_3H_6 + H_2 + e^-$	f(σ)	[1]
63	$e^- + C_3H_7 \rightarrow C_2H_5^+ + CH_2 + e^- + e^-$	f(σ)	[1]
64	$e^- + C_3H_7 \rightarrow C_2H_4^+ + CH_3 + e^- + e^-$	f(σ)	[1]
65	$e^- + C_3H_7 \rightarrow C_2H_3^+ + CH_4 + e^- + e^-$	f(σ)	[1]
66	$e^- + C_3H_7 \rightarrow CH_3^+ + C_2H_4 + e^- + e^-$	f(σ)	[1]
67	$e^- + C_3H_7 \rightarrow C_2H_4 + CH_3 + e^-$	f(σ)	[1]
68	$e^- + C_3H_7 \rightarrow C_2H_3 + CH_4 + e^-$	f(σ)	[1]
69	$e^- + C_3H_7 \rightarrow C_3H_6 + H + e^-$	f(σ)	[1]
70	$e^- + C_3H_7 \rightarrow C_3H_5 + H_2 + e^-$	f(σ)	[1]

71	$e^- + C_3H_6 \rightarrow C_2H_5^+ + CH + e^- + e^-$	f(σ)	[1]
72	$e^- + C_3H_6 \rightarrow C_2H_4^+ + CH_2 + e^- + e^-$	f(σ)	[1]
73	$e^- + C_3H_6 \rightarrow C_2H_3^+ + CH_3 + e^- + e^-$	f(σ)	[1]
74	$e^- + C_3H_6 \rightarrow C_2H_2^+ + CH_4 + e^- + e^-$	f(σ)	[1]
75	$e^- + C_3H_6 \rightarrow CH_3^+ + C_2H_3 + e^- + e^-$	f(σ)	[1]
76	$e^- + C_3H_6 \rightarrow C_3H_5 + H + e^-$	f(σ)	[1]
77	$e^- + C_3H_6 \rightarrow C_2H_2 + CH_4 + e^-$	f(σ)	[1]
78	$e^- + C_3H_5 \rightarrow C_2H_3^+ + CH_2 + e^- + e^-$	f(σ)	[1]
79	$e^- + C_3H_5 \rightarrow C_2H_2^+ + CH_3 + e^- + e^-$	f(σ)	[1]
80	$e^- + C_3H_5 \rightarrow CH_3^+ + C_2H_2 + e^- + e^-$	f(σ)	[1]
81	$e^- + C_3H_5 \rightarrow C_2H_2 + CH_3 + e^-$	f(σ)	[1]
82	$e^- + H_2 \rightarrow e^- + H_2$	f(σ)	[2]
83	$e^- + H_2 \rightarrow H_2(rot.) + e^-$	f(σ)	[2]
84	$e^- + H_2 \rightarrow H_2(rot.) + e^-$	f(σ)	[2]
85	$e^- + H_2 \rightarrow H_2(vib.) + e^-$	f(σ)	[2]
86	$e^- + H_2 \rightarrow H_2(vib.) + e^-$	f(σ)	[2]
87	$e^- + H_2 \rightarrow H_2^* + e^-$	f(σ)	[2]
88	$e^- + H_2 \rightarrow H_2^* + e^-$	f(σ)	[2]
89	$e^- + H_2 \rightarrow e^- + H + H$	f(σ)	[2]
90	$e^- + H_2 \rightarrow e^- + e^- + H_2^+$	f(σ)	[2]
91	$e^- + H_2^* \rightarrow H_2^* + e^-$	f(σ)	[2]
92	$e^- + H_2^* \rightarrow H_2 + e^-$	f(σ)	[2]
93	$e^- + H_2^* \rightarrow H_2^+ + e^- + e^-$	f(σ)	[2]
94	$e^- + H \rightarrow e^- + H$	f(σ)	[2]
95	$e^- + H \rightarrow H^* + e^-$	f(σ)	[2]

96	$e^- + H \rightarrow H* + e^-$	$f(\sigma)$	[2]
97	$e^- + H \rightarrow H* + e^-$	$f(\sigma)$	[2]
98	$e^- + H \rightarrow e^- + H^+ + e^-$	$f(\sigma)$	[2]
99	$e^- + H* \rightarrow H* + e^-$	$f(\sigma)$	[2]
100	$e^- + H* \rightarrow H + e^-$	$f(\sigma)$	[2]
101	$e^- + H* \rightarrow H^+ + e^- + e^-$	$f(\sigma)$	[2]
102	$e^- + N_2 \rightarrow e^- + N_2$	$f(\sigma)$	[2]
103	$e^- + N_2 \rightarrow e^- + N_2(rot.)$	$f(\sigma)$	[2]
104	$e^- + N_2 \rightarrow N_2(vib.) + e^-$	$f(\sigma)$	[2]
105	$e^- + N_2 \rightarrow N_2(vib.) + e^-$	$f(\sigma)$	[2]
106	$e^- + N_2 \rightarrow N_2(vib.) + e^-$	$f(\sigma)$	[2]
107	$e^- + N_2 \rightarrow N_2(vib.) + e^-$	$f(\sigma)$	[2]
108	$e^- + N_2 \rightarrow N_2(vib.) + e^-$	$f(\sigma)$	[2]
109	$e^- + N_2 \rightarrow N_2(vib.) + e^-$	$f(\sigma)$	[2]
110	$e^- + N_2 \rightarrow N_2(vib.) + e^-$	$f(\sigma)$	[2]
111	$e^- + N_2 \rightarrow e^- + N_2*$	$f(\sigma)$	[2]
112	$e^- + N_2 \rightarrow e^- + N_2(a'^1)$	$f(\sigma)$	[2]
113	$e^- + N_2 \rightarrow e^- + N + N$	$f(\sigma)$	[2]
114	$e^- + N_2 \rightarrow e^- + N^+ + N + e^-$	$f(\sigma)$	[2]
115	$e^- + N_2 \rightarrow e^- + e^- + N_2^+$	$f(\sigma)$	[2]
116	$e^- + N_2(vib.) \rightarrow N_2(vib.) + e^-$	$f(\sigma)$	[2]
117	$e^- + N_2(vib.) \rightarrow N_2 + e^-$	$f(\sigma)$	[2]
118	$e^- + N_2(vib.) \rightarrow N_2* + e^-$	$f(\sigma)$	[2]
119	$e^- + N_2(vib.) \rightarrow N_2^+ + e^- + e^-$	$f(\sigma)$	[2]
120	$e^- + N_2* \rightarrow e^- + N_2*$	$f(\sigma)$	[2]

121	$e^- + N_2^* \rightarrow e^- + N_2$	f(σ)	2
122	$e^- + N_2^* \rightarrow N_2(\text{vib.}) + e^-$	f(σ)	2
123	$e^- + N_2^* \rightarrow e^- + N_2^+ + e^-$	f(σ)	2
124	$e^- + N_2(a'^1) \rightarrow N_2(a'^1) + e^-$	f(σ)	2
125	$e^- + N_2(a'^1) \rightarrow e^- + N_2$	f(σ)	2
126	$e^- + N_2(a'^1) \rightarrow N_2^+ + e^- + e^-$	f(σ)	2
127	$e^- + N \rightarrow e^- + N$	f(σ)	2
128	$e^- + N \rightarrow e^- + N^*$	f(σ)	2
129	$e^- + N \rightarrow e^- + N^+ + e^-$	f(σ)	2
130	$e^- + N^* \rightarrow e^- + N^*$	f(σ)	2
131	$e^- + N^* \rightarrow e^- + N$	f(σ)	2
132	$e^- + N^* \rightarrow e^- + N^+ + e^-$	f(σ)	2
133	$e^- + NH \rightarrow NH + e^-$	f(σ)	2
134	$e^- + NH \rightarrow N + H + e^-$	f(σ)	2
135	$e^- + NH \rightarrow N^+ + H + e^- + e^-$	f(σ)	2

Table A III-2. Electron-ion reactions included in the model and the references where these data were adopted from. Some reactions are treated by energy-dependent cross sections, for others the reaction coefficients are given by the Arrhenius function: $k(T) = A\ (T/300\ K)^n \exp(-E/RT)$ where T is the gas mixture temperature (in K) and A is given in units of $cm^3\ s^{-1}$ for two-body collisions and in $cm^6\ s^{-1}$ for three-body collisions. In the latter case, the values for A and n are listed in the table. If no values are listed for n and E/R, it means that these values are assumed to be zero, and the rate coefficient is just equal to A.

No	Reaction	A	n	Ref
1	$e^- + CH_5^+ \rightarrow CH_3 + H + H$	2.57E-07	-0.30	1
2	$e^- + CH_5^+ \rightarrow CH_2 + H_2 + H$	6.61E-08	-0.30	1
3	$e^- + CH_4^+ \rightarrow CH_3 + H$	1.18E-08	-0.50	1

4	$e^- + CH_4^+ \rightarrow CH_2 + H + H$	2.42E-08	-0.50	[1]
5	$e^- + CH_4^+ \rightarrow CH + H_2 + H$	1.41E-08	-0.50	[1]
6	$e^- + CH_3^+ \rightarrow CH_2 + H$	2.25E-08	-0.50	[1]
7	$e^- + CH_3^+ \rightarrow CH + H_2$	7.88E-09	-0.50	[1]
8	$e^- + CH_3^+ \rightarrow CH + H + H$	9.00E-09	-0.50	[1]
9	$e^- + CH_3^+ \rightarrow C + H_2 + H$	1.69E-08	-0.50	[1]
10	$e^- + CH_2^+ \rightarrow CH + H$	1.00E-08	-0.50	[1]
11	$e^- + CH_2^+ \rightarrow C + H_2$	4.82E-09	-0.50	[1]
12	$e^- + CH_2^+ \rightarrow C + H + H$	2.53E-08	-0.50	[1]
13	$e^- + CH^+ \rightarrow C + H$	3.23E-08	-0.42	[1]
14	$e^- + C_2H_6^+ \rightarrow C_2H_5 + H$	2.19E-08	-0.71	[1]
15	$e^- + C_2H_6^+ \rightarrow C_2H_4 + H + H$	3.36E-08	-0.71	[1]
16	$e^- + C_2H_5^+ \rightarrow C_2H_4 + H$	7.70E-09	-0.71	[1]
17	$e^- + C_2H_5^+ \rightarrow C_2H_3 + H + H$	1.92E-08	-0.71	[1]
18	$e^- + C_2H_5^+ \rightarrow C_2H_2 + H_2 + H$	1.60E-08	-0.71	[1]
19	$e^- + C_2H_5^+ \rightarrow C_2H_2 + H + H + H$	8.98E-09	-0.71	[1]
20	$e^- + C_2H_5^+ \rightarrow CH_3 + CH_2$	9.62E-09	-0.71	[1]
21	$e^- + C_2H_4^+ \rightarrow C_2H_3 + H$	8.29E-09	-0.71	[1]
22	$e^- + C_2H_4^+ \rightarrow C_2H_2 + H + H$	3.43E-08	-0.71	[1]
23	$e^- + C_2H_4^+ \rightarrow C_2H + H_2 + H$	5.53E-09	-0.71	[1]
24	$e^- + C_2H_3^+ \rightarrow C_2H_2 + H$	1.34E-08	-0.71	[1]
25	$e^- + C_2H_3^+ \rightarrow C_2H + H + H$	2.74E-08	-0.71	[1]
26	$e^- + C_2H_2^+ \rightarrow C_2H + H$	1.87E-08	-0.71	[1]
27	$e^- + C_2H_2^+ \rightarrow C_2 + H + H$	1.12E-08	-0.71	[1]
28	$e^- + C_2H_2^+ \rightarrow CH + CH$	4.87E-09	-0.71	[1]

29	$e^- + C_2H^+ \rightarrow C_2 + H$	1.34E-08	-0.71	1
30	$e^- + C_2H^+ \rightarrow CH + C$	1.09E-08	-0.71	1
31	$e^- + C_2H^+ \rightarrow C + C + H$	4.29E-09	-0.71	1
32	$e^- + C_2^+ \rightarrow C + C$	1.19E-08	-0.71	1
33	$e^- + H_3^+ \rightarrow H_2 + H$	f(σ)		2
34	$e^- + H_3^+ \rightarrow H + H + H$	f(σ)		2
35	$e^- + H_2^+ \rightarrow H + H$	f(σ)		2
36	$e^- + H^+ \rightarrow H$	f(σ)		2
37	$e^- + N_4^+ \rightarrow N_2 + N_2$	3.21E-07	-0.50	2
38	$e^- + N_4^+ \rightarrow N_2 + N + N$	3.13E-07	-0.41	2
39	$e^- + N_3^+ \rightarrow N + N_2$	3.22E-08	-0.50	2
40	$e^- + N_2^+ \rightarrow N + N$	f(σ)		2
41	$e^- + M + N_2^+ \rightarrow N_2 + M$	4.31E-34	-4.50	2
42	$e^- + N^+ \rightarrow N$	f(σ)		2
43	$e^- + N^+ + M \rightarrow N + M$	2.49E-29	-1.50	2
44	$e^- + H_3^+ \rightarrow H_3^+ + e^-$	f(σ)		2
45	$e^- + H_3^+ \rightarrow e^- + H_2 + H^+$	f(σ)		2
46	$e^- + H_3^+ \rightarrow e^- + H + H + H^+$	f(σ)		2
47	$e^- + H_2^+ \rightarrow e^- + H_2^+$	f(σ)		2
48	$e^- + H_2^+ \rightarrow e^- + H^+ + H$	f(σ)		2
49	$e^- + H_2^+ \rightarrow H^+ + H^-$	f(σ)		2
50	$e^- + H^+ \rightarrow e^- + H^+$	f(σ)		2
51	$e^- + H^+ + e^- \rightarrow e^- + H$	8.80E-27	-4.50	2
52	$e^- + H^- \rightarrow e^- + e^- + H$	f(σ)		2
53	$e^- + H^- \rightarrow e^- + H^-$	f(σ)		2

54	$e^- + N_4^+ \rightarrow e^- + N_4^+$	f(σ)		2
55	$e^- + N_3^+ \rightarrow e^- + N_3^+$	f(σ)		2
56	$e^- + N_2^+ \rightarrow e^- + N_2^+$	f(σ)		2
57	$e^- + e^- + N_2^+ \rightarrow N_2 + e^-$	7.18E-27	-4.50	2
58	$e^- + N^+ \rightarrow e^- + N^+$	f(σ)		2
59	$e^- + N^+ + e^- \rightarrow N + e^-$	5.40E-24	-4.50	2

Table A III-3. Ion-ion reactions included in the model and the references where these data were adopted from. Reaction coefficients are given by the Arrhenius function: $k(T) = A\ (T/300\ K)^n \exp(-E/RT)$ where T is the gas mixture temperature (in K) and A is given in units of $cm^3\ s^{-1}$ for two-body collisions and in $cm^6\ s^{-1}$ for three-body collisions. If no values are listed for n and E/R, it means that these values are assumed to be zero, and the rate coefficient is just equal to A.

No	Reaction	A	n	Ref
1	$H^- + H_3^+ \rightarrow H_2 + H + H$	1.00E-07		2
2	$H^- + H_2^+ \rightarrow H + H_2$	2.00E-07	-0.50	2
3	$H^- + H_2^+ \rightarrow H + H + H$	1.00E-07		2
4	$H^- + H_2^+ + M \rightarrow H + H_2 + M$	2.00E-25	-2.50	2
5	$H^+ + H^- \rightarrow H + H$	2.00E-07	-0.50	2
6	$H^+ + H^- + M \rightarrow H + H + M$	2.00E-25	-2.50	2
7	$H^- + N_4^+ \rightarrow N_2 + N_2 + H$	1.00E-07		2
8	$H^- + N_3^+ \rightarrow NH + N_2$	3.00E-06	-0.50	3
9	$H^- + N_3^+ \rightarrow N + N_2 + H$	1.00E-07		2
10	$H^- + N_2^+ \rightarrow N_2 + H$	2.00E-07	-0.50	2
11	$H^- + N_2^+ \rightarrow N + N + H$	1.00E-07		2
12	$H^- + N_2^+ + M \rightarrow N_2 + H + M$	2.00E-25	-2.50	2
13	$H^- + N^+ \rightarrow N + H$	2.00E-07	-0.50	2

14	$H^- + N^+ + M \rightarrow NH + M$	2.00E-25	-2.50	2

Table A III-4. Neutral-neutral reactions included in the model and the references where these data were adopted from. Reaction coefficients are given by the Arrhenius function: $k(T) = A (T/300\ K)^n \exp(-E/RT)$ where T is the gas mixture temperature (in K) and A is given in units of $cm^3\ s^{-1}$ for two-body collisions and in $cm^6\ s^{-1}$ for three-body collisions. If no values are listed for n and E/R, it means that these values are assumed to be zero, and the rate coefficient is just equal to A.

No	Reaction	A	n	E/R	Ref
1	$CH_4 + CH_2 \rightarrow CH_3 + CH_3$	3.01E-19			1
2	$CH_4 + CH \rightarrow C_2H_4 + H$	9.74E-11			1
3	$CH_4 + C_2H_5 \rightarrow C_2H_6 + CH_3$	1.83E-24			1
4	$CH_4 + C_2H_3 \rightarrow C_2H_4 + CH_3$	2.28E-18			1
5	$CH_4 + C_2H \rightarrow C_2H_2 + CH_3$	1.31E-12			1
6	$CH_4 + C_3H_7 \rightarrow C_3H_8 + CH_3$	4.38E-24			1
7	$CH_4 + H \rightarrow CH_3 + H_2$	8.43E-19			1
8	$CH_3 + CH_3 \rightarrow C_2H_5 + H$	2.71E-19			1
9	$CH_3 + CH_3 + CH_4 \rightarrow C_2H_6 + CH_4$	4.23E-29	-0.784	310	4,5
10	$CH_3 + CH_3 + N_2 \rightarrow C_2H_6 + N_2$	1.41E-29	-0.784	310	5
11	$CH_3 + CH_2 \rightarrow C_2H_4 + H$	7.01E-11			1
12	$CH_3 + C_2H_6 \rightarrow C_2H_5 + CH_4$	7.21E-21			1
13	$CH_3 + C_2H_5 \rightarrow C_2H_4 + CH_4$	1.91E-12			1
14	$CH_3 + C_2H_5 + CH_4 \rightarrow C_3H_8 + CH_4$	1.00E-28			1
15	$CH_3 + C_2H_5 + N_2 \rightarrow C_3H_8 + N_2$	1.00E-28			1
16	$CH_3 + C_2H_4 \rightarrow C_2H_3 + CH_4$	1.94E-21			1
17	$CH_3 + C_2H_3 \rightarrow C_2H_2 + CH_4$	6.51E-13			1
18	$CH_3 + C_2H_3 + CH_4 \rightarrow C_3H_6 + CH_4$	4.91E-30			1

19	$CH_3 + C_2H_3 + N_2 \rightarrow C_3H_6 + N_2$	4.91E-30			1
20	$CH_3 + C_2H_2 \rightarrow CH_4 + C_2H$	7.65E-26			1
21	$CH_3 + C_3H_8 \rightarrow C_3H_7 + CH_4$	1.02E-20			1
22	$CH_3 + C_3H_7 \rightarrow C_3H_6 + CH_4$	3.07E-12			1
23	$CH_3 + C_3H_6 \rightarrow C_3H_5 + CH_4$	1.24E-19			1
24	$CH_3 + H_2 \rightarrow CH_4 + H$	9.60E-21			1
25	$CH_3 + H \rightarrow CH_2 + H_2$	9.96E-22			1
26	$CH_3 + H + CH_4 \rightarrow CH_4 + CH_4$	2.97E-28			1
27	$CH_3 + H + N_2 \rightarrow CH_4 + N_2$	4.09E-29	-1.15	175	5
28	$CH_2 + CH_2 \rightarrow C_2H_2 + H_2$	5.27E-11			1
29	$CH_2 + C_2H_5 \rightarrow C_2H_4 + CH_3$	3.01E-11			1
30	$CH_2 + C_2H_3 \rightarrow C_2H_2 + CH_3$	3.01E-11			1
31	$CH_2 + C_2H \rightarrow C_2H_2 + CH$	3.01E-11			1
32	$CH_2 + C_3H_8 \rightarrow C_3H_7 + CH_3$	1.02E-20			1
33	$CH_2 + C_3H_7 \rightarrow C_2H_4 + C_2H_5$	3.01E-11			1
34	$CH_2 + C_3H_7 \rightarrow C_3H_6 + CH_3$	3.01E-12			1
35	$CH_2 + C_3H_6 \rightarrow C_3H_5 + CH_3$	3.65E-17			1
36	$CH_2 + H_2 \rightarrow CH_3 + H$	5.00E-15			1
37	$CH_2 + H \rightarrow CH + H_2$	2.01E-10			1
38	$CH + C_2H_6 + CH_4 \rightarrow C_3H_7 + CH_4$	1.14E-29			1
39	$CH + C_2H_6 + N_2 \rightarrow C_3H_7 + N_2$	1.14E-29			1
40	$CH + H_2 \rightarrow CH_2 + H$	6.80E-13			1
41	$CH + H \rightarrow C + H_2$	1.00E-10			1
42	$C + H_2 \rightarrow CH + H$	1.50E-10			1
43	$C_2H_6 + C_2H_3 \rightarrow C_2H_5 + C_2H_4$	3.39E-21			1

44	$C_2H_6 + C_2H \rightarrow C_2H_2 + C_2H_5$	5.99E-12			[1]
45	$C_2H_6 + C_3H_7 \rightarrow C_3H_8 + C_2H_5$	3.16E-22			[1]
46	$C_2H_6 + H \rightarrow C_2H_5 + H_2$	4.96E-17			[1]
47	$C_2H_5 + C_2H_5 \rightarrow C_2H_6 + C_2H_4$	2.41E-12			[1]
48	$C_2H_5 + C_2H \rightarrow C_2H_4 + C_2H_2$	3.01E-12			[1]
49	$C_2H_5 + C_3H_8 \rightarrow C_2H_6 + C_3H_7$	3.62E-22			[1]
50	$C_2H_5 + C_3H_7 \rightarrow C_3H_8 + C_2H_4$	1.91E-12			[1]
51	$C_2H_5 + C_3H_7 \rightarrow C_3H_6 + C_2H_6$	2.41E-12			[1]
52	$C_2H_5 + C_3H_6 \rightarrow C_3H_5 + C_2H_6$	2.53E-20			[1]
53	$C_2H_5 + C_3H_5 \rightarrow C_3H_6 + C_2H_4$	5.36E-12			[1]
54	$C_2H_5 + H_2 \rightarrow C_2H_6 + H$	2.97E-21			[1]
55	$C_2H_5 + H \rightarrow CH_3 + CH_3$	5.99E-11			[1]
56	$C_2H_5 + H \rightarrow C_2H_4 + H_2$	3.01E-12			[1]
57	$C_2H_5 + H + CH_4 \rightarrow C_2H_6 + CH_4$	9.20E-30			[1]
58	$C_2H_5 + H + N_2 \rightarrow C_2H_6 + N_2$	9.20E-30			[1]
59	$C_2H_4 + C_2H \rightarrow C_2H_2 + C_2H_3$	1.40E-10			[1]
60	$C_2H_4 + H \rightarrow C_2H_3 + H_2$	4.92E-21			[1]
61	$C_2H_4 + H + CH_4 \rightarrow C_2H_5 + CH_4$	3.66E-30			[1]
62	$C_2H_4 + H + N_2 \rightarrow C_2H_5 + N_2$	8.19E-30			[1]
63	$C_2H_3 + C_2H_3 \rightarrow C_2H_4 + C_2H_2$	1.60E-12			[1]
64	$C_2H_3 + C_2H \rightarrow C_2H_2 + C_2H_2$	1.60E-12			[1]
65	$C_2H_3 + C_3H_8 \rightarrow C_2H_4 + C_3H_7$	3.40E-21			[1]
66	$C_2H_3 + C_3H_7 \rightarrow C_3H_8 + C_2H_2$	2.01E-12			[1]
67	$C_2H_3 + C_3H_7 \rightarrow C_3H_6 + C_2H_4$	2.01E-12			[1]
68	$C_2H_3 + C_3H_6 \rightarrow C_3H_5 + C_2H_4$	6.58E-19			[1]

69	$C_2H_3 + C_3H_5 \rightarrow C_3H_6 + C_2H_2$	8.00E-12			1
70	$C_2H_3 + H_2 \rightarrow C_2H_4 + H$	9.78E-20			1
71	$C_2H_3 + H \rightarrow C_2H_2 + H_2$	2.01E-11			1
72	$C_2H_3 + H + CH_4 \rightarrow C_2H_4 + CH_4$	8.26E-30			1
73	$C_2H_3 + H + N_2 \rightarrow C_2H_4 + N_2$	8.26E-30			1
74	$C_2H_2 + C_2H \rightarrow C_4H_2 + H$	1.50E-10			1
75	$C_2H_2 + H \rightarrow C_2H + H_2$	6.12E-27			1
76	$C_2H_2 + H + CH_4 \rightarrow C_2H_3 + CH_4$	2.81E-31			1
77	$C_2H_2 + H + N_2 \rightarrow C_2H_3 + N_2$	5.05E-31			1
78	$C_2H + C_2H \rightarrow C_2H_2 + C_2$	3.01E-12			1
79	$C_2H + C_3H_8 \rightarrow C_2H_2 + C_3H_7$	5.99E-12			1
80	$C_2H + C_3H_7 \rightarrow C_3H_6 + C_2H_2$	1.00E-11			1
81	$C_2H + C_3H_6 \rightarrow C_3H_5 + C_2H_2$	5.99E-12			1
82	$C_2H + H_2 \rightarrow C_2H_2 + H$	1.52E-13			1
83	$C_2H + H + CH_4 \rightarrow C_2H_2 + CH_4$	9.44E-30			1
84	$C_2H + H + N_2 \rightarrow C_2H_2 + N_2$	9.44E-30			1
85	$C_3H_8 + H \rightarrow C_3H_7 + H_2$	5.15E-17			1
86	$C_3H_7 + C_3H_7 \rightarrow C_3H_6 + C_3H_8$	2.81E-12			1
87	$C_3H_7 + C_3H_6 \rightarrow C_3H_5 + C_3H_8$	2.53E-20			1
88	$C_3H_7 + C_3H_5 \rightarrow C_3H_6 + C_3H_6$	3.00E-12			1
89	$C_3H_7 + H_2 \rightarrow C_3H_8 + H$	7.12E-21			1
90	$C_3H_7 + H \rightarrow C_3H_6 + H_2$	3.01E-12			1
91	$C_3H_7 + H + CH_4 \rightarrow C_3H_8 + CH_4$	3.96E-30			1
92	$C_3H_7 + H + N_2 \rightarrow C_3H_8 + N_2$	3.96E-30			1
93	$C_3H_6 + H \rightarrow C_3H_5 + H_2$	6.94E-15			1

94	$C_3H_6 + H + CH_4 \rightarrow C_3H_7 + CH_4$	3.79E-33			1
95	$C_3H_6 + H + N_2 \rightarrow C_3H_7 + N_2$	3.79E-33			1
96	$C_3H_5 + H + CH_4 \rightarrow C_3H_6 + CH_4$	1.33E-29			1
97	$C_3H_5 + H + N_2 \rightarrow C_3H_6 + N_2$	1.33E-29			1
98	$CH_4 + CN \rightarrow CH_3 + HCN$	1.00E-11		857	6
99	$CH_4 + N + H \rightarrow NH + CH_4$	5.00E-32			7
100	$CH_3 + N \rightarrow HCN + H_2$	1.40E-11			6
101	$CH_3 + N \rightarrow H_2CN + H$	9.61E-11			6
102	$CH_2 + N \rightarrow HCN + H$	5.00E-11		250	6
103	$CH_2 + N \rightarrow CN + H + H$	1.60E-11			6
104	$CH_2 + N \rightarrow H_2 + CN$	1.60E-11			5
105	$C + N_2 \rightarrow CN + N$	1.04E-10		23,000	6
106	$C_2H_4 + N \rightarrow HCN + CH_3$	3.30E-14		353	5
107	$C_2H_2 + N \rightarrow CH + HCN$	2.70E-15			5
108	$C_3H_6 + N \rightarrow HCN + C_2H_5$	1.94E-13		654	5
109	$H_2 + H \rightarrow H + H + H$	4.67E-07	-1.00	55,000	2
110	$H_2 + N \rightarrow NH + H$	1.69E-09		18,095	2
111	$H_2 + N + NH_3 \rightarrow NH_2 + NH_3$	1.00E-36			7
112	$H_2 + CN \rightarrow H + HCN$	4.98E-19	2.45	1,118	6
113	$H + HCN + N_2 \rightarrow H_2CN + N_2$	4.84E-30		2,440	5
114	$H + H + CH_4 \rightarrow H_2 + CH_4$	6.00E-33			1
115	$H + H + H_2 \rightarrow H_2 + H_2$	4.00E-32	-1.00		2
116	$H + H + N_2 \rightarrow H_2 + N_2$	2.00E-32	-1.00		2
117	$H + N + N_2 \rightarrow NH + N_2$	5.00E-32			2
118	$H + N + H_2 \rightarrow NH + H_2$	1.00E-31			2

119	$H + NH_2 \rightarrow NH + H_2$	1.00E-11			[5]
120	$H + NH_2 + M \rightarrow NH_3 + M$	6.00E-30			[7]
121	$H + NH \rightarrow H_2 + N$	1.70E-11			[2]
122	$H + H_2CN \rightarrow HCN + H_2$	5.02E-10	0.50		[5]
123	$N_2 + CN \rightarrow N_2 + C + N$	4.15E-10		70,538.50	[6]
124	$N + CH \rightarrow CN + H$	2.10E-11			[5]
125	$N + CN \rightarrow C + N_2$	6.64E-11			[6]
126	$N + H_2CN \rightarrow HCN + NH$	6.70E-11			[6]
127	$N + N + N_2 \rightarrow N_2 + N_2$	1.38E-34		-500	[2]
128	$N + N + H_2 \rightarrow N_2 + H_2$	2.50E-34		-500	[2]
129	$N_2H_4 + N \rightarrow N_2H_2 + NH_2$	1.30E-13			[7]
130	$N_2H_4 + H \rightarrow N_2H_3 + H_2$	1.20E-11		1,260	[7]
131	$N_2H_3 + H \rightarrow NH_2 + NH_2$	2.70E-12			[7]
132	$N_2H_4 + NH_2 \rightarrow NH_3 + N_2H_3$	5.20E-13			[7]
133	$N_2H_3 + N_2H_3 \rightarrow NH_3 + NH_3 + N_2$	5.00E-12			[7]
134	$N_2H_3 + N_2H_3 \rightarrow N_2H_4 + N_2H_2$	2.00E-11			[7]
135	$N_2H_2 + H \rightarrow N_2 + H_2 + H$	4.50E-13	2.63	-115	[7]
136	$N_2H_2 + NH_2 \rightarrow N_2 + H + NH_3$	1.50E-13	4.05	-810	[7]
137	$NH_3 + H \rightarrow H_2 + NH_2$	6.50E-13	2.76	5,135	[7]
138	$NH_3 + NH + NH_3 \rightarrow N_2H_4 + NH_3$	1.00E-33			[7]
139	$NH_2 + H_2 \rightarrow NH_3 + H$	2.10E-12		4,277	[7]
140	$NH_2 + N \rightarrow N_2 + H + H$	1.20E-10			[7]
141	$NH_2 + NH_2 + NH_3 \rightarrow N_2H_4 + NH_3$	6.90E-30			[7]
142	$NH_2 + NH_2 \rightarrow H_2 + N_2H_2$	6.60E-11		6,000	[5]
143	$NH_2 + NH_2 \rightarrow NH + NH_3$	8.30E-11		5,030	[5]

144	$NH_2 + NH_2 \rightarrow N_2H_4$	8.00E-11			5
145	$NH_2 + NH \rightarrow N_2H_3$	1.20E-10			7
146	$NH + N \rightarrow H + N_2$	2.50E-11			2
147	$NH + NH_2 \rightarrow H + N_2H_2$	5.25E-11		500	5
148	$NH + NH \rightarrow N_2H_2$	3.50E-12			7
149	$NH + NH + M \rightarrow H_2 + N_2 + M$	1.00E-33			6
150	$NH + NH > H + N_2H$	2.29E-11	0.50	500	5
151	$NH + NH \rightarrow NH_2 + N$	5.72E-12	0.50	1,000	5
152	$NH + NH \rightarrow N_2 + H + H$	1.20E-09			2
153	$NH + NH \rightarrow N_2 + H_2$	1.70E-11			2

Table A III-5. Ion-neutral reactions included in the model and the references where these data were adopted from. Reaction coefficients are given by the Arrhenius function: $k(T) = A\ (T/300\ K)^n \exp(-E/RT)$ where T is the gas mixture temperature (in K) and A is given in units of $cm^3\ s^{-1}$ for two body collisions and in $cm^6\ s^{-1}$ for three body collisions.

No	Reaction	A	n	E/R	Ref
1	$CH_5^+ + CH_2 \rightarrow CH_3^+ + CH_4$	9.60E-10			1
2	$CH_5^+ + CH \rightarrow CH_2^+ + CH_4$	6.90E-10			1
3	$CH_5^+ + C \rightarrow CH^+ + CH_4$	1.20E-09			1
4	$CH_5^+ + C_2H_6 \rightarrow C_2H_5^+ + H_2 + CH_4$	2.25E-10			1
5	$CH_5^+ + C_2H_4 \rightarrow C_2H_5^+ + CH_4$	1.50E-09			1
6	$CH_5^+ + C_2H_2 \rightarrow C_2H_3^+ + CH_4$	1.60E-09			1
7	$CH_5^+ + C_2H \rightarrow C_2H_2^+ + CH_4$	9.00E-10			1
8	$CH_5^+ + C_2 \rightarrow C_2H^+ + CH_4$	9.50E-10			1
9	$CH_5^+ + H \rightarrow CH_4^+ + H_2$	1.50E-10			1
10	$CH_4^+ + CH_4 \rightarrow CH_5^+ + CH_3$	1.50E-09			1

11	$CH_4^+ + C_2H_6 \rightarrow C_2H_4^+ + CH_4 + H_2$	1.91E-09			[1]
12	$CH_4^+ + C_2H_4 \rightarrow C_2H_5^+ + CH_3$	4.23E-10			[1]
13	$CH_4^+ + C_2H_4 \rightarrow C_2H_4^+ + CH_4$	1.38E-09			[1]
14	$CH_4^+ + C_2H_2 \rightarrow C_2H_3^+ + CH_3$	1.23E-09			[1]
15	$CH_4^+ + C_2H_2 \rightarrow C_2H_2^+ + CH_4$	1.13E-09			[1]
16	$CH_4^+ + H_2 \rightarrow CH_5^+ + H$	3.30E-11			[1]
17	$CH_4^+ + H \rightarrow CH_3^+ + H_2$	1.00E-11			[1]
18	$CH_3^+ + CH_4 \rightarrow CH_4^+ + CH_3$	1.36E-10			[1]
19	$CH_3^+ + CH_4 \rightarrow C_2H_5^+ + H_2$	1.20E-09			[1]
20	$CH_3^+ + CH_2 \rightarrow C_2H_3^+ + H_2$	9.90E-10			[1]
21	$CH_3^+ + CH \rightarrow C_2H_2^+ + H_2$	7.10E-10			[1]
22	$CH_3^+ + C \rightarrow C_2H^+ + H_2$	1.20E-09			[1]
23	$CH_3^+ + C_2H_6 \rightarrow C_2H_5^+ + CH_4$	1.48E-09			[1]
24	$CH_3^+ + C_2H_4 \rightarrow C_2H_3^+ + CH_4$	3.50E-10			[1]
25	$CH_3^+ + C_2H_3 \rightarrow C_2H_3^+ + CH_3$	3.00E-10			[1]
26	$CH_2^+ + CH_4 \rightarrow CH_3^+ + CH_3$	1.38E-10			[1]
27	$CH_2^+ + CH_4 \rightarrow C_2H_5^+ + H$	3.60E-10			[1]
28	$CH_2^+ + CH_4 \rightarrow C_2H_4^+ + H_2$	8.40E-10			[1]
29	$CH_2^+ + CH_4 \rightarrow C_2H_3^+ + H_2 + H$	2.31E-10			[1]
30	$CH_2^+ + CH_4 \rightarrow C_2H_2^+ + H_2 + H_2$	3.97E-10			[1]
31	$CH_2^+ + C \rightarrow C_2H^+ + H$	1.20E-09			[1]
32	$CH_2^+ + H_2 \rightarrow CH_3^+ + H$	1.60E-09			[1]
33	$CH^+ + CH_4 \rightarrow C_2H_4^+ + H$	6.50E-11			[1]
34	$CH^+ + CH_4 \rightarrow C_2H_3^+ + H_2$	1.09E-09			[1]
35	$CH^+ + CH_4 \rightarrow C_2H_2^+ + H_2 + H$	1.43E-10			[1]

36	$CH^+ + CH_2 \rightarrow C_2H^+ + H_2$	1.00E-09			1
37	$CH^+ + CH \rightarrow C_2^+ + H_2$	7.40E-10			1
38	$CH^+ + C \rightarrow C_2^+ + H$	1.20E-09			1
39	$CH^+ + H_2 \rightarrow CH_2^+ + H$	1.20E-09			1
40	$CH^+ + H \rightarrow C^+ + H_2$	7.50E-10			1
41	$C^+ + CH_4 \rightarrow C_2H_3^+ + H$	1.10E-09			1
42	$C^+ + CH_4 \rightarrow C_2H_2^+ + H_2$	4.00E-10			1
43	$C^+ + CH_3 \rightarrow C_2H_2^+ + H$	1.30E-09			1
44	$C^+ + CH_3 \rightarrow C_2H^+ + H_2$	1.00E-09			1
45	$C^+ + CH_2 \rightarrow CH_2^+ + C$	5.20E-10			1
46	$C^+ + CH_2 \rightarrow C_2H^+ + H$	5.20E-10			1
47	$C^+ + CH \rightarrow CH^+ + C$	3.80E-10			1
48	$C^+ + CH \rightarrow C_2^+ + H$	3.80E-10			1
49	$C^+ + C_2H_6 \rightarrow C_2H_5^+ + CH$	2.31E-10			1
50	$C^+ + C_2H_6 \rightarrow C_2H_4^+ + CH_2$	1.16E-10			1
51	$C^+ + C_2H_6 \rightarrow C_2H_3^+ + CH_3$	4.95E-10			1
52	$C^+ + C_2H_6 \rightarrow C_2H_2^+ + CH_4$	8.25E-11			1
53	$C^+ + C_2H_5 \rightarrow C_2H_5^+ + C$	5.00E-10			1
54	$C^+ + C_2H_4 \rightarrow C_2H_4^+ + C$	1.70E-11			1
55	$C^+ + C_2H_4 \rightarrow C_2H_3^+ + CH$	8.50E-11			1
56	$C^+ + H- \rightarrow C + H$	2.30E-07			1
57	$C_2H_6^+ + C_2H_4 \rightarrow C_2H_4^+ + C_2H_6$	1.15E-09			1
58	$C_2H_6^+ + C_2H_2 \rightarrow C_2H_5^+ + C_2H_3$	2.47E-10			1
59	$C_2H_6^+ + H \rightarrow C_2H_5^+ + H_2$	1.00E-10			1
60	$C_2H_5^+ + H \rightarrow C_2H_4^+ + H_2$	1.00E-11			1

61	$C_2H_4^+ + C_2H_3 \rightarrow C_2H_5^+ + C_2H_2$	5.00E-10			1
62	$C_2H_4^+ + C_2H_3 \rightarrow C_2H_3^+ + C_2H_4$	5.00E-10			1
63	$C_2H_4^+ + H \rightarrow C_2H_3^+ + H_2$	3.00E-10			1
64	$C_2H_3^+ + C_2H_6 \rightarrow C_2H_5^+ + C_2H_4$	2.91E-10			1
65	$C_2H_3^+ + C_2H_4 \rightarrow C_2H_5^+ + C_2H_2$	8.90E-10			1
66	$C_2H_3^+ + C_2H_3 \rightarrow C_2H_5^+ + C_2H$	5.00E-10			1
67	$C_2H_3^+ + C_2H \rightarrow C_2H_2^+ + C_2H_2$	3.30E-10			1
68	$C_2H_3^+ + H \rightarrow C_2H_2^+ + H_2$	6.80E-11			1
69	$C_2H_2^+ + CH_4 \rightarrow C_2H_3^+ + CH_3$	4.10E-09			1
70	$C_2H_2^+ + C_2H_6 \rightarrow C_2H_5^+ + C_2H_3$	1.31E-10			1
71	$C_2H_2^+ + C_2H_6 \rightarrow C_2H_4^+ + C_2H_4$	2.48E-10			1
72	$C_2H_2^+ + C_2H_4 \rightarrow C_2H_4^+ + C_2H_2$	4.14E-10			1
73	$C_2H_2^+ + C_2H_3 \rightarrow C_2H_3^+ + C_2H_2$	3.30E-10			1
74	$C_2H_2^+ + H_2 \rightarrow C_2H_3^+ + H$	1.00E-11			1
75	$C_2H^+ + CH_4 \rightarrow C_2H_2^+ + CH_3$	3.74E-10			1
76	$C_2H^+ + CH_2 \rightarrow CH_3^+ + C_2$	4.40E-10			1
77	$C_2H^+ + CH \rightarrow CH_2^+ + C_2$	3.20E-10			1
78	$C_2H^+ + H_2 \rightarrow C_2H_2^+ + H$	1.10E-09			1
79	$C_2^+ + CH_4 \rightarrow C_2H_2^+ + CH_2$	1.82E-10			1
80	$C_2^+ + CH_4 \rightarrow C_2H^+ + CH_3$	2.38E-10			1
81	$C_2^+ + CH_2 \rightarrow CH_2^+ + C_2$	4.50E-10			1
82	$C_2^+ + CH \rightarrow CH^+ + C_2$	3.20E-10			1
83	$C_2^+ + H_2 \rightarrow C_2H^+ + H$	1.10E-09			1
84	$H_3^+ + CH_4 \rightarrow CH_5^+ + H_2$	2.40E-09			1
85	$H_3^+ + CH_3 \rightarrow CH_4^+ + H_2$	2.10E-09			1

86	$H_3^+ + CH_2 \rightarrow CH_3^+ + H_2$	1.70E-09			1
87	$H_3^+ + CH \rightarrow CH_2^+ + H_2$	1.20E-09			1
88	$H_3^+ + C \rightarrow CH^+ + H_2$	2.00E-09			1
89	$H_3^+ + C_2H_6 \rightarrow C_2H_5^+ + H_2 + H_2$	2.40E-09			1
90	$H_3^+ + C_2H_5 \rightarrow C_2H_6^+ + H_2$	1.40E-09			1
91	$H_3^+ + C_2H_4 \rightarrow C_2H_5^+ + H_2$	1.15E-09			1
92	$H_3^+ + C_2H_4 \rightarrow C_2H_3^+ + H_2 + H_2$	1.15E-09			1
93	$H_3^+ + C_2H_3 \rightarrow C_2H_4^+ + H_2$	2.00E-09			1
94	$H_3^+ + C_2H_2 \rightarrow C_2H_3^+ + H_2$	3.50E-09			1
95	$H_2^+ + CH_4 \rightarrow CH_5^+ + H$	1.14E-10			1
96	$H_2^+ + CH_4 \rightarrow CH_4^+ + H_2$	1.40E-09			1
97	$H_2^+ + CH_4 \rightarrow CH_3^+ + H_2 + H$	2.30E-09			1
98	$H_2^+ + CH_2 \rightarrow CH_3^+ + H$	1.00E-09			1
99	$H_2^+ + CH_2 \rightarrow CH_2^+ + H_2$	1.00E-09			1
100	$H_2^+ + CH \rightarrow CH_2^+ + H$	7.10E-10			1
101	$H_2^+ + CH \rightarrow CH^+ + H_2$	7.10E-10			1
102	$H_2^+ + C \rightarrow CH^+ + H$	2.40E-09			1
103	$H_2^+ + C_2H_6 \rightarrow C_2H_6^+ + H_2$	2.94E-10			1
104	$H_2^+ + C_2H_6 \rightarrow C_2H_5^+ + H_2 + H$	1.37E-09			1
105	$H_2^+ + C_2H_6 \rightarrow C_2H_4^+ + H_2 + H_2$	2.35E-09			1
106	$H_2^+ + C_2H_6 \rightarrow C_2H_3^+ + H_2 + H_2 + H$	6.86E-10			1
107	$H_2^+ + C_2H_6 \rightarrow C_2H_2^+ + H_2 + H_2 + H_2$	1.96E-10			1
108	$H_2^+ + C_2H_4 \rightarrow C_2H_4^+ + H_2$	2.21E-09			1
109	$H_2^+ + C_2H_4 \rightarrow C_2H_3^+ + H_2 + H$	1.81E-09			1
110	$H_2^+ + C_2H_4 \rightarrow C_2H_2^+ + H_2 + H_2$	8.82E-10			1

111	$H_2^+ + C_2H_2 \rightarrow C_2H_3^+ + H$	4.80E-10			[1]
112	$H_2^+ + C_2H_2 \rightarrow C_2H_2^+ + H_2$	4.82E-09			[1]
113	$H_2^+ + C_2H \rightarrow C_2H_2^+ + H$	1.00E-09			[1]
114	$H_2^+ + C_2H \rightarrow C_2H^+ + H_2$	1.00E-09			[1]
115	$H_2^+ + C_2 \rightarrow C_2H^+ + H$	1.10E-09			[1]
116	$H_2^+ + C_2 \rightarrow C_2^+ + H_2$	1.10E-09			[1]
117	$H_2^+ + H_2 \rightarrow H_2 + H^+ + H$	1.00E-08		84,100	[2]
118	$H_2^+ + H \rightarrow H_3^+ + H$	2.10E-09			[2]
119	$H_2^+ + H \rightarrow H_2 + H^+$	6.39E-10			[2]
120	$H_2^+ + N \rightarrow N^+ + H_2$	5.00E-10			[2]
121	$H^+ + CH_4 \rightarrow CH_4^+ + H$	1.50E-09			[1]
122	$H^+ + CH_4 \rightarrow CH_3^+ + H_2$	2.30E-09			[1]
123	$H^+ + CH_3 \rightarrow CH_3^+ + H$	3.40E-09			[1]
124	$H^+ + CH_2 \rightarrow CH_2^+ + H$	1.40E-09			[1]
125	$H^+ + CH_2 \rightarrow CH^+ + H_2$	1.40E-09			[1]
126	$H^+ + CH \rightarrow CH^+ + H$	1.90E-09			[1]
127	$H^+ + C_2H_6 \rightarrow C_2H_5^+ + H_2$	1.30E-09			[1]
128	$H^+ + C_2H_6 \rightarrow C_2H_4^+ + H_2 + H$	1.40E-09			[1]
129	$H^+ + C_2H_6 \rightarrow C_2H_3^+ + H_2 + H_2$	2.80E-09			[1]
130	$H^+ + C_2H_5 \rightarrow C_2H_4^+ + H_2$	1.65E-09			[1]
131	$H^+ + C_2H_5 \rightarrow C_2H_3^+ + H_2 + H$	3.06E-09			[1]
132	$H^+ + C_2H_4 \rightarrow C_2H_4^+ + H$	1.00E-09			[1]
133	$H^+ + C_2H_4 \rightarrow C_2H_3^+ + H_2$	3.00E-09			[1]
134	$H^+ + C_2H_4 \rightarrow C_2H_2^+ + H_2 + H$	1.00E-09			[1]
135	$H^+ + C_2H_3 \rightarrow C_2H_3^+ + H$	2.00E-09			[1]

136	$H^+ + C_2H_3 \rightarrow C_2H_2^+ + H_2$	2.00E-09			1
137	$H^+ + C_2H_2 \rightarrow C_2H_2^+ + H$	5.40E-10			1
138	$H^+ + C_2H \rightarrow C_2H^+ + H$	1.50E-09			1
139	$H^+ + C_2H \rightarrow C_2^+ + H_2$	1.50E-09			1
140	$H^+ + C_2 \rightarrow C_2^+ + H$	3.10E-09			1
141	$H^+ + H_2 + M \rightarrow H_3^+ + M$	1.50E-29			2
142	$H^+ + H + M \rightarrow H_2^+ + M$	1.00E-34			2
143	$H^+ + N \rightarrow N^+ + H$	5.00E-11			2
144	$H- + CH_3 \rightarrow CH_4 + E$	1.00E-09			1
145	$H- + CH_2 \rightarrow CH_3 + E$	1.00E-09			1
146	$H- + CH \rightarrow CH_2 + E$	1.00E-10			1
147	$H- + C \rightarrow CH + E$	1.00E-09			1
148	$H- + C_2H \rightarrow C_2H_2 + E$	1.00E-09			1
149	$H- + C_2 \rightarrow C_2H + E$	1.00E-09			1
150	$H- + M \rightarrow H + E + M$	2.70E-10	0.50	5,590	2
151	$H- + H \rightarrow H_2 + E$	1.30E-09			2
152	$H- + N \rightarrow NH + E$	1.00E-09			2
153	$N_4^+ + C_3H_8 \rightarrow C_2H_5^+ + CH_3 + N_2 + N_2$	6.70E-10			5
154	$N_4^+ + C_3H_8 \rightarrow C_2H_4^+ + CH_4 + N_2 + N_2$	4.30E-10			5
155	$N_4^+ + M \rightarrow N_2^+ + M + N_2$	2.50E-15			2
156	$N_4^+ + N \rightarrow N_2 + N_2 + N^+$	1.00E-11			2
157	$N_3^+ + NH_3 \rightarrow NH_3^+ + N + N_2$	2.10E-09			3
158	$N_3^+ + N \rightarrow N_2^+ + N_2$	6.60E-11			2
159	$N_3^+ + M \rightarrow M + N + N_2^+$	6.60E-11			2
160	$N_2^+ + C_3H_8 \rightarrow C_2H_5^+ + CH_3 + N_2$	3.90E-10			5

161	$N_2^+ + C_3H_8 \rightarrow C_2H_4^+ + CH_4 + N_2$	2.20E-10			5
162	$N_2^+ + C_3H_8 \rightarrow C_2H_3^+ + CH_3 + H_2 + N_2$	5.20E-10			5
163	$N_2^+ + NH_3 \rightarrow NH_3^+ + N_2$	1.90E-09			3
164	$N_2^+ + N_2 + M \rightarrow N_4^+ + M$	6.80E-29	-1.64		2
165	$N_2^+ + N \rightarrow N_2 + N^+$	7.20E-13	1.00		2
166	$N_2^+ + N + M \rightarrow M + N_3^+$	9.00E-30	1.00	-400	2
167	$N^+ + NH_3 \rightarrow NH_3^+ + N$	2.40E-09			3
168	$N^+ + N + M \rightarrow N_2^+ + M$	1.00E-29			2
169	$N^+ + N_2 \rightarrow N + N_2^+$	4.45E-10			2
170	$N^+ + N_2 + M \rightarrow N_3^+ + M$	9.00E-30		-400	2
171	$N^+ + H \rightarrow N + H^+$	2.00E-09			2
172	$N^+ + NH \rightarrow H + N_2^+$	3.70E-10			2
173	$NH_3^+ + NH_3 \rightarrow NH_4^+ + NH_2$	2.20E-09			7
174	$NH_3^+ + H_2 \rightarrow NH_4^+ + H$	4.00E-13			7
175	$NH_2^+ + NH_3 \rightarrow NH_3^+ + NH_2$	1.10E-09			7
176	$NH_2^+ + NH_3 \rightarrow NH_4^+ + NH$	1.10E-09			7
177	$NH_2^+ + H_2 \rightarrow NH_3^+ + H$	1.00E-09			7
178	$NH^+ + NH_3 \rightarrow NH_3^+ + NH$	1.80E-09			7
179	$NH^+ + NH_3 \rightarrow NH_4^+ + N$	6.00E-10			7
180	$NH^+ + NH_2 \rightarrow NH + NH_2^+$	1.80E-09			7

Table A III-6. Excited-neutral reactions included in the model and the references where these data were adopted from. Reaction coefficients are given by the Arrhenius function: $k(T) = A\ (T/300\ K)^n \exp(-E/RT)$ where T is the gas mixture temperature (in K) and A is given in units of $cm^3\ s^{-1}$ for two body collisions and in $cm^6\ s^{-1}$ for three body collisions.

No	Reaction	A	E/R	Ref

1	H_2(vib.) + N_2 → H_2 + N_2	1.00E-13		[2]
2	H_2(vib.) + N → H_2 + N	1.00E-13		[2]
3	H_2(vib.) + H_2 → H_2 + H_2	1.00E-13		[2]
4	H_2(rot.) + N_2 → H_2 + N_2	1.00E-13		[2]
5	H_2(rot.) + N → H_2 + N	1.00E-13		[2]
6	H_2(rot.) + H_2 → H_2 + H_2	1.00E-13		[2]
7	H_2* + N_2 → H_2 + N_2	1.00E-13		[2]
8	H_2* + N → H_2 + N	1.00E-13		[2]
9	H_2* + H_2 → H_2 + H_2	1.00E-13		[2]
10	H* + N_2 → H + N_2	1.00E-13		[2]
11	H* + N → H + N	1.00E-13		[2]
12	H* + H_2 → H + H_2	1.00E-13		[2]
13	$N_2(a'^1)$ + CH_4 → N_2 + C + H_2 + H_2	3.00E-10		[6]
14	$N_2(A^3)$ + CH_4 → N_2 + CH_3 + H	1.50E-12		[6]
15	$N_2(a'^1)$ + CH_4 → CH_3 + H + N_2	3.00E-10		[5]
16	N_2* + CH_4 → N_2 + CH_2 + H_2	1.35E-13		[6]
17	N_2* + C_3H_8 → C_3H_6 + H_2 + N_2	1.30E-12		[5]
18	$N_2(a'^1)$ + C_3H_8 → C_3H_6 + H_2 + N_2	3.00E-10		[5]
19	N_2* + C_3H_6 → C_3H_5 + H + N_2	1.40E-10		[5]
20	$N_2(a'^1)$ + C_3H_6 → C_3H_5 + H + N_2	1.40E-10		[5]
21	N_2* + C_3H_6 → C_2H_3 + CH_3 + N_2	1.40E-10		[5]
22	$N_2(a'^1)$ + C_3H_6 → C_2H_3 + CH_3 + N_2	1.40E-10		[5]
23	N_2* + C_2H_6 → C_2H_4 + H_2 + N_2	1.80E-10	1,980	[5]
24	$N_2(a'^1)$ + C_2H_6 → C_2H_4 + H_2 + N_2	5.00E-08	1,980	[5]
25	N_2* + C_2H_4 → C_2H_3 + H + N_2	5.50E-11		[5]

26	$N_2(a'^1) + C_2H_4 \rightarrow C_2H_3 + H + N_2$	2.00E-10		[5]
27	$N_2^* + C_2H_4 \rightarrow C_2H_2 + H_2 + N_2$	5.50E-11		[5]
28	$N_2(a'^1) + C_2H_4 \rightarrow C_2H_2 + H_2 + N_2$	2.00E-10		[5]
29	$N_2^* + C_2H_2 \rightarrow C_2H + H + N_2$	2.00E-10		[5]
30	$N_2(a'^1) + C_2H_2 \rightarrow C_2H + H + N_2$	3.00E-10		[5]
31	$N_2^* + CH_3 \rightarrow N_2 + CH_2 + H$	1.00E-13		[6]
32	$N_2^* + H_2 \rightarrow N_2 + H_2$	2.10E-10		[2]
33	$N_2^* + H_2 \rightarrow N_2 + H + H$	3.80E-10	3,500	[2]
34	$N_2(a'^1) + H_2 \rightarrow N_2 + H_2$	2.10E-10		[2]
35	$N_2^* + H \rightarrow N_2 + H$	2.10E-10		[2]
36	$N_2(a'^1) + H \rightarrow N_2 + H$	2.10E-10		[2]
37	$N_2^* + N_2(a'^1) \rightarrow N_4^+ + e^-$	9.00E-12		[2]
38	$N_2^* + N_2(a'^1) \rightarrow N_2^+ + N_2 + e^-$	1.00E-12		[2]
39	$N_2^* + N_2^* \rightarrow N_2 + N_2^*$	2.00E-12		[2]
40	$N_2(a'^1) + N_2(a'^1) \rightarrow N_4^+ + e^-$	1.00E-11		[2]
41	$N_2(a'^1) + N_2(a'^1) \rightarrow N_2^+ + N_2 + e^-$	5.00E-13		[2]
42	$N_2(a'^1) + N_2(a'^1) \rightarrow N_2 + N_2(a'^1)$	2.00E-12		[2]
43	$N_2^* + N_2 \rightarrow N_2 + N_2$	3.70E-16		[2]
44	$N_2(a'^1) + N_2 \rightarrow N_2 + N_2$	3.70E-16		[2]
45	$N_2^* + N \rightarrow N_2 + N$	2.00E-11		[2]
46	$N_2(a'^1) + N \rightarrow N_2 + N$	2.00E-11		[2]
47	$N_2^* + HCN \rightarrow N_2 + CN + H$	6.00E-12		[6]
48	$N_2(rot.) + N_2 \rightarrow N_2 + N_2$	1.00E-13		[2]
49	$N_2(rot.) + N \rightarrow N_2 + N$	1.00E-13		[2]
50	$N_2(rot.) + H_2 \rightarrow N_2 + H_2$	1.00E-13		[2]

51	N_2(vib.) + N_2 → N_2 + N_2	1.00E-13		[2]
52	N_2(vib.) + N → N_2 + N	1.00E-13		[2]
53	N_2(vib.) + H_2 → N_2 + H_2	1.00E-13		[2]
54	N* + H_2 → NH + H	4.60E-11	880	[2]
55	N* + N_2^+ → N^+ + N_2	1.00E-10		[2]
56	N*+ NH_3 → NH + NH_2	5.00E-11		[3]
57	N* + M → N + M	2.40E-14		[2]

2. References

1 R. Snoeckx, R. Aerts, X. Tu and A. Bogaerts, *J. Phys. Chem. C*, 2013, **117**, 4957–4970.

2 W. Van Gaens and A. Bogaerts, *J. Phys. D. Appl. Phys.*, 2014, **47**, 79502.

3 R. Dorai, University of Illinois at Urbana-Champaign, 2002.

4 *http://www.me.berkeley.edu/gri_mech/index.html*.

5 N. Moreau, S. Pasquiers, N. Blin-Simiand, L. Magne, F. Jorand, C. Postel and J.-R. Vacher, *J. Phys. D. Appl. Phys.*, 2010, **43**, 285201.

6 C. D. Pintassilgo, C. Jaoul, J. Loureiro, T. Belmonte and T. Czerwiec, *J. Phys. D. Appl. Phys.*, 2007, **40**, 3620–3632.

7 R. a Arakoni, A. N. Bhoj and M. J. Kushner, *J. Phys. D. Appl. Phys.*, 2007, **40**, 2476–2490.

APPENDIX IV

Additional data dry reforming of methane

1. Comparison of experimental and computational data

Table A IV-1. Overview of the detailed experimental and computational results, used for the model validation; as a function of the CH_4/CO_2 mixture.

		Experimental				Computational			
CH_4/CO_2 Mixture	*SEI (J/cm^3)*	*Conversion (%)* CH_4	*Conversion (%)* CO_2	*Conversion (%)* *Total*	*Energy Efficiency (%)*	*Conversion (%)* CH_4	*Conversion (%)* CO_2	*Conversion (%)* *Total*	*Energy Efficiency (%)*
10 - 90	36	62.1	27.8	**31.23**	**8.71**	97.00	16.28	**24.36**	**6.79**
10 - 90	18	37.3	15.9	**18.04**	**10.06**	67.76	10.34	**16.08**	**8.97**
25 - 75	36	50.6	27.5	**33.28**	**9.28**	57.84	20.97	**30.19**	**8.41**
25 - 75	18	28.6	16.3	**19.38**	**10.80**	37.46	10.51	**17.25**	**9.62**
50 - 50	36	40.9	26	**33.45**	**9.32**	42.00	25.38	**33.69**	**9.39**
50 - 50	18	20.4	14.2	**17.30**	**9.64**	23.20	12.93	**18.065**	**10.07**
75 - 25	36	29.7	23.3	**28.10**	**7.83**	29.93	40.39	**32.55**	**9.07**
75 - 25	18	16.1	11.7	**15.00**	**8.36**	16.24	21.52	**17.56**	**9.79**
90 - 10	36	24.1	43	**25.99**	**7.24**	23.24	67.71	**27.69**	**7.72**
90 - 10	18	12.6	28.6	**14.20**	**7.92**	13.09	42.40	**16.02**	**8.93**

Table A IV-2. Overview of the detailed experimental and computational results, used for the model validation, as a function of the residence time and the SEI for a 1:1 CH_4/CO_2 mixture.

		Experimental				**Computational**			
SEI (J/cm³)	***Residence Time (s)***	***Conversion (%)***			***Energy Efficiency (%)***	***Conversion (%)***			***Energy Efficiency (%)***
		CH_4	***CO_2***	***Total***		***CH_4***	***CO_2***	***Total***	
36	32.57	40.9	26	**33.45**	**9.32**	42.00	25.38	**33.69**	**9.39**
18	16.29	28.4	19.5	**23.95**	**13.35**	26.66	15.01	**20.84**	**11.62**
12	10.86	18.4	8.8	**13.6**	**11.37**	19.80	10.78	**15.29**	**12.78**
9	8.14	15.9	9.3	**12.6**	**14.05**	15.75	8.39	**12.07**	**13.46**
4.5	4.07	7	3.3	**5.15**	**11.48**	8.81	4.52	**6.66**	**14.86**
18	32.57	20.4	14.2	**17.3**	**9.64**	23.20	12.93	**18.06**	**10.07**
9	16.29	13.8	10.3	**12.05**	**13.44**	13.72	7.24	**10.48**	**11.68**
6	10.86	7.4	4.5	**5.95**	**9.95**	9.77	5.05	**7.41**	**12.40**
4.5	8.14	7	4	**5.5**	**12.26**	7.59	3.89	**5.74**	**12.80**
2.25	4.07	2.8	0.9	**1.85**	**8.25**	3.96	2.03	**3.00**	**13.37**
1	1					2.14	1.09	**1.62**	**16.24**
100	100					63.82	43.70	**53.76**	**5.39**
1	2					1.78	0.94	**1.36**	**13.66**
100	200					58.25	39.33	**48.79**	**4.90**
0.5	1					0.89	0.48	**0.68**	**13.73**
50	100					41.02	25.24	**33.13**	**6.65**

2. Computational data

When looking at the influence of the gas mixture in the entire range of conditions (see Figures A IV-1–A IV-15), the following trends can be observed. First of all, the effect of the gas mixture seems to be different, depending on the SEI:

- At the lowest SEI of 0.01 and 0.1 J/cm³, the conversion increases upon increasing CO_2 content ($10 < 25 < 50 < 75 < 90$ % CO_2) for all conditions investigated.
- At an SEI of 1 J/cm³, the conversion also increases upon increasing CO_2 content ($10 < 25 < 50 < 75 < 90$ % CO_2) at all conditions investigated, except at the highest residence time and frequency ($10 = 25 < 50 < 75 < 90$ % CO_2).
- At an SEI of 10 J/cm³ the effect of gas mixture seems to vary, depending on the other conditions, and no clear trend was observed at first sight. However, when we multiply the residence time (τ) with the frequency (f), which is a

measure for the number of micro-discharges that take place within a certain residence time, we can identify the following trends:

  - When $f \cdot \tau = 10^7$, the conversion is almost constant for 10, 25 and 50 % CO_2 and then starts decreasing at 75 and 90 % CO_2.
  - When $f \cdot \tau = 10^6$, the conversion first increases from 10 to 50 % CO_2 and then decreases again at 75 and 90 % CO_2.
  - When $f \cdot \tau = 10^5$ and 10^4 , the conversion increases from 10 to 75 % CO_2 and decreases again at 90 %. Note that the experimental validation shown in the paper was performed for $f \cdot \tau = 3 \cdot 10^4$, and indeed showed the same trend.
  - When $f \cdot \tau = 10^3$, the conversion increases upon increasing CO_2 content (10 < 25 < 50 < 75 < 90 % CO_2).
  - When $f \cdot \tau < 10^3$, the conversion slightly decreases from 10 to 75 % CO_2, but then strongly increases at 90 % CO_2.
- At the SEI of 100 J/cm³ , the conversion shows the same behavior as for the SEI of 10 J/cm³, more specifically:
  - When $f \cdot \tau = 10^7 – 10^5$, the conversion first increases from 10 to 50 % CO_2 and then decreases at 75 and 90 % CO_2.
  - When $f \cdot \tau < 10^5$, the conversion is almost constant for 10, 25 and 50 % CO_2 and increases for 75 and 90 % CO_2.

To summarize, changing the gas mixture will yield different results depending on the conditions (i.e., the other parameters). Especially the SEI plays an important role, i.e., for SEI values of 0.01, 0.1 and 1 J/cm³ a higher CO_2 content in the mixture leads to a higher conversion and subsequently energy efficiency. On the other hand, for the SEI values of 10 and 100 J/cm³, also the frequency and residence time play a role, and depending on the product of both, different trends are observed.

2.1. Total Conversion as a function of residence time and frequency for each SEI value and CH_4-CO_2 mixture investigated (Figure A IV-1–A IV-5)

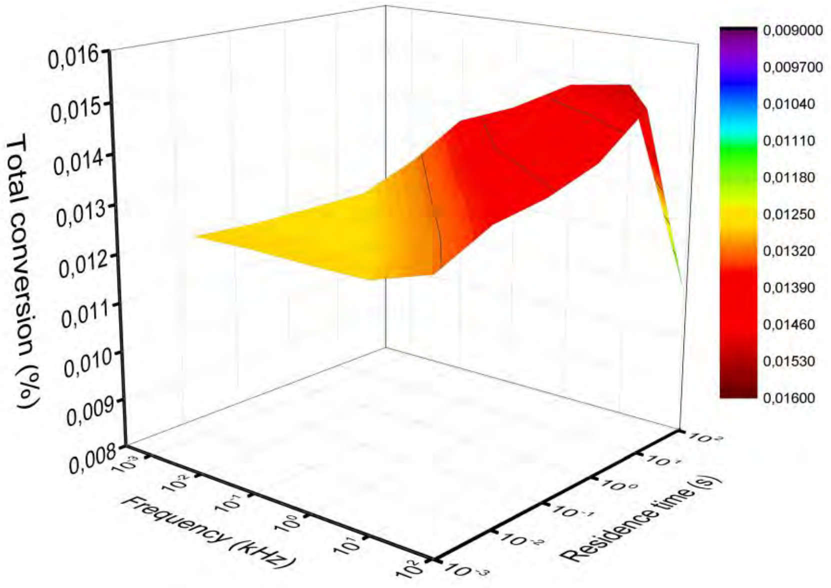

Figure A IV-1(a). Total simulated conversion for a 10-90 CH_4-CO_2 mixture as a function of the residence time and frequency for an SEI of 0.01 J/cm³.

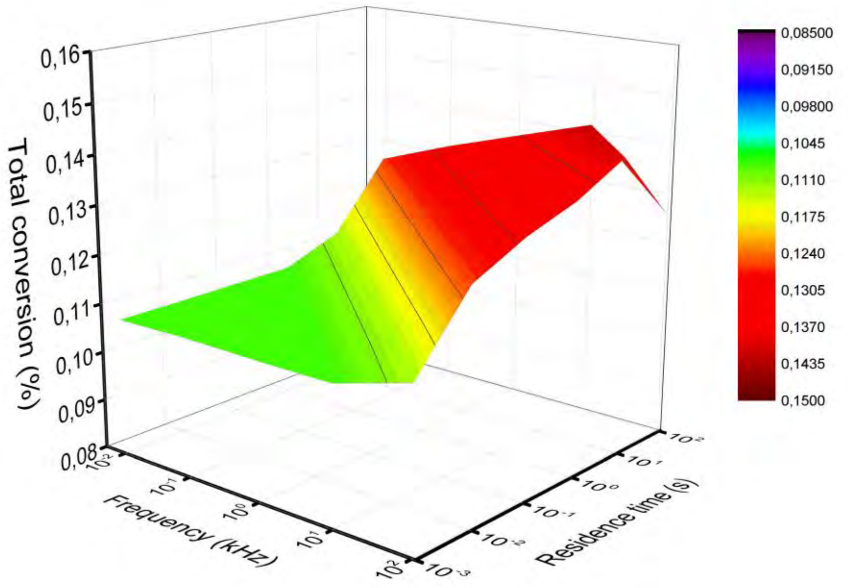

Figure A IV-1(b). Total simulated conversion for a 10-90 CH_4-CO_2 mixture as a function of the residence time and frequency for an SEI of 0.1 J/cm³.

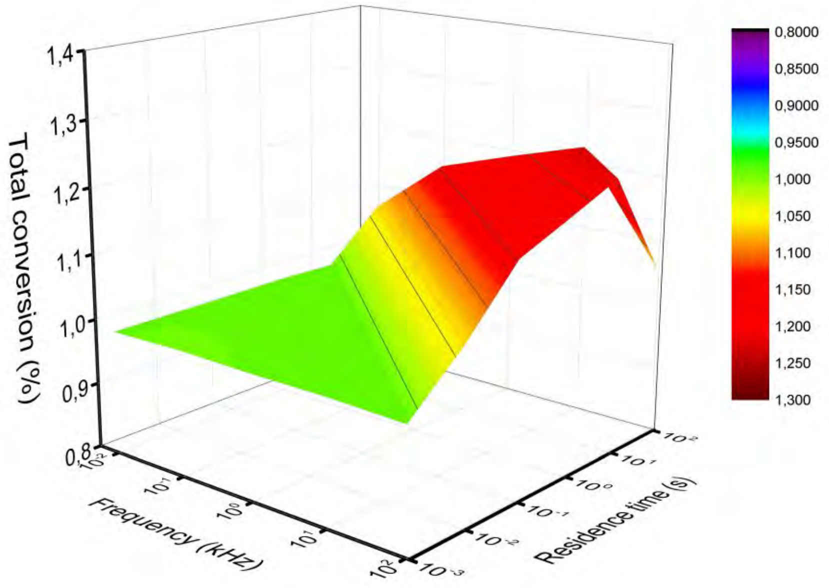

Figure A IV-1(c). Total simulated conversion for a 10-90 CH_4-CO_2 mixture as a function of the residence time and frequency for an SEI of 1 J/cm³.

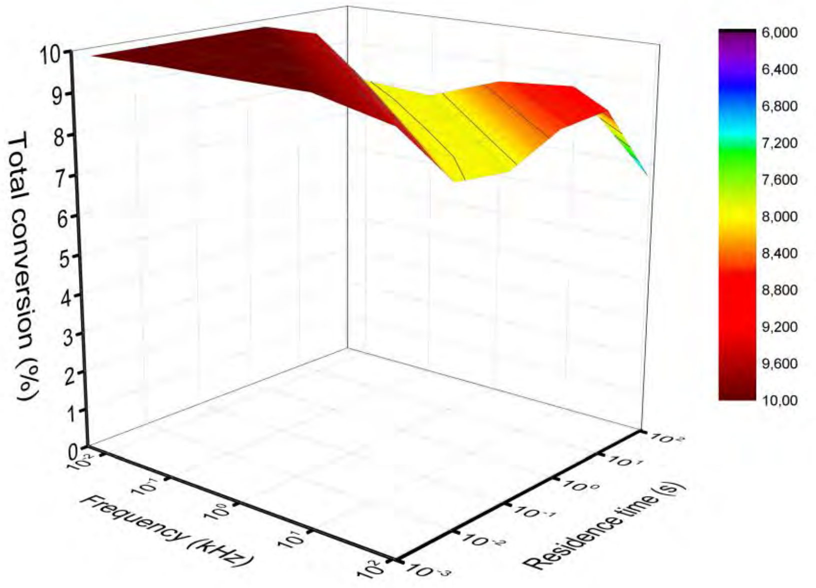

Figure A IV-1(d). Total simulated conversion for a 10-90 CH_4-CO_2 mixture as a function of the residence time and frequency for an SEI of 10 J/cm³.

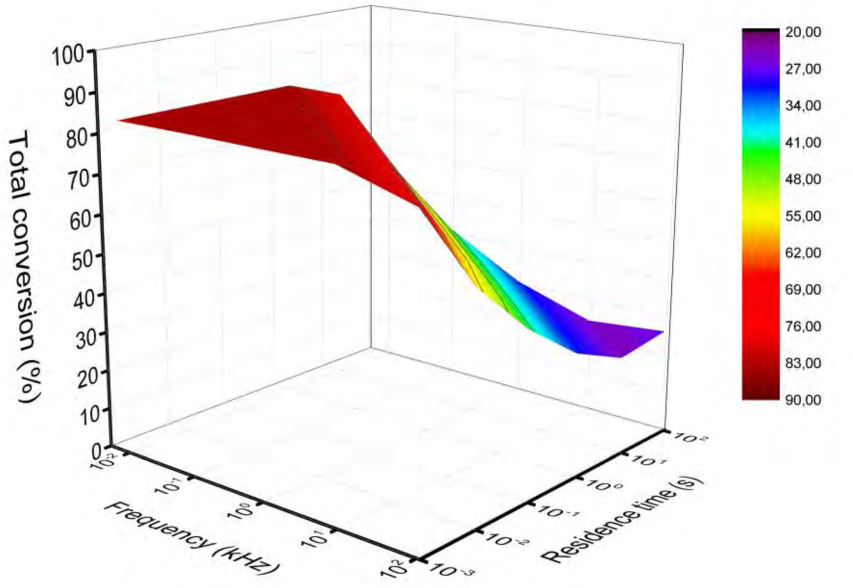

Figure A IV-1(e). Total simulated conversion for a 10-90 CH_4-CO_2 mixture as a function of the residence time and frequency for an SEI of 100 J/cm³.

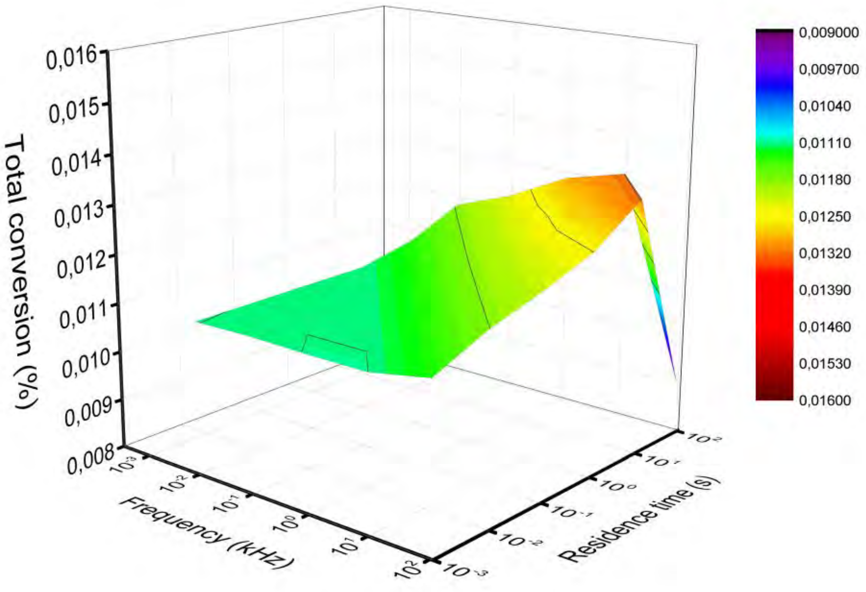

Figure A IV-2(a). Total simulated conversion for a 25-75 CH_4-CO_2 mixture as a function of the residence time and frequency for an SEI of 0.01 J/cm³.

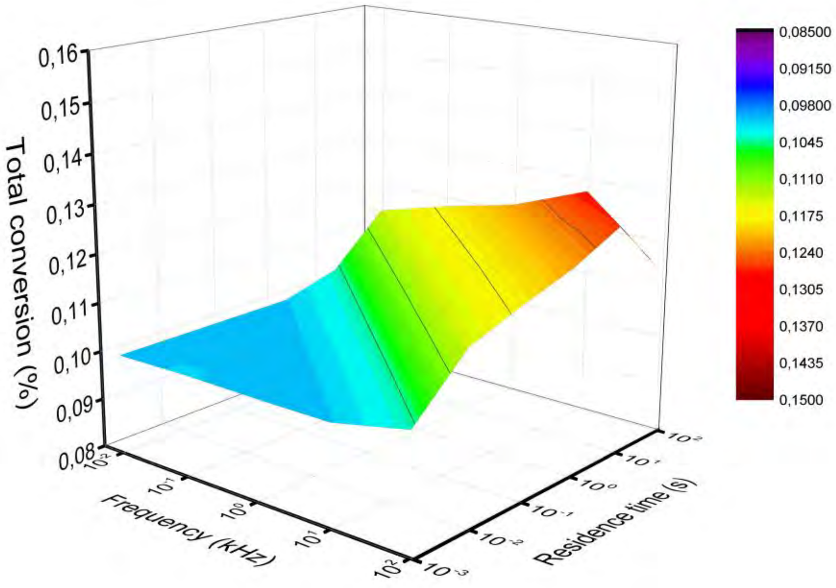

Figure A IV-2(b). Total simulated conversion for a 25-75 CH_4-CO_2 mixture as a function of the residence time and frequency for an SEI of 0. 1 J/cm³.

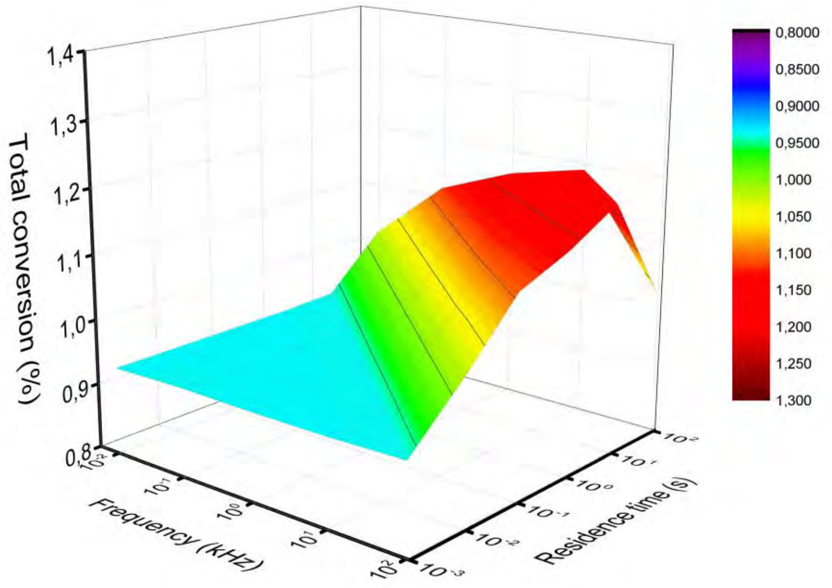

Figure A IV-2(c). Total simulated conversion for a 25-75 CH_4-CO_2 mixture as a function of the residence time and frequency for an SEI of 1 J/cm³.

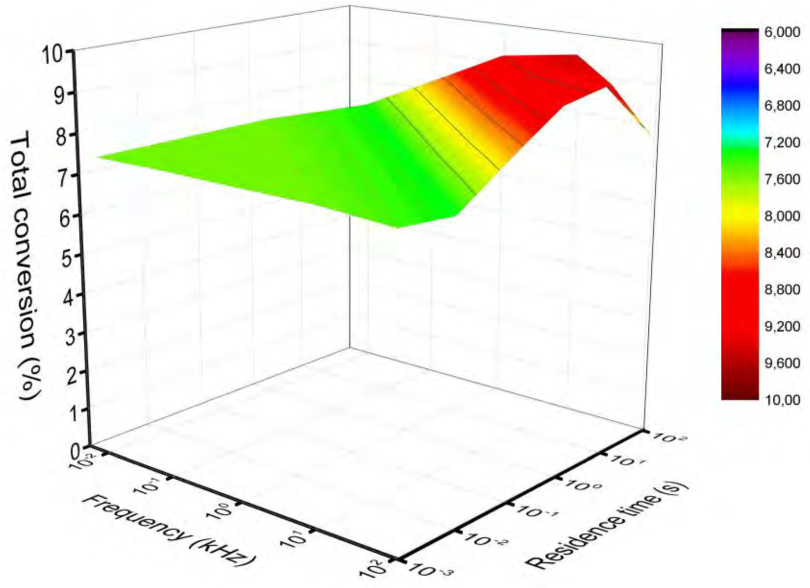

Figure A IV-2(d). Total simulated conversion for a 25-75 CH_4-CO_2 mixture as a function of the residence time and frequency for an SEI of 10 J/cm³.

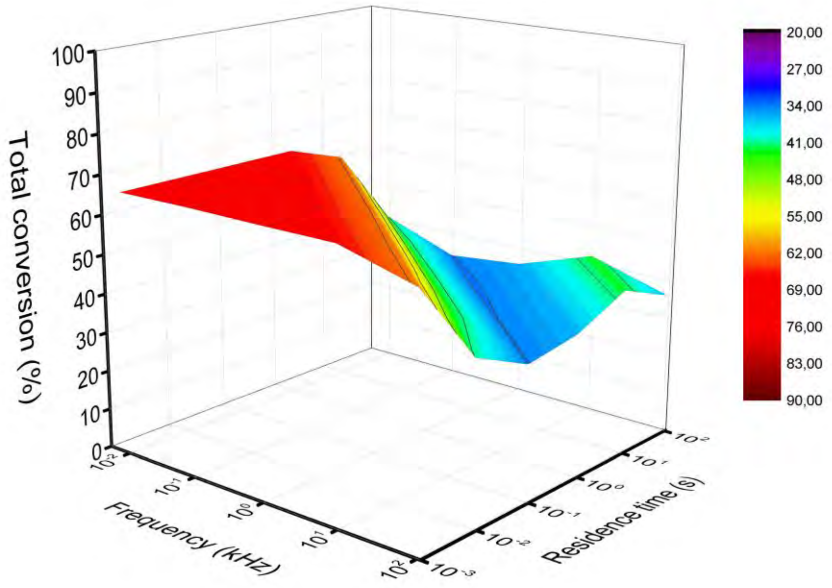

Figure A IV-2(e). Total simulated conversion for a 25-75 CH_4-CO_2 mixture as a function of the residence time and frequency for an SEI of 100 J/cm³.

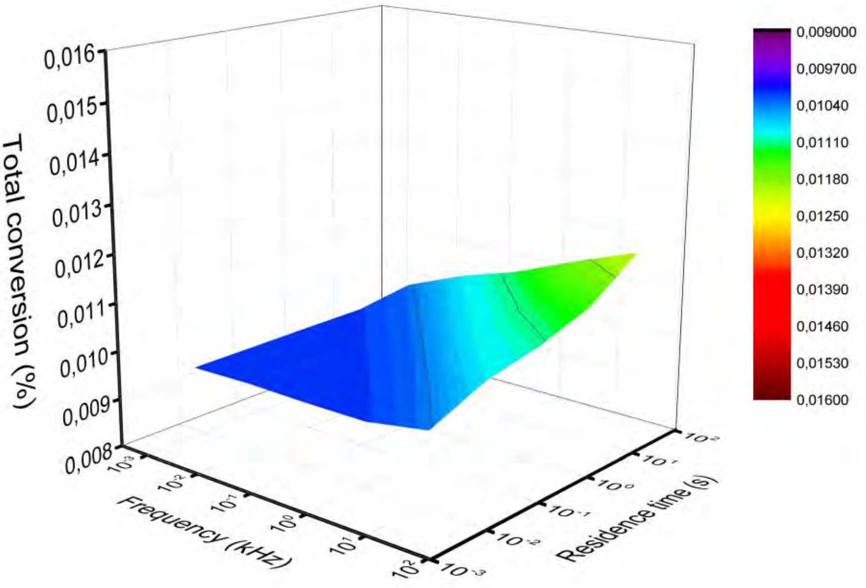

Figure A IV-3(a). Total simulated conversion for a 50-50 CH_4-CO_2 mixture as a function of the residence time and frequency for an SEI of 0.01 J/cm³.

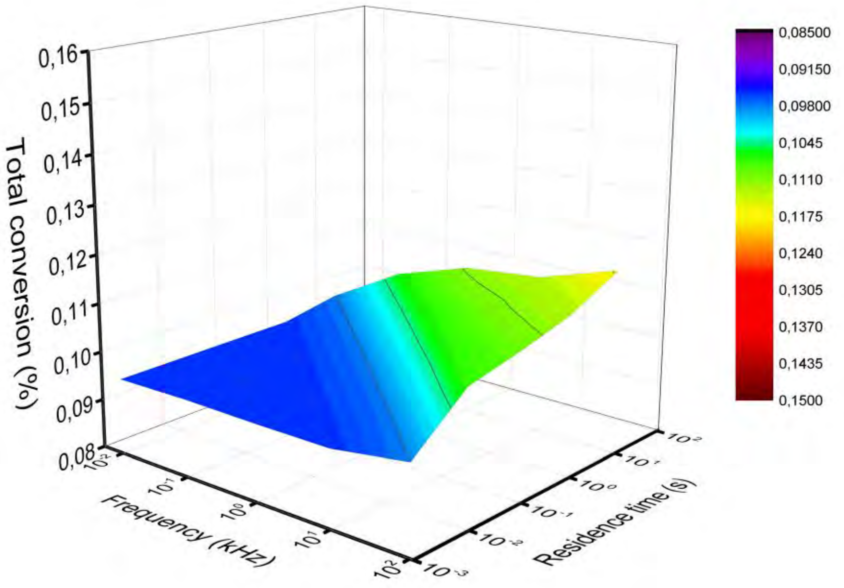

Figure A IV-3(b). Total simulated conversion for a 50-50 CH_4-CO_2 mixture as a function of the residence time and frequency for an SEI of 0. 1 J/cm³.

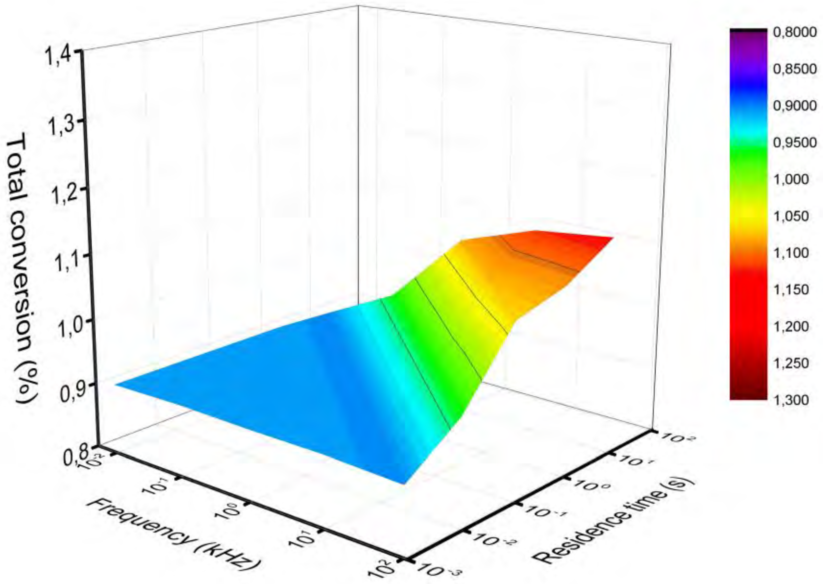

Figure A IV-3(c). Total simulated conversion for a 50-50 CH_4-CO_2 mixture as a function of the residence time and frequency for an SEI of 1 J/cm³.

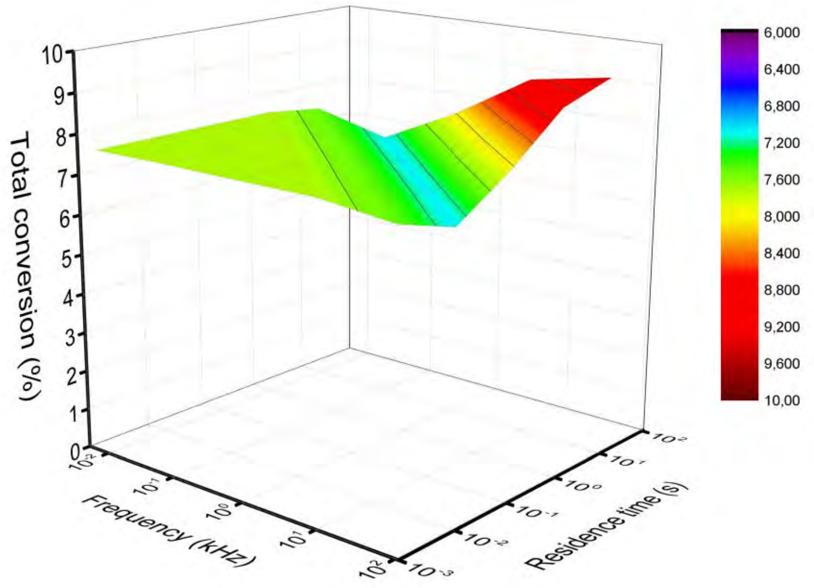

Figure A IV-3(d). Total simulated conversion for a 50-50 CH_4-CO_2 mixture as a function of the residence time and frequency for an SEI of 10 J/cm³.

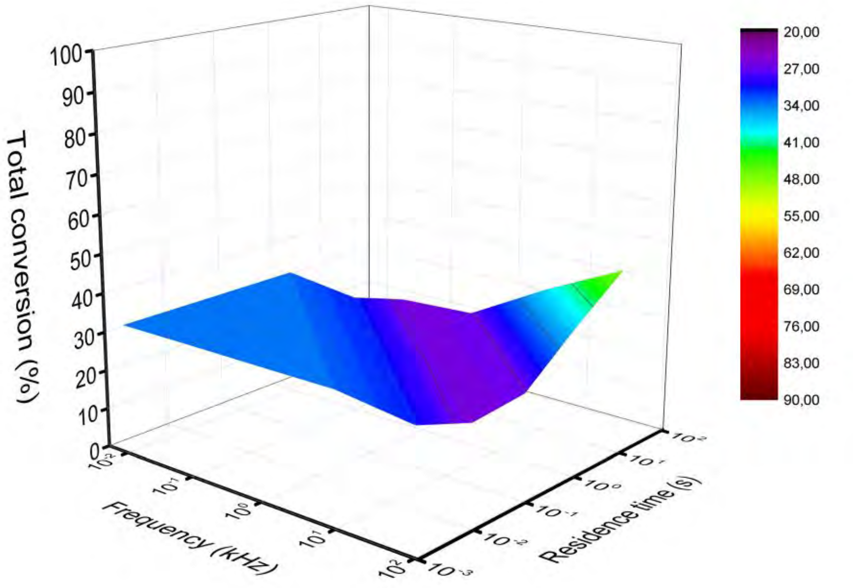

Figure A IV-3(e). Total simulated conversion for a 50-50 CH_4-CO_2 mixture as a function of the residence time and frequency for an SEI of 100 J/cm³.

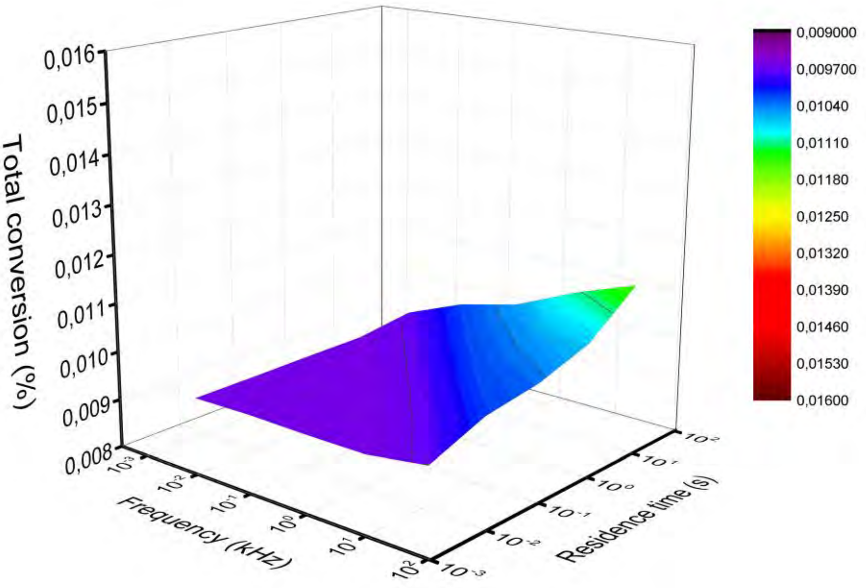

Figure A IV-4(a). Total simulated conversion for a 75-25 CH_4-CO_2 mixture as a function of the residence time and frequency for an SEI of 0.01 J/cm³.

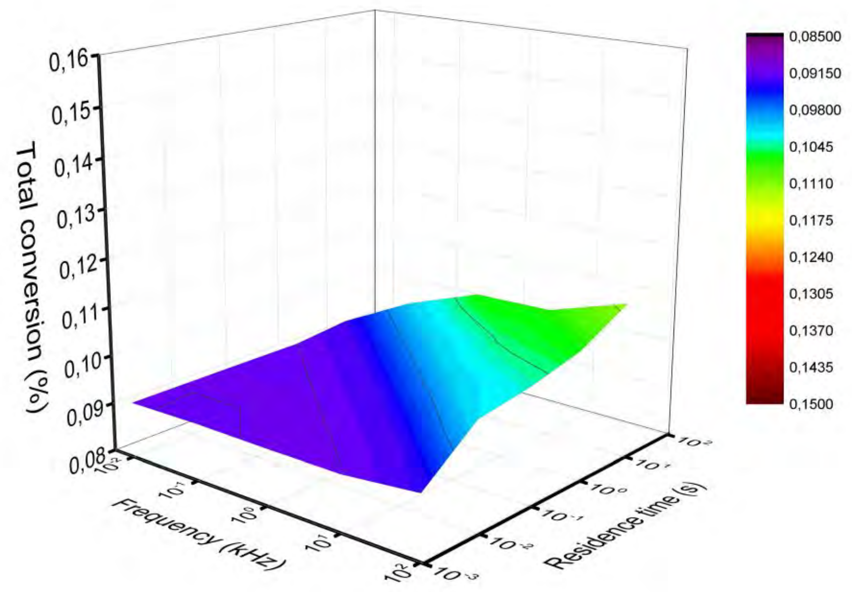

Figure A IV-4(b). Total simulated conversion for a 75-25 CH_4-CO_2 mixture as a function of the residence time and frequency for an SEI of 0. 1 J/cm³.

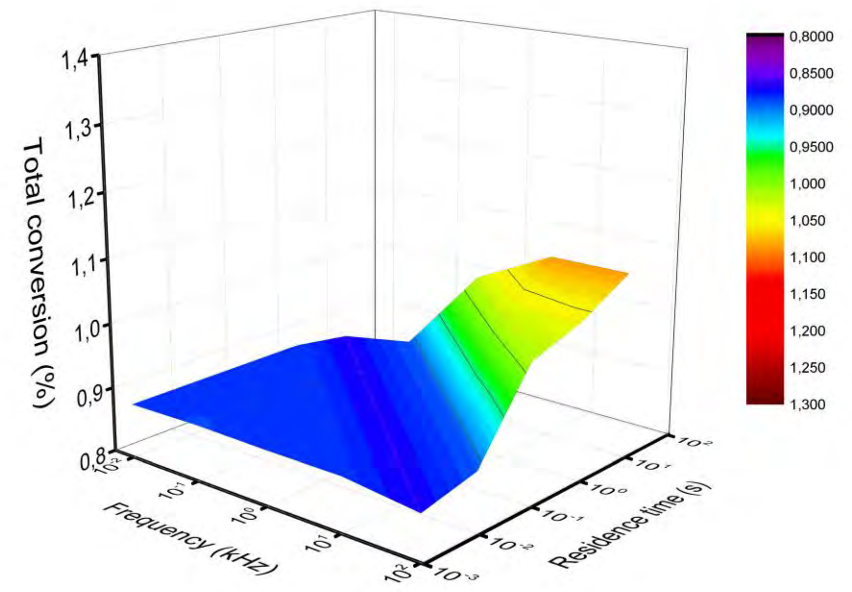

Figure A IV-4(c). Total simulated conversion for a 75-25 CH_4-CO_2 mixture as a function of the residence time and frequency for an SEI of 1 J/cm³.

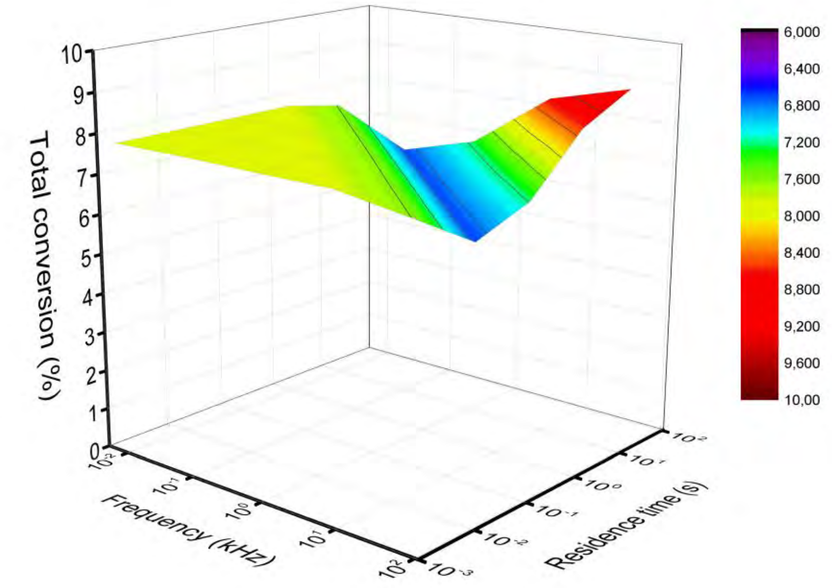

Figure A IV-4(d). Total simulated conversion for a 75-25 CH_4-CO_2 mixture as a function of the residence time and frequency for an SEI of 10 J/cm³.

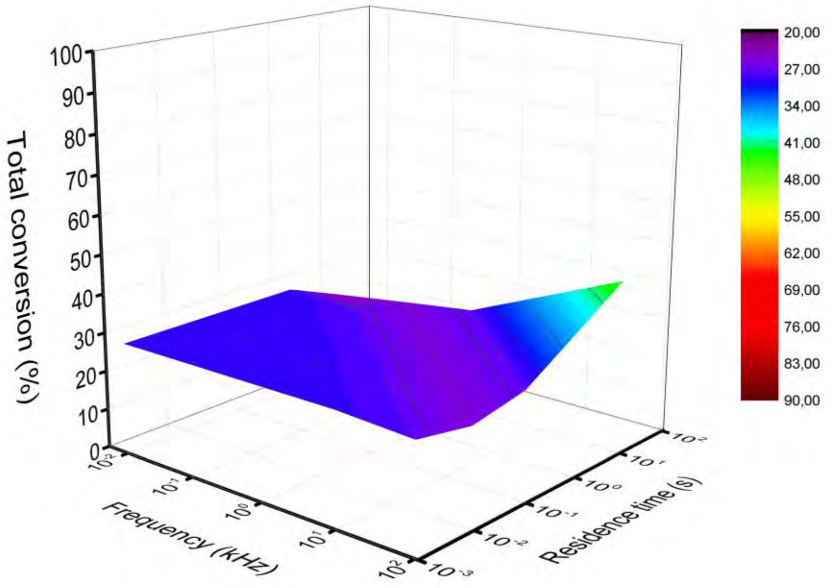

Figure A IV-4(e). Total simulated conversion for a 75-25 CH_4-CO_2 mixture as a function of the residence time and frequency for an SEI of 100 J/cm³.

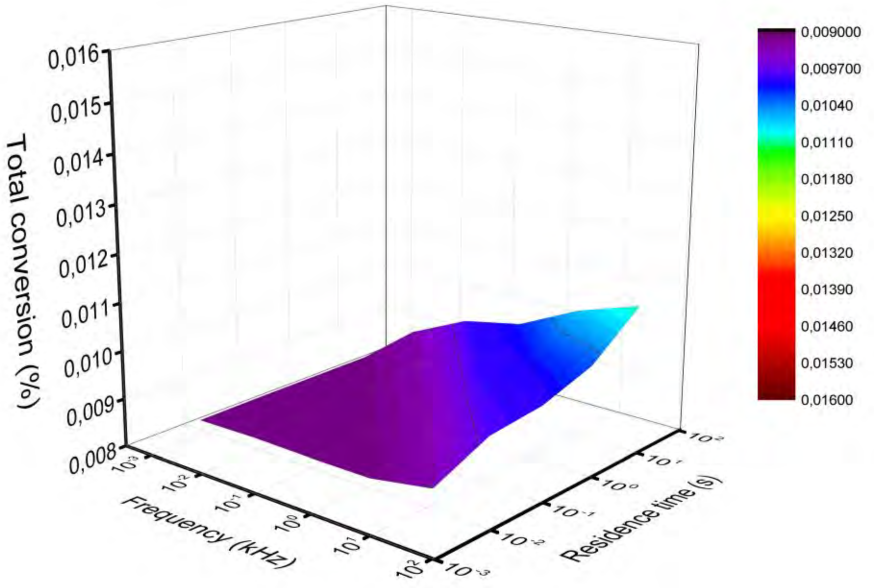

Figure A IV-5(a). Total simulated conversion for a 90-10 CH_4-CO_2 mixture as a function of the residence time and frequency for an SEI of 0.01 J/cm³.

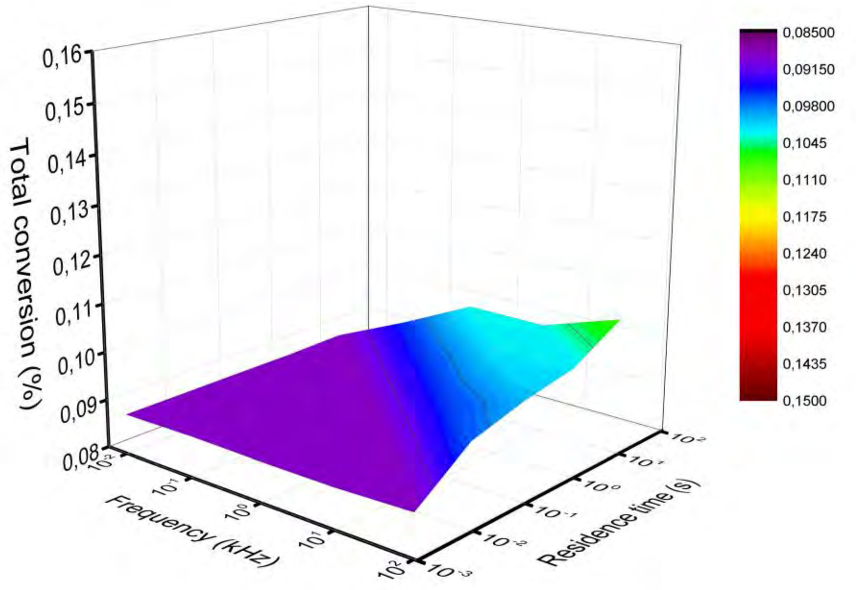

Figure A IV-5(b). Total simulated conversion for a 90-10 CH_4-CO_2 mixture as a function of the residence time and frequency for an SEI of 0. 1 J/cm³.

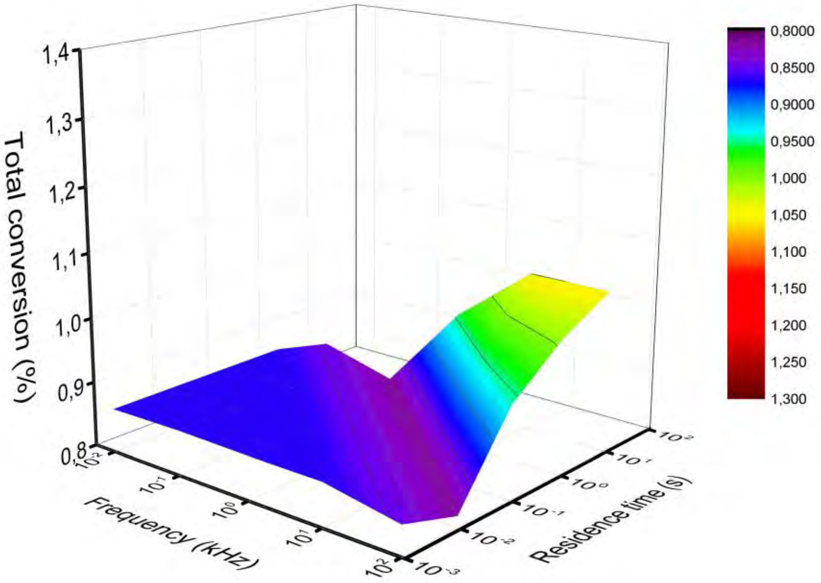

Figure A IV-5(c). Total simulated conversion for a 90-10 CH_4-CO_2 mixture as a function of the residence time and frequency for an SEI of 1 J/cm³.

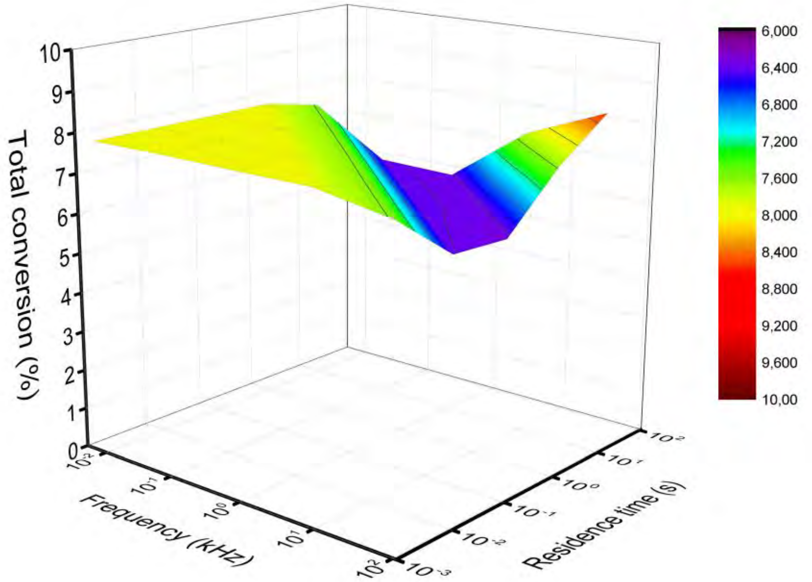

Figure A IV-5(d). Total simulated conversion for a 90-10 CH_4-CO_2 mixture as a function of the residence time and frequency for an SEI of 10 J/cm³.

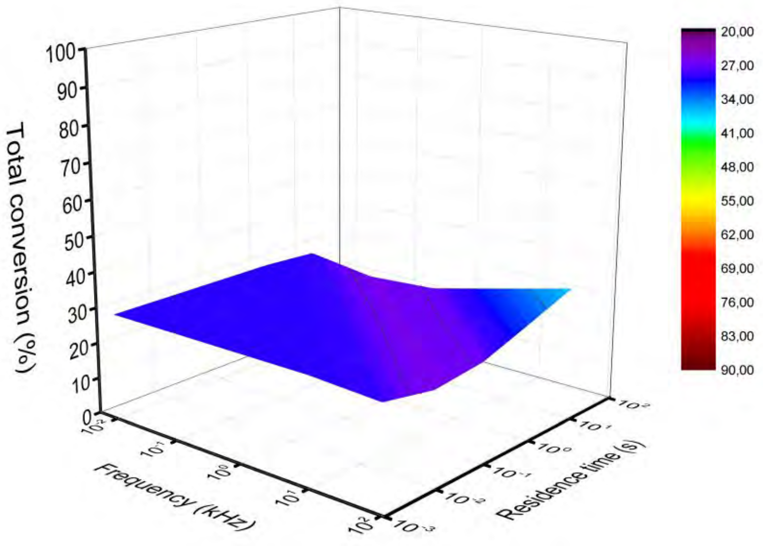

Figure A IV-5(e). Total simulated conversion for a 90-10 CH_4-CO_2 mixture as a function of the residence time and frequency for an SEI of 100 J/cm³.

2.2. Energy efficiency as a function of residence time and frequency for each SEI value and CH_4-CO_2 mixture investigated (Figure A IV-6–A IV-10)

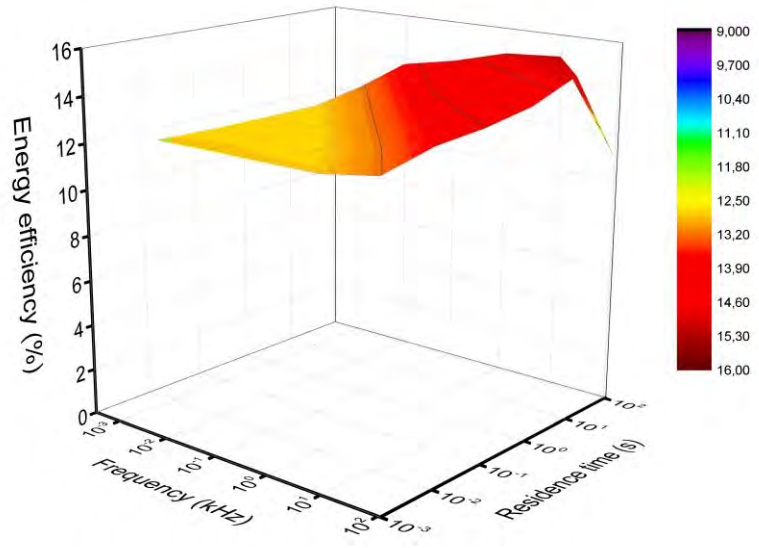

Figure A IV-6(a). Simulated energy efficiency for a 10-90 CH_4-CO_2 mixture as a function of the residence time and frequency for an SEI of 0.01 J/cm³.

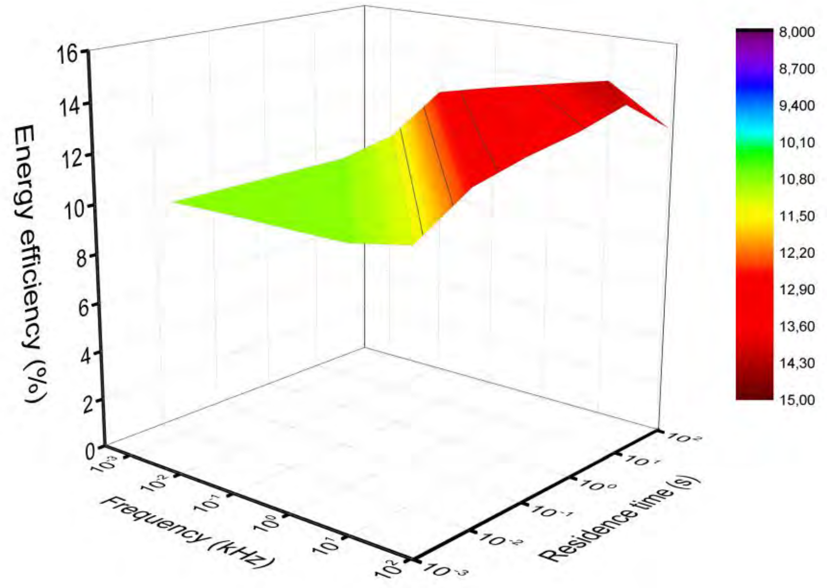

Figure A IV-6(b). Simulated energy efficiency for a 10-90 CH_4-CO_2 mixture as a function of the residence time and frequency for an SEI of 0. 1 J/cm³.

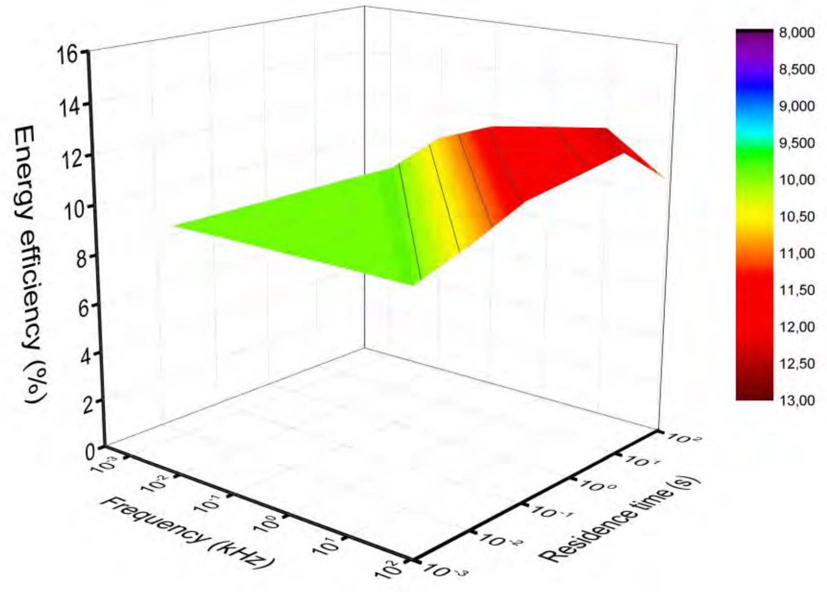

Figure A IV-6(c). Simulated energy efficiency for a 10-90 CH_4-CO_2 mixture as a function of the residence time and frequency for an SEI of 1 J/cm³.

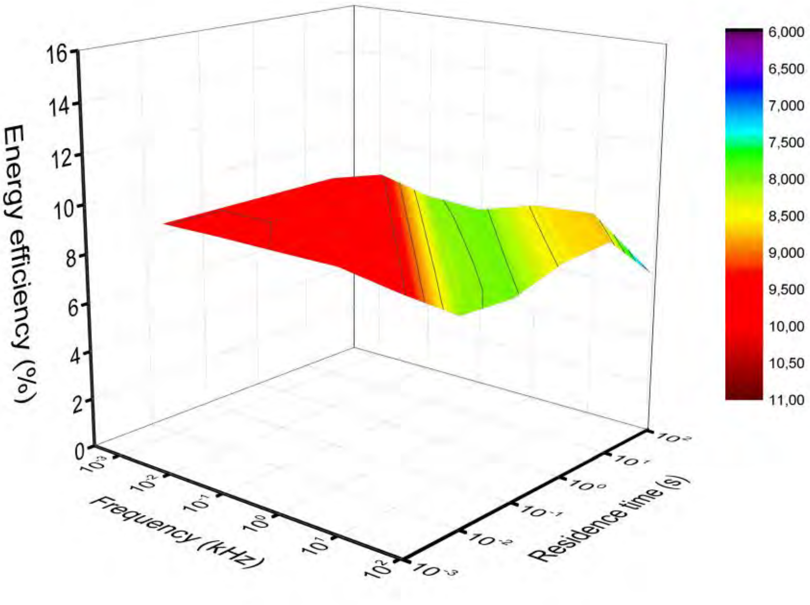

Figure A IV-6(d). Simulated energy efficiency for a 10-90 CH_4-CO_2 mixture as a function of the residence time and frequency for an SEI of 10 J/cm³.

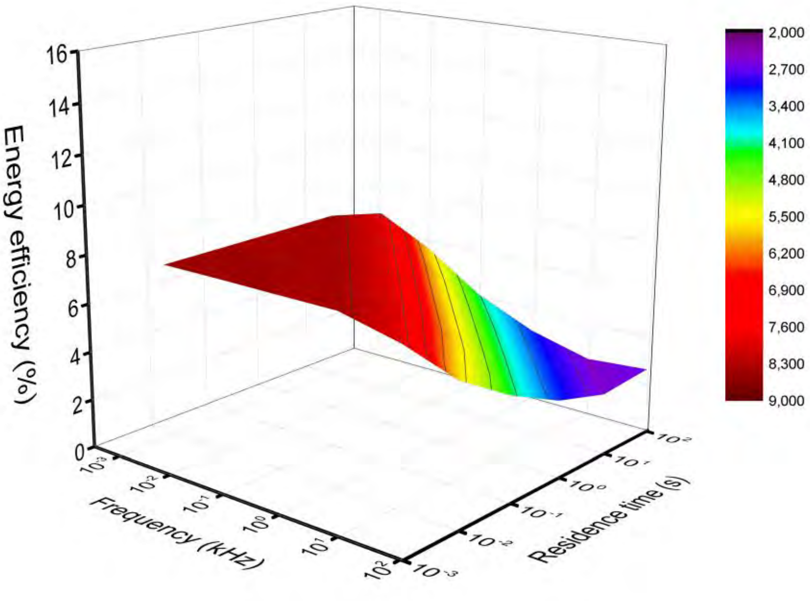

Figure A IV-6(e). Simulated energy efficiency for a 10-90 CH_4-CO_2 mixture as a function of the residence time and frequency for an SEI of 100 J/cm³.

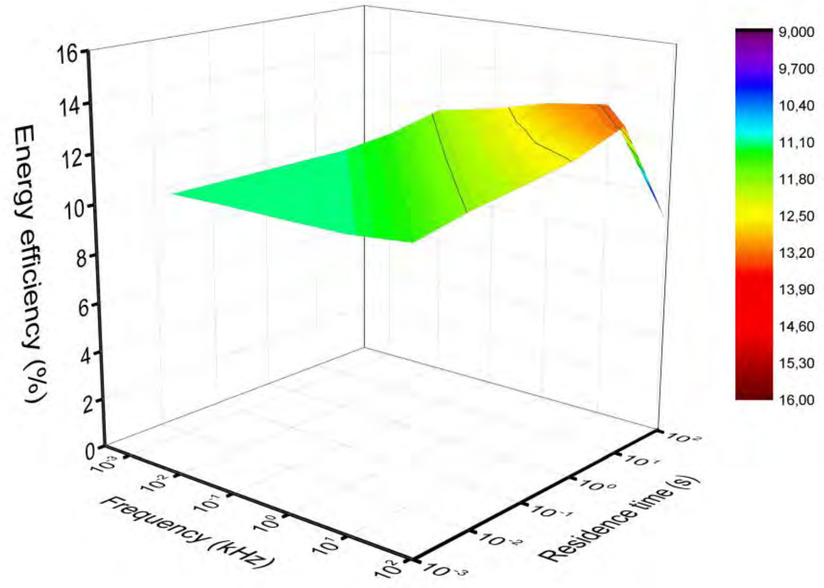

Figure A IV-7(a). Simulated energy efficiency for a 25-75 CH_4-CO_2 mixture as a function of the residence time and frequency for an SEI of 0.01 J/cm³.

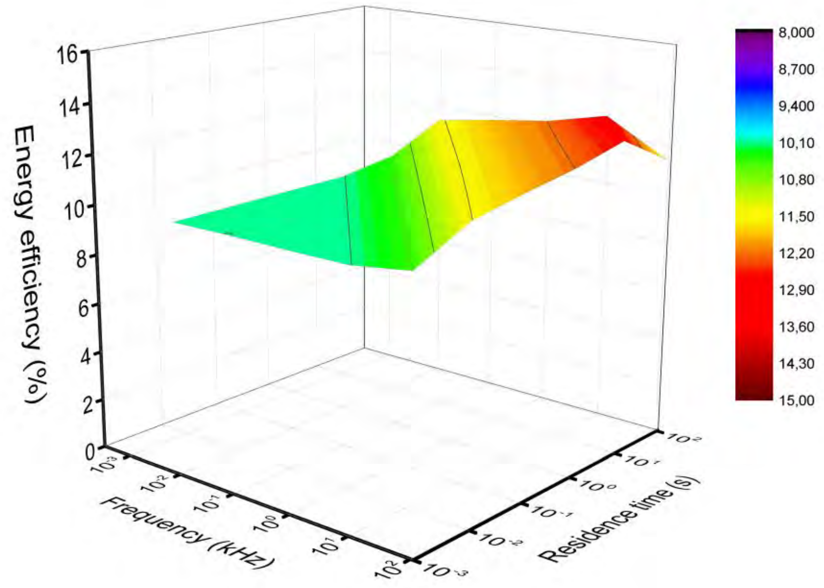

Figure A IV-7(b). Simulated energy efficiency for a 25-75 CH_4-CO_2 mixture as a function of the residence time and frequency for an SEI of 0. 1 J/cm³.

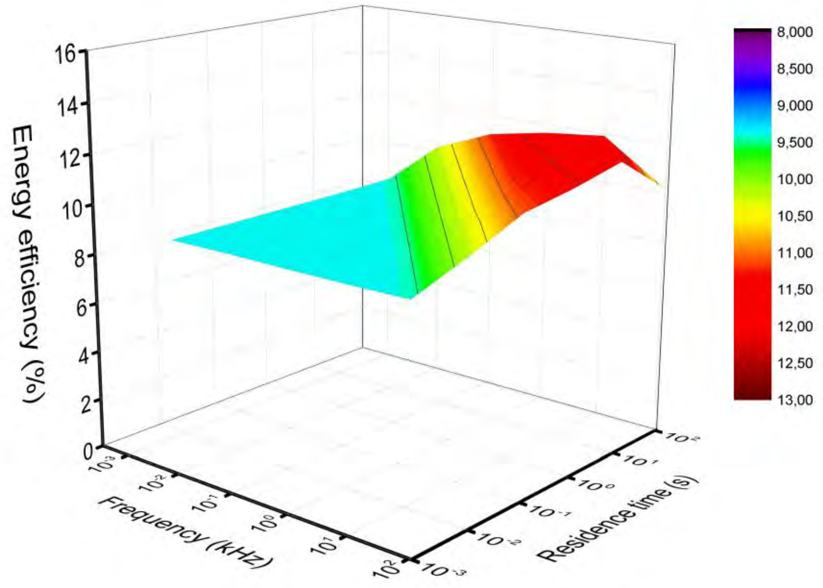

Figure A IV-7(c). Simulated energy efficiency for a 25-75 CH_4-CO_2 mixture as a function of the residence time and frequency for an SEI of 1 J/cm³.

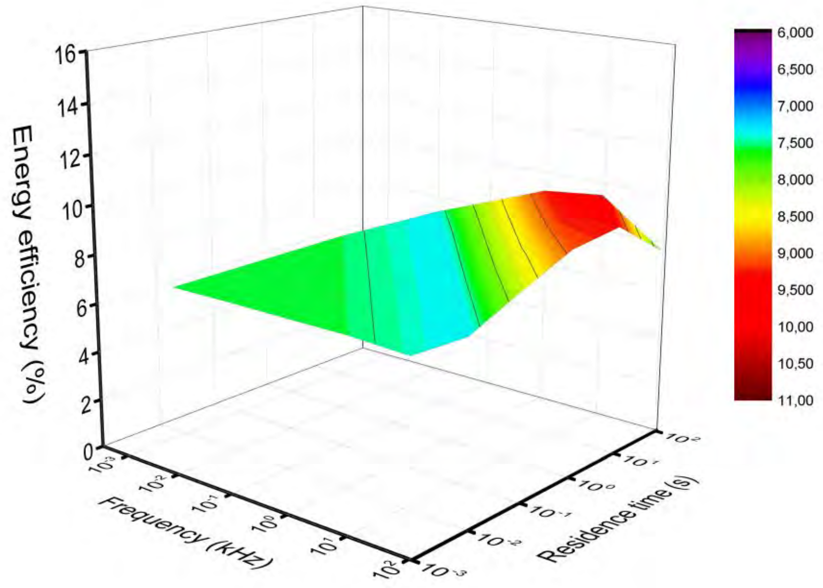

Figure A IV-7(d). Simulated energy efficiency for a 25-75 CH_4-CO_2 mixture as a function of the residence time and frequency for an SEI of 10 J/cm³.

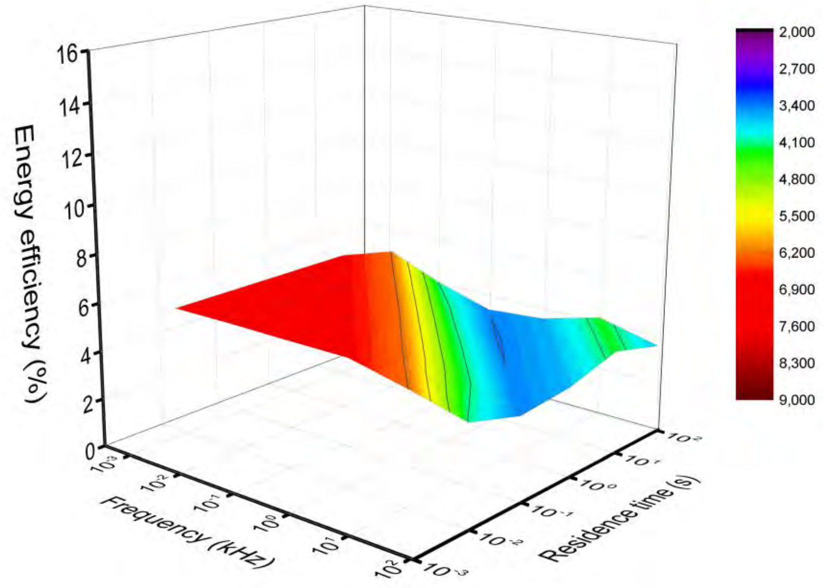

Figure A IV-7(e). Simulated energy efficiency for a 25-75 CH_4-CO_2 mixture as a function of the residence time and frequency for an SEI of 100 J/cm³.

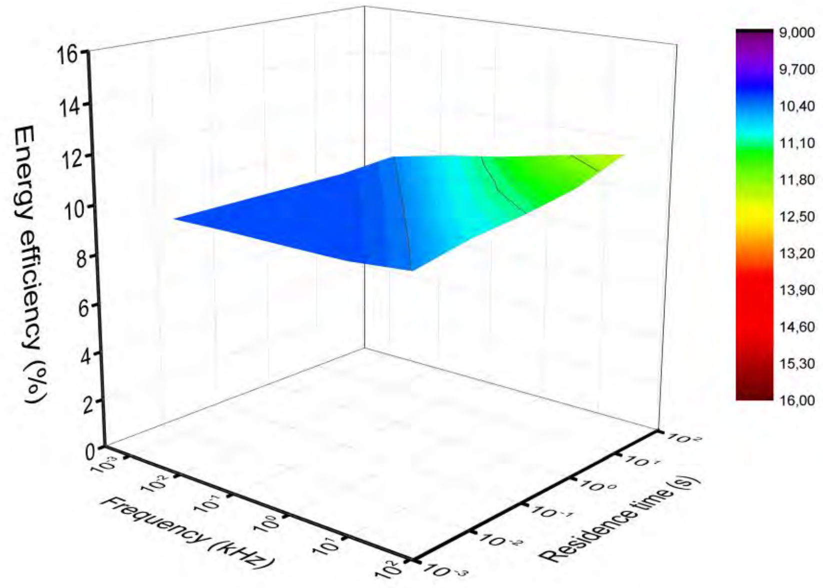

Figure A IV-8(a). Simulated energy efficiency for a 50-50 CH_4-CO_2 mixture as a function of the residence time and frequency for an SEI of 0.01 J/cm³.

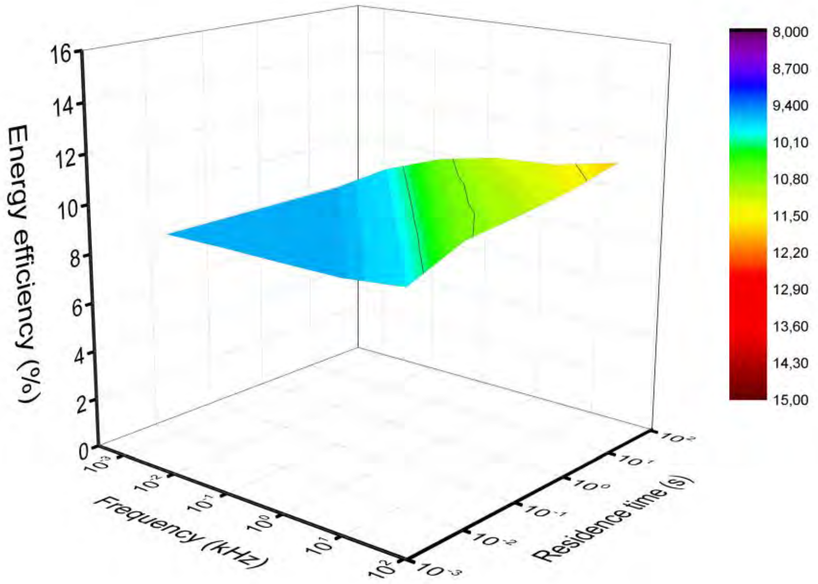

Figure A IV-8(b). Simulated energy efficiency for a 50-50 CH_4-CO_2 mixture as a function of the residence time and frequency for an SEI of 0. 1 J/cm³.

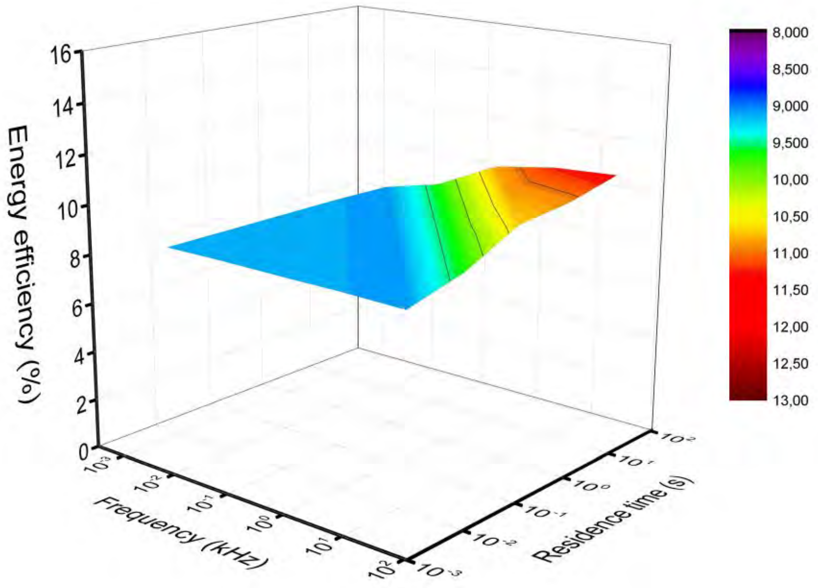

Figure A IV-8(c). Simulated energy efficiency for a 50-50 CH_4-CO_2 mixture as a function of the residence time and frequency for an SEI of 1 J/cm³.

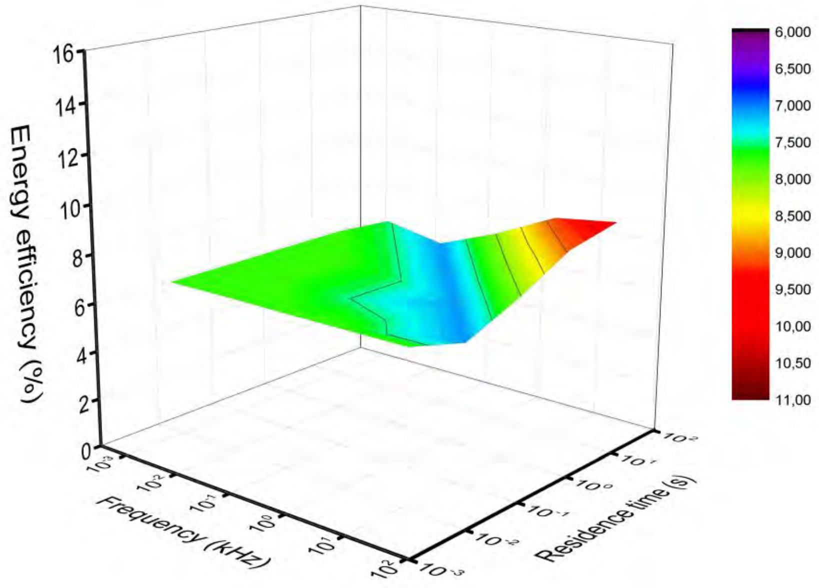

Figure A IV-8(d). Simulated energy efficiency for a 50-50 CH_4-CO_2 mixture as a function of the residence time and frequency for an SEI of 10 J/cm³.

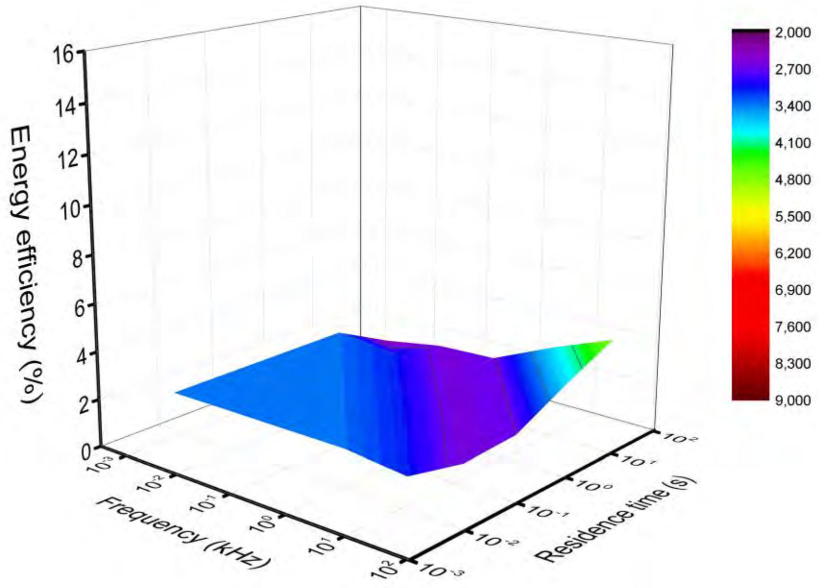

Figure A IV-8(e). Simulated energy efficiency for a 50-50 CH_4-CO_2 mixture as a function of the residence time and frequency for an SEI of 100 J/cm³.

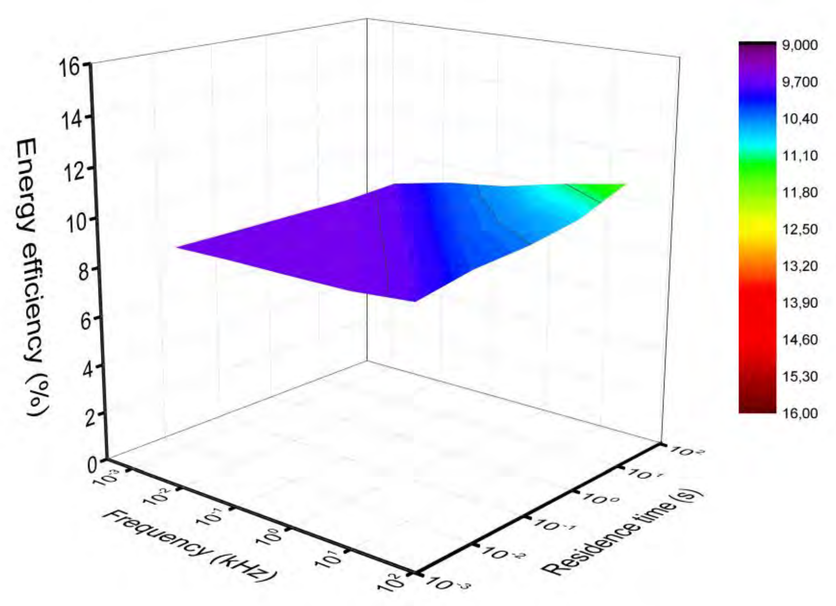

Figure A IV-9(a). Simulated energy efficiency for a 75-25 CH_4-CO_2 mixture as a function of the residence time and frequency for an SEI of 0.01 J/cm³.

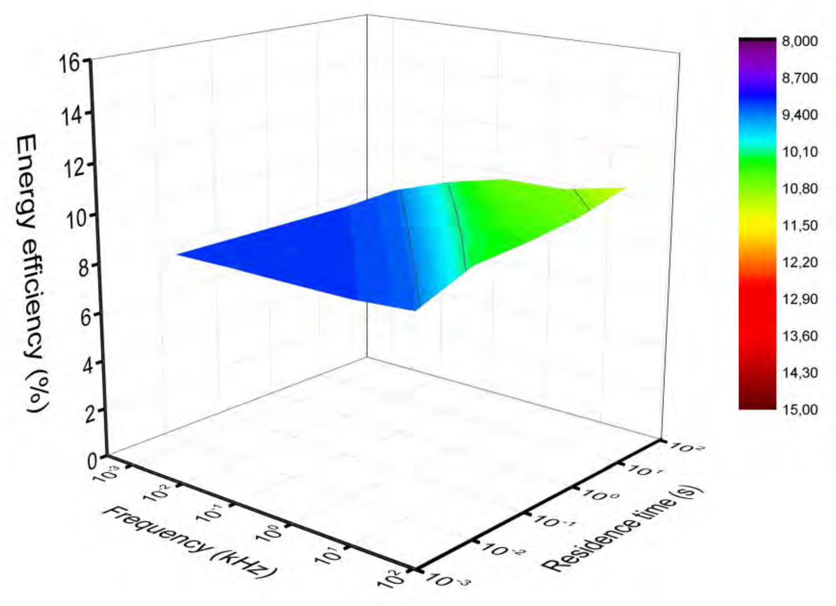

Figure A IV-9(b). Simulated energy efficiency for a 75-25 CH_4-CO_2 mixture as a function of the residence time and frequency for an SEI of 0. 1 J/cm³.

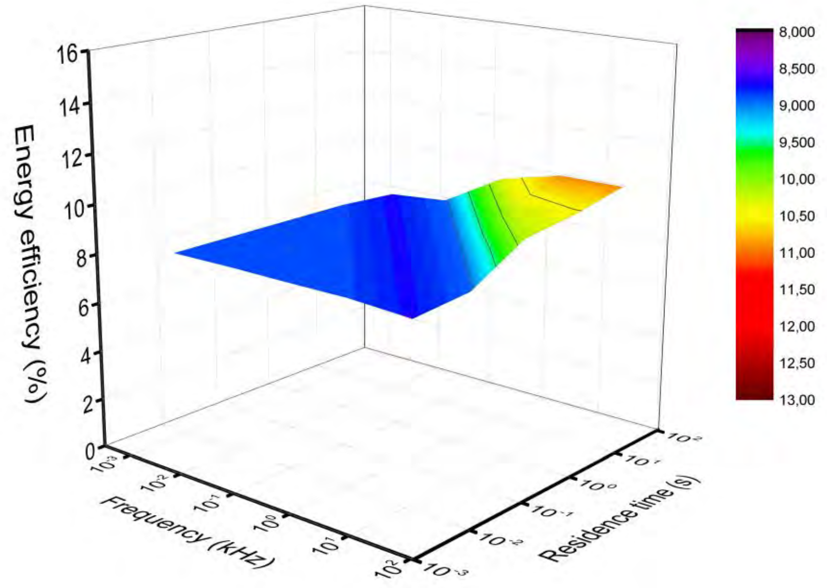

Figure A IV-9(c). Simulated energy efficiency for a 75-25 CH_4-CO_2 mixture as a function of the residence time and frequency for an SEI of 1 J/cm³.

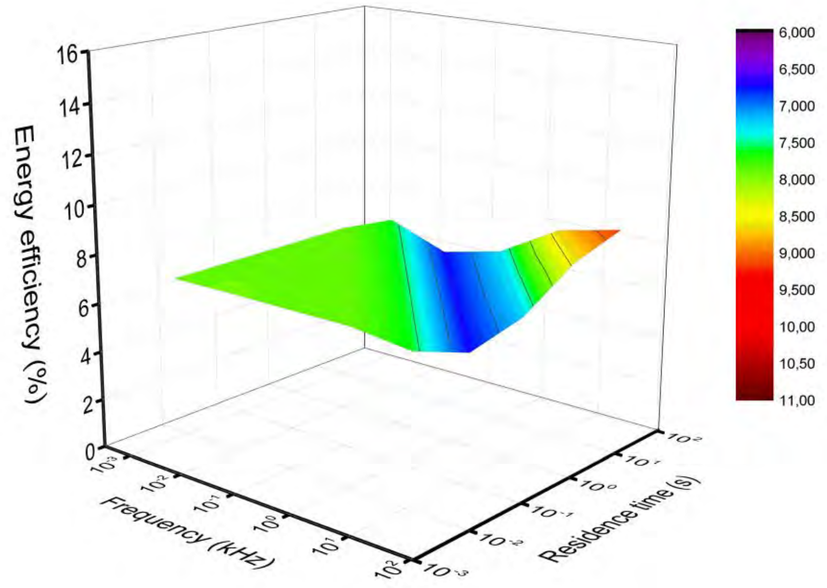

Figure A IV-9(d). Simulated energy efficiency for a 75-25 CH_4-CO_2 mixture as a function of the residence time and frequency for an SEI of 10 J/cm³.

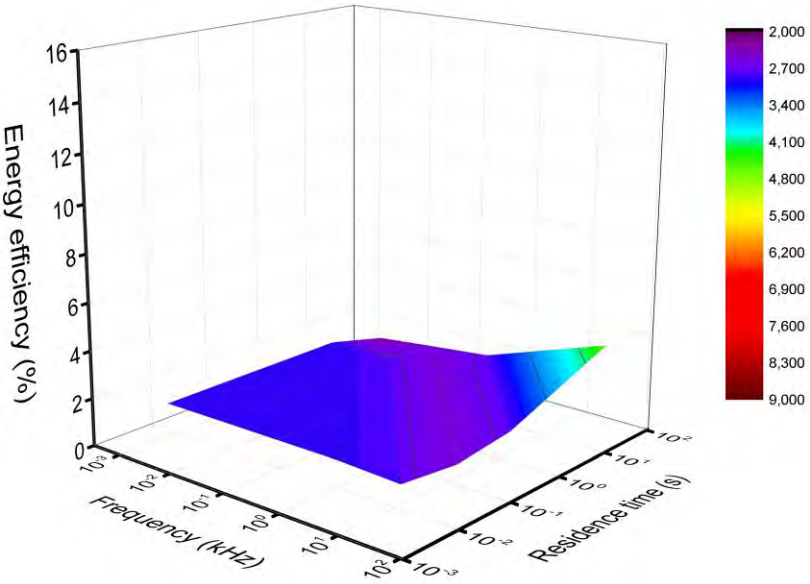

Figure A IV-9(e). Simulated energy efficiency for a 75-25 CH_4-CO_2 mixture as a function of the residence time and frequency for an SEI of 100 J/cm³.

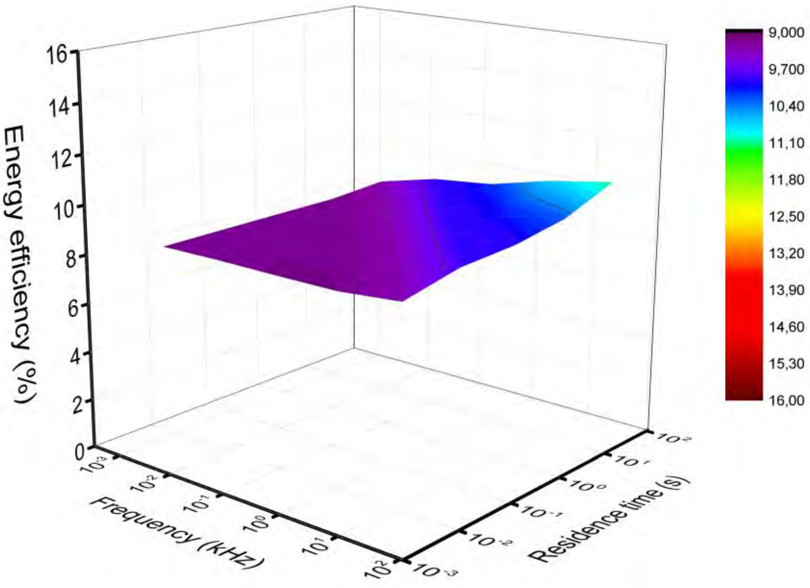

Figure A IV-10(a). Simulated energy efficiency for a 90-10 CH_4-CO_2 mixture as a function of the residence time and frequency for an SEI of 0.01 J/cm³.

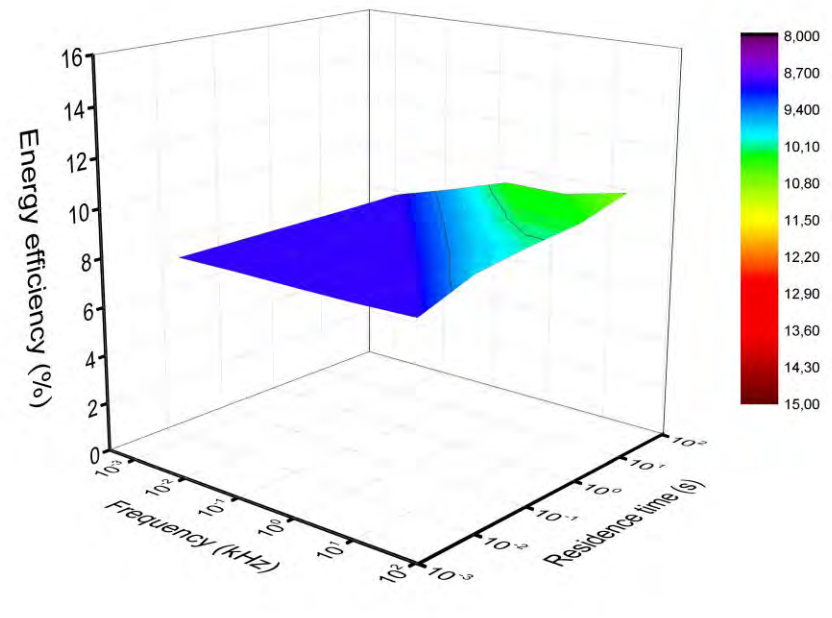

Figure A IV-10(b). Simulated energy efficiency for a 90-10 CH_4-CO_2 mixture as a function of the residence time and frequency for an SEI of 0. 1 J/cm³.

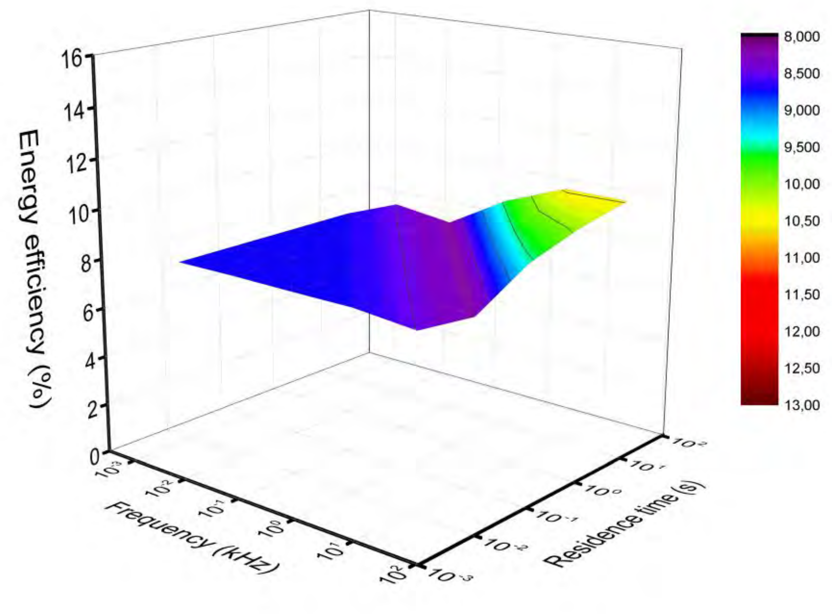

Figure A IV-10(c). Simulated energy efficiency for a 90-10 CH_4-CO_2 mixture as a function of the residence time and frequency for an SEI of 1 J/cm³.

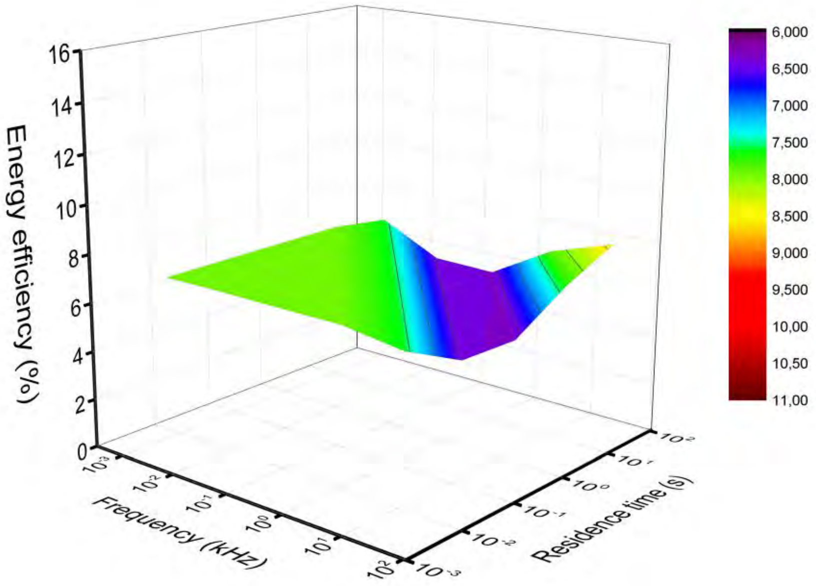

Figure A IV-10(d). Simulated energy efficiency for a 90-10 CH_4-CO_2 mixture as a function of the residence time and frequency for an SEI of 10 J/cm³.

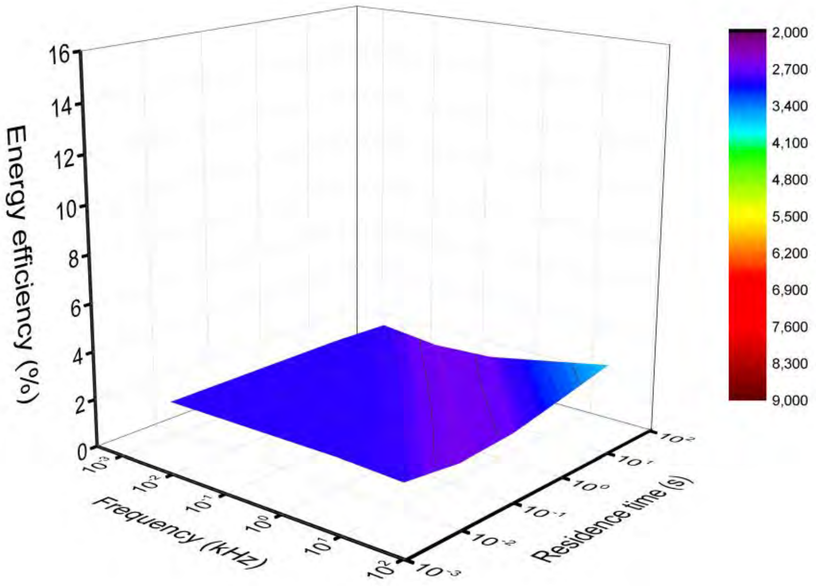

Figure A IV-10(e). Simulated energy efficiency for a 90-10 CH_4-CO_2 mixture as a function of the residence time and frequency for an SEI of 100 J/cm³.

2.3. Calculated Maximum and Minimum Achieved Values of Energy Efficiency vs Total Conversion

Table A IV-3. Overview of the minimum achieved values of energy efficiency vs total conversion as obtained from the calculations, for all conditions investigated.

CH_4/CO_2 Mixture	*SEI (J/cm³)*	*Conversion (%)*	*Energy Efficiency (%)*	*Residence Time (s)*	*Frequency (kHz)*
10 - 90	0.01	0.0111	11.1	100	100
25 - 75	0.01	0.00905	9.08	100	100
50 - 50	0.01	0.00886	8.89	100	100
75 - 25	0.01	0.00848	8.51	100	100
90 - 10	0.01	0.00763	7.66	100	100
10 - 90	0.1	0.108	10.8	1	0.01
25 - 75	0.1	0.100	10.1	0.001	1
50 - 50	0.1	0.0956	9.59	0.001	1
75 - 25	0.1	0.0914	9.17	0.001	1
90 - 10	0.1	0.0883	8.86	0.001	1
10 - 90	1	0.986	9.89	10	0.01
25 - 75	1	0.934	9.37	0.001	1
50 - 50	1	0.903	9.06	0.01	10
75 - 25	1	0.870	8.73	0.01	10
90 - 10	1	0.816	8.19	100	0.01
10 - 90	10	6.70	6.73	100	100
25 - 75	10	7.28	7.30	0.01	100
50 - 50	10	7.04	7.06	0.01	100
75 - 25	10	6.70	6.71	0.01	100
90 - 10	10	6.33	6.35	0.1	100
10 - 90	100	24.6	2.47	100	10
25 - 75	100	33.7	3.38	10	1
50 - 50	100	25.4	2.55	0.01	100
75 - 25	100	22.6	2.26	10	0.1
90 - 10	100	25.7	2.58	0.01	100

Table A IV-4. Overview of the maximum achieved values of energy efficiency vs total conversion as obtained from the calculations, for all conditions investigated.

CH_4/CO_2 Mixture	*SEI (J/cm^3)*	*Conversion (%)*	*Energy Efficiency (%)*	*Residence Time (s)*	*Frequency (kHz)*
10 - 90	0.01	0.0150	15.1	100	10
25 - 75	0.01	0.0132	13.3	10	100
50 - 50	0.01	0.0122	12.2	100	10
75 - 25	0.01	0.0116	11.7	100	10
90 - 10	0.01	0.0113	11.4	100	10
10 - 90	0.1	0.142	14.2	100	10
25 - 75	0.1	0.128	12.8	100	10
50 - 50	0.1	0.119	11.9	100	10
75 - 25	0.1	0.113	11.4	100	10
90 - 10	0.1	0.110	11.0	100	10
10 - 90	1	1.23	12.3	100	10
25 - 75	1	1.19	12.0	100	10
50 - 50	1	1.14	11.4	100	10
75 - 25	1	1.10	11.0	100	10
90 - 10	1	1.06	10.7	100	10
10 - 90	10	9.99	10.0	0.001	0.1
25 - 75	10	9.49	9.52	100	10
50 - 50	10	9.63	9.66	100	10
75 - 25	10	9.32	9.36	100	10
90 - 10	10	8.75	8.78	100	10
10 - 90	100	84.2	8.45	0.001	0.1
25 - 75	100	67.0	6.72	0.001	0.1
50 - 50	100	53.5	5.37	10	100
75 - 25	100	44.7	4.49	100	10
90 - 10	100	36.9	3.70	100	10

2.4. Calculated conversion and energy efficiency as a function of the total number of micro-discharge filaments for each CH_4-CO_2 mixture investigated (Figure A IV-11–A IV-15)

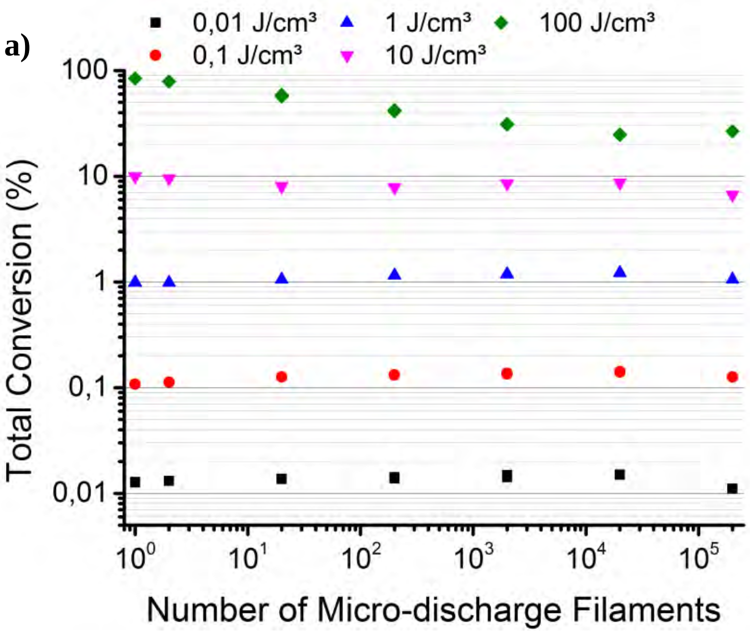

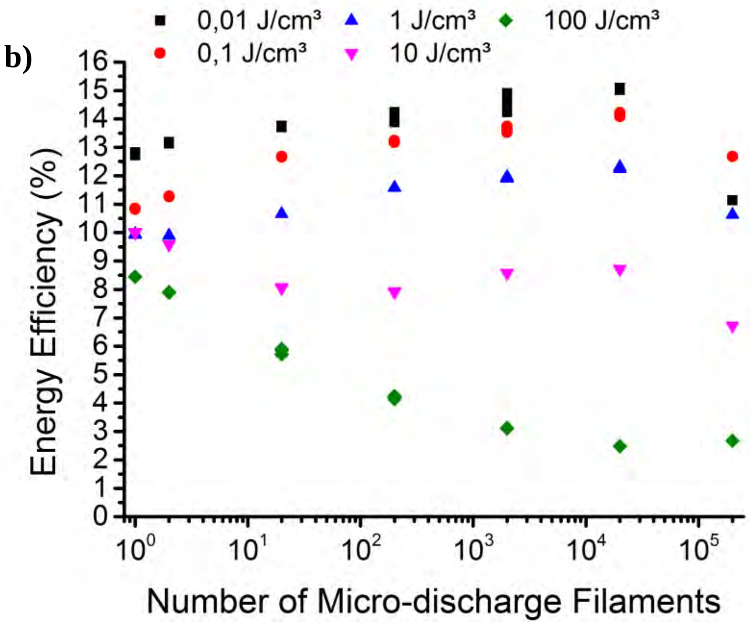

Figure A IV-11. Calculated conversion (a) and energy efficiency (b) as a function of the total number of micro-discharge filaments (i.e., product of residence time and frequency), for all the different residence times, frequencies and SEI values investigated, for a CH_4-CO_2 mixture of 10-90. The values corresponding to the same SEI values are indicated with the same colored symbols.

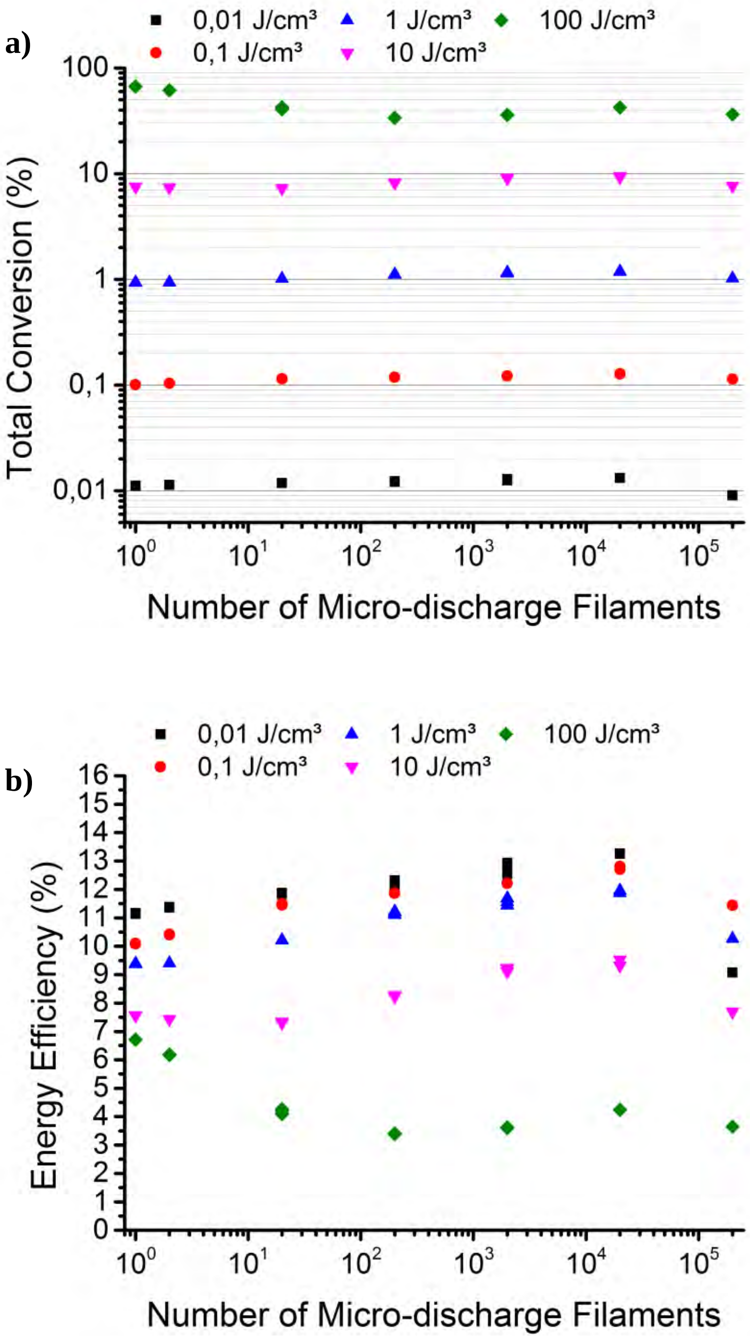

Figure A IV-12. Calculated conversion (a) and energy efficiency (b) as a function of the total number of micro-discharge filaments (i.e., product of residence time and frequency), for all the different residence times, frequencies and SEI values investigated, for a CH_4-CO_2 mixture of 25-75. The values corresponding to the same SEI values are indicated with the same colored symbols.

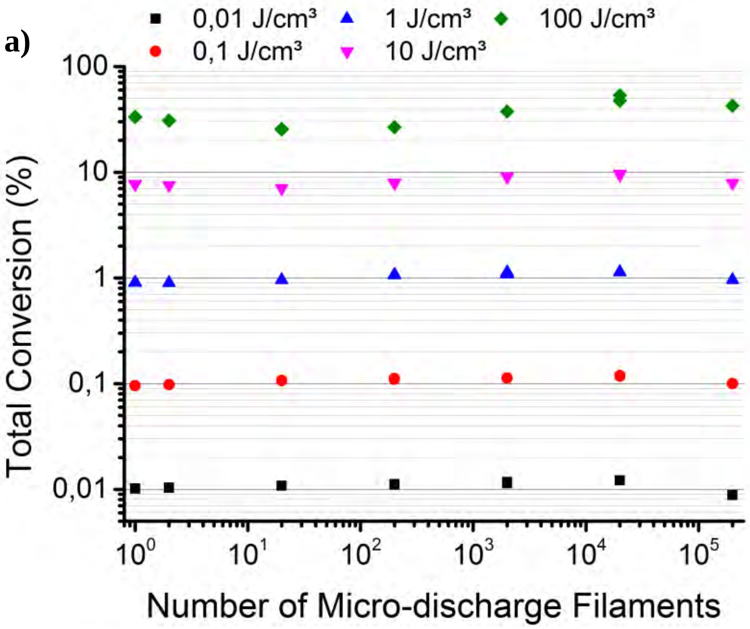

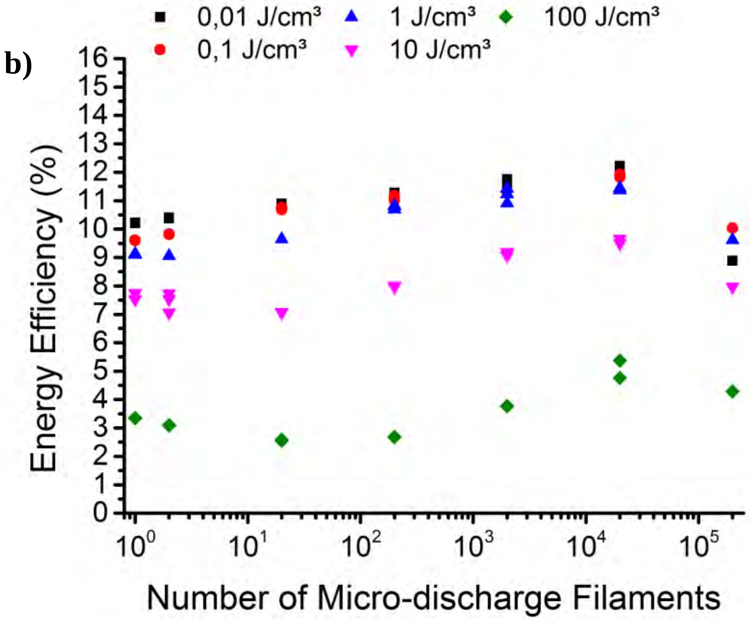

Figure A IV-13. Calculated conversion (a) and energy efficiency (b) as a function of the total number of micro-discharge filaments (i.e., product of residence time and frequency), for all the different residence times, frequencies and SEI values investigated, for a CH_4-CO_2 mixture of 50-50. The values corresponding to the same SEI values are indicated with the same colored symbols.

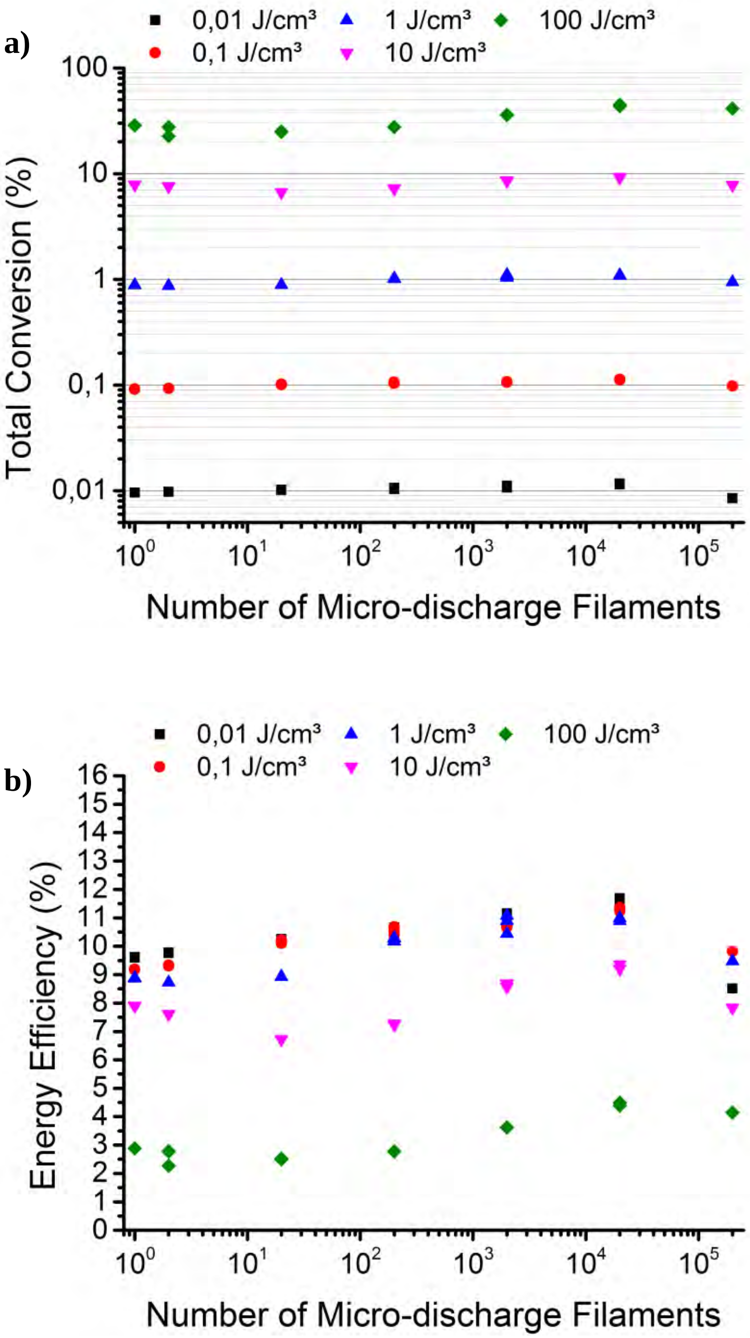

Figure A IV-14. Calculated conversion (a) and energy efficiency (b) as a function of the total number of micro-discharge filaments (i.e., product of residence time and frequency), for all the different residence times, frequencies and SEI values investigated, for a CH_4-CO_2 mixture of 75-25. The values corresponding to the same SEI values are indicated with the same colored symbols.

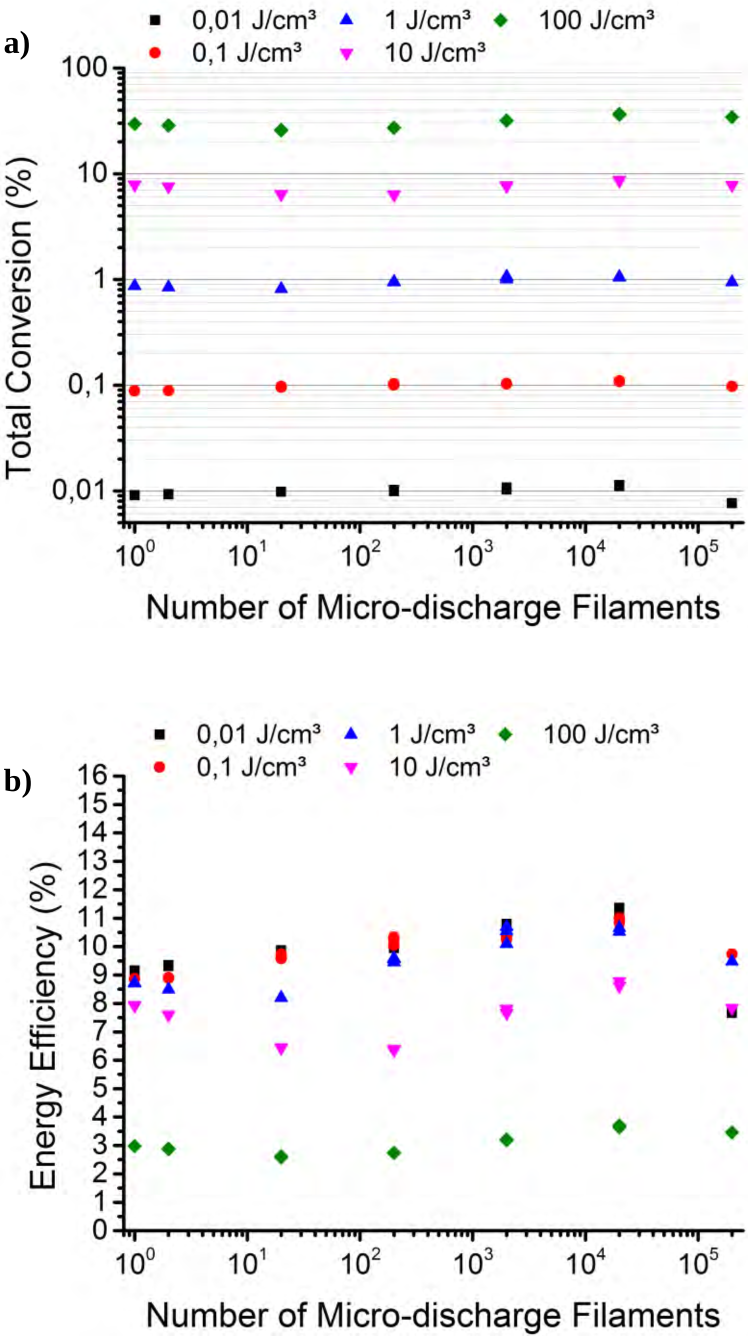

Figure A IV-15. Calculated conversion (a) and energy efficiency (b) as a function of the total number of micro-discharge filaments (i.e., product of residence time and frequency), for all the different residence times, frequencies and SEI values investigated, for a CH_4-CO_2 mixture of 90-10. The values corresponding to the same SEI values are indicated with the same colored symbols.